Satellite remote sensing for improvement of groundwater characterisation

A thesis submitted in fulfilment

of the requirements for the degree

of

Doctor of Philosophy

at

The University of Waikato

by

Rogier Sebastiaan Westerhoff

THE UNIVERSITY OF
WAIKATO
Te Whare Wānanga o Waikato

2017

Abstract

Groundwater, the water stored in the subsurface, plays an essential role in water provision for domestic, industrial and agricultural use. Groundwater is also vital for ecology and environment, since it provides baseflow to many streams, rivers and wetlands. Groundwater demand in New Zealand has grown strongly in recent years and assessment of groundwater volumes, fluxes and flows requires more advanced methods. Exploration of groundwater, the least-known water resource, often requires the combination of multiple research disciplines, such as well-drilling, geophysical techniques and groundwater models. These combined products often are uncertain in areas where ground-observed data are sparse. This uncertainty limits our future scientific capability to better assess our complex groundwater resources.

Satellite geophysical data can help tackle the problem of data sparsity in groundwater research because they commonly cover several regions or a whole nation in one image. On a global scale, in recent years, use of satellite-derived data in hydrogeology has gained considerable attention. Although data access is relatively easy and data are mostly free, similar in-depth hydrogeological studies have not been performed for New Zealand. This is mainly because satellite data can contain much noise, as the signal has to travel far before it reaches the Earth, and because data are often too coarse for the New Zealand aquifer scale. Therefore, satellite data for hydrogeological research in New Zealand are not proven technology and they are generally not used by New Zealand scientists, consultancies or water managers. A break-through is needed.

This thesis researches the added value of satellite data to better estimate groundwater volumes and flows, including their uncertainties, in New Zealand. The thesis uses the concept of 'efficient combination', where satellite data are combined with existing information from ground observations or models, so that they can fill in gaps and trends in data-sparse areas. The satellite data used are those on evapotranspiration, vegetation properties, and soil moisture (the amount of water stored in our top soils). These water budget components are important in-

put for the estimation of rainfall recharge to groundwater: the amount of rainfall that percolates through the soil to eventually replenish the groundwater. Rainfall recharge to groundwater is an important component for groundwater flow models. This thesis shows that satellite data can be used as a tool with other data (e.g., with ground observations and models) to better spatially estimate evapotranspiration, soil moisture, rainfall recharge and groundwater table, including their uncertainty estimates. Satellite data thus help to better estimate groundwater volumes, fluxes, and flows, at both the regional and national scale. This thesis has resulted in the first New Zealand-wide gridded estimates of rainfall recharge and groundwater table.

With my thesis, I hope to have paved the way for further use of satellite-derived data sources in groundwater research. I am confident that the results and recommendations of this thesis will lead to a further increase of New Zealand research and applications of satellite data for groundwater and freshwater studies.

Mihi

He manu hou ahau he pī kā rere

Nga rau rangatira tena koutou

Ma te tika

Te mihi tuatahi ki tatau atua

No nga hau e wha oku tupuna

No te whenua papa

He wa poto i timata ahau raua taku hoa rangatira he haerenga konei

I kimi au oku purakau me mohiotanga o oku tipuna i tautokomai kei runga i taku pamu

Konei i timata au he whanaungatanga i te whenua

Toku hiahia hohonu, i noho kei konei i nga wa katoa

Ko Rogier Westerhoff taku ingoa

Tena koutou, tena koutou, tena tatou katoa

I am a young bird just learning to fly

I greet our esteemed leaders, gods and guardians. My ancestors are from far away. Only a short time ago I started a journey here. The wisdom of my ancestors supported me in this land and on my farm and I have started to connect with this land. My deep desire is to stay here forever. My name is Rogier Westerhoff.

Acknowledgements

This PhD has been funded by the Ministry of Business, Innovation and Employment as part of the 2011-2017 SMART Aquifer Characterisation (SAC) programme. I would like to acknowledge the extra support I received from the European eartH2Observe project. I have been based based at GNS Science in Wairakei, Taupo, New Zealand, with the support of Deltares, The Netherlands.

My chief supervisor in this Doctoral degree study was Prof. Moira Steyn-Ross. Moira has supported me in many ways. Besided her supervisory role, she opened my eyes to the beautiful world of physics underlying the satellite microwave backscatter, of which I realise I have still barely touched the surface. More importantly, she supported me when times were rough with the mental support at moments I needed it most. Thank you, Moira.

Paul White, my supervisor at GNS Science, has taught me the fundamentals of New Zealand hydrogeology and has helped me steer my wild ideas into the proper scientific tracks and the New Zealand context. Furthermore, he did something I needed most: giving me the confidence to become an acceptable writer in the English scientific language, which I can now tell you is not easy as a non-native speaker. Thank you, Paul.

The comments of the two examiners of this thesis, Prof. Geoff Austin and Dr. Ross Woods, were very much appreciated.

I would like to thank two fellow scientists who have added to this research with some very important data: Andrew Tait and Qiaozhen Mu. I also acknowledge the importance of the European Space Agency that has provided New Zealand with its Sentinel satellite data.

My GNS Science colleagues have given me full support for this PhD, have fed me with inspiration for new ideas, have taught me how to play proper table tennis (Alex) and have never once complained about taking up so much of their time. I hope I have repaid you enough by helping you out in some other projects. There

are some folks at GNS Science that I want to acknowledge in person. Chris Daughney and Stewart Cameron for believing in my goals, when others did not. I so truly appreciate that and will not forget.

For my mihi, my introductory regards and compilation of this thesis, I would like to thank GNS Science colleagues Sheena Tawera and Diane Bradshaw for being so supportive with this. Moreover, I would like to thank Lorraine Te Punga and Sandy Lind who have put so much of their time in helping me write my mihi in the beautiful Māori language. It is so warming to be surrounded with good and friendly people who'll volunteer their own time without asking anything in return. Thank you.

Bob Hoogendoorn from Deltares, The Netherlands, has backed me up from the moment I mentioned my ideas of doing a PhD in New Zealand. I appreciate that very much.

Many friendships in my life have helped me become the person that I am (amongst which are Rian, Mike, Freek, Mandy, Dan, Zara). There is one person in particular to thank. Erwin Gardenier is my friend since ages and we manage to always stay in touch, no matter the distance. I thank you for our friendship, life would have been much less fun without you, mate.

My parents, who have my eternal love and gratitude, have raised me as someone who tries to understand others, who thinks twice before judging, and who listens to others. This is a gift that has brought me to a lot of my successes. I cannot thank you enough for that. It was hard for them to initially accept that their son went to the other side of the world. However, they understand why I have fallen in love with the beauty of New Zealand, its landscape, and its people.

To my family. Arlette, Noah, Malik, Nils, I miss you guys and I love you. But we do not intend to come back any time soon!

Last but not least. Hillechien. I have never met a more radiant and positive woman in my life than you, my love. Your spirit and strength help me (and many others surrounding you) to see the truly bright side of life. I fell in love the first instance I saw you. That love has only grown since. We've been on quite some cool adventures now, and look where it has led us so far! I need to truly thank you for being where I am right now, both personality-wise as location-wise. You have backed me up all the way during these last years. You take care of me when I need it, and I have needed it in this last stressful year. Sorry for all the moaning and whining, but you even managed to pick that up in a positive way! I just truly love you for who you are.

List of Figures

List of Tables

Contents

1 Introduction

1.1 Problem statement

Most of the world's freshwater is stored in the subsurface (Margat and van der Gun, 2013) and is called groundwater. Groundwater is an important water resource to New Zealand because it is the source of water for many users (i.e., agriculture, industry and domestic), it flows to springs which are important amenity features and it provides baseflow to many streams, rivers and wetlands (White, 2001). Nationally, groundwater provides approximately 30% of New Zealand's consumptive water use with allocation and actual usage of approximately 9 and 6 Billion m^3 per year, respectively (Rajanayaka et al., 2010). Groundwater flows to many springs that are important for tourism or city water supply, while it also sustains important environmental and ecological assets (Larned et al., 2004), e.g. in streams and lakes in Rotorua or spring-fed streams in the Wairau Plains, Marlborough (White et al., 2016, 2007). Recently, groundwater allocation in New Zealand has grown strongly, and will grow further in the future as surface water is already fully allocated in most catchments (White, 2001) and national groundwater allocation nearly doubled in the period 1999 to 2010 (Rajanayaka et al., 2010). In response, regional councils have implemented regional policies that aim to ensure sustainable management of groundwater resources considering the framework of national policies, plans and rules for the protection of New Zealands aquifers, i.e., the Resource Management Act of 1991 (RMA) and the national policy statements for fresh water (e.g., Ministry for the Environment, 2013).

Groundwater is one of the least-known water resources and its exploration is not straightforward (Margat and van der Gun, 2013). This is mainly due to the fact that groundwater is 'hidden' under our soils and subsurface layers, which can be complex and heterogeneous. Investigation of groundwater is therefore costly and does not always lead to satisfying answers. A traditional way of groundwater exploration is to drill a well. Drill samples from boreholes can be used to investigate the aquifer properties of the underlying subsurface (e.g., sand, silty sand, clay, ignimbrite) and the availability and quality of water. Research from

within the borehole can also be carried out with more advanced geophysical well-logging techniques (Jorgensen and Petricola, 1995; MacCary, 1983). However, one borehole in a complex and heterogeneous geological setting is not enough to characterise an aquifer and therefore a dense network of boreholes would be required. That is often considered too costly. Other, geophysical, techniques for exploration of groundwater, applied from the surface, also exist. These techniques yield a laterally continuous image and can be used to interpolate the sparse borehole information when geology is complex and heterogeneous. Many of those geophysical techniques have been applied in hydrogeological research, e.g., seismic techniques (Brouwer and Helbig, 1998; Kluiving et al., 2003; Meekes et al., 1990); electrical resistivity (Loke and Barker, 1996; Urish and Frohlich, 1990); (airborne) electromagnetics (Danielsen et al., 2003; Faneca Sanchez et al., 2012; Goldman and Neubauer, 1994; Siemon et al., 2009); or ground-penetrating radar (Davis and Annan, 1989; Van Overmeeren, 1998). Those techniques are considered well-known in research applications, but also have their limitations. Most geophysical data translate material properties, e.g. electrical resistivity, to the required parameters, e.g. porosity. They are therefore indirect methods. Furthermore, the geophysical signal is often clouded by the layers it has had to travel through before reaching target depth. Also, the geophysical data is often a combination of multiple material properties and therefore the estimation of a single material property from the geophysical signal (called 'inversion', e.g., Effersø et al. (1999); Günther et al. (2006); Sambridge (1999)) is often noisy, as well as non-unique. Because geophysical techniques are relatively costly, commercial applications for the regional scale are still quite limited: most large-scale applications of geophysical techniques are reserved for the larger industries of mining and exploration for oil and gas. Borehole information and geophysical information are often used in conjunction, since in combination they are more cost-effective for the larger scale and often lead to less uncertainty. For example, Faneca Sanchez et al. (2012) show that the combined use of boreholes samples and logs (giving reliable depth information) and surface geophysics (outlining lateral spatial patterns) can give a good coverage of information, without the need for a dense network of boreholes.

Most models of groundwater flows or fluxes are built and calibrated using ground-observed data, but they are therefore more uncertain in data-sparse areas. An additional information tool is the use of local and hydrogeological system knowledge. For example, knowing the original depositional environment of an aquifer (e.g., porous sand or sandstone) can lead to more insight of the areal and depth dimensions and the porous properties of that aquifer. Hydrogeological system information can also be used as additional tool to groundwater models of an aquifer (e.g., Rawlinson, 2014; White et al., 2015). Such an approach is commonly cost-effective and is therefore often used, but also contains unknown and potentially large uncertainty if ground observations are sparse. All models are therefore best applied in conjunction with, more costly, boreholes and geophysical techniques. The challenge is then to find the balance between best outcome and most cost-efficient approach. However, uncertainty always remains. This is explained in somewhat more detail for an important input of groundwater flow models: recharge, i.e.,

the amount of water that percolates through the soil to replenish the groundwater. Recharge is commonly inferred by models called 'soil water budgets' or 'soil water balance models'. These models rely on measurements of variables in the hydrological cycle (water cycle, Figure 1.1), i.e., rainfall, evapo(transpi)ration, groundwater and/or soil moisture. Recharge can also be measured directly by lysimeters, which measure percolation of water from the surface through the soil in situ (e.g., White et al., 2003, 2014a). However, lysimeter data are sparse, as installation and maintenance of lysimeters are costly. Recharge models, e.g., of rainfall recharge to groundwater, are therefore easiest to apply on a local scale in well-drained plains, where uncertainties can be constrained by the use of (sparse) lysimeter data and model calibration. Within New Zealand, a range of these studies have calculated rainfall recharge mainly for specific aquifer regions, on a weekly or daily basis (Scott, 2004; White et al., 2014b). This localised approach is useful within the policy framework of regional councils, who manage the setting of sustainable water allocation limits at the aquifer and (sub-)catchment scales. However, setting of these limits requires information on areas far greater than the points of abstraction, as groundwater systems and their interactions with rainfall, surface water and the land surface extend over many different spatial and temporal scales (Alley, 2002; Alley and Leake, 2004). Because of this localised approach, a consistent overview of rainfall recharge to groundwater is difficult to obtain at the catchment, inter-catchment and national scale, because there are large spatial data gaps between observations. More specifically, ground observations are sparse in mountainous or sparsely-populated areas. It is shown in studies in the U.S.A. and Taiwan that these areas can add considerably to rainfall recharge (Calmels et al., 2011; Doyle et al., 2015). Thus, considerable error or uncertainty of rainfall recharge estimation can occur. It seems straightforward that all other available measurements of water cycle variables (including in situ or remotely sensed rainfall, evapotranspiration, or soil moisture) in these areas could have potential to improve models of groundwater flow or recharge.

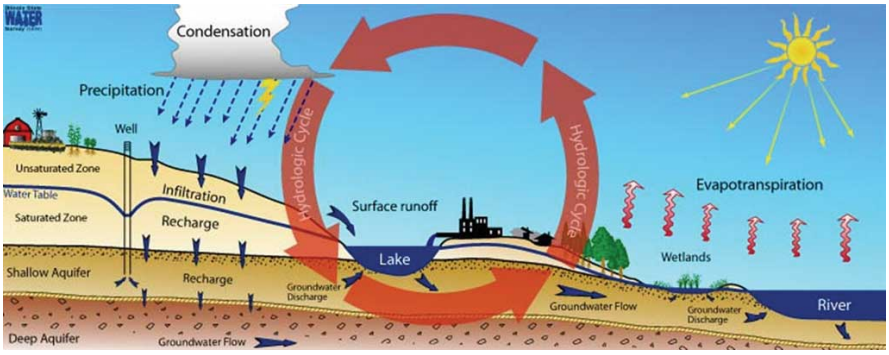

Figure 1.1: Schematisation of components of the water cycle (Lin et al., 2008).

This thesis builds upon methods of 'efficient combination', of which the concept is explained here. In situ point data (i.e., borehole information, soil samples, etc.) are generally the best available data to infer material properties. Point data can therefore be considered 'hard information'. Geophysical data, geological system knowledge and models are indirect and considered 'soft information': they need

extra assumptions, processing and models to infer the required aquifer properties (e.g., Seibert and McDonnell, 2002). The combined soft and hard information can be very powerful, if used efficiently (in an 'efficient combination'). This is not uncommon in hydrogeology. For example, advanced model properties to combine ground-observed point data with a model have been developed by Gunnink et al. (2013), who describe a national model of the geology of the Netherlands built of borehole data and advanced interpolation techniques, which embed geological system knowledge. Marinoni (2003) describe how geological system knowledge helps to avoid the smoothing effect of the normal kriging interpolation; Willis and White (2000) describes a technique that uses the geological system knowledge of sedimentary processes to simulate and automate fluid flow in sandstone. Incorporation of geophysical data as part in an efficient combination has been applied by Faneca Sanchez et al. (2012), who use airborne electromagnetic data in combination with the model of Gunnink et al. (2013) to simulate the effect on groundwater systems in shallow groundwater lenses; Van Overmeeren (1998) uses ground-penetrating radar to interpret hydrogeological properties of shallow subsurface properties; Westerhoff et al. (2014) describe the preliminary interpretation of geophysical measurements from a helicopter survey in Otago, New Zealand, and interpret these to aquifer potential of the subsurface.

Satellite data, a subset of geophysical data, has been shown to play an important role in hydro(geo)logical global studies. Satellite sensors mostly measure and/or transmit electromagnetic waves in the range from optical wavelengths (e.g., satellite photos, like used in Google Earth), in other near-optical bands (e.g., thermal or other infra-red bands for vegetation information), or in the radar domain (e.g., microwaves for soil moisture or land subsidence studies). Satellite measurements are made from high altitudes, up to hundreds or even thousands of kilometres, and therefore images can cover several regions or a whole nation. The downside of the high altitude is that data can contain much noise, as satellite signals have to travel many (atmospheric, clouds, vegetation) layers before reaching the earth. Measured data only covers properties from, or close to, the surface. As groundwater flows in the deeper layers, it is not possible to directly measure groundwater flow. Also, areas of complex geology, such as faults or impermeable layers that contain confined aquifers, cannot be measured directly. However, efficient combination is still possible, similar to the earlier-mentioned, more traditional, field geophysical methods. On a global scale, in recent years, the application of satellite-derived data in hydrogeology has gained considerable attention, where satellite data have been used in studies that look at the modelled long-term behaviour of groundwater (Fan et al., 2013a) and its depletion and recharge on a global scale (Döll, 2009; Döll and Fiedler, 2008; Gleeson et al., 2010, 2012; Wada et al., 2012, 2010). These studies mostly used modelled data from a hydrological model, and incorporated satellite-derived data as input components. These input components are usually precipitation and evapotranspiration (ET), and sometimes soil moisture. Data patterns and trends in long-term data, when combined with ground-based data, could thus have the potential to fill in the gaps of these ground data. A fitting example is shown by climate reanalysis data such as ERA-40 or ERA-Interim

(Dee et al., 2011), which are a description of recent climate parameters, such as rainfall, soil moisture, evapotranspiration (ET). These data are produced by combining models with ground and satellite observations. Satellite data can thus have large potential to be incorporated in the standard practice of hydrogeology or hydrology. This is confirmed by Becker (2006) and Meijerink (2007), who point out that, similar to the above geological and geophysical examples, the strength of satellite remotely-sensed data lies in the combination: satellite data for groundwater must be placed in the hydrogeological and geological context, in combination with available model information and in situ data. Satellite data from different components of the terrestrial water cycle relate to groundwater and its recharge and ideally these must all be taken into account when estimating groundwater volume changes over time. These are mostly data on precipitation, evaporation, land cover, soil moisture, and in other cases surface runoff and snow extent. Sahoo et al. (2011) show the growing potential of satellite data, by calculating the Earth's freshwater budget using multiple satellite data sources (although they are not able to fully close the water budget).

Satellite techniques that focus on groundwater have not been used frequently in New Zealand, even though much of the satellite data are now free. Research on the additional value of satellite remotely sensed data to aquifer characterisation was performed by Zemansky and Westerhoff (2013), but they only focussed on the comparison (e.g., cross-correlation plots) of satellite data to ground observations, and not on efficient combination. Although recommendations were made to combine satellite data with models of rainfall recharge or a groundwater table, no serious efforts of combination were analysed. One of the explanations for the lack of use of satellite data in New Zealand is that most data have only recently become available in long-term data series through research projects in the U.S.A. and Europe (De Jeu et al., 2008; GLOWASIS, 2015; Mu et al., 2011). Another explanation is that there is no guarantee that the success of these methods performed on large continents will translate effectively to New Zealand conditions. For example, the GRACE satellite data relates gravity to mass changes in groundwater (Rodell et al., 2007, 2004) and this could potentially be beneficial for groundwater research. However, GRACE data, having a resolution of 100 km or larger, are spatially too coarse to be used on a sub-catchment level in New Zealand, as aquifer areal extents in New Zealand are in the order of 100 km^2 or less for small aquifers (e.g., Kerikeri/Kaikohe, Waipoa, Wairoa), to 1,000 – 3,000 km^2 for medium aquifers (e.g., Ashburton, Northern Haurakei), to 5,000 – 7,000 km^2 for large aquifers (e.g., Taupo, Southland) (Moreau-Fournier and Cameron, 2011; White, 2001). Furthermore, not much is known about the uncertainty of satellite-derived parameters of the water cycle. Most satellite-derived parameters embed a pseudo-model with a chain of calculations and assumptions, leading to unknown model uncertainty of the desired output parameter. For example, only recently it was suggested that GRACE could overestimate groundwater depletion (Long et al., 2016). Another example is the derivation of ET from inferred vegetation and soil wetness from satellite imagery (Bastiaanssen et al., 1998a; Mu et al., 2011), which is often combined with an estimate of meteorological parameters,

all in advanced ET estimation equations (i.e., the Penman-Monteith equations by Monteith, 1965; Penman, 1948, 1963), that have their own set of assumptions. Soil moisture is inferred through radar measurements using multiple non-linear equations (e.g., De Jeu and Owe, 2003; Wagner et al., 1999). Finally, ground observations are not always easily combined with satellite data, for multiple reasons. First, a satellite image typically covers multiple regions in New Zealand, or multiple countries in a global setting. This requires ground observations to be collected from multiple sources, which is not always straightforward, due to the difference in data policies, inconsistencies of data quality, measurement method, or data formats in these regions or countries. Second, data accuracy of satellite is hindered by steep-sloped landscape and it is known to be less accurate data in such regions. For example, Van der Tol and Parodi (2012) showed that satellite evapotranspiration errors increase with topographic relief. The errors arising from steep topography have been described by Van Zyl et al. (1993). Dorigo (2013) stated that satellite microwave soil moisture data beyond a 20° - 25° topography angle should be flagged as erroneous. To overcome this issue, Westerhoff et al. (2013) applied a filter, based on the elevation and the distance to the nearest surface water drainage, to remove low-quality satellite microwave data. Third, there is the difference in scale between satellite and point data. The resolution of many hydrological satellite-derived data, such as soil moisture, evapotranspiration, precipitation, is often several tens of kilometres. Wagner et al. (2007) showed that correlation between satellite and ground-observed soil moisture data (of 0.25 x 0.25 Arc degree cell) is not only low because of the fact that the geophysical satellite information is indirect and contains noise, but also because of the heterogeneity of soil and soil moisture within the relatively coarse satellite data cell (Figure 1.2). Gedney and Cox (2003) acknowledged the need for sub-grid heterogeneity of soil moisture for large-scale studies. Doubková et al. (2012) proved that soil moisture can be refined from the 25 km to the 1 km scale in Australia using two different satellite signals. However, within this smaller cell, soil data is still heterogeneous. Soil moisture sensors that are placed next to each other can still produce significantly different results, due to differences in: canopy (Breshears et al., 1997); crop; roots; land-management practice leading to preferential draining paths of the soil (Hohenbrink et al., 2016); technical placement of the sensor; or calibration of the sensors.

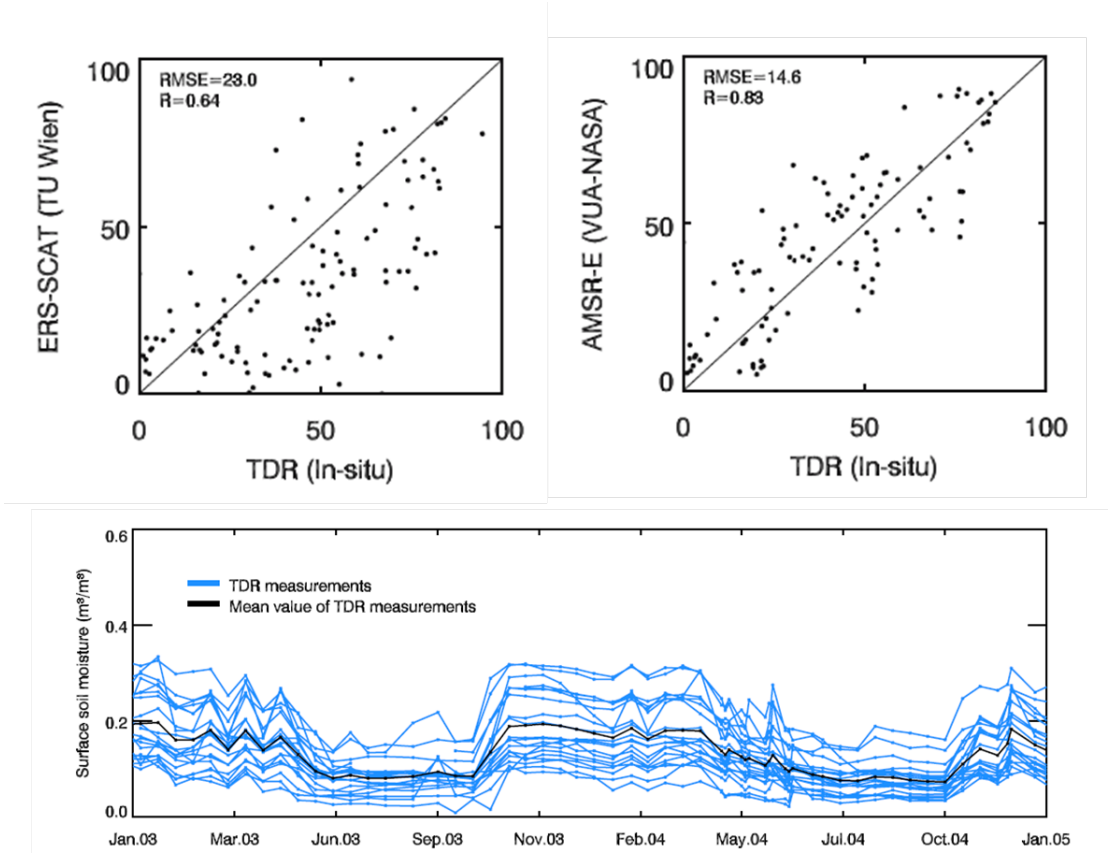

Figure 1.2: Scatter plots of satellite-derived soil moisture (top left and top right) and their correlation with ground-observed soil moisture. Adapted from Wagner et al. (2007), also used in Zemansky and Westerhoff (2013).

1.2 Research gaps and research questions

Groundwater is a valuable resource, and its demand is growing. Groundwater is one of the least-known water resources and its exploration is not straightforward. Most models of groundwater flows or fluxes still know considerable uncertainty in data-sparse areas. Satellite data has been shown to play an important role in hydro(geo)logical global studies, but has not been used frequently in New Zealand, even though much of the satellite data are free. That is mostly due to some gaps in research that were identified in this introduction, and summarised here. First, In New Zealand, research on the additional value of satellite data to aquifer characterisation has not been performed sufficiently. Although satellite data are used more frequently (in global and continental scale studies), uncertainty and errors of satellite-derived products are still mostly unknown. This is partly because spatial scaling of data is not always obvious, given the earth's and soil heterogeneity, and New Zealand's challenging topography. Therefore, satellite data will contain additional potential, but unknown, errors or uncertainty in these areas. The application of satellite remotely sensed data on the local, regional, or New Zealand-wide scale is often too coarse for use in small-scale studies. It requires higher resolution satellite data.

From the identified research gaps, I pose the following research questions:

1. Do satellite-derived data of the terrestrial water cycle, merged with ground observed or modelled data, lead to better estimation of water cycle variables, especially those that are important for the characterisation of groundwater volumes and flux changes and subsurface hydraulic properties in New Zealand?
2. Can we simulate the uncertainties of these above estimations?
3. Can satellite-derived data of terrestrial water cycle parameters aid to better indicate and characterise New Zealand's aquifers?

1.3 Objectives and outline of this thesis

This thesis aims to answer the three research questions using an 'efficient combination' of data. First, two terrestrial water cycle variables are studied in detail: evapotranspiration (ET) and soil moisture. Chapter 2 describes complexity and uncertainty of the estimation of ET, for both ground-observed as for satellite data, and investigates efficient combinations between ground-observed and satellite data. Chapter 3 describes the physics of microwaves in relation to soil moisture and vegetation, and from there proposes and tests models that can be used to estimate high resolution satellite soil moisture and its uncertainty.

Chapter 4 describes how satellite data can be used, in an efficient combination with other datasets and models, to estimate regional and nation-wide rainfall

recharge to groundwater. These rainfall recharge data are taken one step further and are used as one of many other input data in a nation-wide model of a water table, including estimates of other aquifer properties in Chapter 5.

Chapter 6 synthesises each chapter's discussions as relating to the research questions, and then considers how well the research questions have been answered in this thesis. From there it follows with recommendations for further research. Overall conclusions are drawn in Chapter 7.

This thesis also contains three appendices. Appendix A contains soil moisture output graphs of Chapter 3. As some methods were used throughout multiple chapters, these are described in more details in Appendices B (uncertainty propagation) and C (hydraulic conductivity).

1.4 Journal articles, science reports and conference abstracts

This doctoral thesis is written as a monograph. Parts of this monograph have been included in journal articles, refereed conference proceedings or GNS Science reports. These have been outlined below. Reviewer feedback from the journal papers and GNS Science reports has greatly improved the quality of my thesis.

Chapter 2

Journal paper:
Westerhoff, R.S., 2015. Using uncertainty of Penman and Penman-Monteith methods in combined satellite and ground-based evapotranspiration estimates, Remote Sensing of Environment, Vol. 169, pages 102-112. Doi:10.1016/j.rse.2015.07.021.

Refereed conference proceeding and oral presentations:
Westerhoff, R.S., 2014. National monthly satellite evapotranspiration for rainfall recharge estimation. p. 286 In: 2014 Water Symposium : integration, the final frontier : Nov. 24 - 28, Marlborough Convention Centre. Water Symposium 2014.

Westerhoff, R.S., Mu, Q., 2014. Groundwater Estimation Using Remote Sensing Data on a Catchment Scale in New Zealand. AGU Fall Meeting, H34D-05. URL: https://agu.confex.com/agu/fm14/meetingapp.cgi#Paper/2659.

Chapter 3

Journal manuscript:
Westerhoff, R.S., and Steyn-Ross, M., 2016. Explanation of InSAR phase dis-

turbances by seasonal characteristics of soil and vegetation. Submitted to IEEE Transactions of Geoscience and Remote Sensing.

Chapter 4

Published discussion paper and manuscript for finalisation:
Westerhoff, R., White, P., and Rawlinson, Z., 2016. Application of global models and satellite data for smaller-scale groundwater recharge studies, Hydrol. Earth Syst. Sci. Discuss., doi:10.5194/hess-2016-410.

GNS Science Report:
Rawlinson, Z., Westerhoff, R., White, P., Schaller, K., Moore, C., 2015. Estimation of rainfall recharge to groundwater in the Waipa River catchment from three independent models. GNS Science Consultancy Report 2015/212., 81p. GNS Science.

Refereed conference proceeding and oral presentations:
Westerhoff, R.S., White, P., Moore, C., 2015. Rainfall recharge estimation on a nation-wide scale using satellite information in New Zealand. European Geophysical Union General Assembly, Vienna 13-17 April 2015.

Westerhoff, R.S., White, P., 2015. Nation-wide gridded baseflow from recharge and groundwater models. In: New Zealand Hydrological Society 2015 Annual Conference, From Data to Knowledge, 1-4 December 2015, Hamilton, New Zealand.

Chapter 5

Journal manuscript:
Westerhoff, R.S., White, P.A., Miguez-Macho, M., 2016. Application of an improved global-scale groundwater model for water table estimation across New Zealand. Submitted to Journal of Hydrology Regional Studies.

GNS Science Report:
Westerhoff, R.S., White, P.A., 2013. Application of equilibrium water table estimates using satellite measurements to the Canterbury Region, New Zealand, GNS Science Report No. 2013/43.

Refereed conference proceeding and oral presentations:
Westerhoff, R.S., Palmer, K. 2013. Validation of a satellite derived water table. p. 233-234 In: The New Zealand Hydrological Society & The Meteorological Society of New Zealand Joint Conference Handbook, Palmerston North 2013. New Zealand Hydrological Society.

2 Satellite data and the estimation of evapotranspiration

2.1 Introduction

Evapotranspiration (ET) can be defined as liquid water from soil or plants transferring to vapour in the atmosphere (adjusted from Irmak, 2012). It can either be expressed as potential ET (PET: the amount of ET if ample water is available) or actual ET (AET). In New Zealand, ET is on average approximately 53% of mean annual rainfall, but varies considerably throughout the country (Figure 2.1). Mean annual AET was estimated by Woods et al. (2006) as ranging from 100 to 1100 mm/yr. ET is an important part of the water cycle and therefore also for estimation of groundwater fluxes. Wrong estimates of ET can have significant consequences on estimates of rainfall recharge to groundwater. For example, Howard and Lloyd (1979) showed that 10% overestimation of ET leads to 5% underestimation of yearly groundwater recharge and up to 20% in summer groundwater recharge.

Global satellite products could benefit ET estimation on a catchment scale. In recent years, global satellite data products are increasingly developed. Space research on water resources, drought and floods has been increasingly linked into collaborative global efforts to develop data on a global scale. Examples are large-scale efforts and projects such as GEWEX (Global Energy and Water Exchange; GEWEX, 2014), and GEO (Group on Earth Observation; GEO, 2014b), who oversee and coordinate global climate and space research for water (GEO, 2014a). Recent research projects of the European 7th Framework Programme (i.e., EartH2Observe, 2015; GLOWASIS, 2015) aim at providing open data on global water resources datasets for scientific communities. These communities could then use these data for research on their continent, country or catchment. As most policy on water is on a national and regional scale, global satellite data could thus be adding value in countries where ground observations are sparse.

Although ET can be useful on the catchment scale, most global satellite data and derived products are not easily projected to a country or catchment scale. For example, for small catchments, some global ET data (e.g., from Miralles et al., 2011a,b) is often too coarse. Also, most satellite-derived ET products embed a 'pseudo-model', which can hold over-simplified model assumptions and unknown uncertainty (e.g., Miralles et al., 2011a,b; Mu et al., 2007, 2011). The one-on-one use of these data on a catchment scale are thus prone to errors. A future challenge lies ahead: how to use the large amount of available global satellite ET data on a catchment scale without the results becoming unreliable.

Estimation of ET can contain considerable uncertainty. ET cannot be measured directly and estimation methods are complex. ET is inferred through energy budget methods (e.g., Anderson et al., 2007; Bastiaanssen et al., 1998b) or hydrological water balance estimations, with measurements of vegetation status and climate variables (i.e., stomatal conductance, temperature, solar radiation, air pressure, air humidity, wind; Mu et al., 2011). Many different approaches for ET estimation exist, with many uncertain input components and therefore, modelled ET is often different than ground-estimated ET. For example, the modelled AET from Woods et al. (2006) shows much uncertainty at ground observations, e.g. lysimeter-derived AET in the Canterbury Plains (Figure 2.2). The research in this chapter uses Penman (Penman, 1963) and Penman-Monteith (P-M, Monteith, 1965; Penman, 1948) methods. A comprehensive description of many variations of ET methods is given in the overview of McMahon et al. (2013).

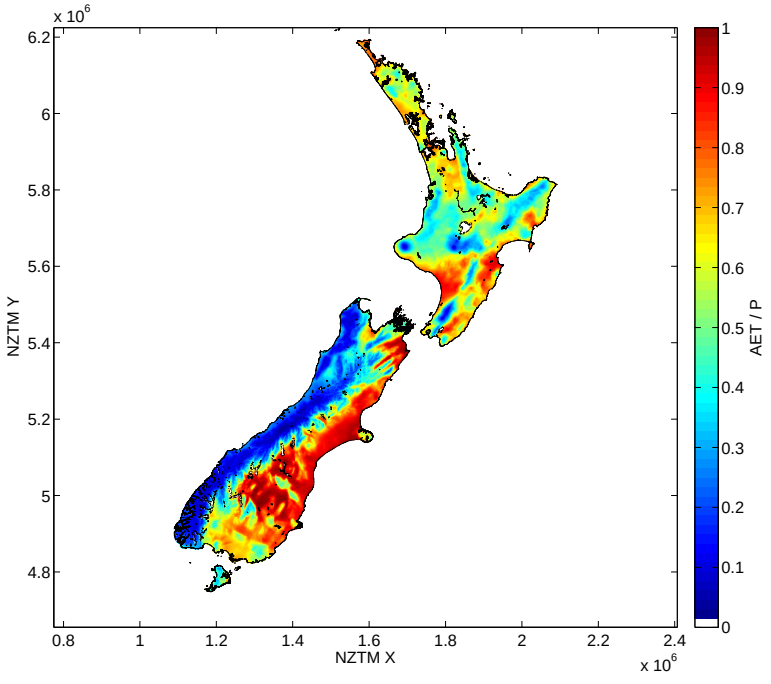

Figure 2.1: An estimated ratio of AET and precipitation P in New Zealand, derived from mean annual values for AET and P, from Woods et al. (2006) and Tait et al. (2006), respectively.

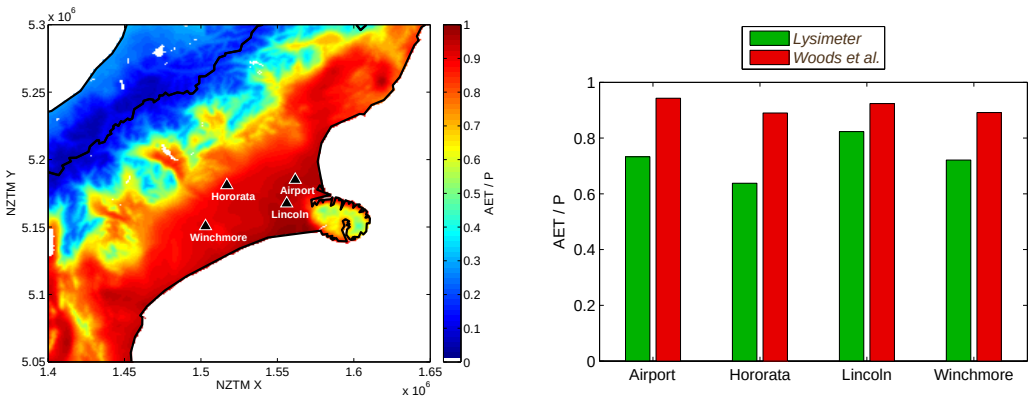

Figure 2.2: **Left**: AET/P in the Canterbury Plains, derived from mean annual values for AET from Woods et al. (2006) and P from Tait et al. (2006). Locations of lysimeters are shown in black triangles. **Right**: AET/P derived from lysimeter data (green; White, 2013) compared to those derived from Woods et al. (2006) (red).

The uncertainty of ground-estimated ET should be taken into account when combining satellite and ground-estimated ET data. In general, if ample ground observations are available, simple interpolation between these observations would lead to a gridded product, the ground-observed value logically being treated as the correct value. However, this is not always the case, as ground observation networks are usually sparse. In that case, additional data (e.g., satellite data) can be used. Interpolation methods that use other variables as an additional constraint in data-sparse environments are, for example, used by Tait and Woods (2007). They use elevation as an additional parameter and describe 5 km x 5 km daily reference crop ET for New Zealand by interpolating long term daily data of 70 climate stations using trivariate thin-spline interpolation. Their resulting gridded data correlate well with ground observations. However, the uncertainty of ground observations of ET is not taken into account. In most studies estimating ET from satellite data (Bastiaanssen et al., 1998b; Miralles et al., 2011b; Mu et al., 2007, 2011; Su, 2002) the satellite estimations are validated with ground observations from (micro-) meteorological or eddy-covariance flux towers. Validations seldom lead to a one-on-one correlation, and it is considered in these studies that the ground observations are correct and that the satellite estimates contain noise and uncertainty. Earth-observing satellites measure from several hundreds of km altitude and atmospheric effects can therefore create incoherent noise. It is also known that satellite ET data can have high errors in areas with high elevation differences (Van der Tol and Parodi, 2012). However, ground observations are also uncertain: it is for example known that flux tower ET estimations can lead to a lack of closure of the energy balance by 20% (Wilson et al., 2002). Also, most PET estimations from climate stations use simplifying assumptions. For example, reference crop ET by Allen (1998) assumes green grass with a constant height of 0.12 m, which is then corrected by a crop factor to get PET. Errors due to different vegetation types or wrong vegetation growth status are often not considered, and the effect on PET is relatively unknown, but potentially large.

Satellite data are able to measure vegetation characteristics and could thus help in a better PET estimation. Ideally, one wants a combination of both satellite ET and ground observations, which takes uncertainty of both datasets into account. Potentially, weak points from both methods could then be scored out against each other.

Uncertainty comes in different forms and is therefore difficult to assess on a uniform spatial and temporal scale. It could stem from measurements, or models that ignore inter-dependency of input components. Literature values of uncertainties cannot always be used in further studies, as they: only represent the local or regional climate and observation strategies; they comprise different time windows (e.g., daily, monthly or annual); have different model origin; or have different statistical origin. Error and sensitivity analyses of ET to its input components have been done in the past, but with different outcomes. For example, Saxton (1975) showed that computed ET was most sensitive to changes or errors in net radiation R_n: in summer, 50-90% was governed by net radiation, and 20-30% by aerodynamic properties (vapour pressure deficit, wind). Gong et al. (2006) showed that ET was most sensitive to relative humidity, followed by S_n, air temperature and wind speed) and that sensitivities changed over the season. Coleman and DeCoursey (1976) estimated standard deviation of several ET methods and found average errors of approximately 0.2 mm/day in winter and 3 mm/day in summer. However, these were for different climatic environments and different ET estimation methods. Estévez et al. (2009) show that in Southern Spain ET is most sensitive to temperature in summer and it causes overestimation of ET; relative humidity in winter causes underestimation of ET. All above-mentioned studies show that sensitivity of ET to its input components depends on climate region and season. Uncertainty of some ET input component have been described by a.o. Tait and Zheng (2007). They established a range of model prediction errors of minimum and maximum median annual temperature of 0.4 and 0.8 °C using the ANUSPLIN method (Australian National University, 2014). For relative humidity, Lin and Hubbard (2004) found uncertainties, both modelled and measured, to be in the range of 0.5 to 5%, depending on the temperature. For wind speed Leathwick and Stephens (1998) used two different methods and found uncertainties in between 0.6 and 1.6 m/s for daily wind speed measurements; Tait and Zheng (2007) found uncertainties in between 0.6 and 1.1 m/s for median annual wind speed. Solar radiation measured from earth's surface is commonly used for measuring cloudiness or surface albedo, but knows uncertainty of site measurements and down-scaling methods (Li et al., 2005). Surface albedo values are derived from solar radiation measurements, and therefore complex, because these again are correlated with cloudiness. The inter-relation of these parameters implies that they are not independent. There is a need for better uncertainty assessment of ET and its many components, taking into account this inter-dependence. To further estimate AET, several approaches are known. For example, using information on soil water deficit leads to a relation between AET and PET (e.g., Miralles et al., 2011b; Verhoef and Egea, 2014; White et al., 2003). Others use an estimation based on a long term water balance approach and a dryness index (Woods et al.,

2006; Zhang et al., 2004). However, most approaches do not always lead to satisfying results. For example, the ratio of AET over rainfall P (AET/P) according to Woods et al. (2006) estimates that there is little rainfall recharge to groundwater in the Canterbury Plains (Figure 2.2), whereas ground observations measure rainfall recharge of 17% to 36% of total rainfall (White et al., 2014a).

This chapter describes a method to combine ground-estimated and satellite remotely sensed ET. It is applied at the national scale and leads to a 1 km x 1 km New Zealand-wide estimation of monthly PET and AET, including uncertainty, for the period 2000-2014. These data could for example be used in other nation-wide estimates, such as rainfall recharge (Chapter 4). Uncertainty of the input components of ET estimation and their propagation in two different ET methods are further described in this chapter. This uncertainty is embedded in an interpolation method that uses the pattern of global satellite data. The interpolation method 'projects' the satellite ET data to ground-estimated ET, abiding the locally used (Penman) estimation methods. The methods and their results are explained for monthly historical ET in New Zealand. Direct application of the original satellite ET, i.e., without projection to the national standard, is furthermore discussed. Finally, the conversion of PET to AET knows different approaches, each with its own strength and weakness. These approaches are described and compared.

2.2 Theory

2.2.1 Introduction to the Penman-Monteith and Penman equations

The Penman-Monteith (P-M) equation (Monteith, 1965; Penman, 1948) calculates ET based on the earth's surface energy balance and atmospheric water demand. In mm/day, it is defined by Hendriks (2010) as:

$$E_a = \frac{1000}{\rho_w \lambda} \times \frac{\Delta \left(R_n - G\right) + \frac{86400 \times \rho_a c_p (e_s - e_a)}{r_a}}{\Delta + \gamma \left(1 + \frac{r_s}{r_a}\right)}, \tag{2.1}$$

where

E_a is actual evaporation [mm day^{-1}];

ρ_w is water density [kg m^{-3}];

λ is latent heat of vaporisation [MJ kg^{-1}]

Δ is the gradient of the saturation pressure curve [kPa °C^{-1}];

R_n is the net radiation of the earth's surface [MJ m^{-2} day^{-1}];

G is heat transfer into the soil, rock or water [MJ m^{-2} day^{-1}];

86400 = a constant for the second to day conversion [s^{-1} day];

ρ_a = air density [kg m^{-3}];

e_s is the saturation vapour pressure at the surface [kPa];

e_a is the actual vapour pressure of the air [kPa];

γ is the 'psychometric' constant [kPa $°C^{-1}$];

r_s is the surface resistance [s m^{-1}];

r_a is the aerodynamic resistance [s m^{-1}];

As G is relatively small, it is often assumed zero (Allen et al., 2001; Bastiaanssen et al., 1998a; Su, 2002).

If all known constants, assumed to have negligible error, are put into the P-M equation, actual ET in mm/day looks like this (Hendriks, 2010):

$$E_a = 0.408 \times \frac{\Delta R_n + \frac{105.028(e_s - e_a)}{r_a}}{\Delta + 0.067\left(1 + \frac{r_s}{r_a}\right)} \tag{2.2}$$

Commonly used simplified equation calculate PET using static and simplified assumptions of land cover and growth: 'reference crop ET', or ET_0. Reference crop ET according to Allen (1998) is most used and is also known as 'FAO56 reference crop ET'. It generally simplifies the expressions of r_s and r_a for a well-watered grass surface of 12 cm and is further mentioned and explained in McMahon et al. (2013). It is called $ET_{0,FAO}$ onwards. The Penman method (Penman, 1963), based on the same input components, is mostly used in New Zealand as an alternative to the $ET_{0,FAO}$. It calculates evaporation (not evapotranspiration) from a well-watered grass surface (Burman and Pochop, 1994; NIWA, 2014). Although not accounting for transpiration, the Penman 'ET' is used as such, and will be called $ET_{0,Penman}$ onwards. Both $ET_{0,FAO}$ and $ET_{0,Penman}$, can be simplified to a function of limited input components:

$$ET_{0,FAO} = 0.408 \times \frac{\Delta R_n + \frac{60.3}{T+273} u_2 (e_s - e_a)}{\Delta + 0.067(1 + 0.34u_2)} \tag{2.3}$$

and

$$ET_{0,Penman} = \frac{\Delta R_n + 0.4244(1 + 0.536u_2)(e_s - e_a)}{(\Delta + 0.067)(2.501 - 0.00236T)} \tag{2.4}$$

where

- ET_0 is in [mm day^{-1}];
- u_2 is wind speed at 2 m above the surface [m s^{-1}];
- T is temperature [°C];

Eq. 2.3 simplifies transpiration for a green grass with a height of 0.12 m, while Eq. 2.4 does not take into account transpiration of the plant through stomata. Both equations assume no soil water deficit.

2.2.2 Explanation of all individual P-M input components and their uncertainties

Uncertainty and sensitivity analyses of the P-M equation have led to different outcomes in the past. The studies mentioned in the introduction of this chapter show that the sensitivity of ET is depending on its input variables but this sensitivity depends on climate region and season. For New Zealand, a sensitivity analysis of the P-M equation, as well as detailed analyses of the overall uncertainty caused by the P-M input variables has not been done. This section aims to quantify uncertainty in ET caused by possible ranges of uncertainty in P-M input variables. It details all uncertainty of input components in the Penman-Monteith equations used in Eq. 2.1 - 2.4.

2.2.2.1 Vapour pressure

e_a is "the actual pressure of the water vapour molecules in the air at a certain temperature"; e_s is "the partial pressure of the water vapour molecules when the air is saturated with water vapour" (Hendriks, 2010), also called *saturation vapour pressure*. The difference between e_s and e_a is often called the *vapour pressure deficit*.

The *saturation vapour pressure* e_s at the surface is a function of air temperature and atmospheric pressure. Several approaches exist for calculating vapour pressure (Hendriks, 2010; Lin and Hubbard, 2004; World Meteorological Organization, 2008). The assumption that constant air pressure (of 100 kPa=1000 mbar) has a negligible effect on e_s (Hendriks, 2010; Lin and Hubbard, 2004). Therefore e_s [kPa] can be approximated as a function of air temperature only through:

$$e_s = 0.6108 \exp\left(\frac{17.27T}{237.3+T}\right), \tag{2.5}$$

It is assumed that uncertainty in T is small (e.g. 0.5 °C) near and larger in between (e.g. max. 2 °C) meteorological stations. When propagating standard deviations in between 0 and 2 °C for normal New Zealand temperatures (-5 to +35°C), values for e_s are in between 0 and 6 kPa, with uncertainties, σ_{e_s}, in between 0 and 0.6 kPa (Figure 2.3). The mean value for σ_{e_s} is 0.16 kPa.

The *actual vapour pressure* e_a can be derived by measuring relative humidity RH [%] (World Meteorological Organization, 2008):

$$RH = 100\frac{e_a}{e_s} \tag{2.6}$$

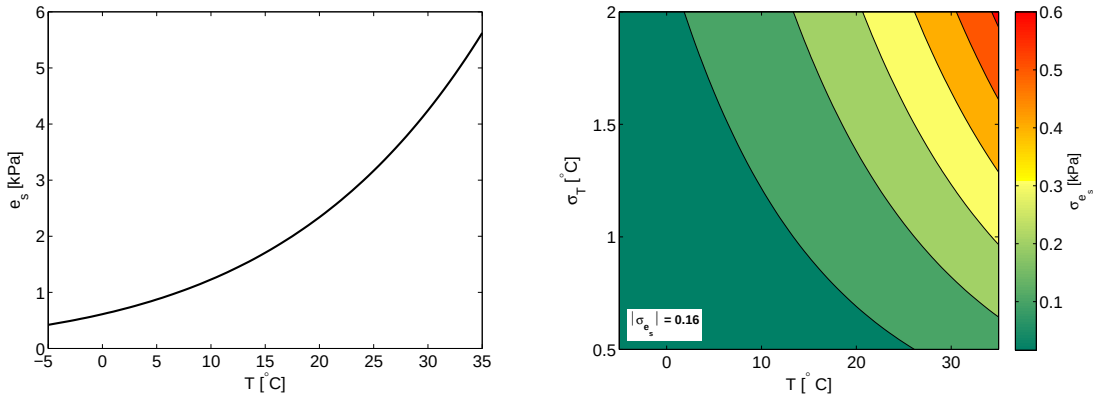

Figure 2.3: Left: saturated water vapour pressure e_s for common New Zealand temperatures T [°C]. Right: Uncertainty σ_{e_s} plotted against T and σ_T.

Putting Eq. 2.5 in 2.6 shows that e_a is depending on the measured parameters T and RH:

$$e_a = 6.108 \times 10^{-3} RH \exp\left(\frac{17.27T}{237.3+T}\right) \tag{2.7}$$

RH can also be derived by measuring dewpoint temperature. Either directly measured or derived, uncertainty in RH, σ_{RH}, can be roughly in between 0.5% and 5% (Lin and Hubbard, 2004), assuming common New Zealand temperatures. Since e_s is a function of temperature, e_a is a function of RH and temperature. When using mean values for σ_{RH} (2 %) and σ_T (1.25 $°C$), values of the uncertainty e_a, σ_{e_a}, can be in between 0 and 0.4, with a mean value of 0.1 kPa (Figure 2.4). Randomly distributed values of σ_{RH} (in between 0 and 5 %) and σ_T (in between 0 and 2 $°C$), show a similar pattern, with slightly larger value for e_a and σ_{e_s} (Figure 2.5, left). For randomly distributed random values of σ_{RH} and σ_{e_s}, the mean value for σ_{e_a} is 0.12 kPa (Figure 2.5, right).

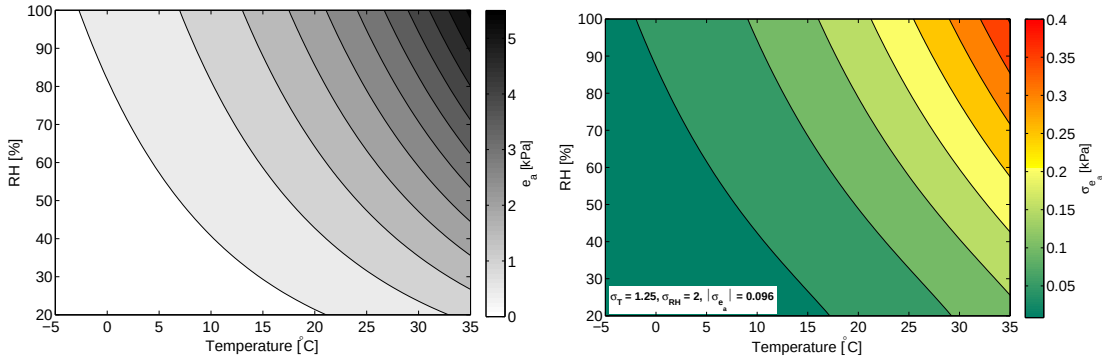

Figure 2.4: Left: actual water vapour pressure e_a as a function of T and RH. Right: Uncertainty σ_{e_a} as a function of RH and e_s for static standard deviations $\sigma_{RH} = 2$ and $\sigma_{e_s} = 0.13$.

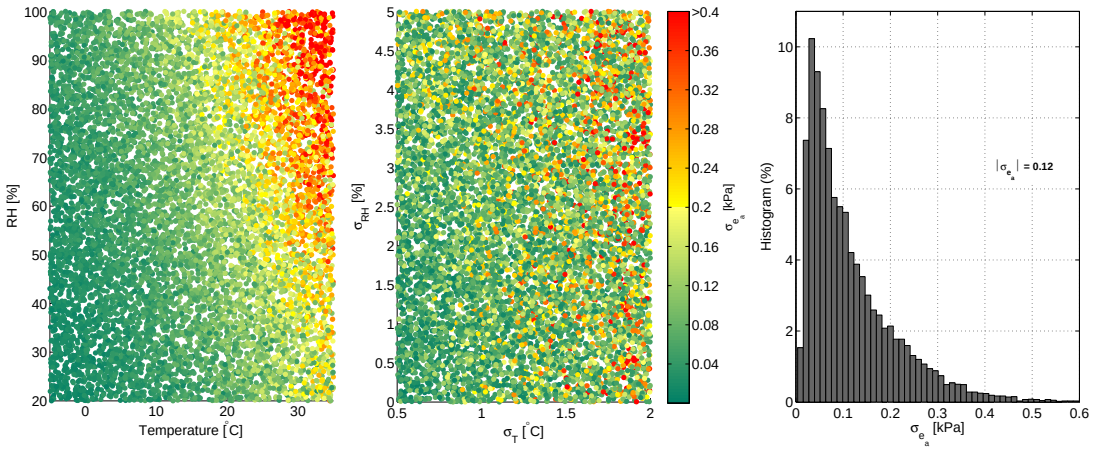

Figure 2.5: Uncertainty in actual water vapour pressure, σ_{e_a}, of 10,000 randomly distributed values of σ_T, σ_{RH} in: **(left)** a T-RH plot; a **(middle:)** σ_T-σ_{RH} plot; and a **(right)** histogram.

2.2.2.2 Gradient of saturation pressure curve (Δ)

Tetens (1930) and Murray (1967) determine Δ, the gradient of saturation vapour pressure over temperature, as function of e_s and T:

$$\Delta = \frac{de_s}{dT} = \frac{4098 e_s}{(237.3 + T)^2}, \tag{2.8}$$

Since e_s is a function of T (Eq. 2.5), uncertainty in Δ, σ_Δ is only a function of T and σ_T. For normal New Zealand temperatures, values of Δ are in between 0.04 and 0.31 °C^{-1} (Figure 2.6, left). Propagating σ_T leads to possible values of σ_Δ in between 0 and 2.5×10^{-2} kPa °C^{-1}, with a mean value of 7×10^{-3} (Figure 2.6, right).

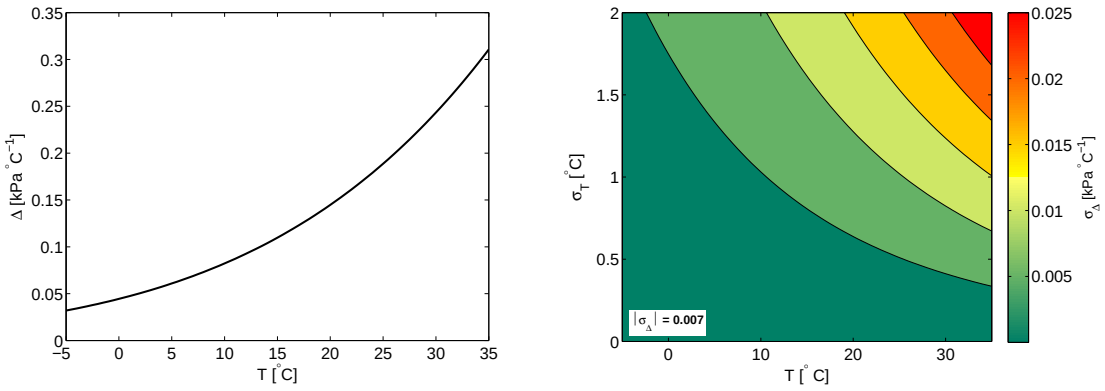

Figure 2.6: Left: gradient of saturated water vapour pressure Δ for common New Zealand temperatures T [°C]. Right: Uncertainty σ_Δ plotted against T and σ_T.

2.2.2.3 Net radiation

R_n is the net radiation. It is determined by the difference between the net incoming shortwave radiation (from the sun) at the earth's surface S_n and outgoing longwave radiation (from the earth) L_n (Hendriks, 2010):

$$R_n = S_n - L_n \tag{2.9}$$

S_n depends on solar reflection properties of the earth's surface, the cloudiness and the earth's atmosphere and is given here as an empirical equation (Hendriks, 2010):

$$S_n = (1 - \alpha)\left(a_s + b_s \frac{n}{N}\right) S_0, \tag{2.10}$$

where;

α the earth's albedo (solar reflection coefficient). Values for α lie in between 0.05 and 0.5 for natural materials (water, ice, soils and rocks) except for snow (Figure 2.7);

n the number of bright sunshine hours per day;

N the total possible hours of sunshine per day. Values of N are well known and vary between 8.5 to 16 hours in southern New Zealand and 10 to 14 hours in northern New Zealand (U.S. Naval Observatory, 2012);

S_0 is the shortwave radiation at the top of the atmosphere. For New Zealand, it ranges from roughly 8 to 40 in winter and summer, respectively, and it slightly changes with latitude (Hendriks, 2010);

a_s is the fraction of S_0 on overcast days (n=0);

$a_s + b_s$ the fraction of S_0 on clear days (n = N).

S_n relates to measured solar radiation Rad at the surface as (Burman and Pochop, 1994; NIWA, 2014).

$$S_n = (1 - \alpha)Rad \tag{2.11}$$

The ratio of S_n over S_0 (S_n/S_0) for water, soils and rocks ranges from 0.15 to 0.75 (Figure 2.8, left). The uncertainty, σ_{S_n}/S_0, propagates as:

$$\frac{\sigma_{S_n}}{S_0} = \sqrt{\left(-a_s - b_s \frac{n}{N}\right)^2 {\sigma_\alpha}^2 + \left(-b_s\left(\alpha - 1\right)\right)^2 {\sigma_{nN}}^2}, \tag{2.12}$$

These assumptions are made:

1) The maximum standard deviation in α, σ_α, is set to 0.1;

2) a_s and b_s are assumed constants of 0.25 and 0.50, respectively (Hendriks, 2010);

3) The standard deviation of n/N, cloud hours per day σ_{nN}, varies between 0.05 nearby meteorological stations and 0.3 in between stations;

4) S_0 is well known with negligible error;

Mean values of σ_α (0.05) and σ_{nN} (0.175) in Eq. 2.12 lead to a σ_{S_n} that is 5-10% of S_0 with a mean value of 7% (Figure 2.8, right). Randomly distributed values of σ_α and σ_{nN} lead to σ_{S_n} values that are 2-15% of S_0 with a mean value of 7% (Figure 2.9). σ_S/S_0 is mostly governed by σ_{nN} (Figure 2.9, left). Higher σ_S/S_0 tends to occur more often at low albedo (Figure 2.9, middle).

For absolute values of S_n (in MJ m^{-2} day^{-1}), we use an S_0 variation from 8 in winter to 40 in summer. S_n then ranges from a lowest value in winter of 1.2 (0.15*8) to a highest value in summer of 30 (0.75*40). Uncertainty σ_S can then vary from a lowest value in winter of 0.16, to a highest value in summer of 6. A mean value of 1.7 (7% of an S_0 of 24) is assumed.

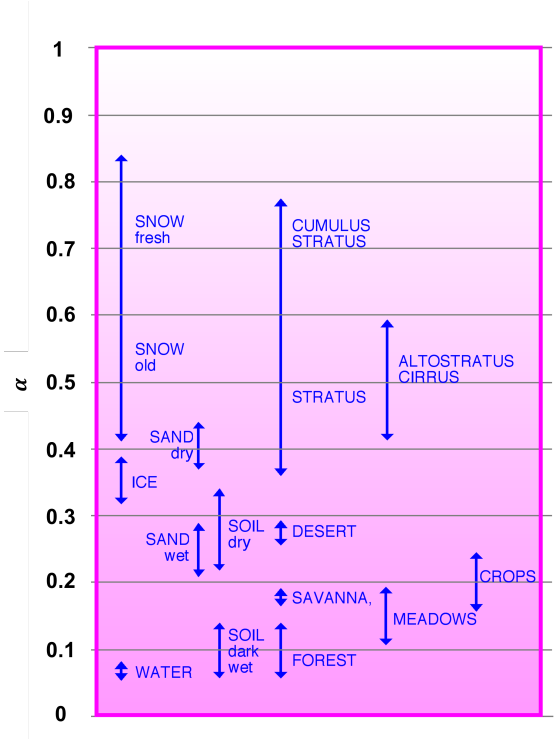

Figure 2.7: Albedo: percentage of reflected sun light in relation to the various surface conditions of the earth. Adapted from Grobe (2000) (Creative Commons CC-BY-SA-2.5 licence).

The net outgoing long wave radiation L_n at the earth's surface is also estimated by an empirical equation. If all known constants are embedded, L_n looks like (Hendriks, 2010):

$$L_n = 4.903 \times 10^{-9} \left(T + 273.2\right)^4 \left(0.34 - 0.14\sqrt{e_a}\right) \left(0.25 + 0.75\frac{n}{N}\right), \qquad (2.13)$$

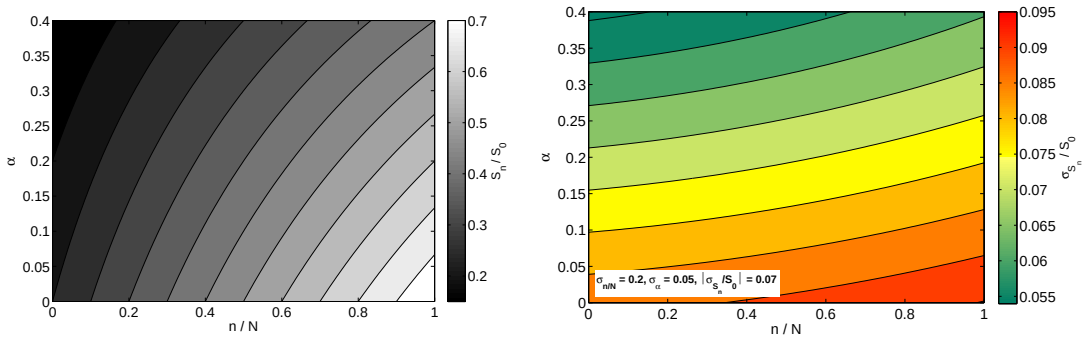

Figure 2.8: **Left:** The ratio for S_n/S_0 for values for cloudiness ratio n/N and albedo α. **Right:** Uncertainty $\sigma_{S_n}/S0$ as a function of n/N and α for mean uncertainties $\sigma_{n/N} = 0.2$ and $\sigma_\alpha = 0.05$.

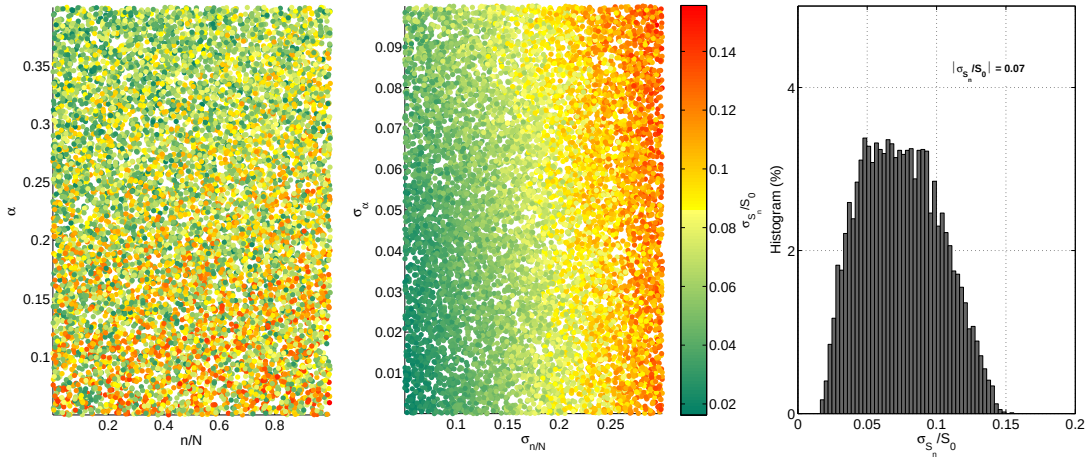

Figure 2.9: Uncertainty in shortwave radiation, σ_{S_n}/S_0, of 10,000 random values of $\sigma_{n/N}$, σ_α, n/N and α in: **(left)** an n/N - α plot; **(middle)** a $\sigma_{n/N}$-σ_α plot ; **(right)** and a histogram.

or, using Eq. 2.7:

$$L_n = 4.903 \times 10^{-9} \left(T + 273.2\right)^4 \left(0.25 + 0.75\frac{n}{N}\right) \left(0.34 - 0.14\sqrt{6.108 \times 10^{-3} RH \exp\left(\frac{17.27T}{237.3 + T}\right)}\right) \tag{2.14}$$

L_n thus depends on T, RH, and n/N. Values of L_n are roughly in between 0 and 5 MJ m^{-2}day^{-1} (Figure 2.10, left). For fixed values of uncertainty ($\sigma_T = 1.25°C$, $\sigma_{RH} = 2\%$, and $\sigma_{n/N} = 0.2$), the uncertainty σ_L ranges in between 0.15 and 0.75 and increases mostly at lower relative humidity (Figure 2.10, right). When propagating all possible uncertainties in T, RH and n/N (Figure 2.11), the range in σ_L slightly increases to 0.05-1.15 MJ m^{-2}day^{-1}, with a mean value of 0.5. σ_L is highest at low relative humidity and high $\sigma_{n/N}$.

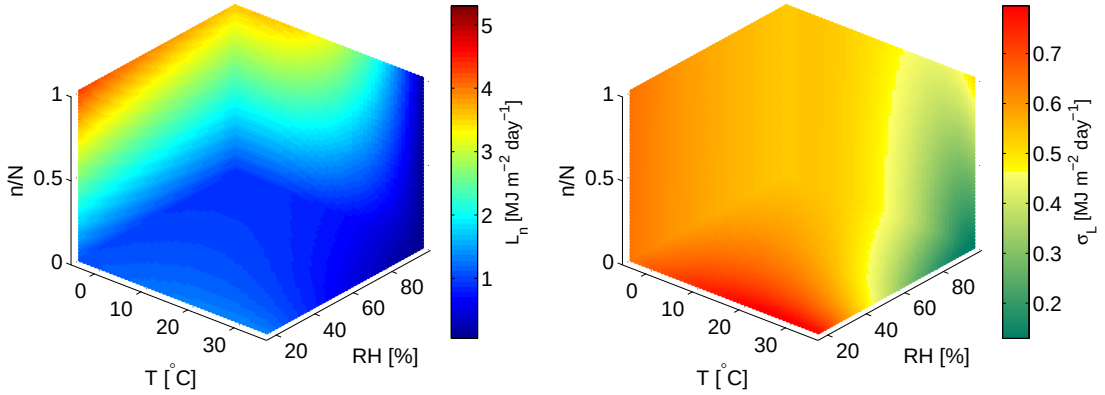

Figure 2.10: **Left:** Longwave radiation L_n as a function of T, RH, and n/N. **Right:** Uncertainty σ_{L_n} as a function of T, RH, and n/N for static values of $\sigma_T = 1.25°C$, $\sigma_{RH} = 2\%$, and $\sigma_{n/N} = 0.2$.

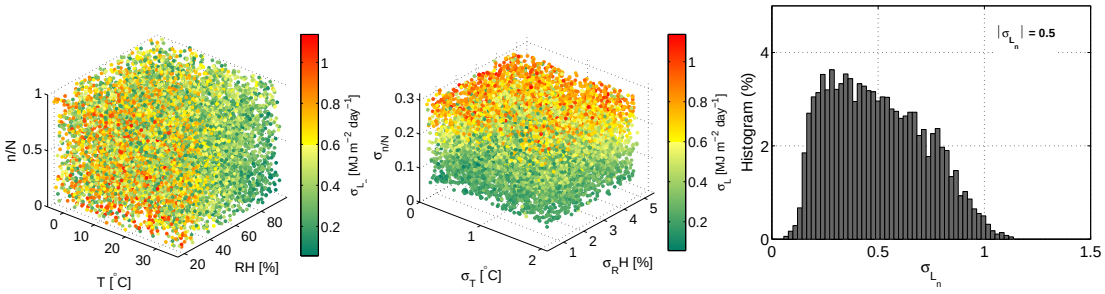

Figure 2.11: Uncertainty in longwave radiation, σ_{L_n}, of 10,000 random values of σ_T, σ_{RH} and $\sigma_{n/N}$ in: **(left)** a T-RH-n/N plot; **(middle)** a σ_T-σ_{RH}-$\sigma_{n/N}$ plot; and **(right)** a histogram.

2.2.2.4 Aerodynamic resistance

The resistance that water vapour encounters when it diffuses from a surface is called aerodynamic resistance, r_a. It is inversely related to the roughness of the earth's surface and the wind speed: a smooth surface and low wind speed cause higher r_a (Hendriks, 2010). For a wide range of crops, r_a [s m^{-1}] is a function of crop height h [m] and wind speed u_2 [m s^{-1}] at 2m height (Allen, 1998):

$$r_a = \frac{\ln\left(\frac{2-\frac{2}{3}h}{0.123h}\right)\ln\left(\frac{2-\frac{2}{3}h}{0.0123h}\right)}{0.1681u_2}, \tag{2.15}$$

where standardized heights for wind speed, temperature, and humidity of 2m have been assumed. Average daily wind speeds in New Zealand range from approximately 1 - 12 m/s, with monthly error estimates at climate stations in between 1 and 1.5 m/s (Leathwick and Stephens, 1998) or annual error estimates at climate station in between 0.6 and 1.1 m/s (Tait and Zheng, 2007). It is assumed that uncertainty in between stations is larger, up to 3 m/s.

Ranges for r_a for forest, grass and water are shown in Table 2.1. According to Eq. 2.15 and shown in Figure 2.12, values of r_a increase to high values at low wind speed and low crop heights. I follow Hendriks (2010) and set the maximum value of r_a to 125, which represents a water surface. The uncertainty σ_{r_a} also increases exponentially at lower wind speed and low crop heights (Figure 2.12, right, and Figure 2.13, left). When mean values for σ_u (1.8 m s^{-1}) and σ_h (0.1) are taken, the median of σ_{r_a} is 3.6 m s^{-1}. The median was chosen, as the range of σ_{r_a} was very large (10^{-4} to 10^6). However, most values are in between 0 and 100. σ_{r_a} is most sensitive to wind speed and crop height and not to their uncertainties (Figure 2.12, left and middle). Using 10,000 random values of σ_u in between and 0.5 and 2 m s^{-1}) and σ_h (in between 0.01 and 0.2 m) leads to a similar range of values of σ_{r_a}, with a median of 2.8.

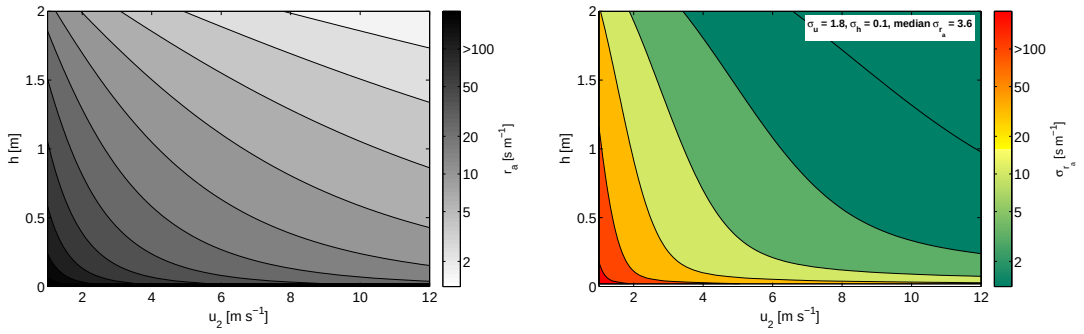

Figure 2.12: **Left:** Aerodynamic resistance r_a as a function of wind speed u_2, and crop height h. **Right:** Uncertainty σ_{r_a} as a function of wind speed u_2, and crop height h for static values of σ_{u_2} =1.8 m s^{-1} and σ_h= 0.1 m.

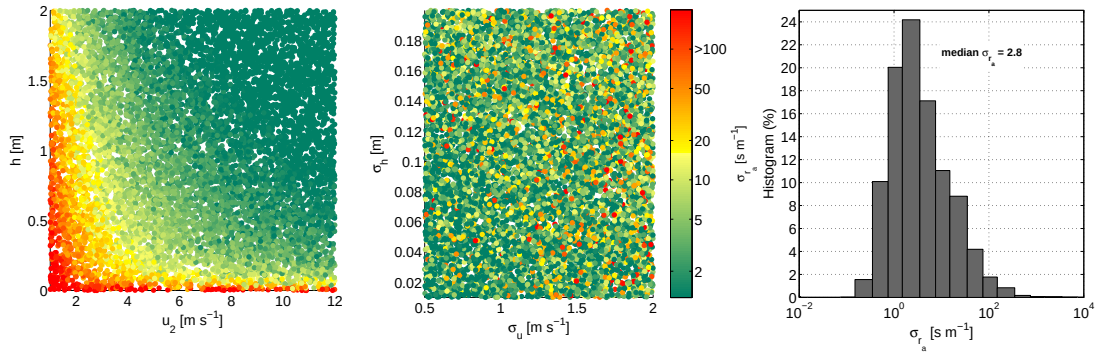

Figure 2.13: Uncertainty in aerodynamic resistance, σ_{r_a}, of 10,000 random values of σ_{u_2} and σ_h in: **(left)** a u_2-h plot; **(middle)** a σ_{U_2}-σ_h plot; and **(right)** a histogram.

2.2.2.5 Surface resistance and the link to AET

The surface resistance r_s is a property that combines the physiological resistance by the stomata of the plant and the resistance of the soil to evaporation. It is the most complex and uncertain property of the P-M equation, as in cases of water stress the surface resistance increases with soil water deficit and actual ET is lower than potential ET. It is thus a measure of soil moisture and plant stomatal resistance. For unstressed conditions and an area of fully covered vegetation, r_s can be described like this (Allen, 1998):

$$r_s = \frac{r_l}{LAI_{active}}, \tag{2.16}$$

where r_l is the bulk stomatal resistance of the well-illuminated leaf, and LAI_{active} the sunlit leaf area index. Possible values for surface resistance under unstressed conditions are given in 2.1.

Table 2.1: Values for aerodynamic and surface resistance (Hendriks, 2010, his Table 2.1)

Land type	r_a **(s m^{-1})**	r_s **(s m^{-1})**
Forest	5 - 10	80 - 150
Grass	50-70	40 - 70
Open water	110-125	0

For conditions of water stress, when the soil dries up, r_s becomes of function of soil moisture. Bastiaanssen et al. (2005) used the Jarvis-Stewart model (Jarvis, 1976; Stewart, 1988) to calculate r_s:

$$r_s = \frac{r_{s,min}}{R_T R_{\Delta e} R_K R_\theta LAI}, \tag{2.17}$$

where the R values denote empirical reduction functions of soil moisture (R_θ) and the stomatal aperture (R_T, $R_{\Delta e}$, R_K: air temperature, vapour pressure deficit, solar radiation, respectively). The use of empirical functions generally implies

that theoretical functions are too complex or cannot be found. For a multitude of (empirical) models, the net effect of soil water stress on ET was evaluated by Verhoef and Egea (2014). They assessed RT (=AET/PET) as a function of the fraction of transpirable soil water (FTSW):

$$FTSW = \frac{\theta - \theta_{WP}}{\theta_{FC} - \theta_{WP}}, \tag{2.18}$$

in which

θ is soil moisture;

WP is wilting point;

FC is field capacity.

Leading to different transpiration reduction functions (TRF).

In terms of the Penman-Monteith equation (Eq. 2.1), r_s can be written as;

$$r_s = \frac{r_a}{0.067}\left(0.408R_n\Delta + \frac{\left(\frac{105.028e_s\left(1-\frac{RH}{100}\right)}{r_a}\right)}{ET} - \Delta - 0.067\right) \tag{2.19}$$

Surface resistance compared for grass and forest as a function of RT is plotted in Figure 2.14, where several random scenarios for r_s and r_a were taken in the ranges given in Table 2.1. As r_a can have large uncertainty (Figure 2.13), values of r_s cover a large range of values and they therefore best plotted in the logarithmic domain. Uncertainty values for r_s are therefore assumed to be very high, and practically hard to be quantified.

Since r_s and its uncertainty are so hard to quantify, other approaches are also used, which are either based on empirical findings or look-up table of vegetation properties or hydrological water balance assumptions. For example, one can use TRFs to calculate AET when soil water deficit is known using empirical findings of vegetation TRFs. An example is shown in Figure 2.15, where empirical TRF from 13 crop-soil combinations Verhoef and Egea (2014) are fitted to a function. The best fit function can be used to calculate RT if soil moisture, field capacity and wilting point are known (Eq. 2.18).

Mu et al. (2011) define a surface resistance that is depending on the Leaf Area Index, stomatal conductance estimate, minimum temperature and vapour pressure deficit:

$$r_s = \frac{1}{C_c}C_c = C_s \times LAIC_s = C_L \times m(T_{min}) \times m(VPD), \tag{2.20}$$

Where:

- C_L is the mean stomatal conductance per unit leaf area, which are found by a look-up table approach;
- $m(T_{min})$ and $m(VPD)$ are multiplication factor that limits C_L by minimum air temperature T_{min} and vapour pressure deficit VPD.

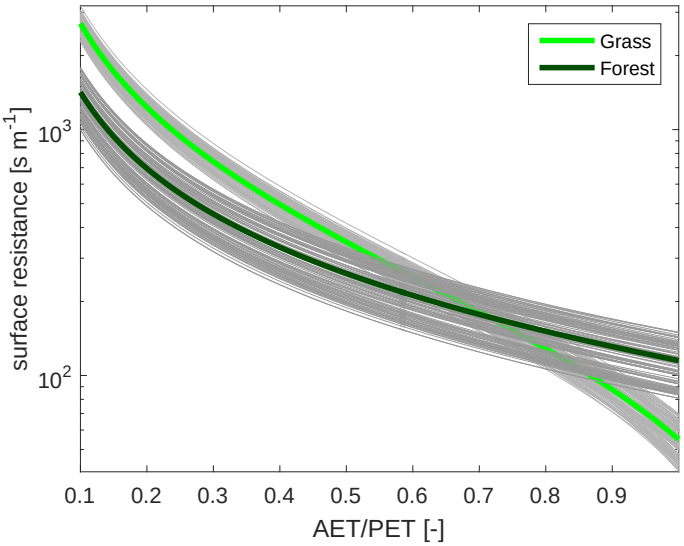

Figure 2.14: Surface resistance r_s as a function of RT (=AET/PET). The thick green lines are the means of random (grey) simulations.

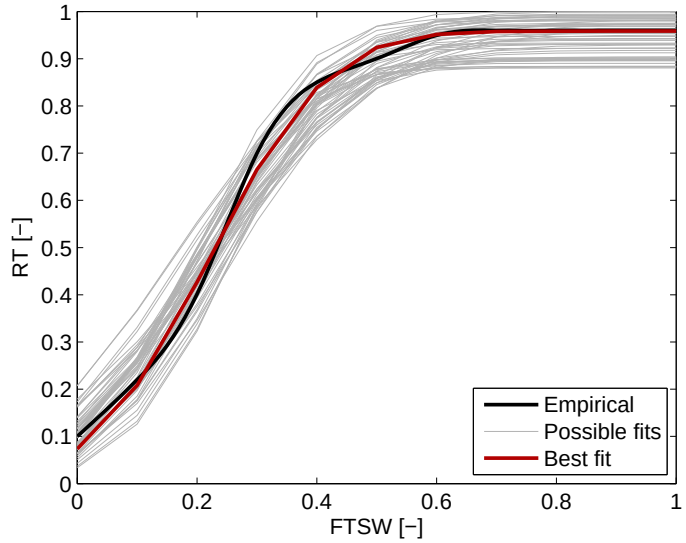

Figure 2.15: Possible fits with models of transpiration reduction functions (TRF) from Verhoef and Egea (2014). RT = relative transpiration, FTSW = fraction of transpirable soil water.

Another, more hydrological, approach is given by Zhang et al. (2004). They calculate long term AET from PET using a 'dryness' index and mean annual values of rainfall and PET:

$$AET_{MOD16_{Zhang}} = P + PET\left(1 - \left[1 + \left(\frac{P}{PET}\right)^{w}\right]^{1/w}\right) \tag{2.21}$$

Another approach is described by White et al. (2003) and Scott (2004) and uses a hydrological soil water balance model with a daily to weekly time step. They use an approach based on a soil moisture balance (SOILMOD, see Chapter 4). If there is a soil water deficit between timestep i and i-1, then:

$$\frac{AET_i}{PET_i} = \frac{S_{i-1}/FC}{(1 - VC/PET_i)}, \tag{2.22}$$

where:

S_{i-1} is soil moisture at timestep i-1;

VC is a vegetation cover factor;

FC is field capacity of soil moisture.

Concluding, estimation of r_s is the most complex in the estimation of AET and includes the need for other measurements and/or empirical relations. Therefore, methods of estimation of r_s are diverse and bring more uncertainty to the estimation of AET when soil water deficit is high.

2.2.2.6 Summary of all input components and their uncertainties based on the findings in this section

Based on the mentioned assumed values and literature values of input components of the ET equations, and error propagation mentioned in this section, all findings of this section are summarised in Tables 2.2 and 2.3. They will be updated with new estimates developed in the method of this chapter (in section 2.3.

2.3 Methodology

This section describes two methods that were developed in my research. First, I am using uncertainties of Penman-Monteith input components (summarised in section 2.2.2.6 and using a method to assess covariance of these input components) to estimate uncertainty of satellite and ground-observed reference crop ET. Using this uncertainty, a method for interpolation of ground-observed data is described, using the synoptic satellite ET data as an interpolator, while still abiding the national (Penman) standard of ET estimation. Second, conversion of satellite PET to AET is tested for some approaches, and existing national products are compared to the satellite AET estimation.

Table 2.2: Estimated values of variables in the Penman-Monteith equation after findings in this section.

	Min	Max	Units	Reference
T	-10	35	°C	
RH	20	100	%	
S_0	8	40	MJ m^{-2} day^{-1}	Hendriks (2010)
$u2$	1	12	m s^{-1}	Tait and Zheng (2007)
α	0.05	0.5	-	Ahrens (2007); Oke (1992)
n/N	0	1	-	
e_s	0.4	5.7	kPa	
e_a	0.4	5.7	kPa	
Δ	0.04	0.31	kPa °C^{-1}	
S_n	1.2	30	MJ m^{-2} day^{-1}	
L_n	0.1	5.2	MJ m^{-2} day^{-1}	
r_a	0	125	s m^{-1}	
r_s	0	150	s m^{-1}	

Table 2.3: Estimated uncertainties in the Penman-Monteith equation after findings of this section

	Min	Max	Median	Units
σ_T	0.5	2	1.25	°C
σ_{RH}	0.5	5	2	%
σ_{S_0}	0	0	0	MJ m^{-2} day^{-1}
σ_{u2}	0.5	1.5	1.0	m s^{-1}
σ_{alpha}	0	0.1	0.05	-
$\sigma_{n/N}$	0.05	0.015	0.01	-
σ_{e_s}	0	0.6	0.13	kPa
σ_{e_a}	0	0.16	0.13	kPa
Δ	0	0.025	0.007	kPa °C^{-1}
σ_{S_n}	0.16	6	1.7	MJ m^{-2} day^{-1}
σ_{L_n}	0.05	1.15	0.5	MJ m^{-2} day^{-1}
σ_{r_a}	0.1	100	3	s m^{-1}
σ_{r_s}	?	?	? (but high)	s m^{-1}

2.3.1 Description of input data

2.3.1.1 Satellite PET

The MOD16 algorithm uses satellite data from the Moderate Resolution Imaging Spectroradiometer (MODIS) sensors, which are onboard NASA's Terra and Aqua satellites. The satellite-derived parameters are land cover, albedo, leaf area index (LAI), fraction of absorbed photosynthetically active radiation (FPAR), and enhanced vegetation index (EVI). Temperature, radiation, air humidity and pressure data are derived from daily global meteorological reanalysis data set from NASA's Global Modeling and Assimilation Office (GMAO). The algorithm, described in Mu et al. (2007) and Mu et al. (2011), uses the P-M approach. Data are available online in HDF (Hierarchical Data Format) files (NTSG, 2013). The spatial resolution of the cells is 0.926 km by 0.926 km, but was re-gridded to 1 km x 1 km for this study. Data are available in 8-daily, monthly, and yearly intervals. The monthly data were used in this study. Four variables are available in the HDF file: PET; AET; potential latent heat flux; and latent heat flux. Mean annual MOD16 PET and AET, compiled from monthly data, is shown in Figures 2.16 and 2.17. MOD16 data currently covers the period January 2000 to December 2015. For this study, monthly MOD16 PET and AET from 2000 to 2014 were used as input in the method, as it could be best evaluated against ground observations. These data will be called *original MOD16 PET* and *original MOD16 AET* onwards.

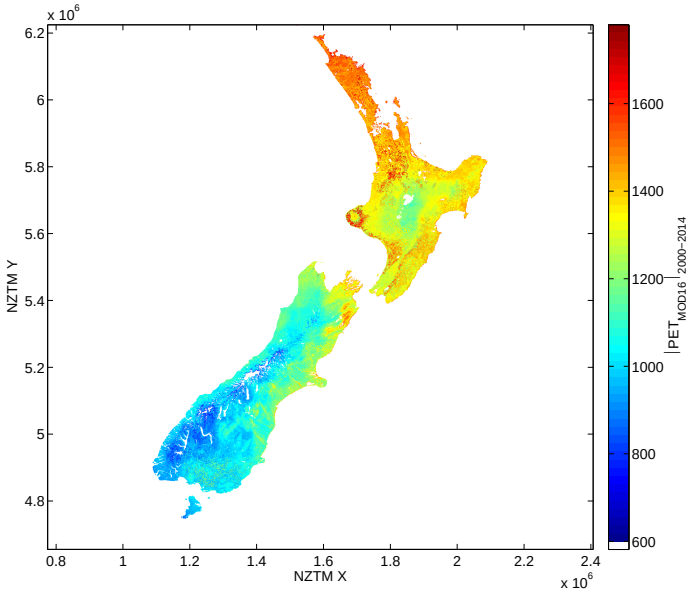

Figure 2.16: Original MOD16 PET. Mean annual value for 2000-2014.

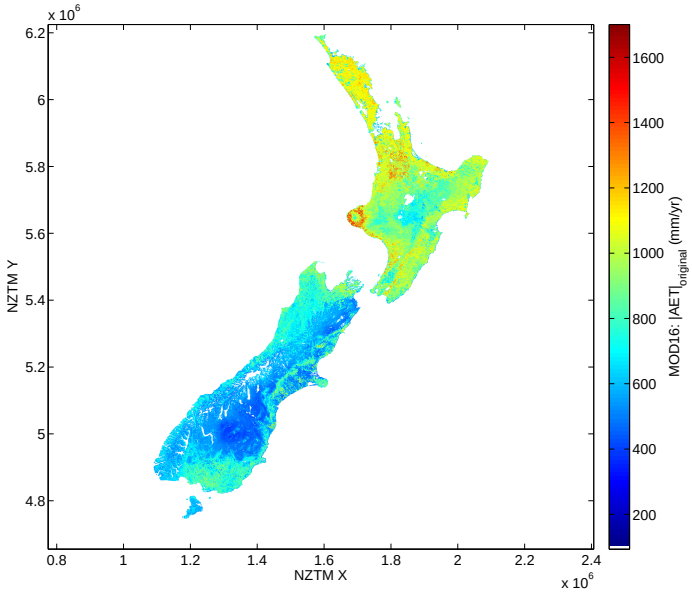

Figure 2.17: Original MOD16 AET. Mean annual value for 2000-2014.

2.3.1.2 Ground-observed reference crop ET

Reference crop ET ground observations from 112 climate stations (Fig. 2.18) were downloaded from the New Zealand's Climate Database web portal CliFlo (NIWA, 2014). Data were compiled to monthly values from January 2000 to December 2014. Some stations do not cover 2000-2014 entirely, and there are also gaps for some years and months in the data. Data from the climate stations use simplified PET estimates: they have been processed using a Penman reference crop ET method based on Penman (1963). The PET values of this dataset are estimates of the PET of a reference crop, and do not reflect the effects of variations in land cover.

2.3.1.3 Climate data from the Virtual Climate Station network

Daily climate data from 1972 to current for New Zealand are available in a regular ∼5 km grid from the Virtual Climate Station (VCS) network (NIWA, 2014; Tait, 2014). The VCS data used in this research were rainfall according to Tait et al. (2006); Penman reference crop ET; relative humidity; solar radiation; maximum and minimum temperature; and wind speed.

2.3.1.4 Mean annual AET from Woods et al. (2006)

Another dataset on mean annual AET that was used for comparison is from Woods et al. (2006). They estimated mean annual AET from the land surface for the period 1960-2006. First, 70 climate stations located throughout New Zealand

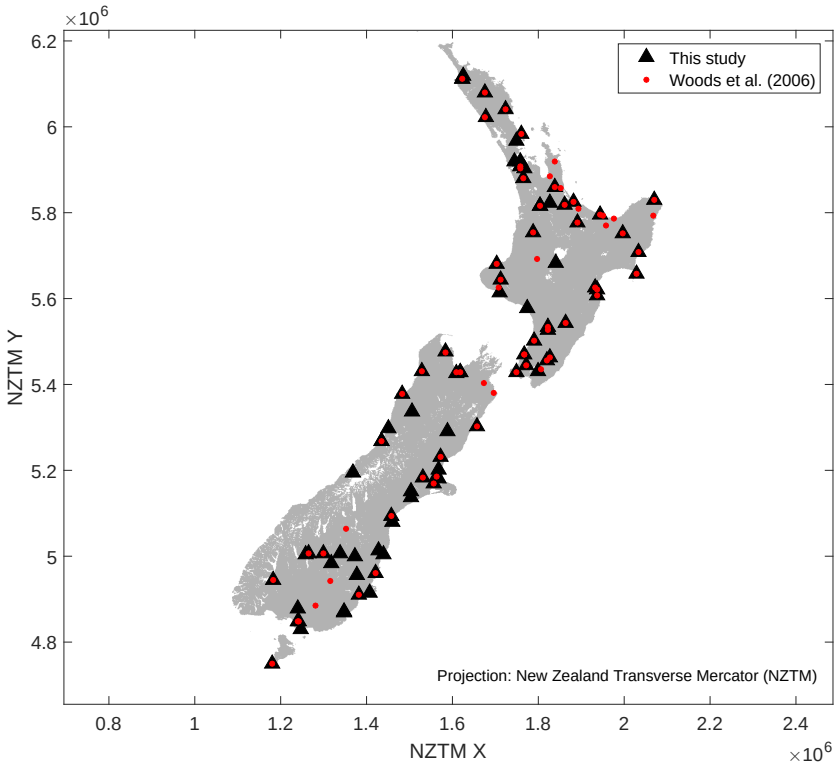

Figure 2.18: Location of 112 ET_0 climate stations used in this study. Locations of 70 climate stations used by Woods et al. (2006) are shown in red dots.

(Figure 2.18, red dots) were used in building the national map of PET. These stations have recorded daily Penman potential ET (Penman, 1948) data for the period 1972 to 2003. No crop corrections to real PET are used. Interpolation of the climate station PET to a national map was done using a trivariate thin-plate spline interpolation method using elevation, latitude and longitude by Tait and Woods (2007). Woods et al. (2006) then calculated AET from PET using an algorithm of Zhang et al. (2004) (Equation 2.21). Data have been re-gridded from original spatial resolution of 500 m by 500 m to 1 km by 1 km for this study. These data are called '*AET Woods*' onwards.

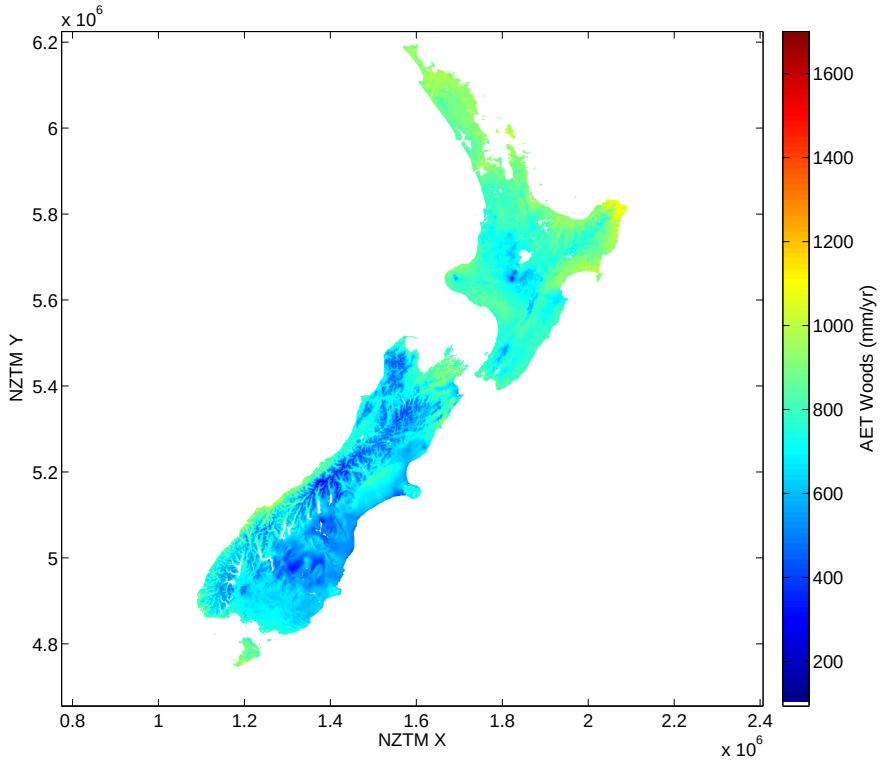

Figure 2.19: AET after Woods et al. (2006).

2.3.1.5 Lysimeters

Lysimeters in the Canterbury Plains were used to derive AET. These dryland lysimeter sites are at 4 locations (Table 2.4). These lysimeter stations have measured rainfall recharge and data have been analysed compared with other model outputs extensively by White et al. (2003, 2014a). Data were compiled for this research by White (2013). Since no surface runoff due to terrain slope is expected at these locations in the plains, a simple assumption was made that long-term AET at these stations equals rainfall minus measured rainfall recharge. These rainfall and rainfall recharge data are described in more detail in Chapter 4 of this thesis.

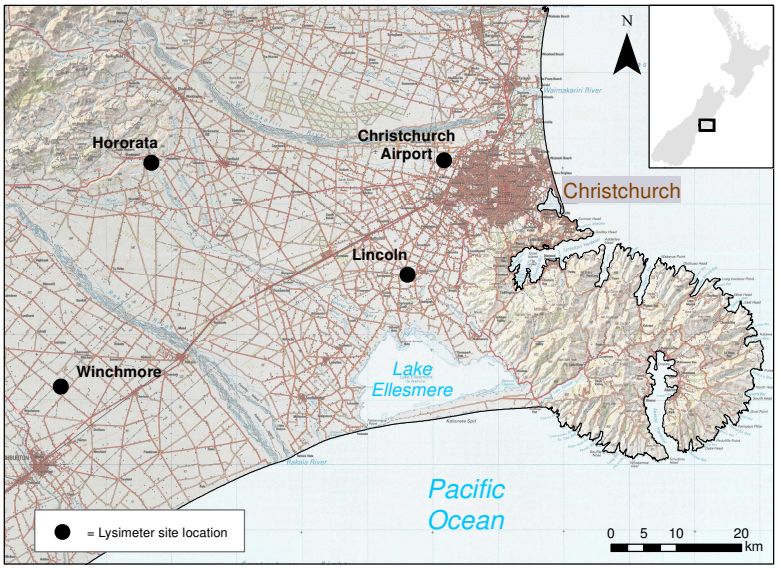

Figure 2.20: Lysimeter sites in the Canterbury Region. Adapted from: White et al. (2014a). The soil property PAW is explained in Chapter 4.

Table 2.4: Description of four dryland lysimeters stations in the Canterbury Plains

	NZMG East	**NZMG North**	PAW (mm)	**Description**
Airport	2471700	5746600	45	Very stony sandy loam
Hororata	2426900	5742600	75	Stony silt loam
Lincoln	2466100	5729100	170	Silt loam on sand
Winchmore	2413000	5712200	95	Stony silt loam

2.3.2 Using uncertainty to combine satellite and ground-observed PET

2.3.2.1 Estimation of uncertainty of P-M derived ET

2.3.2.1.1 Uncorrelated random values

One million uncorrelated random realisations of ET_0 of core input components (T, RH, α, n/N, S0 and u2, according to Table 2.2) were used to calculate e_s, Δ, R_n according to section 2.2.2 and the reference crop Penman-Monteith equation (Allen, 1998). Then, a million random realisations of uncertainties in the core input components, according to Table 2.3, were used to calculate a 'noisy' ET_0. The uncertainty in all realisations were normalised to ET_0 (Figure 2.23). A million values were chosen to have a reasonable amount of values to average over the entire range of parameters, without losing too much computational power (i.e., 1e7 values took significantly longer to test with).

2.3.2.1.2 Correlated random values

For both Penman and FAO reference crop ET, a set of one million correlated random realisations of the core input components were generated using VCS climate data. Correlated random realisations of d components fall within a multivariate normal distribution f (Mathworks, 2014; Rose and Smith, 1996):

$$f(x, \mu, \boldsymbol{V}) = \frac{1}{\sqrt{\mid \boldsymbol{V} \mid (2\pi)^d}} e^{\frac{1}{2}(x-\mu)\boldsymbol{V}^{-1}(x-\mu)}, \tag{2.23}$$

with f a function of 1-by-d vectors x (locations within distribution), μ (means of input components), and d-by-d variance-covariance matrix $\boldsymbol{V}$. The input components were T, RH, S_0, u_2,α and n/N. Before applying Eq. 2.23, these preprocessing steps were taken:

- Daily VCS T_{min}, T_{max}, RH, u_2 and solar radiation Rad were compiled to monthly values;
- T was estimated as $T = (T_{min} + 2T_{max})/3$
- Monthly S_0 throughout the year was estimated from Hendriks (2010) (his Figure B2.12.2);
- Although albedo values for the FAO and Penman methods are fixed ($\approxeq$ 0.25), they were randomly distributed in between 0.08 (water) and 0.4 (dry sand), to look at the sensitivity of the methods to this input component;
- n/N was calculated using Eq. 2.10 and 2.11:

$$\frac{n}{N} = \frac{Rad}{S_0 b_s} - \frac{a_s}{b_s} \tag{2.24}$$

or for the assumptions of a_s and b_s being constants of 0.25 and 0.5, respectively (Eqs. 2.11 and 2.12):

$$\frac{n}{N} = \frac{2Rad}{S_0} - 0.5 \tag{2.25}$$

- μ and $\boldsymbol{V}$ were calculated.

Values and uncertainties for further input components in e_s, e_a, Δ, R_n were then calculated with Eqs. 2.5 to 2.13. This was done with basic error propagation using Eq. B1.

All resulting input components were then used to generate one million realisations of ET_0. Then, a million random realisations of uncertainties in the core input components (from the variances on the diagonal of $\boldsymbol{V}$, according to Table 2.5) were used to calculate a 'noisy' ET_0. The difference between the normal and noisy ET_0 is called the uncertainty in ET_0, or σ_{ET0}. All realisations of σ_{ET0} were then normalised to ET_0.

The ET_0 - σ_{ET0} relation was then averaged per ET_0 value (bin size ~0.33) and fitted to a function with a smoothing spline fit (Mathworks, 2015b). This function, describing the uncertainty of in-situ ET, was used in the further calculations. For further processing, it was assumed that the maximum uncertainty of satellite PET can be 50% larger than ground-observed ET_0 uncertainty (further elaboration of this assumption is in the discussion of this chapter).

2.3.2.2 Projection of satellite PET to ET_0 ground observations

Monthly PET were imported from MOD16 and ground-observed data, with the uncertainty in ET as estimated in section 2.3.2.1.2. A linear relation between original MOD16 PET and ground-observed ET_0 data was calculated for both annual and monthly data using a Monte-Carlo approach. This was done by analysing 1000 realisations of MOD16 PET and ground-observed ET_0 with least squares fitting. The number of 1000 was mostly practically chosen, it was taken to obtain reliable estimates, without the routine becoming too slow, i.e., too much computational effort on a standard desktop. Each realisation used a random deviation within the uncertainties of both datasets. When the linear fit is defined as $y = Ax + B$, the realisation with the lowest χ^2 coefficient was chosen as the best fit. χ^2 is defined by Taylor (1997) as:

$$\chi^2 = \sum_{i=1}^{N} \frac{(y_i - B - Ax_i)^2}{\sigma_y^2}, \tag{2.26}$$

with: x representing the ground observations; y the original MOD16 PET data; σ_y the standard deviation for y; and N the number of ground observations. Using the A and B of the best fit, the original MOD16 PET was then re-written as:

$$MOD16_{orig} = (A \pm \sigma_A)\, ET_0 + B \pm \sigma_B, \tag{2.27}$$

in which σ_A and σ_B are the standard deviations in slope and intercept, respectively. These were derived by calculating the standard deviation of the χ^2 distribution. To account for seasonal variation, original MOD16 PET for each month was fitted to ground-observed ET_0. This led to 12 solutions (January to December) for slope and intercept. These were then used to project original MOD16 PET to ground-observed ET_0 using slope and intercept of the best linear fit for each month:

$$MOD16_0 = \frac{MOD16_{orig} - B}{A}, \tag{2.28}$$

with estimated uncertainty:

$$\sigma_{MOD160} = \sqrt{{\sigma_{MOD16_{orig}}}^2 + {\sigma_A}^2 + {\sigma_B}^2} \tag{2.29}$$

2.3.2.3 Estimation of uncertainty of MOD16 PET and AET

Using the uncertainty of $MOD16_0$ data, I define normalised uncertainty as:

$$\tilde{\sigma}_{ET} = \frac{\sigma_{MOD16_0}}{MOD16_0} \tag{2.30}$$

Uncertainty of MOD16 monthly PET and AET was estimated with Eq. 2.30:

$$\sigma_{MOD16_{PET}} = \tilde{\sigma}_{ET} MOD16_{PET} \tag{2.31a}$$

$$\sigma_{MOD16_{AET}} = \tilde{\sigma}_{ET} MOD16_{AET} \tag{2.31b}$$

2.3.3 Correction of long-term mean PET to AET using a 'dryness index'

MOD16 monthly PET and AET data, including uncertainty, were converted to mean annual values. The mean MOD16 AET was stored for further comparison; the MOD16 mean annual PET data were converted to an alternative AET estimate using the relation from Zhang et al. (2004), as also used by Woods et al. (2006), which calculated AET from mean annual precipitation and PET using Equation 2.21. This approach can only be used for long-term mean annual data.

Uncertainty was estimated by: propagating the RMSE of P (= 15% of P, according to Tait et al., 2006) through Eq. 2.21 to get σ_{AET_P}; propagating $\sigma_{MOD16_{PET}}$ from Eq.2.31a through Eq. 2.21 to get $\sigma_{AET_{PET}}$; and then joining the two uncertainties as:

$$\sigma_{AET,MOD16_{Zhang}} = \sqrt{{\sigma_{AET_P}}^2 + {\sigma_{AET_{PET}}}^2} \tag{2.32}$$

Further analyses and comparison of data followed these corrections. These are described in the results section 2.4.3.

2.4 Results

2.4.1 Estimation of uncertainty of P-M derived ET

2.4.1.1 Uncorrelated random values

Sensitivity of ET_0 to each of the six core input component is shown in Figures 2.21 (FAO56) and 2.22 (Penman). FAO56 ET_0 is less sensitive to components T, RH, and S_0 than Penman ET_0. Therefore, FAO56 ET_0 values are lower than Penman ET_0. Furthermore, the deviation σ because of binning, as well as the deviation ϵ_{noise} caused by a 'noisy' input (see sub-section 2.3.2.1.1), are smaller for FAO56 ET_0 than for Penman ET_0. Normalised uncertainty $\sigma_{\tilde{ET}}$ (Eq. 2.30) is shown as a percentage for the FAO56 and Penman methods in Figures 2.23 and 2.24, respectively. $\sigma_{\tilde{ET}}$ is high for low ET_0 ($\sim$23% for FAO56 and $\sim$30% for Penman). For the FAO56 method, $\sigma_{\tilde{ET}}$ decreases to $\sim$5% for increasing ET_0. For Penman however, a minimum of $\sim$18% is found for $\tilde{\sigma}_{ET}$ at an ET of 2 mm/day, after which it rises again to $\sim$30% for high ET values. Standard deviation of $\sigma_{\tilde{ET}}$ due to binning is lower for the FAO56 method than for the Penman method.

2.4.1.2 Correlated random values

Correlated random values of the core components lead to slightly lower ET for FAO56 ET_0 2.25 compared to Penman ET_0 than for 2.26. Also, uncertainty of both methods are different (Figures 2.27 and 2.28). For FAO56, the uncertainty function σ_{ET} goes to $\sim$ 10 % of ET_0 for high ET and to $\sim$ 35% of ET_0 for low ET (Fig. 2.27). However, the Penmman method, although similar to FAO56 for low ET, shows high uncertainty, up to 30%, for high ET values 2.28. This means that Penman ET can have a higher absolute uncertainty (in mm/day) than the FAO56 method, and that this uncertainty is embedded in the method. Values and uncertainties for all ET input components, resulting from the multivariate random distributions, are shown as percentiles 1 and 99 (p1 and p99) in Tables 2.5 and 2.6. Fig. 2.25 shows that values of $ET_{0,FAO}$ range from approximately 0 to 10 mm/day (for Penman 0 to 15 mm/day, Figure 2.26), and that ET_0 is most sensitive to its input components temperature, followed by cloudiness ratio and relative humidity (the slope of the red line). The grey band denotes the standard deviation of ET_0 outcomes of all random generations, while the black-dotted line

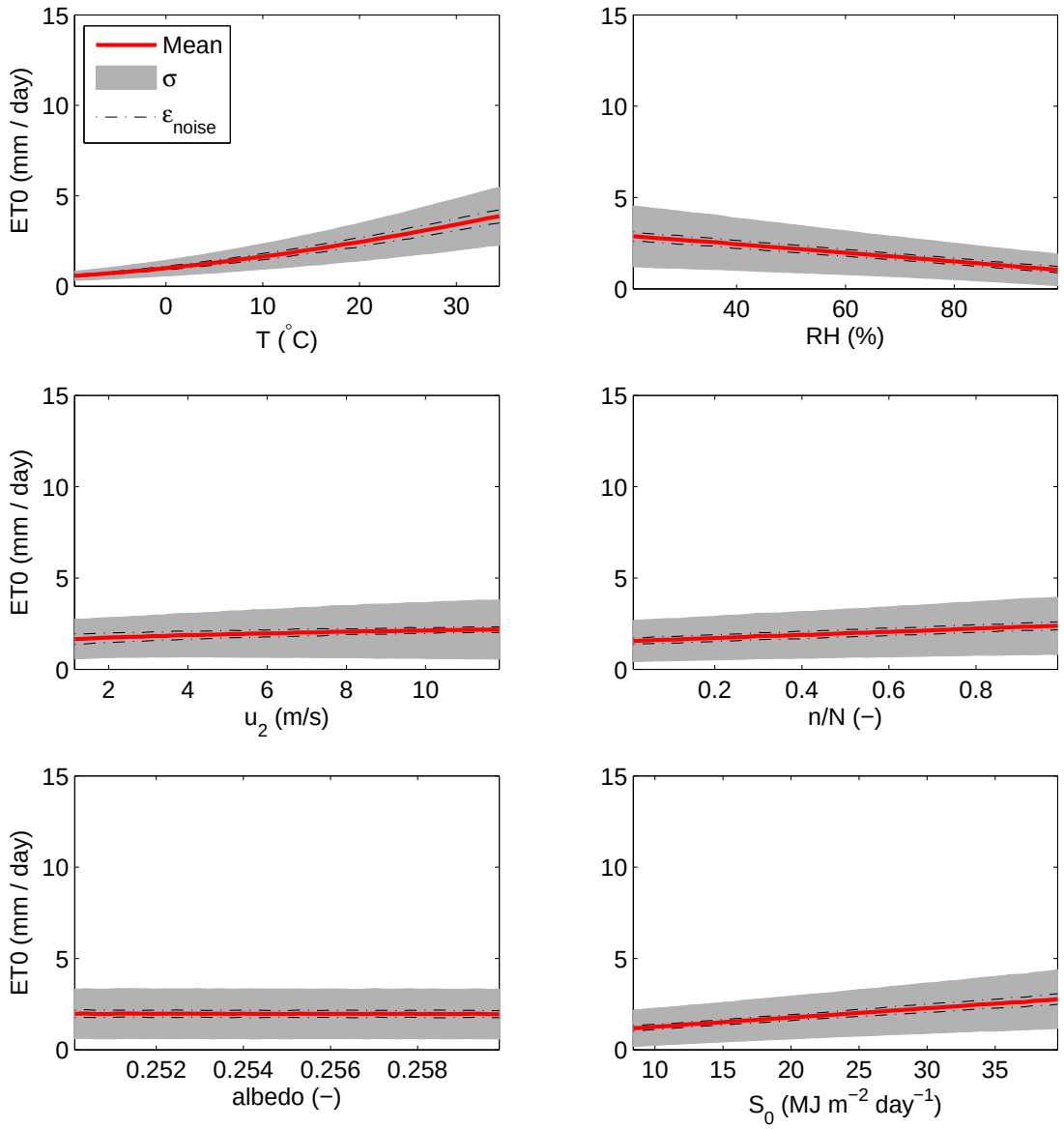

Figure 2.21: Means and standard deviation σ for $ET_{0,FAO56}$ for uncorrelated random values of the core input components T, RH, u_2, n/N, albedo α and S_0. ε_{noise} is the error when noise in the input components is introduced.

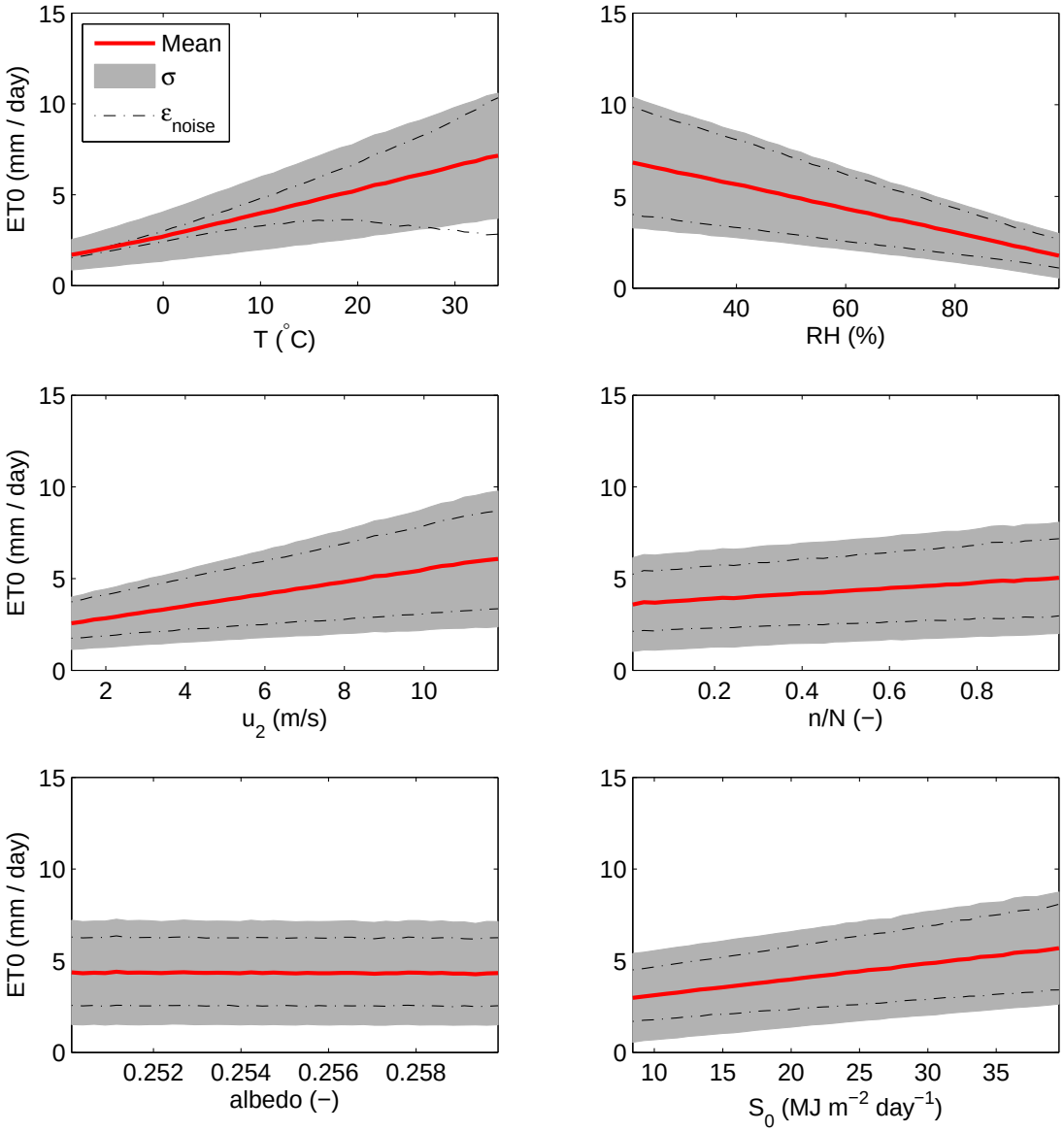

Figure 2.22: Means and standard deviation σ for $ET_{0,Penman}$ of uncorrelated random values of the core input components T, RH, u_2, n/N, albedo α and S_0. ε_{noise} is the error when noise in the input components is introduced.

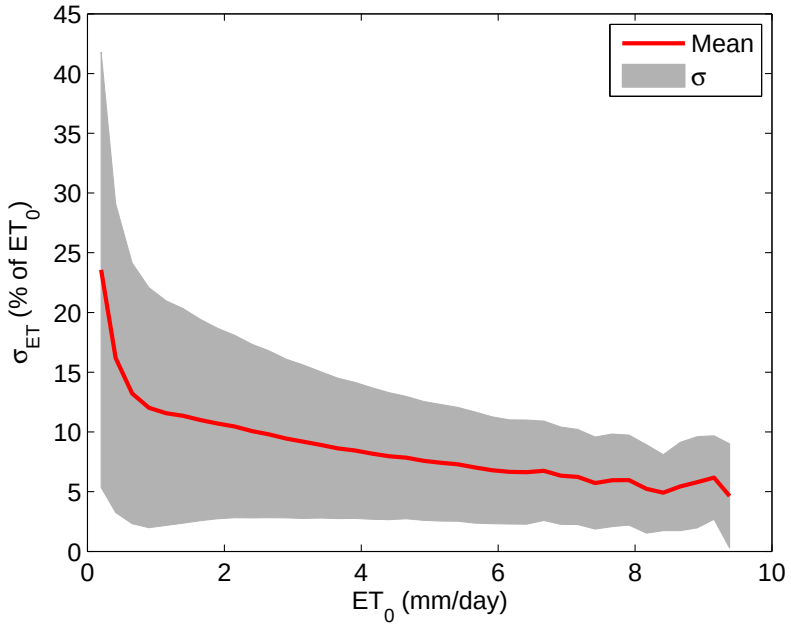

Figure 2.23: Means and standard deviation σ of the normalized uncertainty σ_{ET0} (FAO56) for uncorrelated random values of T, RH, u_2, n/N, albedo α and S_0.

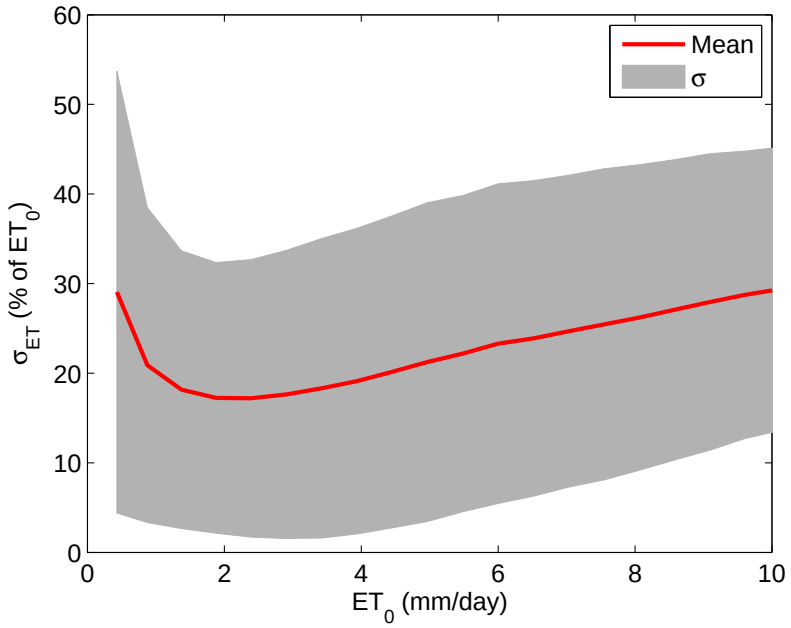

Figure 2.24: Means and standard deviation σ of the normalized uncertainty σ_{ET0} (Penman) for uncorrelated random values of T, RH, u_2, n/N, albedo α and S_0.

gives an estimate of the effect of noise per input component. These results can be used in further sensitivity analyses.

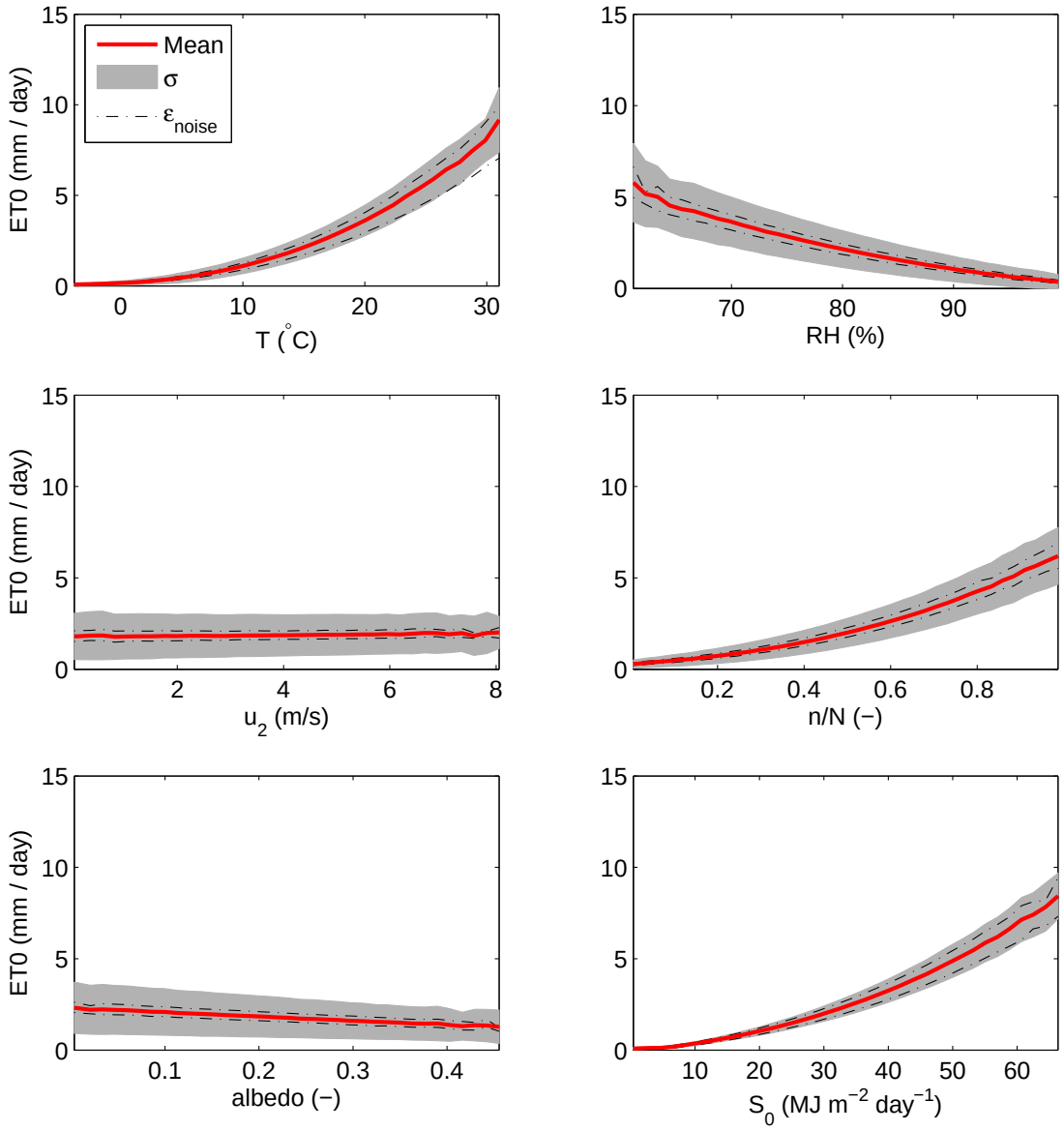

Figure 2.25: Means and standard deviation σ for $ET_{0,FAO}$ for correlated random values of the ET core input components T, RH, u_2, n/N, albedo α and S_0. ε_{noise} is the error when noise in the input components is introduced.

2.4.2 Projection of satellite PET to ET_0

All ground-observed data plotted against original MOD16 data shows that there is a clear linear relation between ground observations and satellite data (Figure 2.29). It also shows that the error bars (Figure 2.29, left) cloud the actual relation and makes this plots not easy to read. Therefore, I decided to plot my monthly plots without these error bars (such as in Figure 2.29,right).

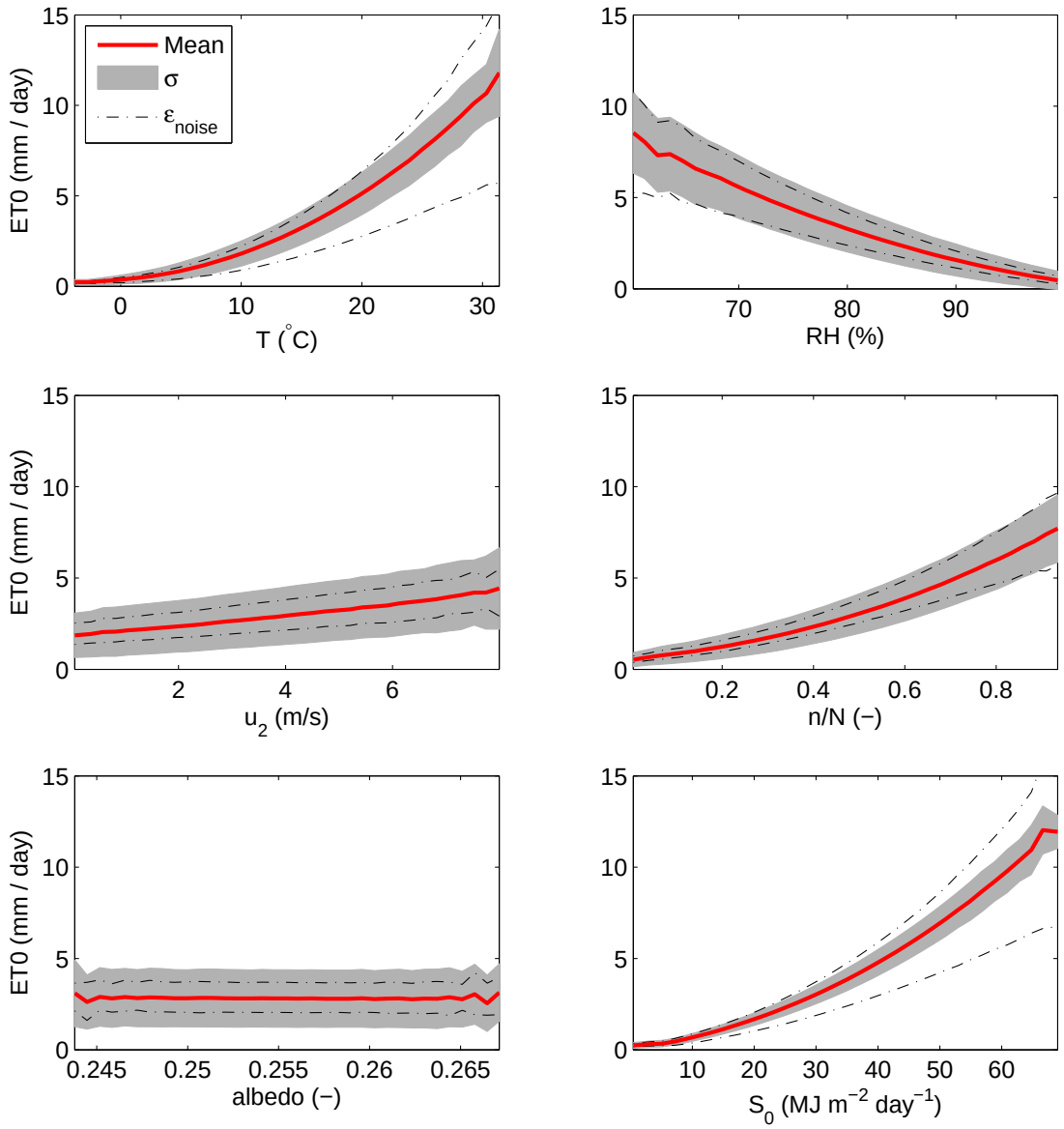

Figure 2.26: Means and standard deviation σ for $ET_{0,Penman}$ for correlated random values of the ET core input components T, RH, u_2, n/N, albedo α and S_0. ε_{noise} is the error when noise in the input components is introduced.

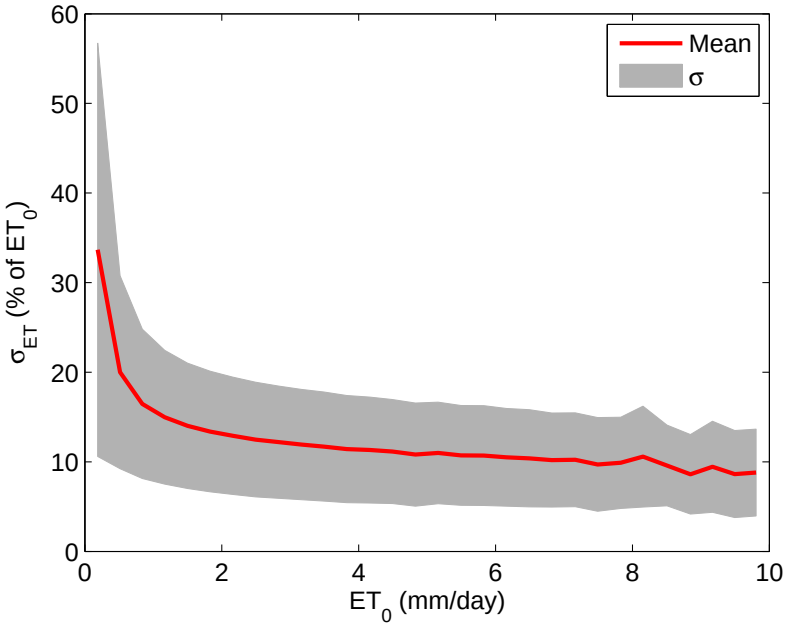

Figure 2.27: Means and standard deviation σ of the normalized uncertainty σ_{ET0} (FAO56) for correlated random values of T, RH, u_2, n/N, albedo α and S_0.

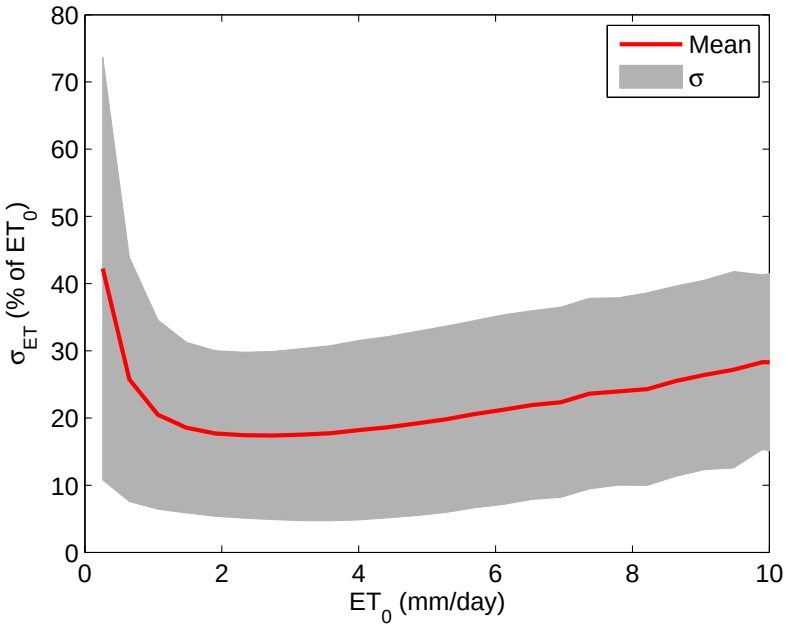

Figure 2.28: Means and standard deviation σ of the normalized uncertainty σ_{ET0} (Penman) for correlated random values of T, RH, u_2, n/N, albedo α and S_0.

Table 2.5: Values of components in the FAO56 and Penman equations through literature and multivariate distributions of VCS data. p1=1st percentile, p99=99th percentile.

	p1	p99	Units	Reference
Core input				
T	2.92	23.3	°C	
RH	69.8	96.2	%	
S_0	3.70	50.7	MJ m^{-2} day^{-1}	Hendriks (2010)
u_2	0.87	6.26	m s^{-1}	Tait and Zheng (2007)
α	0.08	0.40	-	Ahrens (2007); Oke (1992)
n/N	0.07	0.82	-	
Estimated through core input				
e_s	0.75	2.86	kPa	
Δ	0.05	0.17	kPa °C^{-1}	
S_n	1.03	25.4	MJ m^{-2} day^{-1}	
L_n	1.10	2.95	MJ m^{-2} day^{-1}	
R_n	0	22.8	MJ m^{-2} day^{-1}	

Table 2.6: Estimated uncertainties in input components of FAO56 and Penman equations. p1=1st percentile, p99=99th percentile.

	p1	p99	Units
Core input components			
σ_T	0.01	0.99	°C
σ_{RH}	0.55	4.96	%
σ_{S_0}	0	0	MJ m^{-2} day^{-1}
σ_{u_2}	0.51	1.49	m s^{-1}
σ_α	0	0.01	-
$\sigma_{n/N}$	0.05	0.15	-
Propagated with core input			
σ_{e_s}	0	0.14	kPa
σ_Δ	0	0.01	kPa °C^{-1}
σ_{S_n}	0.15	3.18	MJ m^{-2} day^{-1}
σ_{L_n}	0.30	0.46	MJ m^{-2} day^{-1}
σ_{R_n}	0	3.20	MJ m^{-2} day^{-1}

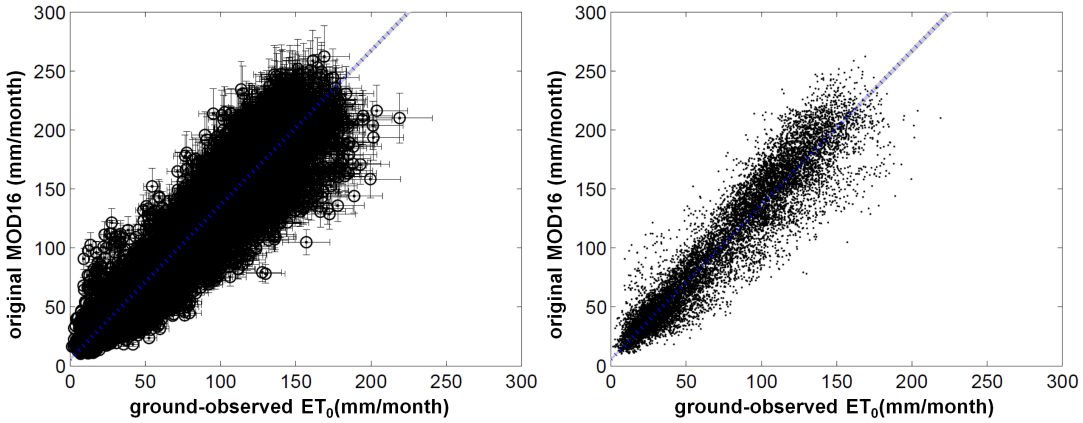

Figure 2.29: Fit of all data. Blue dashed line: best fits for all monthly data (plotted in black with error bars). Grey lines: linear fits within the (very small) standard deviations of slope and intercept. Error bars are shown left, while the point density is highlighted right.

Original MOD16 PET is generally higher than ground-observed ET_0; the difference between the two increases in warmer seasons (with higher PET, Figure 2.30). This is expected, as reference crop ET (ground-observed ET_0) is commonly smaller than real PET. Projection of satellite PET to Penman ET_0 leads to a new variable, MOD16 ET_0, based on monthly linear fits (Figure 2.31). All monthly slopes and intercepts, including standard deviations, are summarised in Table 2.8.

MOD16 ET_0 and ground-observed ET_0 mostly falls within each other's uncertainties (Figure 2.32), with the exception of a few outliers. Monthly MOD16 corrected data at the location of ground stations were compared at six randomly picked locations and years (Figure 2.33). MOD16 corrected data has similar trends and values for most locations. Some seasonal trends can be spotted in the MOD16 data, like an increase from May to August (2.33, topleft). These differences are picked up by the satellite and not by the ground-observed climate station and could be related to vegetation cover or growth.

RMSE values of mean monthly ET compared to ground-observed ET_0 are much smaller for MOD16 ET_0 than for the original MOD16 PET (Table 2.7).

Resulting monthly PET data from January 2000 until December 2013 are available in MATLAB structures, containing the data in two coordinate systems (NZTM2000 / EPSG:2193 and WGS84 / EPSG:4326). Gridded data are presented in a NetCDF (UCAR, 2014) file with 30 arc second resolution (Table 2.9). Mean annual PET and its uncertainty can be derived from this dataset, as shown in Figure 2.34 and Figure 2.35, respectively.

Table 2.7: RMSE (mm/month)of original MOD16 and MOD16 ET_0 compared to ground observed ET_0, based on mean values, excluding the uncertainty information.

Month	**original MOD16**	**MOD16$_0$**
January	57.2	18.8
February	47.6	14.3
March	38.8	12.7
April	26.9	10.4
May	21.3	10.4
June	19.0	9.9
July	17.3	9.4
August	18.9	9.4
September	26.9	11.7
October	37.6	14.1
November	47.0	16.9
December	57.8	18.0

Table 2.8: Sample sizes, slopes A, intercepts B and their uncertainties (σ_A and σ_B) for all monthly linear fits

	Sample size	A	σ_A	B	σ_B
AVERAGE	**1087**	**1.02**	**0.08**	**27.8**	**6.7**
Jan	1065	0.88	0.09	66.6	11.9
Feb	1078	1.12	0.09	28.2	9.1
Mar	1064	1.31	0.08	4.4	7.3
Apr	1082	1.28	0.07	6.4	3.3
May	1087	1.06	0.05	11.7	1.3
Jun	1085	0.93	0.05	13.0	0.8
Jul	1093	0.87	0.05	14.0	1.0
Aug	1105	1.05	0.07	9.8	2.3
Sep	1110	1.25	0.12	2.47	6.8
Oct	1092	1.02	0.11	27.0	9.2
Nov	1095	0.80	0.11	61.7	13.2
Dec	1083	0.70	0.11	88.2	14.6

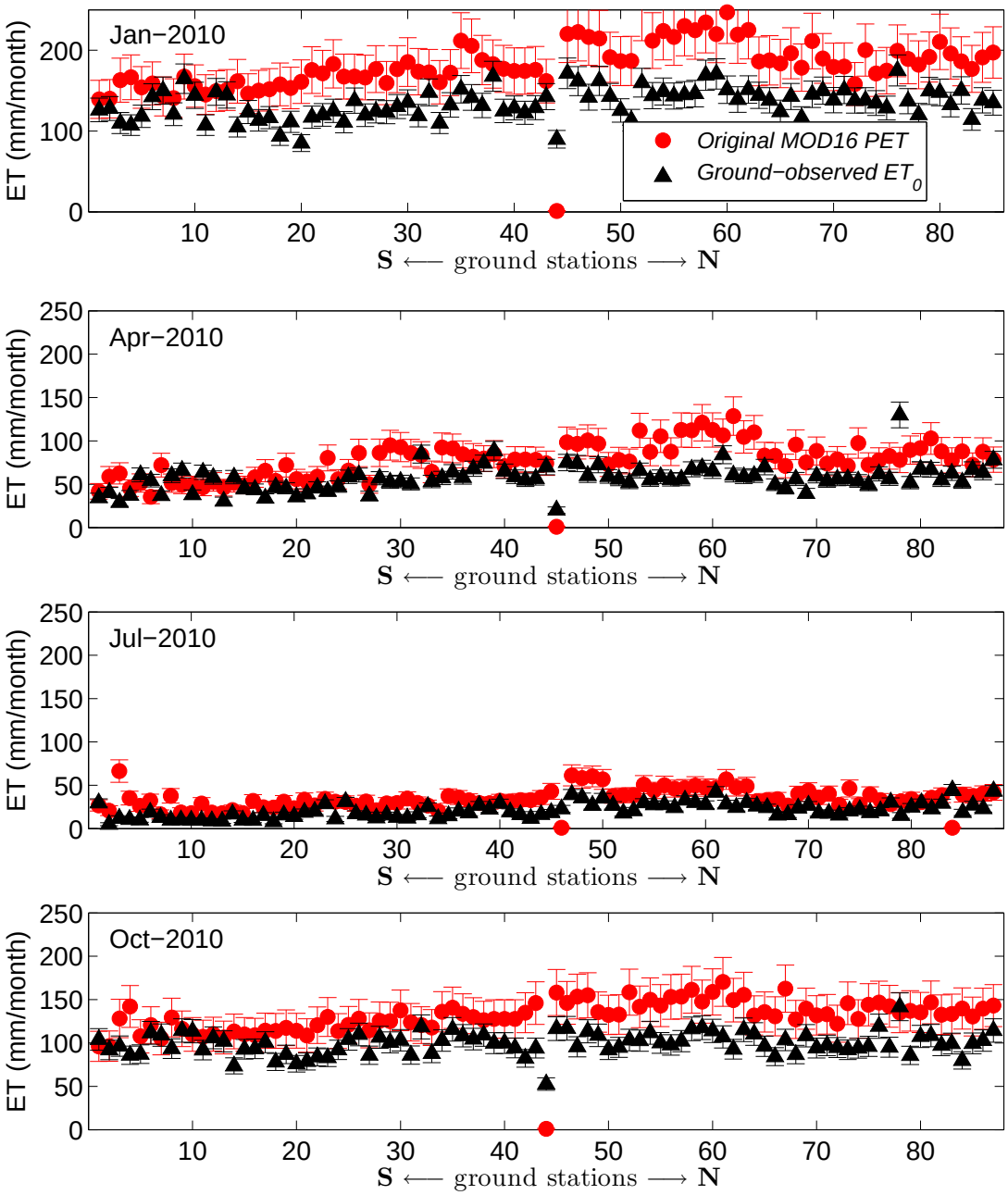

Figure 2.30: Original MOD16 PET for January, April, July and October of 2010 compared to ground-observed ET_0. The stations are plotted from the southernmost (left) to northernmost (right) locations.

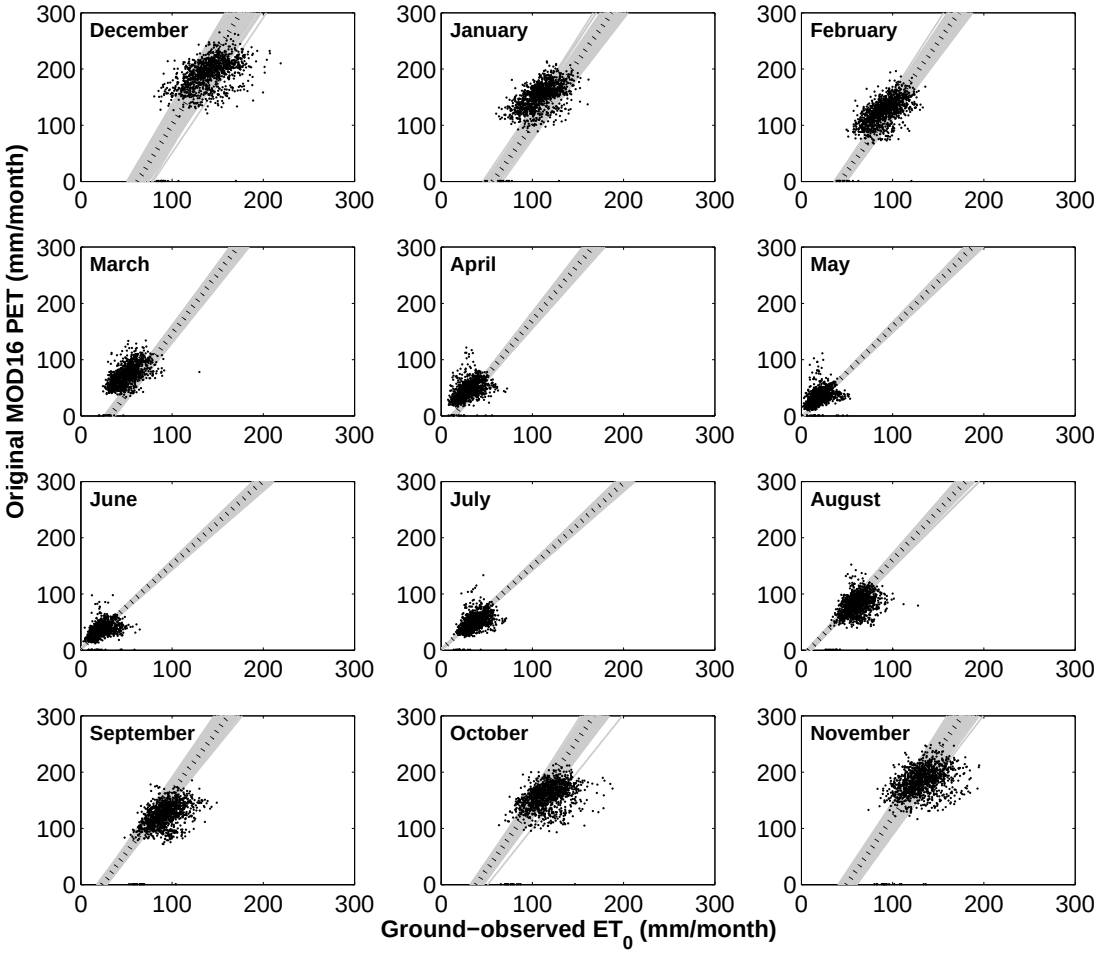

Figure 2.31: Monthly best fits for original MOD16 PET to ground-observed ET_0. Black dashed line: best fit per month. Grey lines: linear fits within the standard deviation of slope and intercept. Error bars are not shown.

Table 2.9: Specifications of MOD16 ET data files. Original MOD16 data has been regridded.

Format	NetCDF (UCAR, 2014), CF-1.6
Spatial resolution	30 arc seconds
Coordinate system	WGS84 (EPSG:4326)
Start	January 2010
End	December 2014
Time interval	monthly
Unit	mm/month
Data layers	monthly ET $MOD16_0$
	uncertainty in $MOD16_0$
	original MOD16 PET
	original MOD16 AET

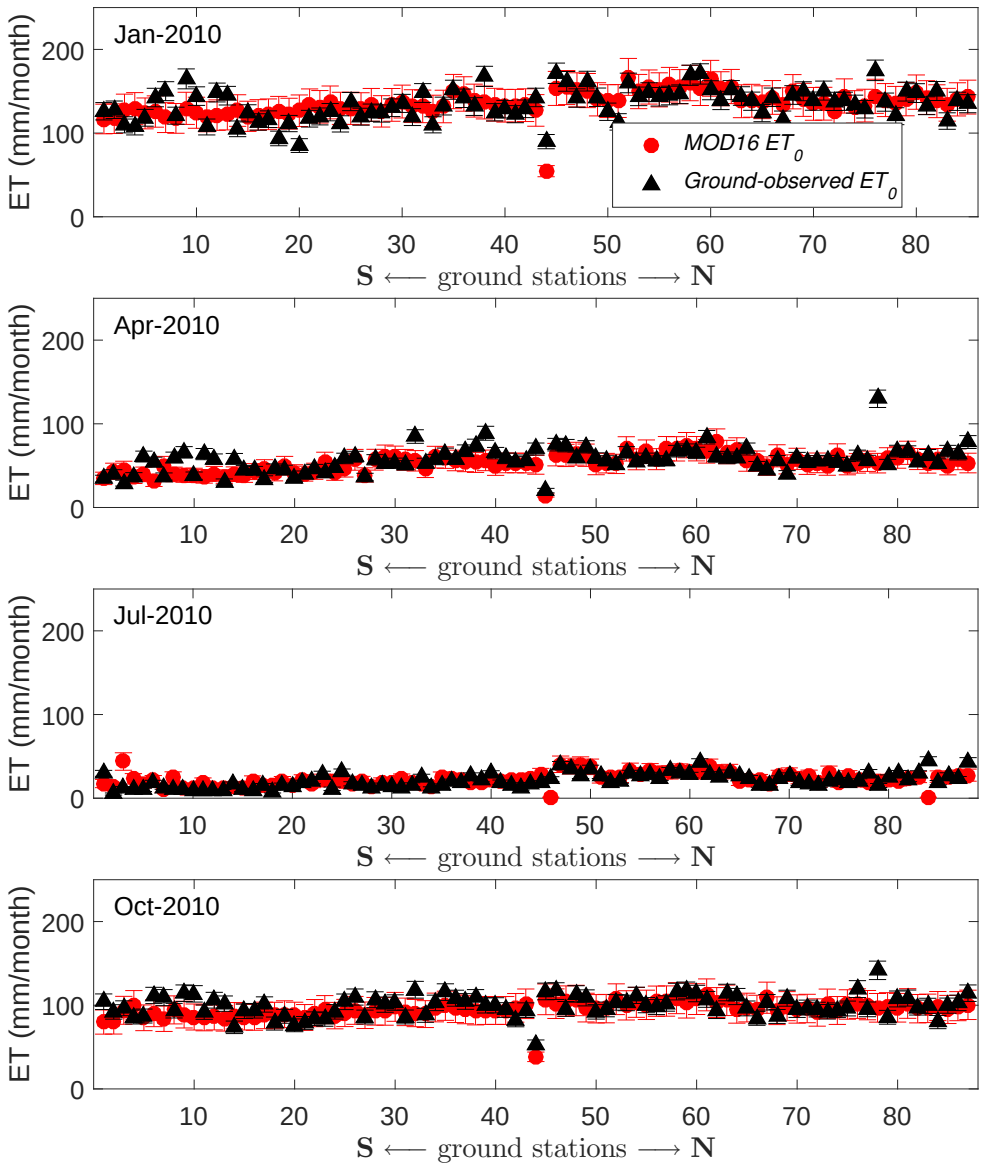

Figure 2.32: Monthly MOD16 ET_0 (red) and ground-observed ET_0 (in black) in January; April; July; and October of 2010.

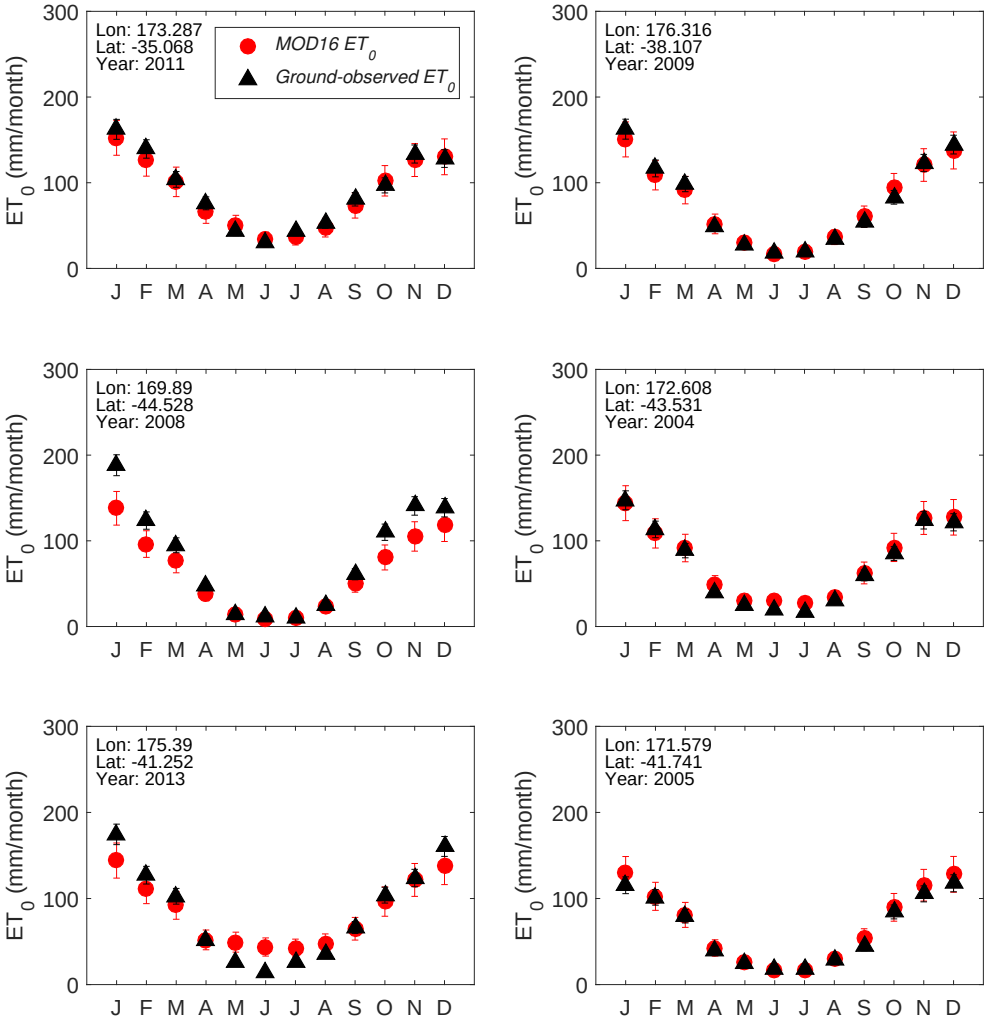

Figure 2.33: Monthly ET for all months at 6 randomly picked climate stations for MOD16 ET_0 (red dots) and ground-observed ET_0 (black triangles).

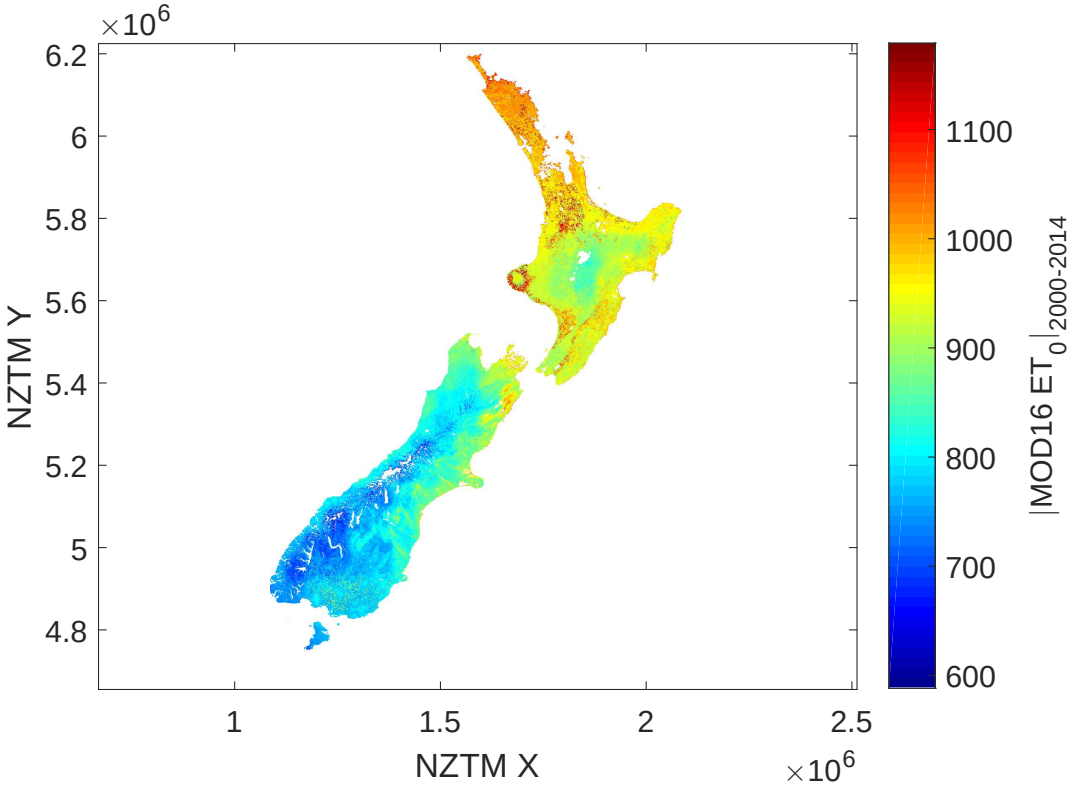

Figure 2.34: Mean annual MOD16 ET_0 (2000-2014).

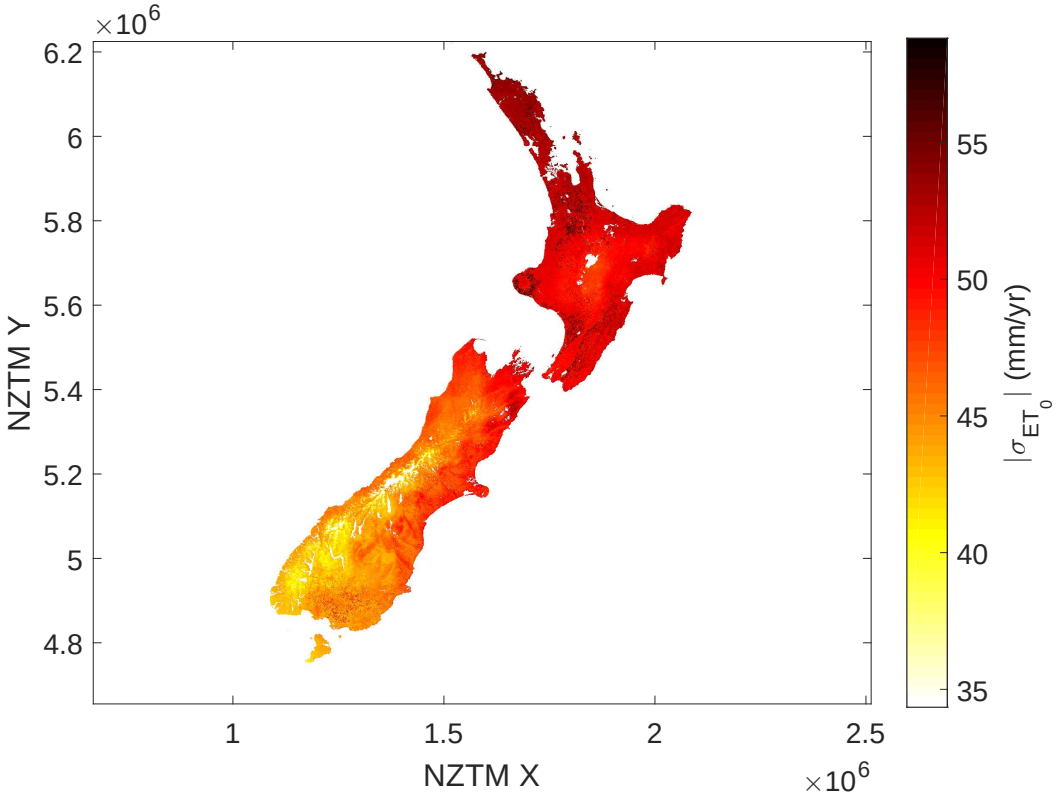

Figure 2.35: Mean annual σ_{ET0} of 2000-2014 MOD16$_0$ ET.

2.4.3 Correction of long-term mean PET to AET using a 'dryness index'

Mean annual values of MOD16 original AET data (Figure 2.36a) differ significantly from those estimated from MOD16 original PET through the algorithm of Zhang et al. (2004) ($AET_{MOD16_{Zhang}}$, Figure 2.36c). Uncertainty of MOD16 original AET, $\sigma_{AET,MOD16,original}$ (Figure 2.36b) is lower than that of $\sigma_{AET,MOD16,Zhang}$ (Figure 2.36d). Also, three datasets compared to each other give significantly different results, where $AET_{MOD16_{Zhang}}$ is higher than the original MOD16 AET (Figure 2.37) and AET Woods (986, 763 and 709, respectively, Table 2.10). The standard deviations (Table 2.10) show that the original MOD16 AET is more spatially diverse than AET Woods, despite having similar mean values. Figure 2.37 also shows that overall, mean annual MOD16 original data is similar to AET Woods, but local differences occur, e.g. in the Waikato and Taranaki Region (AET MOD16 original higher than AET Woods) or in the Marlborough Region and Stewart Island (AET Woods higher than AET MOD16 original).

Differences in uncertainty can be explained quite easily by the incorporation of a coarse error estimate of precipitation in Zhang's calculation (Equations 2.21 and 2.32). Explanation of the large differences in AET values requires further analysis with ground-observed data. Therefore, all mean annual AET values were compared to ground-observed AET: those derived from 4 lysimeter sites in Canterbury (map of sites in Figure 2.20). It was assumed that there was no runoff (so that AET equals rainfall minus recharge measured by the lysimeter, Table 2.11). MOD16 original AET data is closest to the ground-observed value at all lysimeters (Figure 2.38), where AET Woods and AET MOD16 Zhang are consistently too high. At the Hororata site, all AET values are significantly higher than the lysimeter observations. Therefore, it is concluded that, of the three compared datasets, original MOD16 AET values compares best with ground observations in the Canterbury Plains.

Table 2.10: Mean annual AET from three different AET estimates.

	AET (mm/yr)	stdev (mm/yr)
$MOD16_{original}$	764	213
$MOD16_{Zhang}$	986	214
Woods et al. (2006)	709	135

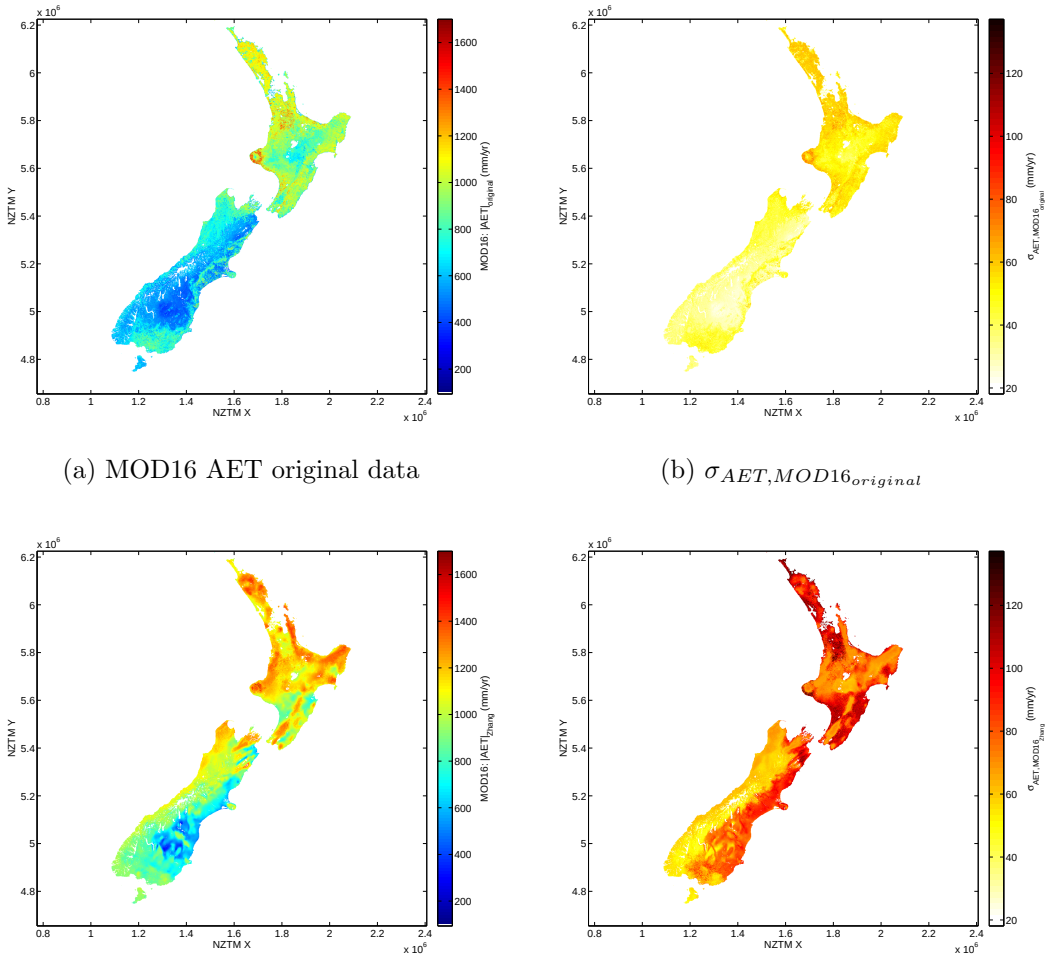

(a) MOD16 AET original data

(b) $\sigma_{AET,MOD16_{original}}$

(c) MOD16 AET, after Zhang et al. (2004)

(d) $\sigma_{AET,MOD16_{Zhang}}$

Figure 2.36: MOD16 corrected mean annual AET, after Zhang et al. (2004)

Table 2.11: AET measured from lysimeters in the Canterbury Plains from 1 July 1990 to June 30 2011 (White, 2013). Coordinate system is New Zealand Map Grid (NZMG)

	NZMG East	**NZMG North**	**RRECH (mm)**	**P (mm)**	**AET (mm)**
Airport	2471700	5746600	2041	7644	5603
Hororata	2426900	5742600	3113	8599	5486
Lincoln	2466100	5729100	1425	8065	6640
Winchmore	2413000	5712200	2483	8907	6424

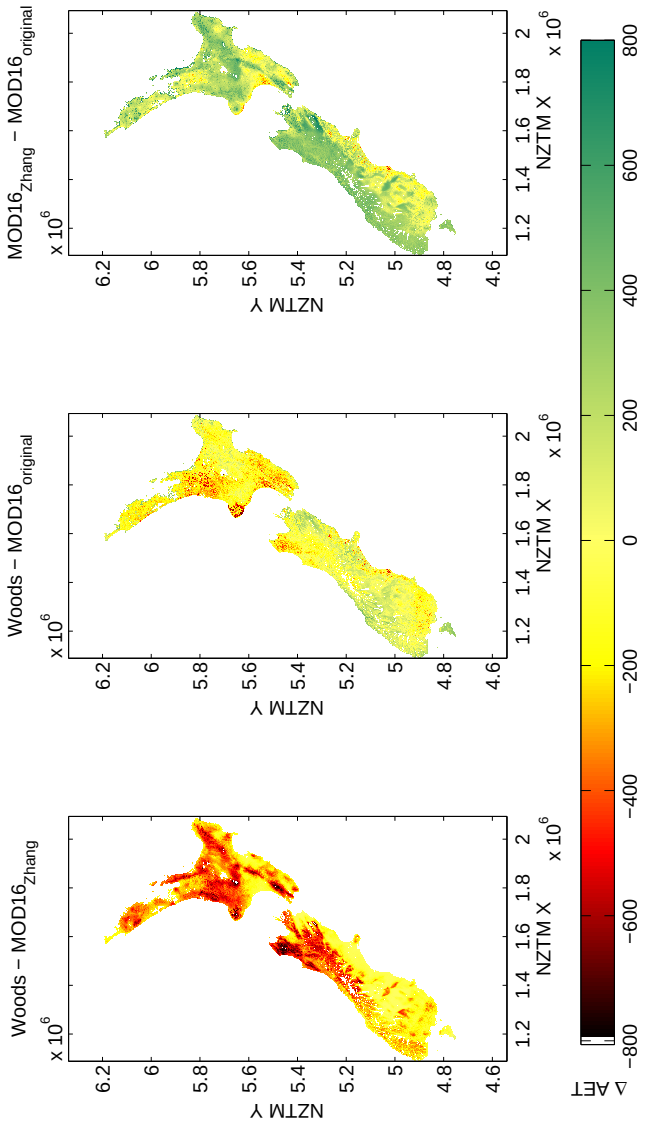

Figure 2.37: Difference between three AET datasets: Woods, MOD16$_{original}$, and MOD16$_{Zhang}$. Unit is [mm]

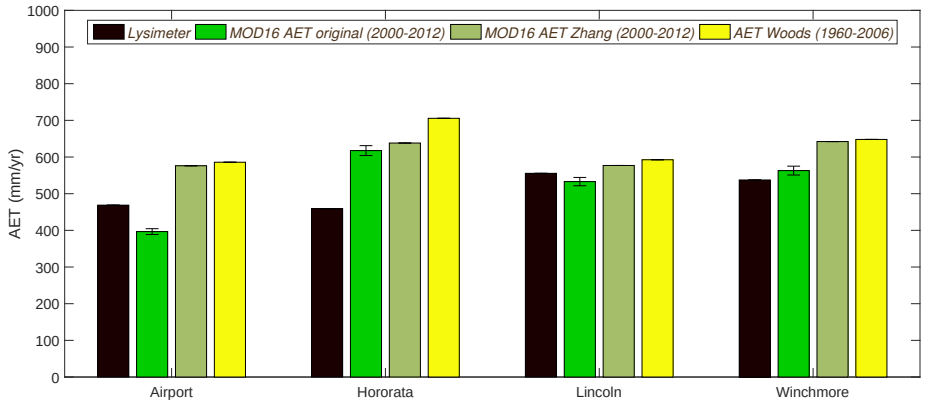

Figure 2.38: AET from lysimeters in Canterbury compared to AET from Woods, $MOD16_{original}$, and $MOD16_{Zhang}$

.

2.5 Discussion

2.5.1 Difference between FAO56 ET_0 and Penman PET

The name 'Penman PET', which is often used for Penman ET_0 (e.g., NIWA, 2014), can lead to some confusion. It might lead to the assumption that this PET does not need to be corrected for vegetation growth by crop factors. This assumption might be theoretically sound when looking at the Penman method: it only calculates the evaporation from a grass surface, does not incorporate any transpiration factors and therefore theoretically cannot contain a crop factor. However, in reality vegetation varies in height and thus in transpiration. Not accounting for transpiration is incorrect and it is therefore recommended that Penman PET should be replaced by FAO56 ET_0. If FAO56 ET_0 according would be used, crop factors K_c could be up to 1.3 (PET=K_c ET_0) in the growing season (depending on the crop type Allen, 1998).

Sub-sections 2.4.1.1 and 2.4.1.2 show that Penman ET_0 and its uncertainty are more sensitive to aerodynamic input components compared to FAO56 ET_0. To further analyse this, daily FAO56 ET_0 was calculated similar as in sub-section 2.3.2.1.1 (but with daily VCS data and albedo of 0.24 for grass) and compared to VCS (Penman) ET_0 estimates. Figure 2.39 (daily FAO56 ET_0 and VCS Penman ET_0 for 6 random locations in the year 2000) and Figure 2.40 (all VCS stations for 1 January 2000) confirm this: Penman ET_0 is higher than FAO56 in warmer areas or seasons, and lower in colder regions or seasons. Daily ET_0 show that the FAO56 is less sensitive than Penman ET_0 and thus appears to be more stable.

Although the Penman method lacks the contribution of transpiration, it artificially makes up for that by being more sensitive to, amongst others, temperature.

It therefore calculates a high evaporation from a grass surface in the warmer seasons and therefore, artificially, partly makes up for its missing transpiration component. The Penman PET thus more or less 'disguises' the fact that it lacks transpiration.

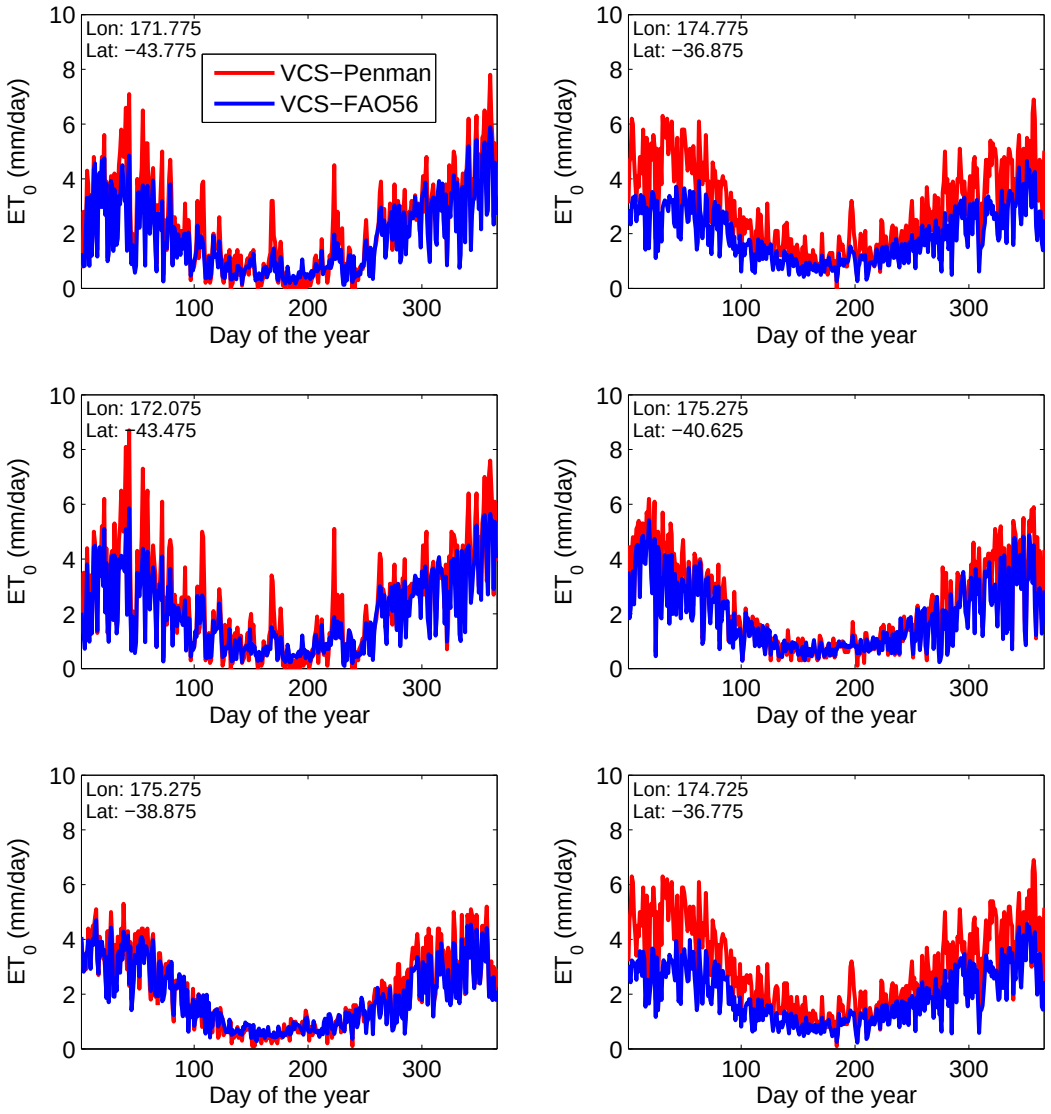

Figure 2.39: FAO56 ET compared to Penman ET for 6 random VCS stations in 2000.

Penman PET is mistakenly used as real PET by New Zealand researchers. For example, White et al. (2003) in their AET estimation (Eq. 2.22) assume a vegetation cover factor, including root factors to incorporate for plant transpiration. However, for Penman PET the vegetation cover only matters in the albedo estimation (soil could have a different albedo than grass for example). The wrong use of PET has thus led to wrong or wrongly calibrated correction methods of PET to AET. That does not necessarily mean that the calculated value of AET is wrong: using a wrong calibration on a wrongly estimated PET could still lead to a

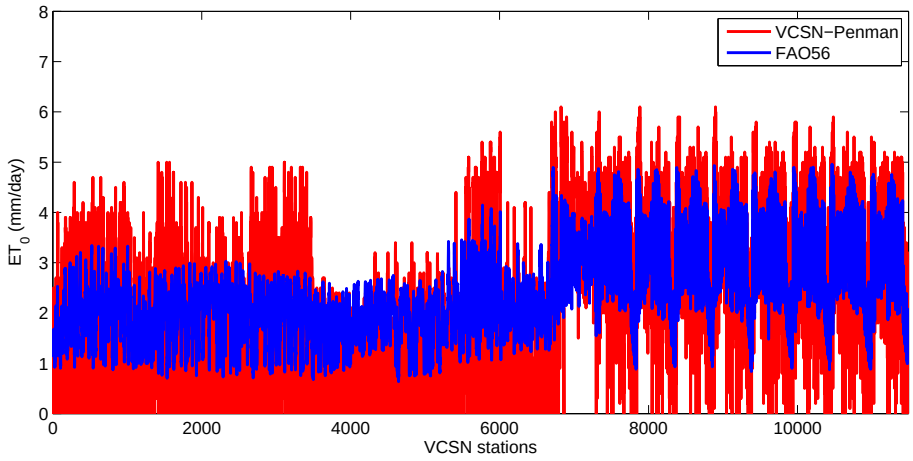

Figure 2.40: FAO56 ET compared to Penman ET for all VCS stations on 1 January 2000.

reasonable value of AET. However, these AET estimations lack scientific credibility. Another example of the wrong use of Penman PET is shown in Woods et al. (2006), who derive AET from mean annual Penman PET for long-term periods using Eq. 2.21 from Zhang et al. (2004). Penman PET values of Woods et al. (2006) (his Table 1) are compared to VCS Penman ET_0 values in Table 2.12. Values of Penman PET at ground observations correspond to VCS cells of Penman ET_0 (except for one outlier). This extra check thus concludes that Woods et al. (2006) did not correct Penman PET for any type of vegetation growth. In theory, this could lead to too low AET values. However, the calibration factor w used in Eq. 2.21 could have made up for this. This does not mean that the method of Zhang et al. (2004) is wrong: it might work with an improved PET estimation or a different calibration factor. Using long-term mean values of original MOD16 PET converted to AET using the same Eq. 2.21 does not show a solution, they perform worse than the Woods AET when compared to lysimeter data (Figure 2.38). Possibly a different calibration factor would be needed.

As the currently used deprecated Penman PET estimation was shown to lack scientific credibility, and calibrations that were used cannot be traced back, it is hard to say if AET from Woods et al. (2006) is wrong and if so, where. In fact, Figure 2.41, a zoom-in of Figure 2.37 for the Canterbury Region, shows that areas where AET Woods is lower than original MOD16 AET are just as plentiful as areas where AET Woods are higher, e.g. at the locations of the lysimeters (Figure 2.38). Higher values of Woods AET could be caused by the fact that Woods et al. (2006) do not incorporate rainfall recharge in their long-term water budget: they assume a long-term water balance of

$$P - AET = Q, \tag{2.33}$$

where Q is the runoff. As rainfall recharge can be tens of percents of the precipitation in plains (e.g., White, 2001; White et al., 2003, 2014b), this could explain the too high AET found at the lysimeter sites. As mentioned, in some regions, AET

Woods is lower than the original MOD16 AET. At this stage, it is not possible to point out which AET is correct.

One advantage to use of the original AET MOD16 data, is that it comes with an uncertainty estimation. For example, Woods et al. (2006) used a trivariate thin-plate splicing interpolation techniques to interpolate PET between 70 climate stations, where they iterated until the error at the climate stations was almost zero. They did not take into account uncertainty of the ground-observed data. As shown in this research and by others (e.g., Baldocchi et al., 2001), climate station ET data can have an uncertainty up to tens of percents.

Table 2.12: Mean annual Penman PET values for long term periods mentioned in Woods et al. (2006) (their Table 1), compared to VCSN Penman PET values NIWA (2014); Tait (2014). All PET values in mm/yr.

	Ohakea Aero	**Kelburn**	**Nelson Aero**	**Christchurch Aero**	**Invercargill Aero**
Period	1972-1990	1962-1995	1972-1990	1972-2001	1972-1994
In situ	1043.6	880.7	923.1	933.8	782.2
VCSN	874.6	897.7	934.9	950.8	798.4

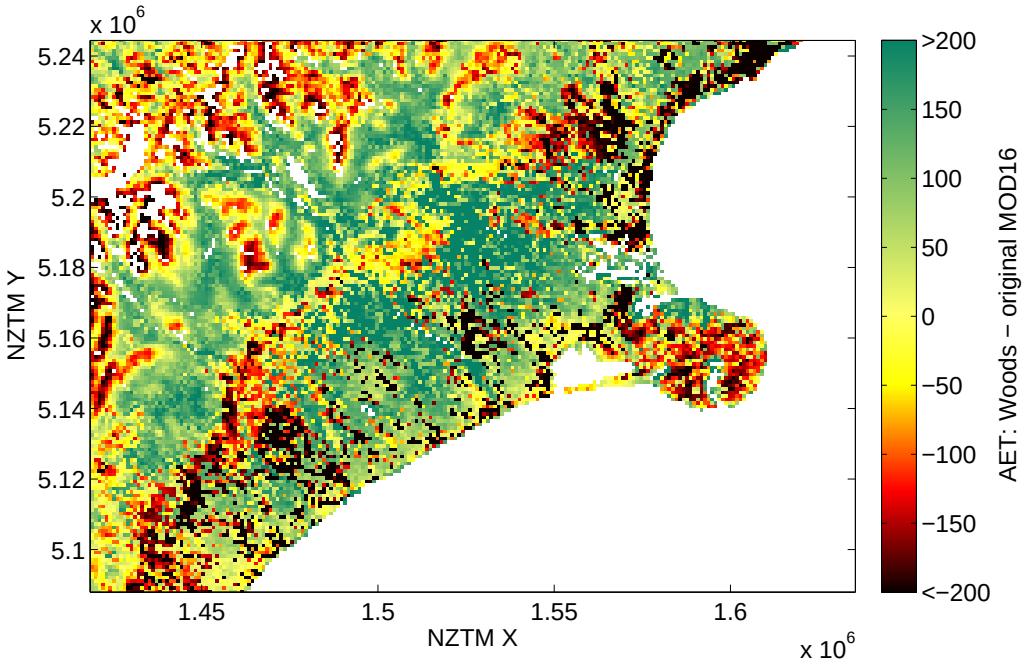

Figure 2.41: AET from Woods et al. (2006) minus AET from original MOD16 data.

2.5.2 Quality of the newly developed MOD16 ET_0

The main advantage of the presented monthly MOD16 ET_0 dataset is that it has a high resolution (1 km x 1 km), has uncertainty information, and takes into account vegetation characteristics (as measured by MODIS), while still abiding to the locally used standards in ground observations. Other gridded ET estimates (i.e., 5 km x 5 km daily Penman PET estimates from Tait and Woods, 2007) are interpolated based on elevation. Elevation is indeed related to ET input component temperature and solar radiation, but not necessarily to e.g. albedo, wind speed or land cover.

A potential drawback of MOD16 satellite data is that input data on global meteorology are from global sources and could maybe not capture climate diversity of countries like New Zealand, making the data less reliable. However, the comparison with original MOD16 data and Penman ground observations in colder months (Fig. 2.30) shows that original MOD16 data is just slightly higher than Penman ET. This is as expected: a slightly higher ET in relatively colder months shows the minor difference that the transpiration causes. The qualitative trend shows this difference increasing in warmer months, which seems to be correct. Although having a potentially larger error, the original MOD16 PET data could be used as a first estimate of PET, as it is the only estimate taking into account vegetation characteristics. This could potentially enhance the capability of this dataset to be used for irrigation studies (i.e., the data could be used to analyse crop growth in irrigated areas). However, there are no ground observations through which the original MOD16 PET can be validated, except for the mentioned correct qualitative trend. Satellite MOD16 data as presented in this research could be used to improve existing daily (VCS) estimates: merge of $MOD16_0$ datasets with those from Tait and Woods (2007), followed by a second merge to PET estimates using the original MOD16 data, could help score out the potential drawbacks of each method, and could aid in better estimation of crop coefficient factors using the best-fit values from Table 2.8. A conversion of ET ground observations from Penman to FAO56 would help improve this merge.

Another potential drawback of the correction method is that I have corrected a reference ET_0 with PET ('compared apples with pears'). PET from MOD16 contains vegetation information. By correcting to Penman PET, which does not contain this information, I introduce vegetation information, but at the same I thus more or less 'cloud' this vegetation information by correcting it to Penman PET. This is a very important drawback and the only solution found for that is again converting the ground observations to the FAO56 standard. If these, corrected with a crop factor, would be used as the ground-observed ET to be corrected with, the interpolation method would honour the vegetation information of the satellite PET more. That is a recommendation for further research. By including this vegetation information, we could also find out if differences landcover should also be part of he correction methods. For example, the MOD16 uses different transpiration functions for different landcover, and the validity of these could then be assessed more appropriately.

The FAO56, Penman, and $MOD16_0$ reference crop ET estimates do not take into account soil moisture deficit. Soil moisture deficit is represented in the P-M equation in the parameter *surface resistance* r_s, which has complex inter-relations with soil moisture, and stomatal conductance of different plant and tree types (Verhoef and Egea, 2014). As ground observations calculate a reference crop ET, this complexity was not tackled in this research. Suggestions for a simplified conversion of ET_0 to AET are: (1) to use the original MOD16 AET; (2) to use the original MOD16 PET in a hydrological soil water balance approach (e.g., Thornthwaite, 1948; Thornthwaite and Mather, 1957; White et al., 2003) to estimate AET based on soil water deficit from the soil storage component. As satellite data in this study were processed to ET_0, the error analysis is therefore also simplified. Recommended further consideration of ET uncertainty analyses could therefore be in-depth analyses and comparison of differences between ground observations of soil moisture, MOD16 ET_0, MOD16 AET and MOD16 PET data from this study, and ground-observed vegetation characteristics. Similarly, a better spatially varying estimated value for albedo could improve ET estimation.

Satellite data are considered to be of lower quality than ground observations (Chapter 1). The ratio of uncertainty of satellite data to ground observations was therefore chosen as a conservative 1.5. This estimate is debatable, as the exact figure is not known. The reason for that is that the uncertainty in global meteorology data, cloud cover, land cover, vegetation characteristics are unknown. Further research of the combined effect of cloud cover and vegetation characteristics, and the difference of global with national meteorological data could help to better quantify this, and is a recommendation for further research.

Satellite data are known to have more uncertainty in areas with high elevation differences (Van der Tol and Parodi, 2012). Furthermore, a known weak point of satellite data is that it does not perform well in tropical forest (e.g., it typically overestimates ET, Mu et al., 2011). It is not sure if very dense primary forest in New Zealand creates a similar bias. If it does, dense forest, either at high or low elevations, would cause an overestimation of ET on the satellite data. Further research is recommended on quantification of that bias in New Zealand. Possibly, a merge between MOD16 AET and other AET (e.g. AET Woods) is therefore recommended, where the elevation is used a weighting factor. However, as this chapter shows that the source data for that AET estimation (Penman PET) is unreliable and deprecated, more research on the effect of incorporating a better (FAO56) PET should then first be performed.

2.5.2.1 Linear regression as an interpolation method

In this study, the spatial pattern of satellite data was used to interpolate between ground-observed values. The simple linear regression technique was used, as it best maintains the spatial pattern of the MOD16 satellite data. Other interpolation techniques, like polynomial regression, thin-plate smoothing spline interpolation (e.g., Tait et al., 2006) or kriging-based interpolation could yield to a better

fit of the satellite data at the locations of the ground-observed data. However, the uncertainty of the ground-observed data at the climate station data can be large. For this study, the standard deviation of ground-observed data is calculated using only the yearly variations. It has thus embedded climate variation and incoherent measurement errors. However, it has not embedded the difference in PET algorithms (i.e., Penman PET (Penman, 1948) or the Priestley-Taylor algorithm (Priestley and Taylor, 1972)): only Penman PET was used. Also, it has not taken into account the systematical uncertainty of the ground-based Penman PET data and algorithms (10-30%, Glenn et al., 2008; Mu et al., 2011). Also, Baldocchi et al. (2001) suggest that climate stations can systematically underestimate ET fluxes with (10-30%). If we take these into account, uncertainty of ground-observed data would increase and other interpolation techniques than linear regression would not necessarily yield better results. Further study should be undertaken to investigate whether polynomial regression or other interpolation techniques, e.g, thin-plate smoothing spline interpolation (Tait et al., 2006) or fractal characterisation (Korvin et al., 1990), using ground-observed uncertainty would yield better results than following the spatial pattern of the satellite data in the linear regression.

2.6 Conclusions and Recommendations

As global satellite data have potential for use on regional or catchment scale, MODIS MOD16 data have been tested to improve PET estimation in New Zealand. Original MOD16 PET data were projected to Penman reference crop ET_0 (or 'Penman PET'). This has resulted in a nationwide 1km x 1km monthly ET_0 estimation (2000-2014). This nation-wide gridded dataset contains an uncertainty estimate, calculated through propagation of the uncertainty of its input components through the ET model equations. The satellite MOD16 data show to provide a credible and realistic means of interpolation. The newly developed satellite MOD16 ET_0 dataset fits almost all ground observations.

While existing techniques consider ground-estimated data as the 'gold standard', this research incorporates uncertainty of both ground-estimated and satellite ET. Uncertainty analysis performed on ground-estimated ET_0 shows that its uncertainty varies between 10% and 40% of ET_0, where Penman PET is more uncertain at high ET_0 than the global standard, FAO56 ET_0. It also shows that ET_0 is most sensitive to temperature, followed by solar radiation, cloudiness ratio and relative humidity. Using this analysis, a set of correlated random variables, and a Monte-Carlo fitting approach, satellite data becomes a soft 'interpolator' between the ground estimations. The resulting ET_0 estimates also contain an uncertainty estimate. The proposed method enhances the capability of using global satellite data products on a catchment scale, able to conform to any local measurement standards used.

Comparison of ground-estimated ET_0 with original MOD16 PET data leads to

the conclusion that original MOD16 PET data could well be used as an initial estimate of PET, as: the difference in original MOD16 PET and reference crop ET_0 seems to follow the expected trends (the same or slightly higher MOD16 PET in winter and higher MOD16 PET in summer); and it is the only estimate taking into account vegetation characteristics on a national scale. However, more quantitative data to further test this are lacking. Recommendations for further research are therefore further quantitative analyses. Also, temporal up-scaling to daily estimates with existing gridded (VCS) data is recommended.

This research shows that one should be careful with the use of Penman PET, as it is not real PET, and does not incorporate transpiration of the vegetation. Penman PET has shown to be mistaken for real PET in some studies in New Zealand. Further research should apply the more modern version of reference crop ET (FAO56) as it is better able to be corrected with factors than include vegetation information.

Original MOD16 PET and AET data were used in this research to generate New Zealand-wide AET estimates that included an uncertainty estimate. These AET estimates could serve as an alternative to the existing dataset from Woods et al. (2006). I surmise that the AET estimation performs better at plains. Original MOD16 AET resembles expected values, and also compares better than alternative modelled data at lysimeters in Canterbury. As quality of satellite data decreases with topography and dense forest, a merge between MOD16 AET and the AET from Woods et al. (2006) is therefore recommended. However, future research should then first focus on the incorporation of a better (FAO56) PET in the current national PET dataset.

3

Satellite microwave backscatter and soil moisture

3.1 Reading guide for this chapter

This chapter on soil moisture is the largest of this thesis. Therefore, a short reader guide is given.

The introduction outlines the importance of soil moisture to studies of rainfall recharge to groundwater. The potential capability of recently launched satellites for soil moisture in New Zealand is described; at the same time the importance and impact of the uncertainty of soil moisture data and models is stressed.

The theory, section 3.3 outlines the physics of satellite 'microwaves', often used for soil moisture research. It mostly describes terms as material properties, transmission, reflection, scattering, polarisation, surface roughness, soil, soil type, soil moisture, vegetation, topography.

Three different methods are described in section 3.4. First, a method that proves a new theory on why measurements of terrain motion are often disturbed by vegetation and soil moisture (section 3.4.1). Second, the sensitivity of microwave backscatter to important input components (e.g. soil moisture, terrain slope, vegetation, clay fraction) is estimated in section 3.4.2. Third, an algorithm to calculate soil moisture from satellite data is developed, which is then tested for both synthetic as well as real satellite data (section 3.4.3).

The results (section 3.5) and the discussion (section 3.6) are sectioned as to the three different methods.

Important results and discussion topics are concluded in section 3.7.

More detailed results of the soil moisture algorithm at locations of ground stations are shown in Annex A of this thesis.

3.2 Introduction

Soil moisture is an important hydrological water cycle variable and is recognised as an esssential climate variable (ECV, Bojinski et al., 2014; GCOS, 2010), i.e., a fundamental variable that needs to be measured to support climate research and the assessment of climate change. Soil moisture is a key component for models that calculate rainfall recharge to groundwater, i.e. soil water budget or soil water balance models (Hong and White, 2014; Rushton et al., 2006; Scott, 2004; Westenbroek et al., 2010; White et al., 2003).

Models of rainfall recharge to groundwater commonly estimate the amount of soil moisture through other (measured) variable, such as rainfall, evapotranspiration, and soil type. Soil moisture is thus mostly modelled and not measured directly. For example, in my rainfall recharge estimation (see Chapter 4) the soil starts with an initial soil moisture and is then filled with rainfall or drained of water (through evapotranspiration or rainfall recharge) at each time step. The resulting remaining water in the soil at each model time step is a proxy for soil moisture. However, there is much uncertainty in this modelled parameter, as there is uncertainty in all input data (e.g., rainfall, evapotranspiration) feeding the model, as well as in the model equations.

Measurements of soil moisture could help improve rainfall recharge estimations. However, ground-observed soil moisture is often uncertain due to measurement calibration and heterogeneity of the soil (see Figure 1.2, bottom, in Chapter 1). Ground-observed soil moisture is also often data-sparse, so that interpolation of ground-observed soil moisture data creates additional uncertainty.

Satellite data has the potential to be used for better spatial estimation of soil moisture in areas where ground observations are sparse. The combination of the synoptic satellite data and ground-observed soil moisture data could help assess and improve uncertainty estimates of rainfall recharge models. Soil moisture is generally measured with radar waves, electromagnetic waves that occur in the microwave domain (cm scale, more in section 3.3. Satellite microwave sensors measures microwaves that originate from the Earth. Microwaves are sensitive to moisture and therefore differences in soil moisture in the top centimetres (also called Surface Soil Moisture or SSM) can be measured by microwaves.

There are active and passive microwave antenna systems. Active sensors transmit an microwave signal to Earth, and measure the returning signal, called 'microwave backscatter'. Some well known soil moisture data services have been developed over the last years with active sensors (e.g., ASCAT, Wagner et al., 2007). Passive sensors, which measure the natural microwave emission from Earth are also well known in global research on soil moisture (e.g. SMOS, AMSR-E, De Jeu and Owe, 2003; Kerr et al., 2012, respectively). However, all passive and most active microwave satellite data are often too coarse (approximately 25 km grid resolution or coarser) to be used on the scale that would typically be needed in New Zealand.

Another type of active microwave backscatter comes in the form of Synthetic Aperture Radar (SAR), which often comes at a much higher spatial resolution. High resolution active microwave backscatter (10m x 10m) data have recently become available with ESA's Sentinel-1 SAR satellite mission. These new data create a valuable opportunity to estimate soil moisture on a fine scale in New Zealand. The downside of the high resolution of SAR data is that the derivation of microwave soil moisture through SAR data is much more uncertain than the coarser existing soil moisture (e.g. ASCAT) products. SAR-derived data on soil moisture have some known accuracy limitations, which was explored by Doubková et al. (2012), who found a solution by using a relative 1km x 1km SAR signal (from Envisat-ASAR) to downscale the coarse ASCAT in Australia to finer spatial resolution.

Explanations for the limitation in SAR accuracy can be due to many reasons, such as atmospheric noise (Hanssen, 1998), vegetation (Barrett, 2012), or soil heterogeneity (Wagner et al., 2007). Not only soil moisture studies suffer from these accuracy limitations. SAR data is also used for measurements of terrain motion, and the sensitivity to atmospheric noise, vegetation and soil moisture there causes uncertainty in terrain motion measurements using the Interferometric SAR (InSAR) technique, InSAR has become widely applied for studies on earthquakes (Funning et al., 2005), volcanism (Lundgren et al., 2004), landslides (Carnec and Fabriol, 1999), or excessive pumping or abstraction of gas, oil or water resources (Hooijer et al., 2012; Ortega-Guerrero et al., 1999; Wu et al., 2007). InSAR uncertainties due to atmospheric noise is well documented (Barnhart and Lohman, 2013; Hanssen, 1998, 2001). However, uncertainty due surface characteristics such as soil, soil moisture, vegetation are reported (Lauknes et al., 2010; Reeves et al., 2011; Tomás et al., 2016), but are poorly understood and actual physics-based explanations remain poorly documented and thus poorly understood. To be able to implement SAR derived data in soil moisture studies, more insight is needed on the factors that create noise and uncertainty on these SAR data.

The Sentinel-1 satellite mission produces imagery (ESA, 2015c) that amounts up to tens of GB per week for New Zealand. These amounts of data require efficient processing chains before they can be used in hydrological estimates, such as soil moisture or vegetation parameters. Data assimilation methods, widely applied in hydrology, are a strategy to still work with data of unknown uncertainty. These methods typically combine high resolution but uncertain measurements with well-known but data-sparse measurements by their statistical relation and they are used in many hydrological applications (Clark et al., 2008; Weerts and El Serafy, 2006) and could also be applied for soil moisture. However, if no physics-based explanations can be given for causes of uncertainty of SAR to soil moisture and vegetation, then these efficient processing chains might not be optimised well enough. Another way to describe uncertainty is to go back to the fundamentals of physics used to derive soil moisture from their original measurement method. This approach is more based on (geo)physics, and less on the statistical relations between two data streams, and might lead to better explanations of the origin of the uncertainties of some satellite microwave measurements; these explanations

might be useful for future improvements of high-volume ('big data') satellite data processing sequences.

This chapter creates more insight in the effects of soil moisture and vegetation on microwave data. It will dig deeper into the properties of microwaves in different materials. It defines physics of propagation, reflection and scattering of microwaves and the sensitivity of soil moisture and vegetation on the portion of the microwaves scattered back to a satellite. It then explains some common forms of uncertainty that occur in SAR research (such as: noise in InSAR due to soil and vegetation; the sensitivity of microwaves to several model input components; non-uniqueness of soil moisture solutions from microwave data). Finally, it develops a framework for efficient processing of large amounts of microwave data for practical use in applications that require soil moisture information.

3.3 Theory of microwave backscatter

3.3.1 General

This section describes some theory of electromagnetic waves in the microwave domain. It is not considered a complete review of all theory, but provides information to elucidate the further used methods of this chapter. For example, I will not describe the theory about the large variety of radar antennas, as this is considered out of scope for the aim of this theory section. More advanced and extensive theory from Fung et al. (1992); Lorrain et al. (1988); Pain (2005); Ulaby (1981); Ulaby et al. (2014, 1982, 1986) are cited in this section and are recommended for further reading.

Most earth-observing satellite methods measure electromagnetic waves in the range from optical wavelengths (hundreds of nanometers) to microwaves (roughly from millimetres to tens of cm wavelength, often called radar). The optical and microwaves are shown in the full electromagnetic spectrum in Figure 3.1. Compared to optical waves, microwaves have a larger wavelength, which make them specifically useful for hydrological purposes, e.g., soil moisture estimation. This is because they are able to penetrate the first few centimetres of the soil, and can therefore pick-up soil moisture differences in that top layer. Also, microwaves do not depend on daylight and are able to penetrate clouds almost completely, whereas optical waves do not yield any information in clouded area, nor at night time (except for infra-red waves). Microwaves are thus useful for day and night imagery, and independent of cloud cover. Finally, microwaves are able to penetrate (light) vegetation. They can therefore used to estimate vegetation properties, whether or not in conjunction with optical data. The wavelength spectrum are subdivided in *bands* (Figure 3.1, bottom left). For satellite microwave research, L-band (wavelength $\lambda \sim$22 cm, frequency $f \sim$ 1.4 GHz), C-band ($\lambda \sim$6 cm, $f \sim$5 GHz), or X-band ($\lambda \sim$3 cm, $f \sim$10 GHz) In this study, C-band microwave data will be mostly used.

The microwaves used in this research are measured with Synthetic Aperture Radar (SAR) antennas. SAR antennas transmit microwaves, mostly in the L-, C-, or X-band. Antenna are 'side-looking', with very low return of water surfaces, and relatively much backscatter from rougher surfaces (Figure 3.2). SAR measurements can be used for soil moisture or vegetation purposes. They can also be used for measuring terrain motion over time, e.g. for earthquake or land subsidence research. The changes in signal over time are measured with interferometric measurements, i.e., the small differences of repeated overpasses of the satellite over time are used to establish whether the terrain has moved. These measurements are called Interferometric SAR or InSAR. In this study, the aim will be to work with high resolution SAR backscatter to estimate soil moisture. The C-band SAR data used will be from the Sentinel-1 mission of the European Space Agency, which are freely available for research purposes ESA (2015b).

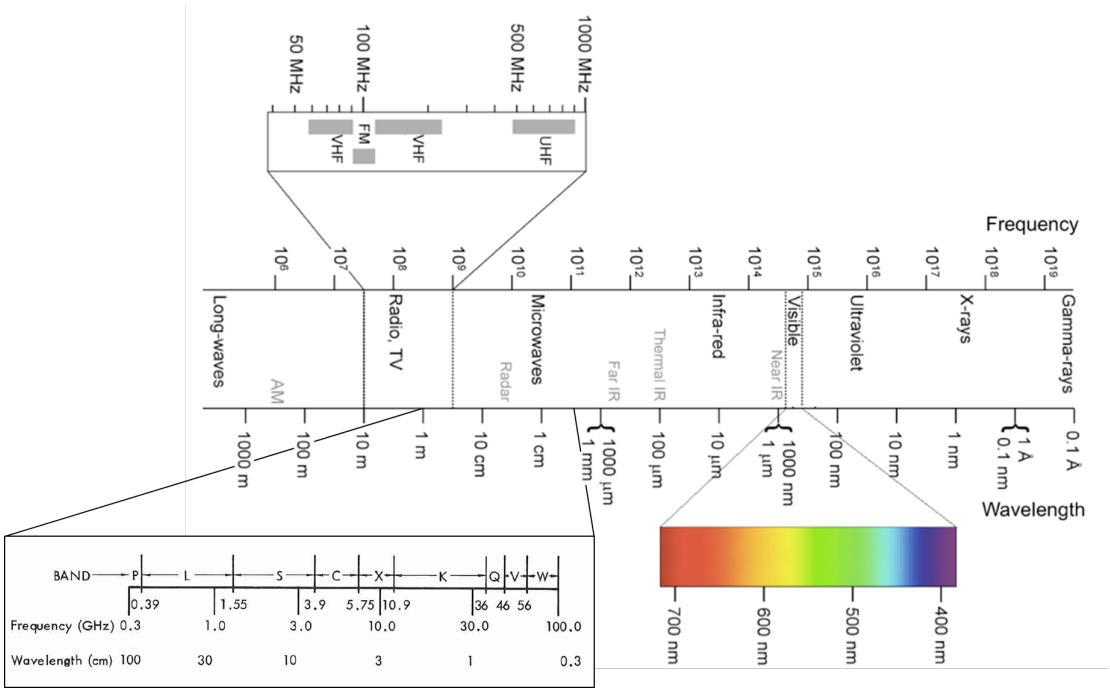

Figure 3.1: The electromagnetic spectrum, adapted from Dean (2013) and Ulaby et al. (1982)

An electromagnetic field is either transmitted or received by one or multiple antennas. The antenna measuring configuration where a signal is transmitted and received from the same active antenna is called a *monostatic* or *backscatter* configuration (Figure 3.3).

3.3.2 Material properties

Electromagnetic wave energy and motion is mostly affected by three material properties (e.g. Pain, 2005):

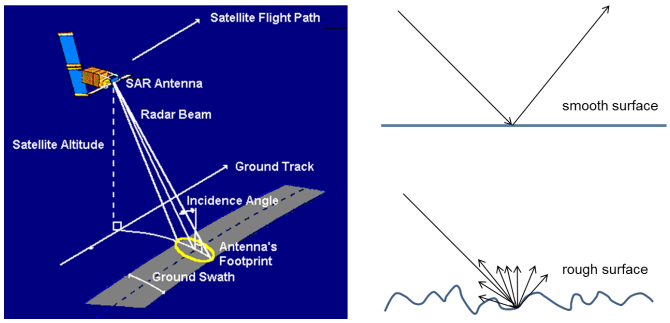

Figure 3.2: Synthetic Aperture Radar (SAR) backscatter basics: **(left)** SAR satellite measurement configuration; **(right)** backscatter on smooth and rough surfaces. Based on Westerhoff et al. (2013), their figure 1.

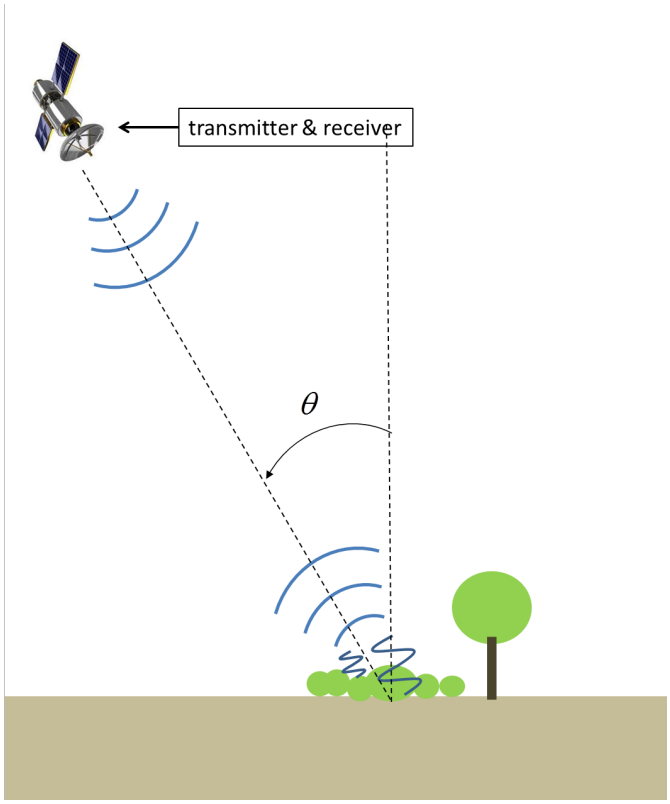

Figure 3.3: Backscatter configuration, where transmitter and receiver are at the same location.

1. Magnetic permeability $\mu = \mu_0\mu_r$. In free space, $\mu_0 = 4\pi \times 10^{-7}$ (SI unit $\frac{V \cdot s}{A \cdot m}$), and μ_r is the *relative magnetic permeability*;
2. Electrical conductivity σ (SI unit S/m);
3. Dielectric permittivity $\varepsilon = \varepsilon_r\varepsilon_0$, where, in a free space, ε_0 has a value of ε_0=8.854187817.. x 10^{12} (SI unit F/m) and is defined as $\varepsilon_0 = \mu_0/c^2$, with c being the speed of light in a vacuum (299,792,459 m/s). ε_r is called the *relative permittivity* or *dielectric constant*.

It is further assumed that for most of Earth's materials, μ is more or less constant, and focus is put on σ and ε. Beside material composition, ε also depends on frequency, pressure and temperature, and is a complex parameter in most of Earth's media (, i.e., with a real and imaginary part, more later). The dielectric permittivity becomes complex when it has conductivity $\sigma \neq 0$ embedded and is then defined as (Böttcher, 1978; Ulaby et al., 1982):

$$\hat{\varepsilon} = \varepsilon - j\frac{\sigma}{\omega} \triangleq \varepsilon' - j\varepsilon'', \tag{3.1}$$

where:

- $\hat{\varepsilon}$ is the complex dielectric constant;
- ε is the 'static dielectric constant', i.e., the real part of the dielectric constant which is only affected by temperature, pressure and composition (Böttcher, 1978), and not by conductivity. In other words, $\hat{\varepsilon}$ equals ε in a dielectric medium, where $\sigma = 0$;
- ω is the angular frequency (=$2\pi f$);
- $\varepsilon^{'}$ and $\varepsilon^{''}$ are the real and imaginary parts of $\hat{\varepsilon}$, respectively.

The dielectric constant and its complex members are mostly shown in relative values (relative to ε_0). In this research they will be called ε_r, $\hat{\varepsilon}_r$, $\varepsilon_r^{'}$, or $\varepsilon_r^{''}$. Complex relative permittivities for loams and clays are depicted in Figure 3.4. Some material properties at ambient pressures and temperatures are shown in Table 3.1.

3.3.2.1 The effect of geology

Permittivities are related to rock type if bare rock occurs at the surface. Ulaby et al. (1990) show that values for ε_r' for dry rocks are in between 4 and 7 and relate to the bulk density of the rock ρ_b: their empirical finding is that, if ρ_b is in [g/cm^3] and is used dimensionless:

$$\varepsilon'_{rock} \approxeq 2\rho_b, \tag{3.2}$$

while ε'' varies between 0.02 and 0.08 for C-band frequencies.

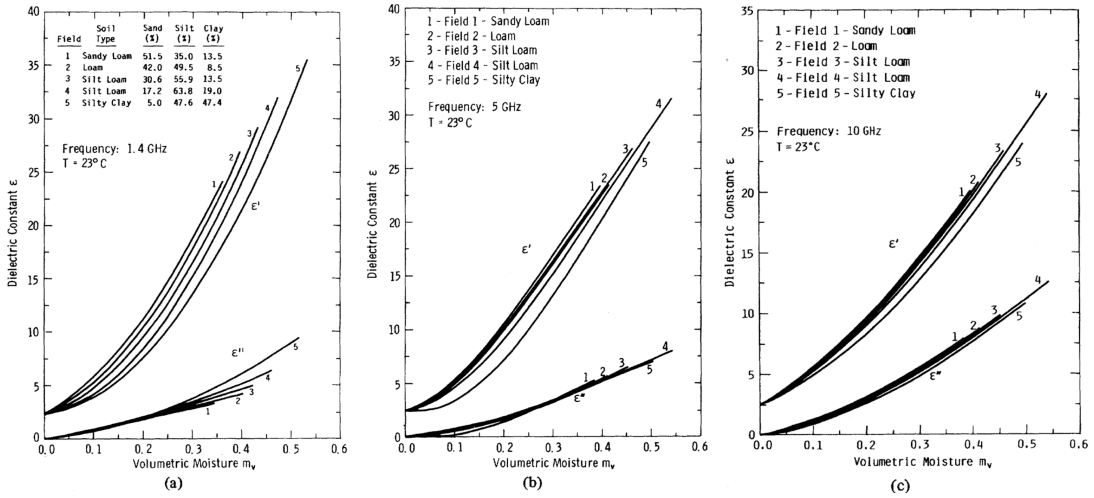

Figure 3.4: Complex dielectric permittivitties $\varepsilon_r^{'}$ and $\varepsilon_r^{''}$ for loams and silty clay at L-, C- and X-band (adapted from Hallikainen et al., 1985, their Fig.7).

Table 3.1: Approximate material properties μ, σ, and $\hat{\varepsilon}$ for some of Earth's materials (at normal pressure and temperature). For sand (soil moisture M_v of 0.4 m^3m^{-3}) permittivity values have been taken from Hallikainen et al. (1985). Typical value for normal freshwater and seawater at C- or L-band are given (Ellison et al., 1998; Gadani et al., 2012; The Engineering Toolbox, 2012), these depend on concentrations of ions in the water.

Material	μ/μ_0	$\sigma(S/m)$	$\varepsilon_r^{'}$	$\varepsilon_r^{''}$
Air	1	≈ 0	≈ 1	0
Dry sand	1	$> 10^3$	3	0
Pure Water	1	10^{-4}	75	15
Fresh-Brackish Water (<5000 ppm)	1	$< 10^{-2}$	75	30
Sea water	1	4.8	80	100
Silty Clay (M_v=0.4)	1	0.05	24	5

3.3.2.2 The effect of soil and soil moisture

For dielectric properties of dry soil, empirical findings of Dobson et al. (1985) and Ulaby et al. (2014) are:

$$2 \lesssim \varepsilon'_{soil} \lesssim 4 \tag{3.3a}$$

$$\varepsilon'' < 0.05 \tag{3.3b}$$

$$\varepsilon'_{soil} = (1 + 0.44\rho_b)^2 \tag{3.3c}$$

where ρ_b is the bulk density in [g/cm^3] and is used dimensionless in the empirical relation. Also following from Eq. 3.3, ρ_b is usually in between 1 (light soil) and 2 (heavy soil) [g/cm^3].

The amount of clay and silt in a soil influences the conductivity and thus the dielectric properties. Soil texture is usually defined as a composite of sand, clay and silt (USDA, 1987, Figure 3.5). In terms of particle size and chemical composition (Table 3.2), and in terms of electrical conductivity (, e.g., Milsom, 2003, his Tables 5.1 and 10.1), silt is somewhere in between clay and sand. For the calculations in this chapter, a simplifying assumption is made: that silt is half clay and half sand.

Table 3.2: Soil texture as assumed in this chapter (Source: Foth, 1990).

	Particle size (μm)	Chemical composition
Sand	50 - 2000	silica, quartz
Silt	2 - 50	quartz, feldspar
Clay	< 2	clay minerals (e.g., feldspar)

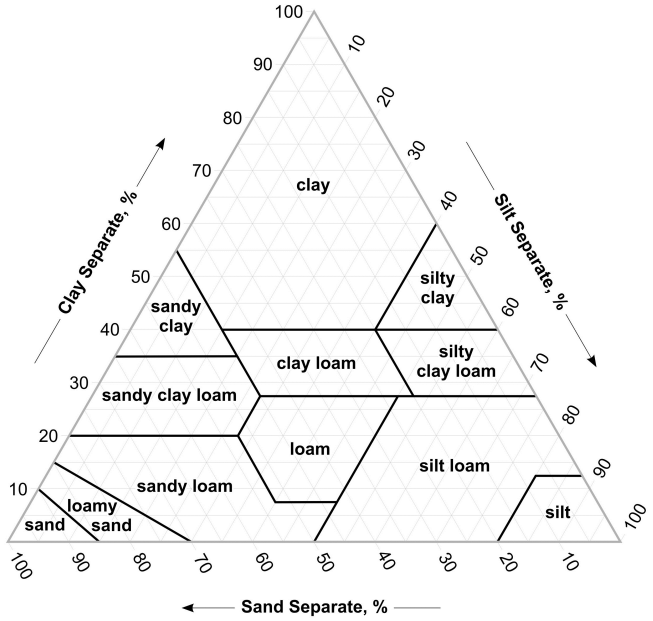

Figure 3.5: USDA soil texture triangle Source: USDA (2015), with approval.

Water has an important effect on dielectric properties of soil (see Table 3.1). For soil, this effectively means that the amount of sand and clay content in the soil play an important role, not only in soil texture, but mostly for their ability to hold water. Dobson et al. (1985) define a model of dielectric properties as a function of temperature, sand and clay fraction, soil moisture, and frequency:

$$\varepsilon'_{soil} = \left[1 + 0.66\rho_b + M_v^{\beta_1}\left(\varepsilon'_w\right)^{\alpha} - M_v\right]^{1/\alpha} \tag{3.4a}$$

$$\varepsilon''_{soil} = M_v^{\beta_2}\varepsilon''_w \tag{3.4b}$$

with ρ_b in [g cm^{-3}], and where M_v is the volumetric moisture content [m^{3}m^{-3}], β_1 and β_2 empirically determined expressions related to sand and clay content, α an empirically determined constant, and ε'_w and ε''_w dielectric constants of water. All variables in this equation are again dimensionless for the sake of the empirical relation. For freshwater (, i.e., no dissolved salts), ε'_w and ε''_w can be determined by a *Single Debye Model* (, e.g., Ulaby et al., 2014):

$$\varepsilon'_w = \varepsilon_{w\infty} + \frac{\varepsilon_{w0} - \varepsilon_{w\infty}}{1 + \left(2\pi f \tau_w\right)^2}, \tag{3.5a}$$

$$\varepsilon''_w = \frac{2\pi f \tau_w \left(\varepsilon_{w0} - \varepsilon_{w\infty}\right)}{1 + 2\pi f \tau_w}, \tag{3.5b}$$

with $\varepsilon_{w\infty}$ a dimensionless constant (= 4.9, according to Lane and Saxton, 1952). Klein and Swift (1977) and Stogryn (1971) fitted polynomials to experimental

data and estimated best fits for ε_{w0} and $2\pi\tau_w(T)$ to values of temperature T in °C:

$$\varepsilon_{w0}(T) = 88.045 - 0.4147T + 6.295 \times 10^{-4}T^2 + 1.075 \times 10^{-5}T^3 \quad (3.6a)$$

$$2\pi\tau_w(T) = 1.1109 \times 10^{-10} - 3.284 \times 10^{-12}T + 6.938 \times 10^{-14}T^2 - 5.096 \times 10^{-16}T^3 \quad (3.6b)$$

Note that the units before and after the equality sign do not match because of their experimental polynomial fitting approach.

3.3.3 Transmission and reflection in earth's media

Electromagnetic wave theory can be described by four vector relations known as Maxwell's equations (Maxwell, 1865). There are two time-varying and two steady state equations. The time-varying equations are:

$$\nabla \times \mathbf{E} = -\mu \frac{\partial \mathbf{H}}{\partial t} \quad (3.7)$$

$$\nabla \times \mathbf{H} = \sigma \mathbf{E} + \varepsilon \frac{\partial \mathbf{E}}{\partial t} \quad (3.8)$$

where $\mathbf{E}$ is the electric field vector, $\mathbf{H}$ the magnetic field intensity vector, and σ the electrical conductivity. The two equations tell us that $\mathbf{E}$ and $\mathbf{H}$ are always propagating perpendicular to each other in a transverse motion. In a dielectric medium (, e.g., free space/vacuum) equation 3.8 simplifies as $\sigma\mathbf{E}$ vanishes, and the transverse motion looks as shown in Figure 3.6. The two steady state equations are:

$$\nabla \cdot \mathbf{D} = \varepsilon \left(\frac{\partial E_x}{\partial x} + \frac{\partial E_y}{\partial y} + \frac{\partial E_z}{\partial z} \right) = \rho \quad (3.9)$$

$$\nabla \cdot \mathbf{B} = \mu \left(\frac{\partial H_x}{\partial x} + \frac{\partial H_y}{\partial y} + \frac{\partial H_z}{\partial z} \right) = 0 \quad (3.10)$$

where $\mathbf{D}$ is the displacement charge ($= \varepsilon\mathbf{E}$), ε is constant and ρ is the charge density. Eq. 3.9 states that over a small volume element (dx dy dz) of charge density ρ the number the change of D depends on the value of ρ. Eq. 3.10 states that an equal number of magnetic induction lines enter and leave the volume element dx dy dz (e.g. Pain, 2005).

When assuming harmonic (sinusoidal) wave motion, the E_x amplitude of an electromagnetic wave travelling with frequency f in a homogeneous and source free medium in the positive z-direction can be written as (Ulaby et al., 1982):

$$E_x(z,t) = Re\left\{ E_{x_0} e^{j(\omega t - \hat{k}z)} \right\}, \quad (3.11)$$

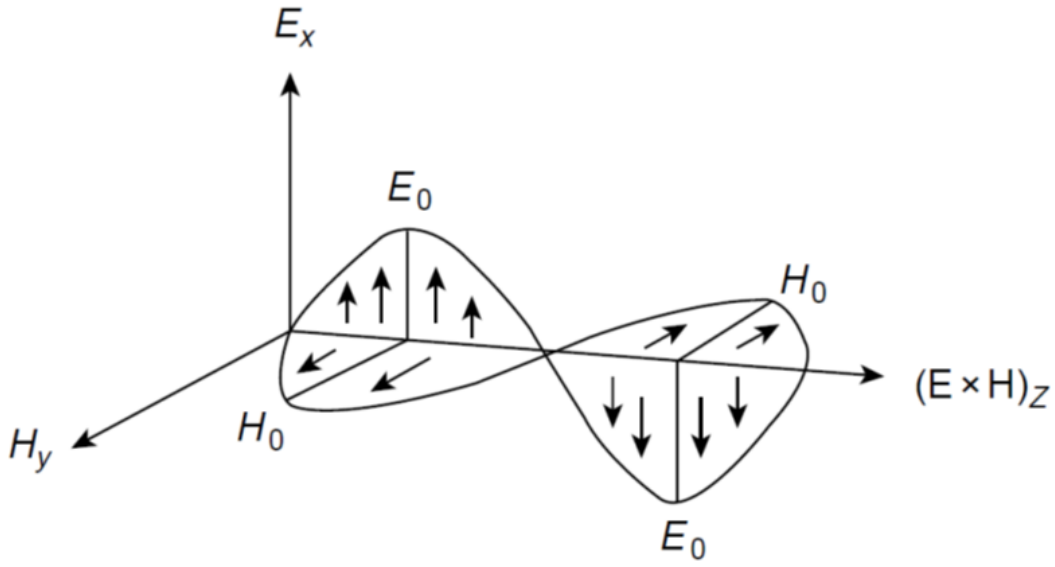

Figure 3.6: EM transverse wave motion. Adapted from Pain (2005).

where $\omega = 2\pi f$, and $\hat{k} = \omega\sqrt{\mu\hat{\varepsilon}}$ is the (complex) wave number. In a similar representation, **H** in the perpendicular y direction is defined as:

$$H_y(z,t) = Re\left\{\frac{E_{x_0}}{\hat{\eta}} e^{j(\omega t - \hat{k}z)}\right\}, \tag{3.12}$$

where $\hat{\eta} = \sqrt{\mu/\hat{\varepsilon}}$ is known as the *impedance*, which for electromagnetic waves is defined as:

$$\hat{\eta} = \frac{E_x}{H_y} = \sqrt{\frac{\mu}{\hat{\varepsilon}}}, \tag{3.13}$$

If $\sigma = 0$, permittivity and impedance lose their complex form. Then, phases of the E and H field are equal, as mentioned in Pain (2005), and as shown for a dielectric (e.g., air) in Figure 3.7 (top). A phase difference between E_x and H_y occurs if $\sigma \neq 0$, because $\hat{\eta}$ is now complex. This means that for a 'lossy media' ($\sigma > 0$), H lags E (Figure 3.8, which shows the E_x and H_y for a silty clay).

When a wave travels from one medium to another, some of the incoming ('i') wave energy could be reflected ('r'), with the remaining part transmitted ('t'). In that case, some boundary conditions apply to the E and H fields. Lorrain et al. (1988), their Eqs. 30-21 and 30-22, state that at a boundary between two media, the total E and H fields in medium 1 should be equal to those in medium 2:

$$\boldsymbol{E}_{i,1} + \boldsymbol{E}_{r,1} = \boldsymbol{E}_{t,2} \tag{3.14a}$$

$$\boldsymbol{H}_{i,1} + \boldsymbol{H}_{r,1} = \boldsymbol{H}_{t,2} \tag{3.14b}$$

The phase and amplitude of the reflected signal thus depend on the impedances of the two media (and thus on material properties μ,ε, and σ). Assuming normal

incidence (incidence angle $\theta = 0$) on the boundary of medium 1 and medium 2 the reflected signals are (, e.g., Pain, 2005):

$$E_{x,r} = E_{x,i}\frac{\hat{\eta}_2 - \hat{\eta}_1}{\hat{\eta}_1 + \hat{\eta}_2} \tag{3.15a}$$

$$H_{y,r} = -H_{y,i}\frac{\hat{\eta}_2 - \hat{\eta}_1}{\hat{\eta}_1 + \hat{\eta}_2}, \tag{3.15b}$$

Which is shown in Figure 3.7 (middle, with medium 2 a dry sand with $\varepsilon = 3$). Note that the phase of the reflected E_x field reverses (shifts by 180°) if $\hat{\eta_2} < \hat{\eta_1}$. The transmitted part travelling from medium 1 into 2 is:

$$E_{x,t} = E_{x,i}\frac{2\hat{\eta}_2}{\hat{\eta}_1 + \hat{\eta}_2} \tag{3.16a}$$

$$H_{y,t} = H_{y,i}\frac{2\hat{\eta}_1}{\hat{\eta}_1 + \hat{\eta}_2} \tag{3.16b}$$

and shown in Figure 3.7 (bottom) for a dry sand ($\varepsilon = 3$).

For the above examples, normal incidence ($\theta = 0$) was assumed. However, reflection and transmission also depends on the incidence angle. For any incidence angle θ, reflection is given by:

$$E_{x,r} = E_{x,i}\frac{\hat{\eta}_2 \cos\theta_1 - \hat{\eta}_1 \cos\theta_2}{\hat{\eta}_1 \cos\theta_2 + \hat{\eta}_2 \cos\theta_1} \tag{3.17}$$

$$H_{y,r} = -H_{y,i}\frac{\hat{\eta}_2 \cos\theta_1 - \hat{\eta}_1 \cos\theta_2}{\hat{\eta}_1 \cos\theta_2 + \hat{\eta}_2 \cos\theta_2} \tag{3.18}$$

where θ_2 is derived from Snell's Law:

$$\hat{k_2} \sin\theta_2 = \hat{k_1} \sin\theta_1 \tag{3.19}$$

and wave numbers $\hat{k}$ for both media obey the relationship:

$$\hat{k} = 2\pi/\hat{\lambda}, \quad \hat{\lambda} = 1/f\sqrt{\mu\hat{\epsilon}} \tag{3.20}$$

The reflection adjusted for incidence angle is called Fresnel reflection. However, in this chapter normal incidence angles will be used mostly, unless stated otherwise.

The reflected and transmitted E- and H-fields can also be defined in terms of their wave numbers. Let's assume a EM wave travelling in a medium 1:

$$E_{x,i} = E_{x,0}e^{j\left(\omega t - \hat{k}z\right)} \tag{3.21a}$$

$$H_{y,i} = H_{y,0}e^{j\left(\omega t - \hat{k}z\right)}, \tag{3.21b}$$

with $H_{y,0} = E_{x,0}/\hat{\eta}_1$. If we define the ratio between the wave numbers $\hat{k_1}$ and $\hat{k_2}$ as ζ, the reflected and transmitted E- and H-fields at the boundary B are (Lorrain et al., 1988, their Equations 32-5 and 32-14, and assuming normal incidence):

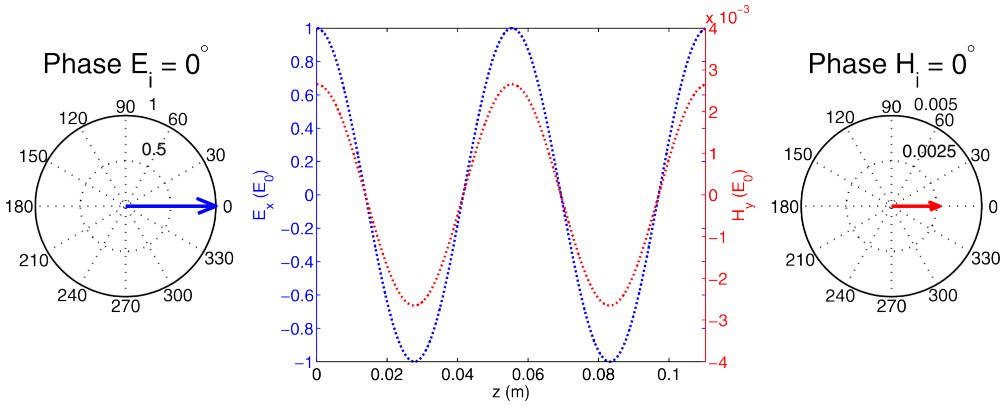

(a) Incoming EM wave in air

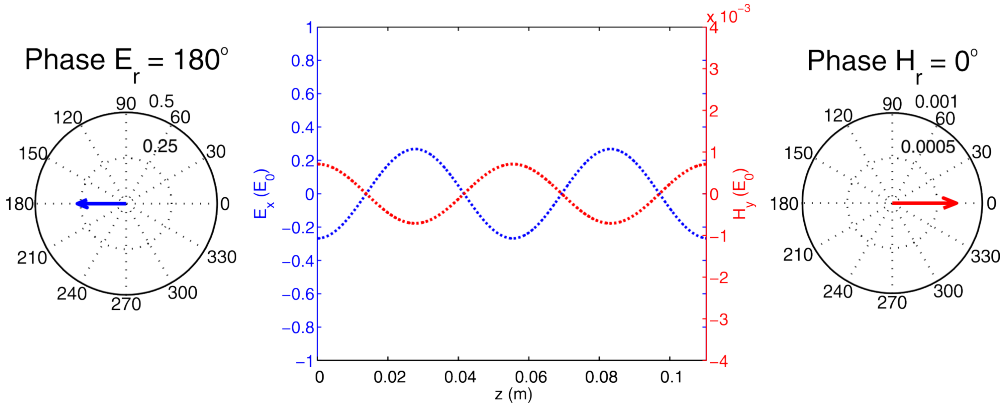

(b) Reflected EM on dry sand, $\varepsilon = 3$

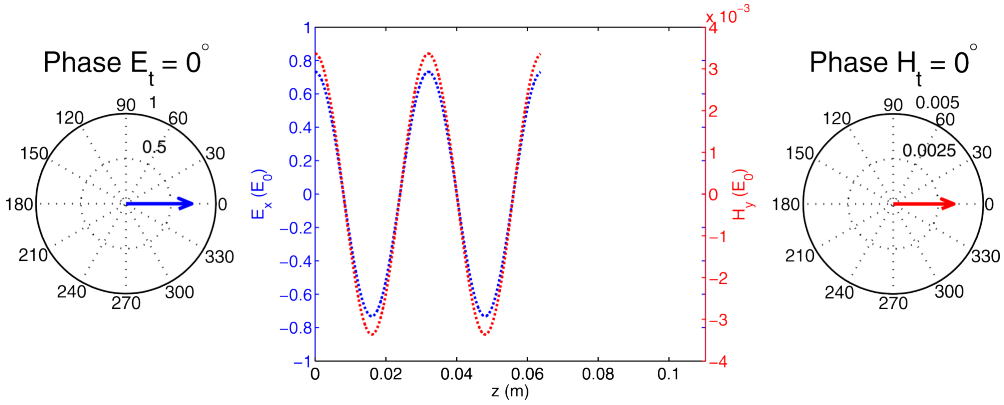

(c) Transmitted wave through dry sand, $\varepsilon = 3$

Figure 3.7: Motion of the reflected E_x and H_y field over two wavelengths from a dielectric to a non-conductive medium (e.g. dry sand) at t=0 and normal incidence. For simplicity E_0=1 is chosen. Left and right are the relative phase differences of the incoming (i), reflected (r) and transmitted (t) E and H field.

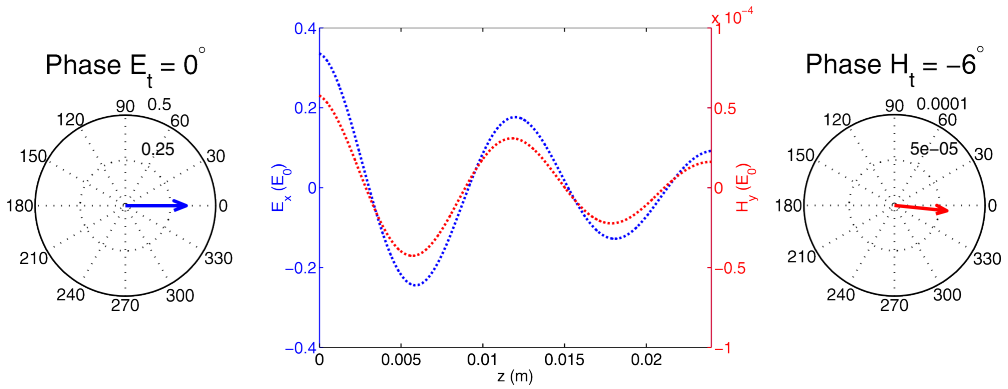

Figure 3.8: Motion of the E_x and H_y field over two wavelengths in a silty clay at t=0. For simplicity E_0=1 is chosen. Left and right are the relative phase differences of E_x and H_y.

$$\frac{E_{r_B}}{E_{i_B}} = \frac{\zeta - 1}{\zeta + 1} \tag{3.22a}$$

$$\frac{E_{t_B}}{E_{i_B}} = \frac{2\hat{k}_1}{\zeta + 1} \tag{3.22b}$$

$$\frac{H_{r_B}}{H_{i_B}} = -\frac{\zeta - 1}{\zeta + 1} \tag{3.22c}$$

$$\frac{H_{t_B}}{H_{i_B}} = \frac{\hat{\eta}_1}{\hat{\eta}_2}\frac{2\zeta}{\zeta + 1} \tag{3.22d}$$

and the reflected and transmitted wave fields in the media can be written as:

$$E_{x,r} = E_{r_B} e^{j\left(\omega t + \hat{k_1} z\right)} \tag{3.23a}$$

$$H_{y,r} = H_{r_B} e^{j\left(\omega t + \hat{k_1} z\right)} \tag{3.23b}$$

$$E_{x,t} = E_{t_B} e^{j\left(\omega t - \hat{k_2} z\right)} \tag{3.23c}$$

$$H_{y,t} = H_{t_B} e^{j\left(\omega t - \hat{k_2} z\right)} \tag{3.23d}$$

3.3.4 Polarisation of an EM wave

The orthogonal wave motion described in the former sections was assumed to be in the orthogonal x and y planes for the sake of simplicity. In reality, these orthogonal planes are usually represented as a *phasor* formulation. For example, the electric field travelling in the z-direction, may be represented by an x and y component:

$$\mathbf{E}(z) = \hat{\mathbf{x}} E_x(z) + \hat{\mathbf{y}} E_y(z), \tag{3.24}$$

where

$$E_x(z) = E_{x0}e^{-ikz}, \tag{3.25a}$$
$$E_y(z) = E_{y0}e^{-ikz}, \tag{3.25b}$$

with E_{x0} and E_{y0} the amplitudes of $E_x(z)$ and $E_y(z)$ and $\hat{\mathbf{x}}$ and $\hat{\mathbf{y}}$ the directions or *polarisations* of the electric field. In a spherical coordinate system (with radial distance R, polar angle θ and azimuthal angle ϕ, Figure 3.9), the electric field phasor can be represented as orthogonal polarisation components h and v travelling in direction $\hat{\mathbf{k}}$. In this case,

$$\mathbf{E} = \left(\hat{\mathbf{v}}E_v + \hat{\mathbf{h}}E_h\right) e^{-ik\hat{\mathbf{k}}\cdot\hat{\mathbf{R}}}, \tag{3.26}$$

where $\hat{\mathbf{k}}$, $\hat{\mathbf{v}}$, $\hat{\mathbf{h}}$ relate to the local (x,y,z) coordinate system as:

$$\hat{\mathbf{k}} = \hat{\mathbf{x}}\sin\theta\cos\phi + \hat{\mathbf{y}}\sin\theta\sin\phi + \hat{\mathbf{z}}\cos\theta, \tag{3.27a}$$
$$\hat{\mathbf{h}} = -\hat{\mathbf{x}}\sin\phi + \hat{\mathbf{y}}\cos\phi, \tag{3.27b}$$
$$\hat{\mathbf{v}} = -\hat{\mathbf{x}}\cos\theta\cos\phi + \hat{\mathbf{y}}\cos\theta\sin\phi - \hat{\mathbf{z}}\sin\theta. \tag{3.27c}$$

The *polarisation* of a wave is defined as the electric (or magnetic) field in the direction of the h and v planes. Sometimes, the terminology p and q are used instead of $\hat{\boldsymbol{h}}$ or $\hat{\boldsymbol{v}}$.

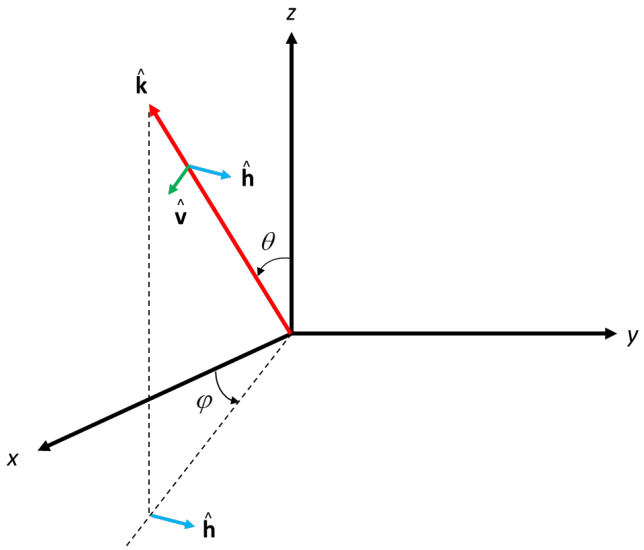

Figure 3.9: Spherical coordinate system ($\hat{\boldsymbol{R}}$,$\hat{\boldsymbol{\theta}}$,$\hat{\boldsymbol{\phi}}$) for a wave travelling in $\hat{\boldsymbol{k}}$ direction. Based on Ulaby et al. (2014), their Figure 5.1.

3.3.5 Surface roughness

A perfectly smooth surface is called *specular*. However, in reality specular surfaces do not often exist, as it has a certain 'roughness'. This roughness can be caused by small variations of the terrain, but also by variation of complex permittivity within a terrain, producing an electromagnetic surface different than the terrain surface (, i.e., because of small variations in soil texture or moisture). Most backscatter processing methods use the assumption of a distributed target area: an area consisting of a distribution of elements with electromagnetic height. The combined roughness of terrain and electromagnetic surface of that distributed target area is called *electromagnetic roughness* ks and is defined as:

$$ks = \frac{2\pi s}{\lambda}, \tag{3.28}$$

with:

- $k = \frac{2\pi}{\lambda}$ the wavenumber;
- s the root-mean-square *rms height*: the standard deviation of the distribution of electromagnetic terrain heights.
- λ the wavelength.

Most distributed target areas are furthermore defined with a correlation function, which describe the height variation over distance, or rather put the measure of correlation between two locations (x, y) and (x', y') (, e.g., Ulaby et al., 2014):

$$\rho(\xi) = \frac{\langle z(x,y)\, z(x',y')\rangle}{s^2} \tag{3.29}$$

where $\xi = \sqrt{(x-x')^2 + (y-y')^2}$ is the separation between the two locations. The *correlation length* L is defined as the distance ($\xi = L$) where the correlation is e^{-1} compared to distance ($\xi = 0$). By combining L and s, one can also infer a distribution of electromagnetic terrain slopes. The standard deviation of these slopes is then called the *rms slope* m.

3.3.6 Scattering from Earth's media

When wavelengths are small and a target is large, all reflected energy from that target would be considered a 'reflection'. However, when wavelengths increase or a target size decreases, some of the energy is 'scattered' in multiple directions. Such small targets are called *point targets*. They can also be defined as having a much smaller solid angle than a radar beam (Ulaby et al., 2014). Scattering is used here as a collective term: it is defined as all reflected energy from a random target in all directions. For example, an incoming and a received (reflected/scattered)

E-field could be:

$$\mathbf{E}^i = \hat{\mathbf{v}}_t E_v^i + \hat{\mathbf{h}}_t E_h^i, \tag{3.30a}$$
$$\mathbf{E}^r = \hat{\mathbf{v}}_r E_v^r + \hat{\mathbf{h}}_r E_h^r. \tag{3.30b}$$

The fields $\mathbf{E}^i$ and $\mathbf{E}^r$ are related by

$$\mathbf{E}^r = \frac{e^{-jkR_r}}{R_r} \mathbf{S}\, \mathbf{E}^i, \tag{3.31}$$

where $\frac{e^{-jkR_r}}{R_r}$ is a *spherical propagation factor*, and $\mathbf{S}$ holds information on the reflection or scattering properties of the illuminated area for each polarisation of the E field. $\mathbf{S}$ is called the *scattering matrix*, and is defined as:

$$\mathbf{S} = \begin{pmatrix} S_{vv} & S_{vh} \\ S_{hv} & S_{hh} \end{pmatrix}, \tag{3.32}$$

where S_{vv} is the scattering coefficient for a wave that is transmitted and received in the same direction $\hat{v}$; S_{hv} is the scattering coefficient for the wave that is transmitted in direction $\hat{h}$ and received in the direction $\hat{v}$; etc. $\mathbf{S}$ can be complex, as it holds the information of impedance η. It furthermore consists of the angular relations between transmitted and received E field. If a (near-)specular surface would be illuminated by an EM-field from a satellite at normal incidence ($\theta = 0$), scatter would be equal to a normal reflection, and $\boldsymbol{S}$ would then look like this:

$$\boldsymbol{S} = \begin{pmatrix} \dfrac{\hat{\eta}_2 - \hat{\eta}_1}{\hat{\eta}_1 + \hat{\eta}_2} & 0 \\ 0 & \dfrac{\hat{\eta}_2 - \hat{\eta}_1}{\hat{\eta}_1 + \hat{\eta}_2} \end{pmatrix}, \tag{3.33}$$

which are the familiar reflection coefficients of Eq. 3.15. For a monostatic (backscatter) radar configuration, no coherent signal would be received from a specular surface. More common for radar waves, the terrain has a certain surface roughness ks, and will both have specular and non-specular reflections, called 'coherent' and 'non-coherent' components, respectively. With increasing surface roughness, the incoherent component will be larger. Scatter is defined as the collective term of both the coherent and incoherent components.

Let's assume normal incidence on a specular surface again, where all of the backscatter would be coherent (, i.e., normal reflection). All of the signal transmitted in h-polarisation would also be scattered in h-polarisation, i.e., no de-polarisation would occur. With increasing surface roughness, non-coherent scatter increases, and more de-polarisation can occur. The backscatter from an h-polarised transmitted signal received in the v-direction, is called *cross-polarised* scatter; backscatter from the same signal received in the h-direction is called *co-polarised*.

Next, assume a backscatter configuration, where the antenna is side-looking (Figure 3.3). For a specular surface, no normal incidence occurs, and no backscatter

would return. Both co-polarised and cross-polarised backscatter increases with increasing surface roughness. The co-polarised backscatter is then typically caused by the signal scattering back from small variations in the (electromagnetic) terrain that are normal incident. Although not often defined as such, co-polarised backscatter can thus be seen as a coherent signal from the micro-variations within the em-terrain. Other co-polarised signal can also be a result of diffractions, where a beam is spread out in multiple directions because it meets a small em-terrain variation (in the range of a wavelength or smaller). Cross-polarised signals can come from backscatter from outside of the area that is also illuminated, but leads to the same travel time, e.g. because of slightly higher elevation. It can also be caused by multiple reflections/scatter within the area, e.g. because of heterogeneity or vegetation. Finally, diffractions can also cause cross-polarised signals.

The fields $\mathbf{E}^t$ and $\mathbf{E}^r$ are related by

$$\mathbf{E}^r = \frac{e^{-jkR_r}}{R_r}\mathbf{S}\,\mathbf{E}^t, \tag{3.34}$$

where $\frac{e^{-jkR_r}}{R_r}$ is a *spherical propagation factor*, and $\mathbf{S}$ thus holds information on the reflection or scattering properties of the illuminated area for each polarisation of the E field. For the case of a point target with scattering matrix $\boldsymbol{S}$, its pq-polarised backscattering strength is defined by the *radar cross section*, given by Ulaby et al. (2014) as:

$$\sigma_{pq} = 4\pi|S_{pq}|^2, \tag{3.35}$$

where the factor $4\pi^2$ represents the spherical spreading from the point target. If a target area is distributed, it consists of N point scatterers and has area A. Its *reflectivity* σ^0_{pq}, also called *backscattering cross section*, is then defined for pq-polarisation as:

$$\sigma^0_{pq} = \frac{4\pi}{AN}\sum_{i=1}^{N}|S^i_{pq}|^2 \tag{3.36}$$

3.3.7 Known methods for estimation of backscatter from a soil

3.3.7.1 Kirchhoff Scattering

Kirchhoff scattering assumes that plane-boundary reflection can occur at every point of the reflected surface. In other words, all of the scatter is coherent. Kirchhoff scattering methods calculate radar scatter for surfaces with gentle undulations. Assuming that the horizontal dimension of these undulations are large compared with the incident wavelength, local diffraction is neglected. For the case

of monostatic scattering, where the transmitter and receiver look in the same direction with an incidence angle θ (Figure 3.3), the Kirchhoff stationary phase method calculates backscatter as (Ulaby et al., 1982, their Eq. 12.45):

$$\sigma^r_{pp}(\theta) = \frac{|R_{pp}(0)|^2 e^{-(\tan^2\theta/2\sigma^2|\rho''(0)|)}}{2\sigma^2|\rho''(0)|cos^4\theta}, \tag{3.37}$$

where

- $\sigma^0_{pp}(\theta)$ is the backscatter coefficient of the pp polarisations (e.g., HH or VV);
- θ is the angle of incidence;
- $R_{pp}(0)$ is the Fresnel reflection coefficient evaluated at normal incidence (and equal to S_{vv} or S_{hh} of Eq. 3.32);
- σ^2 is the height variance. If the height distributions of the rough surface is Gaussian, σ is the rms height s.;
- $\rho''(0)$ is the second derivative of the correlation function of the rough surface. For a Gaussian surface that is $-2/L^2$, where L is the correlation length;

Furthermore, multiple scattering is neglected, and thus no depolarisation occurs (e.g., Fung and Eom, 1979):

$$\sigma^r_{pq}(\theta) = 0 \tag{3.38}$$

Eq. 3.37 is depicted for different soil types and rms slopes. The rms slope m is known for a Gaussian surface as (e.g., Ulaby et al., 2014):

$$m = \sqrt{-s^2\rho''(0)}. \tag{3.39}$$

The Kirchhoff stationary can only be applied with gentle undulations, i.e., where the radius of curvature is large enough to assume plane-boundary reflection. This leads to the following constraints (Ulaby et al., 1982):

$$k_1 L > 6 \tag{3.40a}$$
$$L^2 > 2.76 s\lambda_1 \tag{3.40b}$$
$$k_1 s > \approx 2, \tag{3.40c}$$

where L is the correlation length, s is the rms height, and in which 1 specifies medium 1 (e.g. air). These conditions limit the applicability of the Kirchhoff scattering method.

3.3.7.2 Small-Perturbation model

While the Kirchhoff model has to work with gentle, undulating slopes, the Small-Perturbation model allows surfaces to vary within the distance of a wavelength.

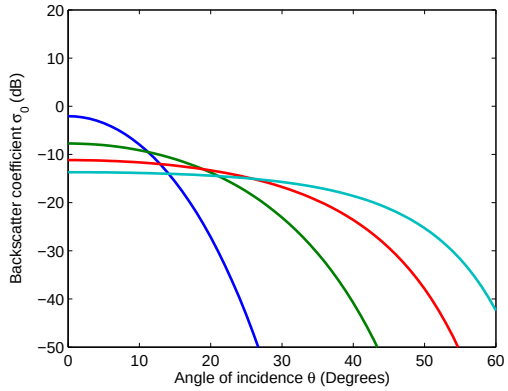

(a) After Ulaby et al. (1982), their Figure 12.2, $\varepsilon = 1.6$

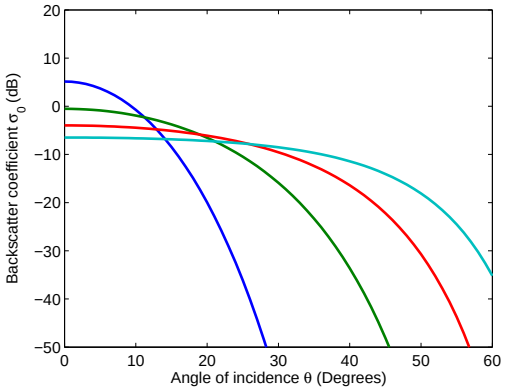

(b) Dry sand, $\varepsilon = 3$

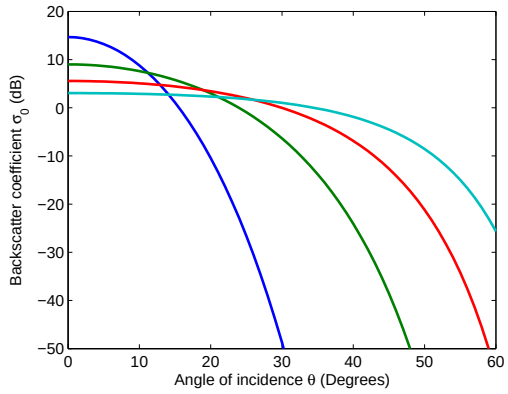

(c) Fresh-brackish water-saturated sand, $\hat{\varepsilon} = 75 - 30i$

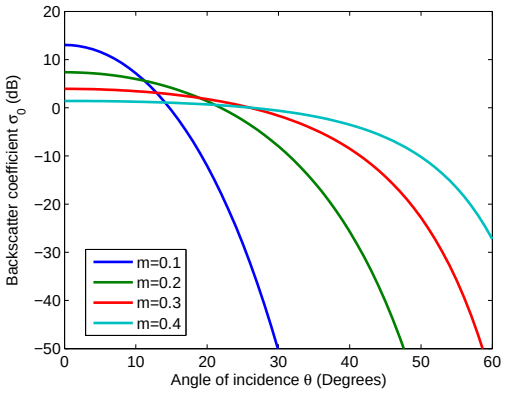

(d) Silty clay, after Hallikainen et al. (1985), $\hat{\varepsilon} = 24 - 5i$

Figure 3.10: Backscatter coefficient from a rough surface vs. incidence angles according to the Kirchhoff stationary phase method. Figure made with for rms slopes (m) of 0.1-0.4, and different permittivities (a-d).

If a Gaussian distribution of electromagnetic heights is assumed, then the Small-Perturbation model defines the backscattering cross section as (Ulaby et al., 1982, , their equation 12.110):

$$\sigma^0_{pq} = 8k^4 s^2 \cos^4\theta |\alpha_{pq}|^2 W \tag{3.41}$$

where,

$$W = \frac{L^2}{2}\exp\left[-\left(kL\sin\theta\right)^2\right] \tag{3.42a}$$

$$\alpha_{hh} = \left[\mu_r\cos\theta - \left(\mu_r\varepsilon_r - \sin^2\theta\right)^{1/2}\right] / \left[\mu_r\cos\theta + \left(\mu_r\varepsilon_r - \sin^2\theta\right)^{1/2}\right] \tag{3.42b}$$

$$\alpha_{vv} = \left(\varepsilon_r - 1\right)\frac{\sin^2\theta - \varepsilon_r\left(1+\sin^2\theta\right)}{\left[\varepsilon_r\cos\theta + \left(\varepsilon_r - \sin^2\theta\right)^{1/2}\right]^2} \tag{3.42c}$$

$$\alpha_{vh} = \alpha_{hv} = 0 \tag{3.42d}$$

where,

- k is the wavenumber in medium 1 (usually air);
- s is the rms height;
- L is the correlation length;
- θ is the incidence angle;
- μ_r is the permeability of medium 2 relative to medium 1;
- ε_r is the permittivity of medium 2 relative to medium 1.

The Small-Perturbation model works for a 'slighty rough surface', i.e., a surface with s much less than 5 percent of the incident wavelength and an average surface slope comparable or less than s times the wave number k. This leads to these constraints (Ulaby et al., 1982):

$$s/L <\sim 0.21 \tag{3.43a}$$

$$k_1 s < 0.3, \tag{3.43b}$$

3.3.7.3 IEM method

The Kirchhoff and Small-Perturbation models have limited applicability because of their constraints (Eqs. 3.40 and 3.43). Fung et al. (1992) bridged the gap between these existing models by developing the Integral Equation Method (IEM), which is able to calculate backscatter from a surface with any degree of roughness. The method is mathematically advanced, based on an approximate soilution of a pair of integral equations, and is able to calculate multiple scattering contributions and de-polarised signal from a soil. Although this method might give the

theoretical most correct results, application is computationally intensive: application of existing Matlab code (accompanying Ulaby et al., 2014) on a 2.80 GHz computes backscatter for one pixel in approximately 10 minutes. Application to entire high resolution satellite images, consisting of million of pixels and multiple images over time, is therefore not feasible. The IEM is therefore not considered for application to Sentinel-1 data.

3.3.7.4 Semi-empirical approach: the PRISM forward model

As the Kirchhoff scattering and small perturbation methods are limited to a small range of surface roughness and correlation lengths, and other methods for further calculation are too computationally intensive, semi-empirical methods were developed by Oh et al. (1992). They first defined the co-polarised ratio p and cross-polarised ratio q as:

$$p = \frac{\sigma^0_{hh}}{\sigma^0_{vv}}, \tag{3.44a}$$

$$q = \frac{\sigma^0_{hv}}{\sigma^0_{vv}}, \tag{3.44b}$$

after which they developed empirical models fitting the ratios. These were first defined in terms of surface roughness and Fresnel reflection coefficients (the PRISM-1 model):

$$p = \frac{\sigma^0_{hh}}{\sigma^0_{vv}} = \left[1 - \left(\frac{2\theta}{\pi}\right)^{\alpha} e^{-ks}\right]^2, \tag{3.45a}$$

$$q = \frac{\sigma^0_{hv}}{\sigma^0_{vv}} = 0.23\sqrt{\Gamma_0}\left[1 - e^{-ks}\right], \tag{3.45b}$$

$$\sigma^0_{vv} = 0.7\left[1 - e^{-0.65(ks)^{1.8}}\right]\frac{\cos^3\theta}{\sqrt{p}}\left[\Gamma_v(\theta) + \Gamma_h(\theta)\right], \tag{3.45c}$$

where Γ_0 is the Fresnel reflection coefficient for normal incidence, $\alpha = 1/3\Gamma_0$, and $\Gamma_v(\theta)$ and $\Gamma_h(\theta)$ are the Fresnel reflection coefficients for horizontal and vertical polarisations, as a function of incidence angle θ.

Oh et al. (2002) and Oh (2004) then developed a semi-empirical model (PRISM-2) that substituted Γ and ε with soil moisture (M_v):

$$p = \frac{\sigma^0_{hh}}{\sigma^0_{vv}} = 1 - e^{-0.4(ks)^{1.4}}\left(\frac{2\theta}{\pi}\right)^{0.35M_v^{-0.65}}, \tag{3.46a}$$

$$q = \frac{\sigma^0_{vh}}{\sigma^0_{vv}} = 0.095\left(0.13 + \sin 1.5\theta\right)\left[1 - e^{-1.3ks^{0.9}}\right], \tag{3.46b}$$

$$\sigma^0_{vh} = 0.11M_v^{0.7}\left(\cos\theta\right)^{2.2}\left[1 - 0.32\left(ks\right)^{1.8}\right], \tag{3.46c}$$

This model agrees with field observations for soil moisture $0.04 < M_v < 0.29$ $[m^3/m^3]$ and surface roughness values of $0.13 < ks < 6.98$, at incidence angles 10°

$< \theta < 70°$. The PRISM method can calculate backscatter in pp and pq directions for either inputs of s and *epsilon* (PRISM1, Oh et al., 1992), or inputs of s and soil moisture (PRISM2, Oh, 2004). In general, both PRISM-1 and PRISM-2 lead to similar, but slightly different, backscatter values.

Modelled PRISM backscatter compared to Kirchhoff backscatter (Figure 3.11) shows that Kirchhoff backscatter calculations calculate a much higher backscatter for low incidence angles, and a much lower backscatter for high incidence angles. The main difference is interpreted as a result of the assumption in Kirchhoff backscatter: that the surface exists of gentle undulations. A more realistic surface consists of smaller undulations and will therefore result in more 'non-coherent' backscatter at larger incidence angles. As the empirical findings of the PRISM methods are based on many observations, they are deemed more reliable than the limited Kirchhoff scattering method.

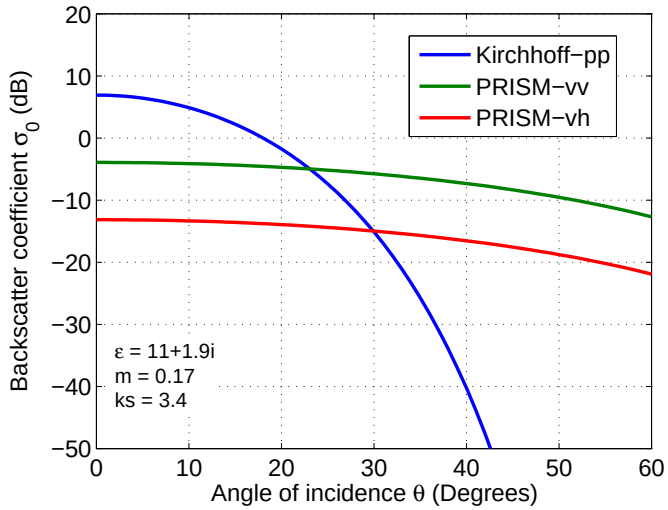

Figure 3.11: Backscatter σ_0 of the Kirchhoff stationary phase and PRISM methods.

3.3.8 Topography

Terrain slope (β) can cause the angle of incidence (θ) to be locally different. The resulting *local incidence angle* α, relies on θ and β (e.g., Westerhoff et al., 2013):

$$\alpha = \theta - \beta. \tag{3.47}$$

where β is positive if terrain slopes towards the satellite (Figure 3.12). The incidence angle θ is usually defined as the nominal angle between the satellite sensor and the normal to the surface of an earth ellipsoid without local terrain variation. The value α is the 'true' angle. Backscatter calculation methods could thus hold errors due to wrong assumptions on the local terrain. This assumption is tested using the PRISM method with M_v=0.1 and ks =1. Not incorporating a

terrain model can cause considerable error (, i.e., 10 dB at 10° wrongly assumed terrain slope, Figure 3.13, left). Error due to a too coarse or inaccurate terrain model causes small errors (i.e., $<$ 1 dB at 1° error in the terrain slope, Figure 3.13, left), also suggested by Westerhoff et al. (2013). Accounting for terrain slope is thus important: over the whole spectrum of θ and β, maximum error in backscatter calculations up to approximately 20 dB (Fig. 3.13, right).

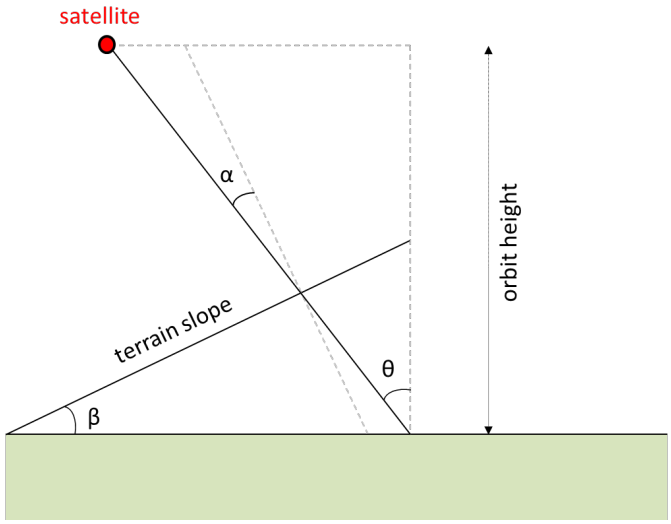

Figure 3.12: The relation between terrain slope β, incidence angle θ and local incidence angle α.

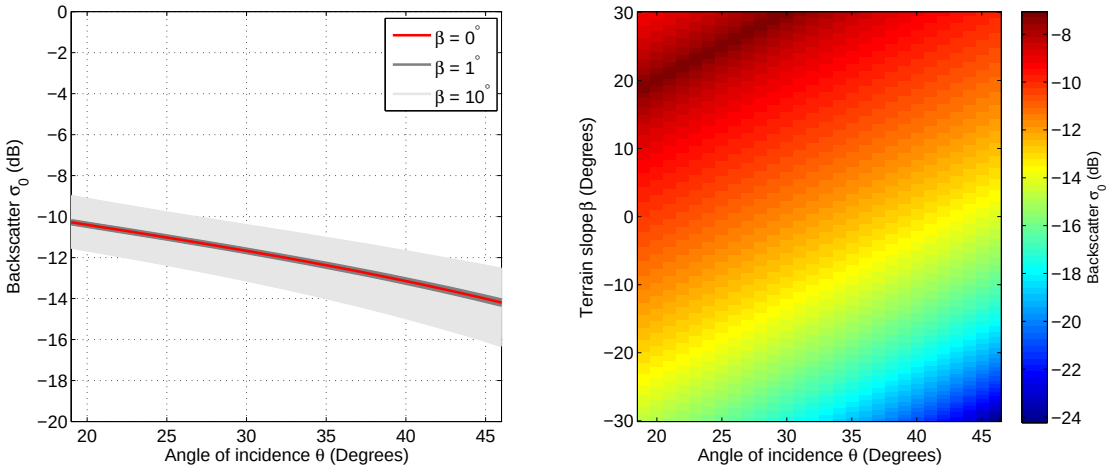

Figure 3.13: Backscatter coefficient σ_0 vs incidence angle θ for different terrain slope β. **Left**: backscatter of a terrain slope from 0 (red) and differences with increasing terrain slope, from 1° (dark grey) up to 10° (light grey). **Right:** σ_0 for θ and β ranging from zero to 45 °.

3.3.9 Vegetation

Dielectric properties change with different vegetation types and growth. They can be assumed by a simplified *mixing model*: a model where different substances occur in one volume. For example, Ulaby et al. (1987) introduced a linear model for the dielectric constant of a vegetation:

$$\varepsilon_{veg} = \varepsilon_r + \nu_{fw}\varepsilon_{fw} + \nu_{bw}\varepsilon_{bw}, \tag{3.48}$$

where ε_r is the dielectric constant of the actual plant fibre, volume fractions are given by ν and the dielectric properties of free water (ε_{fw}, water free to move within the plant) and bound water (ε_{fw}, water inhibited by the plant molecules, further details in Ulaby and Long, 2014). At C-band frequencies, El-Rayes and Ulaby (1987) measured values for corn leaves that varied, from low to high moisture values, in between 1 and 43 for ε' and 0 and 13 for ε''. Ulaby et al. (1987) found similar values and also separated for the effect of stalks and leaves. For volumetric moisture M_v of 0.65 for leaves (l) and 0.47 for stalks(s), they found:

$$\hat{\varepsilon}_l = \varepsilon_0 \left(27 - i7\right), \tag{3.49a}$$

$$\hat{\varepsilon}_s = \varepsilon_0 \left(14 - i4\right). \tag{3.49b}$$

Assuming a pp signal transmitted by a satellite, vegetation affects the backscatter as follows:

- it depolarises the backscatter, as multiple scattering takes places in all directions against the leaves and stalks (possibly via the ground);
- it attenuates the pp backscatter, as more signal will be scattered in all directions, and thus less to the satellite. It could however result in a slight increase in pq signal at the receiver, although this depends on the attenuation properties of the vegetation.

Therefore, sometimes more advanced vegetation backscatter models are necessary. The *single-scattering radiative transfer model* (S^2RTR) approximation combines several models in one and accounts for the different types of the vegetation (Figure 3.14):

- the scattering of a bare soil;
- the volume scattering of the illuminated area, according to e.g. Attema and Ulaby (1978);
- the multiple scattering through canopy to ground and vice versa:
  i. from canopy to ground to satellite;
  ii. from ground to canopy to satellite;
  iii. from canopy to ground to canopy to satellite.

It is based on an energy balance, i.e., that the total (incoming, reflected, and transmitted) energy is conserved when the microwaves travel through the vegetation. The energy balance is defined by scattering matrices (, e.g., Eq. 3.32) and extinction properties of particles (more detail in Chandrasekhar, 1960; Ulaby et al., 2014). These particles could be defined as spherical Rayleigh scatterers: particles that are small compared to the wavelength of the electromagnetic signal. If multiple scattering between leaves and/or stalks is ignored, an approximate form of the S^2RTR model for spherical Rayleigh scatterers is (Ulaby et al., 2014, their equations 11.77 and 11.78):

$$\sigma^0_{vv}(\theta_i) = \Upsilon^2 \sigma^0_{s_{vv}}(\theta_i) + \frac{3}{4} a \cos\theta_i \left(1 - \Upsilon^2\right)\left(1 + \Gamma^2 \Upsilon^2\right) + 6\kappa_s d \Gamma \Upsilon^2, \quad (3.50a)$$

$$\sigma^0_{hv}(\theta_i) = \Upsilon^2 \sigma^0_{s_{hv}}(\theta_i), \quad (3.50b)$$

in which:

- the *transmissivity* Υ is the ratio of power transmitted through the vegetation and the incoming power. It is here assumed to be the same for p- and q-polarisation and is defined as:

$$\Upsilon = e^{-\tau_p}, \quad (3.51)$$

- the *optical depth* with τ is defined as:

$$\tau = \kappa_e d \sec\theta_i \quad (3.52)$$

- κ_e is the *extinction coefficient*. It accounts for loss of energy due to absorption and scattering ($\kappa_e = \kappa_a + \kappa_s$) and is assumed here to be uniform throughout the vegetation.
- The single-scattering albedo is defined as

$$a = \frac{\kappa_s}{\kappa_e} \quad (3.53)$$

- vegetation height is denoted by d.

The unit of τ is [Np], which is equivalent to $\frac{20}{\ln 10} \approx 8.685889638$ dB. Since the unit of d is [m], the unit of κ_e, κ_a, and κ_s is [Np/m].

3.3.10 Sensitivity analyses of known methods of backscatter towards soil moisture and vegetation

Results of sensitivity of soil moisture and vegetation to backscatter of backscatter forward models have been applied in the past. Chunfeng Ma et al. (2015) concluded, through analyses of sensitivity indices using the IEM method, that

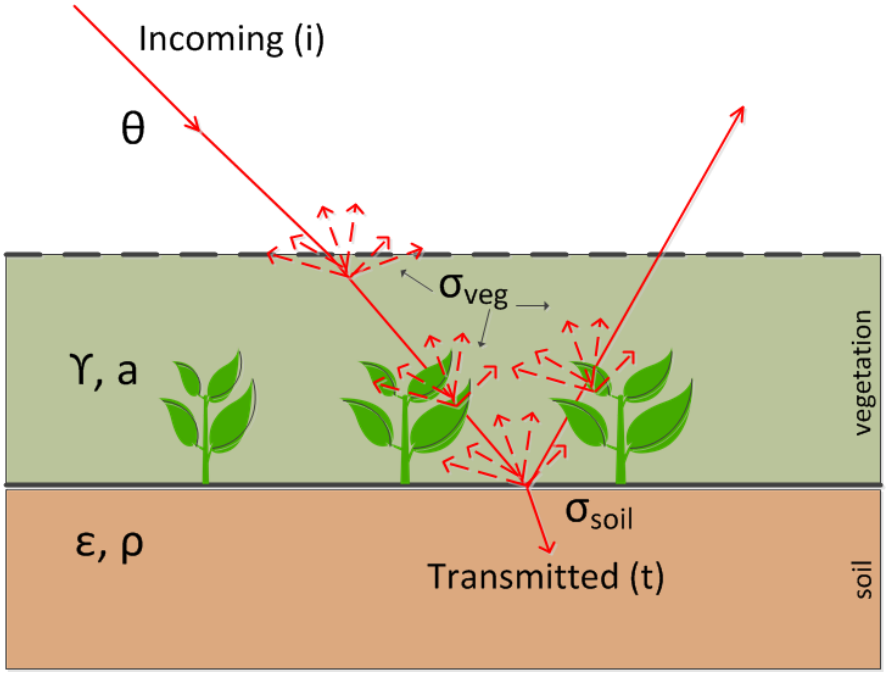

Figure 3.14: Microwave backscatter from soil and vegetation.

backscatter is most sensitive to rms height and soil moisture. However, the use of a sensitivity index did not gave insight on variability of the combined effect of these sensitivity. Also, they did not include vegetation information in their analyses. Wang et al. (1998) had similar findings, i.e., they found that C-band backscatter data was mostly sensitivity to rms height, correlation length and soil moisture. They used different backscatter models, amongst which were the PRISM model (Oh et al., 1992). Additionally, they included a canopy backscatter models for pine forest and found that different tree maturity had large influence on the sensitivity. Du et al. (2000) found, using the small-perturbation model and the S^2RTR model for vegetation, that backscatter is sensitive to both soil moisture, surface roughness, and vegetation, but that more vegetation does not necessarily always means that sensitivity to soil moisture decreases. They ignored the effect of terrain slope.

3.3.11 Known methods for inversion of backscatter to soil moisture

Models like Kirchhoff scattering, Small-Perturbation, IEM and PRISM (section 3.3.7) are called *forward models* onwards: they are fed with input components, i.e., soil type, surface roughness, soil moisture, vegetation, and they calculate the according backscatter. Inverse models are considered to be able to calculate components surface roughness, soil moisture, vegetation etc. from the backscatter.

A well-known problem in geophysics is called non-uniqueness: there are multiple

solutions for an inverse model to fit the answer. In the case of radar backscatter, the answer is backscatter and the solutions are the multiple input components surface roughness, soil moisture, vegetation, if we assume that other input components (i.e., soil type, soil density, clay fraction, sand fraction, temperature) have a negligible effect on the backscatter.

De Roo et al. (2001) researched an inverse relation between soil moisture and vegetation, using field measurements and full polarimetric (i.e., all HH, VV and HV components) data. This involved a best fit approach for both the polarised (σ^0_{hh} and σ^0_{vv}) and depolarised signals σ^0_{hv}. Methods that calculate soil moisture from radar backscatter are described in Dubois et al. (1995a,b) (SMART), and Oh et al. (1992, 2002) (PRISM). However, these methods need to work with all three σ_{hh}, σ_{vv} and σ_{hv} polarities. Also, they do not take into account vegetation characteristics and only work with limited soil types.

A genetic algorithm (GA) can solve for optimization problems based on a natural selection process that mimics biological evolution. A GA is typically used when problems are highly non-linear and a direct inversion is hard to calculate. The forward model in this research is highly non-linear, since it is a combination of non-linear backscatter calculations of the soil and its moisture and vegetation corrections. The GA mimics the behaviour of 'survival of the fittest'. By modifying a population of individual solutions, the GA randomly selects individuals from a current population and uses them as parents to produce the children for the next generation. For multiple time steps (generations) the population then evolves toward an optimal solution (Mathworks, 2015a). Jin and Wang (2001) explain the evolutionary part of a GA as follows (which is depicted in Figure 3.15): "In the GA algorithm, each parameter is encoded into a gene, which is simply a binary representation. A trial solution of a set of genes composes a chromosome. A number of different chromosomes forms a population. The initial population is generated randomly. Then the population undergoes natural selection, i.e. the chromosomes are tested for their fitness to the cost function. All of the chromosomes with higher fitness survive as the parents for the next generation, while all of the chromosomes with lower fitness are discarded. Cloning of the surviving parents improves the population quality. Mating parents produce new offspring, which inherit their parents' fitness. During this operation, the size of the population remains constant. The binary-encoded parents can mate with each other by swapping their binary bits with their partner. To maintain population diversity and avoid the algorithm being trapped at a local minimum, a random operation of mutation or new blood is introduced into the new population." Jin and Wang (2001) then used a GA to solve for soil moisture, correlation length l, backscatter, and complex permittivity. Using the Small Perturbation model (section 3.3.7.2), they solved for soil moisture using single polarised (hh) backscatter. However, the underlying non-uniqueness and its effect on the solution was not discussed or explained. Furthermore, only two ground-observations were used as validation. Finally, using the Small-Perturbation model only works for areas that comply to the model's boundary constraints (i.e., a 'slightly rough surface'). Although this work seems as potentially valuable, it also seems to incomplete and this approach

was not followed up afterwards.

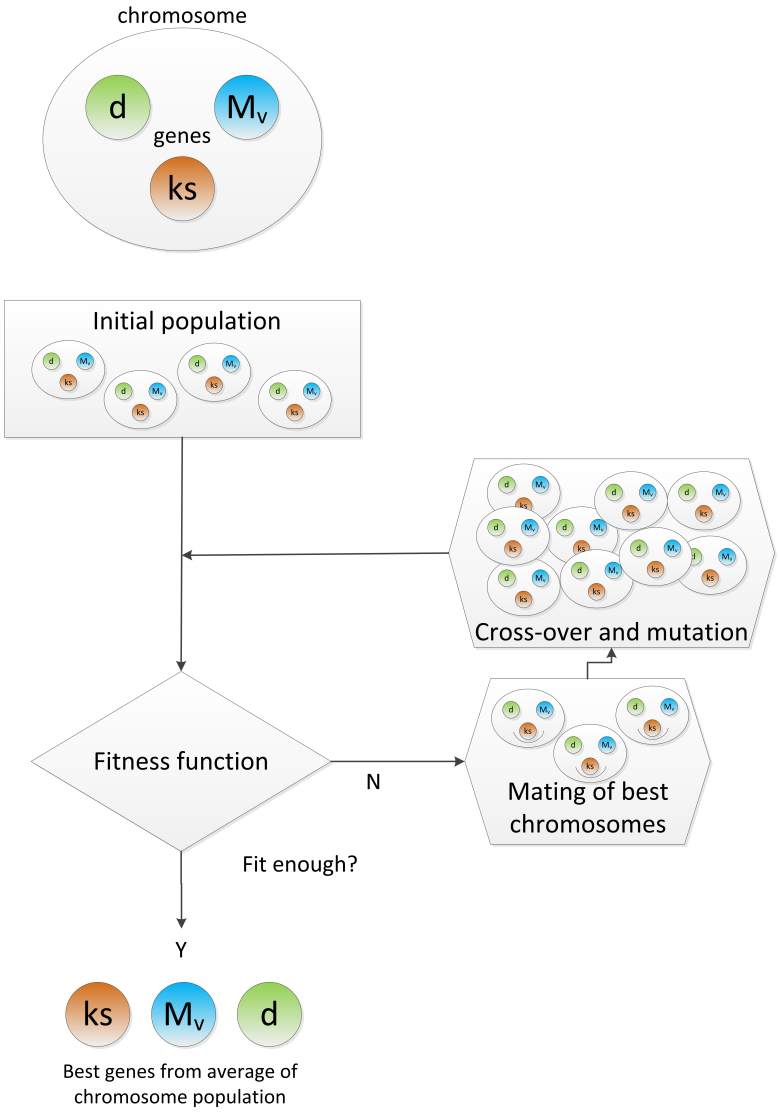

Figure 3.15: Flow chart explanation of a genetic algorithm.

Oh (2006) acknowledged the advantage of a GA algorithm over traditional optimisation techniques, since a GA does not tend to get stuck in a local minimum of non-unique solutions. He then used a GA to solve for soil moisture using the vh and vv polarised backscatter and co-polarised ratio p. However, as this inversion technique works on dual-polarised data, it does not work for single polarised data (like vv-polarised data which is the standard data delivery for Sentinel-1 SAR data in New Zealand).

Yi-Cheng Lin and Sarabandi (1999) used a genetic algorithm in combination with a simplified fractal-based scattering forward model to retrieve forest parameters, such as trunk properties, branching, and wood and soil moisture. Their approach seems to fit ground-observed soil moisture values well for single polarisation C-band VV data (similar to standard Sentinel-1 data for New Zealand). However,

soil moisture only plays a negligible part in their algorithm and canopy properties play the major role. As forest floors are covered with leaves, and the backscatter is not likely to penetrate to the surface at all, it seems that the method infers a soil moisture indirectly from the other model parameters, without basing it on actual backscatter from the soil layer. All further described research in their article focus on the vegetation part of this model and not on the soil moisture.

3.4 Methodology

This section describes three methods that have been developed during the PhD research. These methods will attribute to a better understanding of uncertainty and noise in SAR methods, and might help to better estimate soil moisture from microwave backscatter. First, small differences in vegetation or soil moisture can cause an unexpected phase disturbance in the scattered signal. A method is developed to better understand this phenomenon. Second, a method to calculate the sensitivity of modelled backscatter to its input components is described. Finally and most importantly, a method is described to calculate soil moisture from radar backscatter. This method consists of a forward and an inverse part and is tested on high-resolution satellite backscatter data from the Sentinel-1 satellite.

3.4.1 Phase disturbances in radar backscatter

Reflection from a dielectric to lossy media can cause a phase disturbance (shift) between the original incoming and the reflected wave field; transmission through the media can also cause a phase shift between the E and H field (section 3.3.3). To gain more insight in the effect that seasonal variation of soil moisture and vegetation has on the phase shift between the E and H field, some experiments were performed: these are described here.

Propagation and reflection from a dielectric to a lossy medium was calculated using Eqs. 3.14, and 3.21 to 3.23. Kirchhoff scattering was assumed (see section 3.3.7.1), i.e., that all energy of a backscattered signal is caused by normal incidence. As common in interferometric SAR (InSAR) processing (ESA, 2007), correlation coefficients were calculated to estimate the coherence. For that, a complex coherence $\hat{\gamma}$ of the H- and E-signals between dry sand and brackish water-saturated sand was calculated (as described by Ferretti et al., 2007):

$$\hat{\gamma} = \frac{\sum_{i=1}^{N} x_i y_i*}{\sqrt{\sum_{i=1}^{N} \mid x_i \mid^2} \sqrt{\sum_{i=1}^{N} \mid y_i \mid^2}} \tag{3.54}$$

where x and y are amplitudes of two different satellite overpasses, and N is the number of spatial samples that are tested. The * denotes the complex conjugate value.

First, a bare soil was assumed. E and H fields were calculated for a EM field travelling from air (medium 1) and reflecting on a soil (medium 2) with $\hat{\varepsilon} = 75 - i30$, corresponding to a brackish water-saturated sand. Similar motion plots to Figures 3.7 and 3.8 in the theory section were then analysed.

Second, E and H fields were calculated for a EM field travelling from air (medium 1) and reflecting on a soil (medium 2) surface for a range of permittivity values ($2 < \varepsilon' < 80$ and $0 < \varepsilon'' < 50$) of that soil. This range was assumed to cover most soil types and soil moisture, both fresh and brackish (see also Table 3.1). Then, a reference soil of dry sand ($\hat{\varepsilon}$=3) was assumed. The results for E and H fields were plotted as $\hat{\gamma}$ - coherence plots, showing the difference in angle and amplitude between the soil and the reference soil.

Third, an extra vegetation layer in between air and soil was introduced with a height of approximately 12 cm (i.e., twice the wavelength for C-band radar). Transmission through that layer was modelled with permittivity values ranging in between $0 < \varepsilon' < 10$ and $0 < \varepsilon'' < 2$. These are based on the findings of El-Rayes and Ulaby (1987) and Ulaby et al. (1987) for corn (section 3.3.9). A simplifying assumption was made, i.e., that multiple scattering in between stalks and leaves are ignored. Dielectric properties of a vegetated area were then approximated by a mixing model approach (e.g., see Eq. 3.48) of the entire vegetated volume, including air:

$$\hat{\varepsilon}_{total} = \hat{\varepsilon}_{air} + \nu_{leaf}\hat{\varepsilon}_{leaf} + \nu_{stalk}\hat{\varepsilon}_{stalk}, \tag{3.55}$$

where ν_{leaf} and $+\nu_{stalk}$ represent the relative contribution of the vegetation in a volume. For example, using the estimated values of Eq. 3.49, and assuming a vegetated volume, with 20% of the volume filled with vegetation (15% leaves, 5% stalks), the transmitted signal through the vegetation then travelled through a volume with permittivity of

$$\hat{\varepsilon}_{total} = 5.55 - 1.25i \tag{3.56}$$

before reflecting at the surface. The vegetation coherence plots were calculated for two underlying soils: dry sand and a water-saturated silty clay ($\hat{\varepsilon}$=24-i5).

3.4.2 Simplified sensitivity of backscatter to model input parameters

Summary: a method was developed to calculate a simplified sensitivity of backscatter to its input components, and from there conclude which model parameters are most sensitive to backscatter.

Inspired by findings of Du et al. (2000) (section 3.3.10), and the sensitivity analyses for ET in chapter 2, a method was developed to give more insight in sensitivity of backscatter to its different input components. Therefore, a set of random values were generated for incidence angle θ, surface roughness ks, soil moisture M_v, and clay fraction cf (See Table 3.3). The number of random values (10^5) was

tested first, and chosen on the simple condition that the resulting sensitivity plots created smooth lines. Ranges for these value of input components were based on the validity of the PRISM model (section 3.3.7.4) and assuming that for optical depth larger than 2 backscatter to the soil is insignificant. First, the PRISM model was used to calculate vv, hh, and hv polarised backscatter for bare soils for all random combinations. Then, vegetation was added (through optical depth τ), and the PRISM and S2RTR models were subsequently used in the same exercise to calculate backscatter.

Table 3.3: Minimum and maximum of the random input components for the forward backscatter model used in the sensitivity analysis θ, M_v, ks, cf. Soil density ρ was assumed a constant 1.7 [g/cm^3]

	min value	max value
θ [Deg]	0	60
M_v [m^3 m^{-3}]	0	0.35
ks [-]	0.1	5
cf [-]	0	1
τ [m]	0	2

Then, 40 discrete bins were assumed in between the minimum and maximum value of each input component. For each bin, mean and standard deviation of backscatter in vv, hh, and vh polarisations were calculated. The means were then, per input components ks, M_v, θ, cf, ρ_b, and τ, fitted as a function of the backscatter value (in dB). These functions were then differentiated and fitted again. The fitting function module was written in such a way that the best fit was chosen between 3 polynomial (linear, quadratic and cubic)and 2 exponential functions (i.e., $f(x) = a*e^{bx}$ or a sum of two different ones $f(x) = a*e^{bx}+c*e^{dx}$). This led to estimates of partial derivatives of backscatter per input component. These partial derivatives, the *sensitivity*, could for example be used to calculate variance of the backscatter, according to Eq. 3.57 (see Appendix B for more details on variance and error propagation):

$$VAR_{\sigma_{pq}} = \sum_{i=1}^{i=N} \frac{\partial \sigma^0_{pq}}{\partial x_i} VAR_{x_i} \tag{3.57}$$

3.4.3 Calculation of soil moisture from microwave backscatter

Summary: a method is described to estimate soil moisture from radar backscatter. The method applies forward models to calculate backscatter from soil and vegetation and an inverse model to estimate soil moisture from the backscatter.

3.4.3.1 Input data and pre-processing steps

Sentinel-1 Synthetic Aperture Radar backscatter

Sentinel-1A data was downloaded from Sentinels Scientific Data Hub (ESA, 2015c). Gridded VV polarised data from the IW sensor mode were downloaded for all of New Zealand from October 2014 to December 2015. Data is provided in the SAFE format (ESA, 2015a). Locations and swath information is stored in xml annotations, and the measurement is stored in a GeoTiff file.

Table 3.4: Specification of Sentinel-1 data

Satellite	Sentinel-1A
Time period	October 2014 - December 2015
File format	Geotiff (SAFE: ESA, 2015a)
Format	Ground Range Detected (GRD)
Mode	Interferometric Wide Swath (IW)
Global incidene angles	29 - 46 Degrees
Pixel spacing	10 x 10 m
Polarisation	VV

Ground-observed soil moisture from NIWA's Cliflo network

Hourly soil moisture ground observations have been compiled to monthly statistics at 62 soil moisture stations in New Zealand in the period of October 2014 to November 2015 (NIWA, 2015). These values are the soil moisture measured at approximately 20 cm depth below the ground surface, expressed as a percentage by volume. Maximum value of soil moisture is assumed to be 65%. Data from the sensors is uncalibrated (Srinivasan, 2015). Station names and coordinates are given in Annex A.

Table 3.5: Station names and coordinates for all used soil moisture ground observations.

Station name	**Latitude**	**Longitude**
Kerikeri Ews	-35.183	173.926
Hanmer Forest Ews	-42.534	172.851
Te Puke Ews	-37.822	176.324
Blenheim Research Ews	-41.499	173.963
Paraparaumu Ews	-40.904	174.984
Invercargill Aero 2 Ews	-46.417	168.330
Waione Raws	-40.453	176.308
Dunedin, Musselburgh Ews	-45.901	170.515

Continued on next page

Table 3.5 – *Continued from next page*

Station name	Latitude	Longitude
Whakatu Ews	-39.607	176.911
Matamata, Hinuera Ews	-37.877	175.735
Kaitaia Ews	-35.135	173.262
Rangiora Ews	-43.329	172.611
Lincoln, Broadfield Ews	-43.626	172.470
Warkworth Ews	-36.434	174.668
Middlemarch Ews	-45.518	170.136
Ranfurly Ews	-45.124	170.100
Windsor Ews	-45.008	170.823
Pukekohe Ews	-37.206	174.864
Appleby 2 Ews	-41.317	173.095
Martinborough Ews	-41.252	175.390
Takaka Ews	-40.864	172.806
Stratford Ews	-39.337	174.305
Te Kuiti Ews	-38.334	175.153
Greymouth Aero Ews	-42.460	171.192
Franz Josef Ews	-43.365	170.134
Lake Tekapo Ews	-44.002	170.443
Gisborne Ews	-38.627	177.922
Dargaville 2 Ews	-35.931	173.853
Turangi 2 Ews	-38.975	175.791
Arapito Ews	-41.271	172.156
Arthurs Pass Ews	-42.943	171.563
Hamilton, Ruakura 2 Ews	-37.776	175.305
Balclutha, Telford Ews	-46.293	169.732
Cromwell Ews	-45.034	169.196
Waipara West Ews	-43.070	172.653
Dannevirke Ews	-40.217	176.117
Waipawa Ews	-39.952	176.617
Ohakune Ews	-39.419	175.413
Cheviot Ews	-42.829	173.224
Orari Estate Cws	-44.125	171.311
Wairau Valley, Mill Road Cws	-41.572	173.497
Waiau School Cws	-42.653	173.043
Hakataramea Valley Cws	-44.635	170.647
Akaroa Ews	-43.809	172.966
Methven Cws	-43.640	171.652
Waimate Cws	-44.741	171.063
Masterton, Te Ore Ore Cws	-40.957	175.707
Methven, Three Springs Cws	-43.678	171.588
West Eyreton, Larundel Farm Cws	-43.357	172.432
Reefton Ews	-42.117	171.860
Clyde 2 Ews	-45.203	169.318

Continued on next page

Table 3.5 – *Continued from next page*

Station name	Latitude	Longitude
Chertsey Cws	-43.794	171.961
Lismore, Racemans House Cws	-43.921	171.486
Tutira Cws	-39.224	176.839
Ashcott Road Cws	-39.958	176.380
Waipounamu Cws	-45.825	168.716
Five Rivers Cws	-45.626	168.367
Whitianga Ews	-36.828	175.672
Taumarunui Ews	-38.862	175.238
Diamond Harbour Ews	-43.633	172.728
Oamaru Ews	-45.057	171.023
Rotorua Ews	-38.146	176.258

Clay and sand fractions

Although microwave backscatter is not very sensitive to clay and sand fraction (see section 3.4.2), this information is available and is thus taken into account for the cases where there is more information on it. For that, S-MAP data from Landcare (Landcare Research, 2015) were assigned clay and sand fractions. This was done with the following processing steps:

- polygons were related to lookup tables, denoting percentages of (a.o.) clay, loam, sandy loam, silty loam, peat, and bare rock;
- percentages of clay, loam, sandy loam, silty loam were converted to sand, silt, and clay percentages using the soil texture triangle (Figure 3.5);
- it was assumed that silt is 50% clay and 50% sand fraction (section 3.3.2.2);
- bare rock was considered to not add to the clay or sand content: $sf + cf + br = 1$, with cf= clay fraction, sf= sand fraction, and br = bare rock.
- all other pixels were assumed to have sand and clay fractions of 0.8 and 0.2, respectively.

Resulting sand and clay fractions are shown in Figures

Leaf Area Index

Monthly Leaf Area Index, ranging from 0 to 10, was imported for New Zealand for the period January 2000 up to December 2014. Data originates from NASA's MODIS sensor and has been described by Park (2015) and Samanta et al. (2011). The data was processed to mean monthly values, including standard deviations. It was assumed that microwave loss of energy due to absorption and scattering

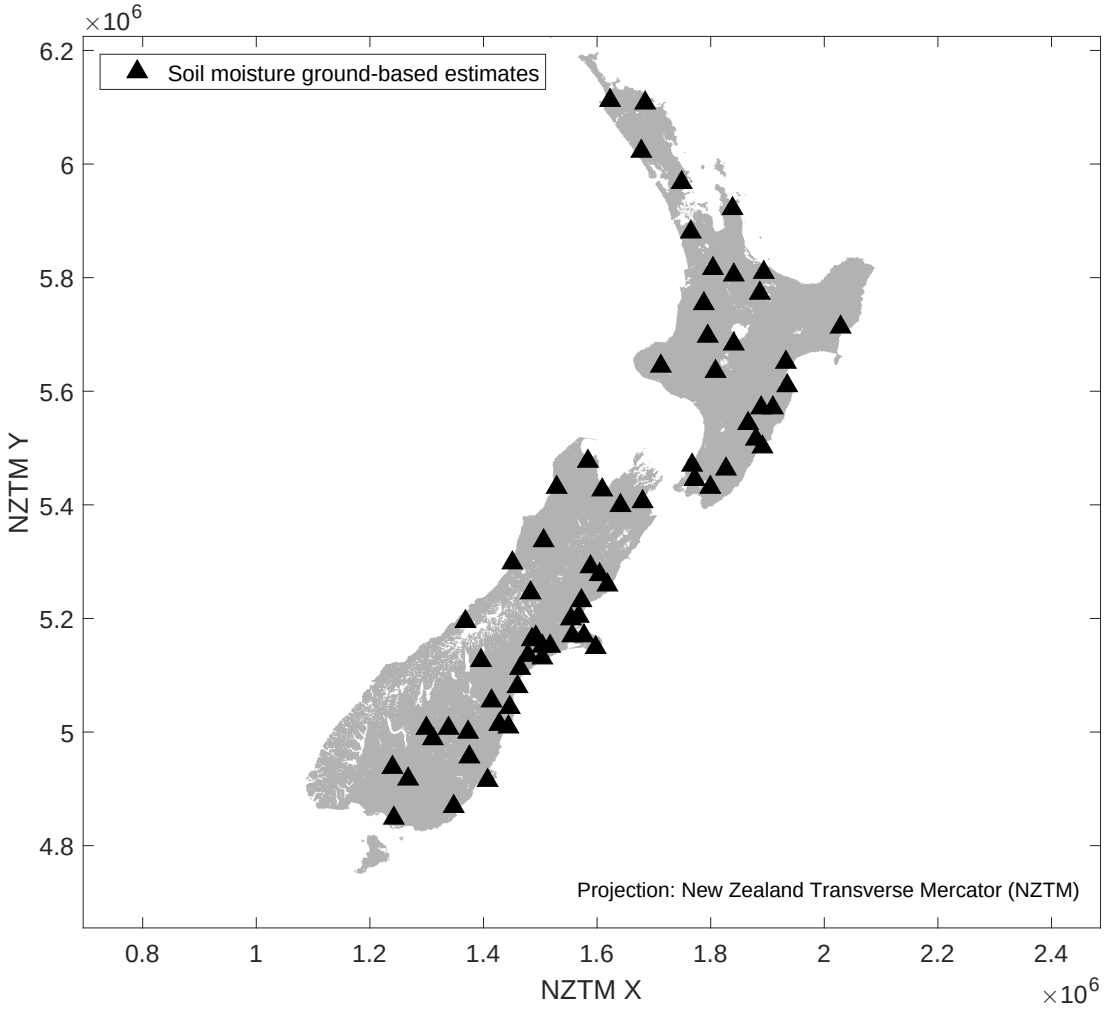

Figure 3.16: Location of soil moisture ground-based estimates used in this study.

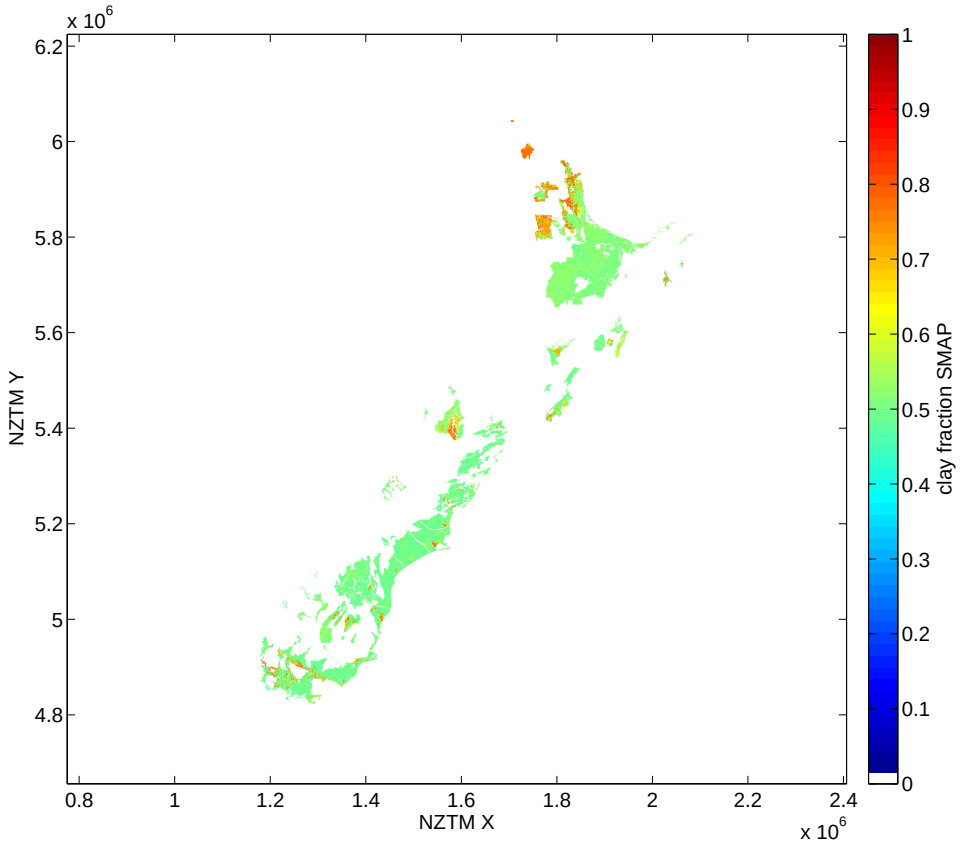

Figure 3.17: Clay fraction from SMAP.

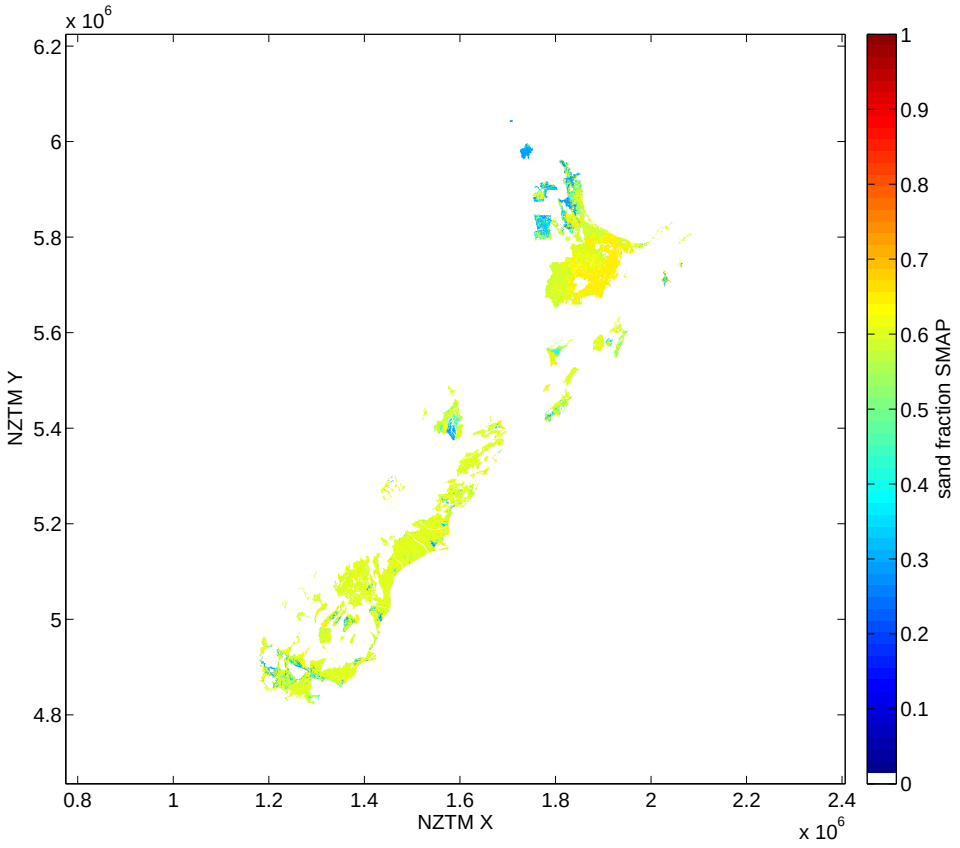

Figure 3.18: Sand fraction from SMAP.

of vegetation is uniform throughout the vegetation (section 3.3.9). Values for the LAI can then used as a proxy for the extinction coefficient κ_e:

$$\kappa_e = \frac{LAI}{10} \tag{3.58}$$

Topography

The Geographx New Zealand DEM 2.1 Geographx (2012) has used New Zealand based topographic data from Land Information New Zealand (LINZ) and data from the satellite derived Shuttle Radar Topography Mission (SRTM, USGS, 2006) data. The original resolution of the data is 8m x 8m. It was resampled to 20 m x 20 m. Then, the conversion of incidence angle to local incidence angle in line of sight of the satellite was calculated for each image by these steps (and depicted in Figure 3.20):

- the azimuth of line of sight ϕ was assessed by calculating the gradient of the incidence angle over the entire satellite image. This angle is uniform over the image and was defined as the angle from the positive Easting in the NZTM grid;
- the terrain slope was estimated in Easting (px) and Northing (py) direction [m/m] by calculating the gradient of the elevation in its NZTM coordinate grid;
- the slope β in the line of sight is then:

$$\beta = \arctan\left(\frac{px}{\cos\phi} + \frac{py}{\sin\phi}\right); \tag{3.59}$$

- the local incidence angle α is then, according to Eq. 3.47 and Figure 3.12, $\theta - \beta$.

The difference between global and local incidence angle is shown in Figure 3.21 (b and d).

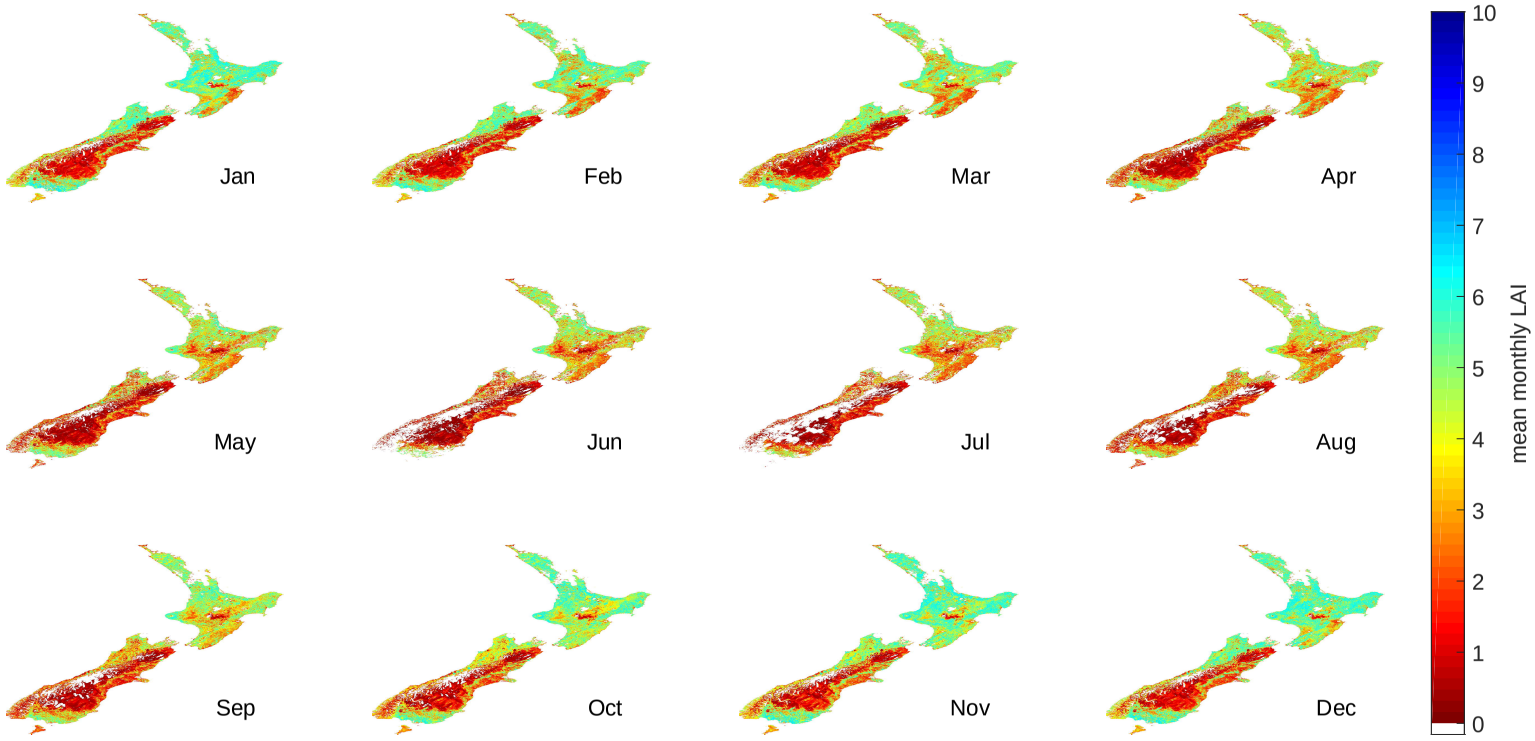

Figure 3.19: LAI climatology (2000-2014), compiled from Park (2015) and Samanta et al. (2011).

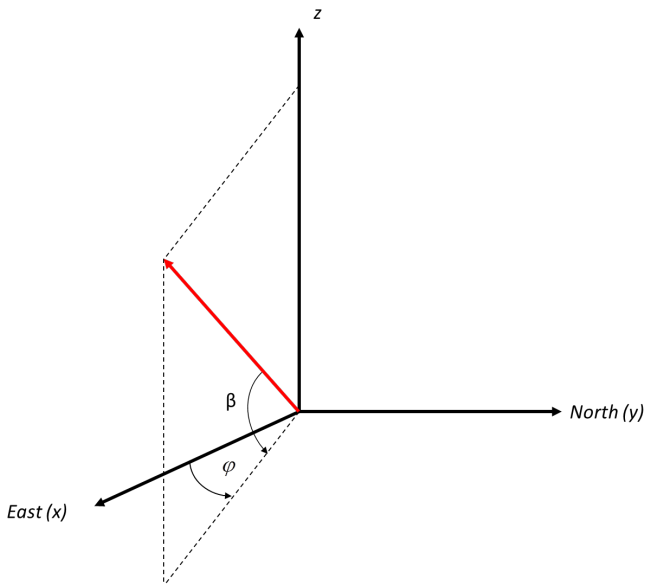

Figure 3.20: Slope in line of sight β in a spherical coordinate system.

3.4.3.2 A forward model for calculating microwave backscatter of soil moisture and vegetation

The effect of soil moisture on dielectric properties was calculated with a Single Debye Model (see section 3.3.2.2), assuming fresh water with a constant temperature of 15 °C and a soil density of 1.7 g/cm^3. Backscatter was calculated using the PRISM-1 model of Oh (2004). Only the σ^0_{vv} backscatter was used for this study. The effect of vegetation was calculated with a single-scattering radiative transfer (S^{2}RTR) method based on canopy elements as Rayleigh scatterers (section 3.3.9), using the LAI as a proxy for the extinction coefficient κ_e (Eq. 3.58). As a simplification, a single unit was used as input: vegetation height d.

3.4.3.3 An inversion algorithm for estimation of soil moisture and vegetation

A genetic algorithm was applied find the minimum of the absolute difference between observed backscatter and modelled backscatter. This absolute difference is called the fitness function. Backscatter was modelled with the forward model (see section 3.4.3.2) as a function of soil type, soil density, vegetation extinction coefficient, soil moisture, surface roughness, and incidence angle. The GA was then run with three of the input components considered variables, i.e. soil moisture, surface roughness, vegetation height. The other input components were considered static and known:

- local incidence angle, which was calculated from the global incidence angle of the satellite image, and the terrain slope (see section 3.3.8);

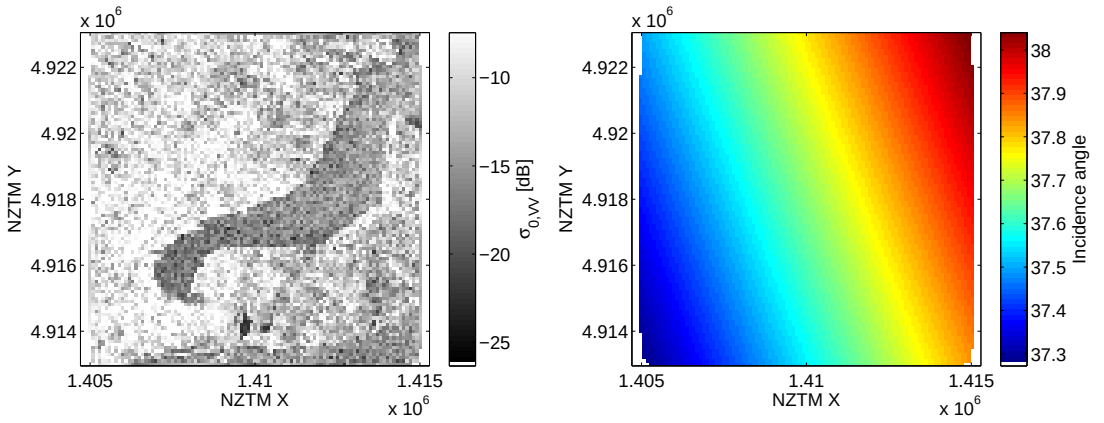

(a) Sentinel 1A $\sigma_{0,vv}$ backscatter for a 10kmx10km area

(b) incidence angle θ

(c) accompanying DEM

(d) local incidence angle

Figure 3.21: Backscatter $\sigma_{0,VV}$ from a Sentinel 1A image, regridded to 100mx100m.

- soil density, which has a very small effect on the backscatter and was considered 1.7 g cm^{-3};
- extinction coefficient $\kappa_{e,LAI}$, which was inferred from MODIS derived Leaf Area Index data (section 3.4.3.2);
- sand and clay fraction of soil type (section 3.4.3.2);

The three variables were randomly initialised for each generation within their lower and upper boundaries (0 and 0.35 for M_v, 0.01 and 6 for surface roughness, 0 and 1 for vegetation height, respectively). The algorithm was set to standard convergence criteria, i.e. not more than 100 generations, or sooner if the fitness function is smaller than 10^{-4};

Experiments for non-uniqueness

Experiments were run to see if the GA solutions can be used to ultimately solve for soil moisture, and how non-unique solutions for M_v and ks are. For all itemised experiment I. to VII., mentioned below, soil type and soil density, who do not affect the modelled backscatter significantly (section ...), were set to constant values (clay fraction = 0.3, sand fraction=0.7, density=1.7 g/cm^3). These were the experiments:

I. Using one observed backscatter value σ^0_{vv} and one incidence angle θ, solutions of the GA solving for soil moisture and surface roughness were analysed assuming a bare soil (i.e., no vegetation);

II. The GA was used to solve for multiple σ^0_{vv}-θ pairs. First, theoretical 'true observed' backscatter was simulated with the forward model. For that, a homogeneous bare soil area of five cells was assumed, each cell having a random combination of ks and incidence angle θ (with ks in between 0.01 and 5 and θ in between 0 and 60 degrees). The number of five was chosen, so visual analyses was still easy, while remaning enough samples for numerical analysis. Each resulting σ^0_{vv} - θ was then analysed in the ks-M_v domain panel, similar to experiment I. This was repeated for eight different soil moisture scenarios (0.01, 0.05, 0.1, 0.15, 0.2, 0.25, 0.3, 0.35). Then, RMSE and standard deviation between GA solutions of soil moisture and the 'true observed' soil moisture value were calculated.

III. The same experiment as II was run. However, now soil moisture was set to one single value of 0.15, while the $\kappa_{e,LAI}$ value was varied in six scenarios (i.e., 0.01, 0.1, 0.2, 0.3, 0.4, 0.5).

IV. Instead of five random values for ks and θ for bare soil (II), 30 random value were chosen. Subsequently, the 30 outputs were filtered in two steps: (1) filter out all values outside the 50th and 90th percentile of σ^0; (2) filter out all values lower than the median (50th percentile) of the incidence angle. The remaining (usually 5 or 6) σ^0-θ pairs were then processed as experiment II. The number of 30 was chosen, so enough cells are left for numerical analyses.

V. Instead of five random values for ks and θ for a vegetated soil (III), 30 random value were chosen. Subsequently, the 30 outputs were filtered and processed similar to experiment IV.

VI. This method was developed with newly developed insights after analyses of the experiments I to V. The same subsetting was applied as experiment V, with an extra following filtering step after GA application and before calculating the median. The median was taken for only GA solutions higher than ks=2.

VII. This method was developed after analyses of the experiments I to VI. It is the same as experiment VI, but with an extra correction for the noise due to vegetation. This correction involved filtering out data above a cut-off percentile $Pctile_{co}$, which depends on the LAI: $Pctile_{co} = 50/LAI$. A reliability factor (REL) was estimated as well, which depends on the LAI, and assumes that for LAI > 5 data is too unreliable:

$$REL = 1 - 0.2LAI \tag{3.60}$$

with values of $REL < 0$ set to 0. Standard deviations might not represent the uncertainty well enough in these cases, because of the small subset taken if reliability is low (because of much vegetation). Standard deviation was therefore set to these values:

$$STDEV = \begin{cases} \text{STDEV} & \text{if STDEV} > \text{(1-REL)*med}(M_v) \\ (1 - REL) * \text{med}(M_v) & \text{if STDEV} < \text{(1-REL)*med}(M_v), \end{cases} \tag{3.61}$$

with 'med' denoting the median.

3.4.3.4 Application of the GA algorithm at soil moisture ground observations

Soil moisture derived from C-band Sentinel-1A SAR (Table 3.4) were compared to ground-observed soil moisture from NIWA Cliflo stations (section 3.4.3.1, or Figure 3.16)). The GA inversion algorithm was tested at all locations of ground-observed soil moisture. These were the steps taken for each location, which are based on non-uniqueness experiment VII (see above):

- A polygon was defined, i.e., a circle with the station as mid-point and 500 m radius;
- Sentinel-1 backscatter data within the polygon were imported (approximately 8000 pixels);
- LAI data were projected to the polygon. If no LAI data were available, a low value of 0.1 was assumed;

- Local incidence angles were calculated, based on the 20 m x 20 m terrain model;
- All σ^0_{vv} outside the $p1$ percentile and 90th percentile of σ^0_{vv} were filtered out, where $p1$ was estimated to maintain 100 samples;
- All local incidence angles α lower than the median were filtered out;
- 25 σ^0_{vv}-α, chosen randomly from the remaining subset (of approximately 50), were inverted in 25 GA generations. Each GA generation had a random start values of M_v, ks and d in between their boundary constraints. This lead to 225 (= 25 x 25) solutions;
- If LAI was higher than 1, soil moisture solutions corresponding to $ks < 2$ were filtered out (based on experiment VI) and vegetation filtering was performed (based on see experiment VII);
- Median soil moisture values and standard deviations (or reliability, see experiment VII) were calculated;

Inverted timeseries of soil moisture were organised and plotted in three different ways:

1. All data, considered one time series, were plotted in chronological order;
2. First, data were sorted in 'bins', i.e. per value of global incidence angle θ. These (typically two or four) timeseries were then plotted in chronological order;
3. Bins were resampled to all dates of time series 1. Then the median values soil moisture and standard deviation (or reliability) of each time step were estimated, including a bias to describe the different solutions per incidence angle bin. This bias, δ_θ, was defined as the range of soil moisture solutions per time step.

3.5 Results

3.5.1 Phase disturbances in radar reflections

Results of the method (section 3.4.1) are described and analysed here.

The reflected E_x and H_y fields at the interface between air and brackish water-saturated (lossy medium, Figure 3.22), compared to that of dry sand (Figure 3.7), has a slightly higher amplitude and shows a phase difference in both E and H of 2°, which is an effect of the boundary constraint at a lossy medium. This phase difference for a C-band wave translates to 0.3 mm, assuming C-band wavelength is 6 cm. The coherence of the two signals according to Eq. 3.54 is high (0.999). If this would be a difference between dry sand in summer and water-saturated sand in winter, then the seasonal effect between the two would cause a negligible effect if

this backscatter would be used in interferometry (i.e., InSAR): the large difference in soil moisture would result in a small 'noise' of 0.3 mm. For this case, this can be considered negligible. Because two extremes of soil moisture were taken, at first instance it could be concluded that the impact of wrongly assuming soil moisture, or soil type, does not cause a significant difference in amplitude and phase between two recurring satellite overpasses. However, the results of the second experiment shows that this conclusion would be wrong. Amplitude and phase (like in Figures 3.22 and 3.7) are projected as a function of ε' and ε'' for a large range of possible permittivity values in Figure 3.23. This shows that small values of ε' and ε'' lead to larger phase and amplitude differences.

When differential phase, amplitude and coherence are calculated between two overpasses with dry sand as a reference soil (overpass 1), and the whole range of all possible values of soil type and soil moisture are modelled for a recurring satellite record (overpass 2), figures 3.24 and 3.25 (= a zoom-in of 3.24) show that the relation of permittivity with phase and amplitudes is not straight-forward. Maximum phase and amplitude difference and minimum coherences can occur at slightly deviating values of permittivity. At the revisit overpass, very small deviations from the reference soil (the soil at overpass 1) can lead to a maximum phase difference of maximum of 30° ($\simeq$ 5 mm for C-band data). Very small differences in soil moisture can thus cause a change of phase, that can be significant noise for interferometric measurements like InSAR.

Transmission of a wave travelling through a vegetated medium as specified in section 3.4.1 results in substantial amplitude and phase differences between the incoming and reflected H and E field (Figure 3.26) if the underlying soil has low permittivity (e.g. sand).

A vegetation layer of approximately 12 cm, with possible ranges in between $0 < \varepsilon' < 10$ and $0 < \varepsilon'' < 2$ can lead to a decrease in amplitude of 70-100% and phase shifts anywhere between -180 and 180 °. The largest differences are found when the permittivity of the vegetation layer is close to that of the soil. Although this seems counter-intuitive (one expects a small difference at a small contrast between permittivities), it is a result of the boundary conditions at an interface mentioned in section 3.3.3. Coherence plots for two overpasses are shown in figures 3.27 (with dry sand as an underlying soil) and 3.28 (with silty clay as an underlying soil). If it is assumed that for repetitive measurements data with an absolute value of coherence lower than 0.25 is not taken into account for InSAR analyses, phase differences of 30° (silty clay) to 50° (dry sand) are still significant. These phase angles translate to 5 - 8 mm interferometric difference for C-band data.

3.5.2 Simplified sensitivity of backscatter to its input parameters

Results of the method described in section 3.4.2 are analysed, leading to better insight in the sensitivity of backscatter to soil type, soil moisture, terrain slope,

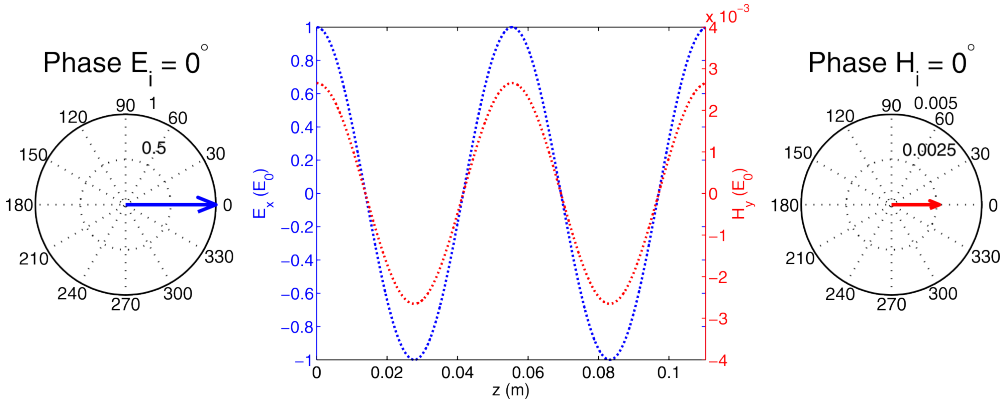

(a) Incoming EM wave in air

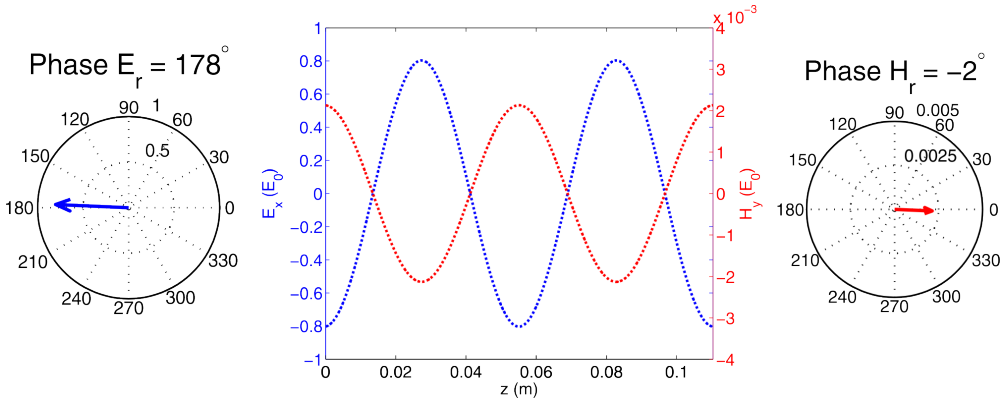

(b) Reflected EM on fresh-brackish water saturated sand, $\varepsilon = 75 - j30$

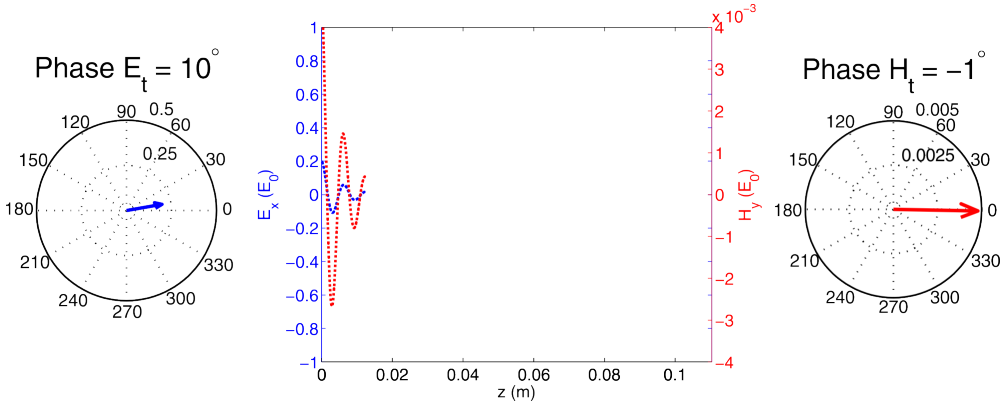

(c) Transmitted wave through fresh-brackish water saturated sand, $\varepsilon = 75 - j30$

Figure 3.22: Motion of the reflected E_x and H_y field over two wavelengths from air to fresh-brackish water saturated sand at a constant t (t=0) and normal incidence. For simplicity E_0=1 is chosen. Left and right are the phase differences of the incoming (i), reflected (r) and transmitted (t) E and H field at the boundary.

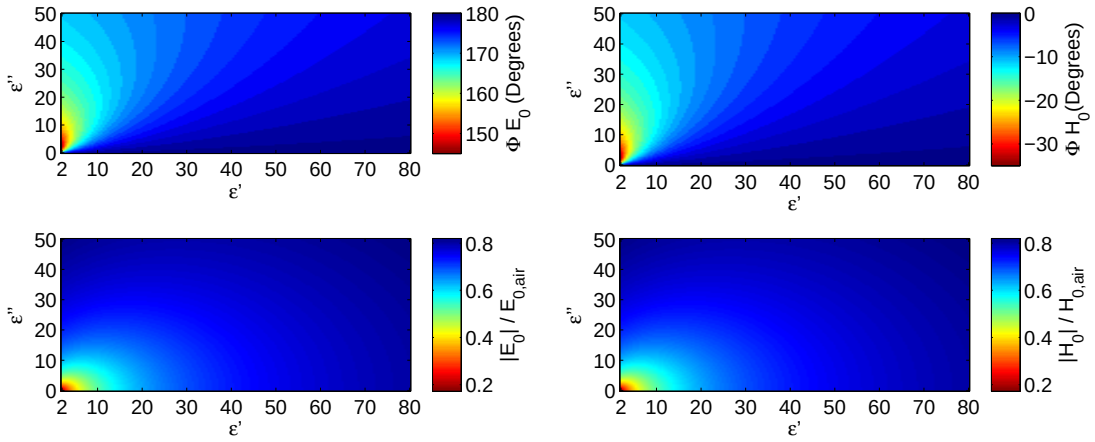

Figure 3.23: Phase (top) and amplitude (bottom) of the reflected E (left) and H (right) field for a range of complex permittivities.

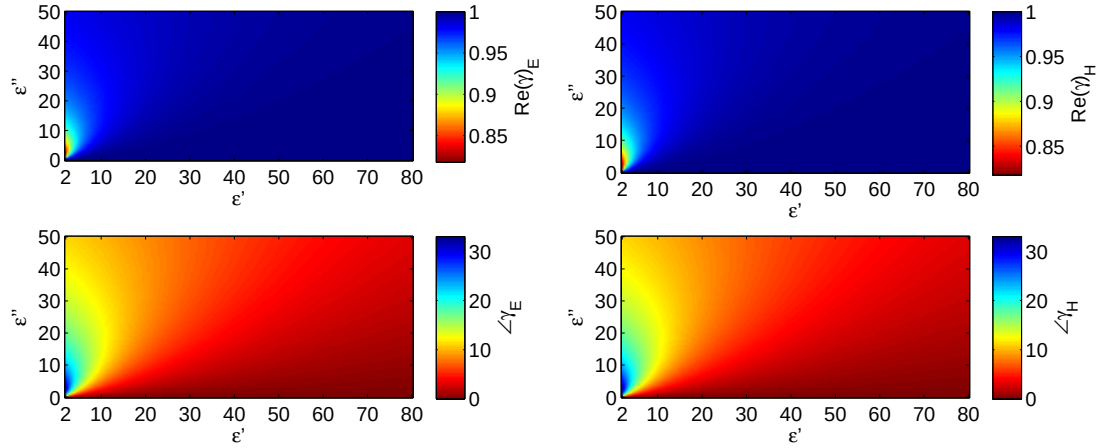

Figure 3.24: Coherence of amplitude (top) and phase(bottom) of reflected E (left) and H (right) fields for a range of complex permittivities. Reference soil is dry sand.

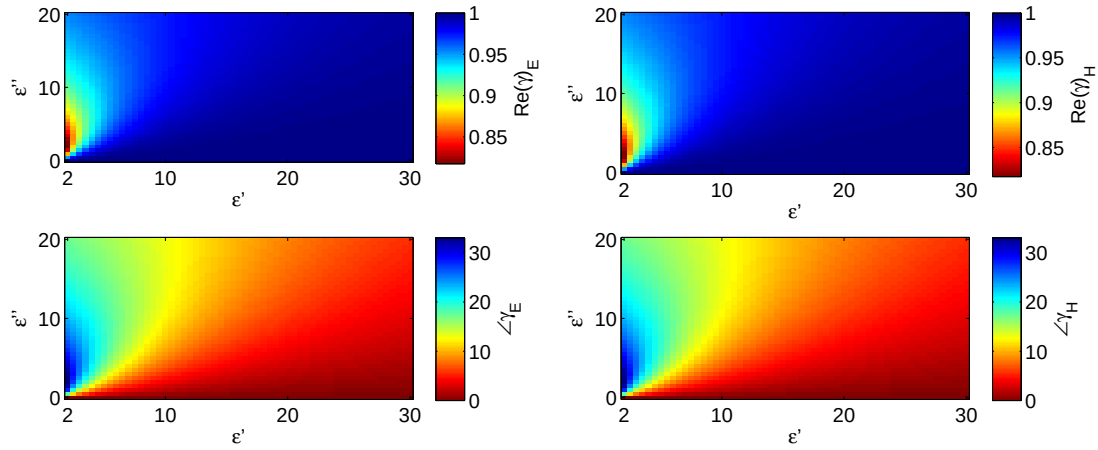

Figure 3.25: Zoom-in of Figure 3.24.

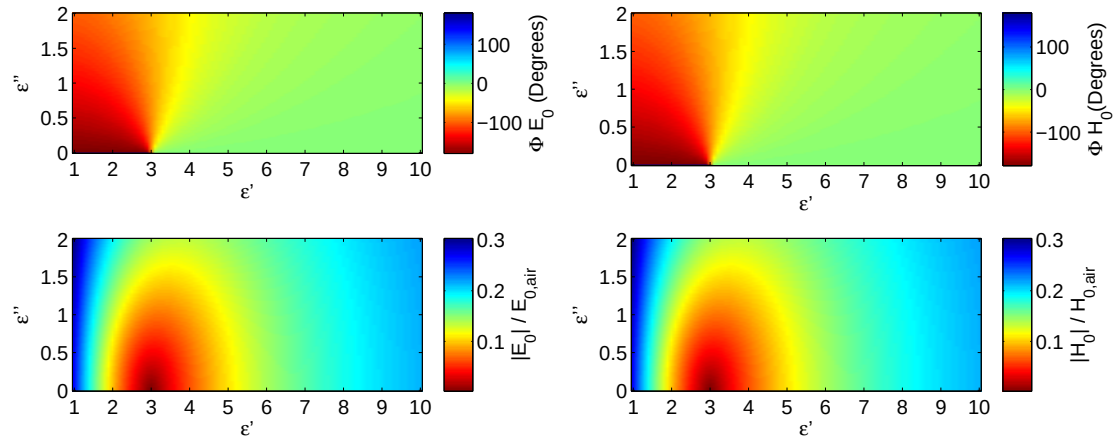

Figure 3.26: Phase and amplitude of reflected E and H field for a range of complex permittivities when a vegetation layer (vegetation height 12 cm) is present. The underlying soil is dry sand (ε=3).

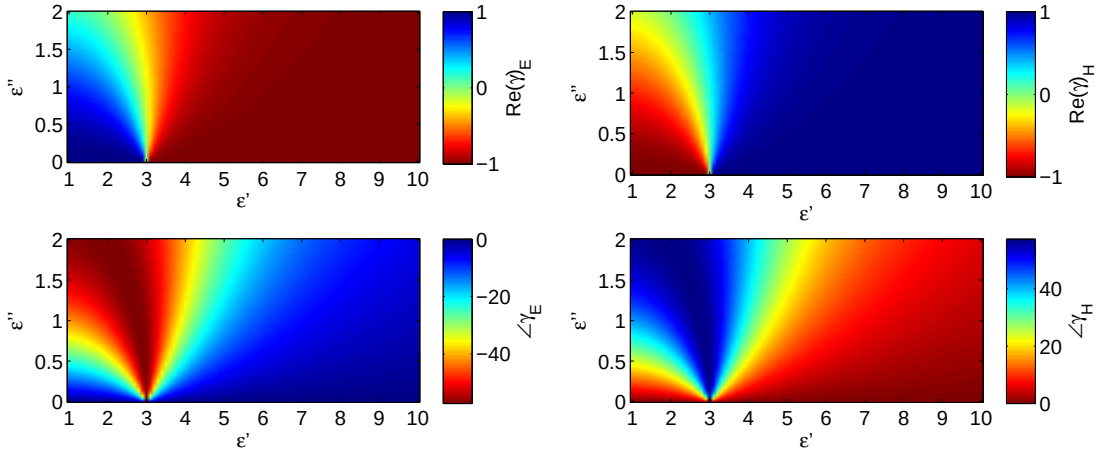

Figure 3.27: Coherence of reflected E and H field for a range of complex permittivities when a vegetation layer (vegetation height 12 cm) is present. The underlying soil is dry sand (ε=3).

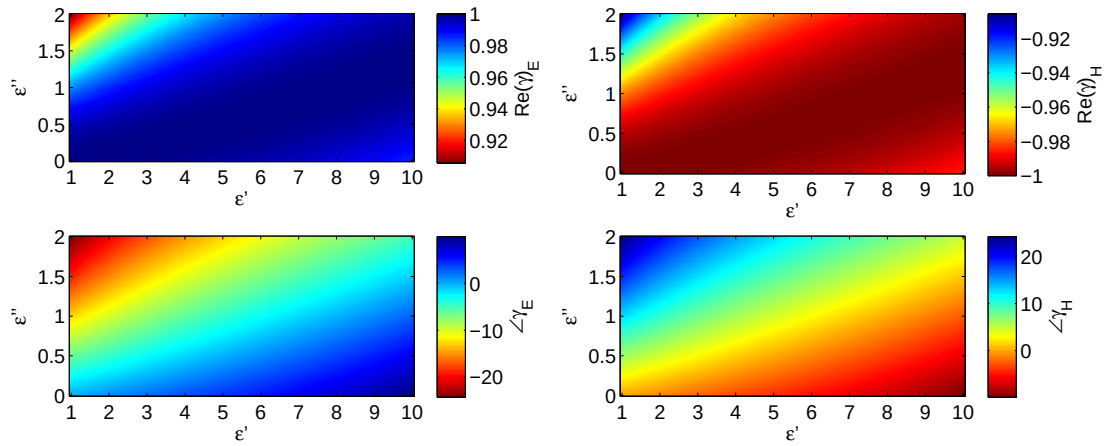

Figure 3.28: Coherence of E and H field for a range of complex permittivities when a vegetation layer (vegetation height two wavelengths) is present. The underlying soil is silty clay (ε=24-i5)

vegetation and surface roughness.

For bare soils, random values for incidence angle θ, surface roughness ks, soil moisture M_v, and clay fraction cf projected in the panels of the 4 dimensions of input variables (Figures 3.29 and 3.30) show that all vv, hh and vh backscatter on bare soils is mostly sensitive to surface roughness, followed by soil moisture, and slightly on incidence angle. The vv and hh backscatter have similar amplitudes, while the de-polarised signal has an overall lower (approx. -10 dB) amplitude. When vegetation is added, represented by the fifth dimension of optical depth τ, the projected panels for vv and hh backscatter (Figures 3.32 and 3.33) show a clear sensitivity to τ, some on θ, while the sensitivity to soil moisture and surface roughness seems to have decreased (only for small τ, the effect of ks can be seen). Adding vegetation shows that backscatter is now most sensitive to τ and incidence angle, and less to the properties of the underlying soil. The de-polarised vh backscatter is also sensitive to τ (Figure 3.34). However, this effect is less than for vv and hh backscatter. The vh signal shows to be sensitive to surface roughness for low ks. Also, a slight dependence on soil moisture and incidence angle can still be distinguished in the vh signal, where it could not be seen in the vv and hh backscatter.

Plots of mean and standard deviation of backscatter in vv, hh, and vh polarisations as a function of each input parameter (Figures 3.35, 3.36, and 3.37) give further insight in sensitivity. These also show that backscatter on bare soils is most sensitive to ks (when ks values are small) and soil moisture. Backscatter is also sensitive to incidence angle, which shows that correcting for terrain features to local incidence angles is important. Adding vegetation information (Figures 3.38, 3.39, and 3.40) shows that backscatter is sensitive to optical depth τ and as a result becomes relatively less sensitive to all other input components.

The fitted functions in Figures 3.35 to 3.40 (black-dotted line), when further differentiated (section 3.4.2), lead to the partial derivatives of backscatter to its

input components and are shown in Equations 3.62 to 3.64 for bare soils and 3.65 to 3.67 for vegetated soils.

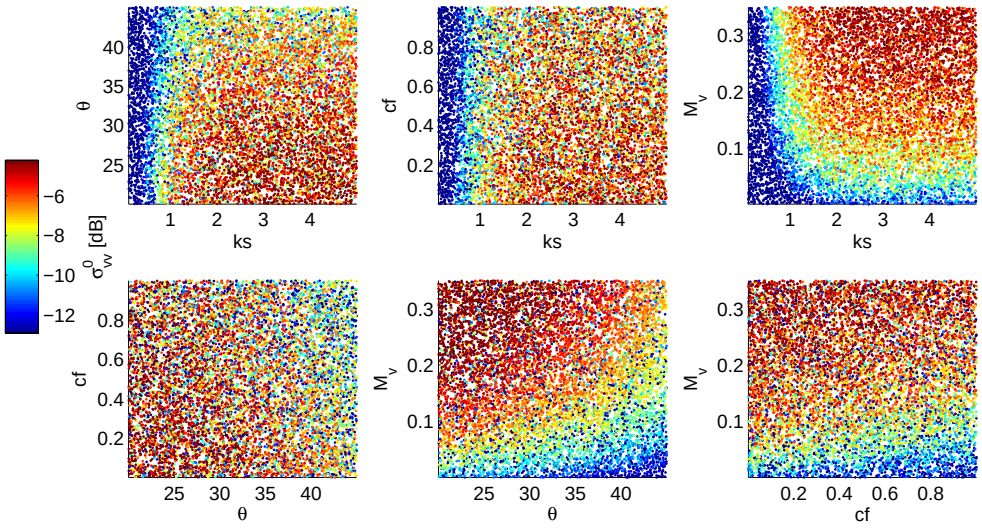

Figure 3.29: Backscatter coefficient σ^0_{vv} for bare soils, projected to all planes of the 4 dimensional space θ, ks, M_v, and cf.

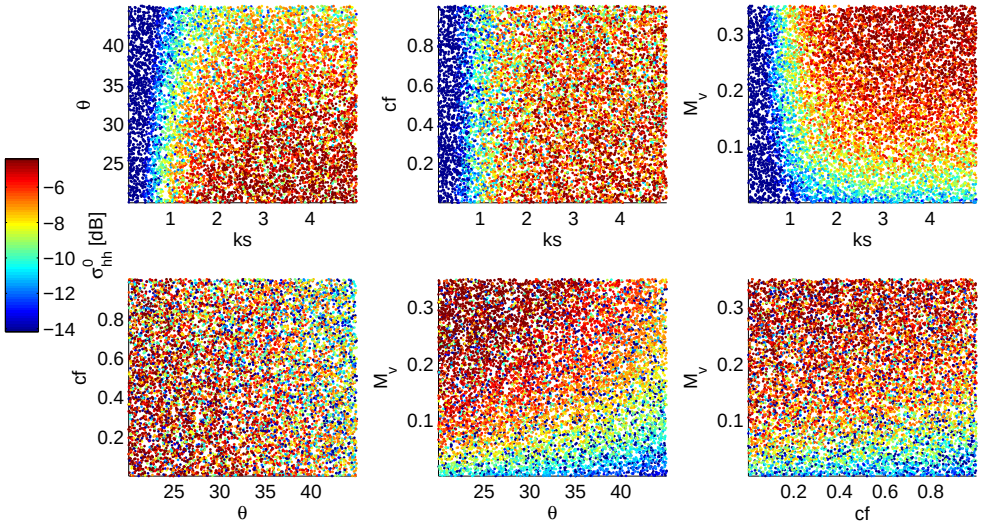

Figure 3.30: Backscatter coefficient σ^0_{hh} for bare soils, projected to all planes of the 4 dimensional space θ, ks, M_v, and cf.

For bare soils, the approximate sensitivity equations of the input components to the backscatter become, for three polarisations vv (Figure 3.35), hh (Figure 3.36),

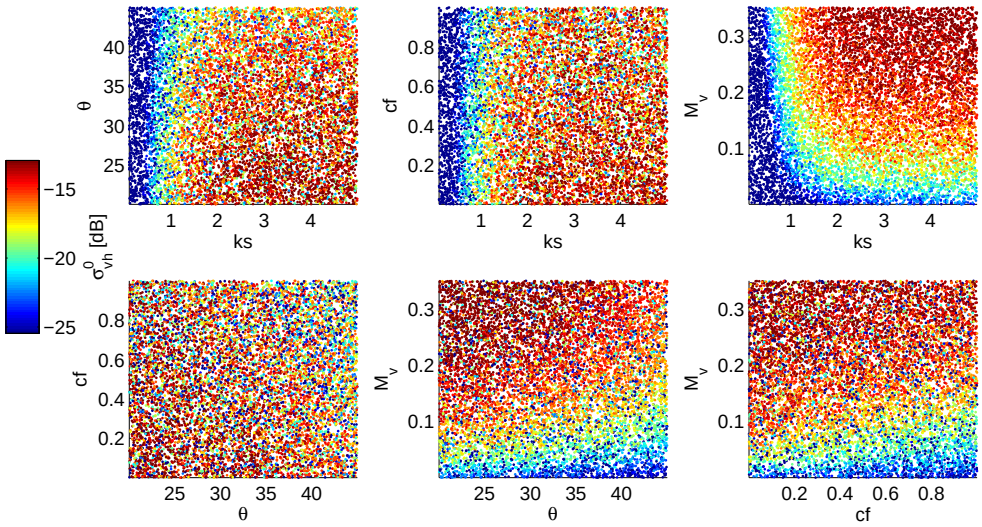

Figure 3.31: Backscatter coefficient σ^0_{vh} for bare soils, projected to all planes of the 4 dimensional space θ, ks, M_v, and cf.

and vh (Figure 3.37):

$$\frac{\partial \sigma^0_{vv}}{\partial ks} \approxeq 44e^{-2.16ks} \quad (0.04 < ks < 6) \tag{3.62a}$$

$$\frac{\partial \sigma^0_{vv}}{\partial M_v} \approxeq 865M_v^2 - 440 * M_v + 63 \tag{3.62b}$$

$$\frac{\partial \sigma^0_{vv}}{\partial \theta} \approxeq -5.3 \times 10^{-3}\theta + 0.03 \tag{3.62c}$$

$$\frac{\partial \sigma^0_{vv}}{\partial cf} \approxeq -1.66cf \tag{3.62d}$$

$$\frac{\partial \sigma^0_{vv}}{\partial \rho_b} \approxeq -0.7 * \rho_b + 1.9 \tag{3.62e}$$

$$\frac{\partial \sigma^0_{hh}}{\partial ks} \approxeq 46e^{-2ks} \tag{3.63a}$$

$$\frac{\partial \sigma^0_{hh}}{\partial M_v} \approxeq 855M_v^2 - 426 * M_v + 59 \tag{3.63b}$$

$$\frac{\partial \sigma^0_{hh}}{\partial \theta} \approxeq -5.4 \times 10^{-3}\theta + 0.02 \tag{3.63c}$$

$$\frac{\partial \sigma^0_{hh}}{\partial cf} \approxeq -1.48cf \tag{3.63d}$$

$$\frac{\partial \sigma^0_{hh}}{\partial \rho_b} \approxeq -0.44 * \rho_b + 1.5 \tag{3.63e}$$

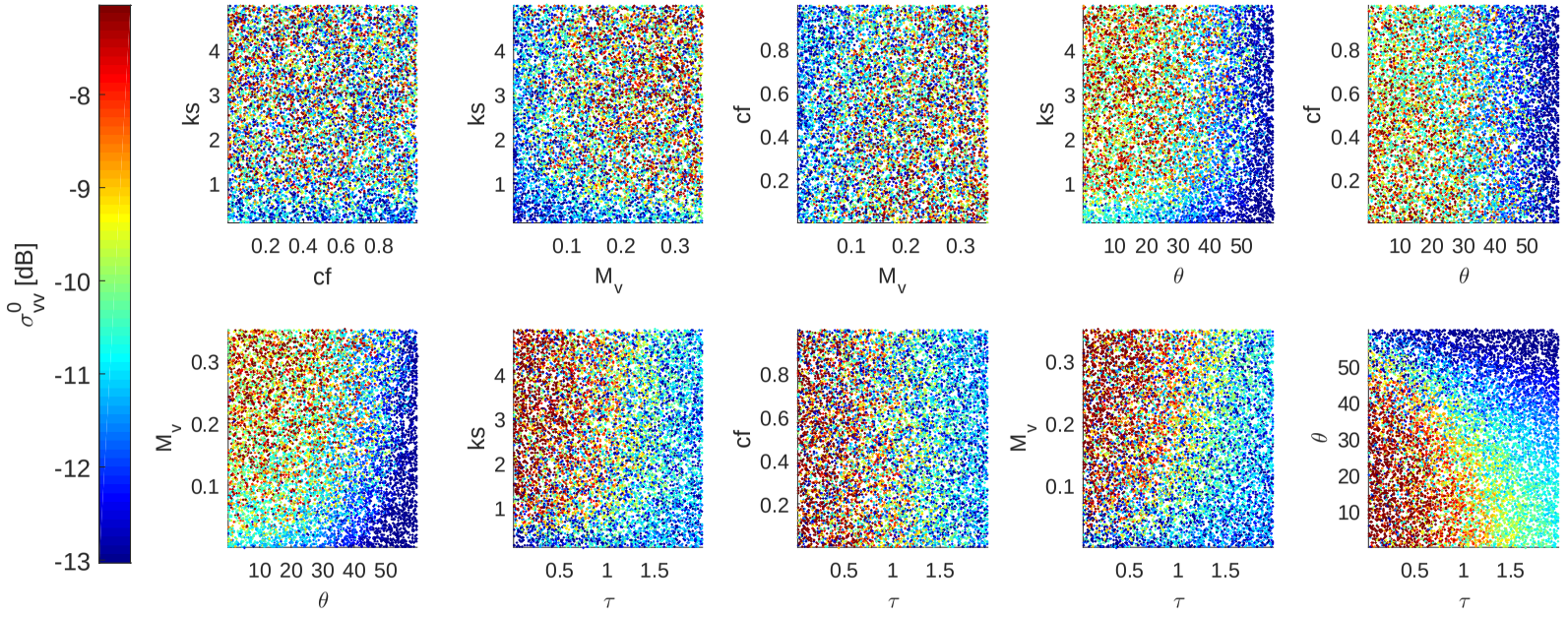

Figure 3.32: Backscatter coefficient σ^0_{vv} for a vegetated surface, projected to all planes of the 5 dimensional space θ, ks, M_v, cf, and τ.

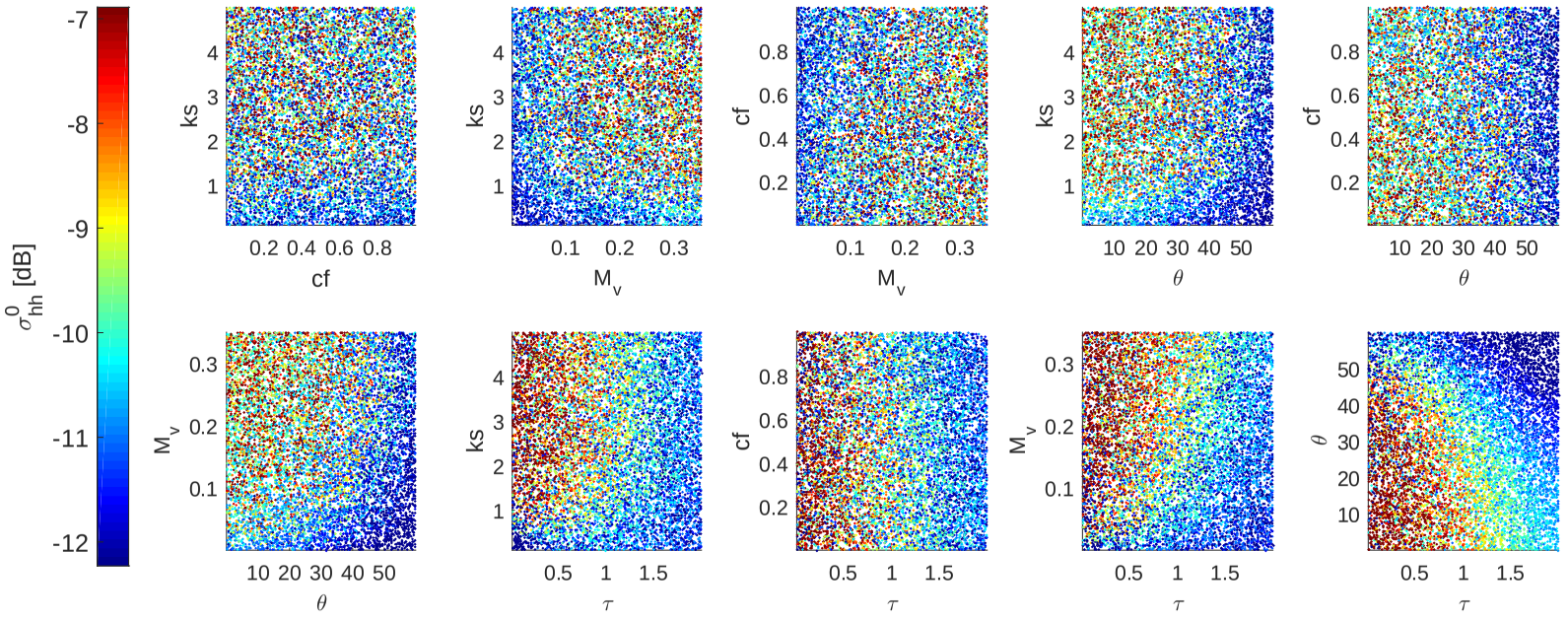

Figure 3.33: Backscatter coefficient σ^0_{hh} for a vegetated surface, projected to all planes of the 5 dimensional space θ, ks, M_v, cf, and τ.

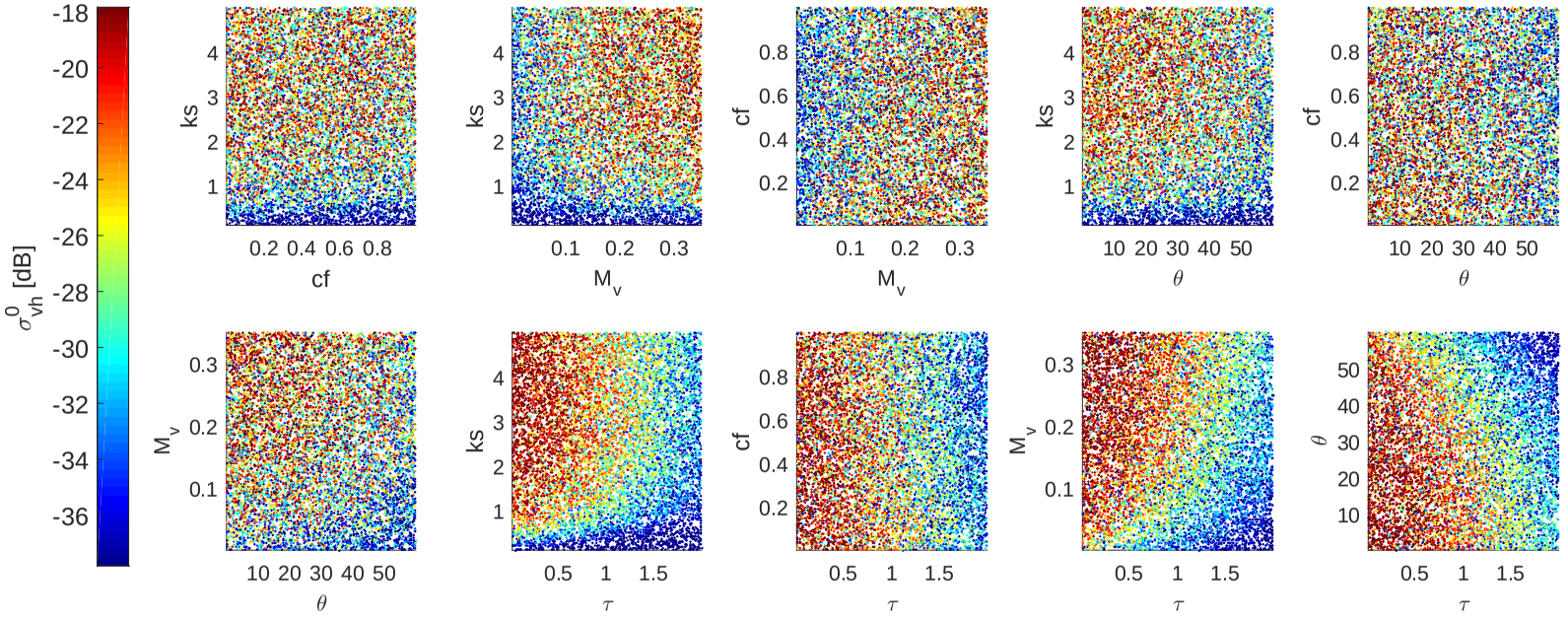

Figure 3.34: Backscatter coefficient σ^0_{vh} for a vegetated surface, projected to all planes of the 5 dimensional space θ, ks, M_v, cf, and τ.

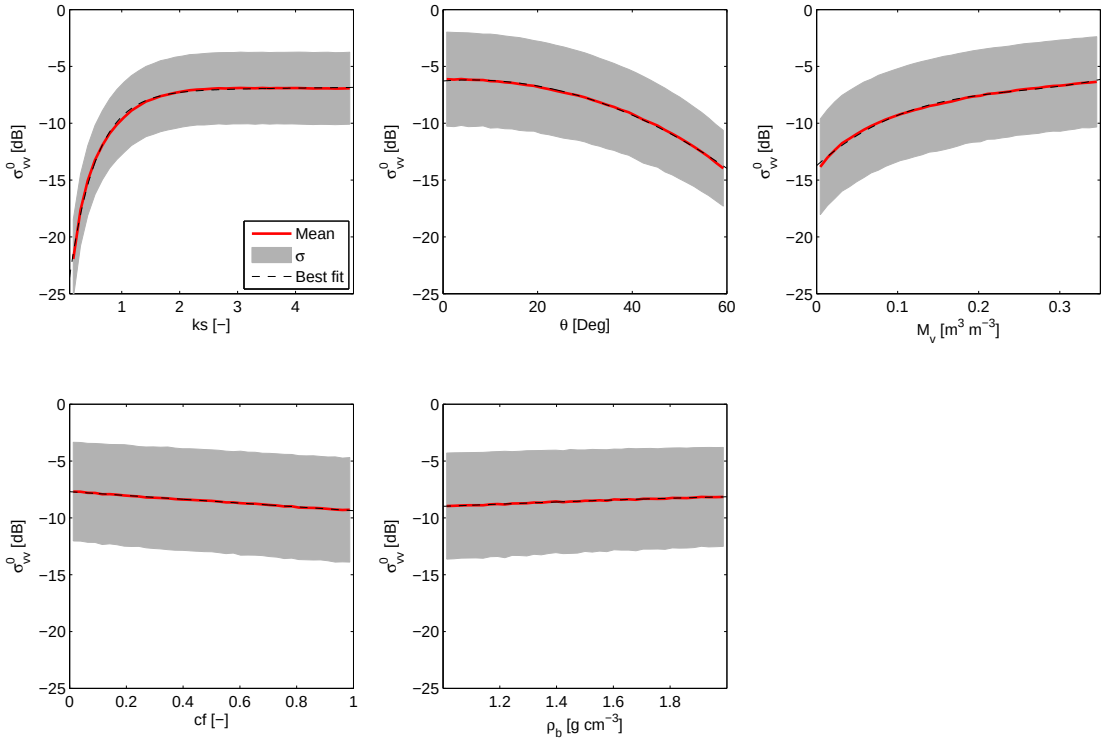

Figure 3.35: Simplified sensitivity for σ^0_{vv} for bare soils, to its input components θ, ks, M_v, and cf. The red line is the mean value, while the grey zone is the standard deviation. The dash-dotted line represents the best fitted function.

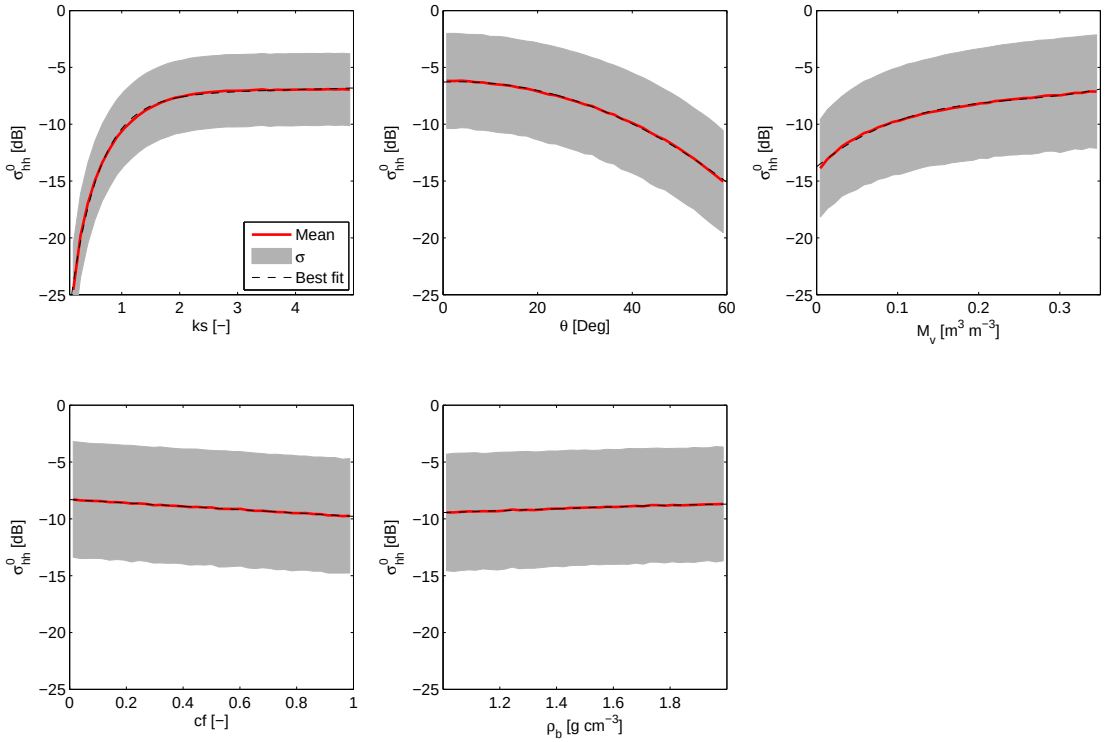

Figure 3.36: Simplified sensitivity for σ^0_{hh} for bare soils, to its input components θ, ks, M_v, and cf. The red line is the mean value, while the grey zone is the standard deviation. The dash-dotted line represents the best fitted function.

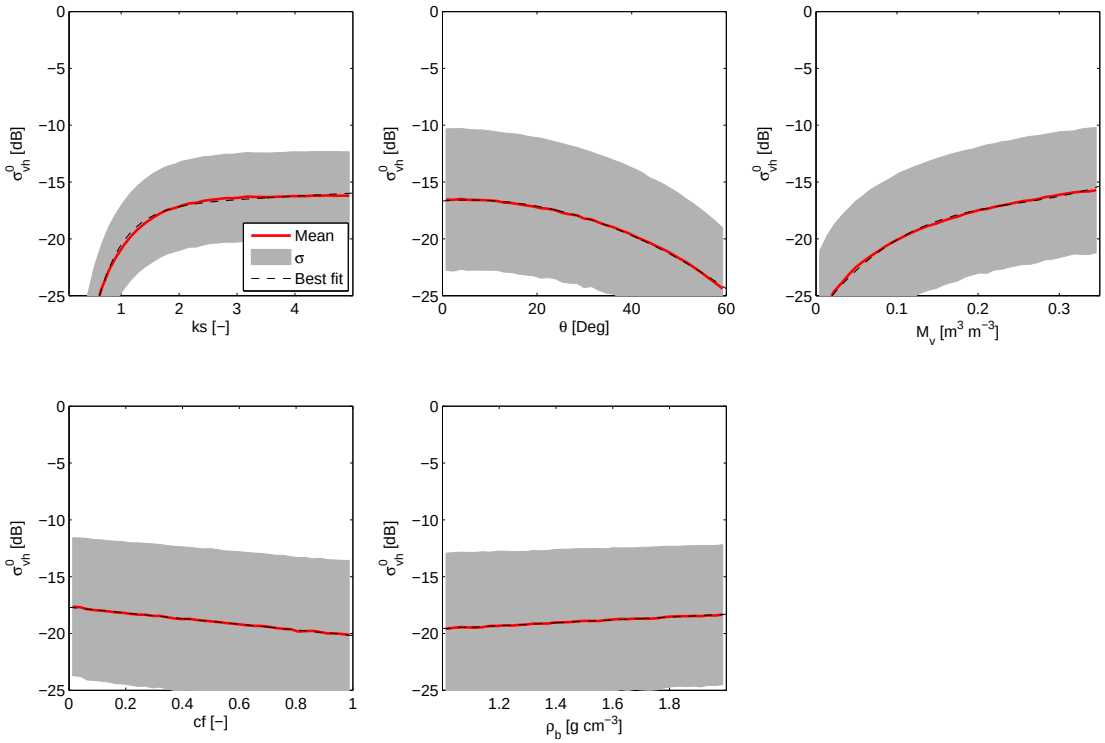

Figure 3.37: Simplified sensitivity for σ^0_{vh} for bare soils, to its input components θ, ks, M_v, and cf. The red line is the mean value, while the grey zone is the standard deviation. The dash-dotted line represents the best fitted function.

$$\frac{\partial \sigma^0_{vh}}{\partial ks} \approxeq 66e^{-2.1ks} \tag{3.64a}$$

$$\frac{\partial \sigma^0_{vh}}{\partial M_v} \approxeq 1319M_v^2 - 670 * M_v + 96 \tag{3.64b}$$

$$\frac{\partial \sigma^0_{vh}}{\partial \theta} \approxeq -5.3 \times 10^{-3}\theta + 0.03 \tag{3.64c}$$

$$\frac{\partial \sigma^0_{vh}}{\partial cf} \approxeq -2.51cf \tag{3.64d}$$

$$\frac{\partial \sigma^0_{vh}}{\partial \rho_b} \approxeq -0.44 * \rho_b + 2 \tag{3.64e}$$

When a vegetation layer is present, approximate equations for figures 3.38, 3.39

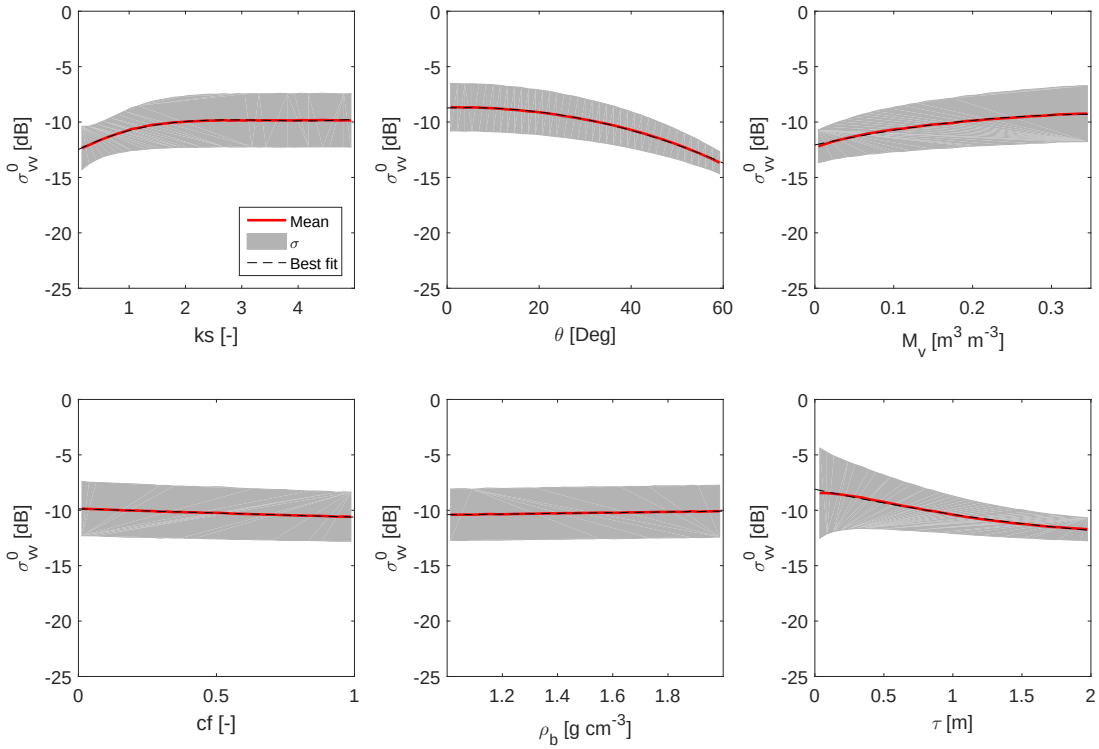

Figure 3.38: Simplified sensitivity for σ^0_{vv} for a vegetated soil, to its input components θ, ks, M_v, and cf, and optical depth τ. The red line is the mean value, while the grey zone is the standard deviation. The dash-dotted line represents the best fitted function.

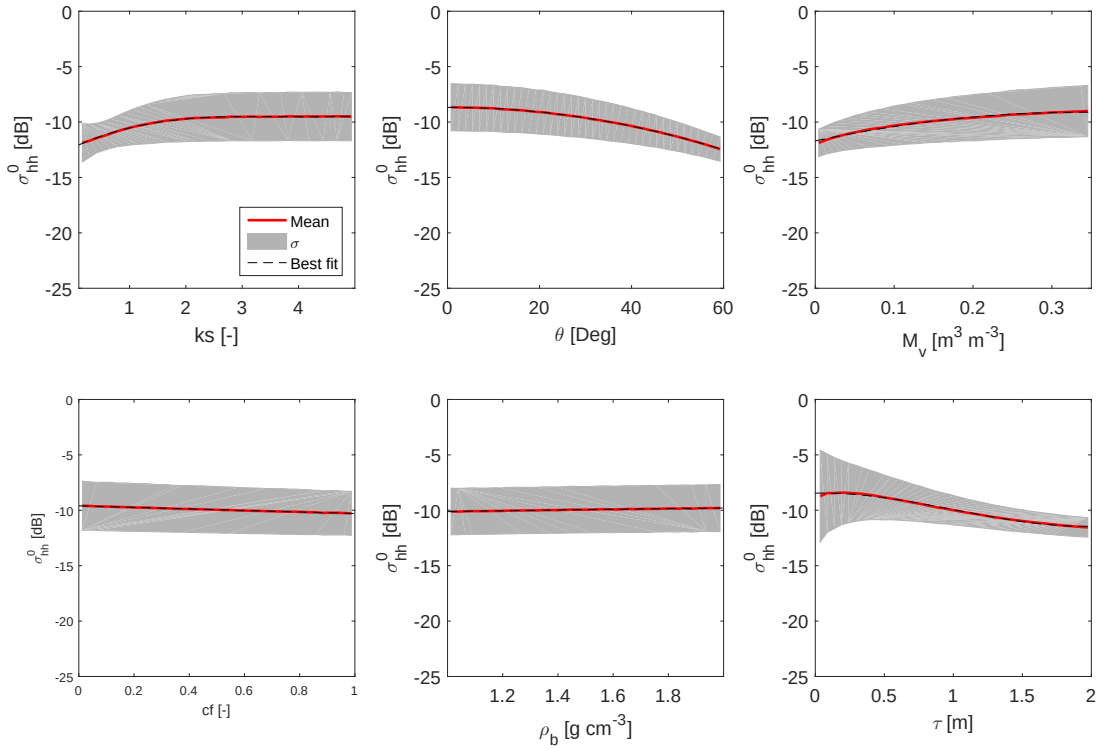

Figure 3.39: Simplified sensitivity for σ^0_{hh} for a vegetated soil, to its input components θ, ks, M_v, and cf, and optical depth τ. The red line is the mean value, while the grey zone is the standard deviation. The dash-dotted line represents the best fitted function.

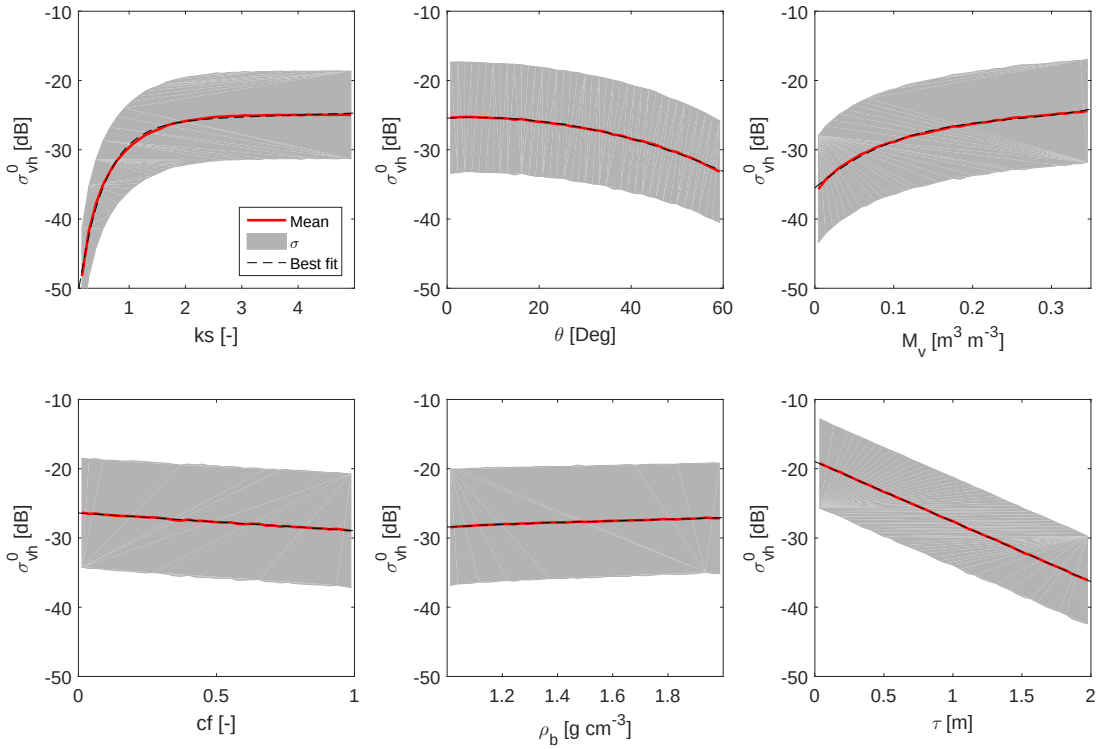

Figure 3.40: Simplified sensitivity for σ^0_{vh} for a vegetated soil, to its input components θ, ks, M_v, and cf, and optical depth τ. The red line is the mean value, while the grey zone is the standard deviation. The dash-dotted line represents the best fitted function. Note the different dB scale when compared to Figures 3.38 and 3.39

and 3.40, respectively, become:

$$\frac{\partial \sigma^0_{vv}}{\partial \tau} \cong 0.83\tau^2 - 12.8\tau - 2.7 \qquad (0 < \tau[m] < 2) \tag{3.65a}$$

$$\frac{\partial \sigma^0_{vv}}{\partial ks} \cong 0.3ks^2 - 1.6ks + 2.69 \qquad (0.04 < ks[-] < 6) \tag{3.65b}$$

$$\frac{\partial \sigma^0_{vv}}{\partial M_v} \cong -43.3M_v + 15.5 \quad (0 < M_v\,[g\,cm^{-3}] < 0.35) \tag{3.65c}$$

$$\frac{\partial \sigma^0_{vv}}{\partial \theta} \cong -3.2 \times 10^{-3}\theta + 0.01 \qquad (0 < \theta\,[Deg] < 60) \tag{3.65d}$$

$$\frac{\partial \sigma^0_{vv}}{\partial cf} \cong -0.75 \qquad (0 < cf[-] < 1) \tag{3.65e}$$

$$\frac{\partial \sigma^0_{vv}}{\partial \rho_b} \cong -0.23\rho_b^2 + 0.51\rho_b - 0.1 \qquad (1 < \rho_b\,[g\,cm^{-3}] < 2) \tag{3.65f}$$

$$\frac{\partial \sigma^0_{hh}}{\partial \tau} \cong 2.65\tau^2 - 5.3\tau + 0.3 \qquad (0 < \tau[m] < 2) \tag{3.66a}$$

$$\frac{\partial \sigma^0_{hh}}{\partial ks} \cong 0.18ks^2 - 1.31ks + 2.36 \qquad (0.04 < ks[-] < 6) \tag{3.66b}$$

$$\frac{\partial \sigma^0_{hh}}{\partial M_v} \cong -45M_v + 15.3 \quad (0 < M_v\,[g\,cm^{-3}] < 0.35) \tag{3.66c}$$

$$\frac{\partial \sigma^0_{hh}}{\partial \theta} \cong -2.1 \times 10^{-3}\theta \qquad (0 < \theta\,[Deg] < 60) \tag{3.66d}$$

$$\frac{\partial \sigma^0_{hh}}{\partial cf} \cong -0.7 \qquad (0 < cf[-] < 1) \tag{3.66e}$$

$$\frac{\partial \sigma^0_{hh}}{\partial \rho_b} \cong -0.14\rho - 0.53 \qquad (1 < \rho_b\,[g\,cm^{-3}] < 2) \tag{3.66f}$$

$$\frac{\partial \sigma^0_{vh}}{\partial \tau} \cong -8.7 \qquad (0 < \tau[m] < 2) \tag{3.67a}$$

$$\frac{\partial \sigma^0_{vh}}{\partial ks} \cong 65.6e^{-2.1ks} \qquad (0.04 < ks[-] < 6) \tag{3.67b}$$

$$\frac{\partial \sigma^0_{vh}}{\partial M_v} \cong 1.3 \times 10^3 M_v^2 - 0.68 \times 10^3 M_v + 96 \quad (0 < M_v\,[g\,cm^{-3}] < 0.35) \tag{3.67c}$$

$$\frac{\partial \sigma^0_{vh}}{\partial \theta} \cong -5 \times 10^{-3}\theta + 0.03 \qquad (0 < \theta\,[Deg] < 60) \tag{3.67d}$$

$$\frac{\partial \sigma^0_{vh}}{\partial cf} \cong -2.6 \qquad (0 < cf[-] < 1) \tag{3.67e}$$

$$\frac{\partial \sigma^0_{vh}}{\partial \rho_b} \cong 3.1\rho_b^2 - 10.1\rho_b + 9.3 \qquad (1 < \rho_b\,[g\,cm^{-3}] < 2) \tag{3.67f}$$

3.5.3 Soil moisture derived from from microwave backscatter

Results from the forward and inverse model approach (section 3.4.3) are analysed here.

3.5.3.1 Experiments for non-uniqueness

Experiment I - multiple solutions of the GA for one σ^0-θ pair

For the bare soil for example, many individual runs of the GA lead to many different solutions for M_v and ks (Figure 3.41). This called 'non-uniqueness' and is clearly shown, as soil moisture can have any value between 0 and 0.35, depending on the surface roughness. The non-uniqueness in this case is constrained by a simple 2D non-linear asymptotic function in the M_v-ks plane.

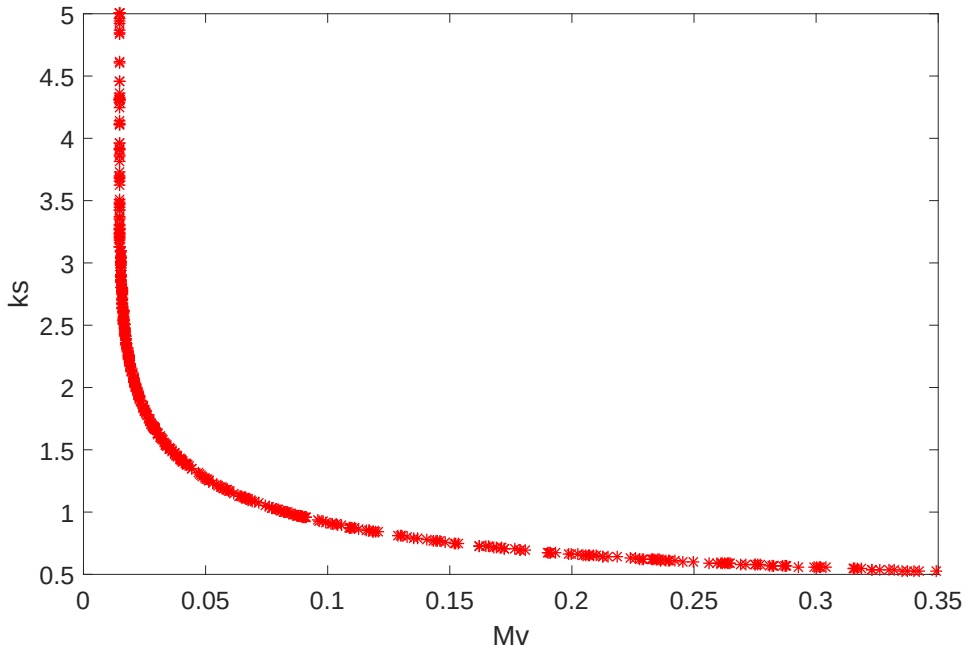

Figure 3.41: 500 GA inverted solutions for M_v and ks for bare soil (σ^0=-10, θ=30°).

II - Five bare soil random σ-θ pairs for six different soil moisture scenarios.

The asymptotic function in the M_v-ks plane depends on the value of incidence angle and backscatter (Figure 3.42). The median of all value estimates the simulated 'true observed' soil moisture reasonably well. Except for very low soil moisture, the RMSE between true observed soil moisture and GA soil moisture median is

low (i.e., close to zero). Standard deviation of the distribution, a measure of the non-uniqueness, varies between 0.05 and 0.1 soil moisture volume percentage.

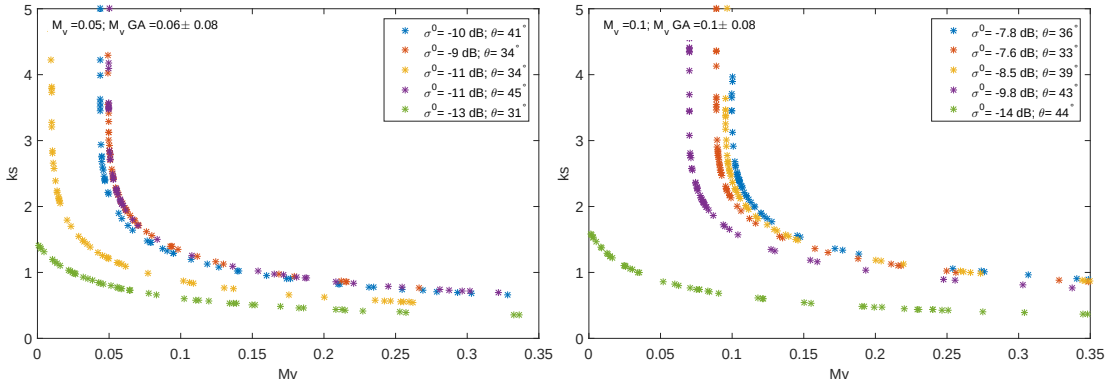

(a) $M_v = 0.05$

(b) $M_v = 0.10$

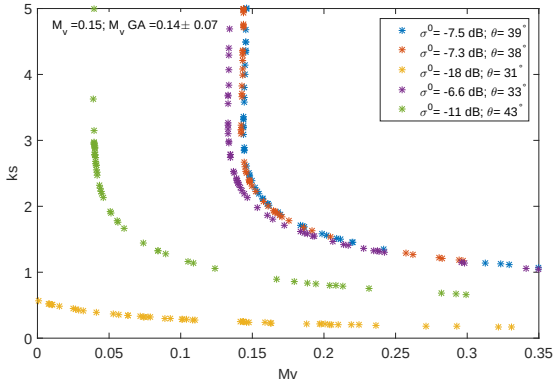

(c) $M_v = 0.15$

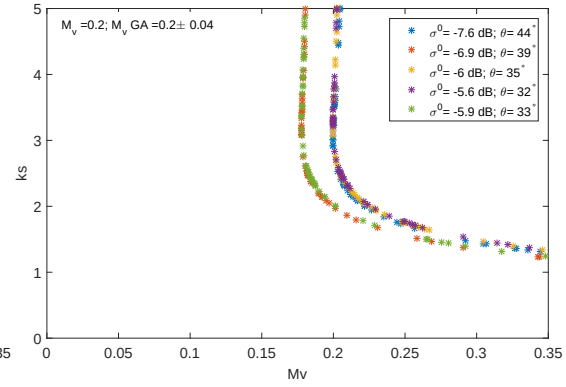

(d) $M_v = 0.20$

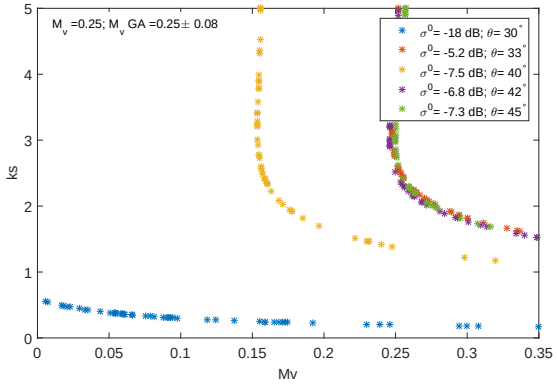

(e) $M_v = 0.25$

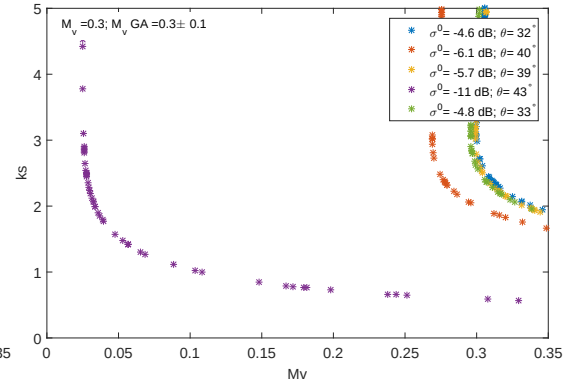

(f) $M_v = 0.30$

Figure 3.42: Soil moisture (M_v) inversion solutions of the genetic algorithm (M_v GA) for different values of M_v on a bare soil.

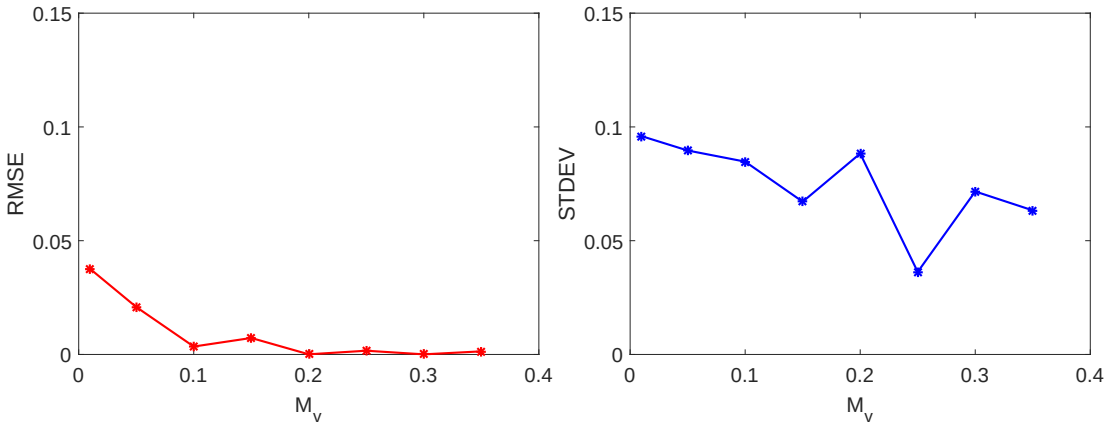

Figure 3.43: RMSE(a) and standard deviation (b) of the genetic algorithm for different values of M_v on a bare soil. All values given as the soil moisture volume ratio [m^3 m^{-3}]

III - Five random σ-θ pairs for six different vegetation scenarios.

Vegetation adds considerable noise (scatter) to the data when plotted in the M_v-ks plane (Figure 3.44). This is not unexpected as backscatter is sensitive to vegetation (see sensitivity analysis in section 3.5.2). For LAI higher than 0.2 the M_v-ks solutions scatter so much that soil moisture estimation through a median value seems unreliable. RMSE values increase with higher LAI to values higher than 0.05 (Figure 3.45). Standard deviation of the distribution increases only slightly with higher LAI. RMSE and standard deviation are variable per experiment run, as the five random scenarios can lead to random M_v-ks hyperbolic functions. Ideally, experiment II and III should be run with more scenarios. However, too many scenarios also lead to longer run time. These results led to further experiments IV and V.

IV - 30 bare soil random σ-θ pairs filtered to a subset.

The GA results improve considerably when a subset of 30 random σ-θ pairs are processed, where the subset only contain the higher backscatter and higher incidence angle pairs. The subset contains six σ-θ pairs (similar to the five pairs of experiment II and III), but solutions of different soil moisture have similar medians (Figure 3.46), smaller RMSEs and the standard deviation decreases with soil moisture (Figure 3.47). Choosing a smart subset thus improves the soil moisture estimation for a bare soil, without necessarily increasing the computing time.

V - 30 vegetation random σ-θ pairs filtered to a subset.

The same subsetting was applied with an increasing LAI value and a fixed value of M_v=0.15. Due to the subsetting, the noise due to increasing LAI only scatters to values of higher soil moisture. Taking the median of this distribution leads to overestimation of the true soil moisture value. These results led to further experiments VI and VII.

VI - 30 bare soil random σ-θ pairs filtered to a subset with ks >2.

While the GA procedure was not changed, further filtering of the subset to values of ks >2 leads to a better estimate of soil moisture, i.e., smaller RMSE and standard deviation (Figure 3.50). This method seems to work very well for soil moisture values from 0.01 to 0.3.

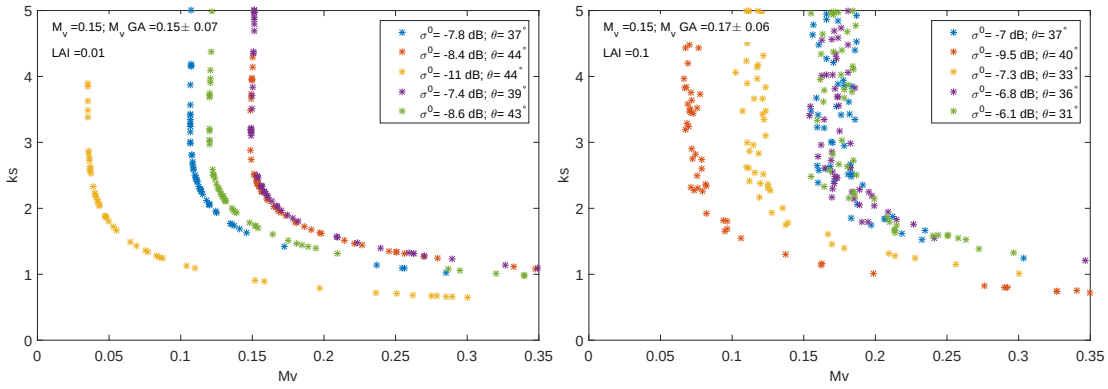

(a) $M_v = 0.15$, LAI=0.01

(b) $M_v = 0.15$, LAI=0.1

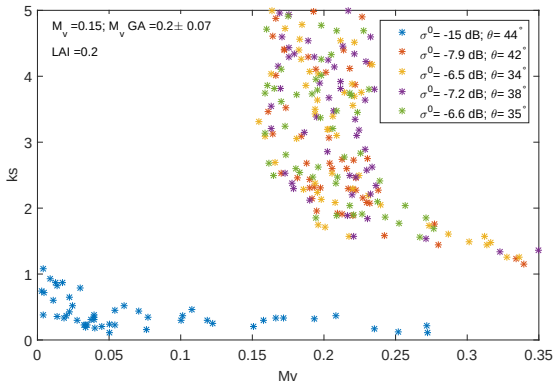

(c) $M_v = 0.15$, LAI=0.2

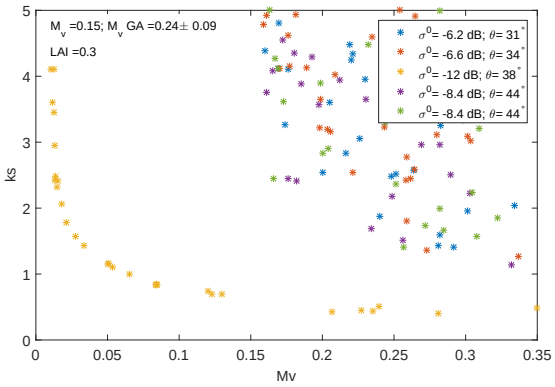

(d) $M_v = 0.15$, LAI=0.3

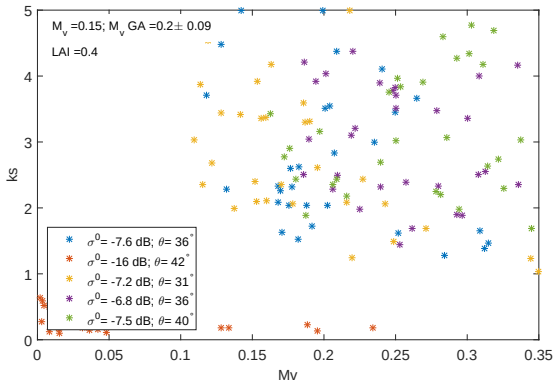

(e) $M_v = 0.15$, LAI=0.4

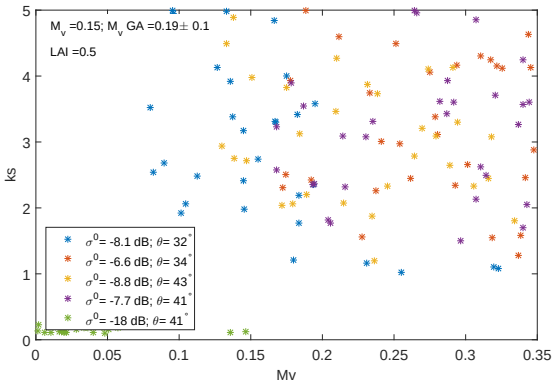

(f) $M_v = 0.15$, LAI=0.5

Figure 3.44: Soil moisture (M_v) inversion solutions of the genetic algorithm (M_v GA) for different values of M_v on a vegetated soil.

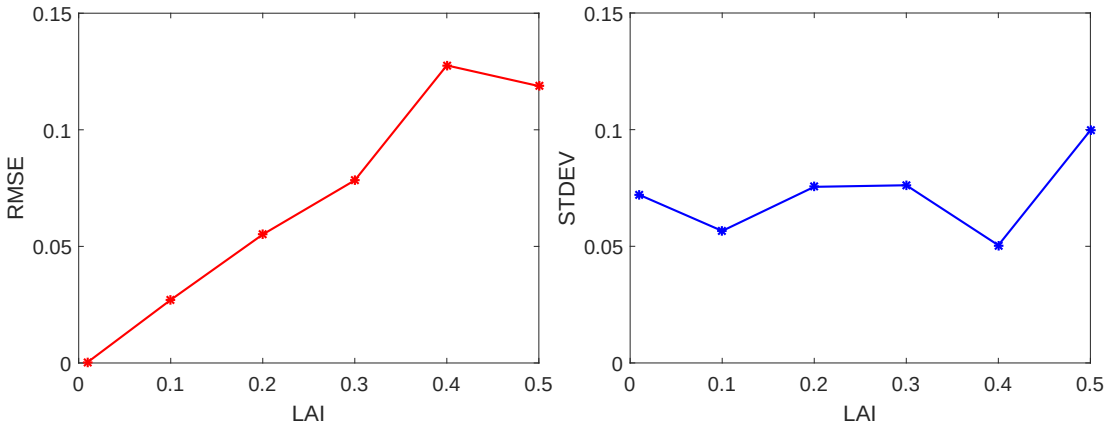

(a) (b)

Figure 3.45: RMSE(a) and standard deviation (b) of the genetic algorithm for different values of LAI on a vegetated soil.

VII - 30 vegetation random σ-θ pairs filtered to a subset with ks >2.

Additional filtering of the solutions depending on the value of LAI leads to smaller RMSE values. The values for standard deviation are small, because of the small subset taken. As taking the artificial smaller subset does not seem to reflect the uncertainty well, the calculated reliability was plotted where this was bigger than the standard deviation.

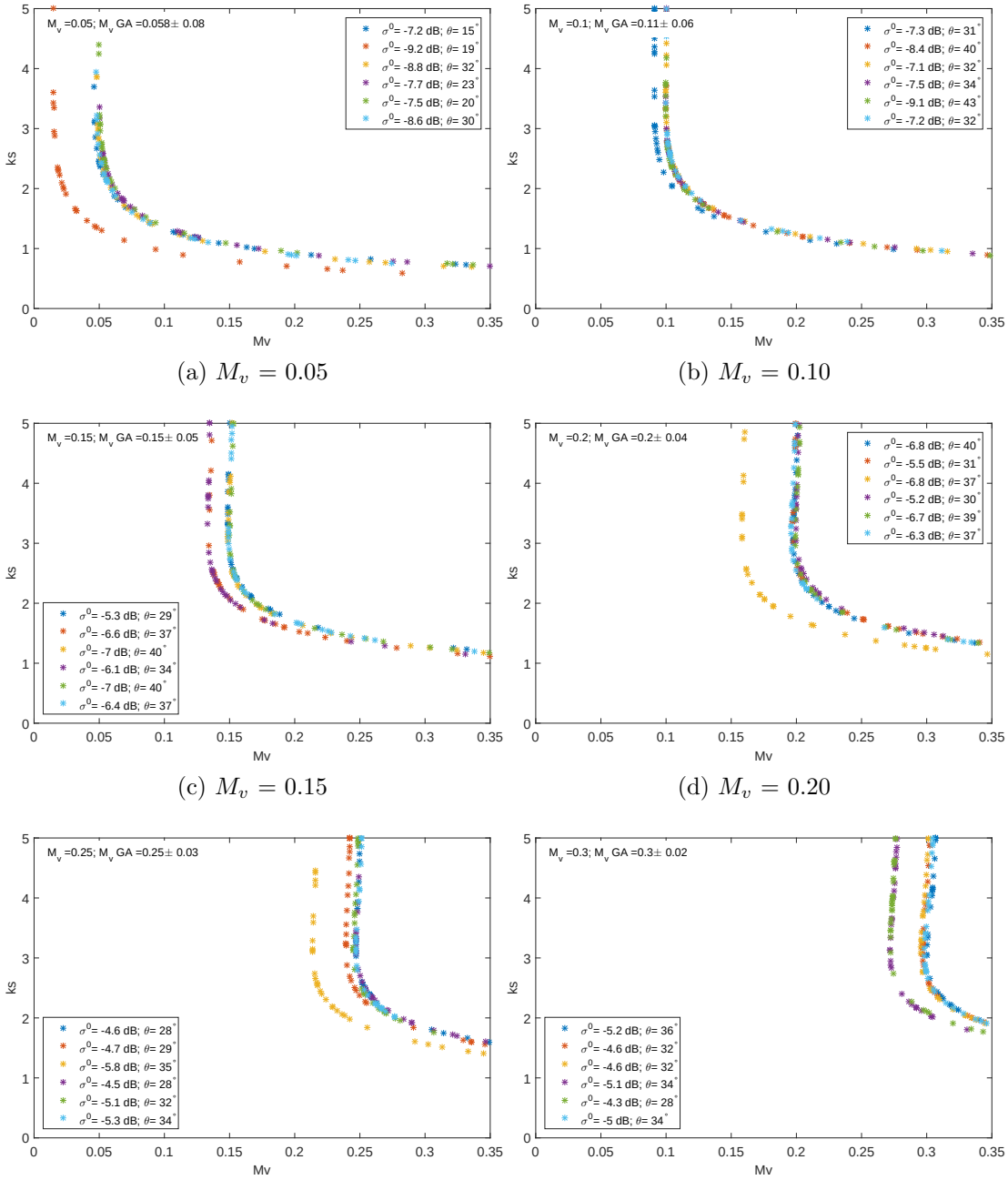

(a) $M_v = 0.05$ (b) $M_v = 0.10$

(c) $M_v = 0.15$ (d) $M_v = 0.20$

(e) $M_v = 0.25$ (f) $M_v = 0.30$

Figure 3.46: Soil moisture (M_v) inversion solutions of the genetic algorithm (M_v GA) for different values of M_v on a bare soil, for a subset of higher backscatter and incidence angles.

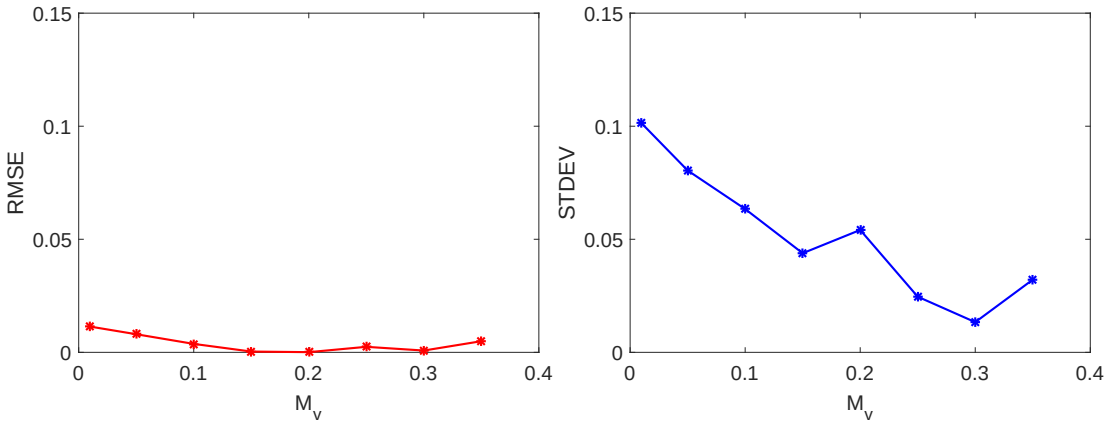

Figure 3.47: RMSE(a) and standard deviation (b) of the genetic algorithm for different values of M_v on a bare soil, for a subset of higher backscatter and incidence angles.

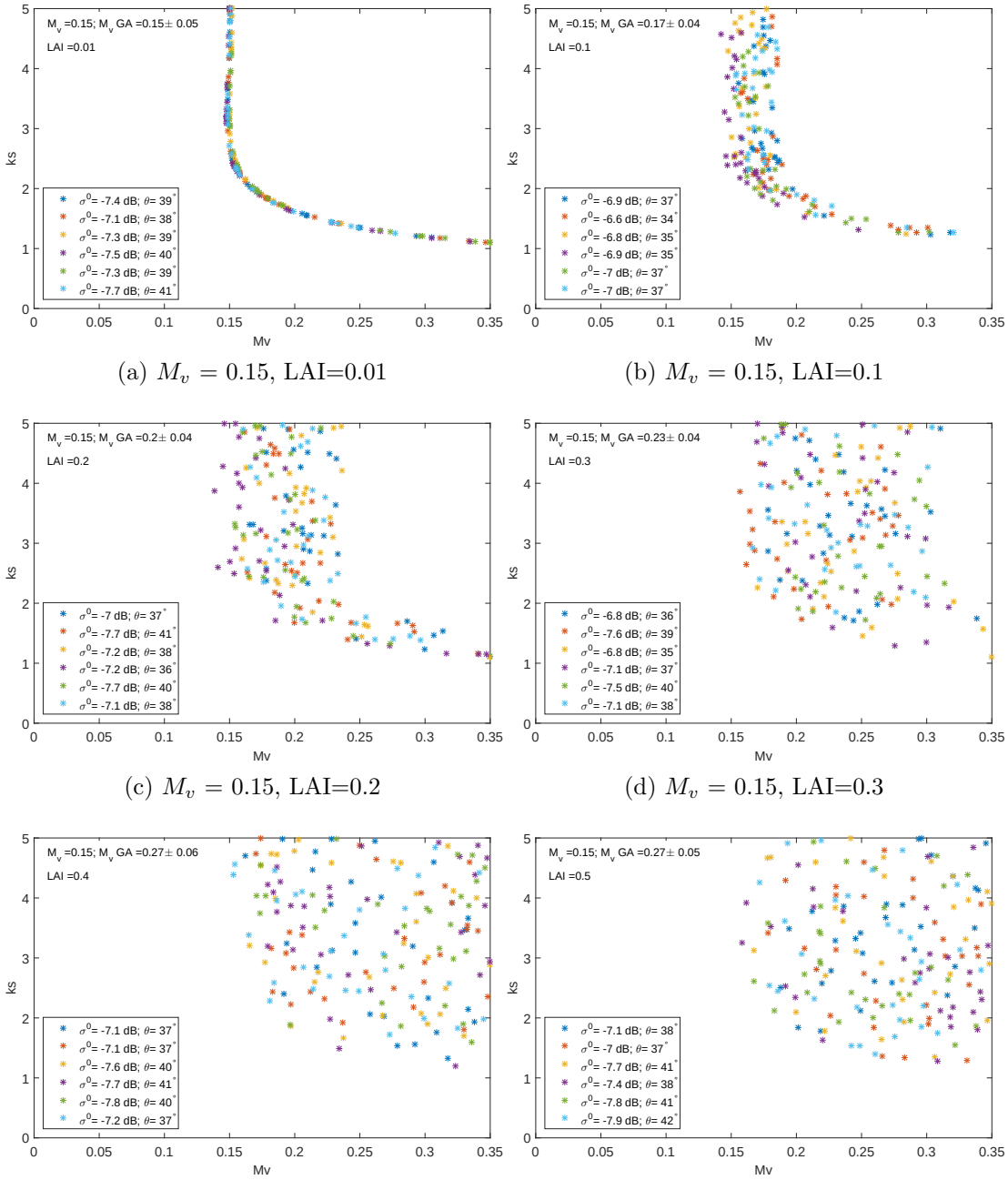

(a) $M_v = 0.15$, LAI=0.01

(b) $M_v = 0.15$, LAI=0.1

(c) $M_v = 0.15$, LAI=0.2

(d) $M_v = 0.15$, LAI=0.3

(e) $M_v = 0.15$, LAI=0.4

(f) $M_v = 0.15$, LAI=0.5

Figure 3.48: Soil moisture (M_v) inversion solutions of the genetic algorithm (M_v GA) for different values of M_v on a vegetated soil, for a subset of higher backscatter and incidence angles.

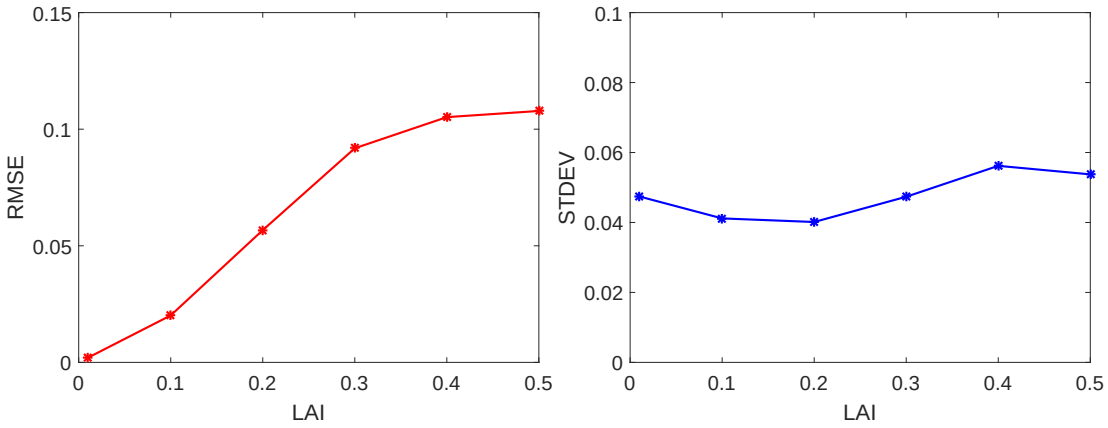

(a) (b)

Figure 3.49: RMSE(left) and standard deviation (right) of the genetic algorithm for different values of LAI on a vegetated soil, with a subset of higher backscatter and higher incidence angle. Soil moisture was fixed at 0.15 m^3m^{-3}.

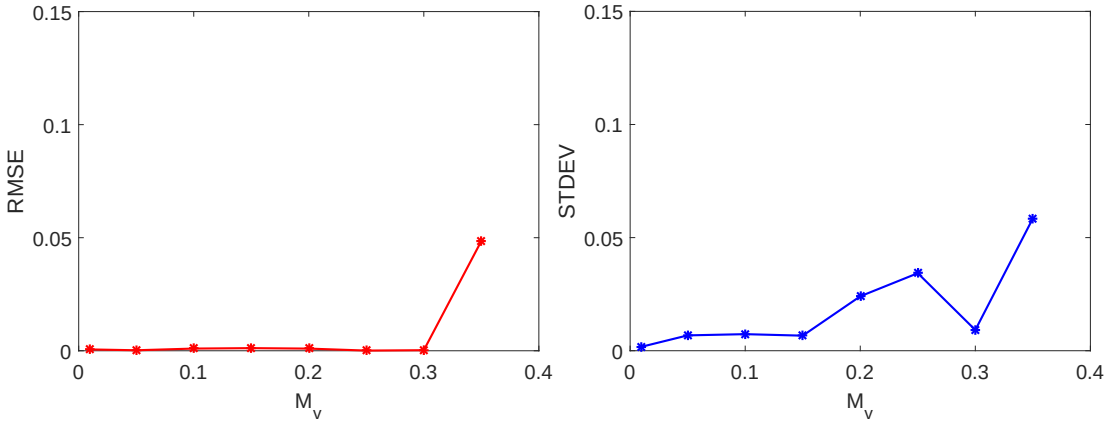

(a) (b)

Figure 3.50: RMSE(left) and standard deviation (right) of the genetic algorithm for different values of M_v on a bare soil, with a subset of higher backscatter and higher incidence angle. Only GA solution ks >2 were used for the soil moisture estimate.

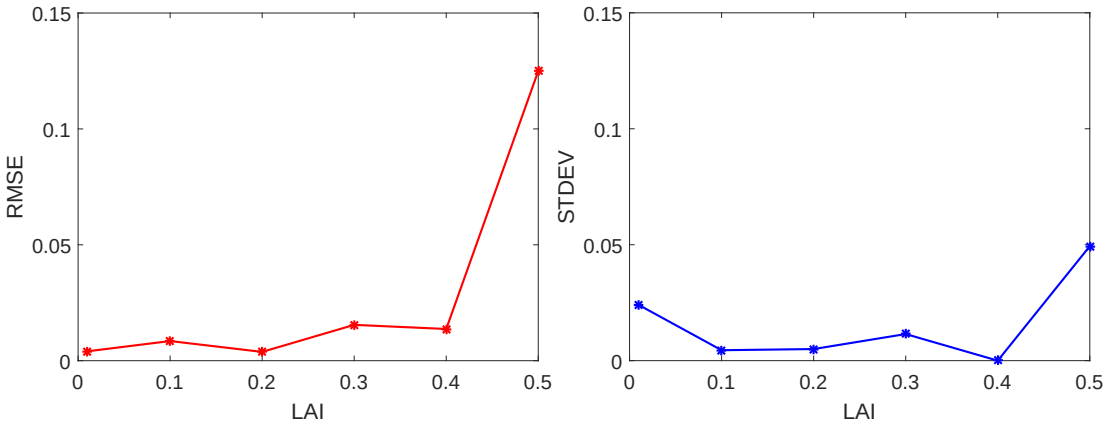

(a) (b)

Figure 3.51: RMSE(left) and standard deviation (right) of the genetic algorithm for different values of LAI on a vegetated soil, with a subset of higher backscatter and higher incidence angle. Only GA solution ks >2 were used for the soil moisture estimate. Soil moisture was fixed at 0.15 m^3m^{-3}.

3.5.3.2 Application of the inverse model at soil moisture stations

Most Sentinel-1 inverted soil moisture are lower than ground-observed soil moisture (Figure 3.52). Possible reasons are discussed in section 3.6. Some outputs, i.e. Figure 3.52a and b, follow expected seasonal trends of wet winters and dry summers. However, many outputs do not follow the trend of ground-observed data, and show a saw-tooth pattern with a wide range in soil moisture values (Figure 3.52c).

Separation of the inverted soil moisture in different global incidence angles (Figs. 3.53 to 3.55) shows that the inverted soil moisture shows a relation with the global incidence angle. It also shows that: there is no clear difference between inverted results from ascending (satellite travelling from south to north) or descending (satellite travelling from north to south) satellite images; and there is no clear relation between the difference in LAI and the spread of the inverted results, i.e. increasing vegetation do not necessarily give a larger spread δ_θ.

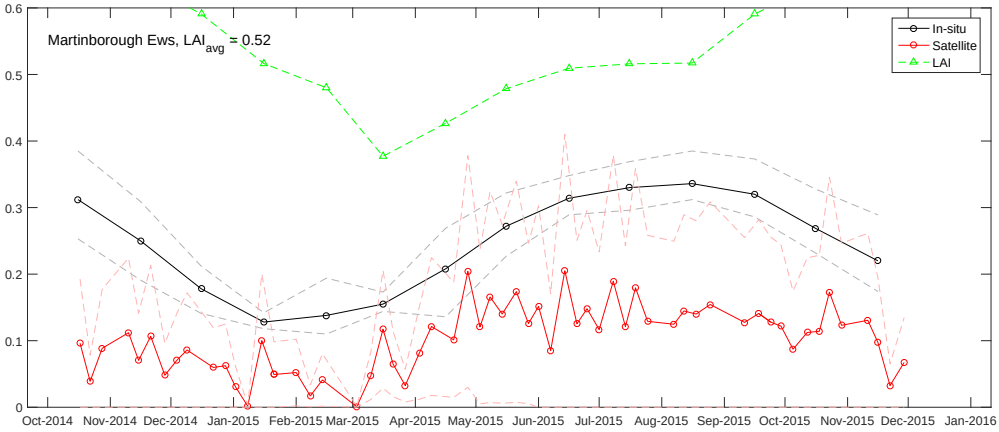

(a)

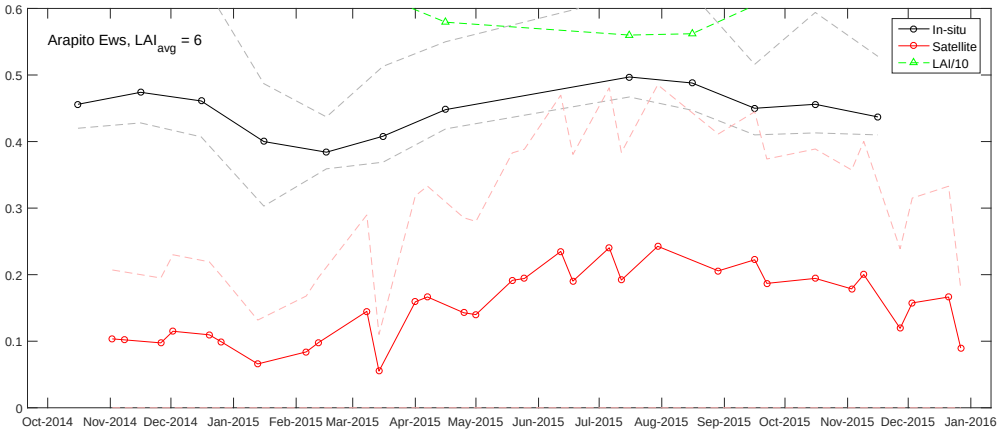

(b)

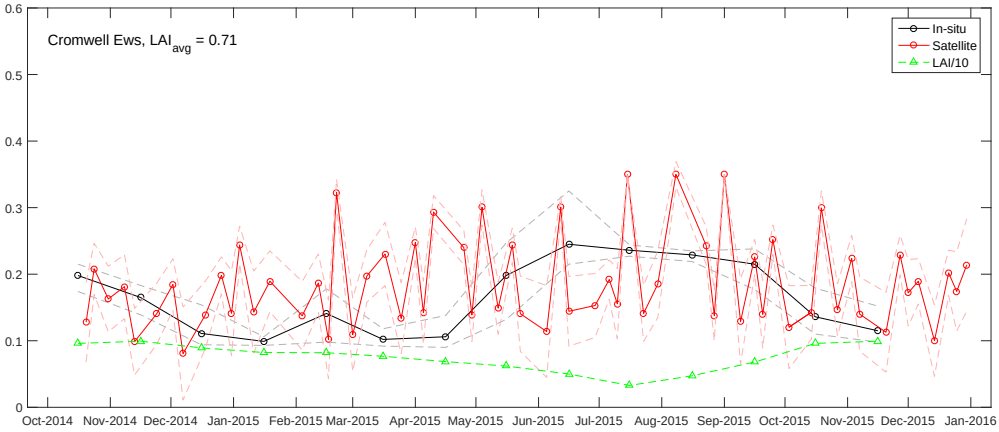

(c)

Figure 3.52: Inverted soil moisture at the location of three ground stations.

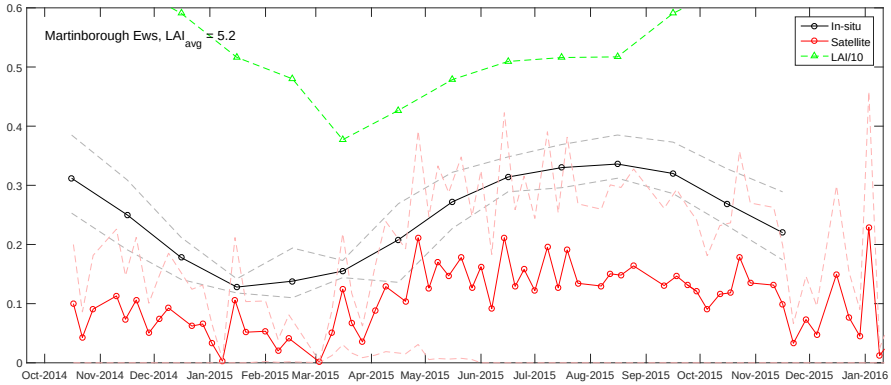

(a) All

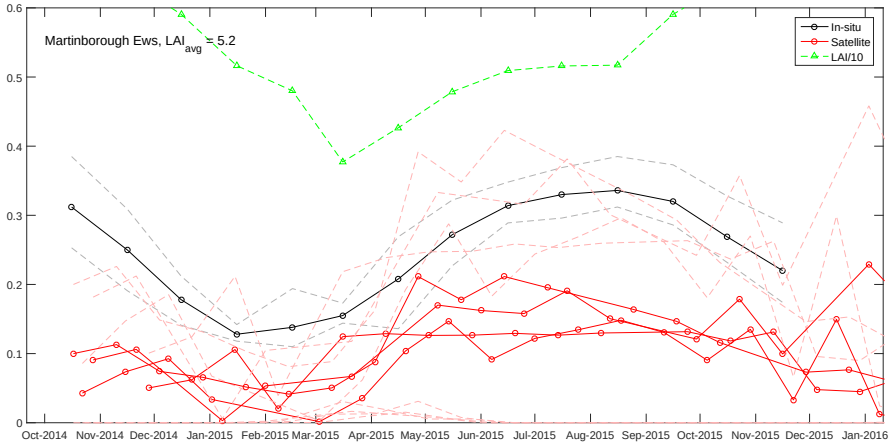

(b) Four separate timeseries binned to global incidence θ

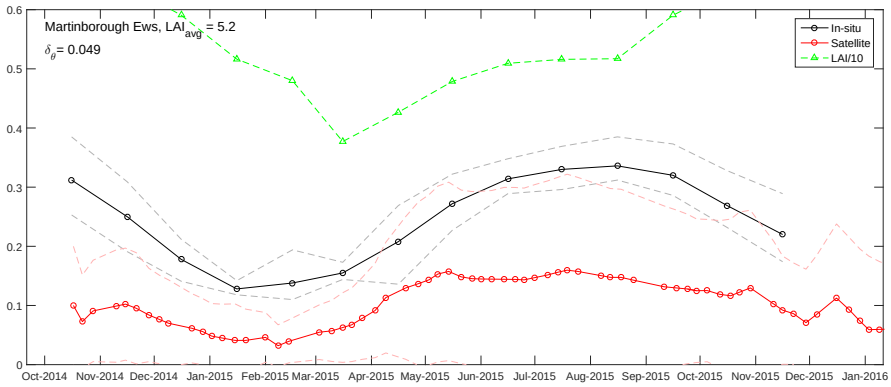

(c) Mean values, based on the four θ time series

Figure 3.53: Inverted soil moisture at NIWA soil moisture ground station 'Martinborough Ews'.

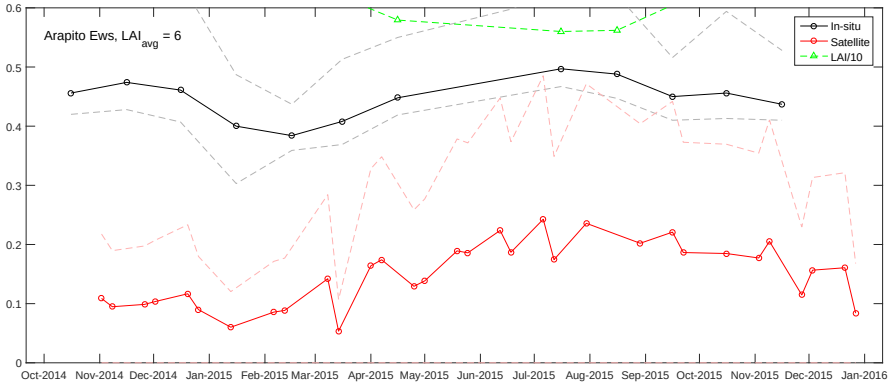

(a) All

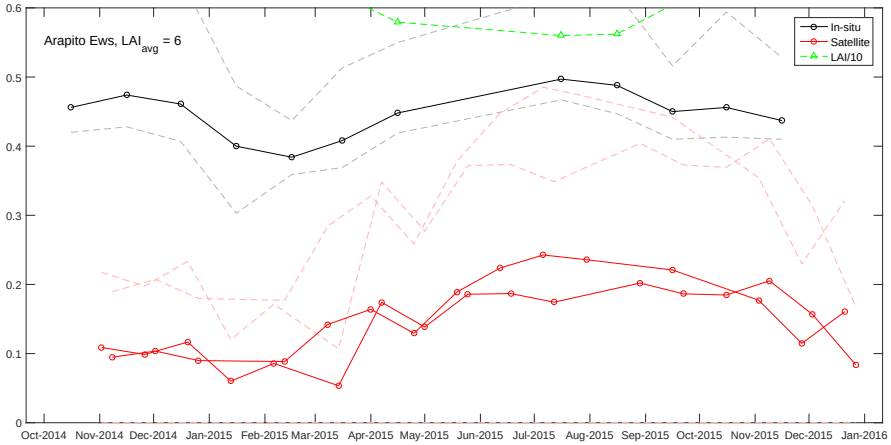

(b) Four separate timeseries binned to global incidence θ

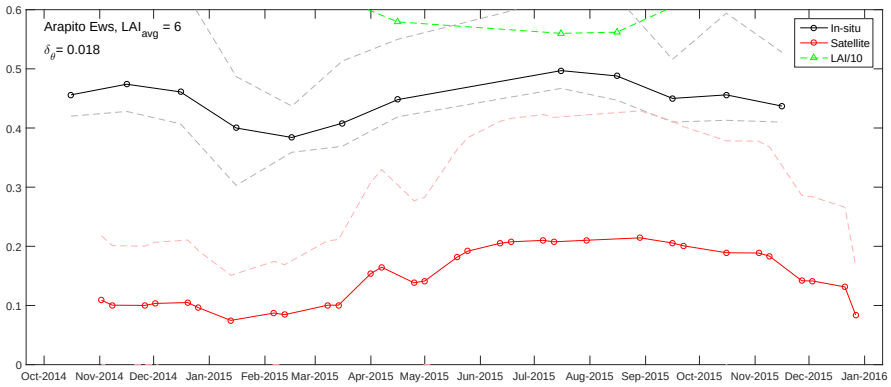

(c) Mean values, based on the four θ time series

Figure 3.54: Inverted soil moisture at NIWA soil moisture ground station 'Arapito Ews'.

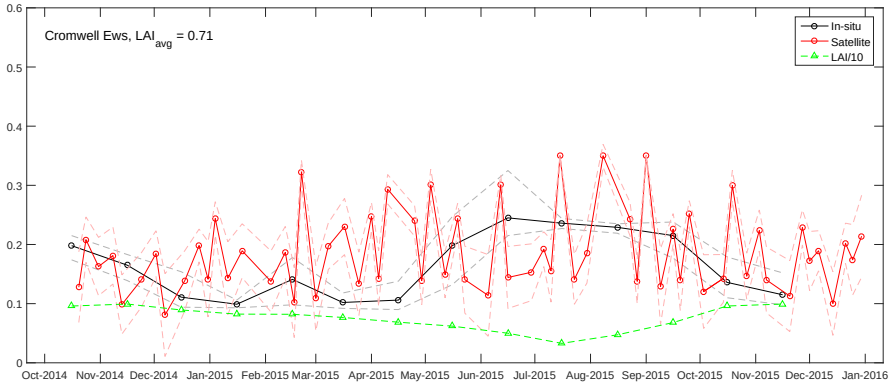

(a) All

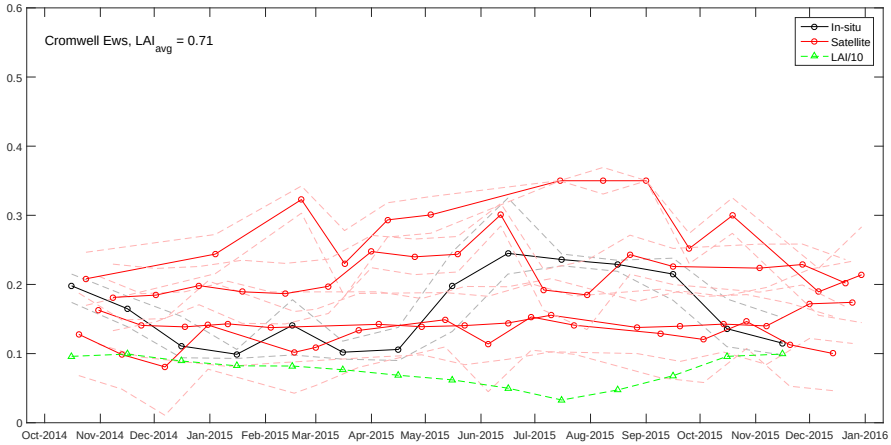

(b) Four separate timeseries binned to global incidence θ

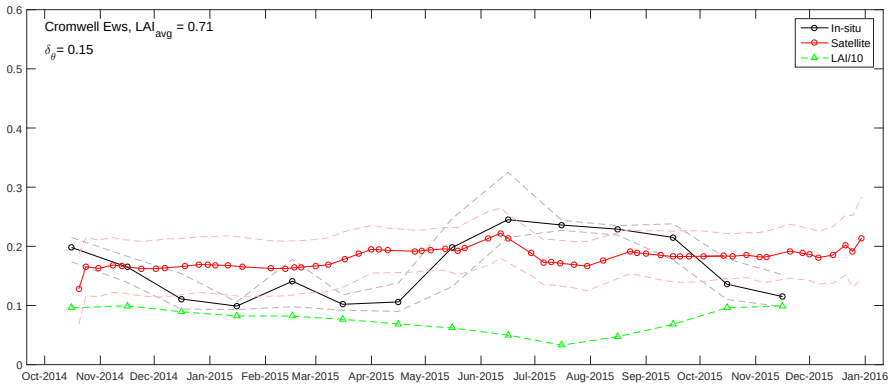

(c) Mean values, based on the four θ time series

Figure 3.55: Inverted soil moisture at NIWA soil moisture ground station 'Kaitaia Ews'.

3.6 Discussion

3.6.1 Phase disturbances in microwave reflections

The results of this study show that small temporal differences in permittivity can have large effect on phase disturbance, while large differences only have a negligible effect. This is a result of the reflection-transmission boundary conditions (Eq. 3.14). The results explain the differences found in studies mentioned in the introduction. For example, Lundgren et al. (2004) find long-term patterns of uplift of Mt. Etna, that related to magmatic inflation. However, they could not explain seasonal trends and variations that are of the order of 1 cm or less. Lauknes et al. (2010) find seasonal patterns in InSAR data in the autumns of 1996 and 1998, where line-of-sight displacement suggests a seasonal upwards terrain motion of almost 10 mm. However, no explanation of the reasons is given. Tomás et al. (2016) confirm that variations of 10 mm in line-of-sight displacement are seasonal. They then relate this to change in groundwater level. Reeves et al. (2011) surmise, from seasonal variations of InSAR of approximately 1 cm or less, that InSAR might capture seasonal variation of hydraulic head. They show high correlation of hydraulic head with lin-of-sight displacement in areas between irrigation circles, where there is little vegetation. They then derive a model of hydraulic head, using the elastic skeletal properties of the subsurface. Although the correlation with hydraulic head and the InSAR data might actually exist, the actual cause of the seasonal variations might well be explained by the small variations of phase disturbance caused by soil moisture and vegetation, e.g. in dryland areas with little vegetation.

More advanced use of the phase disturbance model might not add much more information to the exact quantification of the phase disturbance. One might want to use this model to forecast the phase disturbance if vegetation and soil is known. However, permittivity of vegetation and soil can not be modelled with that detail, especially since very small differences in permittivity can already cause large phase differences. Future research could include the use of pre-modelled coherence plots to match with actual measurement-based coherence plots, to infer relative changes to soil or vegetation. In that case, more advanced backscatter models might be needed, that take into account more than only gently undulating surfaces and (Fresnel) reflection coefficients that take into account incidence angles.

3.6.2 Inverse models for soil moisture estimation

Genetic algorithm (GA) solutions for bare soil, when tested with 'pseudo-field data' (section 3.5.3) yield reliable results. However, comparisons of in situ soil moisture with Sentinel-1 derived soil moisture GA solutions show that the satellite soil moisture is often lower than the in situ measured soil moisture, and that large variations occur in satellite-derived soil moisture, compared to ground observa-

tions (section 3.4.3.4). Discussions on possible explanations for these differences are structured in five items below:

Uncertainty of field data. The GA soil moisture algorithm is designed to calculate soil moisture up to 35% volume percentage. Most satellite soil moisture values are lower than in situ soil moisture. Soil moisture sensors measure values up to 65%. Soil moisture values this high do not occur in most of earth's materials, except for water-saturated peats or soft, wet, clays. The soil moisture sensor data are not calibrated. Therefore, only trends in data between satellite and in-situ data should be compared. Furthermore, in situ soil moisture is typically measured in the first tens of centimetres of the soil, while satellite-derived soil moisture is only from the top few centimetres ('Surface Soil Moisture or SSM'). In-situ and satellite SSM thus do not necessarily have to comply.

Uncertainty of terrain model. GA inverted soil moisture solutions vary with incidence angle. That could be explained by inaccuracy of the used terrain model. This terrain model is used for the conversion from global incidence angle to local incidence angle. Inaccurate elevations could cause the angle used in the forward model to be wrong and this could explain the wrongly calculated output of the GA inversion module.

Heterogeneity and anisotropy. Soil heterogeneity can cause the soil moisture observed by sensors to be very heterogeneous, as shown by e.g. Wagner et al. (2007) (see Chapter 1). It should therefore not be assumed that all soil moisture in a 10m x 10m pixel is the same. For example, soil moisture could go through vertical preferential drainage paths. Furthermore, heterogeneity in soil moisture can cause anisotropy when viewed from multiple incidence angles. For example, preferential drainage paths could give different backscatter from different incidence angles. If soil moisture changes, surface roughness will also change and it could therefore be that both soil moisture and surface roughness are angle-dependent and anisotropic.

Vegetation model. It could be that modelled vegetation backscatter is different from actual vegetation backscatter due to the use of a simple model. The current S^2RTR model does not incorporate the true complexity of vegetation, and does not distinguish between the different de-polarising effects that of, for example, stalks and leaves. Since the aim of this chapter was to solve for soil moisture, other or more advanced models were not used, as these can introduce unknown uncertainty.

Boundary conditions. Small differences in soil moisture can cause a significant variation in phase and amplitude (section 3.5.1). The implication of the boundary conditions have not been implemented in the inversion, since they are not known beforehand and are too complex to be modelled (section 3.6.1).

Although some solutions of the GA inversion seem to follow the expected trends of ground station data, many others are not deemed reliable at this stage. Therefore,

more research is needed to improve reliability. Following the above discussion topics, future research should aim at these topics:

- Use of longer term time series to derive relative ratios of soil moisture, only based on satellite data. For example, if the Sentinel-1 data would contain data of a time span of several years, estimates of relative soil water deficits could be made, which would give an indication of the anomaly of soil moisture;
- Research on the improvements of this algorithm using more accurate terrain model data;
- Find correlations between large differences of in situ with satellite data and other land classifications, such as soil type, land-use, vegetation, terrain slope;
- Anisotropy of surface roughness in relation to the incidence angle;
- Change of amplitudes with small changes in soil moisture or vegetation.

The inversion in this chapter focused on soil moisture. Vegetation density and height is also estimated, but not used in further analyses. Since vegetation is fully embedded in the inversion, further research is also recommended on the use of this inversion scheme dedicated to calculation of vegetation and its height.

3.6.3 Satellite soil moisture and groundwater characterisation

Despite many challenges still to overcome, satellite-derived soil moisture can in principle be used to support soil water budgets or soil water balance models in New Zealand as: the data shows to follow the seasonal trends at many places; is of sufficiently high resolution to be incorporated in gridded rainfall recharge models. If data have been quality controlled and follow the expected patterns of the season or ground observations in the area, trends and patterns in the satellite soil moisture can be used as an interpolator between ground observations. A similar interpolation technique was described in Chapter 2, section 2.3.2, for evapotranspiration.

However, incorporation of many satellite soil moisture estimates still requires manual checks and quality control, as many inconsistencies between ground observations and satellite data still exist. If the seasonal trends of satellite-derived soil moisture in a certain area follow the expected pattern or data from ground observations, then the relative trend in these soil moisture estimates can be used to incorporate in soil water balance models. But in many areas this is not the case, as shown by the comparison of the genetic algorithm at ground observations (section 3.5.3.2). Whether or not data quality is sufficient should be checked manually before incorporation in such a model. The need for this manual check means that the method is, at many places in New Zealand, not yet ready for automated or

operational use. Therefore, efficient processing chains to calculate soil moisture should only be done in smaller areas where quality control is easier to perform, and preferably after the recommendations for future research in this chapter have been further explored.

3.7 Conclusion

More soil moisture data coverage is important to studies of rainfall recharge to groundwater. Satellite microwave data have the potential capability to improve soil moisture estimation in New Zealand. This chapter described the theory that outlines the physics of satellite microwaves, and three novel methods that: (1) explain uncertainty in microwave backscatter that influences InSAR measurements of terrain motion; (2) quantify the sensitivity of microwave backscatter to important input components (e.g. soil moisture, terrain slope, vegetation, clay fraction); and (3) define an algorithm to calculate soil moisture from satellite data.

Minor differences in reflection properties caused by seasonal soil moisture changes can cause substantial differences in phase and amplitude of the backscatter. These differences are caused by the boundary conditions of electromagnetic reflection and transmission and lead to phase 'disturbances' between different satellite overpasses. These phase difference translated to a distance of 5 - 8 mm for C-band microwave data, which can pose significant noise for interferometric (e.g. InSAR) data analyses of terrain motion.

A synthetic model was built that calculates backscatter, based on a semi-empirical existing method to calculate backscatter from a soil (PRISM) and a method to calculate backscatter from vegetation (S^2RTR). This model was used in an analyses of the method to its input components (e.g., soil type, soil moisture, incidence angle, soil density, vegetation optical depth). These numerical and visual analyses show that, for bare soil, microwave backscatter is most sensitive to surface roughness (when surface roughness is small), soil moisture, and incidence angle. Backscatter should be corrected for local terrain features when applied in synthetic models. Backscatter is also sensitive to vegetation, and as a result of that becomes relatively less sensitive to the other input components.

To solve for surface soil moisture (SSM) from backscatter data, the synthetic model was combined with a genetic algorithm-based inverse model. This iterative model, 'the inverse model', demands multiple pairs of backscatter (σ_0) and incidence angle θ as input data, i.e. it uses multiple neighbouring pixels of a satellite image. Using these $\sigma_0 - \theta$ pairs solves for the non-uniqueness of the soil moisture solution and also solves for soil moisture in (light) vegetation scenarios. However, use of multiple pixels downscales the resolution of the solution (in my example from 10x10m to 1000x1000m).

This model was tested with randomly 'pseudo-field' data, covering a range of incidence angles and backscatter values. The pseudo-field test shows that the

genetic algorithm solves well for soil moisture in the range of 0 and 0.35 m^3 m^{-3} with an RMSE and standard deviation that are both lower than 0.05, if smart subsets are chosen (i.e. high incidence angle, high backscatter, and further filtering if vegetation is dense).

Comparison of in-situ soil moisture from sensors at 62 stations with inverted SSM from real satellite (Sentinel-1) data show that inverted soil moisture is generally smaller than in situ measured soil moisture. At some locations soil moisture data follow the seasonal trends also shown in ground observations. However, at many locations a large bias occurs, which is shown to be related to different overpasses (different global incidence angles). Multiple explanations can be given, but need to be explored further. Therefore, future research should focus on: the use of longer satellite time series; a more accurate terrain model; correlation between large model-data discrepancies and other land classifications (i.e. soil type, land-use, vegetation patterns, terrain slope); and anisotropy.

As this chapter mainly focuses on soil moisture, further research is also recommended on similar dedicated inversion schemes that focus on vegetation and its height.

In principle, satellite-derived soil moisture as described in this chapter can be used to support soil water budgets or soil water balance models in New Zealand as the data follows measured and expected seasonal trends at some places and is of high temporal and spatial resolution. However, automated incorporation of satellite soil moisture estimates over the entire nation cannot be rolled out yet. That would require additional study, manual checks and quality control for each location, as many inconsistencies between ground observations and satellite data still exist. Development of efficient processing chains to calculate soil moisture should therefore only be done in smaller areas where quality control is easier, and preferably only after following up on the recommendations of this chapter.

4 New Zealand-wide estimation of rainfall recharge to groundwater

4.1 Introduction

The most important source of groundwater for many aquifer systems is rainfall recharge, i.e., vertical drainage from the soil to the aquifer. In New Zealand, rainfall recharge models are typically developed to estimate at the local (i.e. sub-regional or aquifer) scale, e.g., (Rushton et al., 2006; Scott, 2004; White et al., 2003). The importance of these models is emphasised by application of these models to the calculation of sub-regional groundwater allocation limits. For example, groundwater allocation limits in Canterbury were set as '50% of average annual land-surface recharge including the recharge component contributed by intermittent streams' (Scott, 2004). However, shortcomings in local rainfall recharge models indicate that a rainfall recharge model at the national scale has an important place in groundwater management in New Zealand. These shortcomings include the definition of sub-regional model boundaries. These boundaries are commonly set on geographic criteria that do not represent aquifer boundaries. For example, the Waimakariri River was used as the boundary between two rainfall recharge model zones in Canterbury, i.e., Zone 1 (Ashley - Waimakariri) and Zone 2 (Waimakariri - Rakaia); White et al. (2003)). However, the aquifer (i.e., the Waimakariri gravel fan; White et al., 2012) includes Zone 1 and only part of Zone 2. It also follows that partition of aquifers into geographic units can produce model domains (i.e., the extent of conceptual groundwater flow budgets and groundwater flow models) that represent only part of the aquifer area. As groundwater systems and their interactions with rainfall, surface water and the land surface extend over many different spatial (and temporal) scales (Alley, 2002; Alley and Leake, 2004), incomplete water budgets may result from the use of sub-regional models. In addition, boundary conditions must be considered by models and therefore rainfall recharge models of land areas adjacent to the model domain are always relevant to flow budgets and groundwater flow models. For example, a water budget of the transition zone, Wairau Plains, uses an estimate of ground-

water inflow that was derived, in part, from rainfall recharge estimate of the land up-gradient of the zone (White et al., 2016). Similarly, groundwater recharge from mountainous areas could be considered in the water budgets of plains aquifer systems, e.g., the Waimakariri gravel fan. Recharge from mountainous areas was suggested in studies in Taiwan (Calmels et al., 2011), Canada (Doyle et al., 2015) and New Zealand (Sims et al., 2015).

An understanding of the uncertainty in rainfall recharge is important. For example, the impact of rainfall recharge uncertainty was demonstrated by White et al. (2003), who used three rainfall recharge models for the Central Plains of Canterbury. They showed that estimated groundwater use as a percentage of rainfall recharge was highly model-dependent and, because of that dependency, varied between 63% and 80% in a relative dry year (1997/1998). However, uncertainty has not typically been assessed by sub-regional models in New Zealand. Within this country, a range of local model studies have estimated rainfall recharge on a weekly or daily basis and on a range of grid dimensions (e.g., Scott, 2004; White et al., 2003, 2014a,b). Therefore, quantification of rainfall recharge has not been consistent across the country. Better coverage of rainfall recharge data on these larger scales could give more comprehensive knowledge about rainfall recharge on a catchment-wide scale, and could aid aquifer management, e.g., by better definition of the recharge source location at the aquifer scale, or by relating differences in existing local models.

A national rainfall recharge model could address these shortcomings and could lead to a more consistent inter-regional overview, including uncertainty, because all input data and model equations come from the same source. Nation-wide recharge estimates could further aid in estimating national aquifer volume stocktakes and flows, e.g. by the Ministry for the Environment (Moreau and Bekele, 2015; Statistics New Zealand, 2011), and in estimating rainfall recharge in unexplored territory. National water budgets for New Zealand have been developed for New Zealand, i.e., long-term estimates of precipitation, evapotranspiration and flow for the North Island and South Island (Toebes, 1972) or per 500 m x 500 m model cell (Woods et al., 2006). However, these did not include a separate groundwater component. Inclusion of long-term rainfall recharge could help separate baseflow from quickflow estimates (e.g., Arnold and Allen, 1999). Rainfall recharge has been estimated at the global scale and at the national scale. On the global scale, Döll and Fiedler (2008) calculated that long-term average rainfall recharge is approximately 400,000 m^3/s. Their rainfall recharge for New Zealand in the period 1960 - 1990 was 2835 m^3/s (equal to 334 mm/yr) $\pm$ 10%. However, their larger-scale rainfall recharge models were challenged by the need to combine coarse and uncertain estimates of rainfall, evapotranspiration, terrain, slope, soil and geology. Uncertainty is also a key issue with New Zealand's national hydrological model (Topnet; Bandaragoda et al., 2004; Clark et al., 2008), because: rainfall recharge data uncertainties are currently inconsistent across the country; the density of ground observations differs across regions; rainfall recharge is modelled in few regions and each region typically uses different local models to estimate rainfall recharge; and different methods and ground observations are

used for calibration and validation of these local models.

This chapter describes a model that estimates nation-wide rainfall recharge on a 1km x 1km grid at monthly intervals. The model is called the National Groundwater Recharge Model (NGRM). Input components currently exist of: nation-wide gridded estimates of rainfall; satellite-derived evapotranspiration (ET) and vegetation (Leaf Area Index) information; a national terrain model; and nation-wide soil and geology datasets. The recharge estimates have an associated uncertainty, derived from all model input components and error propagation through the model equation. The use of satellite-derived ET in rainfall recharge models is novel and the ET used is the original MOD16 AET as described in Chapter 2. Validation is described in three case studies (two in the Canterbury Plains and one at sub-catchment-scale in the mid-Mataura catchment, Southland). Recommended model improvements aim to contribute to a national water budget with incorporation of other recharge components, e.g. of river recharge, and better uncertainty estimates. This water budget could have multiple applications including provision of the science behind the setting of realistic limits for the allocation of groundwater and surface water.

4.1.1 Introduction to water budgets and relation to rainfall recharge

Rainfall recharge is a groundwater flux, i.e., there is water transport from surface to groundwater. Other important water fluxes from groundwater to the surface exist. For example, groundwater flux can be upwards (i.e., from the groundwater to surface) through

- groundwater discharging to the surface as springs or in the river, also known as 'baseflow' or 'gaining streams';
- groundwater abstraction, e.g. for agriculture;
- groundwater uptake from (tree) roots, leading to transpiration back in the atmosphere.

Groundwater fluxes can also be downwards (i.e., from surface to groundwater) through

- rivers feeding our groundwater (also known as 'losing streams');
- artificial water injection, e.g., for geothermal purposes;
- rainfall recharge to groundwater.

Many techniques have been developed to calculate rainfall recharge. Some of these will be explained in this section. First, the concept of water budgets and water balances are explained.

A water budget is the estimation of water volumes or fluxes for a certain area. A water balance, also known as a hydrological budget equation (Freeze and Cherry,

1979), is the equation of all ingoing and outgoing water components of an area. For a catchment, a water balance is commonly defined as:

$$P = Q + AET + \Delta S, \tag{4.1}$$

with:

P = precipitation (rainfall + snow);

Q = flow, i.e., surface flow and groundwater flow. Surface flow can be over land or through rivers;

AET = actual evapotranspiration;

ΔS = change in soil and groundwater storage. This is often assumed zero for the long term, assuming that average long term storage does not change. Averaging over a long term (i.e., many hydrological years) implies that there is no climate change and increasing or decreasing water abstractions.

The balance of Eq. 4.1 does not differentiate between inflow and outflows. When using this on a catchment scale, groundwater flow is often ignored as, for a general catchment, net groundwater flow is often assumed zero (no inflow from out of the catchment, no outflow to other catchments), and inflow from surface flow is negligible. However, for a general model area, the water balance should be further expanded, as one has to look at inflows and outflows in the area in more detail. This was done by Scanlon et al. (2002), and some of their terminology is used in this Chapter. Figure 4.1 (left) depicts a conceptual water balance of a generalised model area. If we assume that transfers within the unsaturated (4.1, right, green) zone are not changing over the long term (i.e., ΔS for the unsaturated zone is 0), the water balance of a random area can be defined as:

$$P + Q_{GW,IN} + Q_{SW,IN} = AET + Q_{GW,OUT} + Q_{SW,OUT} \tag{4.2}$$

where

P = precipitation (into the area);

AET = actual evapotranspiration (out of the area);

$Q_{GW,IN}$ = groundwater entering the area (either from a neighbouring cell, or from rainfall recharge to groundwater);

$Q_{GW,OUT}$ = groundwater leaving the area;

$Q_{SW,IN}$ = surface flow entering the area;

$Q_{SW,OUT}$ = surface flow leaving the area.

Many inter-connections of these inflows and outflows exist. For example, precipitation can runoff directly to surface flow (which is often called 'quickflow', Figure 4.1,a); groundwater can come close to surface and evaporate or transpire through plants (Figure 4.1,b); rainfall can recharge into groundwater (Figure

4.1,c); groundwater can discharge to surface flow (which, is often called 'base-flow', Figure 4.1,d); or runoff can directly feed groundwater (Figure 4.1,e). If we define surface flow as the sum of baseflow ($Q_{SW,BF}$) and quickflow ($Q_{SW,QF}$), Equation 4.2 can be further expanded as:

$$P+Q_{GW,IN}+Q_{SW,IN,BF}+Q_{SW,IN,QF} = AET+Q_{GW,OUT}+Q_{SW,OUT,BF}+Q_{SW,OUT,QF} \quad (4.3)$$

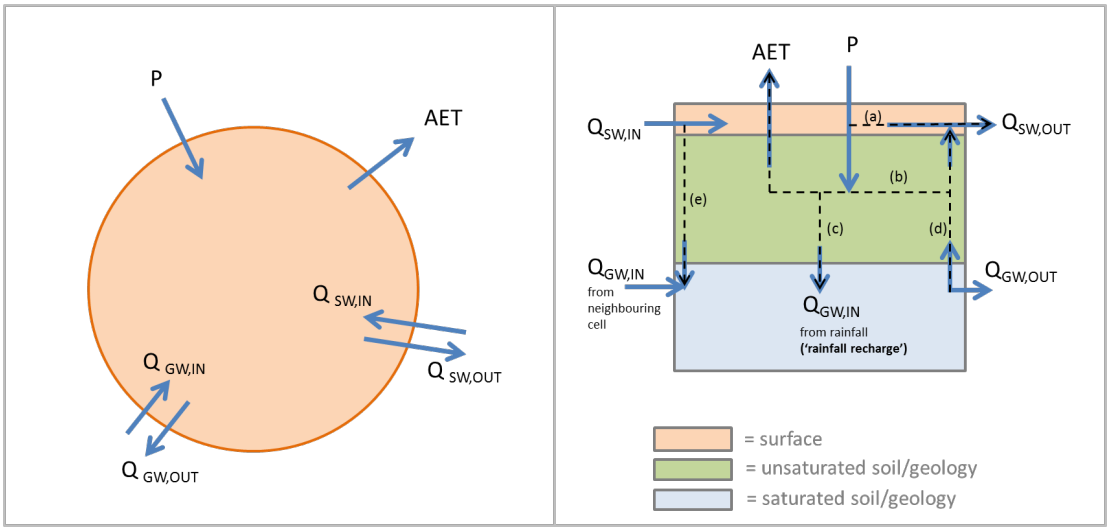

Figure 4.1: Conceptual water budget for a generalised model area. **Left:** top view showing inflows and outflows. P=precipitation (into the area), AET=actual evapotranspiration (out of the area), $Q_{GW,IN}$=groundwater flow in (either through a neighbouring cell or through rainfall recharge), $Q_{GW,OUT}$=groundwater flow out of the area, $Q_{SW,IN}$= surface flow into the area, $Q_{SW,OUT}$ = surface flow out of the area. **Right:** inflows, outflows, and their interactions: (a) surface flow of precipitation, (b) surface flow of soil water (also known as 'interflow'), (c) $Q_{GW,OUT}$ from rainfall recharge into groundwater, (d) groundwater discharge to the surface (also known as 'baseflow'), (e) river recharge into groundwater.

The interest in this study is in the rainfall recharge into groundwater (='$Q_{GW,IN}$ from rainfall' in Figure 4.1). Rainfall recharge into groundwater is defined here as the amount of rainfall that travels through the soil and subsurface and then replenishes the groundwater. If rainfall recharge is named $RRECH$, its long-term balance for a catchment can be defined as:

$$RRECH = P - AET - Q_{SW,QF} \quad (4.4)$$

where $Q_{SW,QF}$ is the remainder of rainfall that leaves the cell through surface flow.

However, the balance of surface flow $Q_{SW,QF}$ is also more complex when taking into account other factors, like the interaction of surface water with groundwater,

or evaporation of surface water. For the whole catchment, i.e. when inflows are assumed negligible, the balance is then:

$$Q_{SW} = Q_{SW,QF} + Q_{SW,BF} - Q_{GW,losing} - E_{SW} \tag{4.5}$$

in which:

$Q_{SW,QF}$ is quicfklow generated through rainfall in the area;

$Q_{SW,BF}$ is baseflow the enters the area, i.e. gaining streams;

$Q_{GW,influent}$ is the loss of runoff due to losing streams;

E_{SW} is evaporation of the surface water.

For a generalised area, Equation 4.5 needs to be expanded to incorporate for the inflows in the area. As one can see, water budgets and balances can be quite complex. Therefore, hydrological budget equations that focus on groundwater need to make simplifying assumptions. Arnold and Allen (1999) explain that, in a simple groundwater budget, groundwater recharge can be estimated if baseflow is known. Their simplified groundwater budget is:

$$RRECH = BF + AET + Q_{GW,OUT} + \Delta S \tag{4.6}$$

where:

R is groundwater recharge;

BF is baseflow;

AET is actual evapotranspiration;

$Q_{GW,OUT}$ is subsurface seepage out of the basin;

S_t is change in groundwater storage.

They further detail multiple baseflow separation techniques (i.e., to separate baseflow from surface runoff or quickflow).

Cherkauer and Ansari (2005) use a similar simplified groundwater budget and separated baseflow in small watersheds to estimate groundwater recharge in the United States. Their simplified groundwater budget is:

$$I + Q_{GW,IN} = Q_{bf} + Q_{GW,OUT} + AET + NP + \Delta S/t \tag{4.7}$$

where:

I is infiltration to the groundwater system (e.g. rainfall);

$Q_{GW,IN}$ is groundwater influx to the catchment through inter-catchment aquifers;

Q_{bf} is groundwater discharge through baseflow;

GW_{out} is groundwater outflux out of the catchment through subsurface seepage;

AET is actual evapotranspiration;

NP is net pumpage out of the catchment;

$\Delta S/t$ is the change in groundwater storage over time period t.

If recharge is equal to $I - ET$, and all parameters $Q_{GW,IN}$, $Q_{GW,OUT}$, NP, and $\Delta S/t$ are set to zero, recharge is equal to baseflow. Yeh et al. (2014) follow the same approach to estimate groundwater recharge in mountainous basins in Taiwan.

4.1.2 Introduction to soil water balance models

When shorter time frames are considered, or when components of long-term balance are prone to changes due to seasonal changes, climate change or water abstraction, estimates of water budgets over smaller time steps are necessary. Ideally, water storage of soil and groundwater should then be fully taken into account. Commonly, these calculations take into account the storage of the underlying soil S, and calculate the recharge to groundwater. Rainfall recharge into groundwater is then defined as the part of the rainfall that, after surface flow, evaporation, and saturation of the soil, permeates through the subsurface and replenishes the groundwater. 'Soil water balance' models are commonly used for that: they calculate a mass balance between water inflow and outflow in a one- or multi-layer soil, and assume that any surplus water in the soil layer either drains to groundwater or goes to surface flow. These models generally revolve around the calculation of soil moisture (or its deficit from the maximum). Most soil water balance models are similar, and differ from each other only in the calculation of AET or surface flow. Some soil water balance models are explained below.

White et al. (2003, 2014a,b) apply a soil water balance model (SOILMOD/DRAIN) based on a model of Scott (2004) (SOILMOD). It calculates a daily soil water budget for plain areas without runoff. The soil storage S for time step i is then defined as:

$$S_i = S_{i-1} + R_i + IRR_i - AET_i - RRECH_i, \tag{4.8}$$

with

R_i is rainfall at day i;

IRR_i is irrigation at day i;

S_i is soil moisture at day i (i=1: at day i-1);

In most soil water balance models it is assumed that, when rainfall exceeds PET, AET is equal to PET; when PET exceeds rainfall, AET is equal to the amount of soil water that can be extracted between timestep i-1 and i. White et al. (2003) solve for the relation between AET and soil storage by assuming known field

capacity FC and vegetation cover factor VC. AET at timestep i then looks like (re-written from White et al. (2003)):

$$AET_i = \frac{S_{i-1}\, PET_i^2}{FC\,(PET_i - VC)}, \tag{4.9}$$

Hong and White (2014) do not define a fixed relation between AET and PET, but try and optimise this relation between AET and PET using a non-linear Bayesian technique. Their model is called 'soil moisture balance using sequential Monte-Carlo filtering' (SMB-SMC). Both the SMB-SMC and SOILMOD/DRAIN models have been compared and validated with lysimeters in the Canterbury Plains (Hong and White, 2014) and will be used for further comparison in this study.

A soil moisture balance model by Rushton et al. (2006) also calculates soil moisture deficit. It uses the Penman-Monteith equation from Allen (1998), and includes crop and vegetation factors. It also includes runoff, which is a function of soil moisture deficit and rainfall intensity, through a look-up table approach.

Westenbroek et al. (2010) describe a soil water balance model, USGS-SWB, that uses a different runoff estimation. This method used the NCRS curve number approach. To calculate which part of precipitation becomes runoff, the empirical NCRS curve number (CN) method was established by Cronshey (1986). It states that surface runoff Q can be determined by;

$$Q = \frac{(P - 0.2S)^2}{(P + 0.8S)} \tag{4.10}$$

and that soil moisture deficit can be empirically determined by:

$$S = \frac{1000}{CN} - 10, \tag{4.11}$$

where CN ranges from 30 to 100, and is found through a look-up table for different soil type, use and cover. This method, although widely used, is depending on the right soil type information. It is developed with data from gently sloping farmland, but it has not defined a relation to topography. CN number are also developed for urban landscapes.

Döll and Fiedler (2008) apply a soil water balance approach to calculate recharge on the global (i.e.,world-wide) scale. They compute recharge as

$$RRECH = min(RRECH_{max}, f_g R_l); f_g = f_r f_t f_h f_{pg}, \tag{4.12}$$

with

$RRECH_{max}$ is the soil texture-specific maximum groundwater recharge (infiltration capcity);

R_l is the total runoff of land area per cell;

f_g is a groundwater recharge factor;

f_r is a slope related factor;

f_t is a soil-texture related factor;

f_h is a hydrogeology related factor;

f_{pg} is a permafrost/glacier related factor;

The slope-related factor Döll and Fiedler (2008) corrects for the terrain slope by correcting the initial recharge with a factor:

$$RRECH = RRECH_0 * f_{slope} \tag{4.13}$$

The linear fit found for their empirical values of Döll and Fiedler (2008), shown in Figure 4.2, is:

$$f_{slope} = -1.1\alpha + 1, \tag{4.14}$$

with the slope angle α in radians.

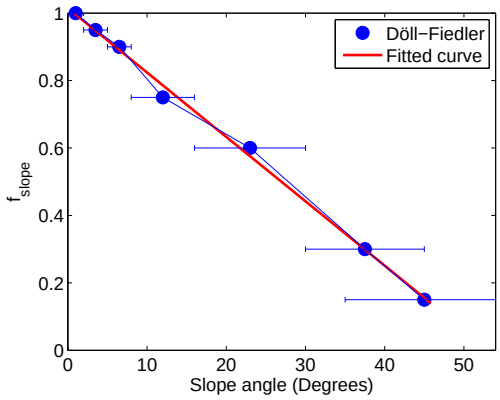

Figure 4.2: Slope angle vs. f_{slope} used in this study compared to Döll and Fiedler (2008).

Döll and Fiedler (2008) furthermore apply a similar correction factor for geology. However, they also mention that this correction factor on a global scale is quite uncertain, as at that time no global geohydrological information was available on a global scale. Gleeson et al. (2011) developed a mapping method for the calculation of hydrogeological properties over the world, which could be applied for further improvements of such a geological factor.

All of these recharge models estimate what could be called a 'potential recharge', since they are not coupled to any groundwater related information or model. Potential recharge would diminish (to 'actual recharge') in areas where groundwater is (temporarily) very shallow or discharges to the surface; it is zero at places where groundwater constantly discharges to the surface. The models described in this chapter, are not coupled to any groundwater information. For those scenarios, some coupling with a groundwater model should take place to be able to correct a 'potential' rainfall recharge to an 'actual' rainfall recharge. That will be part of Chapter 5.

4.2 General methodology

The NGRM model calculates 1km x 1km rainfall recharge to groundwater at monthly time steps and is a simple soil water balance approach, i.e., it calculates a mass balance between water inflow and outflow in a one-layer soil, and it assumes that any surplus water in the soil layer either drains to groundwater or goes to runoff. Surface runoff data (e.g. rainfall runoff, rejection of recharge due to low permeability of soil or geology) is archived in the model, so it can be compiled later for comparison or validation to flow recorders, surface water flow models, or conceptual water budgets. The NGRM model is considered uncalibrated: it has not been calibrated on the national scale to runoff or other measured estimates of the water cycle. However, lessons learned from local comparison described in this chapter, have been used to improve the nation-wide NGRM model equations. The NGRM was developed newly, because there was no one model found that incorporates the following components:

1. a deeper 'geology' layer with hydraulic conductivity estimates, based on the national geology map of New Zealand; this enables the possibility of inhibiting recharge due to deeper impermeable layers. The NGRM model was inspired by the WaterGAP model, which has this possibility. However, since WaterGAP is a global model, it is based on very coarse geology data and much improvement is needed for application to the finer scale;
2. use of a nation-wide high-resolution (1 km) satellite-derived datasets of: potential evapotranspiration; actual evapotranspiration; and Leaf Area Index;
3. an estimate of model uncertainty in rainfall recharge through variance-covariance error propagation of its model input components utilised.

Monthly time steps were chosen because the input data of satellite actual evapotranspiration was monthly (see 'Input data'), and to efficiently calculate, develop and test this model without too much computational effort.

A more detailed methodology section follows after description of the model input data.

4.3 Input data

The NGRM model uses input data on precipitation, evapotranspiration, vegetation, topography, soil parameters, and geology. These are summarised below.

4.3.1 Precipitation

Daily precipitation data from 1972 to current for New Zealand are available in a regular ∼5 km grid from the Virtual Climate Station (VCS) network (NIWA, 2014; Tait, 2014). These data, described by Tait et al. (2006), were resampled to monthly values for the period 1-Jan-2000 to 31-Dec-2013, and to 1 km x 1 km to fit the NGRM model cells.

4.3.2 Leaf Area Index

Monthly 1km x 1km Leaf Area Index (LAI) is derived from surface reflectance in the red and near infrared bands measured by NASA's MODIS sensor. LAI is defined as the one-sided green leaf area per unit ground area in broad-leaf canopies, and one half the total surface area per unit ground area in needle leaf canopies (Samanta et al., 2011). LAI data of New Zealand for the period January 2000 up to December 2013 was used. The 1km x 1km grid cells with monthly time step were classified as values between 0 (minimum LAI = no vegetation) and 100 (maximum LAI) data and obtained from the C5 LAI dataset from Park (2015). These data were gridded to fit the model cells and scaled between values of 0 and 10. Compiled 2000-2013 data of mean monthly LAI is shown in Figure 3.19.

Additional pre-processing was applied to both monthly precipitation to correct for canopy interception (Ic). Based upon studies of Gerrits (2010), who assessed and measured Ic for a range of vegetation types, and Zhou et al. (2006), who defined Ic as a function of precipitation and LAI, we define Ic as Eq 4.15:

$$Ic = \frac{P * LAI}{3E03}, \tag{4.15}$$

so that a conservative estimate of 2% of rainfall will be intercepted by the canopy at maximum LAI (approximately 6). The interception was subtracted from the precipitation dataset. It was assumed that the satellite-measured MOD16 AET already embeds the evaporation of the intercepted water and therefore Ic was not added to AET.

4.3.3 Evapotranspiration

The MOD16 algorithm uses satellite data from NASA's MODerate resolution Imaging Spectroradiometer (MODIS) sensor. The satellite-derived parameters are land cover, albedo, leaf area index (LAI), fraction of absorbed photosynthetically active radiation (FPAR), and enhanced vegetation index (EVI). Temperature, radiation, air humidity and pressure data are derived from the daily global meteorological reanalysis data set from NASA's Global Modeling and Assimilation Office (GMAO). The MOD16 algorithm, Mu et al. (2007) and Mu et al. (2011),

uses the Penman-Monteith approach to calculate evapotranspiration. Data are available online in HDF (Hierarchical Data Format) files (NTSG, 2013). The spatial resolution of the cells is approximately 1 km x 1 km. Data are available in 8-daily, monthly, and yearly intervals. Monthly MOD16 PET data has been tested in the New Zealand setting by Westerhoff (2015) (or 2), who also derived a MOD16 Penman PET conversion and uncertainty estimate for these data. Westerhoff (2015) furthermore suggests that MOD16 AET could be used in New Zealand studies, since: they seem to fit expected values and patterns in large parts of New Zealand; and the data already take into account vegetation characteristics. Monthly MOD16 Penman PET and MOD16 AET, covering the period January 2000 to December 2013, were gridded to fit the 1km x 1km model cells and used in this study. They are called PET and AET onwards.

4.3.4 Terrain model

The Geographx New Zealand DEM 2.1 Geographx (2012) has used New Zealand based topographic data from Land Information New Zealand (LINZ) and data from the satellite derived Shuttle Radar Topography Mission (SRTM, USGS, 2006) data. The 8 m x 8 m DEM was resampled to 1 km x 1 km mean elevation values for this study.

4.3.5 Soil

Profile of Avalailable Water (PAW) and soil permeability data from the Fundamental Soil Layer (FSL) Database (Landcare Research, 2014) as described by Newsome et al. (2008) were used as they generally cover the entire nation. Other datasets, that might be better on the local scale, but do not have nation-wide coverage, i.e., SMAP (Landcare Research, 2015), were not used.

4.3.5.1 PAW

PAW is a soil property defining the amount of water that can be held by a soil column. It is defined here as the difference between field capacity and permanent wilting point, following Smith and Mullins (2001), and is given as an average value for a soil column. Table 4.1 states the different soil PAW classes, after Newsome et al. (2008), with each soil class having a minimum, maximum, and modal value. The PAW data are available from the LRIS portal Landcare Research (2014) as an ArcGIS shapefile. The data were rasterised to the NGRM model cells. The regridded modal PAW values for the soils are shown in Figure 4.3.

Table 4.1: PAW classes and their descriptions, after Newsome et al. (2008).

PAW Class	min. PAW (mm)	max. PAW (mm)	Description
1	250	350	Very high
2	150	249	High
3	90	149	Moderately high
4	60	89	Moderate
5	30	59	Low
6	0	29	Very low

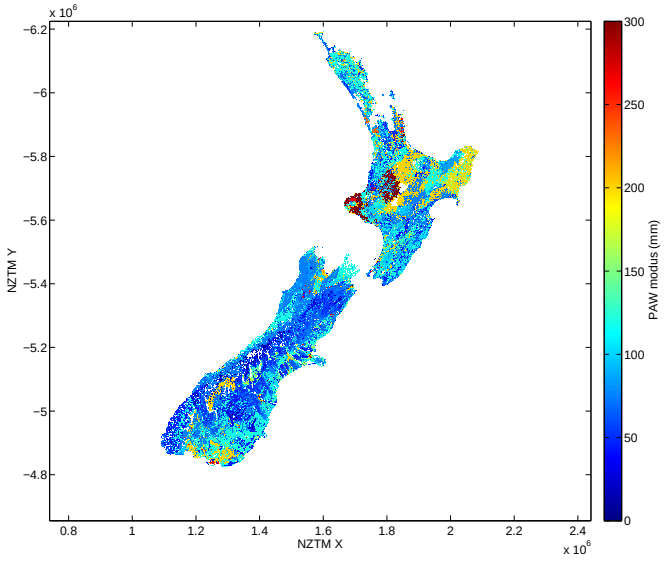

Figure 4.3: PAW modal values for New Zealand.

4.3.5.2 Soil permeability

Soil permeability is the rate that water moves through saturated soil. New Zealand-wide soil permeability data is available from the Land Resource Information Systems (LRIS) portal (Landcare Research, 2014) as an ArcGIS shapefile Newsome et al. (2008). Soil permeability and standard deviation were interpreted to relative permeability ratios in between 0 and 1 from qualitative classes (e.g., 'Slow (S)','Rapid over moderate (R/M)'). It was assumed that the permeability ratios had uncertainty (σ) of 0.1, except for the lowest ratio of 0.05 (where σ was chosen 0.05). The permeability ratio is shown Table 4.2 and depicted in Figure 4.4.

Table 4.2: Soil permeability ratios, empirically chosen from soil qualitative permeability classes from Newsome et al. (2008).

Class name	Qualitative class	Permeability ratio	σ
S	Slow	0.05	0.05
S/M	Slow over moderate	0.15	0.10
S/R	Slow over rapid	0.25	0.10
M/S	Moderate over slow	0.15	0.10
M	Moderate	0.5	0.10
M/R	Moderate over rapid	0.6	0.10
R	Rapid	0.95	0.05
R/M	Rapid over moderate	0.8	0.10
R/S	Rapid over slow	0.25	0.10

4.3.6 Geology

The geology is defined as the deeper subsurface underlying the soil. Most global and New Zealand-based rainfall recharge studies take into account information on soil, i.e., the first 1 to 1.5 metre of the subsurface. In those studies it is furthermore assumed that the geology is permeable enough to allow the drained water to travel to the groundwater. This is sensible, as most studies are performed in unconfined aquifers. When estimating in unexplored territory though, ideally one would need geological information, as water can only drain from the soil to the geology if it is permeable enough. Döll and Fiedler (2008) use a global soil map of the United Nations, and very limited geological information, as it is hardly available on a global scale. Recently, Gleeson et al. (2011) presented a method in which hydraulic permeabilities were estimated on a global scale and over North America using a range of sources, including data from Freeze and Cherry (1979) and calibration data of hydrological models. The findings of Gleeson et al. (2011) were improved with national geological information available in New Zealand. The 1:250,000

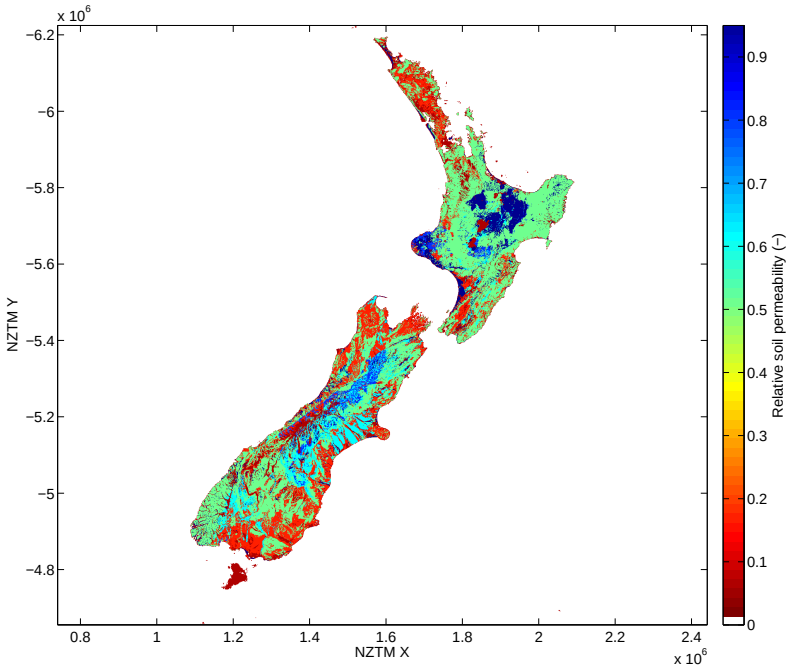

Figure 4.4: Soil permeability ratio for New Zealand.

geological map of New Zealand (GNS Science, 2012) shows surface geology: the geology at near the surface underlying the soil. Information on main rock type is stored in ArcGIS attributes. Median values and standard deviation of the hydraulic permeability κ was gridded on the QMAP scale, using . This was done using data from Gleeson et al. (2011), improved with data from Tschritter et al. (2014). Figure 4.5 shows the resulting categorisation to hydraulic conductivities. A more detailed explanation, including all values of the look-up table, are in the Annex.

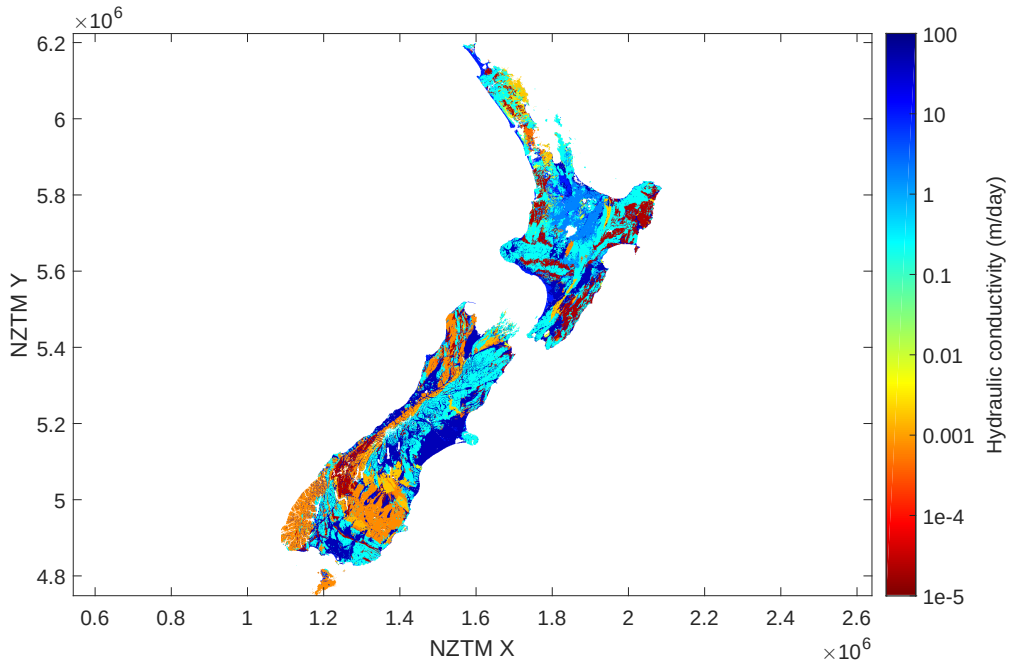

Figure 4.5: Hydraulic conductivity estimate of surface geology for New Zealand.

4.4 Methodology for estimating rainfall recharge

Monthly rainfall recharge was estimated with an approach that was based on some of water balance theories explained in sub-section 4.1.1.

In monthly time steps, rainfall recharge RRECH (in mm) was calculated for time step i as:

$$RRECH_i = [R_i f_{slope} - AET_i - S_{i-1}] f_{soil} f_{geol} \quad ; RRECH_i > 0, \qquad (4.16)$$

where:

R_i is surface rainfall (in mm, after correction for interception and snow);

f_{slope} is a correction factor for rainfall runoff due to slope [0 to 1];

AET is actual evapotranspiration (in mm);

S is soil storage (mm);

f_{soil} is a correction factor for permeability of soil [0 to 1];

f_{geol} is a correction factor for the geology [0 to 1].

If $RRECH_i < 0$ (Eq. 4.16), then $RRECH_i$ is set to zero and the resulting storage deficit $S_i < S_{i-1}$ is used for the calculation of $RRECH_{i+1}$.

The slope correction factor f_{slope} was calculated from the terrain model. After calculating a slope α (in degrees) from the terrain model, this was then used to calculate an initial runoff of the rainfall due to slope:

$$f_{slope} = 1 - erf(2\alpha) \tag{4.17}$$

where the error function (erf) fits the empirical slope - runoff relation used by Döll and Fiedler (2008). The NGRM model prefers to use the simple relation to terrain slope, instead of other alternatives that use a relation between rainfall intensity and soil type (e.g., Rushton et al., 2006; Westenbroek et al., 2010).

Runoff or infiltration from rainfall excess using the runoff curve number (CN) method Cronshey (1986) was not used. This was done for several reasons. First, the CN method does not include a clear relation with terrain slope. As the New Zealand terrain is quite topographically challenging, runoff due to terrain slope and independent of soil type, may be preferential. Second, the soil classes used for the CN method are not necessarily better defined than the input component of the PAW values.

Also, the NGRM model prefers the f_{slope} to directly affect rainfall, and not affect AET and S, as in Döll and Fiedler (2008). Possible model limitations arising because of this simplification are explained in the discussion.

The initial value of water that is held in the soil column was estimated using the PAW values (Table 4.1). Known areas get the modal value of the PAW class. Some unknown areas are interpolated between known values. The standard deviation of the PAW was sampled assuming a normal distribution between the minimum and maximum values, where unknown areas got a standard deviation of twice that size.

At each following time step water is either added or removed from the storage. If the soil column is saturated, water will flow to the geology, unless constrained by the permeability of the soil. In case of an almost saturated soil and high rainfall events, some of the rainfall will not be able to permeate down and will become part of surface runoff. To be able to account for this, a simplified assumption is used: for saturated soils with very low permeability (lower than 4 mm/hr), only 25% will recharge; the remaining part will become surface runoff.

$$f_{soil} = \begin{cases} 0.25 & \text{if permeability} \ll \\ 1 & \text{in all other cases} \end{cases} \tag{4.18}$$

The assumption for this percentage us explained in the discussion of this chapter.

The ratio of rainfall recharge that enters the deeper subsurface, the geology, relates to the hydraulic conductivity K. It is assumed that if the available water per time

unit, W, is larger than K, only the portion equal to K will recharge: the remaining part will be considered runoff. For cases where K is larger, all of W will recharge. The factor combining soil and geology will look this (Equation 4.19).

$$f_{soilgeol} = \begin{cases} (K f_{soil})/W & \text{if } K < W \\ f_{soil} & \text{if } K \geq W. \end{cases} \tag{4.19}$$

Per time step, all water that does not recharge is considered runoff. It is budgeted per time step as the sum of $(1 - P_i f_{slope})$ and the recharge rejected by the soil and geology permeability. This runoff can be used for further constraining and calibration of the method if needed.

4.4.1 Uncertainty of rainfall recharge

In the above defined method of rainfall recharge estimation, the uncertainty of rainfall recharge is calculated using two approaches: 'bottom-up' and 'top-down'.

The 'bottom-up' approach uses ground observations of lysimeters as the 'ground-truth'. The standard estimation errors was calculated (SEE) for all monthly measurements. The SEE is the standard deviation of the difference between the NGRM modelled recharge and recharge measured at lysimeter stations.

The 'top-down' approach uses basic error propagation of the equations in the method and the uncertainty of the input components in these equations through (e.g., Tellinghuisen, 2001):

$$\sigma_f{}^2 = \boldsymbol{g}^T \boldsymbol{V} \boldsymbol{g} \tag{4.20}$$

where $\sigma_f{}^2$ is the variance of a function f, which has $n = 1 : N$ input components; $\boldsymbol{V}$ is the variance-covariance matrix of all input components; $\boldsymbol{g}$ is a vector of input component $\partial f / \partial n_i$; and $\boldsymbol{g}^T$ is the transpose of $\boldsymbol{g}$. Considering Eq. **??**, the components of $\boldsymbol{g}$ are ($RRECH$ is denoted as R):

$$\boldsymbol{g} = (\frac{\partial R}{\partial P}, \frac{\partial R}{\partial f_{slope}}, \frac{\partial R}{\partial AET}, \frac{\partial R}{\partial S}, \frac{\partial R}{\partial f_{geol}}) \tag{4.21a}$$

$$\frac{\partial R}{\partial P} = f_{slope} f_{soilgeol} \tag{4.21b}$$

$$\frac{\partial R}{\partial f_{slope}} = P f_{soilgeol} \tag{4.21c}$$

$$\frac{\partial R}{\partial AET} = -f_{soilgeol} \tag{4.21d}$$

$$\frac{\partial R}{\partial S} = -f_{soilgeol} \tag{4.21e}$$

$$\frac{\partial R}{\partial f_{soilgeol}} = P f_{slope} - AET - S \tag{4.21f}$$

The components of $\boldsymbol{V}$ are:

$$\boldsymbol{V} = \begin{bmatrix} \sigma_P^2 & \dots & \dots & \dots & \dots \\ \dots & \sigma_{f_{slope}}^2 & \dots & \dots & \dots \\ \dots & \dots & \sigma_{AET}^2 & \dots & \dots \\ \dots & \dots & \dots & \sigma_S^2 & \dots \\ \dots & \dots & \dots & \dots & \sigma_{f_{soilgeol}}^2 \end{bmatrix} \tag{4.22}$$

Where the dots indicate all covariances between the parameters. Covariance is estimated by analysing three years of data on the input parameters of Eq. **??**. Rescaling the covariance matrix to the values of the errors in the input components is done as follows:

$$\sigma_{xy,scaled}^2 = \sigma_{xy}^2 \frac{\sigma_{x,new}\sigma_{y,new}}{\sigma_x \sigma_y}, \tag{4.23}$$

where:

- $\sigma_{xy,scaled}^2$ is the scaled variance;
- σ_{xy}^2 is the variance from the covariance analysis;
- $\sigma_{x,new}$ and $\sigma_{y,new}$ are the errors in the input components;
- σ_x and σ_y are the standard deviations from the covariance analysis;

4.5 Results

Application of the NGRM leads to nation-wide estimates of rainfall recharge at monthly intervals at 1 km grid resolution (mean annual values shown in Figure 4.6). The time series of recharge and some model components for three randomly chosen locations are shown in Figure 4.8. Mean rainfall recharge varies over the country, is least in the areas with low rainfall (e.g., Otago) and areas where it is rejected by the geology (e.g., the Southern Alps, Gisborne). It is highest in the areas with high rainfall and high permeability of soil and geology.

The rainfall recharge estimates include uncertainty. Mean annual values of uncertainty is highest at places where rainfall is high (Figure 4.7, left). However, relative uncertainty, i.e. as a percentage of the mean annual recharge (Figure 4.7, right), is largest in areas where hydraulic conductivity is low. While recharge is low, it is most sensitive to the geology in these areas.

The total New Zealand average rainfall recharge for the period 2000 2013 estimated from the NGRM model is 3414 m^3/s or 406 mm/yr, with a model uncertainty σ of 15% (Table 4.3). Total rainfall recharge values for the North Island is 1599 m^3/s (444 mm/yr, σ 13%); for the South Island it is 1815 m^3/s (378 mm/yr,

σ 17%). The national estimate falls within the 2835 m^3/s (σ 10%) recharge estimate of Döll and Fiedler (2008). Although their estimate is for a different period (1972-1990), rainfall in the different analysis periods appears relatively similar (1972 to 1990: 1881 mm/yr; 2000 2013: 1839 mm/yr, according to VCS rainfall estimates).

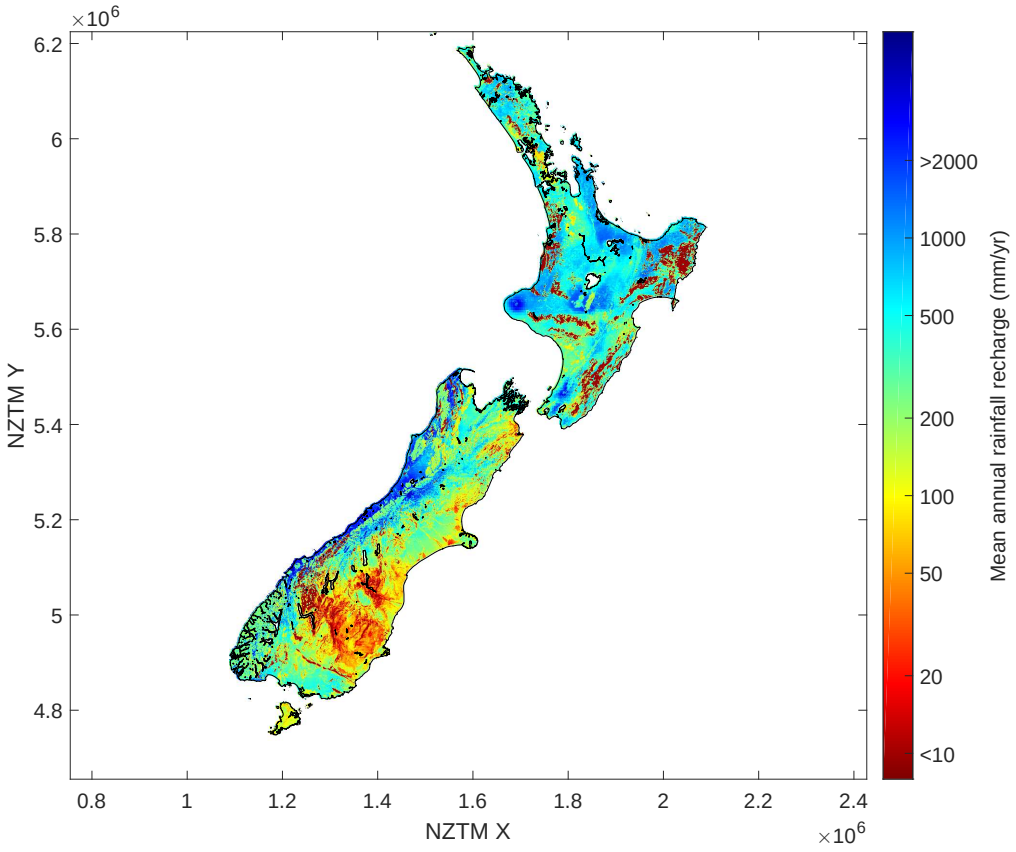

Figure 4.6: Nation-wide rainfall recharge from the NGRM compiled to mm/year.

Table 4.3: 2000-2013 mean rainfall recharge values of the NGRM compiled for New Zealand, the North Island and the South Island, including model uncertainty.

	Rainfall recharge (m^3/s)	**Rainfall recharge (mm/yr)**
New Zealand	3,414 ± 511	406 ± 61
North Island	1,599 ± 210	444 ± 58
South Island	1,815 ± 301	378 ± 63

4.5.1 Validation to lysimeters in the Canterbury Plains

The rainfall recharge data were compiled for ground observations in the Canterbury Plains. A total of four dryland lysimeters were used. These were already

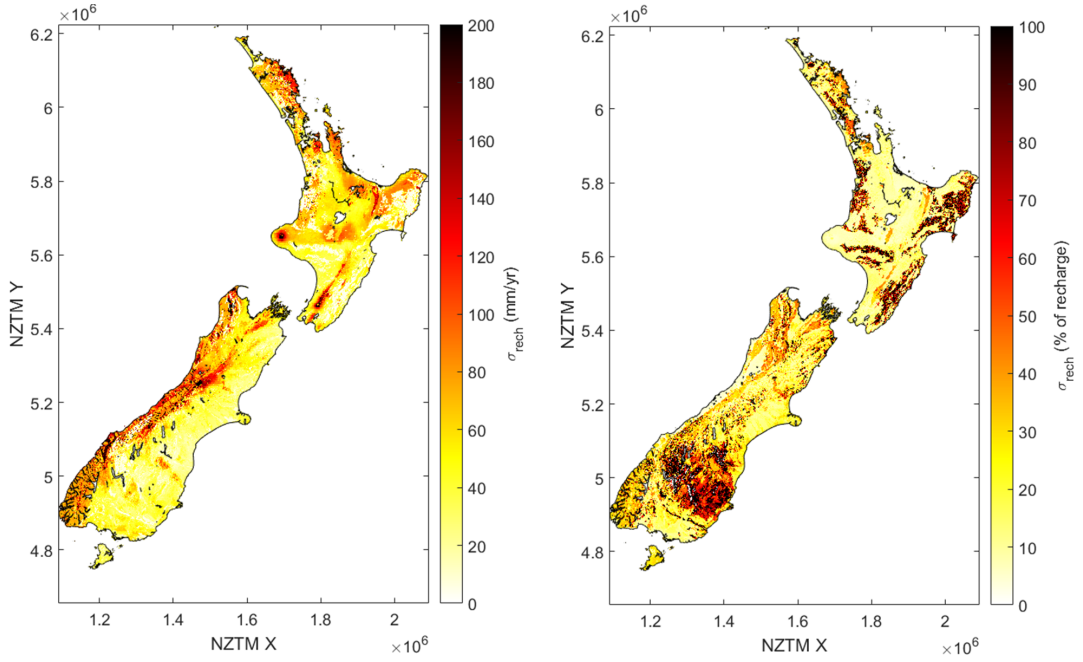

Figure 4.7: Uncertainty σ_{rech} of mean annual rainfall recharge estimated with the NGRM model as mm/yr (left) and as a percentage of total recharge (right).

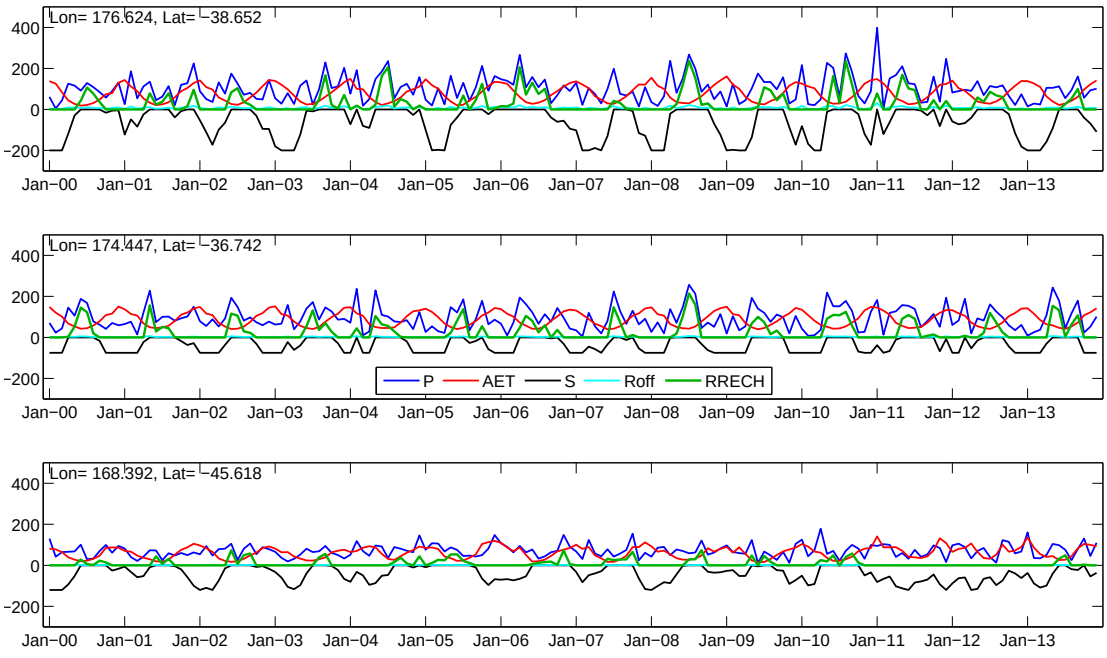

Figure 4.8: NGRM model components for three randomly chosen locations over the entire simulation period: rainfall (P), actual evapotranspiration (AET), soil storage (S), surface quickflow (Roff), and rainfall recharge (RRECH).

described in Chapter 2, Figure 2.20 and Table 2.4. Three lysimeters are located in the plains between the Waimakariri and Rakaia rivers ('Christchurch Airport', 'Hororata', and 'Lincoln') and one just south of the Rakaia River ('Winchmore'). These lysimeter stations have measured rainfall recharge and data have been analysed and compared with other model outputs extensively by White et al. (2003, 2014a). Cumulative monthly recharge of the NGRM model from 2000 to 2013 shows that recharge is mostly occuring in autumn and winter (Figure 4.10, with uncertainty in the grey bands).

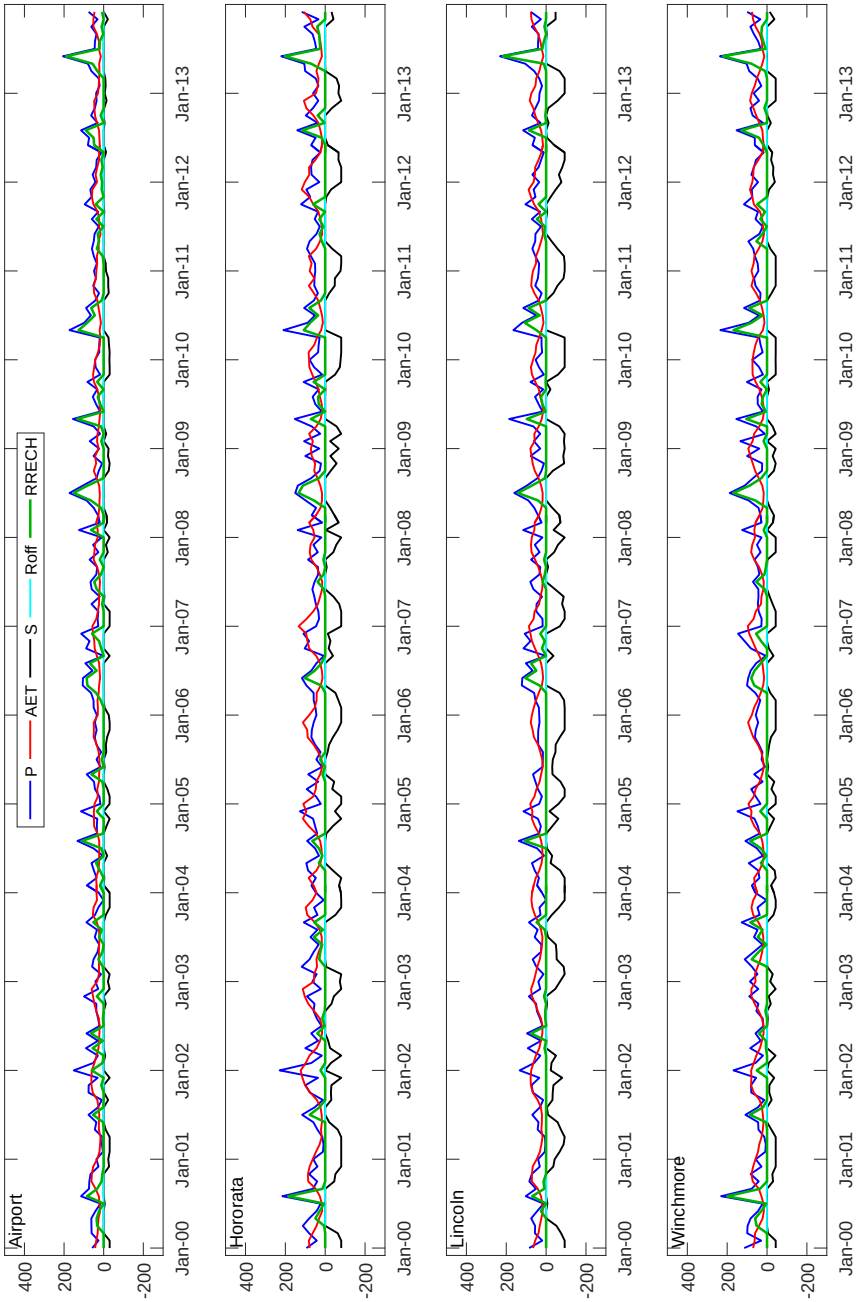

Figure 4.9: Monthly recharge (RRECH) estimated by the NGRM model at four Canterbury locations, including rainfall (P), soil storage (S), AET, and runoff (Roff).

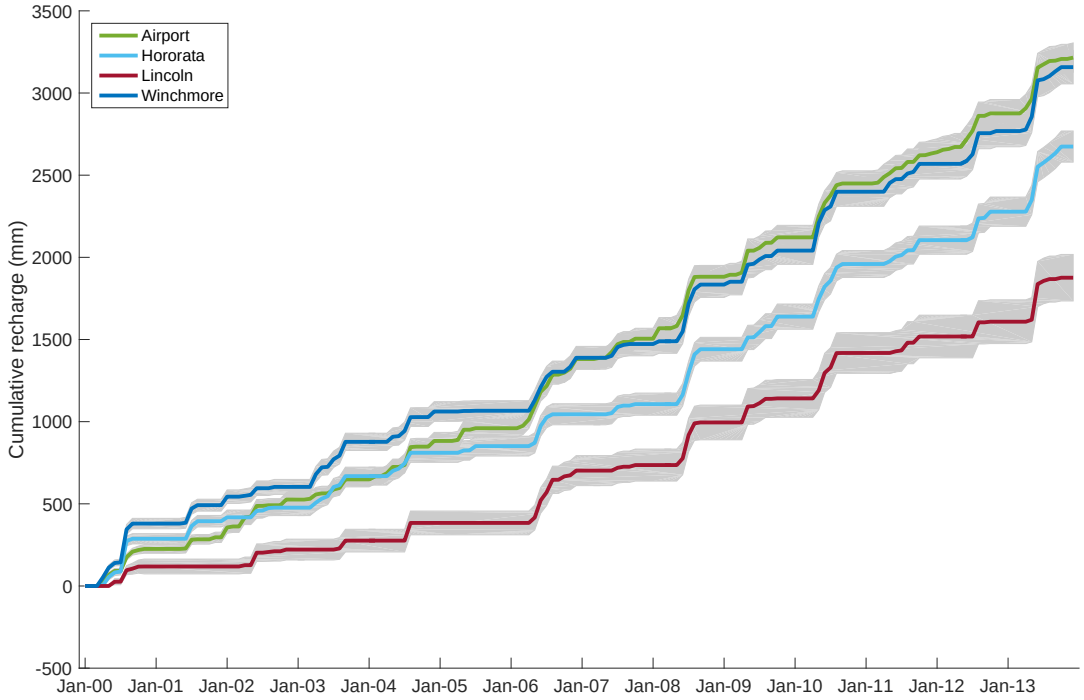

Figure 4.10: Cumulative recharge estimated by the NGRM model at four Canterbury locations. Grey bands indicate the cumulated uncertainty (1σ).

Hong and White (2014) compared lysimeter recharge for the period 2000 to 2004 with two other models, i.e. SOILMOD/DRAIN and SMB-SMC (see section 4.1.1). For this period, the NGRM modelled rainfall recharge compares well to measured recharge from three of four Canterbury lysimeter stations (Table 4.4 and Figure 4.11). However, a large difference is found for the Hororata station for the NGRM: 230 mm/yr for the lysimeter versus 139 $\pm$ 27 for the NGRM estimate. Monthly comparison of lysimeter and NGRM estimates (Figure 4.12) show that this is mainly caused by one anomalous wet January in 2002, where torrential rains occurred on the 1st of January, and heavy rain wreaked havoc along the east coast of Canterbury from 11 - 13 Jan, resulting in surface flooding throughout Canterbury (NIWA, 2002a,b).

The overall NGRM top-down model error (see section 4.4.1) is in the range 7-10 mm/month for the Airport, Hororata and Winchmore locations, and largest for the Lincoln location (13 mm/month: Figure 4.13, left). Generally, these uncertainties are smallest in summer, when rainfall recharge is minimal (Fig. 4.14, right). The slightly higher uncertainties at the Lincoln location might be induced by the higher PAW value used in the soil storage calculation.

Bottom-up standard estimation errors (SEE, see Figure 4.14, left) are generally higher than top-down uncertainties, with the exception of Lincoln. Bottom-up errors vary in between 10 and 18 mm/month, with the highest error at Hororata. Monthly SEE at Hororata shows an anomalous high value in January (Figure 4.14, right). These anomalous values might be caused by the model being unable to adequately handle high rainfall events. However, unknown bias in rainfall data

or other input components of the models (i.e. AET, soil storage), might also add to this model limitation. As NGRM is a simplified and uncalibrated model, these differences will remain, unless the model is calibrated to the local scale for local applications. Furthermore, local models, as the SOILMOD/DRAIN (Figure 4.15) and SMB-SMC (Figure 4.16) show smaller, but similar anomalous values for the total error and monthly errors. It is therefore concluded that, despite the NGRM being simplified and uncalibrated, it does not under-perform for the two other locally calibrated models.

Table 4.4: Mean annual recharge for July 2000 - June 2004 for four Canterbury lysimeters stations and the NGRM model. All values are in mm/yr.

Location	Lysimeter	NGRM
Airport	156	163 ± 23
Hororata	230	139 ± 27
Lincoln	68	67 ± 33
Winchmore	212	195 ± 25

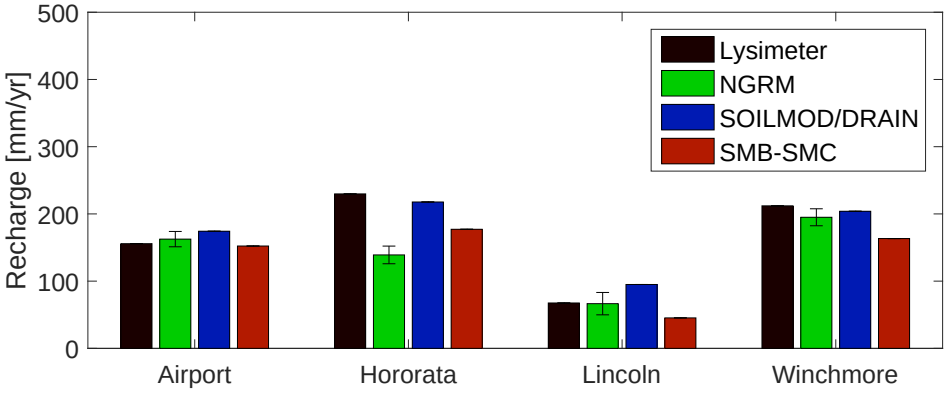

Figure 4.11: Comparison of recharge from lysimeter measurements to the NGRM model and other models (SOILMOD/DRAIN and SMB-SMC) for the period July 2000 - June 2004. The error bars indicate the NGRM model uncertainty.

4.5.2 Comparison with a local model in the Canterbury Plains

NGRM rainfall recharge data were compared to a locally calibrated in the Waimakariri Catchment Water Management Strategy Zone, North of the Waimakariri River (Figure 4.17), Canterbury, for which (Alkhaier, 2016) from Environment Canterbury (ECAN) developed an advanced land surface recharge model. This 'ECAN' model was built with the MIKE SHE hydrological platform (DHI, 2016) and includes a sensitivity analysis with the PEST package (Doherty, 2016). His model resolution is 200m, and time period is 1972 - 2015.

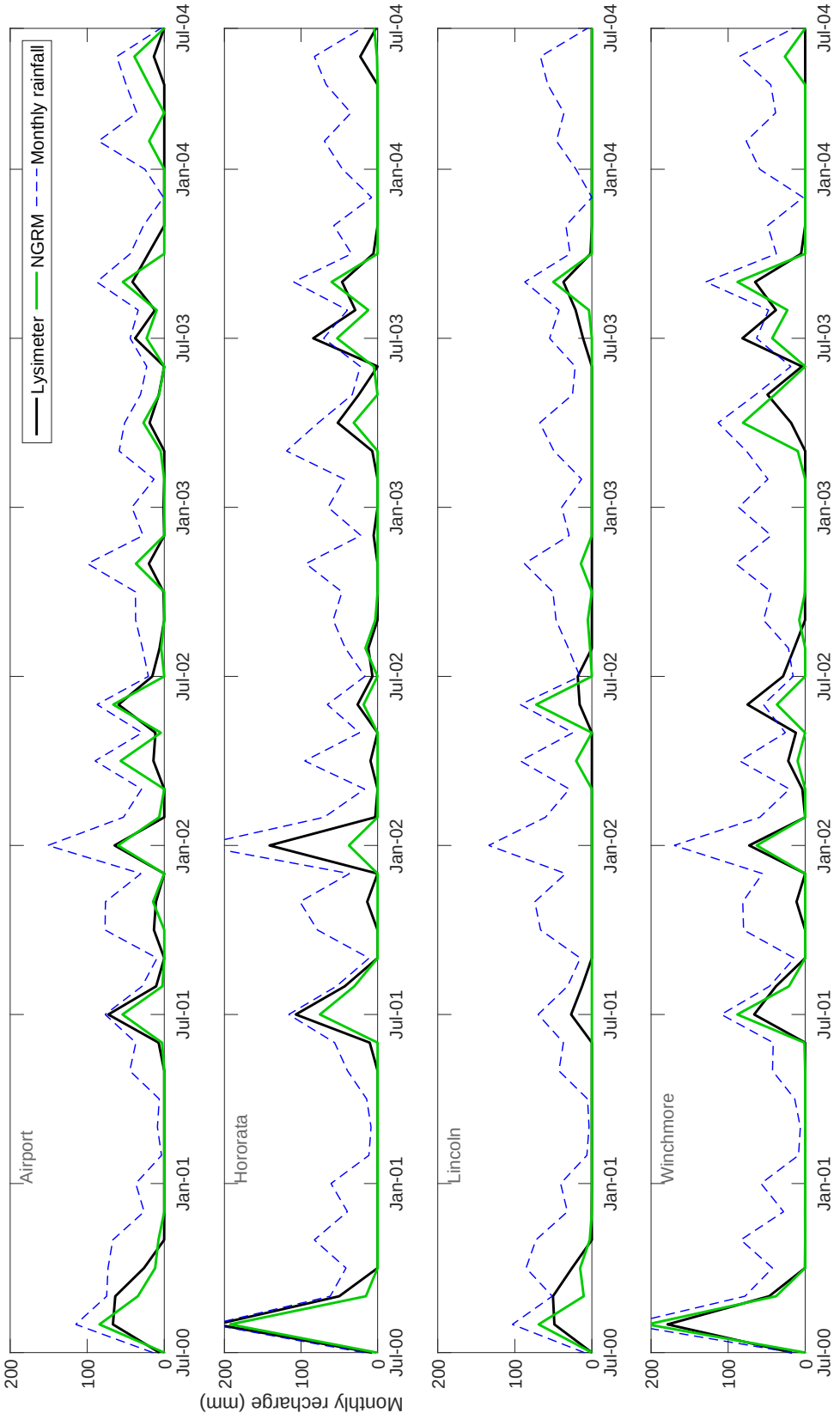

Figure 4.12: Comparison of recharge observed by lysimeter measurements to NGRM rainfall recharge for the period July 2000 - June 2004.

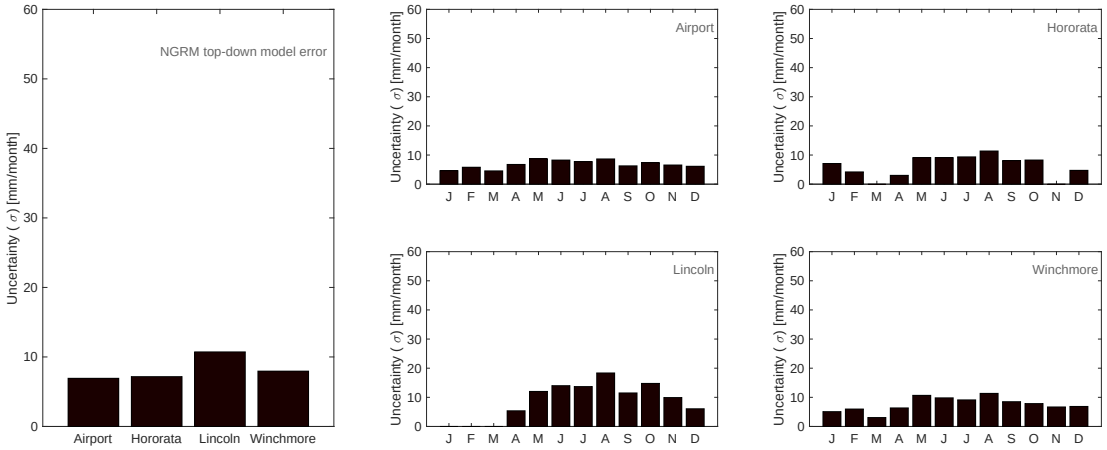

Figure 4.13: Top-down uncertainty (1σ) [mm/month] of the NGRM simulated recharge at the location of four lysimeter stations in Canterbury. Left: total uncertainty, right: uncertainty per month.

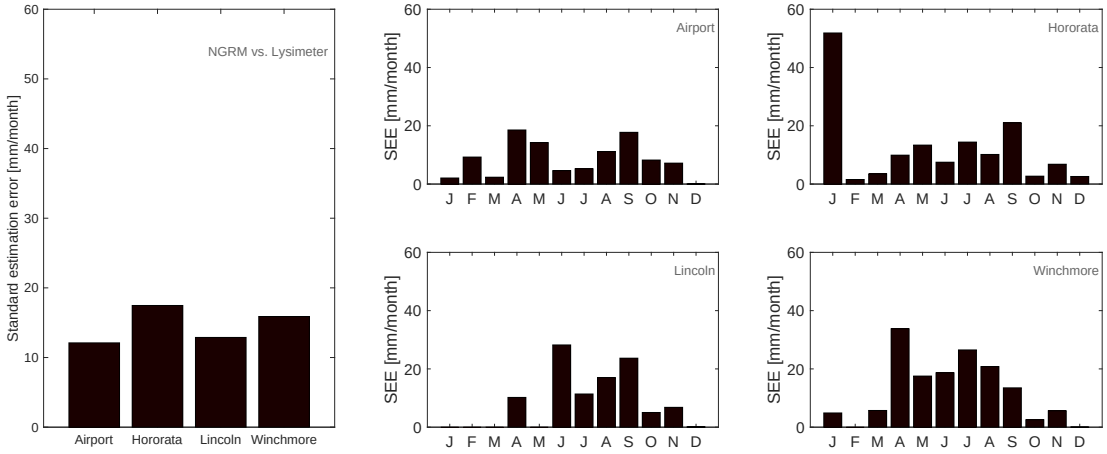

Figure 4.14: Standard estimation errors (SEE) [mm/month] of the NGRM simulated recharge with lysimeters at four Canterbury locations. Left: total SEE, right: total SEE per month.

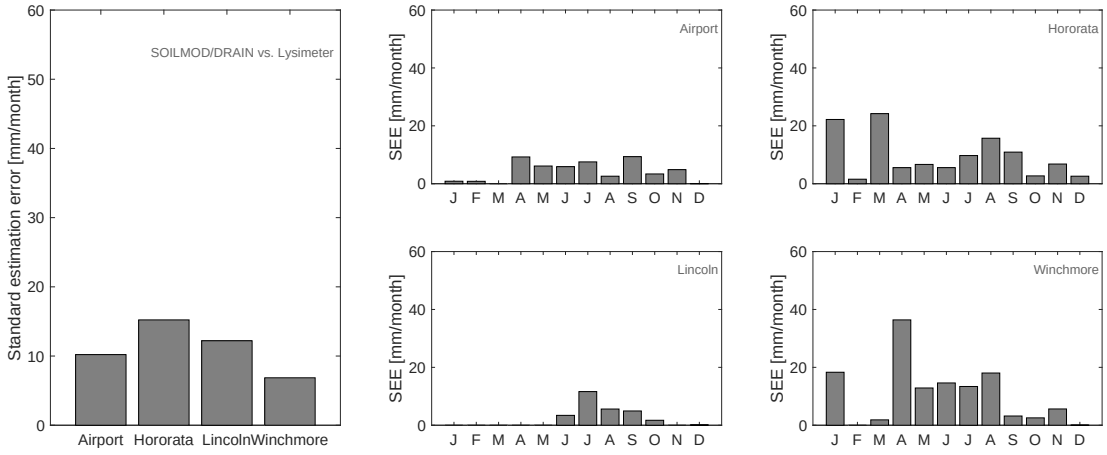

Figure 4.15: Standard estimation errors (SEE) [mm/month] of the SOILMOD/DRAIN recharge model estimates with lysimeters at four Canterbury locations. Left: total SEE, right: total SEE per month.

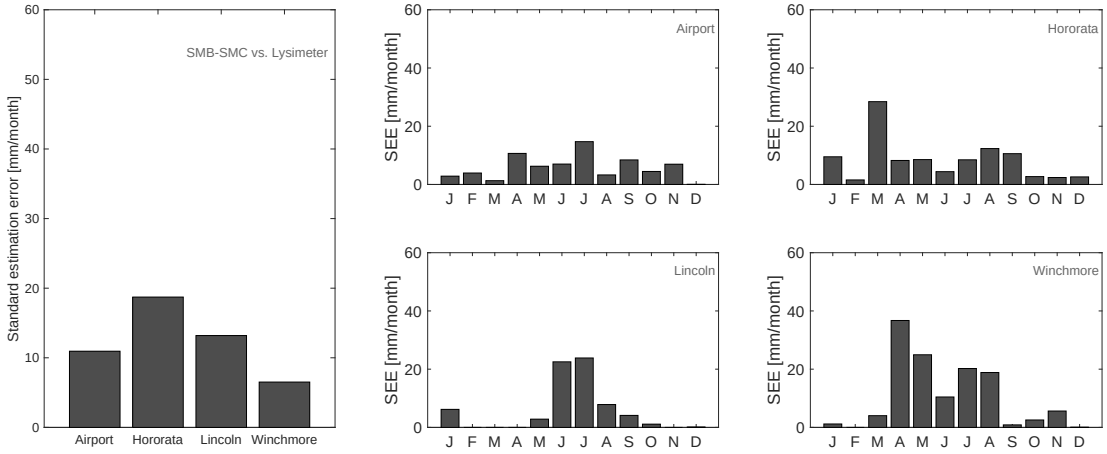

Figure 4.16: Standard estimation errors (SEE) [mm/month] of the SMB-SMC recharge model estimates with lysimeters at four Canterbury locations. Left: total SEE, right: total SEE per month.

Alkhaier (2016) finds values of mean recharge for three different model set-ups: a minimum recharge scenario, average, and maximum land surface recharge scenario. The NGRM 2000-2013 mean annual recharge (192 $\pm$ 27 mm/yr) agrees well with the ECAN minimum (195 mm/yr) and average (247 mm/yr) scenarios (Table 4.5). Comparing recharge for the two different time periods only creates a negligible estimation error of approximately 12 mm/yr, since mean VCS rainfall for the model area for 1972-2013 was 798 mm/yr; for 2000-2013 it was 763 mm/yr; and rainfall recharge was in between approximately 0.25 and 0.45 of rainfall for the different scenarios.

The spatial distributions of the mean annual recharge, quantified as a standard deviation, are similar for the NGRM and the ECAN models (106 mm/yr for NGRM compared to approximately 125 mm/yr for the three ECAN scenarios). However, there are visual spatial differences between the NGRM and the ECAN recharge models, of which the clearest difference is in river areas, where ECAN recharge is high and NGRM recharge is low (see discussion on river recharge). It seems more likely that the ECAN model is more realistic than the NGRM in these areas, since the ECAN model is calibrated. However, both models lead to the same mean annual recharge. To investigate which of the two models is best in which area requires more in-depth research that takes into account factors as: recharge in areas outside of the model boundary (see discussion), groundwater table depths; spring locations, and baseflow separation methods at multiple gauging locations in the rivers.

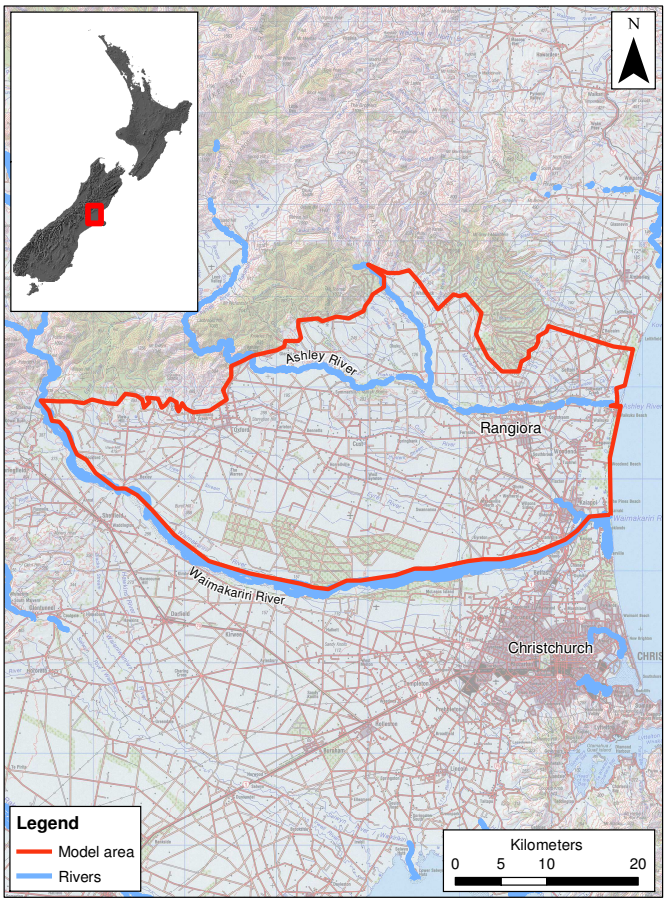

Figure 4.17: Model area in the Waimakariri catchment management strategy zone, Canterbury.

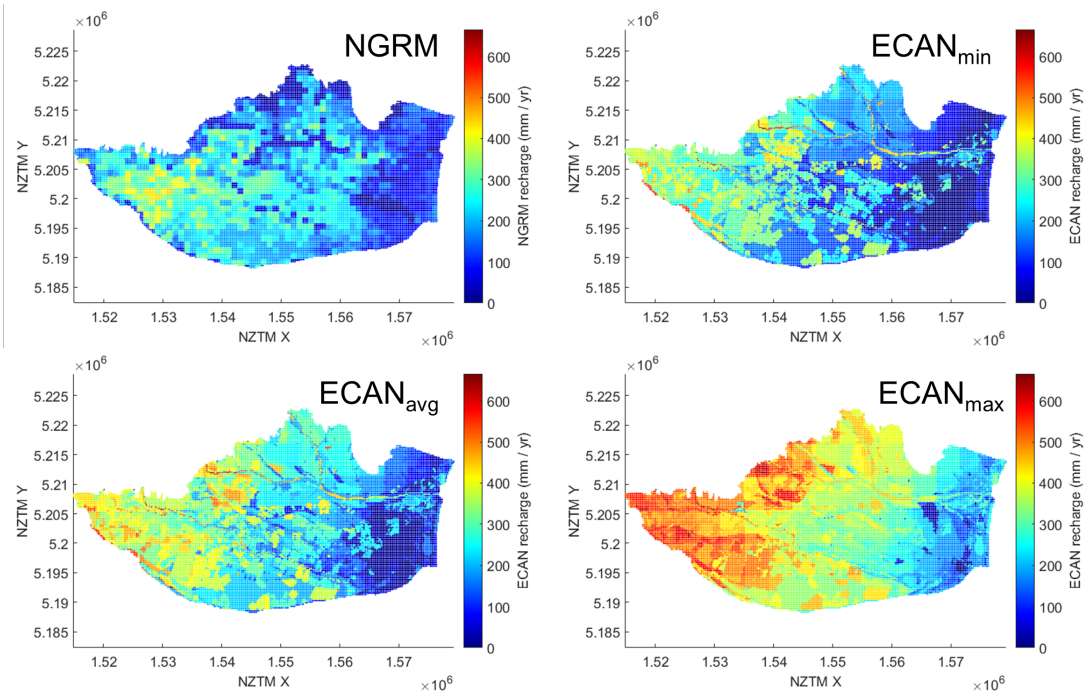

Figure 4.18: Mean annual recharge in Waimakariri catchment management strategy zone. Left: NGRM recharge. Right: Recharge as evaluated by the ECAN land surface recharge model.

Table 4.5: Mean annual recharge for the Waimakariri catchment management zone model area (mm/yr)

	NGRM	ECAN Min	ECAN Average	ECAN Max
Minimum	8	0	0	0
Maximum	440	661	661	664
Mean	192 ± 27	195	247	363
StDev of spatial distribution	106	126	127	120

4.5.3 Comparison with modelled recharge in the mid-Mataura catchment

Introduction

The mid-Mataura catchment is located in the Southland Region, in the plains areas Northwest of Gore. The area for this case study consists of five groundwater management zones (Figure 4.19). Groundwater in these zones has been studied, because the shallow aquifers are hydraulically connected to rivers and springs, and groundwater abstraction has increased in recent years. Therefore, the regional council, Environment Southland (ES), commissioned development of

a groundwater flow model of the mid-Mataura catchment, which was then developed by Phreatos (2007) and further described by Burberry et al. (2013). The recharge as used in that groundwater model was estimated through the Rushton method (Rushton et al. (2006), see section 4.1.1). It has been used for comparison to the NGRM estimates in the model area.

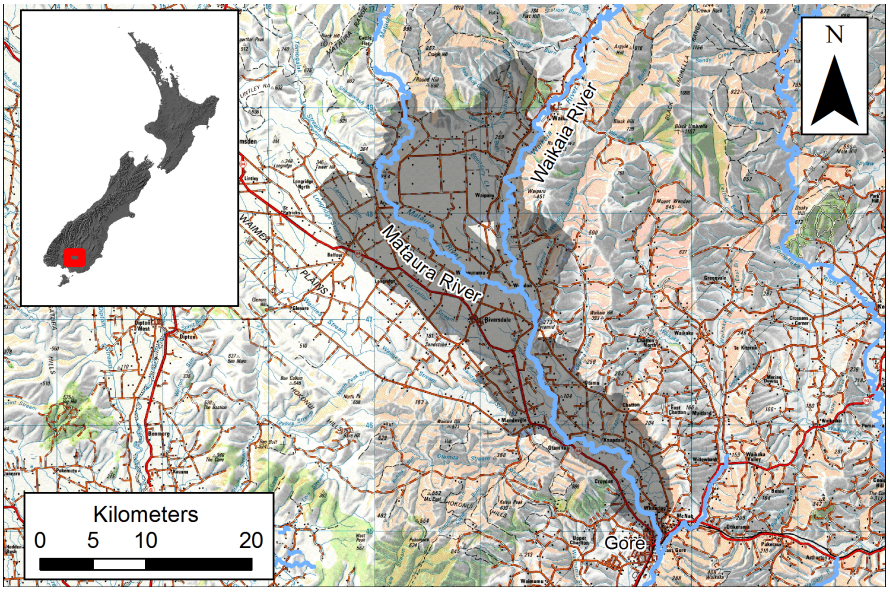

Figure 4.19: Groundwater zones in the mid-Mataura catchment, Southland.

Data used for comparison

The monthly NGRM recharge was compared to 7-daily recharge input files, which will be called the Rushton recharge onwards. Both NGRM and Rushton recharge data were compiled to mean annual recharge. Rushton recharge was read from MODFLOW-2000 recharge input files. To avoid bias from different time periods, only the overlapping period of both datasets, between 1 July 2000 and 31 June 2007 was compared.

Results of the comparison

Total mean annual NGRM recharge is lower than the Rushton estimate (144 ± 28 mm/yr and 215 mm/yr, respectively, see Table 4.6). This is partly caused by the difference in rainfall used for both models (809 mm/yr for the NGRM model vs. 903 mm/yr for the Rushton model). However, the ratio of recharge and rainfall of NGRM (0.18 ± 0.03) is still lower than the Rushton model (0.24). The Rushton polygons have an unknown but potentially large uncertainty, since there are so few polygons compared to the NGRM model cells (Figure 4.20). If Rushton and NGRM uncertainties would be similar, then recharge estimates of both models would match. Rushton recharge estimates exclude areas outside the model boundaries that are still in the catchment. This could have implications

for recharge occurring in areas in the catchment, but outside the model boundary (see discussion). Further local comparison should thus include an uncertainty estimate of the Rushton recharge, and should include the whole (sub-)catchment and not only the model boundary.

Table 4.6: Mean annual rainfall and recharge for the Mid-Mataura model area (mm/yr) for the NGRM and the Rushton model

	NGRM	Rushton
Rainfall	809	903
Recharge	144 ± 28	215
RR ratio	0.18 ± 0.03	0.24

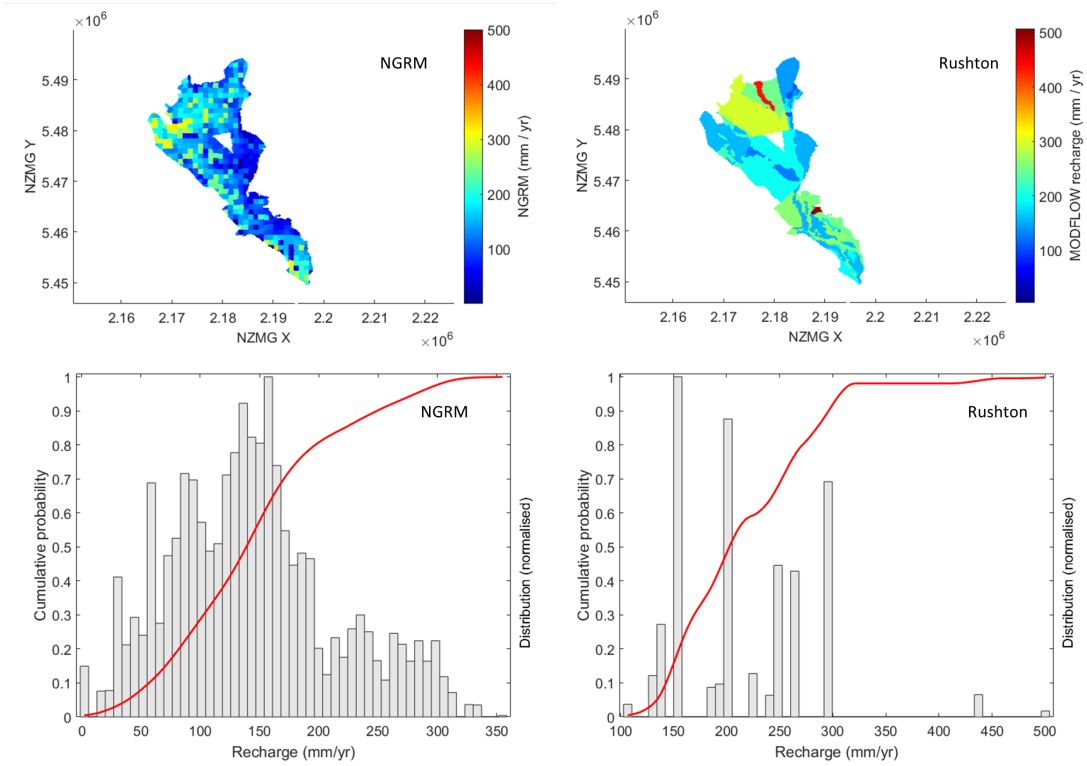

Figure 4.20: Mean annual recharge and its spatial distribution in the mid-Mataura catchment model area, according to the NGRM (left) and the Rushton (right) models. Cumulative probability in the bottom figures is shown in red.

4.6 Discussion

NGRM rainfall recharge estimates are a valuable new addition to existing national datasets of terrestrial water cycle variables (e.g., Booker and Woods, 2014; Tait et al., 2006; Westerhoff, 2015; Woods et al., 2006). For example, national water

budgets based on long-term means can be aided by: estimates of baseflow using the long-term mean rainfall recharge; estimates of AET that include irrigation and interception; estimates of unrouted quickflow using the surface runoff that is calculated by the model; and estimates of rainfall that are corrected for interception and snow. Theoretically, a water budget can be made using all NGRM data. However, we acknowledge that implementation of a national water budget requires a much larger effort. This is because of many reasons, of which some are explained here. First, the NGRM model has model limitations, mostly due to its simplifications. Although NGRM matches case studies well in this paper, the model may be too simple in other (sub-)catchments. These model limitations are described below under 'Model equation limitations'. Second, current national input datasets might not be good enough for application at the local scale. This is discussed under 'Limitations and advantages of nation-wide model input data'. Third, considerable uncertainty remains in data-sparse regions such as irrigated and mountainous areas, which is discussed under 'Uncertainty of NGRM in mountainous areas' and 'Uncertainty of the NGRM in irrigated areas'. Recommendations are compiled and discussed in a final topic 'Future research'.

Model equation limitations

The NGRM is considered a simplified model that aims for a national and inter-regional overview; relating differences in existing local models; and estimating rainfall recharge in unexplored territory. The modelled rainfall recharge and its uncertainty estimates are therefore also considered simplified, although recharge estimates and their uncertainty fit well to observed differences with measurements and other local models. Because the model has not been calibrated on a smaller scale, like local models, it has to use generic or simplified assumptions. These assumptions are discussed below.

The slope-runoff relation is based on a sparse dataset of empirical values by (Döll and Fiedler, 2008), who relate total recharge to a slope correction factor. Other relations were explored, but none better were found for use on the national scale. Probably the best-known alternative is a 'curve number' (CN) approach relating soil type and land cover to runoff Cronshey (1986). Although this method has been applied to calculate runoff at the local scale in Auckland Auckland Regional Council (1999), it has been developed for gently sloping hills in the United States, and might not be able to deal with steeper slopes, e.g., New Zealand mountainous terrain. Other rainfall recharge models use a relation between rainfall intensity and soil (Rushton et al., 2006; Westenbroek et al., 2010) without taking into account terrain slope. The NGRM prefers to use the simple relation to terrain slope. First of all, rainfall intensity is not captured well on a monthly scale. Second, we are of the opinion that steeper slopes lead to rainfall 'splash' (Hendriks, 2010) and can form preferential flow channels, ultimately adding to surface runoff. Third, terrain slope is inherently related to soil. For example, regardless of mean annual precipitation, long-term mean denudation rate in river basins is proportional to basin relief (Ahnert, 1970; Summerfield and Hulton, 1994), leaving less erodible

material (e.g., soil) on the steep slopes, which amplifies the splash effect.

A simple snow correction was assumed to estimate rainfall from precipitation. This correction factor was based on a coarse assumption that precipitation is snow when temperature is below zero degrees Celsius. A better defined snow-rainfall relation should be implemented in future updates of the NGRM. Another shortcoming of this simple correction is snowmelt: in spring a substantial amount of the snow will melt, which is likely to substantially recharge the groundwater and have a large impact on the whole water budget White (2007). Seasonal snow was simulated for the South Island by Clark et al. (2009). Further research should apply these studies to implement a module of 'snow correction and snowmelt recharge'.

Heterogeneity and model up-scaling and down-scaling could cause a large, but unknown uncertainty, e.g., averaging high resolution soil and subsurface parametrisation over a 1 km grid cell. Furthermore, averaging slope for 1 km grid cells could lead to a wrong estimate of runoff, which would loop back to wrong recharge and more uncertainty in the slope-runoff relation. A higher resolution representation of elevation and slope was not implemented at the national scale, since that would require significantly more computational power. For example, a typical run for 2000 to 2013 now takes 1 hour on a standard desktop computer. Using higher resolution data, such as 100 m, would make the input datasets 100 times larger, and parallelisation would need to be implemented for more efficient computation. However, smart solutions can be explored, e.g., by compiling the high resolution only as spatial statistics of a 1 km x 1 km pixel, instead of using the full high resolution data arrays. Future research on application of the NGRM model on the local scale should therefore address these issues of scaling and heterogeneity.

For the effect of low-permeability soils, a simplified assumption was used: for saturated soils with very low permeability (lower than 4 mm/hr), only 25% will recharge; the remaining part will become surface runoff. The 25% was chosen on the basis that high rainfall events are on average 10-16 mm/hr, corresponding to a quarter of soil that can accept 4mm/hr or less. That crude assumption should be tested further, and is a recommendation for further research.

Hydraulic conductivities of the underlying geology in this research are given for saturated flow. K values for unsaturated flow can be lower than for saturated flow, but they are non-linear and not easy to estimate Fitts (2013); Hendriks (2010). The simple NGRM model does not calculate unsaturated K vales for several reasons. First, since the uncertainty in K is already high and was therefore in the model equation already clipped to the actual value of K. Second, it was considered to adjust K relative to soil water deficit by simply choosing a lower value of saturated K, e.g., 75% of saturated K. This option is very arbitrary, and in most cases it does not inhibit any recharge in porous and wet media (i.e. aquifers), as the recharge values are much smaller than the hydraulic conductivity. Third, we assume that preferential flow paths through soil can play a much larger role than the decreased hydraulic conductivity in most unconsolidated aquifers, as well as in most rock types (through faults and cracks). Therefore, and for

the sake of simplicity of the NGRM model, it was chosen not to incorporate any calculations of unsaturated flow.

The rainfall recharge estimated by the NGRM model is a 'potential recharge', i.e., the recharge that would occur if the groundwater table is deep enough. Shallow groundwater tables will result in partial rejection of rainfall recharge, and a larger component might go to runoff or evaporation in these areas, which at this stage cannot be modelled by the NGRM model. Therefore, it is recommended to couple the NGRM with groundwater models, so that recharge can be corrected in areas such as wetlands or springs. This coupling process can then indicate areas where potential recharge can be corrected for actual recharge: it is described and developed in Chapter 5.

Finally, the NGRM model does not calculate the recharge of rivers to groundwater (except for when rainfall falls on dry riverbeds). In some areas with large braided gravel river systems, losing rivers can recharge groundwater substantially (e.g., White et al., 2012), especially when streamflow is high and groundwater level is low (e.g., after heavy rainfall following a long dry period in autumn). Recent research on nation-wide work on losing and gaining rivers is reported by Yang et al. (2015). Therefore, future development of the NGRM is recommended to use results of that work.

Limitations of model input data

Application of the NGRM model on the local scale, as is the case for every model, should always embed a careful consideration of its model equations limitations, but more importantly consider the quality of model input components.

For rainfall, the largest model input component, NGRM application at the local scale reveals bias rather than uncertainty. For example, VCS rainfall within the Waipa River catchment of the Waikato region had to be increased by 15% by Rawlinson et al. (2015) in order to make it fit with the values of three independent models (NGRM, USGS-SWB and a conceptual water budget). Systematic errors or biases in model input components propagate differently from uncertainty as calculated by the NGRM model equations. For example, a consistent bias in monthly rainfall, where there is 'under-catch' (i.e., actual rainfall is higher than measured rainfall), would lead to a different uncertainty of rainfall recharge model estimates.

Although evapotranspiration is smaller than rainfall, the estimation of PET and AET also has considerable uncertainty. Westerhoff (2015) demonstrated that uncertainty in daily Penman PET in New Zealand can be 10 40%. For this study, it was assumed that the uncertainty of AET decreases with the AET/PET ratio. Because AET depends on more parameters than PET, e.g., soil moisture and vegetation health, the effect of the uncertainty of those parameters is unknown. This is one of the reasons that AET is often estimated from PET at the local scale White et al. (2003); White and Tschritter (2014); White et al. (2014b), because soil

parameters are considered to be better known at that scale. Furthermore, satellite-derived AET is known to contain errors in areas with steep topography. Although MOD16 AET (2000-2013) compares better to lysimeter-derived AET (1999-2011) in the Canterbury Plains than the average 1960-2006 AET as described by Woods et al. (2006) (Figure 4.21), it does not necessarily mean it is better in every region. Rawlinson et al. (2015) conclude that satellite MOD16 AET within the Waipa River catchment seems to estimate higher values than the Woods-AET and that MOD16 AET would only fit in the Waipa River catchment if rainfall was increased by an overall 24% above the VCS rainfall estimates. Such a large increase was not considered highly plausible and therefore the AET in that regional study was calibrated to fit the NGRM recharge to baseflow out of the Waipa River catchment.

Another way to try and minimise uncertainty of the AET and PET for rainfall recharge estimates is the use of soil moisture measurements. Measurement of soil moisture lead to better parametrisation of the soil storage component in the rainfall recharge model, and could play a role in an improved estimation of AET. From October 2014 onwards, the Sentinel-1A satellite mission ESA (2015c) measures microwave backscatter with a 10m x 10m spatial resolution, currently approximately twice a month for each location in New Zealand (and more often with the future launch of its second, 1B, satellite). Although these data can contain much noise (Chapter 3) soil moisture estimates at some locations of ground stations follow the trend of the ground-observed soil moisture and the expected seasonal trends.

More detailed research of canopy interception of the rainfall, and LAI, will improve model estimates. However, since the uncertainty of interception was assumed small in comparison with rainfall and ET this will not be discussed here.

Comparison of the NGRM with the ECAN model in the Waimakariri catchment showed that land surface recharge of the ECAN model is much higher in the river. This is not caused by a shortcoming of the model equation (as the ECAN model also does not embed a river recharge model), but by the differences in available soil data. The ECAN recharge model uses a local, more spatially detailed, soil data set, which is not available at the national scale. These local data account better for recharge in the very permeable river areas.

Uncertainty of the NGRM in mountainous areas

The NGRM model indicates that rainfall recharge can be larger in mountainous areas, e.g. the flanks of the Southern Alps (Figure 4.6). Although the existence of large exploitable aquifers is unlikely in mountainous areas, rainfall recharge is likely to occur in these areas. This recharge is mostly caused by a high rainfall climate: although the geology seems relatively impermeable and much runoff is expected, substantial amounts of rainfall can still permeate into the ground. These amounts could, for example, recharge to small, perched, aquifers to enter as baseflow at relatively short distance. This is likely to occur in the higher regions of

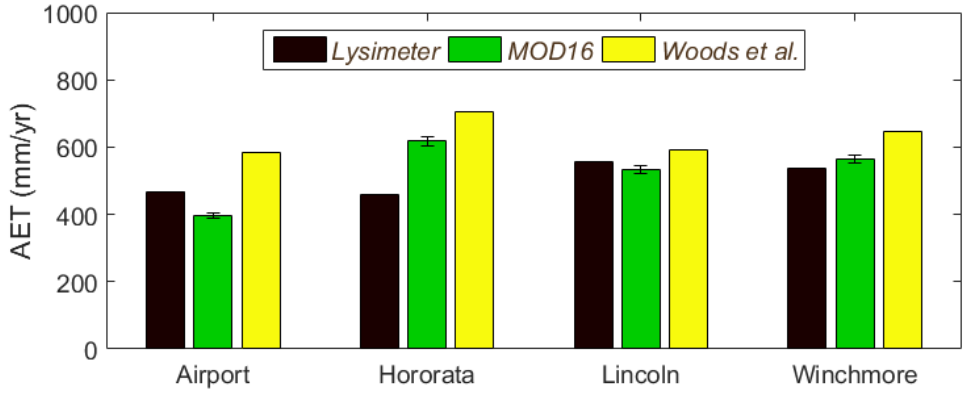

Figure 4.21: Mean annual AET derived from lysimeters in the Canterbury Plains compared to MOD16 AET and AET from Woods et al. (2006).

Canterbury or most of the West Coast. Alternatively, groundwater could recharge to (unknown zones of) deep groundwater. For example, Calmels et al. (2011) find deep groundwater, likely to come from the mountainous region in Taiwan, with a similar high-rainfall climate and terrain. Uncertainty of rainfall recharge is however largest in mountainous regions. First, because at low hydraulic conductivity the large uncertainty of K plays a role in the recharge model uncertainty. Second, because low permeability and high rainfall can cause overestimation of recharge in monthly estimates: the model assumes that this falls evenly over the month, but the monthly rainfall is realistically the result of a few high-rainfall events that lasted not more than days or shorter. Daily estimates would improve recharge estimation in mountainous regions, but this would also impact the speed and simplicity of the model. Third, recharge can also be underestimated due to fractures and faults in mountainous areas. Fractured zones are currently only partly embedded in the estimation of K, as the method of Gleeson et al. (2011) is partly based on calibration of multiple hydrological models in hard-rock formations. It is therefore recommended to perform more research on mountain recharge, its relation to deep groundwater, to model time steps and its relation to fracture zones.

The NGRM model indicates that rainfall recharge can be larger in mountainous areas, e.g., the flanks of the Southern Alps (Figure 4.6). Although the existence of large exploitable aquifers is unlikely in mountainous areas, rainfall recharge is likely to occur in these areas. This recharge is mostly caused by a high rainfall climate: although the geology seems relatively impermeable and much runoff is expected, substantial amounts of rainfall can still permeate into the ground. For example, Sims et al. (2015) surmise that a maximum of 20% of rainfall could infiltrate schist bedrock in the Southern Alps, New Zealand. These amounts could recharge to small, perched, aquifers and/or could enter as baseflow at relatively short distance. This is likely to occur in the higher regions of Canterbury or most of the West Coast. Alternatively, groundwater could recharge to (unknown zones of) deep groundwater. For example, Calmels et al. (2011) find deep groundwater, likely to come from the mountainous region in Taiwan, with a similar high-rainfall

climate and terrain. Doyle et al. (2015) show that 45% of aquifer recharge originates from mountain blocks in their study area in British Columbia, Canada.

The uncertainty of rainfall recharge is, however, largest within mountainous regions. This is because for low hydraulic conductivity the large uncertainty of K plays a significant role in the recharge model uncertainty (e.g., Figure 4.7, right). Additionally, low permeability and high rainfall can cause overestimation of recharge in monthly estimates: the model assumes that this falls evenly over the month, but the monthly rainfall is realistically the result of a few high-rainfall events that lasted not more than days or shorter. Daily estimates would improve recharge estimation in mountainous regions, but this would also impact the speed and simplicity of the model. Finally, recharge can be underestimated due to under-representation of fractures and faults in the model. Fractured zones, common in mountainous areas, are currently only partly embedded in the estimation of K (as the method of Gleeson et al. (2011) is partly based on calibration of multiple hydrological models in hard-rock formations).

Comparisons with locally calibrated models in this chapter (Waimakariri and Mataura) show that NGRM estimates a low mean recharge (when uncertainty is not taken into account). However, calibrated models do not take into account recharge that occurs outside the model boundaries. Recharge in the foothills or in mountainous area is thus not taken into account in these models, since they are not within the model boundary. If recharge outside the model boundaries would occur in reality, but models do not take this into account, then those models would be calibrated wrongly. Future local recharge models should therefore consider taking into account at least the scale of the whole catchment, i.e. including the foothills and mountains. It is recommended to perform more research on mountain recharge, its relation to deep groundwater, and its relation to fracture zones, and implications for model calibration and model time steps.

Uncertainty of the NGRM in irrigated areas

In irrigated areas, the soil storage S receives an additional irrigated amount of water. This is only partly incorporated for in the NGRM model. The effect of irrigation on vegetation status is taken into account by the AET, since the independent satellite-derived signal picks up vegetation health. Use of an independent satellite-derived signal is thus advantageous: it means that the AET is higher in these areas, for vegetation health has increased. Other parts of the model cannot always cope well with irrigation. For example, if irrigation is not fully efficient, (i.e., the water drains to groundwater instead of feeding the crop), the excess water will recharge and create an unknown bias in the monthly soil storage of the NGRM model. If water abstraction for irrigation comes from groundwater, the long-term effect of this excess irrigation recharge (a positive flux to recharge) will balance the water abstraction (a negative flux to recharge). However, if irrigation comes from surface water, this could impact both the monthly and the long term estimates of the rainfall recharge estimation. If irrigation data is available, it is

recommended to add to the model equation. However, estimating exact volumes of irrigation is not straightforward and could result in other, much larger, bias of the model estimates. Use of the satellite-derived AET could help in better estimates of irrigated and non-irrigated areas.

Use of additional independent data on soil moisture, e.g. from satellites might also aid in better soil storage estimation. From October 2014 onwards, the Sentinel-1A satellite mission ESA (2015c) makes available microwave backscatter data with a 10m x 10m spatial resolution, currently approximately twice a month for each location in New Zealand (and more often after data becomes available from the recently launched second, 1B, satellite). Although these data can contain much noise, Doubková et al. (2012) show that averaging satellite backscatter over larger areas (e.g., 1km x 1km) could lead to better soil moisture estimates. Future research for recharge in irrigated is recommended to aim for better estimates of irrigation volumes, followed by soil storage estimation and improved model implementation of the irrigation in the NGRM model.

Future research

This discussion highlights the need for further research on the NGRM model equations and a better uncertainty assessment of nation-wide datasets on terrestrial water cycle variables, such as rainfall and AET. Future research following these recommendations should be completed at the catchment scale with the best available data, i.e., regional streamflow data and water budgets per sub-catchment, if existing. In data-sparse regions, the regional data could then be completed with national flow data and statistics (e.g., Booker and Woods, 2014; Woods et al., 2006). This recommended research can therefore be best applied in a collaborative environment, with regional councils, and research organisations in the fields of groundwater and surface water. Therefore, all the mentioned topics of research lead to one overall recommendation, i.e., more and better collaboration between the research fields of groundwater and surface water. Summarised, these topics are:

- model improvements on rainfall-runoff, river recharge, snow and snowmelt, soil heterogeneity, and hydraulic conductivity;
- better uncertainty assessment of national input data, such as rainfall and AET;
- incorporation of larger (catchment-based) model boundaries in future local and regional recharge studies;
- correction of potential recharge to actual recharge through coupling with groundwater models in wetlands and springs;
- the effect of mountain recharge to groundwater modelling in New Zealand; and

- the added value of satellite-derived AET and soil moisture for model improvement, e.g., in irrigated areas.

4.7 Conclusions

This chapter developed an approach to estimate rainfall recharge across New Zealand with a nation-wide model (NGRM). The NGRM estimates 1 km gridded monthly nation-wide rainfall recharge from January 2000 to December 2013. A valuable addition to the recharge estimation is the model uncertainty estimate, which is not typically produced by existing rainfall recharge models), based on variance and covariance analyses of all input components in the model environment. The model utilises state-of-the-art nation-wide gridded input data of rainfall, soil, elevation, geology, and novel satellite-derived data of evaporation and vegetation. The average New Zealand recharge of the NGRM model results is estimated as approximately 3,414 m^3/s, or 406 mm/yr, with a model uncertainty (1σ) of 15%. Although the NGRM model is uncalibrated, its recharge estimates compare well to Canterbury lysimeter stations and the local models that have been applied there. For example, NGRM mean annual recharge matches the low rainfall recharge scenario of the Waimakariri catchment in Canterbury, although also showing distinct spatial differences in the western plains and in the rivers of this catchment. Mean NGRM annual recharge matches rainfall recharge locally modelled in the mid-Mataura if model uncertainty is taken into account. However, mean annual NGRM recharge is less than the mid-Mataura model. Typically NGRM estimates of rainfall recharge are lower than estimates by local models. This might be due to the locations of boundaries on local models, i.e., the boundaries do not include the whole catchment, including foothills and mountains. From the case study comparisons, it is concluded that the nation-wide rainfall recharge model gives a valuable initial estimate when applied at the local or regional scale, and can thus also be used in areas as a valuable initial estimate in data-sparse areas. Local applications might require the NGRM model to be calibrated and, as with any model, it is therefore recommended to carefully consider the NGRM model limitations for local application, but moreover the limitations of its nation-wide input components (such as rainfall and evapotranspiration), as these seem to cause the largest uncertainty. This research also provides improved insights into the uncertainty of rainfall recharge models, including the role of recharge model input components. It shows that recharge is most sensitive to rainfall in areas where recharge is high, but that uncertainty in hydraulic conductivity plays an important role in areas where recharge is impeded by geology. Further research recommendations include collaborative research in the fields of national water budget estimates and groundwater and surface-water coupling: improvement of rainfall-runoff, snowmelt and river recharge, improvement of estimates of rainfall and evapotranspiration, and the added value of satellite-derived AET, and possibly satellite-derived soil moisture, in irrigated areas. Satellite data might improve uncertainty of heterogeneity, because of its high resolution nation-wide coverage.

The impact of heterogeneity and spatial scaling in elevation, soil and geology input data sets, as well as the impact of fracture zones on rainfall recharge within mountainous areas require more research.

5

Estimates of water table depth in New Zealand using the long-term equilibrium of recharge and groundwater flow

Reading guide

This chapter first describes the importance of nation-wide models and the need for a national-scale groundwater model (section 5.1) and a list of terms used in this chapter (section 5.2). It then describes a method to estimate a long-term average of groundwater table depth, the Equilibrium Water Table (EWT) method. This is an existing method and originally applied on a global, i.e., world-wide, scale. Therefore, this chapter contains sectioning into two major parts, i.e., about the '**original EWT** method' and about the '**improved EWT** method'. The theory of the original EWT method is described in section 5.3. The original EWT depths are evaluated in the Canterbury Plains in section 5.4. From that evaluation, it is concluded that the EWT method correctly points out shallow water table in New Zealand's alluvial aquifer systems, but it also shows the need for better input data and contains recommendations of better terrain models, geology and rainfall recharge input data. Using those recommendations, the improved EWT method is described in section 5.5. The improved methods include new features of: rainfall recharge correction at very shallow water tables; estimates of baseflow; and estimates of groundwater flow directions and relative amplitudes. The improved EWT depths are re-evaluated in the Canterbury Plains (section 5.6), where it is concluded that improved EWT depths match ground observations better than original EWT depths. However, large spatial features remain, i.e., gravel beds in the Canterbury Plains, where the difference between modelled and observed groundwater depth is large. Tests to explain why this feature remains lead to some further local improvements of the model, i.e., the ability to improve hydraulic conductivity estimates. Comparison of the data in the Waipa River catchment shows that EWT depths correlate well with ground observations. From the re-evaluation it is concluded that the improved EWT method is valuable

for estimating water tables in data-sparse areas or higher resolution water table depths for first input in groundwater flow models.

5.1 Introduction

Groundwater is a key water resource for New Zealand that is growing in importance as surface waters reach full allocation. However, the current characterisation of aquifer systems is generally less than required to meet future groundwater management challenges (White, 2006). Groundwater models are usually applied on the local to regional scale, which also fits the policy requirements of regional councils. At the same time, nation-wide models provide us with national estimates of water resources other than groundwater (e.g., rainfall recharge, Chapter 4). At the present, there is a national surface water model that is able to estimate quantity of our surface water resources (TopNet, e.g., Yang et al., 2015). These nation-wide model fill in trends and patterns in New Zealand areas where data is very sparse or non-existent.

Similar to the existing nation-wide hydrological models, a nation-wide groundwater model would help fill the gaps in data-sparse areas. Also, it will stimulate more collaboration between surface water modellers and groundwater modelling communities (see discussion in Chapter 4). This would especially benefit research of surface water - groundwater interaction, which is still largely unknown in many areas of New Zealand. Nation-wide models of both groundwater and surface water would also bridge the gap of data standardisation: until present, regional councils each use their own formats and models, which makes it harder to estimate water resources on the inter-regional scale.

In a changing climate, running large-scale (nation-wide) models sometimes requires a fast-running model. For example, one might want to know how future weather patterns impact our groundwater if: droughts are more persistent; if floods occur more often; or what the combined effects of these will be in a climate with more extremes. To apply fast, nation-wide, groundwater models might require simplification, as this computation is sometimes needed to run in parallel with other existing hydrological models (e.g. TopNet). How much simplification is accepted, is still unknown and there is a need for more insight in application of large-scale groundwater models.

This chapter explains the application of a simplified nation-wide groundwater model, using the Equilibrium Water Table (EWT) method. First, the concept of the original EWT model equations, that were recently used on the global and continental scale, is explained. Then, data from the original EWT method are evaluated. Following the recommendation of that evaluation, improvement to the original EWT model are made. The improved EWT model is evaluated again. This evaluation and comparisons in another region lead to further local improvements.

5.2 Terminology of water table, groundwater and EWT depth

The terms water table, groundwater head and EWT depth are often used in this chapter. These and other important terms are further clarified. Most of the definitions are according to Heath (1995), including the direct "quotes":

- Water table: "the level in the saturated zone at which the pressure is equal to the atmospheric pressure".
- Groundwater head: 'head' is "the height above a datum plane of a column of water. In a groundwater system, it is composed of elevation head and pressure head";
- Artesian water: groundwater head in a confined aquifer is higher than the bottom elevation of the confining layer because of overpressure. Artesian water occurs where the groundwater head is above the ground surface.
- Confined aquifer: saturated material in which the groundwater head rises above the bottom elevation of the overlying, low permeability, bed.
- Elevation head: level of water according to a reference level, commonly the ground surface or sea level.
- Groundwater depth: depth to water as measured in wells.
- Hydraulic conductivity: the ability of a water-saturated material to transmit water. Unit include m/s and m/day.
- Transmissivity: the hydraulic conductivity multiplied by the aquifer thickness. Units include m^2/s and m^2/day.
- Unconfined aquifer: an aquifer in a hydraulically conductive layer located between the ground surface and the first impermeable layer.

  EWT depth: in the report we use the term 'equilibrium water table depth' (or EWT depth), because the inventors of the method refer to it as such. I will use their term, by which I mean the equilibrium water table reference to surface, in metres below ground level (mBGL). If data is referenced to the sea level, the term 'EWT hydraulic head' will be used.

5.3 Theory of the original EWT method

5.3.1 Review

The original EWT method, described by Fan et al. (2013a), calculates EWT depth at the global scale using a variety of ground-based, satellite observed and modelled parameters (Fan and Miguez-Macho, 2010b; Fan et al., 2007; Miguez-Macho et al.,

2007, 2008). EWT depth represents a long-term average at a broad scale without human-induced effects of pumping, draining or irrigation.

To calculate EWT depth, the long-term balance between the groundwater recharge and horizontal groundwater flow is calculated using a simple groundwater flow equation. The groundwater flow is constrained by the sea level, assuming that the hydrology is in equilibrium with the climate and sea level Marshall and Clarke (1999). Model input data include a global topography model, a long-term time series of global groundwater recharge, and a global soil model. Satellite data have been used to build the model input data, consisting of climate data and topography. Ground-observed water level data have been used for calibration of the model parameter for hydraulic conductivity on a continental scale (Fan et al., 2013b). However, the model has not been calibrated for New Zealand conditions.

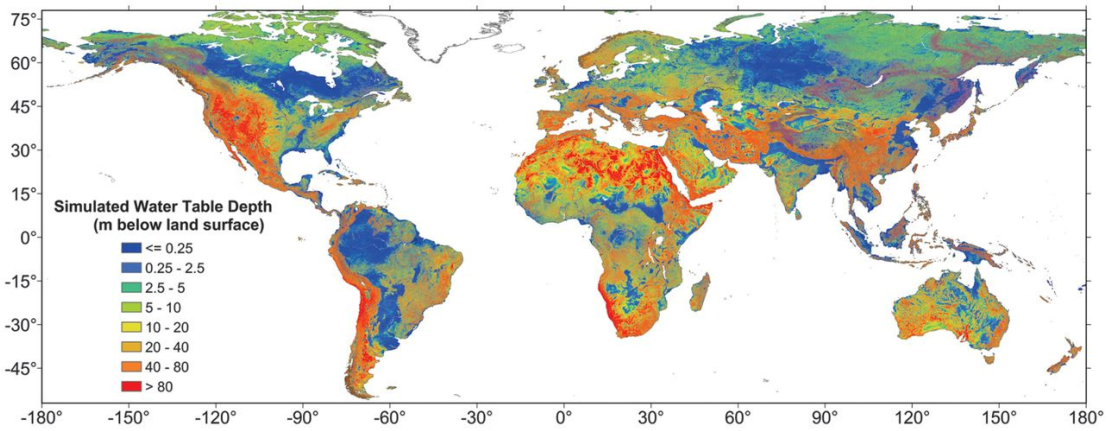

Figure 5.1: Original EWT depth at 30 arc-second grid resolution on the WGS84 grid (Fan et al., 2013a).

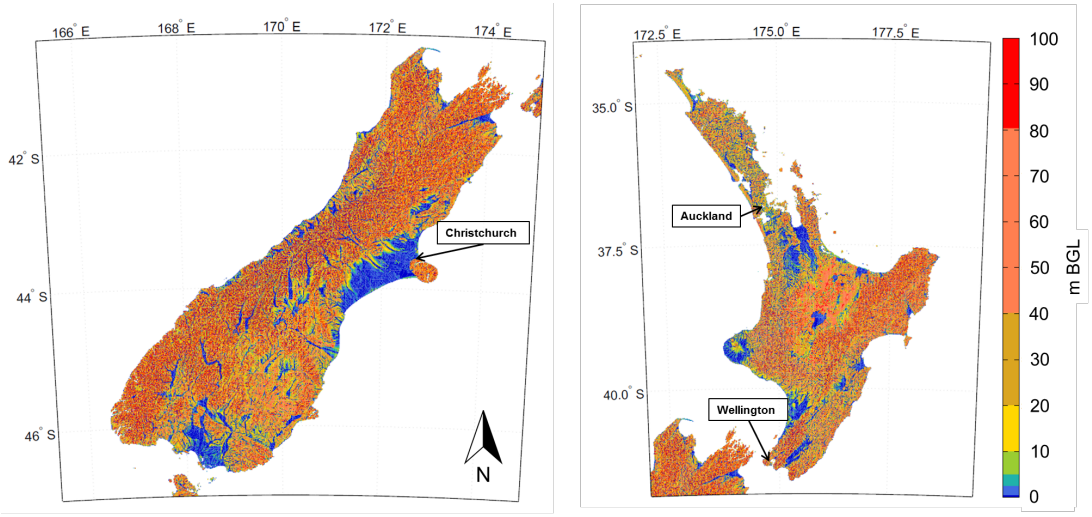

Figure 5.2: Original EWT depth in New Zealand, shown in metres below ground level (m BGL): GLOWASIS (2015) and Fan et al. (2013a).

5.3.2 Method

EWT depth is calculated for a mesh of cells that each have the following properties:

- cell size in the horizontal (x,y) directions;
- elevation of the ground surface above sea level;
- transmissivity, embedded in a hydraulic conductivity-depth relation;
- annual vertical groundwater recharge from rainfall;
- annual horizontal groundwater inflow and outflow, which is calculated by the EWT method;
- groundwater head, which is calculated by the EWT method.

The cell size for global models is typically measured in fractions of degrees of latitude and longitude in the WGS84 projection (Figure 5.1 and 5.2) and therefore cell size in metres depends on location. This is because the east-to-west cell dimension is a function of latitude, while north-to-south cell dimensions are mostly independent of latitude and longitude (ESRI, 2000). For example, east-west cell size in northern New Zealand is larger than southern New Zealand whilst north-south cell size is invariant across the country (Table 5.1).

Table 5.1: Approximate resolution in kilometres of the WGS84 projection for New Zealand. For northern (Cape Reinga, latitude approximately 34.45°S) and southern (Stewart Island, latitude 47°S) locations.

Decimal degree	**East-west, north-south Cape Reinga (km)**	**East-west, north-south Stewart Island (km)**
30 arc-second	0.764, 0.926	0.632, 0.926
5 arc-minute	7.64, 9.26	6.32, 9.26
0.5 arc-degree	45.82, 55.82	37.90. 55.82

Elevation data comes from global topography models; it is described in section 5.3.3. The cell transmissivity is the hydraulic conductivity integrated over depth. Hydraulic conductivity (K) between the ground surface and 1.5 m depth, K_0, is derived from a global soil database (Reynolds et al., 2000). Below 1.5 m, K is assumed to decrease exponentially with depth (Beven and Kirkby, 1979), Figure 2.3. The exponential decrease of K at depth z below 1.5 m depth is defined in Equation 5.1:

$$K = K_0 e^{-z/f}, \tag{5.1}$$

where z is the depth below ground level, and f is called the 'e-folding depth', Equation 5.2:

$$f = \frac{a}{1+bs}; f > f_{min} \tag{5.2}$$

Where a, b, and f_{min} are calibration constants, and s is the terrain slope (Fan et al., 2013b). The inverse relationship of f with s is a function of climate, geology and biota (Ahnert, 1970; Summerfield and Hulton, 1994). It causes steeper terrain to have a large gradient in K with depth (i.e., a thin regolith) and flat land to have a small gradient (i.e., a deep soil). The values of a, b, and f_{min} are set to 120, 150, and 5, respectively. This has been done on the experience of calibration of the model with ground-observed data in North America (Fan et al., 2013b).

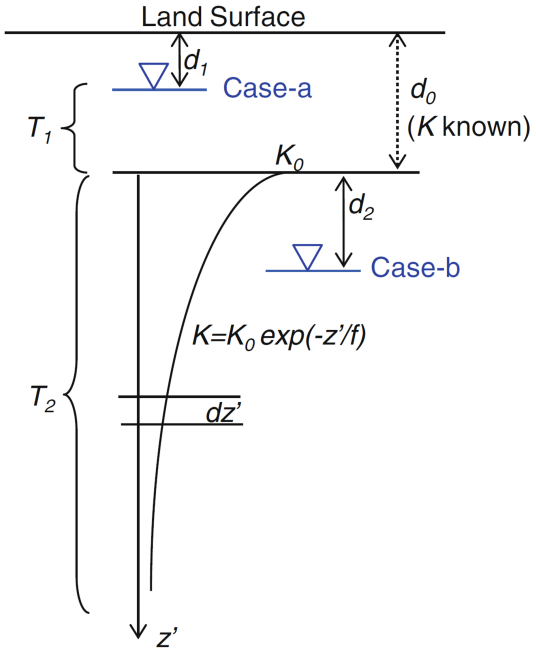

Figure 5.3: The calculation of transmissivity in the EWT model. Case-a: the water table depth at d_1 is within the depth d_0 of known soil hydraulic conductivity (K_0), and $T = T1 + T2$. Case-b: the water table depth at d_0+d_2 is below the known depth from which K is assumed to decrease exponentially with depth z' (Fan and Miguez-Macho, 2010b, their figure 4b).

Groundwater recharge (R) comes from long-term averages of yearly rainfall recharge to groundwater according to Döll and Fiedler (2008). The horizontal flow between cells (Q) is calculated by Equation 5.3. This equation represents two-dimensional groundwater flow based on mass balance, Darcy's law (e.g. Dingman, 2002; Hendriks, 2010) and the Dupuit-Forcheimer approximation (e.g., Freeze and Cherry, 1979):

$$Q = wT\left(\frac{h - h_n}{L}\right) \tag{5.3}$$

where

- w is the width of the cell;
- T is the transmissivity of the cell;
- h is the groundwater head in the centre of the cell relative to sea;
- h_n is the groundwater head in neighbouring cell;
- L is the distance between the two cells.

Groundwater discharge into rivers and wetlands (Q_r) is assumed when the calculated horizontal flow Q causes the groundwater head to be above the ground level (Fan et al., 2013b), Figure 5.4. Calculations are done iteratively. The calculation stops when an equilibrium between recharge and groundwater flow has been reached, i.e. that mean recharge in a cell equals mean groundwater flow out of the cell Equation 5.4:

$$\overline{R} = \sum \overline{Q} \tag{5.4}$$

Computationally, this means that the calculation in Equation 5.3 is repeated until a computational convergence has been reached, i.e., that the difference in groundwater head between two following iterations is less than 1 mm in most of the total number of land cells. Where the groundwater head rises above the land surface, it is reset to the land surface to mimic the effect of surface drainage and evaporation.

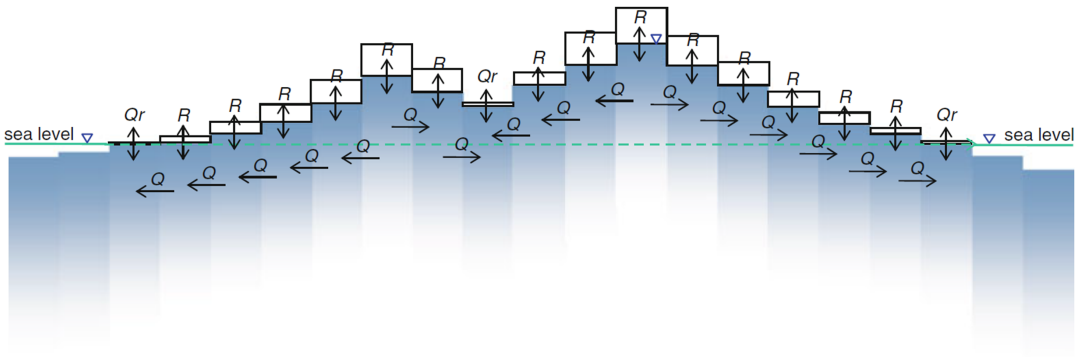

Figure 5.4: Schematic groundwater flow model to simulate the interaction of recharge (R), horizontal groundwater flow (Q), groundwater discharge in rivers (Q_r) and sea level (boundary condition) on water table depth over a continent. The blue fading colours indicate the decrease of hydraulic conductivity with depth (Fan and Miguez-Macho, 2010b, their figure 4a).

Two important assumptions made in the model are that there is only one water table at any location (thus neglecting local, perched aquifers) and that groundwater use (i.e., pumping, abstraction) is zero. Large-scale water abstraction could explain differences in modelled EWT depths and observed data (Fan et al., 2013a). In addition, the New Zealand EWT depth model is uncalibrated as no ground-observed data have been used to calibrate the model.

5.3.3 Input data

Input data for the original EWT model (Table 5.2) include:

- sea level. Fan et al. (2013a,b) do not state the datum for a mean sea level estimate; the writers assume the estimate is mean sea level over the last 30 years;
- global topography derived from satellite data (GTOPO30) (Gesch et al., 1999; Harding et al., 1999), Shuttle Radar Topography Mission (SRTM) (Smith and Sandwell, 2003) and Advanced Spaceborne Thermal Emission and Reflection Radiometer (ASTER) Topography data (Buis, 2011);
- rainfall recharge to groundwater from the global-scale WaterGAP Global Hydrology Model (WGHM) (Döll and Fiedler, 2008) based on a fully-coupled vegetation-soil-groundwater model simulation over the period 1961 - 1990. The simulation uses satellite and ground observation-based global precipitation estimates as input;
- soil hydraulic conductivity to 1.5 m below the ground surface. This is derived from the United Nations Food and Agriculture Organisation (FAO) global soil database which has 14 soil classes (Reynolds et al., 2000).

Table 5.2: Input data for the original EWT model of Fan et al. (2013a)

Input data	Data description	Resolution	Reference
ASTER	Topography	30 arc-second	Buis (2011)
GTOPO30	Topography	30 arc-second	Harding et al. (1999), Gesch et al. (1999)
SRTM	Topography	30 arc-second	Smith and Sandwell (2003)
WGHM	Groundwater recharge	0.5 arc-degree	Döll and Fiedler (2008)
FAO soil map	Soil map	5 arc-minute	Reynolds et al. (2000)
Sea level	Mean sea level	N/A	N/A

5.3.3.1 Uncertainty in input datasets

Topography errors at the regional scale are generally small for flat surfaces and high in mountainous areas. The root mean square error of ASTER topography data over the contiguous United States is 9 m (Gesch et al., 2012). The averaged absolute height errors of SRTM data per continent can be 10 m (Rodriguez et al., 2006). GTOPO30 topography data can reach even higher errors of 30 m (Harding et al., 1999). Rainfall recharge is based on global estimates of rainfall recharge. Groundwater recharge from surface water bodies is not taken into account, as this cannot be estimated on a global scale (Döll and Fiedler, 2008). The uncertainty in initial hydraulic conductivities for New Zealand from global FAO (Reynolds et al., 2000) input data is assumed to be large, but is not given. Information

about the way in which soil properties were measured to produce the FAO soil maps is not available. More importantly, soil material is usually different than the underlying geology, which causes more uncertainty.

5.3.4 Tests of the method

EWT depth estimates at the global scale were compared with ground-observed groundwater depths gridded to the EWT cell size (Figure 5.5) by Fan et al. (2013a). The fraction of EWT depths that were less than 1 m was approximately 0.14. In contrast, the fraction of observations less than 1 m was approximately 0.05. The large difference between these two fractions is because few groundwater level observations are recorded in many shallow aquifers that supply groundwater to surface water features and in the vast boreal and interior swamps of many continents. The relatively high occurrence of observations in the depth range 2 to 30 m reflects observational bias with more observation points in areas where groundwater pumping occurs Fan et al. (2013a,b). However, the effects of this bias are difficult to assess on a global scale. Miguez-Macho et al. (2008) compare estimates of groundwater elevation by the EWT method with observations in the contiguous United States (Figure 5.6). Observed groundwater elevation is a maximum of approximately 3000 m above sea level (Figure 5.6, left). Most differences between groundwater elevation calculated by the EWT method and observed groundwater elevation (Figure 5.6, right) are relatively small. However, residuals can be as large as plus, or minus, 100 m.

Water table depth estimates with the EWT method have been tested on most continents and the method generally works well, according to Fan et al. (2013b). However, the performance of the method is unknown in New Zealand, because no ground-observed data have been used in their comparison. Westerhoff and White (2013) concluded that generally the EWT model correctly calculates shallow water tables in New Zealand's alluvial aquifers (Figure 5.2). They also performed an evaluation in the Canterbury Plains, which is described in the next section.

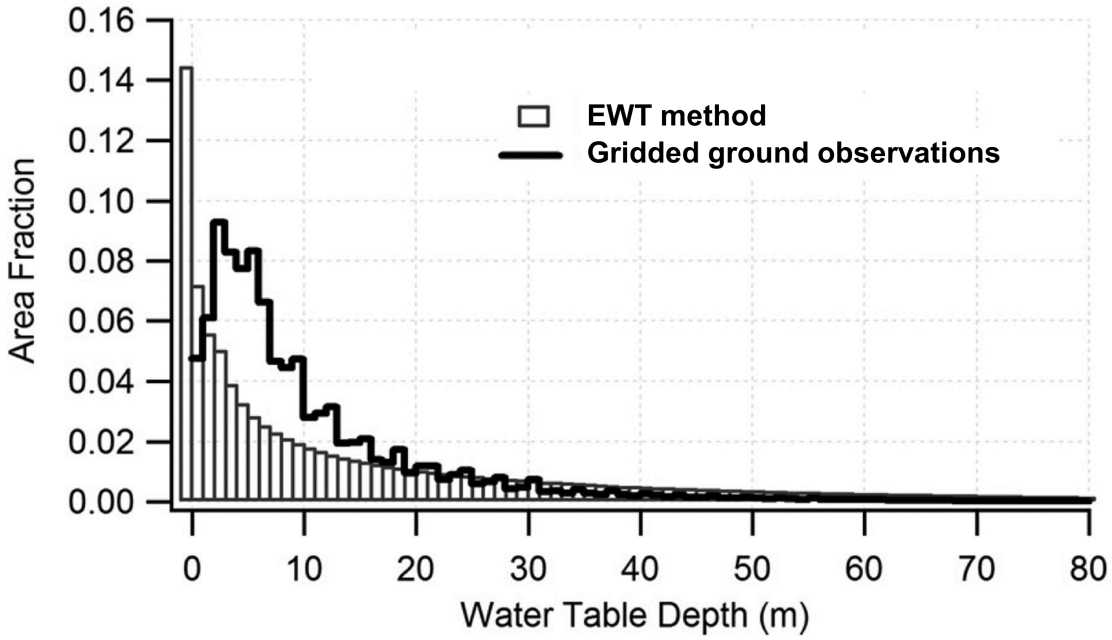

Figure 5.5: Global distribution of EWT depths (grey bars) and observed (bold black line) groundwater depths. The area of fraction is similar to a normalised distribution of data values (adapted from Fan et al., 2013a)

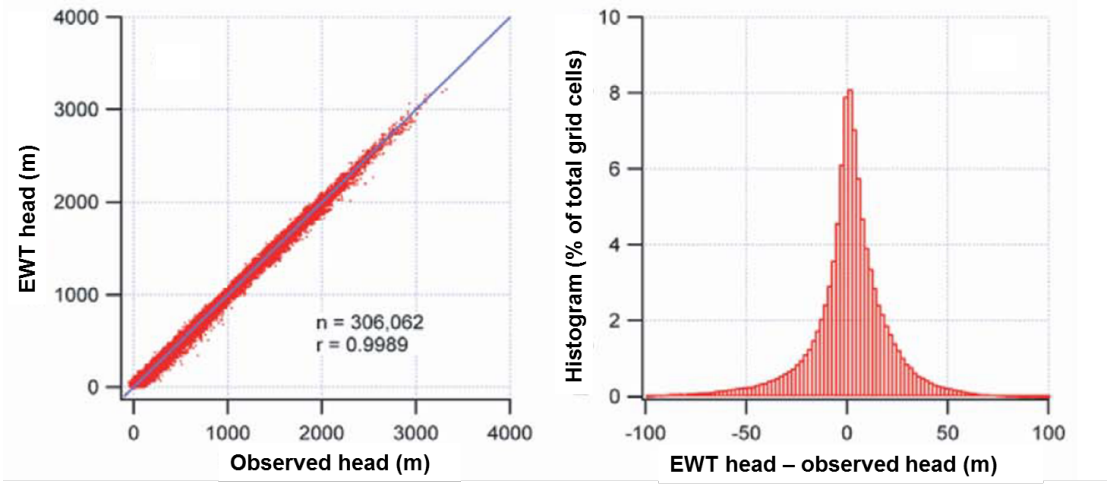

Figure 5.6: Cross plot of EWT hydraulic head (masl) calculated with the original EWT method vs. observed groundwater heads (left) and distribution of the residuals (right) using 306,062 measurements in the contiguous United States. (Adapted from Miguez-Macho et al., 2008)

5.4 Evaluation of the original EWT method in the Canterbury Region

5.4.1 Summary of hydrogeology in the Canterbury Region

Surface geology in the Canterbury Region is dominated by metamorphic rock and floodplains (Figure 5.7). Metamorphic rock includes a large area of greywacke that form much of the Southern Alps. Greywacke can contain groundwater in faults and fractures (Brown, 2001) but is little-used for water supply. Nationwide, regional groundwater allocation is largest in the Canterbury Region (Rajanayaka et al., 2010). The majority of groundwater use in the region is from the Canterbury floodplains. The Canterbury Plains, extending approximately 200 km from Waipara in the north to Waitaki in the south, is New Zealand's largest alluvial plain. General features of hydrogeology in the Canterbury Plains are summarised with the example of the Central Plains, largely from Brown (2001).

The Central Plains is located between the braided Waimakariri and Rakaia rivers. Greywacke basement has been identified below the plains at depth of 1112 m below Leeston (near Lake Ellesmere, Figure 5.7). Glacial outwash deposits form gravel fans, of predominantly Pleistocene age, and the rivers are connected to the aquifer systems. Natural recharge to groundwater systems comes from rainfall and rivers, augmented by artificial recharge from irrigation scheme drainage (i.e., three groundwater allocation zones; Scott, 2004). For example, rainfall recharge and artificial recharge were approximately 24.6 m^3/s and 2.9 m^3/s, respectively, in the period 1972 to 2003. Recharge to groundwater from the braided rivers is also a significant source of groundwater with the Waimakariri and Rakaia rivers contributing an estimated 12.9 m^3/s (White et al., 2012, Figure 5.8) and up to 15 m^3/s (White, 2008), respectively, to the Central Plains groundwater system. Groundwater use is an estimated 13.4 m^3/s in the Central Plains area (White, 2008). Unconfined conditions are common in the upper Plains. Aquifers in the lower Plains are typically confined and supply groundwater to extensive networks of spring-fed streams around Lake Ellesmere (Figure 5.7) and Christchurch City (Figure 5.8). These confining conditions are due, in part, to the occurrence of marine sediments deposited near the current coast during interglacial periods (Figure 5.8). However, Hanson and Abraham (2009) and Lough and Williams (2009) showed that the pattern of groundwater flow is not influenced by any extensive, low-permeability layers of sediment within the upper 100 to 150 m below the water table. Application of the EWT method, which assumes unconfined aquifers, is thus justified in the Central Plains.

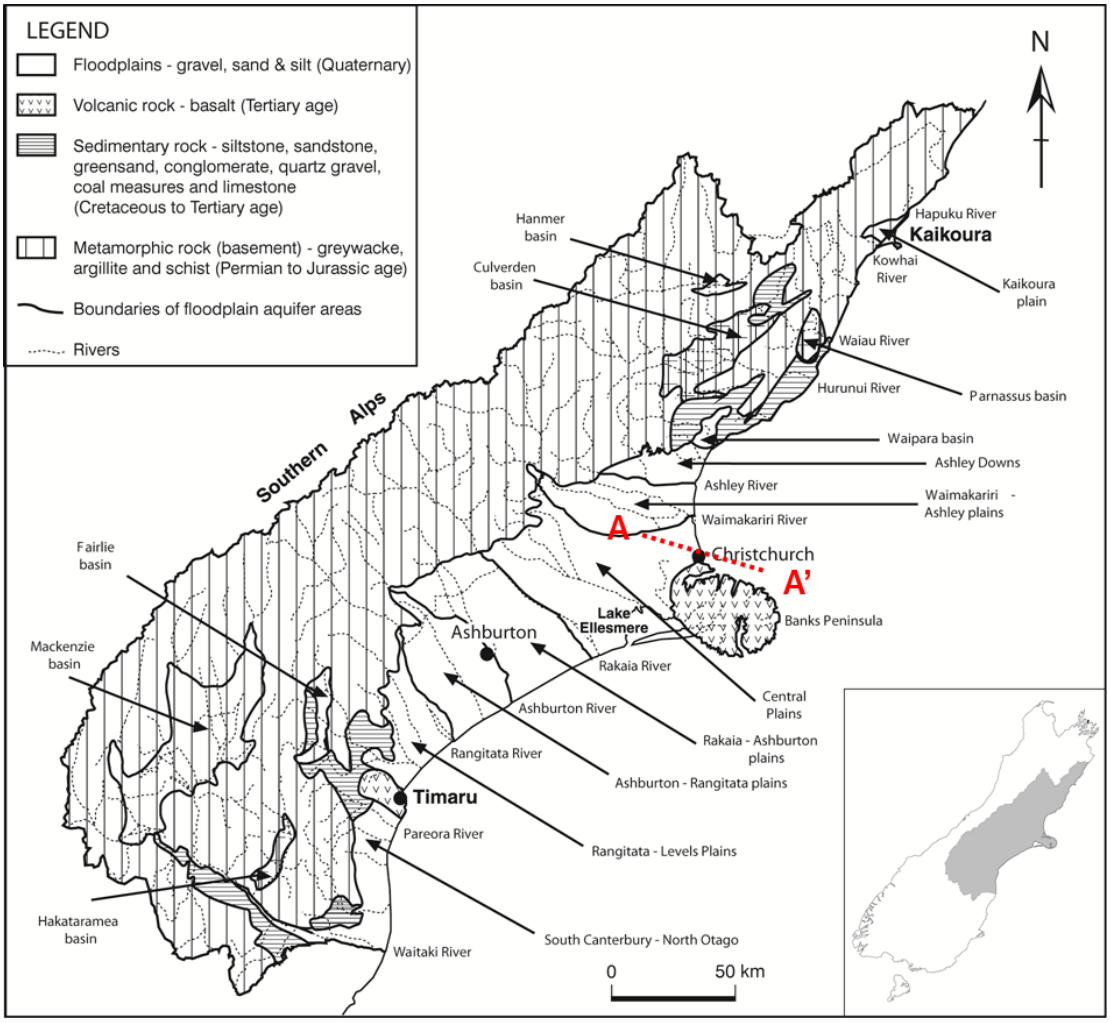

Figure 5.7: Hydrogeological setting of the Canterbury Region (adapted from Brown (2001)). A cross section of line A-A' is shown in Figure 5.8.

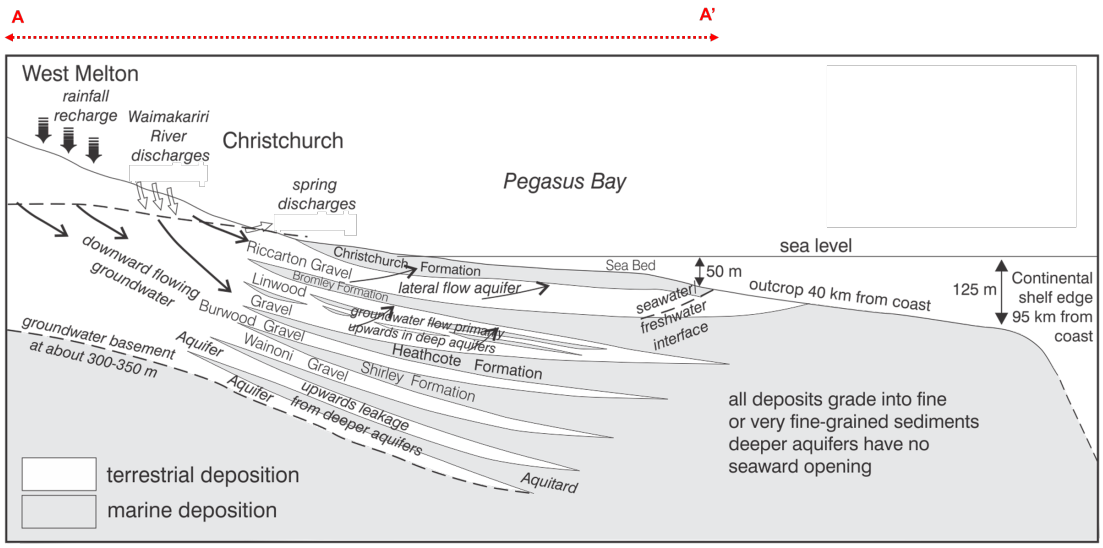

Figure 5.8: Cross-section through the Canterbury Plains near Christchurch (White, 2001). The location of line A-A' is shown in Figure 5.7.

5.4.2 Ground-observed groundwater depths

Groundwater depth observations from 8664 Canterbury time series have been made in wells during the period 1894 to 2013 by Environment Canterbury, and its predecessor organisations (Palmer, 2013). It is assumed that these groundwater depth observations represent the water table and can thus be compared to EWT depths. All groundwater depth observations were corrected for the measurement reference level and quality checked. The following data were filtered from the dataset during the quality check:

- missing or 'no data' values;
- time series from the same well, but with a different logging method: these were averaged;
- time series that ended before 1980;
- time series with durations shorter than 1 full year;
- data containing less than 3 measurements;
- data containing redundant measurements (e.g., some wells have multiple time series from different instruments) to select the longest time series with the largest dataset;
- data containing groundwater levels that are above ground level (42 wells), as it could not be established if these were artesian or a measurement error.

The result is a dataset containing groundwater depth referenced to ground surface from 3286 wells (Figure 5.9). Most of these wells are located in the Canterbury Plains (Figure 5.7). The average length of the used time series is 12.4 years,

with a median of 7 years. The longest time series in the dataset is from 1894 - 2013.

An overall average and median observed groundwater depth for the entire dataset were calculated. Median groundwater depths were then calculated for each well. From here, these will be referred to as 'median observed groundwater depths'.

Ground-observed depths (in metres below ground level - mBGL) were also referenced to metres above mean sea level (masl), using the input terrain model of the original EWT method. From here, these will be referred to as 'median observed groundwater table (masl)'.

The values of the EWT depth (in both mBGL and as EWT hydraulic head in masl) covering the locations of 3286 wells were collected from the original EWT dataset. This resulted in 3286 EWT depth values. Also, the average and median of all EWT depths were calculated.

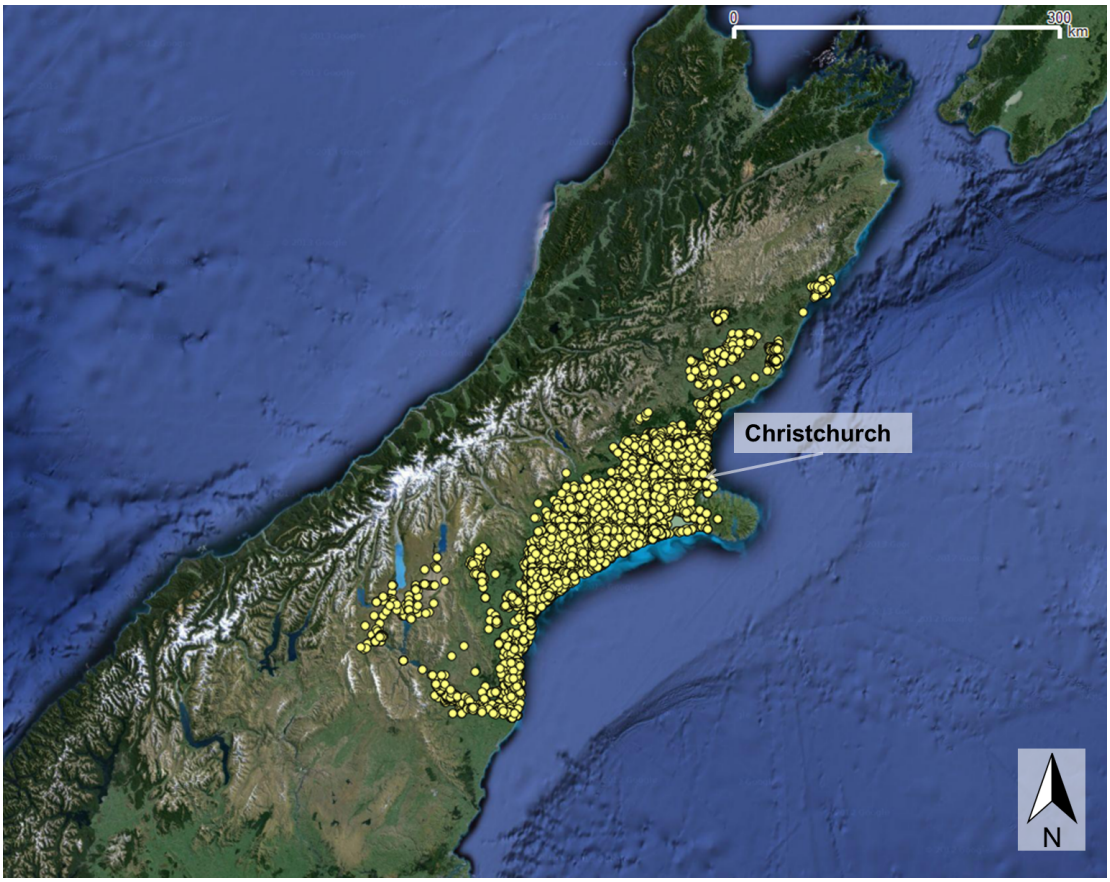

Figure 5.9: Location of 3286 wells with median observed groundwater depth estimates in the Canterbury Region.

5.4.3 Comparison of original EWT depth with median observed groundwater depths

The comparison of median observed groundwater depth with EWT depth (Figure 5.10) shows a similar pattern to that of the global model comparison (Figure 5.5); many EWT depths are less than 1 m and more median observed groundwater depths than EWT depths are in the range 2 to 30 m. The fraction of EWT depths in the Canterbury Region that are less than 1 m is more than 0.4, which is much more than in the global comparison (Figure 5.5). The fraction of observations in the Canterbury Region less than 1 m was approximately 0.05, about the same as the global comparison. Overall, the average and median of the 3286 observed groundwater depth time series in the Canterbury Region are deeper than those of EWT depth (Table 5.3).

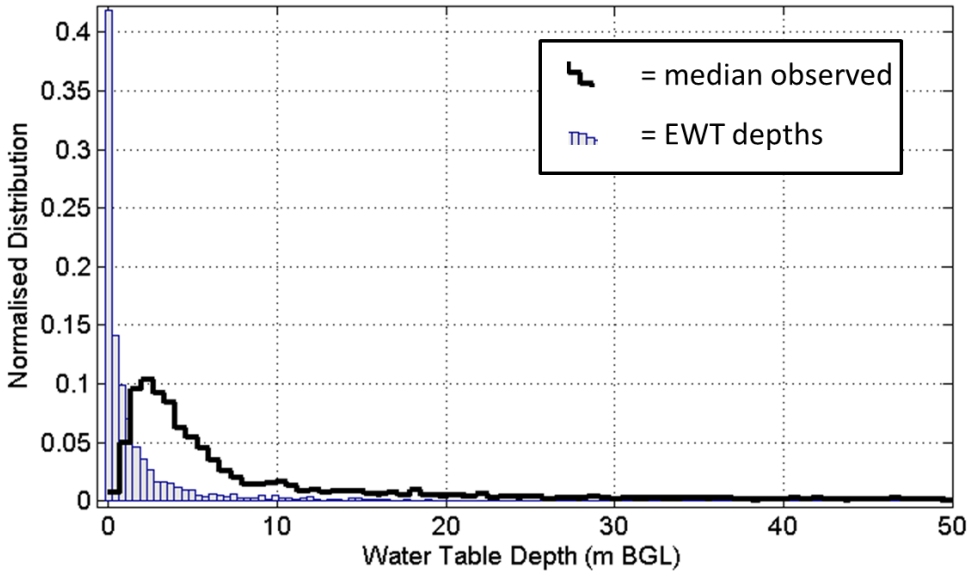

Figure 5.10: Histogram of median observed groundwater depths (thick black line) and calculated EWT depths (grey histogram bars) for the Canterbury Region. Values are shown up to 50 m, the full range (i.e., the maximum median observed groundwater depth is 198 m) is not shown.

Table 5.3: Overall average and median of all observed groundwater depths and calculated original EWT depths in the Canterbury Region.

	Observed groundwater depth (m BGL)	**EWT depth (m BGL)**
Average	12.6	2.0
Median	4.6	0.4

The EWT hydraulic head (masl) correlates well with ground-observed data (R^2=0.96, Figure 5.11a), but some ground-observed data is deeper than the modelled EWT.

Median observed groundwater level is not correlated with EWT depth in mBGL (Figure 5.11b). This is because EWT depths are commonly less than 1 m. However, 13%, and 42%, of EWT depths are within 1 m, and 3 m, of median observed groundwater depths, respectively. Median observed depths are generally larger than EWT depths (Figure 5.12).

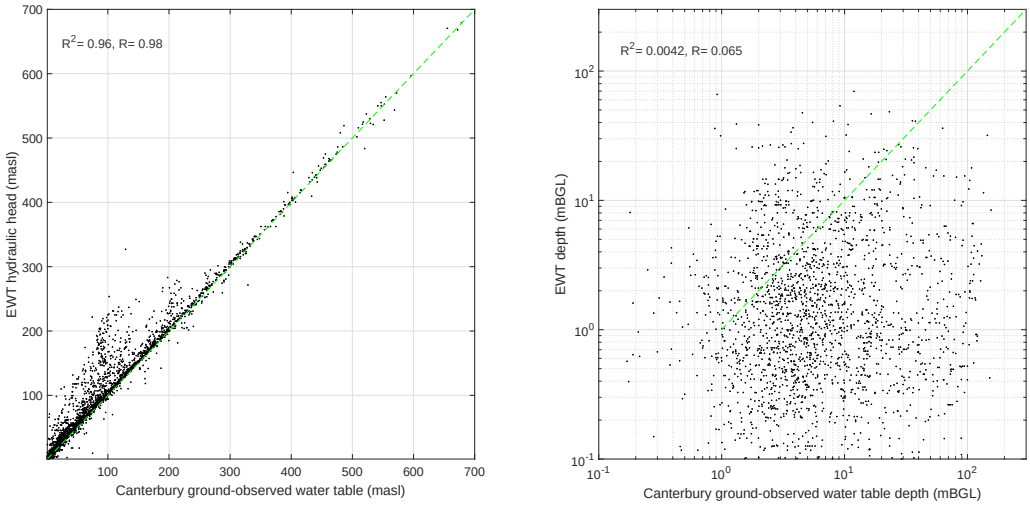

(a) metres above sea level (masl) (b) metres below ground level (mBGL)

Figure 5.11: Cross plots of median observed groundwater depths and calculated EWT hydraulic head and EWT depths in the Canterbury Region.

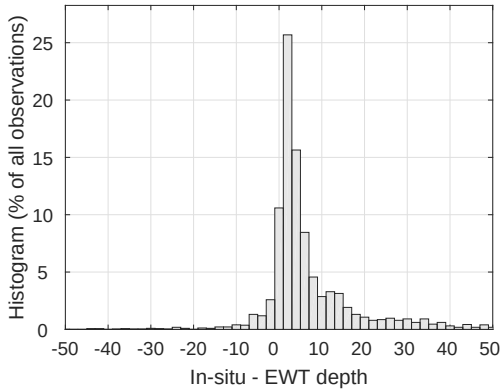

Figure 5.12: Histograms of the difference between median observed groundwater depths and calculated EWT depths in the Canterbury Region.

Median observed groundwater depths and EWT depths (mBGL) are mapped in Figure 5.13. Median observed groundwater depths are greater than EWT depths in the area between the Ashburton and Rakaia rivers and between the Rakaia and Waimakariri rivers. The absolute differences between these two depths are large (i.e., greater than 25 m) in these areas (Figure 5.14). These differences are largest, by more than 150 m, between the major rivers (i.e., the Ashburton,

Rakaia, and Waimakariri rivers) in the hydraulically-conductive gravels of the upper Plains (Figure 5.15). The original EWT model might provide a better match to observations with revised model components including terrain, soil properties, transmissivity, and rainfall recharge (see more in section 5.4.4).

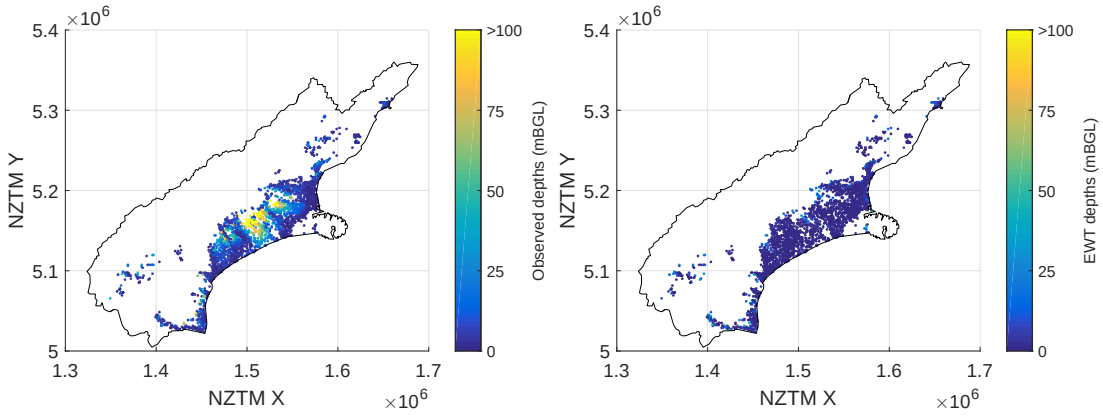

(a) metres above sea level (masl)

(b) metres below ground level (mBGL)

Figure 5.13: Median observed groundwater depths (left) and calculated water table depth by the EWT model (left) and median groundwater depths (right) in the Canterbury Region. Values greater than 100 m are all shown in red.

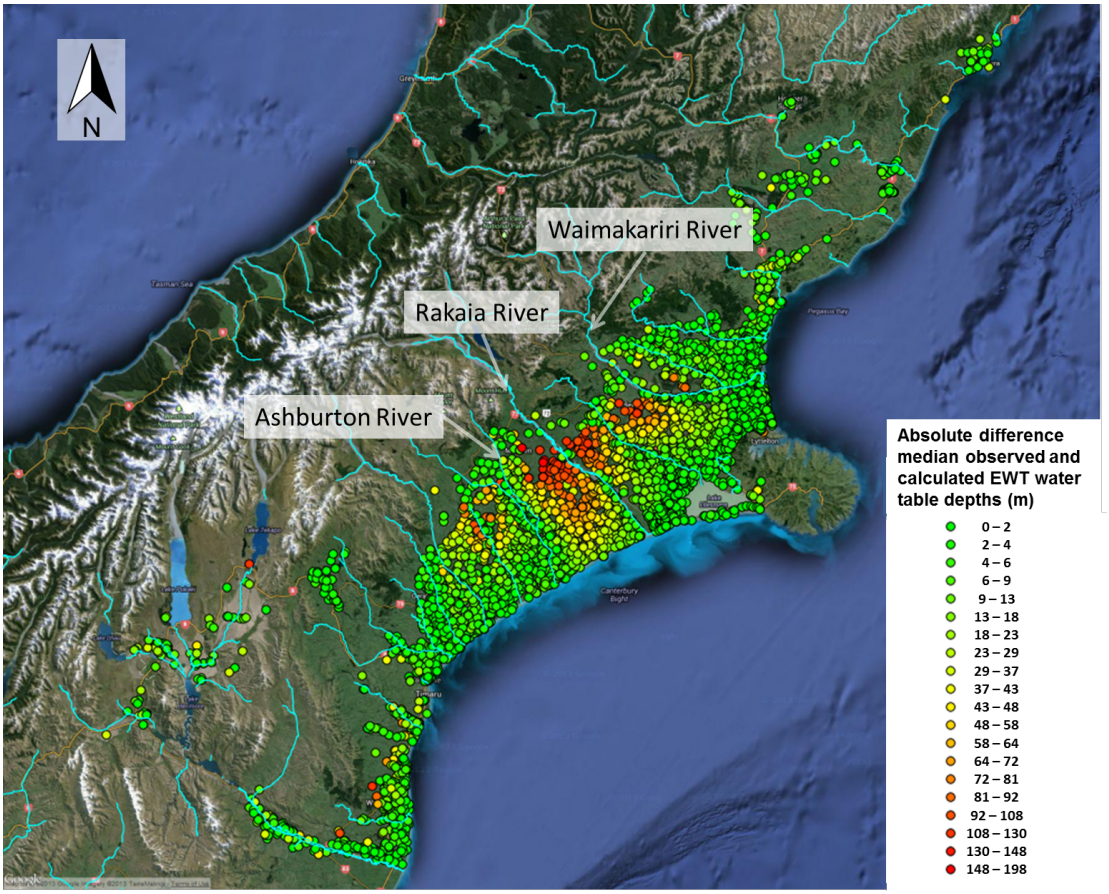

Figure 5.14: Absolute difference of median observed and calculated EWT water table depths in the Canterbury Region.

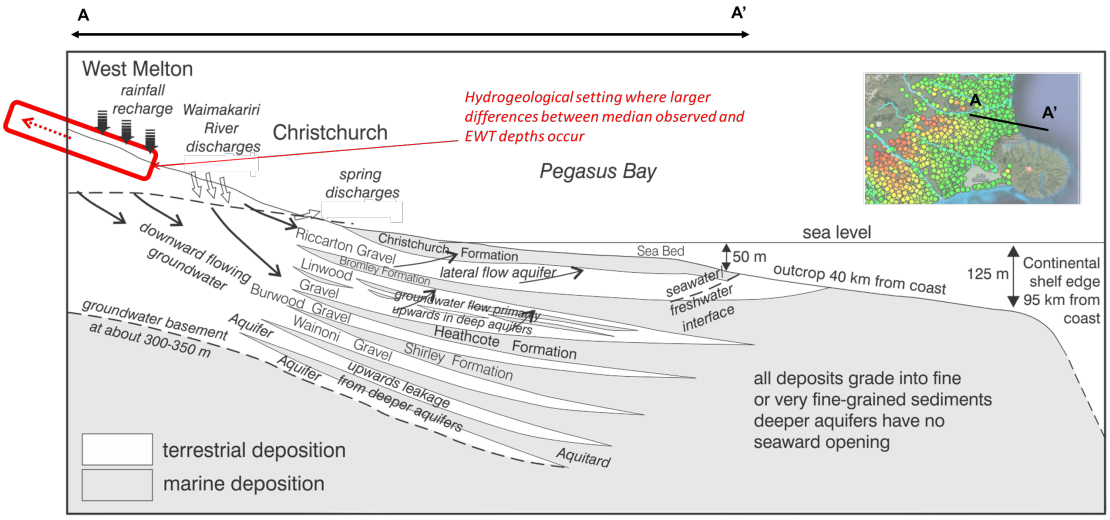

Figure 5.15: Cross section through the Canterbury Plains of Figure 5.8 (adapted from White, 2001). Areas with the larger differences between median observed water table depth and EWT depths are shown in red spots in the right inset.

5.4.4 Explanation of differences found in this evaluation

Generally, the original EWT model correctly calculates shallow water tables in New Zealand's alluvial aquifer systems (Figure 5.2). However, several problems with the original EWT model include:

1. A bias to calculation of shallow EWT depths (< 1 m) at the global and regional scales (i.e., Figures 5.5 and 5.10, respectively). This could be caused by two factors. Firstly, the EWT model cannot solve for surface drainage features that are within the 30 arc-second cell of the terrain model. For New Zealand, with its steep and highly varying topography, this could cause larger differences between observed groundwater depths and EWT depths than elsewhere in the world.

2. The EWT model generally calculates relatively few EWT depths in the range approximately 2 to 30 m at the global (Figure 5.5) and regional (Figure 5.10) scale. This could be due to the low resolution terrain model not solving for catchment drainage; the groundwater recharge input data not incorporating the large differences in rainfall in the area; and/or a hydrogeology that is too complex to be captured by the simple model. These limitations are addressed in the recommendations for EWT model improvement (Section 5.4.5).

3. Large errors are noted in the calculated EWT depths at the regional scale in the Canterbury Region. For example, the absolute differences between median observed groundwater depths and EWT depths are commonly greater than 25 m in the areas between the Ashburton and Rakaia rivers and between the Rakaia and Waimakariri rivers.

This section considers the possible reasons for large differences between median observed groundwater depth and EWT depths, including: (A) EWT input data, including climate and terrain; (B) hydrogeological complexity; and (C) observational bias.

A. EWT input data

The EWT model uses climate and terrain input data with a coarse resolution that does not capture the finer representation at the catchment scale. To build improved input datasets some national and regional datasets are recommended in Section 5.4.5. These model input data would have to cover the spatial variability of New Zealand's rainfall recharge at a catchment scale for three reasons:

1. At a catchment scale, e.g., catchments on the Canterbury Plains, it is important to represent the large gradient in rainfall between the mountains and the coast.

2. The EWT model rainfall recharge input data only represents 'diffuse recharge' (Döll and Fiedler, 2008) and does not capture recharge from rivers into the

groundwater, as is known to occur in the braided river systems in the Canterbury Region. However, including groundwater recharge from rivers in the EWT model in the Canterbury Region would result in even higher water tables in the EWT model. So although this is noted as a shortcoming of the model, it does not explain the difference between EWT and median observed water tables in this study.

3. The EWT model does not calculate groundwater discharge to the surface where the terrain model is too coarse to capture these surface drainage channels.

B. Hydrogeological complexity

The EWT depth at the New Zealand-wide scale follows general patterns of shallow water tables (Figure 5.2). However, the EWT model is not applicable in all aquifers, because it fails to represent hydrogeological complexity due to the following three reasons:

1. The EWT model calculates groundwater head, which does not always equate to the water table: the hydraulic head in a confined aquifer maybe different from the water table elevation in an overlying unconfined aquifer. Therefore, a better term for 'equilibrium water table' would be 'equilibrium groundwater head'.

2. Regional information on soil, subsurface type and hydraulic conductivity is not used. Use of this information will add to the capability of the EWT model.

3. The EWT model does not incorporate non-Darcian flow through fractures, karsts and faults. Theoretically, an EWT model could include lateral 'veins' of very high permeability, but it is unlikely that the EWT model would be the most suitable model for implementing this. A more advanced groundwater model such as FRAC3DVS (e.g., Cook et al., 2001) would be more appropriate for such settings. Such models are underutilised in New Zealand, and only a few examples of research application exist in this country (e.g. White et al., 1996).

Hydraulic conductivity is the least understood of the EWT model input variables. The EWT model could potentially be used to characterise hydraulic conductivity at the sub-regional scale, e.g., by applying Equation 5.1 to improved input data of a New Zealand soil or geology database. Potentially, the characterisation of hydraulic conductivity could lead to an improved understanding of the relation between hydraulic conductivity and depth. Furthermore, the transmissivity can possibly be derived by assuming a long term equilibrium (where rainfall recharge is the sum of groundwater flow in all directions) for regions where the rainfall recharge into groundwater and the water table are known and water abstraction is negligible.

C. Observational bias

The EWT depths in this study, and in that of Fan et al. (2013a), over-represent the occurrence of a very shallow water table compared to observations. Fan et al. (2013a) attributed this to absence or lack of observations at surface water features (rivers, lakes, and wetlands) fed by groundwater discharge; for instance, there are few observations in the vast boreal and interior swamps. However, in the Canterbury Plains, the model simulated very shallow water tables where observation wells showed a deeper water table. I surmise that this discrepancy is not due to a lack of observational data, but rather to shortcomings in the model and its input data, as discussed in A and B above. An alternative explanation is that the modelled EWT depth in confined aquifers is shallower than the observed water table in shallow unconfined aquifer wells. If so, shallow wells above the confining layer should be removed from the comparison dataset.

The differences between median observed groundwater depths and EWT depths in the 2 to 30 m range is explained by Fan et al. (2013a) as sampling bias: "..., observations are made for resource monitoring where humans settle (excluding large swamps and deserts) and where the water table is lowered by pumping or drainage". This explanation would mean that the integrated difference between the median observed groundwater depths and EWT depths would give an indication of groundwater depletion effects due to human pumping and abstraction. Given the current shortcomings of the model, such an assessment could be undertaken only after the EWT model has been improved according to the recommendations in section 5.4.5.

5.4.5 Recommendations for improvements to the original EWT method for nation-wide and regional application in New Zealand

Further research on the original EWT method for national application is recommended. On a national scale, the original EWT method calculates depths that seem to follow the general patterns of shallow water tables. However, EWT depth estimates compare poorly with groundwater depth observations in large areas of the Canterbury Region. To address this shortcoming, it is recommended that three EWT model input data sets be improved for further use in New Zealand settings as follows:

1. Topography models with a better vertical accuracy would lead to better estimates of the water table surface by the EWT model as elevation is the main driver for groundwater flow. A common datum is also recommended for the EWT model and observations of water table depth. Also, improved estimates of runoff will result from a digital terrain model (DTM) with better resolution of horizontal position. A New Zealand DTMs that could be tested could be the 8 x 8 m cell-size model of Geographx (2012).

2. The hydraulic conductivity, or transmissivity, distribution used in the EWT model should be adjusted considering maps of soil Landcare Research (2014) and surface geology (GNS Science, 2012) at the national scale. The use of these maps should provide better estimations of hydraulic conductivity with depth in the EWT model. However, calculation of hydraulic conductivity is not always straightforward.

3. Recharge data should have better data accuracy in the EWT model. Better accuracy could be obtained with estimates of groundwater budget components: e.g., rainfall Tait et al. (2006); potential evapotranspiration and actual evapotranspiration from national databases (Tait and Woods, 2007) or satellite data (Mu et al., 2011, , see Chapter); or runoff. Rainfall recharge measurements in lysimeters would also contribute to regional models of rainfall recharge (, e.g. White et al., 2003).

The next phase of EWT model development for further use in New Zealand should also include some reprogramming of the model to:

1. Process high-resolution data sets efficiently. For example, higher-resolution DTMs proposed in the above require more processing time than the current EWT model.

2. Use NIWA data sets as input variables to the EWT model. This will also improve the efficiency of EWT calculation and the robustness of the input data.

3. Establish the sensitivity of the EWT model to three important input variables (i.e., topography, rainfall recharge and hydraulic conductivity). In this way, the EWT method could be built into an assessment of the uncertainty of these variables at regional and sub-regional scales.

4. Characterise the distribution of hydraulic conductivity at the sub-regional scale. This would be particularly useful as hydraulic conductivity is the least understood of the EWT method's input variables. Potentially, the characterisation of hydraulic conductivity could lead to improved understanding of the relation between hydraulic conductivity and depth.

5.4.6 Conclusion of this evaluation

This section described the original global Equilibrium Water Table (EWT) model (Fan et al., 2013a) which calculates the depth of groundwater in the shallowest aquifer. The original EWT model correctly calculates that the water table is generally shallow in New Zealand's alluvial aquifer systems. The model was evaluated by comparing observations of water table depth in the Canterbury Region with water table depth estimated by the global EWT model. This evaluation demonstrates that the EWT model commonly estimates very shallow water table depths of less than 1 m, whereas observations of very shallow water table depths are rare. Conversely, EWT model water table depths are rare in the range 2 to

30 m but are commonly observed in wells. These two findings are consistent with the global data set of Fan et al. (2013a).

It is therefore concluded that the EWT method can be used in New Zealand on a catchment-wide scale; however the model will need improvement and more suitable input datasets are required. Improvements to model data sets that are recommended include: 1) topography models with a better vertical and horizontal accuracy leading to better estimates of the water table surface by the EWT model as elevation is the main driver for groundwater flow; 2) hydraulic conductivity maps of soils and surface geology in New Zealand; and 3) recharge data including satellite and national data sets on major water budget components (e.g., climate variables such as rainfall and potential evapotranspiration, runoff estimates, and rainfall recharge measurements).

5.5 Improvements in the EWT method for a nation-wide application

Following the recommendation of section 5.4, improvements to the EWT method were made by (1) using better model input components; (2) improvements in the method; and (3) additional features in the EWT method. Unvalidated results are shown for a smaller region in New Zealand, i.e., the Hauraki catchment in the Waikato Region. This region was researched by GNS Science during my PhD (e.g. White and Tschritter, 2014). However, these results have not been validated (such as in section 5.6) and are only shown for the purpose of clarification of the method improvements.

5.5.1 Improved input datasets

The original EWT method mostly used global datasets as input parameters (Section 5.3.3). The improved EWT method uses nation-wide and higher resolution data:

- A high-resolution terrain model. An 8 m x 8 m DTM from Geographx (2012). The Geopgraphx DTM is prepared from New Zealand topographic data, with additional satellite terrain data (SRTM, USGS, 2006). This terrain model was resampled to 200 m x 200 m.
- A rainfall recharge dataset, described in Chapter 4. These data were compiled to a mean annual recharge of 1 km x 1 km cell resolution. This dataset includes a satellite 1km x 1km AET as described in Chapter 2;
- Hydraulic conductivities on a 1 km x 1 km scale, derived from the geological map of New Zealand, using a method based on Gleeson et al. (2011) and described in Appendix C of this thesis.

5.5.2 Improved methodology

Model cell resolution, time steps and convergence

Model cell resolution was chosen as 200 m x 200 m. This was mainly done to match the terrain model resolution. The model was run in daily time steps. This was done taking into account the model cell resolution and the maximum distance that groundwater can travel without passing more than one cell. As the highest hydraulic conductivity in the model was that of gravel (median K = 90 m/day, uncertainty 90 m/day), daily time steps were chosen to be computationally efficient.

The original EWT method had a convergence criterion, i.e., that the water table reaches an equilibrium and does not change. This criterion is not used in the new

method. I decided to use the original EWT as the initial estimate of hydraulic head (a 'well-educated guess') and leave the model run for 100 years. The reasons for that are:

- that an equilibrium might never be reached in reality, because climate factors keep on changing;
- that some cells in the model will not reach an equilibrium, because they will iteratively interchange groundwater amongst neighbouring cells back and forth, without changing the net groundwater flow;
- that the seasonality and inclusion of rainfall recharge uncertainty makes the convergence criteria less straightforward.

The convergence is still monitored in the cells in the model, at a time step of 365 days. An example is shown in Figure 5.16.

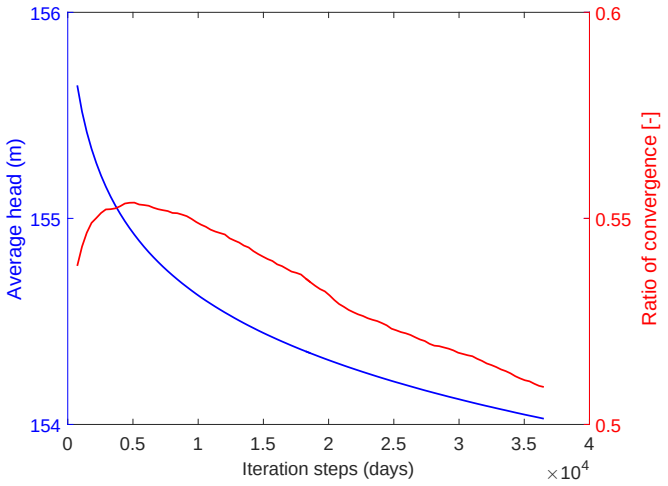

Figure 5.16: Example of convergence output (red) of a model run, including the average head of all model cells (blue). The convergence was set as the ratio of model cells that change less than 1 cm between consecutive years.

Hydraulic conductivity and its decrease over depth

The original EWT method used an estimated map of hydraulic conductivity K, which was based on a world-wide map of soil (Section 5.3) and an exponential decrease of hydraulic conductivity (Equation 5.1) from 1.5 m and deeper.

The improved EWT method uses geology data (and not soil) from the nation-wide digital geological data of New Zealand QMAP (GNS Science, 2012). Estimation of hydraulic conductivity was based on hydrolithological classes described by Gleeson et al. (2011) and improved with knowledge on typical New Zealand geology (e.g., Tschritter et al., 2014). Details of this K estimation are described in Appendix C. The exponential decrease was assumed to start from 10 m and deeper, because the QMAP represents the surface geology, i.e., the geology of layers at or near the surface.

As cell resolution was changed to 200 m, the values of a, b and f_{min} of Equation 5.2 were changed accordingly, to 75, 150 and 4, respectively. These values were also used by a 200 m resolution EWT model of Fan and Miguez-Macho (2010a) in the Amazon basin.

Further adjustments to K are based on more detailed regional evaluation in two case studies and are therefore discussed in the following section 5.6.

Seasonality and uncertainty of rainfall recharge

It was chosen to include seasonality, where rainfall varies over the seasons (i.e., dry in summer, intermediate in spring and autumn, and wet in winter). Main reason to do this was that in reality seasons of higher rainfall recharge can cause more groundwater discharging to the surface in a model cell. If seasonality would not be included, the total recharge averaged over the year might not lead to this same groundwater discharge to surface. To include seasonality, the mean annual recharge was divided over the year with a normal distribution, i.e. a Gaussian distribution with 365 time steps (Eq. 5.5 and Figure 5.17):

$$f = \frac{1}{\sigma\sqrt{2\pi}} e^{-\frac{(x-\mu)^2}{2\sigma^2}}, \tag{5.5}$$

where:

σ is the standard deviation of a normal distribution, i.e. 1/6 of the 365 days in this case;

μ is the mean, in this case 182.5;

x is the day in the year, i.e. a vector with values in between 1 and 365.

It was not deemed necessary to add leap years, since the seasonality is only included to account for the discharge to surface in case of a surplus of recharge.

For each time step, recharge was fed into the model, including a random deviation of uncertainty based on the uncertainties described in Chapter 4.

Modelling on a catchment scale

The original EWT model used the assumption that all of the model region needs to be constrained by sea (Figure 5.4). In the improved EWT method, regional models are also possible assuming that there is no groundwater flowing in or out of the catchment. Computationally, the model boundaries where then set slightly larger than the catchment, and all boundary pixels were then given very low hydraulic conductivities (i.e., these cells are impermeable).

Improved EWT depth for the Hauraki catchment (Figure 5.18) shows a shallow water table near the coast (Hauraki Gulf). Most of the catchment boundaries show large EWT depths, which is an indication that groundwater flow in or out

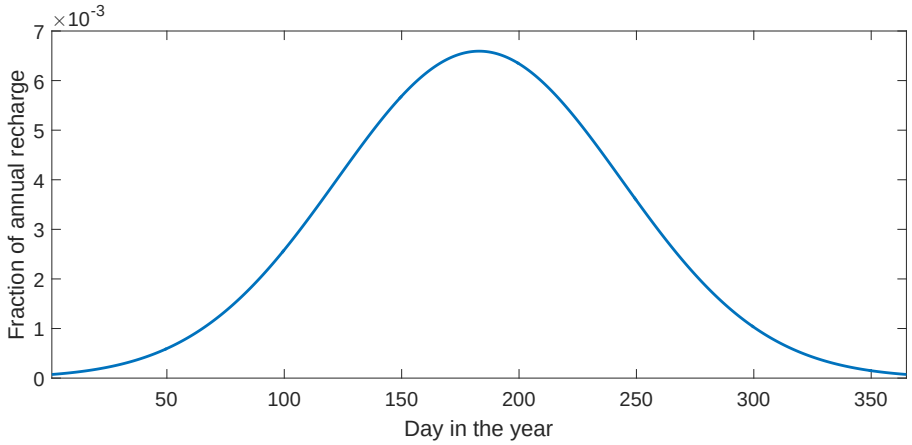

Figure 5.17: Inclusion of seasonality: fraction of annual recharge per daily time step used in the improved EWT method.

of the catchment is not likely at these boundaries. However, EWT depths show shallow water table in the southeast and in the west. Both of these shallow water table indicate that water might still able to flow out of the catchment. The corresponding EWT hydraulic head is shown in Figure 5.19.

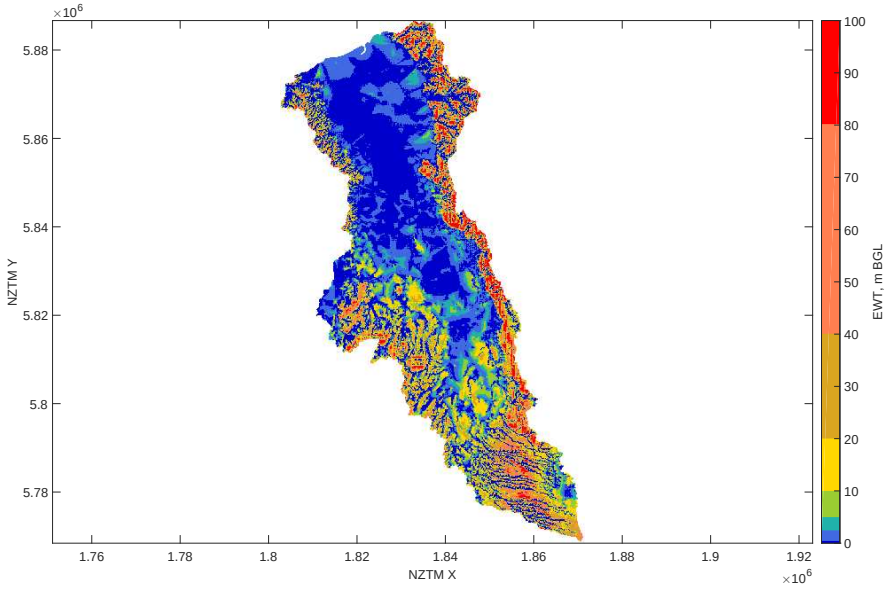

Figure 5.18: EWT depths for the Hauraki catchment in metres below ground level (mBGL).

Correction of recharge estimation

Rainfall recharge data was used as input in the model. These data are described in Chapter 4, where it was also discussed that this recharge should be considered 'potential recharge', as it can be rejected at areas of shallow groundwater. In the improved EWT method, this recharge is corrected for cases where the model

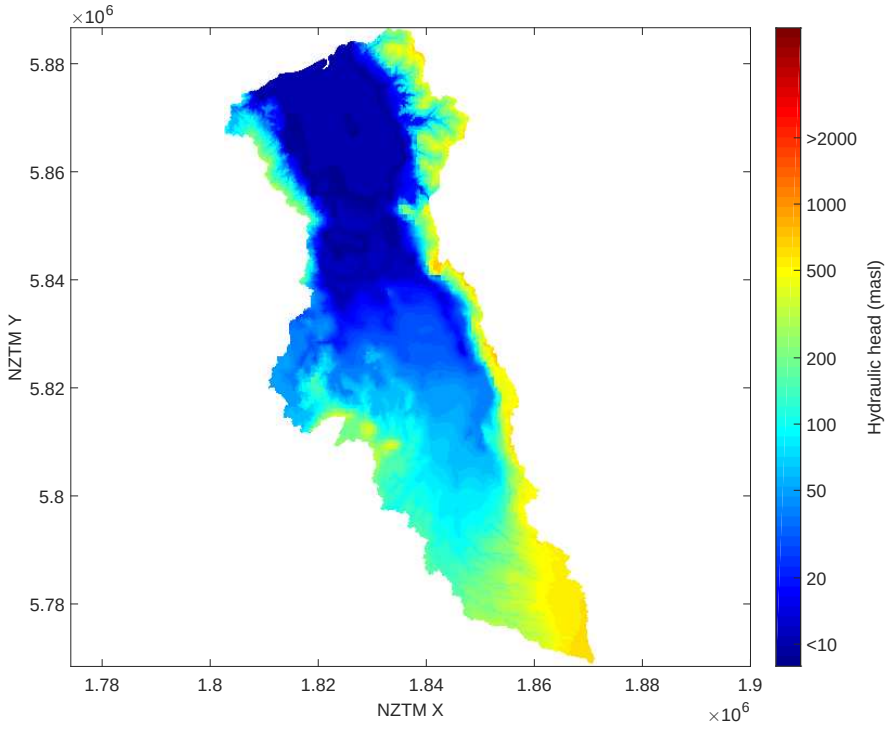

Figure 5.19: Hydraulic head for the Hauraki catchment in metres above sea level (masl).

calculates a very shallow water table or water discharging to the surface. These corrections are performed per (daily) model time step. In case of a very shallow water table, recharge that fits is accepted, while the remainder is rejected. In case of water discharging to the surface, all recharge is rejected. This is considered a loose form of model coupling between the recharge model (Chapter 4) and the EWT method.

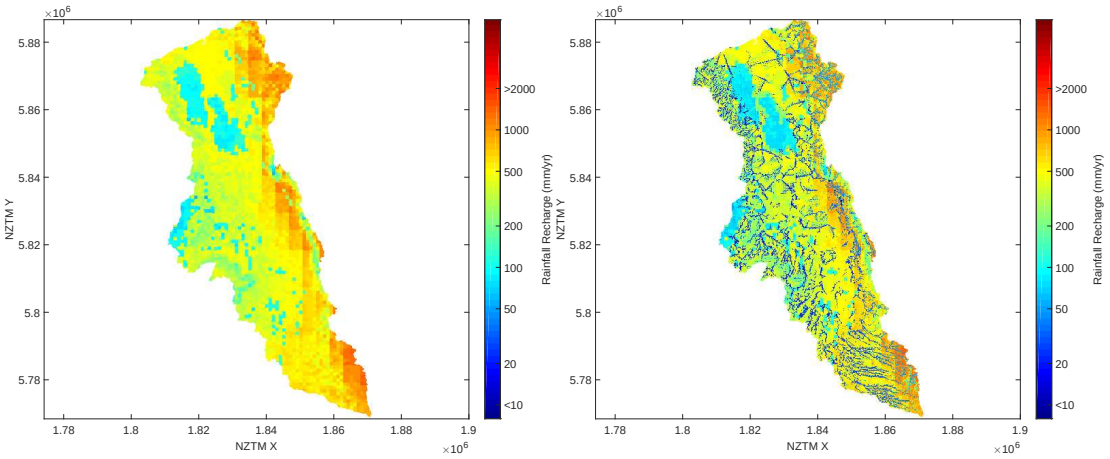

(a) Potential recharge

(b) Actual recharge

Figure 5.20: 'Potential' recharge (the model input, left) and 'actual'recharge (corrected by the improved EWT method, right) for the Hauraki catchment.

Calculating discharge of surface water to groundwater

After running the model for a long period (e.g., more than 100 years), it is assumed that a near-equilibrium state is reached. From that point, groundwater that discharges to surface is stored for every pixel. After running the model for another long period (e.g., another 100 years), these stored data is averaged to m^3/s and defined as baseflow. Although absolute values of this baseflow have not been validated, the pattern can be used to point out zone where much, some or no baseflow is expected (Figure 5.21).

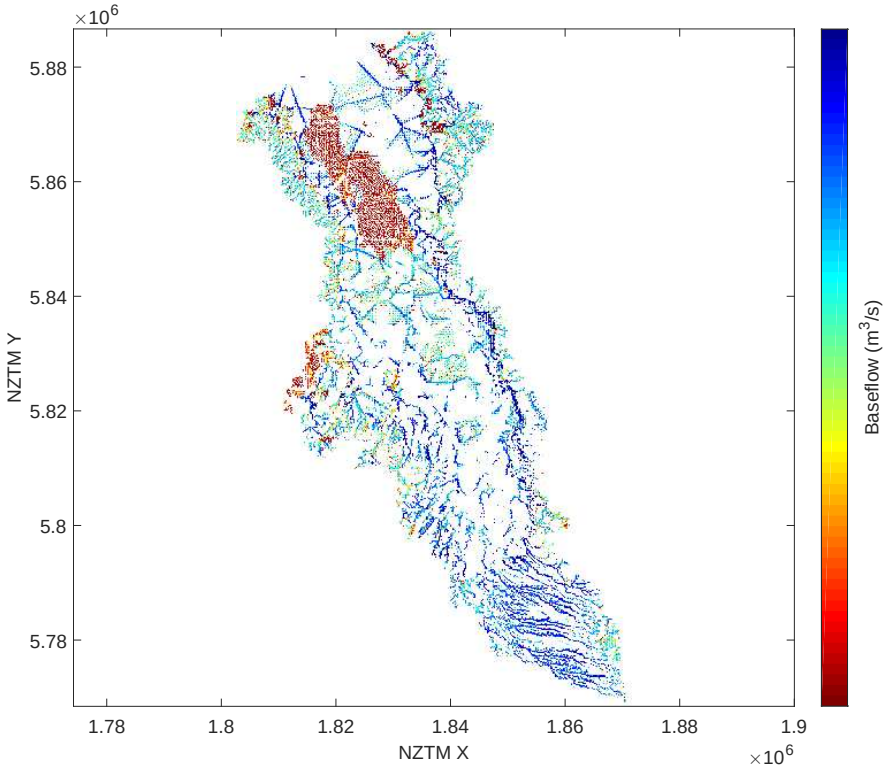

Figure 5.21: Estimates of baseflow for the Hauraki Gulf. Red = low, blue = high, white = none.

Calculating unconfined aquifer depth

The EWT model calculates transmissivity using estimated hydraulic conductivity K at the surface (explained in section 5.5.2 and Appendix C, and equation 5.1, that calculated the decrease of K over depth. Using this initial value of K at the surface, it decreases depending on the terrain slope (Section 5.3.2). If a cut-off value of 0.1 m/day is assumed, i.e., values smaller than 0.1 m/day are not an aquifer, the depth of this cut-off value can be calculated and is defined as 'aquifer thickness' (Figure 5.22). Although the method uses the simple assumptions of the EWT method, and assumes that the aquifer is unconfined, major alluvial aquifers and their indicative depth are identified quickly with this method. The

aquifer depth is merely a 'first guess' and should only be used indicatively. More local studies should incorporate more local data and knowledge of the aquifer system. Also, further improvements are recommended to improve the initial K values by incorporating more data of the geology maps of New Zealand (e.g. age, or secondary/tertiary rock types besides the main lithology).

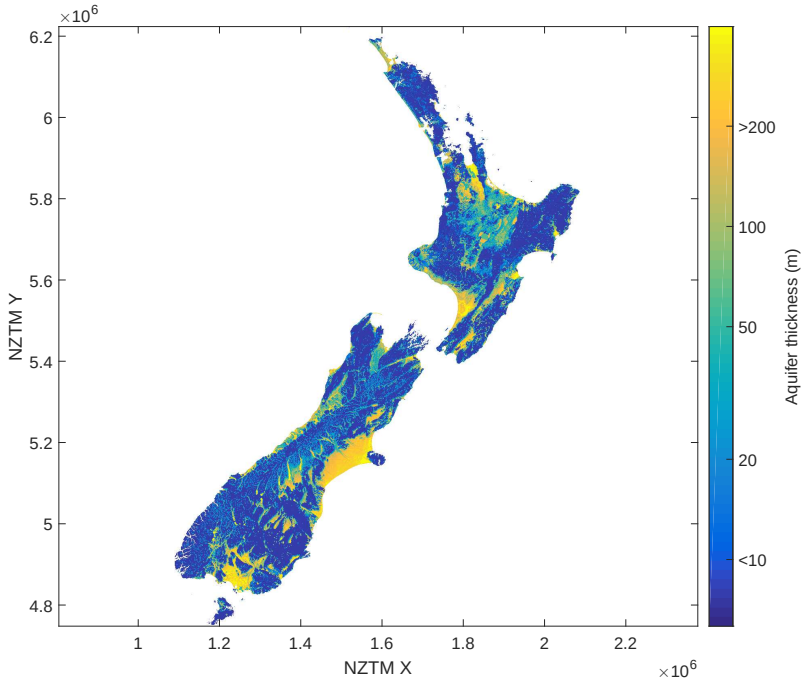

Figure 5.22: Estimates of aquifer thickness in New Zealand.

Calculating groundwater flow per section

Average groundwater flow was estimated for each EWT model cell, using the calculated hydraulic head and the transmissivity values of the EWT model run are translated to groundwater flow per cell (value and direction). First, the gradient of the hydraulic head (the 'hydraulic gradient') in x and y direction was calculated with Equation 5.6:

$$\nabla F = \frac{\partial F}{\partial x}\hat{x} + \frac{\partial F}{\partial y}\hat{y}. \tag{5.6}$$

The groundwater flow is reverse to the gradient (i.e., a uphill gradient is positive, while downhill flow is considered a positive number). Then, the value of this gradient was scaled by the value of transmissivity in each model cell. The groundwater flow vectors are then scaled so that the largest components are clearly visible, but not too large for the map (Figure 5.23). This depiction shows the main drivers of groundwater flow in the catchment, i.e., for the Hauraki catchment the eastern

(Kaimai-Mamaku) mountain range is a clear driver. This simplified groundwater flow model can only be used in unconfined aquifers, as multi-layer aquifers demand a much more complex model environment.

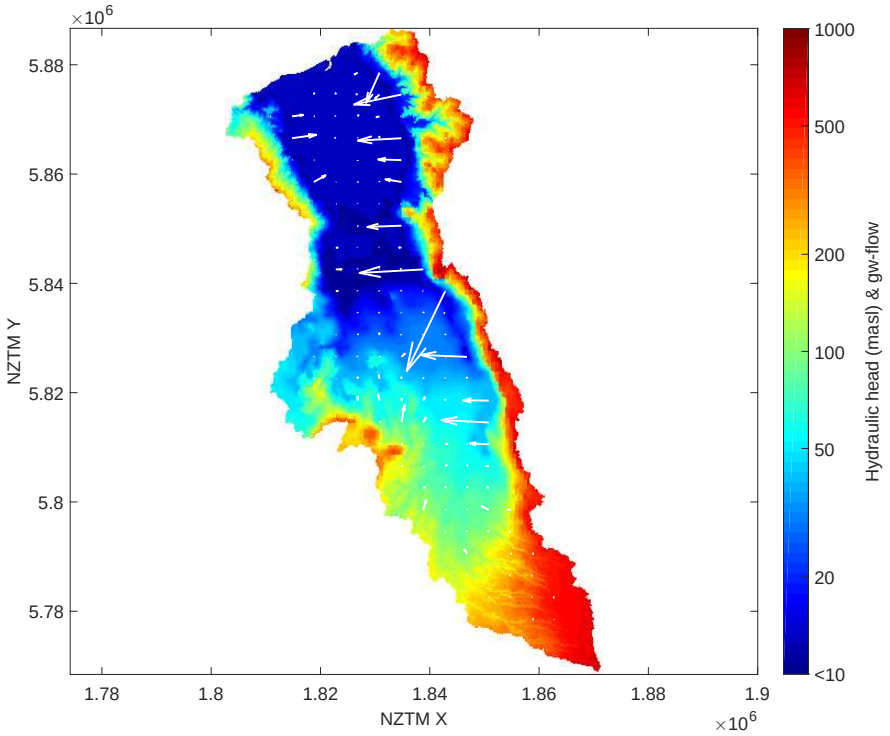

Figure 5.23: Groundwater flow estimates in the Hauraki catchment.

5.5.3 Nation-wide improved EWT depths

Nation-wide maps of improved EWT depths for the North Island 5.24 and South Island 5.25 show that the improved method still points out the main alluvial aquifers. However, the finer detail of the improved EWT method (200m resolution) show that these aquifers show more variation of EWT depth than the original EWT depths (Figure 5.2). These nation-wide plots show so much detail, that it is better to zoom in on smaller region for more analyses, such as done for the Hauraki catchment (Figure 5.18) or in the following sections for the Canterbury Region and Waipa catchment.

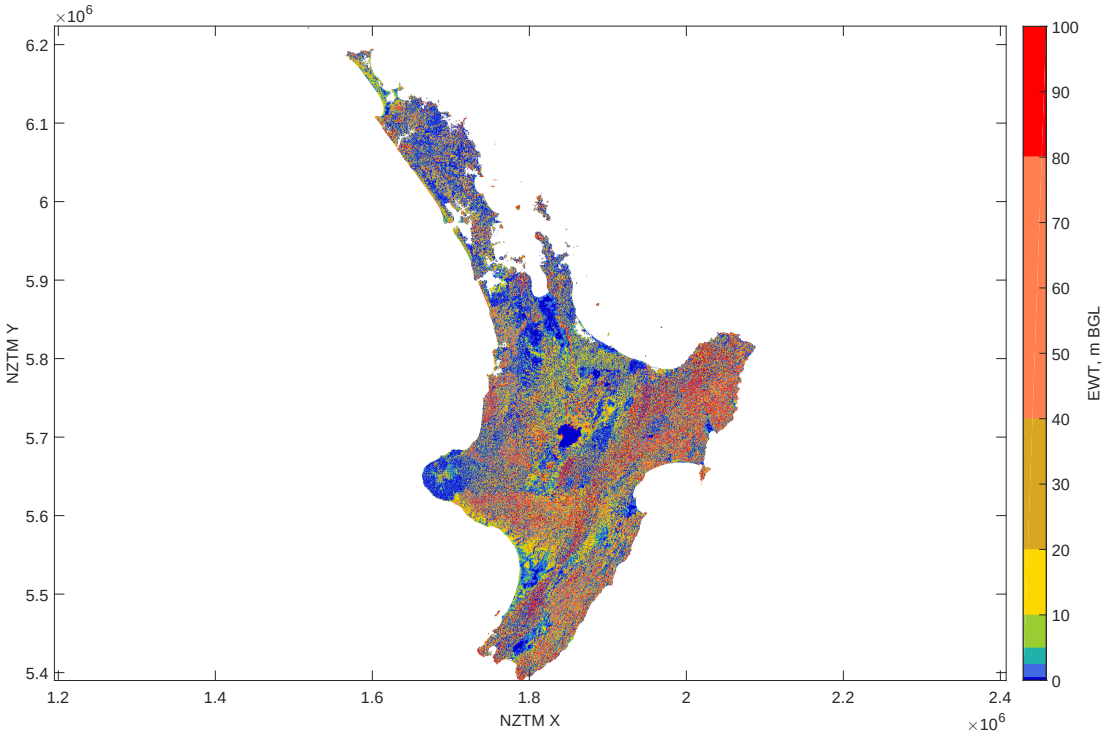

Figure 5.24: Improved Equilibrium Water Table for the North Island.

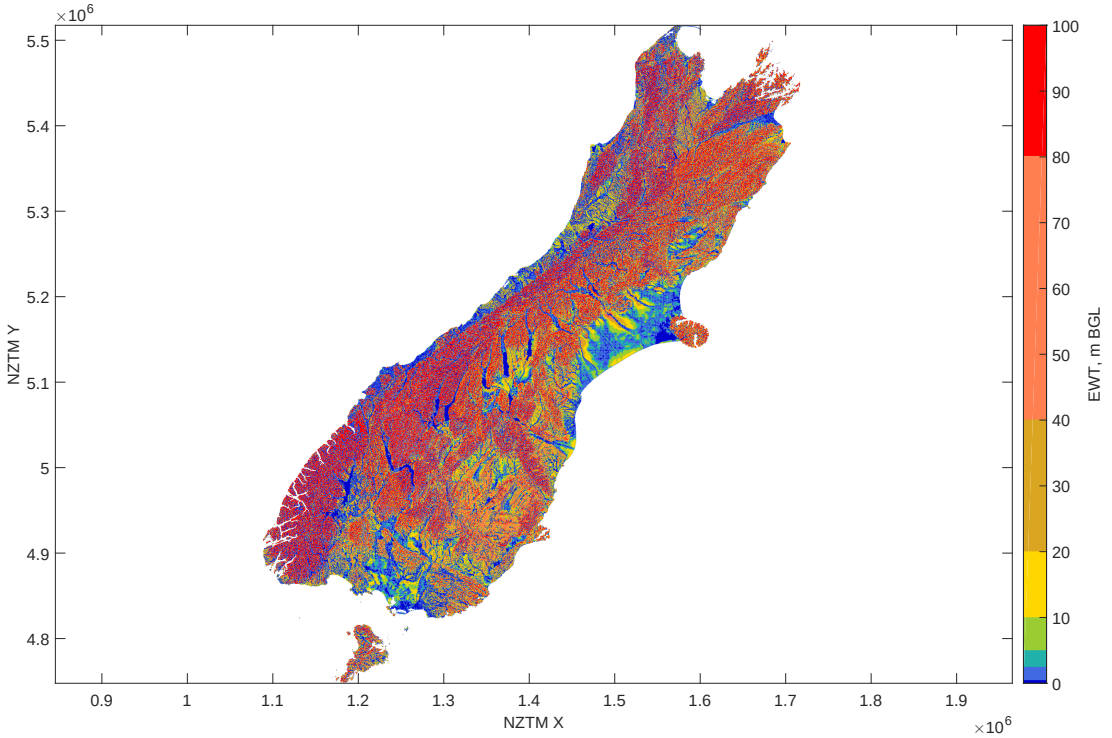

Figure 5.25: Improved Equilibrium Water Table for the South Island.

5.6 Re-evaluation of improved EWT depths in the Canterbury Region

Maps of EWT depths of the original EWT method consistently showed very shallow water tables in the plains area (Figure 5.26a). Compared to those original EWT depths, many improved EWT depths are less shallow (Figure 5.26b) in the plains. This is confirmed by the distribution of EWT depths: compared to the ground-observed medians, the original EWT depths showed very many values close to zero (Figure 5.27, left), while the improved EWT depths follow the distribution of the ground-observed medians better (Figure 5.27, right)).

Overall, more EWT depths are closer to ground-observed values (Figure 5.29 and Table 5.4). For example, 21%, and 51% of improved EWT depth are within 1m and 3m from ground-observed median, respectively; this was 13%, and 42% for the original EWT depths, Section 5.4.3. However, the same large differences, in the area between the Ashburton and Rakaia rivers and between the Rakaia and Waimakariri rivers (originally shown in Figures 5.13 and 5.14 and re-plotted in Figure 5.28b) are still found in the improved EWT depths (Figure 5.28d), although somewhat smaller and showing the same trends as Figure 5.14.

Besides the EWT depths, other outputs of the improved EWT model include: EWT hydraulic head (Figure 5.30); the correction from potential to actual recharge (Figure 5.31); and an estimate of locations and relative volumes of baseflow (Figure 5.32). These will not be evaluated.

Table 5.4: Percentage of occurence of absolute difference between EWT depths and ground-observed median values of water tables in Canterbury

	Original EWT (%)	Improved EWT (%)
< 1	13	21
< 3	42	51
> 50	6.0	5.8
> 100	1.2	0.85
> 150	0.045	0.030

5.6.1 Explanations of large differences between the major rivers and subsequent further local adjustments to the EWT method

Improved EWT depths match ground observations better then the original EWT depths in the Canterbury Plains. However, large differences between ground observations and EWT depths still remain in the areas between the larger rivers. I test three possible theories to explain these large differences: (1) groundwater

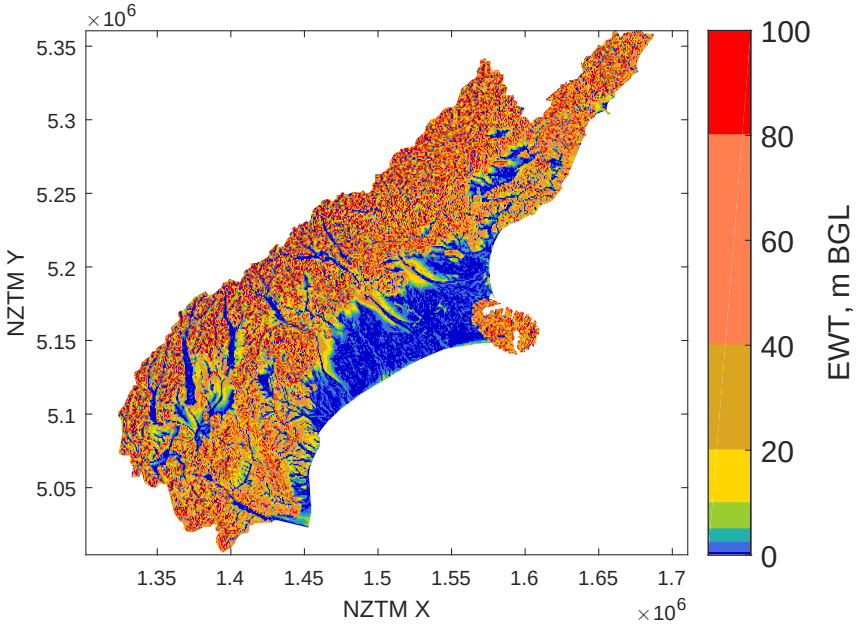

(a) original EWT

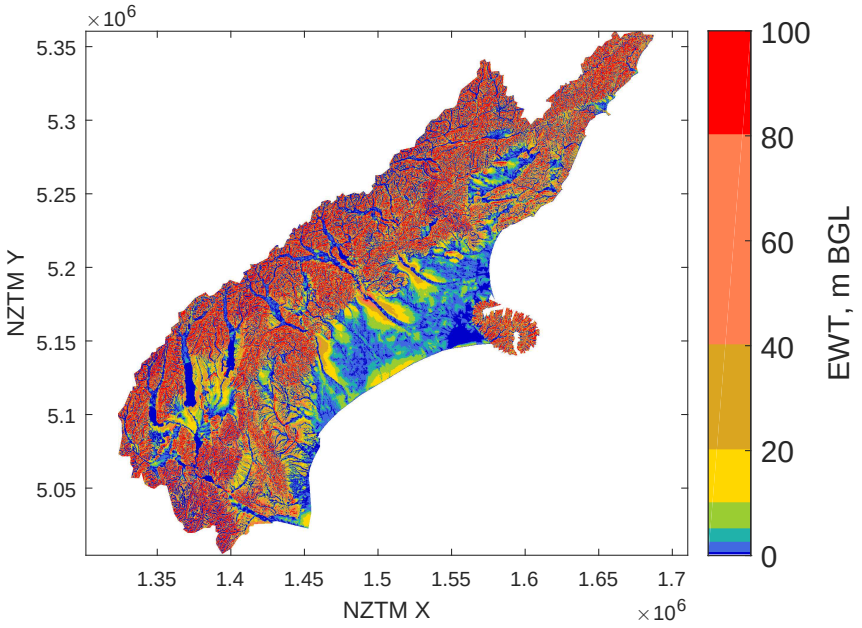

(b) improved EWT

Figure 5.26: EWT depths for the original (a) and improved (b) EWT method for the Canterbury Region.

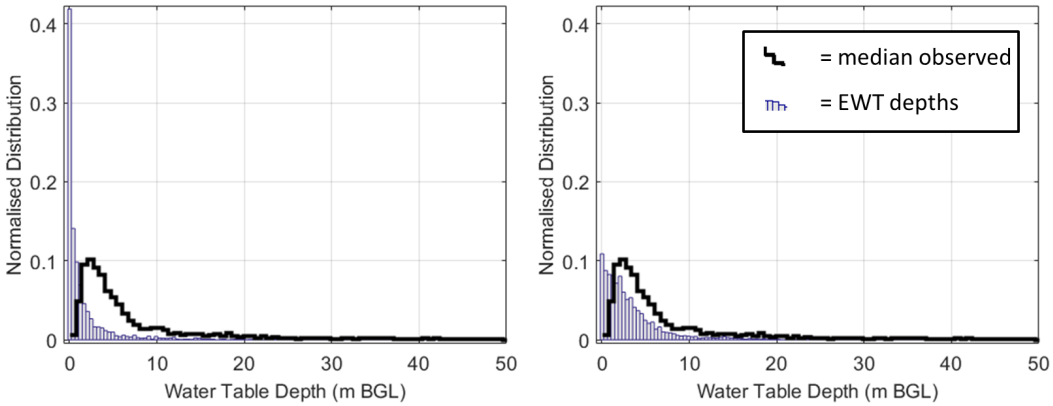

Figure 5.27: Distribution of median observed depths compared to the original EWT depths (left) and to the improved EWT depths (right).

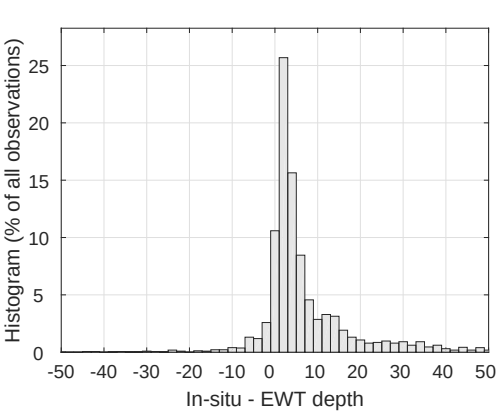

(a) original EWT: histogram

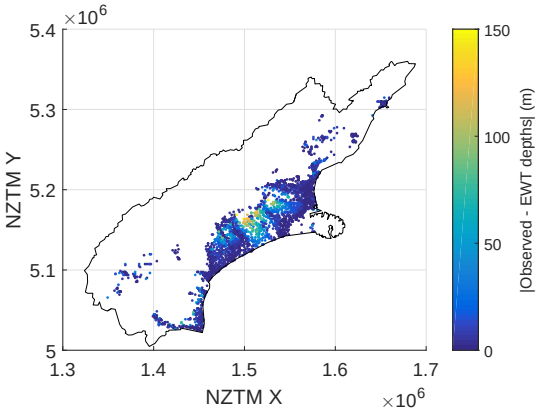

(b) original EWT: absolute differences

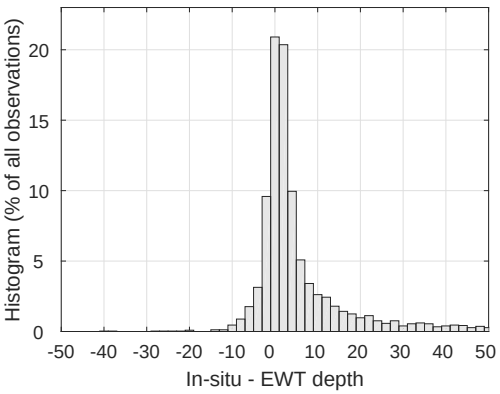

(c) improved EWT: histogram

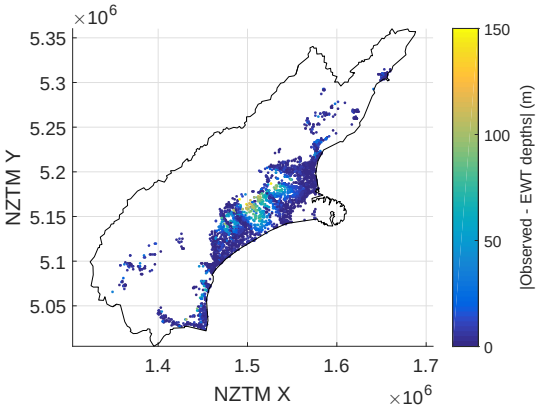

(d) improved EWT: absolute differences

Figure 5.28: Differences between Canterbury EWT depths and median of observed water tables for the original (top) and improved (bottom) EWT method.

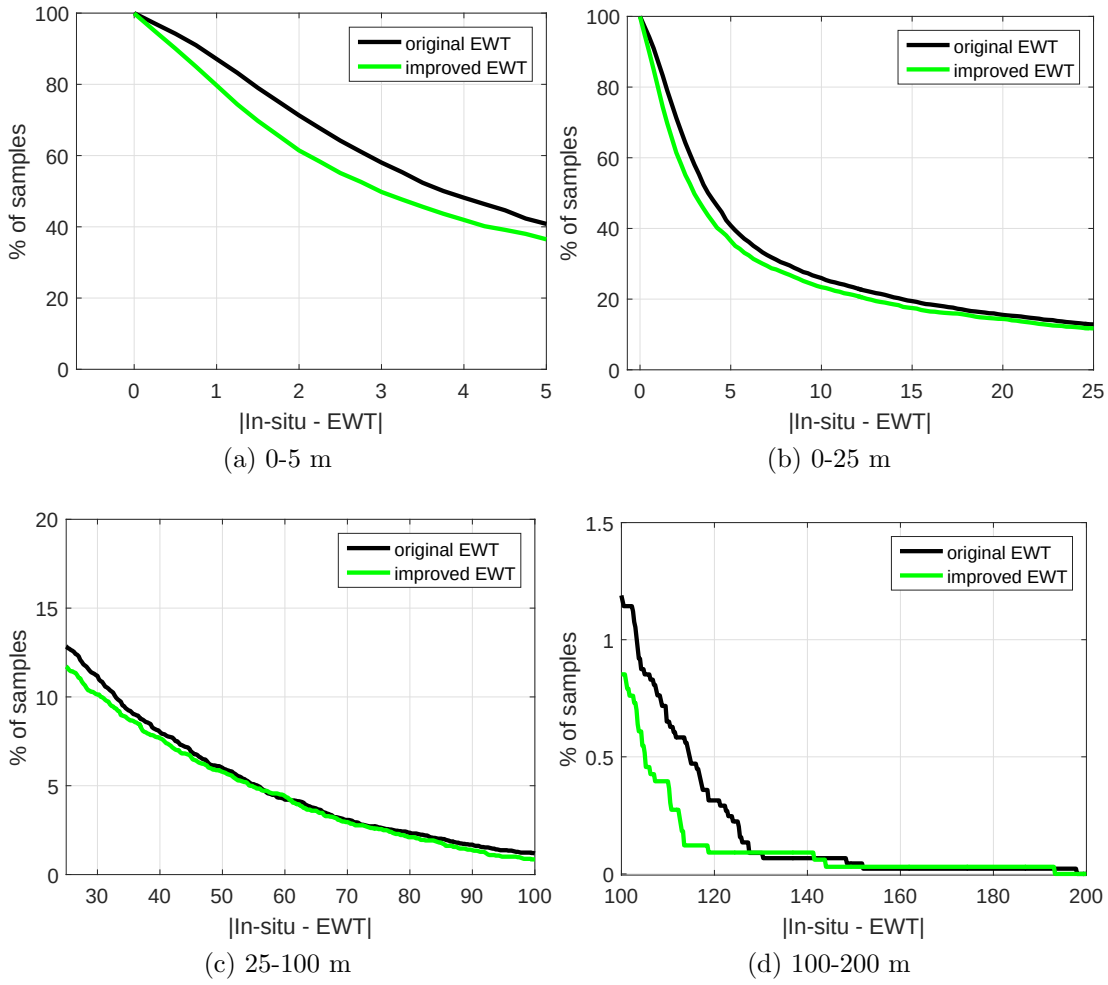

(a) 0-5 m (b) 0-25 m

(c) 25-100 m (d) 100-200 m

Figure 5.29: Absolute difference between improved EWT depths and ground-observed median values in Canterbury.

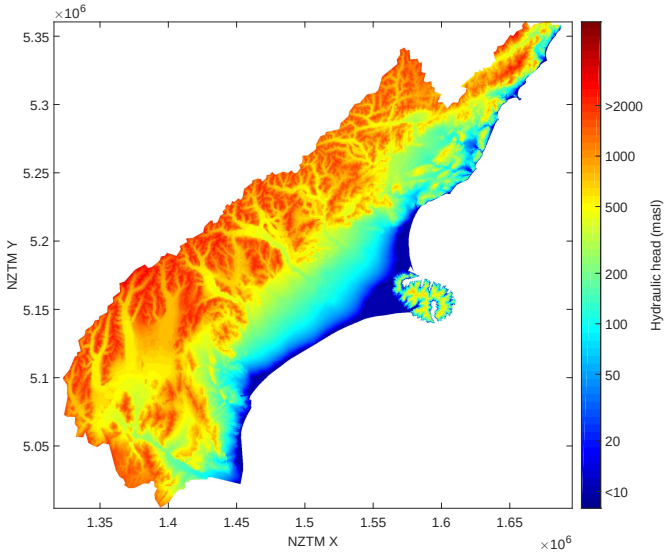

Figure 5.30: Hydraulic head for the Canterbury Region (masl).

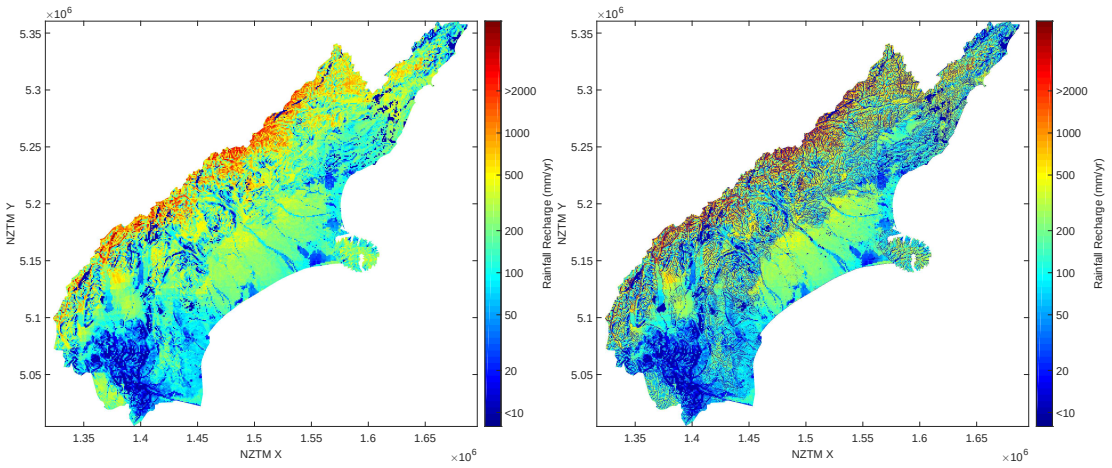

(a) original recharge (b) corrected recharge

Figure 5.31: Original recharge and corrected recharge for the for the Canterbury Region.

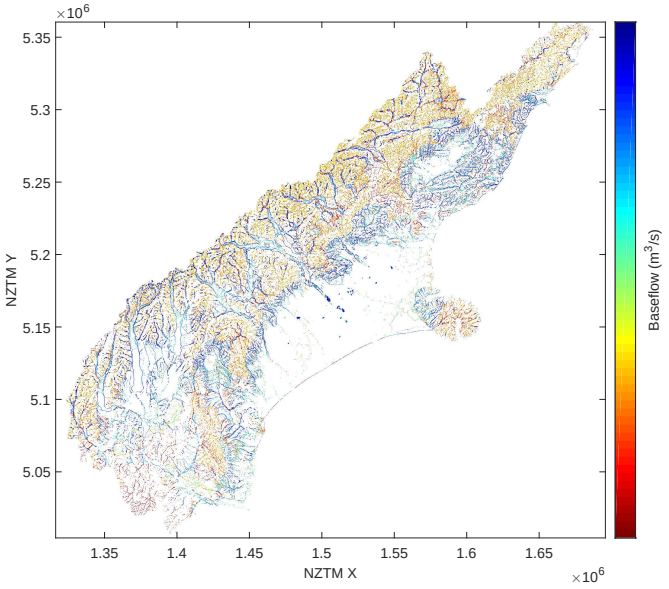

Figure 5.32: Estimate of location and relative volume of baseflow. Red=low, Blue=high, White = no baseflow

discharge to submarine springs; (2) the effects of major water abstraction; or (3) a wrong assumption of hydraulic conductivity of the subsurface.

Groundwater discharge into the ocean

Hanson and Abraham (2009) showed that seepage from alpine rivers to deeper groundwater flow in the Central Plains of Canterbury re-emerges near the coast in a groundwater chemistry study. Given the hydrogeology of the Canterbury Plains, described in section 5.4.1 and depicted in Figure 5.8, this water can also re-emerge on the continental shelf, in submarine springs. If groundwater flow patterns from the area with deeper ground-observed water table to these submarine springs would exist, they could (partly) explain the large difference between EWT depths and ground-observed water tables. Since the EWT model boundary constraints are at the land-sea interface, the model cannot incorporate for possible outcrops under the sea. Although the occurrence of submarine springs near the Canterbury Region has been suggested long since (e.g., Mandel, 1974), the existence of these continental shelf springs has not been proven. Since there are no readily available data to test this theory, I will leave this as a possible explanation.

Water abstraction, including downward and upward trends in groundwater

EWT depths only take into account a natural water table, i.e., no human interference. Major water abstraction, causing a long-term gradual decline of the water table, could explain why observed water tables are deeper than modelled ones. This theory was tested by analysing a subset of ground-observed water depths over time at locations where the difference between EWT depths and ground-observed median of that water depth is larger than 50 m. At some wells trends show a declining water table between 1976 and 1985 and between 2000 and 2007, but also upward trends from 1985 to 1988 and from 2007 to 2013 (Figures 5.33 and 5.34). No trend causing a total water level decline more than 50 m was found, except for in one well (Figure 5.34c). Declining water trends, whether or not caused by water abstraction, could cause differences between ground-observed water tables and EWT depths that are in the order of tens of metres. However, they are not the main cause of the large differences ($>$ 50 m) found. Relative groundwater level for the entire subset also does not show changes larger than 10 m (Figure 5.35). This relative groundwater level was estimated by calculating the median of monthly ground-observed groundwater depth of the subset, with each well in the subset first corrected by its overall median groundwater depth.

Downward and upward trends in groundwater could be caused by climate (drier or wetter years), which makes rainfall and river recharge lower, and could be amplified, as groundwater use might be higher in drier periods. For example, annual rainfall in the Canterbury Region, as derived from VCS data (see Chapter 4), was relatively low in the period 2001-2007 (Figure 5.36), which coincides with

the declining groundwater depths in wells. Other wetter periods (e.g., 1986-1988, 1994-1996) coincide with higher groundwater levels in wells (Figures 5.33, 5.34 and 5.35). However, the years 1978 - 1980 were relatively wet, which does not agree with a declining water table (Figures 5.33c, 5.34a,b, and 5.35).

There can be more explanations for the difference in groundwater trends. For example:

- downward and upward groundwater trends can be an effect of water policy, e.g., the effect of lower allocation limits for an area;
- while some parts of an aquifer are directly recharged by rainfall, others could have a delayed supply from further or deeper aquifer layers, which cannot be incorporated for in the EWT model;
- irrigation using river water could supply extra groundwater;
- colder winters could store water as snow in the mountains, which would then largely disappear as runoff in spring and summer (and recharge groundwater, but relative little through river recharge).

This non-extensive list shows that further conclusions can only be drawn with more detailed research and possibly more detailed and advanced groundwater flow models. Improvement to the EWT method might be possible and are therefore recommended for further research. However, they are deemed beyond the scope of the study described in this thesis.

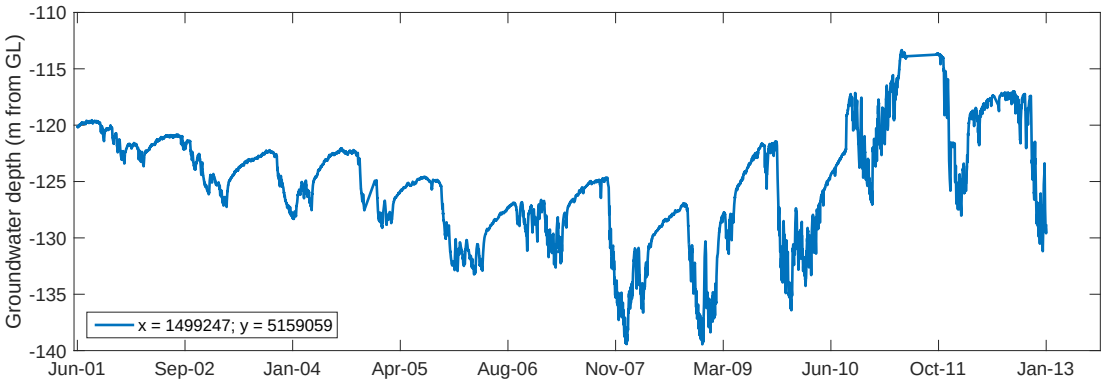

(a)

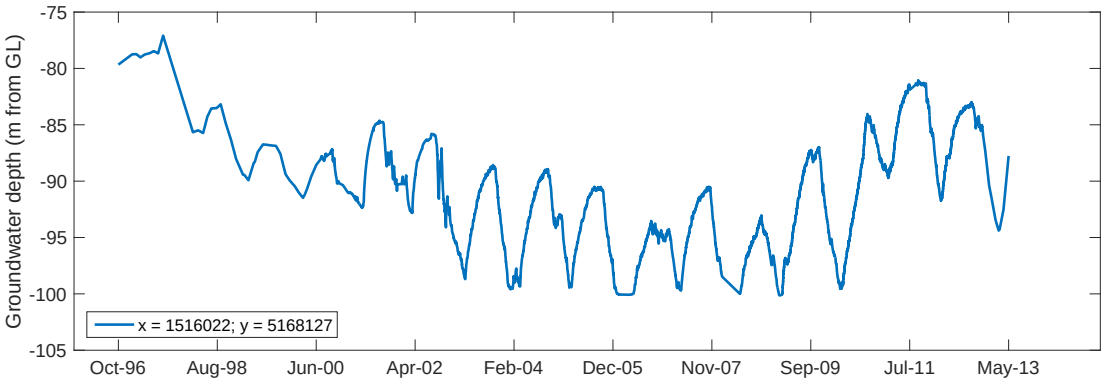

(b)

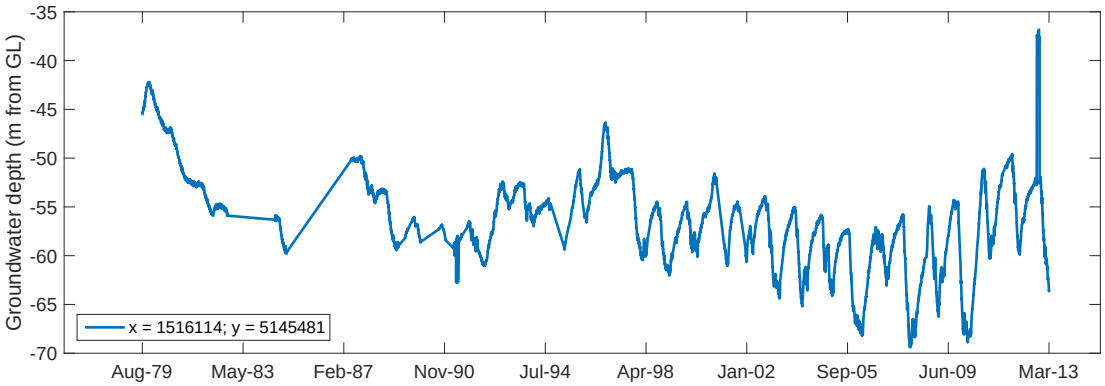

(c)

Figure 5.33: Groundwater depths in some Canterbury Wells. Courtesy of Environment Canterbury.

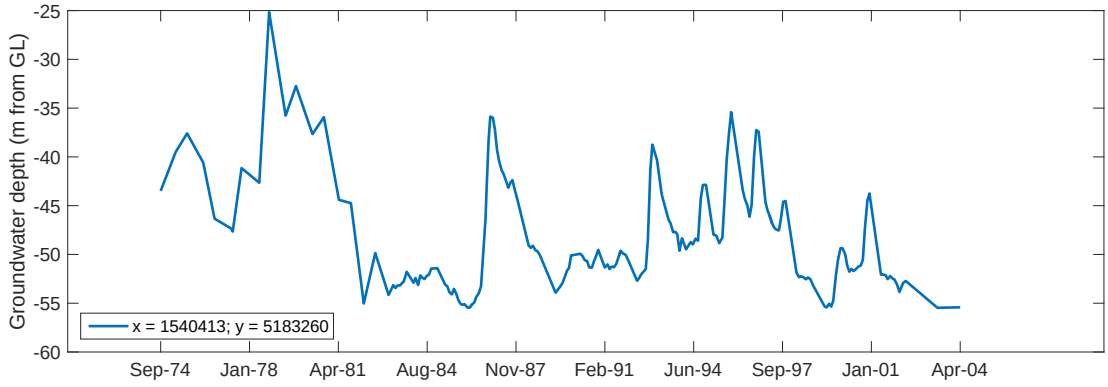

(a)

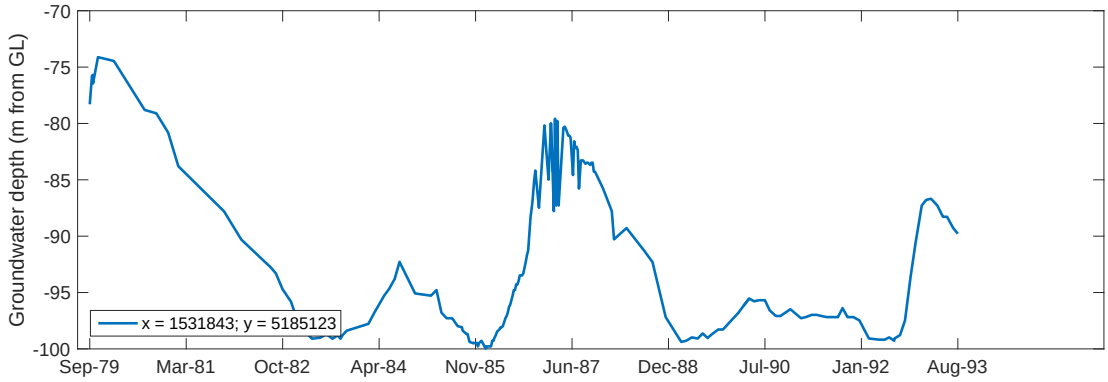

(b)

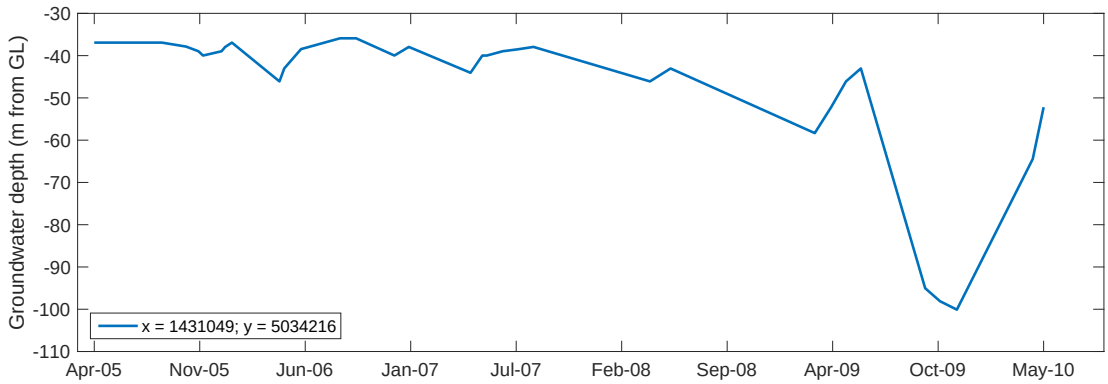

(c)

Figure 5.34: Groundwater depths in some Canterbury Wells. Courtesy of Environment Canterbury.

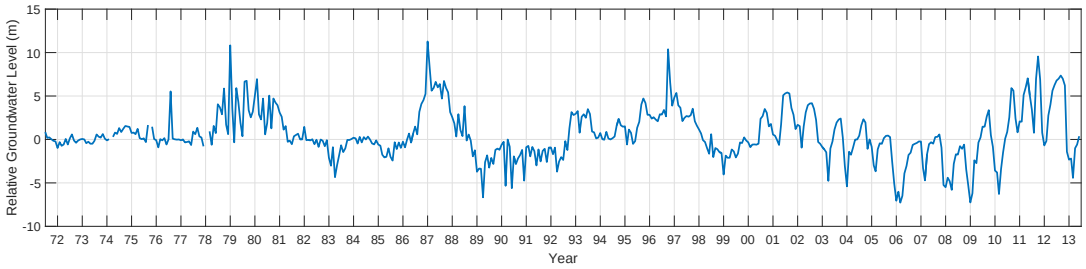

Figure 5.35: Relative groundwater depth for the Canterbury Region from 1972 to 2013, estimated for subset of wells that differ more than 50 m from the EWT depths.

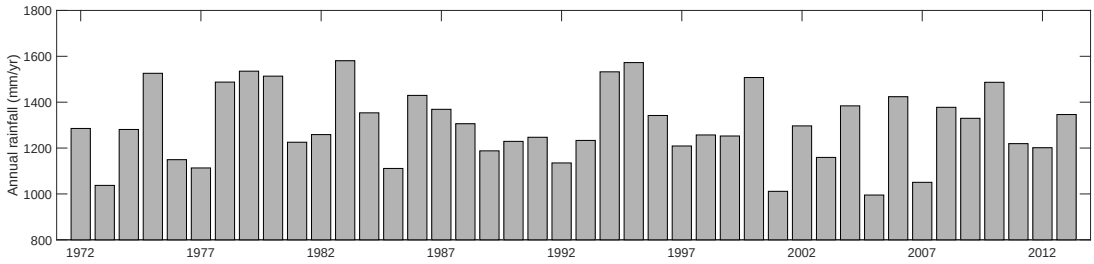

Figure 5.36: Annual rainfall for the Canterbury Region from 1972 to 2013.

Hydraulic conductivity

Initial assumed values, taken from a look-up table approach (see Annex), cannot account well for geological heterogeneity. A large part of the Canterbury Plains are considered gravel: the EWT model assumes a same median values of 90 m/day for all of these formations, which is only slightly lower than values of 103 m/day used by Lough and Williams (2009). However, in reality these gravels are very heterogeneous. The standard deviation of K, which can be as large as the value of K itself, is only taken into account by randomly changing the K value for each model time step. A theory was therefore tested: depending on the differences between EWT depths and ground-observed water tables, the value of K was changed for another model run. This was done based on the difference between ground-observed median (GM) water table and EWT depths:

$$K_{new} = K + K_{adj} \tag{5.7}$$

with all K having unit [m/day] and with K_{adj} scaled with a factor α (unit: [day]).

$$K_{adj} = \frac{GM - EWT}{\alpha} \tag{5.8}$$

The factor α is, arbitrarily and after some test runs, chosen as 0.66. Equation 5.7 was applied iteratively: after each 10 years of model runs K was further adjusted.

EWT model runs with the adjusted K lead to EWT depths that compare better with the ground-observed median values. First, the map of further adjusted EWT depths shows deeper groundwater in the areas between the major rivers (Figure 5.37). Second, absolute difference between further improved EWT (Figure 5.38) are smaller than before (Figure 5.28 for the original and Figure 5.29 for the improved), indicating the EWT improves even further when hydraulic conductivity is adjusted. Third, the correlation of EWT depths with ground-observed data (Figure 5.39) is much higher than the evaluation of the original EWT method (Figure 5.11b). Cross-plots of water table depth (mBGL, Figure 5.39b) however, do show a significant improvement as a result of the K adjustment (Table 5.5). Adjusted values of K (Figure 5.40) suggest that hydraulic conductivity of the Canterbury Plains gravels can be much higher than the median value from the nation-wide K estimate. The EWT model adjusts K to values in between 100 and 700 m/day, with values increasing closer to the foothills (Figure 5.40).

The interpreted results of this adjustment, i.e. that values of K might be much higher than their initial assumed value, are considered a qualitative indication. After all, they are analysed of having the most influence on larger differences between the observed and modelled groundwater table, but they can still also partly be caused by water abstraction, submarine springs, or be a combined effect of all factors. Furthermore, the model is not (yet) adjusted properly for K values higher than 200 m/day, as the model gives an unknown uncertainty if groundwater flow travels further than one cell per daily time step. Ideally, the EWT model should therefore be adjusted to run with smaller time steps in these areas for better results. Further recommended better estimation of K is a more detailed incorporation of the geology than the approach described in Appendix C. This approach should then take into account other file attributes of the digital geological map (such as age, or other infill - silt, sand, clay etc - of the main sediment type gravel).

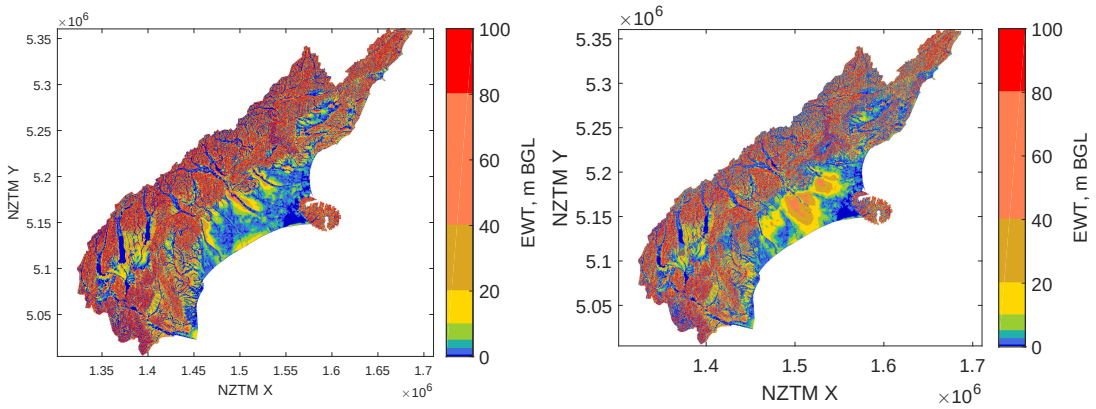

(a) improved EWT

(b) improved EWT with adjusted K

Figure 5.37: Water table depths for the improved EWT method (a) and the improved EWT method + adjusted K (b) for the Canterbury Region.

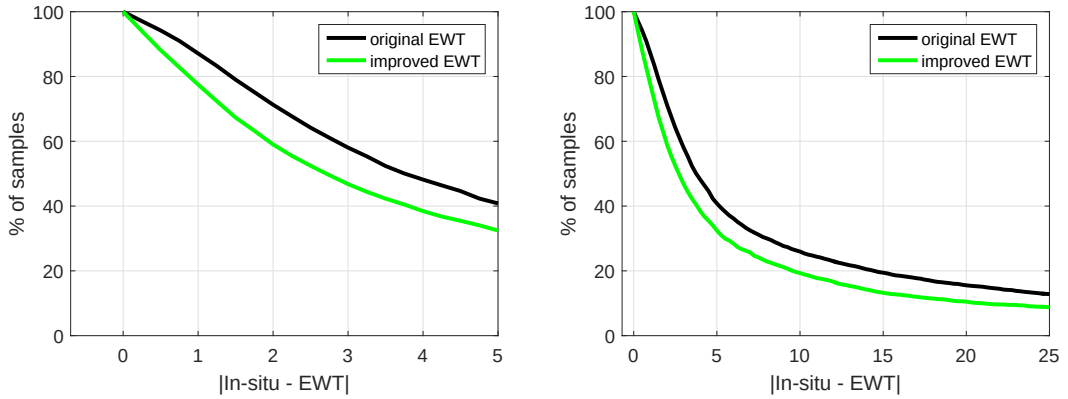

(a) 0-5 m (b) 0-25 m

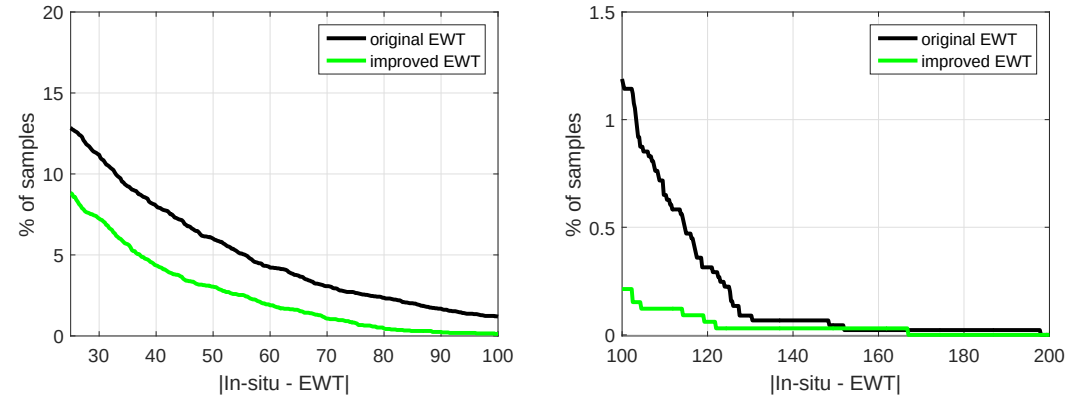

(c) 25-100 m (d) 100-200 m

Figure 5.38: Absolute difference between improved 'EWT + K adjustment' depths and ground-observed median values in Canterbury.

Terrain model

Correlation of EWT depth (mBGL) is still lower than that of the EWT hydraulic head (masl). I give two explanations for this. First, the model calculates head, which is then referenced to metres below ground level (mBGL). That correction, using a terrain model with uncertainties. Second, measured static water levels do not necessarily represent the true median water level. Both differences are significant, i.e. several metres or more, when shown on the scale of the relative low values of EWT depth in mBGL, but become less significant when using the data in masl. It is recommended to use the data in masl for implementation in groundwater flow models, as hydraulic head is a direct input in such models.

Table 5.5: Percentage of occurrence of absolute difference between EWT depths and ground-observed median values of water tables in Canterbury

	Original EWT (%)	Improved EWT (%)	Improved EWT + adjusted K (%)
< 1	13	21	22
< 3	42	51	53
> 50	6.0	5.8	3.0
> 100	1.2	0.85	0.12

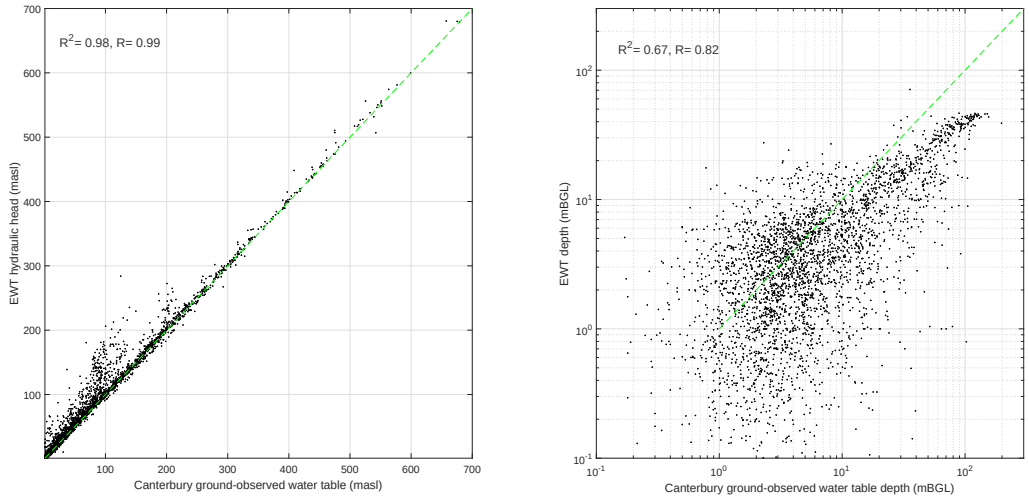

(a) metres above sea level (masl)

(b) metres below ground level (mBGL)

Figure 5.39: Cross plots of median observed groundwater depths and calculated improved EWT depths, including adjustment of K, in the Canterbury Region. The green line is the 1:1 relation.

Table 5.6: Comparison of correlation coefficient R for the (1) original, (2) improved and (3) improved including K adjustment.

	EWT original	EWT improved	EWT improved + K adjustment
masl	0.98	0.98	0.99
mBGL	0.07	0.34	0.82

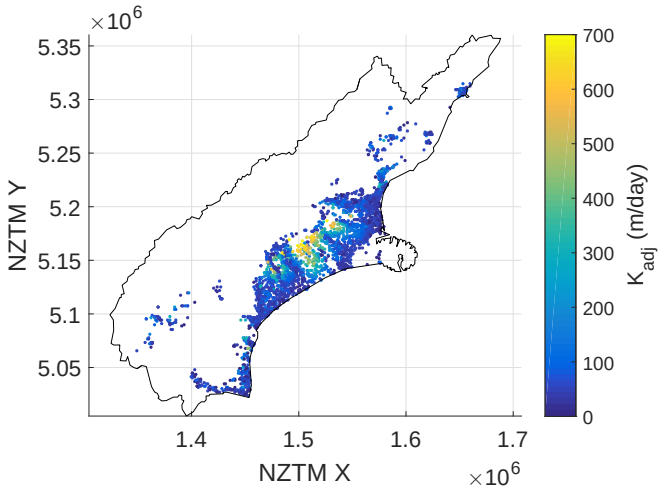

Figure 5.40: Adjusted hydraulic conductivity for the Canterbury Region.

5.7 Comparison of improved EWT depths in the Waipa River catchment

Rawlinson (2014) performed a review on existing information in the Waipa River catchment (Figure 5.41). They used information on water level from 758 wells located in the Waipa River catchment. These ground-observed water levels, either static levels or the median of multiple observations over time, were used to create a surface of the water table (i.e., a potentiometric surface). Although using relatively many ground observations, the data over the catchment is sparse. This is mainly because data is concentrated more in some areas than others and most wells are located in the centre and north-east of the catchment. EWT depths can thus provide a better spatial insight in the water table in these data sparse areas, provided that they correlate well enough with the ground observations.

The EWT model was run on a catchment level, where K values were adjusted using the ground-observed water levels, as described in section 5.6.1.

The spatial pattern of the EWT depths visually matches the potentiometric surface of (Figure 5.43) well. It shows more detail than the potentiometric surface, and also reveals water table depth at places where the potentiometric data does not yield data. In a cross-plot, the EWT hydraulic head (Rawlinson, 2014) shows a high correlation with the ground-observed data plotted in masl (Figure 5.44a, R=0.95). Correlation with ground-observed data is low (Figure 5.44b, R=0.25), where many EWT depths are lower than ground-observed values.

A too detailed terrain model in nation-wide application would require a, currently, too significant computational effort. However, on the regional scale, this might be applicable. Three different elevation models with resolutions of 200m, 100 m and 50 m were tested. These models were derived from a LIDAR-based 10m resolution terrain model, which is expected to have a better vertical accuracy than the national terrain model by Geographx (2012). The difference between the nation-wide terrain model Geographx (2012) and the regional model, both scaled to 100 metre resolution, can be more than 150 m (Figure 5.45). Approximate median difference is 9m for all terrain data, 5 m for low-lying areas ($<$ 20 m masl), and increases with altitude, up to 30 m for elevations higher than 800 m (Table 5.7). These differences are greater than most groundwater levels referenced to ground level. Because of this observational bias, correlation plots referenced to mBGL should not be used as a means to quantify the results of the EWT model. However, these correlation plots can be used to measure possible model improvement through the use of different elevation models. Better model results are expected due to a more accurate elevation, and a higher resolution terrain input allows the model to discharge more water to surface, resluting in less shallow water tables. This was already suggested in section 5.4.6. Therefore, some further testing was done, where the effect of using better accuracy and higher resolution elevation was tested. The 100 metre resolution EWT depths, both in masl and mBGL, (Figure 5.48) yields improved correlation (R=0.41, Figure 5.46). Using

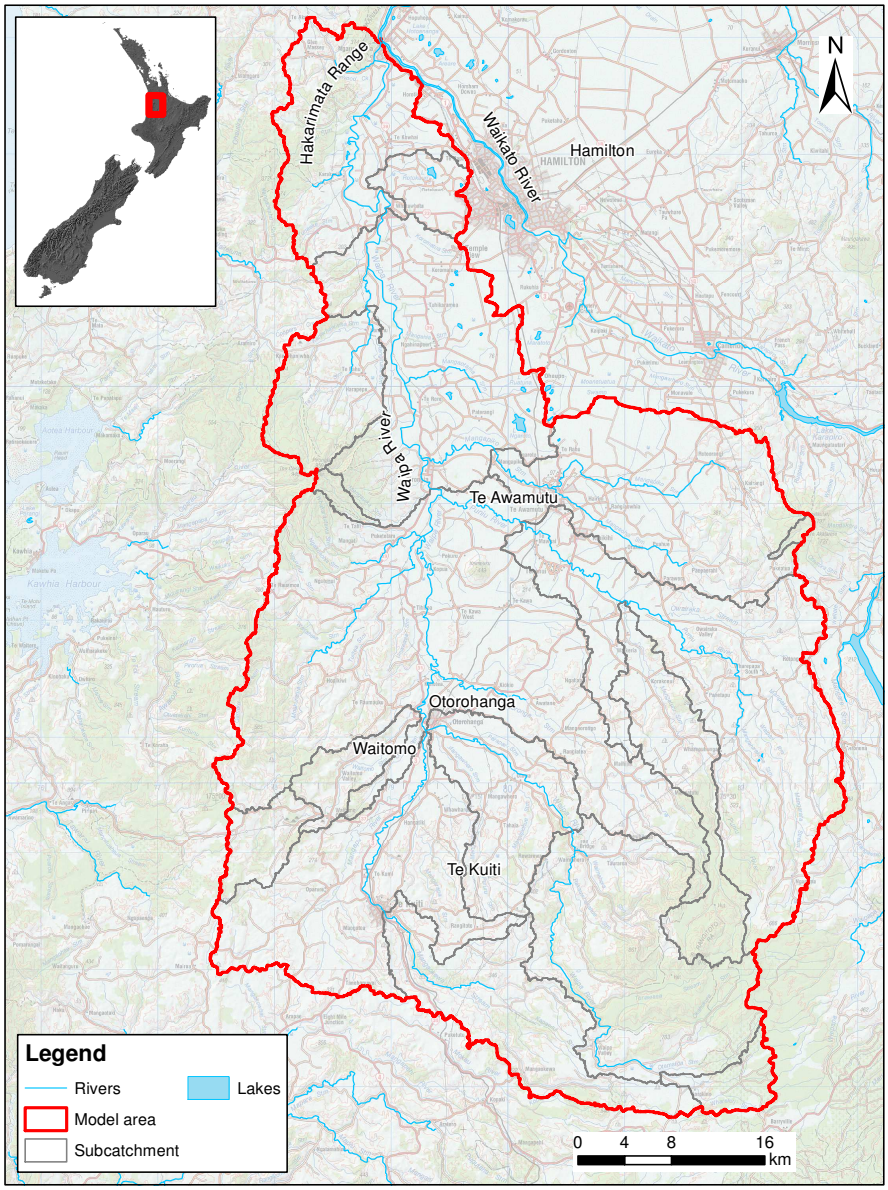

Figure 5.41: Waipa River catchment, Waikato.

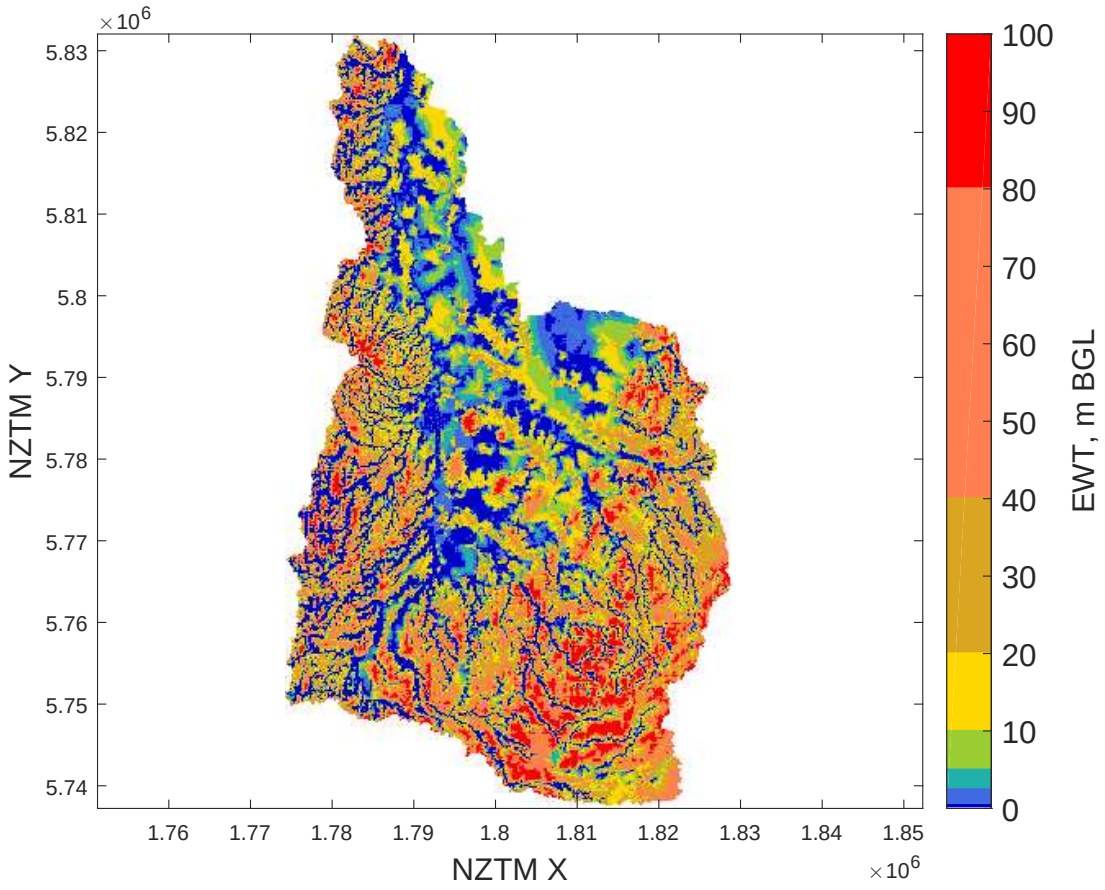

Figure 5.42: Improved Equilibrium Water Table for the Waipa Region.

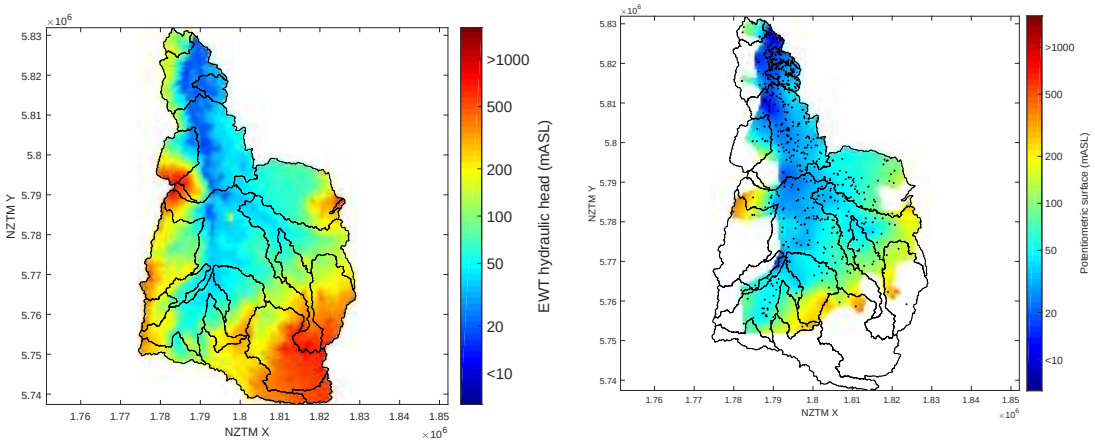

(a) EWT 2016

(b) Potentiometric surface (Rawlinson, 2014)

Figure 5.43: EWT hydraulic head (a) and potentiometric surface (b) from Rawlinson (2014) in the Waipa catchment. Ground observations used for this surface are shown in black dots.

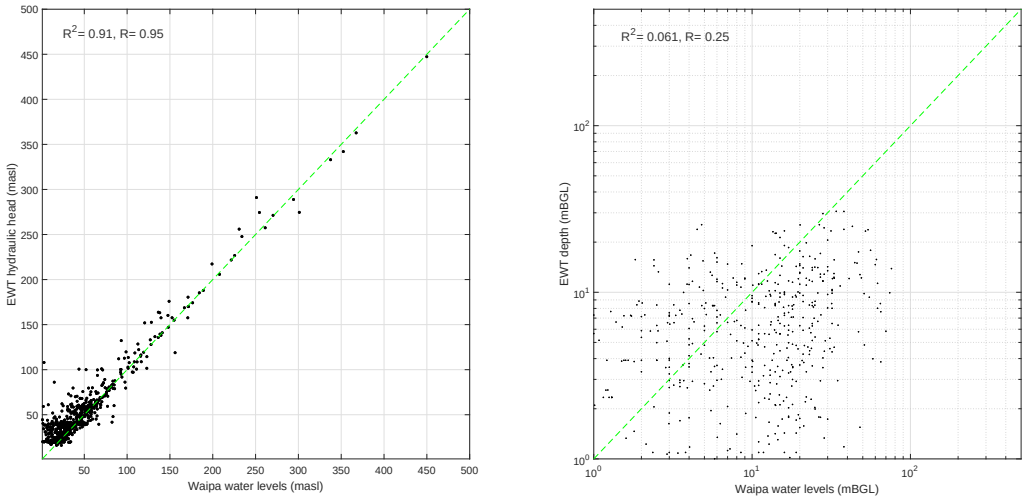

(a) masl (Rawlinson, 2014)

(b) mBGL (Rawlinson, 2014)

Figure 5.44: Cross-plot of the **(a)** EWT hydraulic head with ground-observed water levels in metres above sea level (masl) and **(b)** EWT depth with ground observed water levels in metres below ground level (mBGL) Rawlinson (2014). The green line is the 1:1 relation.

the 50 metre resolution model does not yield significantly better results (R=0.43) and more model areas show artefacts as shown in Figure 5.47 (see discussion in section 5.8).

Some further testing was done, where the whole Waikato Region was taken as a model area, to incorporate for possible groundwater flow out of the Waipa catchment into the Waikato. This did not lead to any substantial differences.

Table 5.7: Absolute differences between regional and national terrain model.

	Median absolute difference (m)
Overall	8.7
$<$ 20 m elevation	4.2
20 m $<$ elevation $<$ 50 m	4.6
50 m $<$ elevation $<$ 100 m	7.1
100 m $<$ elevation $<$ 200 m	12.1
200 m $<$ elevation $<$ 400 m	14
400 m $<$ elevation $<$ 800 m	13.3
elevation $>$ 800m	30

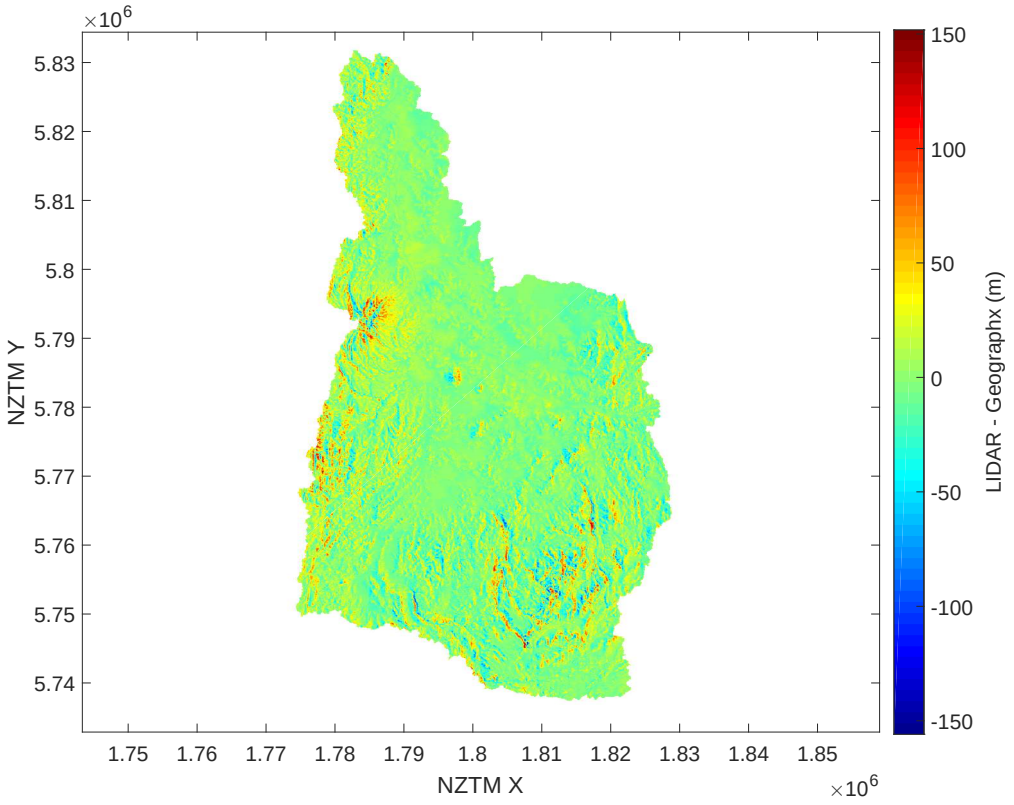

Figure 5.45: Difference between the national terrain model and the LIDAR based regional terrain model in the Waipa River catchment.

Table 5.8: Correlation coefficients of improved EWT depths (masl and mBGL) and ground observations, using different terrain models.

	R-masl	R-mBGL	runtime (minutes)
200m Geographx based	0.95	0.25	18
200m LIDAR based	0.96	0.26	18
100m LIDAR based	0.97	0.41	118
50m LIDAR based	0.97	0.43	328

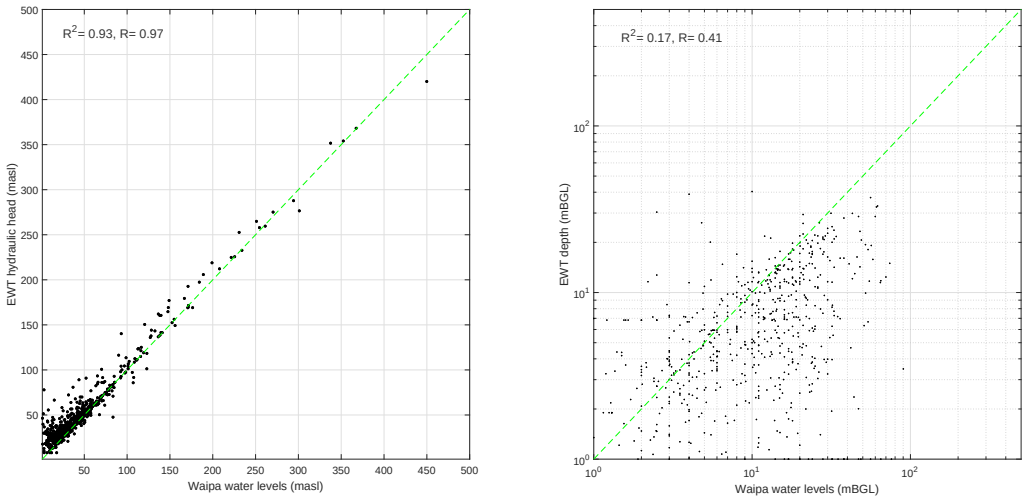

(a) masl (Rawlinson, 2014)

(b) mBGL (Rawlinson, 2014)

Figure 5.46: Cross-plot of the **(a)** EWT hydraulic head with ground-observed water levels in metres above sea level (masl) and **(b)** EWT depth with ground observed water levels in metres below ground level (mBGL) after Rawlinson (2014). EWT data are based on the 100m LiDAR based elevation model. The green line is the 1:1 relation.

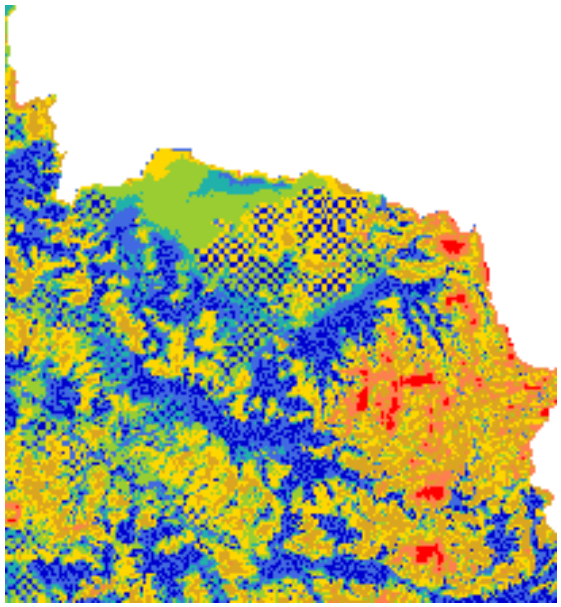

Figure 5.47: Model artefacts occurring at 50 m resolution.

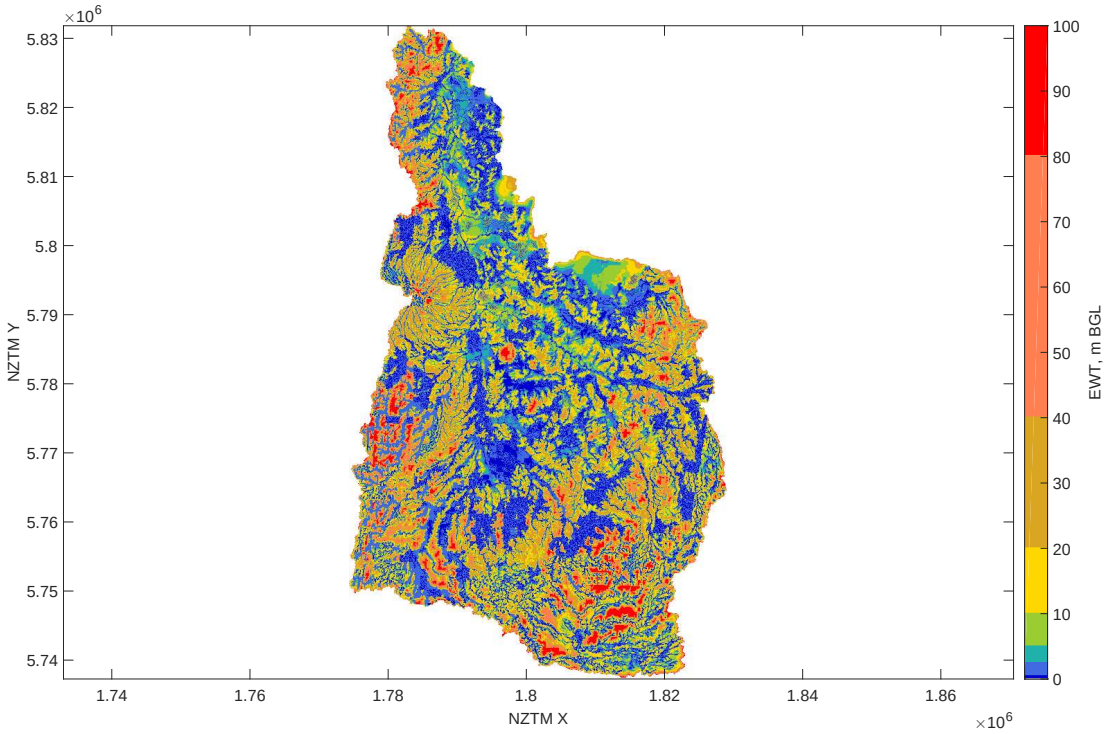

Figure 5.48: EWT depth for the Waipa River catchment, based on a 100m resolution LIDAR based terrain model.

5.8 Discussion

The EWT method is useful for pointing out locations of possible alluvial aquifers on a regional to national scale, including its most likely water table. The improved EWT method furthermore shows that the high-resolution (i.e., 200 m x 200 m in my experiment) hydraulic head can be used on the regional scale,where it fills in the gaps or interpolates between sparse ground observations. These can for example be used as initial estimate for groundwater flow models.

The improved EWT method also calculates groundwater flow direction and amplitude, as well as a qualitative indicator of where groundwater will discharge to surface and contribute to baseflow. This indicator can be useful for further research. For example, if groundwater in an area is known to contain high nitrate concentration or other polluting nutrients, 'nutrient hotspots' can indicate where this pollution is likely to come to surface. However, exact number on baseflow remains a topic for improvement. Since the EWT depths tend to be more shallow than ground-observed data, the baseflow indication could yield different numbers. However, it could also be that this shallow water indeed is drained to surface, either by preferential flow paths, or by trees (leading to more evapotranspiration). More research in the field of groundwater-surface water(-atmosphere) model interaction is therefore recommended.

Large errors in EWT depths (in mBGL) remain. In the evaluation of the original

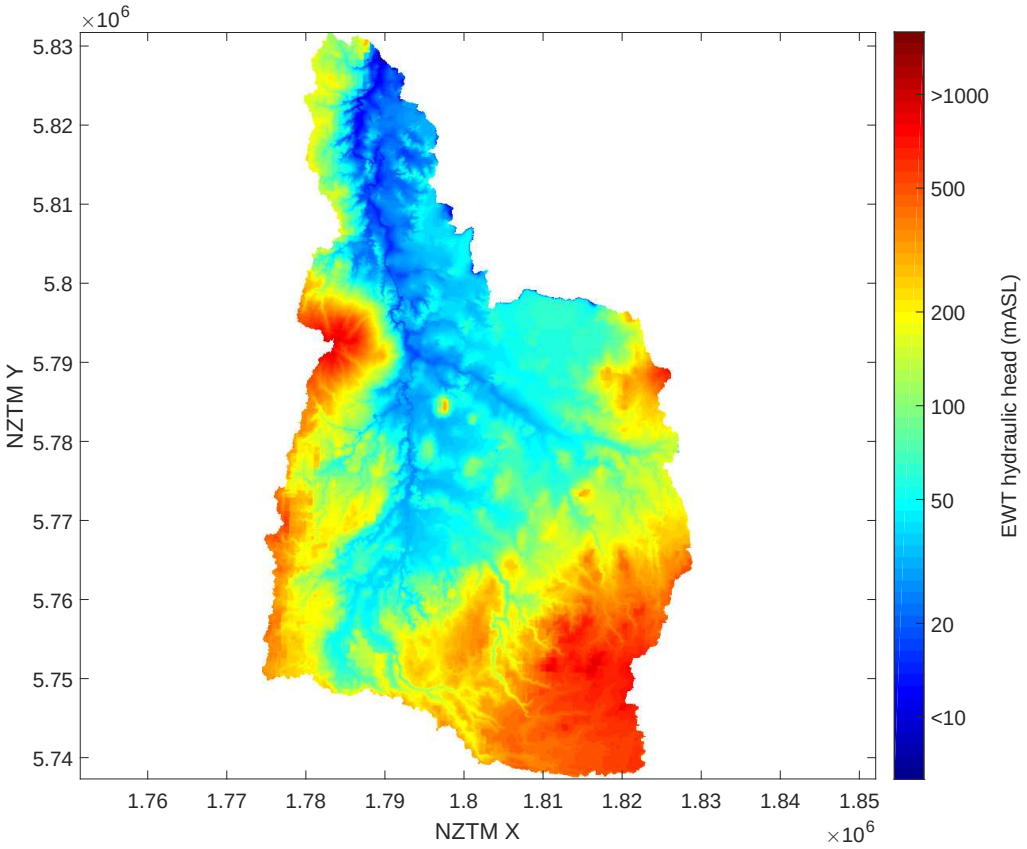

Figure 5.49: EWT hydraulic head (masl) for the Waipa River catchment, based on a 100m resolution LIDAR based terrain model.

EWT method in Canterbury main causes for these errors were deemed: input data; hydrogeological complexity; and observational bias. Input data was improved in this chapter by using better nation-wide input data. This improved correlation between modeled and ground-observed water levels in mBGL, but still large errors remain, where (1) EWT depth models a shallower water table in many places, and (2) the cross-plots show much 'scatter' around the 1:1 relation of the cross-plot. Explanations for (1) and (2) are mainly found in the hydrogeological complexity and the terrain. These and other explanations are described below.

Hydrogeological complexity

Adjustment of the K values on a model pixel cell improves the model, with improvement of the mBGL correlation in the Canterbury Plain, and some improvements on the Waipa Region. The issue remaining is the hydrogeological complexity. Although better geological data was used, the hydrogeological complexity on the smaller scale still remains. For example, in Canterbury, gravels are very heterogeneous and the most likely cause for the differences found between EWT depths and ground-observed data. Based on that analysis, some of the heterogeneity issues can now be solved, leading to better estimates of K and to better EWT depth estimates. More research on these topics is recommended, and could be: (1) running the model to convergence of K,, which would require a significantly larger computational effort (2) A physics-based approach to derive hydraulic conductivity with direct inversion of the model equation. Another main factor of hydrogeological complexity is the occurrence of preferential flow paths, e.g., through cracks and faults. This can still not be tackled by the simplified EWT model, nor by any other model commonly applied in New Zealand.

Terrain model

The difference between a regional terrain model in the Waipa River catchment and the national input data was far greater than many EWT depth in mBGL,i.e., up to 10 metres or more. This is not new, as large errors in SRTM-based data was already noted by e.g. (Westerhoff et al., 2013) This bias leads to significant noise in the EWT depth (mBGL). Therefore, to reduce the significance of this observational bias, correlation between EWT depth and water table should therefore be done in metres above sea level (masl). Practically, this means that hydraulic head should be compared to ground-observed water levels or potentiometric surface in masl. However, comparison of correlation plots in mBGL are still important for model improvement. For the Canterbury Plains, the mBGL correlation was a much better metric for model improvement than the masl correlation. Correlation of data in mBGL also leads to better metrics of the measuring improvement of terrain model input data, e.g., further improvement of the terrain model leads to higher mBGL correlation in the Waipa River catchment (from 0.25 to 0.41, using the national model and the 100m LiDAR regional elevation model,respectively).

Use of a better terrain model leads to better results, but also to further limitations. First, model runtime increases. Second, EWT model artefacts start to occur. These model artefact were noted in both the Waipa River catchment and the Canterbury Plains. They are mainly caused by the model cell and flow limitations: due to too small model cells the model cannot transport groundwater over more than one cell distance. This model limitation is recommended to be improved by a flexible time interval of the EWT model time steps, which are currently fixed at daily. Third, use of a LiDAR-based elevation model can still lead to errors up to several metres. Although LiDAR data can be quite accurate (in the order of centimeters, Begg and Mouslopoulou, 2010), averaging data over larger areas and subsequent comparison with ground-observed data can lead to an observational bias of some metres, which increases at steeper sloped terrain.

Other possible explanations for differences between EWT depths and ground observations

Other issues and possible explanations for differences between EWT depth and ground-observed water level were raised in the case study discussions in the Canterbury Plains and Waipa River catchment is the effect of major water abstraction and the irrigation of that water back into groundwater recharge. In the Canterbury Plains, long-term time series were analysed for a significant decrease of water table. This study showed that wrongly assumed K values explain the very deep water tables better than data on water abstraction, however it is likely that deeper water tables are a combined effect of high K values, water abstraction, or even unknown discharge to coastal submarine springs or other catchments. Both groundwater abstraction and irrigation can be put in the model without any theoretical problems, but the data is not available in most regions. Furthermore, these data are water allocation values and not values of real used water. Therefore, those data were deemed too uncertain and were not used in the model.

Possible improvements to the EWT method might be dealing with incorporation of the effect of water allocation limits, irrigation from surface water, the effect of snow storage, recharge from rivers from losing streams, and the effect of deeper, confining layers. However, they are deemed beyond the scope of the study described in this thesis, as inclusion of such advanced methodology also decreases the computational strength of the model, which is fast computation on a nationwide, inter-regional and regional scale. Although inclusion of these topics might benefit the EWT model for research on drought impact, some input needed is not widely known or, if known, have a large uncertainty (e.g. exact water take, irrigation). Inclusion of these data could therefore lead to erroneous are very uncertain model outputs of EWT depths. Furthermore, inclusion of these data might incur the model to go beyond its possibilities: after all, the EWT method applies a simplified model with known limitations. I therefore decided not to include these additional data in my research.

5.9 Conclusion

The EWT method is useful for pointing out locations of possible alluvial aquifers on a regional to national scale, including its most likely water table. The original EWT model correctly calculates that the water table is generally shallow in New Zealand's alluvial aquifer systems, but an evaluation of the original EWT method applied in the Canterbury Plains showed many differences with ground observations. Therefore, the improved EWT method was applied, which contains improvements in model input data (recharge, geology, terrain) and model improvements (resolution, time step, advanced model algorithms). Re-evaluation of improved EWT depths shows that the high-resolution (i.e., 200 m x 200 m in my experiment) hydraulic head can be used on the regional scale, where it fills in the gaps or interpolates between sparse ground observations. In the Canterbury Plains and Waipa River catchment correlation of EWT hydraulic head with ground observations is high, and it can be used as an initial high-resolution estimate for groundwater flow models in data-sparse areas. Improved EWT depths match ground observations better then the original EWT depths in the Canterbury Plains. The improved EWT method yields a higher resolution water table (200 m) than the original EWT (1000 m). It also calculates a correction for the rainfall recharge (i.e., where water tables are too shallow for the recharge to fit), and a qualitative indicator of where groundwater will discharge to surface and contribute to baseflow. However, large errors in the EWT depth remain, which are mostly visible when comparing modelled and observed data in metres below ground level. Localised an in-depth analyses in the Cantebury Plains and Waipa River catchment shows that these differences are most likely caused by wrong estimates of hydraulic conductivity K and errors in terrain models, but that water abstraction and groundwater discharge to submarine springs or other catchments can also play a role. Localised iterative adjustments in hydraulic conductivity K, embedded in the model, show that the EWT method can be further improved on the local scale: K values in between the Canterbury major rivers can be further adjusted and these show that K is much higher than initially assumed; and iterative adjustment of these K values leads to better estimates of water tables in the Canterbury Plains and Waipa River catchment. These estimates of K are considered qualitative: they lead to better fitting EWT depths, but errors remain. As the current strength of the model is fast computation of initial water tables in data-sparse areas, the model was chosen not to be further improved, as such advanced use would make the model too computationally demanding for current computing facilities. However, further research on such advanced use could be: (1)further estimation of K; (2) flexible model time steps; (3) better terrain model input (if available on the national scale); and (4) inclusion of reliable water abstraction data.

6

Synthesis of research questions and efficient combination

This thesis has described the application of satellite data to groundwater studies. Chapters 2 to 5 of this thesis describe a wide variety of implementation of satellite data for use in hydro(geo)logical research. I have shown that estimation of evapotranspiration, soil moisture, and rainfall recharge to groundwater can be improved by satellite data, and that uncertainty information from such estimates can also be calculated. The introduction of this thesis identified three research questions:

1. Do satellite-derived data of the terrestrial water cycle, merged with ground-observed or modelled data, lead to better estimation of water cycle variables, especially those that are important for the characterisation of groundwater volumes and flux changes and subsurface hydraulic properties in New Zealand?
2. Can we simulate the uncertainties of these above estimations?
3. Can satellite-derived data of terrestrial water cycle parameters aid to better indicate and characterise New Zealand's aquifers?

The answer to question 1 is mostly 'yes'. Chapter 2 describes a national dataset on evapotranspiration based on (MODIS) satellite data. That dataset is both useful as an individual product in a wide range of hydro-meteorological research, as well as for estimates of rainfall recharge to groundwater (as shown in chapter 4). The satellite ET data, combined with ground observations, make a good interpolator, which is most useful in data-sparse regions. Furthermore, the satellite data contain vegetation information, which is shown to be useful for New Zealand, as the national standard data (of Penman PET) does not contain that information. Chapter 3 describes application of satellite microwave (Sentinel-1) data that can be used to estimate soil moisture. Although the large data volume can be problematic, and local application can compare poorly to ground observations, rolling out this method for national use is possible if future recommendations are followed up and high-performance computing facilities are used for that nation-wide

application. However, more research is needed on why some results compare well with most ground observations and some not. Satellite soil moisture is best combined with modelled and ground-observed data, for various reasons, and similar to satellite ET is therefore best used as a tool to interpolate or constrain ground-observed data (i.e., use the data trend and not the absolute values). Chapter 4 shows that nationwide datasets, i.e., satellite ET and vegetation, create more opportunity for development of nation-wide models in combination with other national data, such as soil and geological databases. The rainfall recharge dataset is the first nationwide dataset of its kind, and can thus lead to more valuable insights in hydrogeological research, such as the quantification of mountain recharge. If this rainfall recharge model is then used as input in a groundwater flow model (Chapter 5), estimates of fluxes of groundwater to the surface (i.e., baseflow) can be made on the national scale, and estimates of hydraulic conductivity can be adjusted where groundwater level is known.

The answer to question 2 is 'yes'. Uncertainty of satellite-derived data was estimated for ET (Chapter 2) by a comprehensive error propagation of the Penman-Monteith evapotranspiration model, and taking into account the error that already exists at ground-estimated ET. The 'non-uniqueness' of the soil moisture inversion algorithm is shown to give uncertainty to the estimated soil moisture from satellite backscatter, but this uncertainty can be quantified. Incorporation of ET data, including uncertainty, into a nation-wide model of rainfall recharge (Chapter 4) that also propagates all errors into its model equation, is shown to be beneficial to the estimation of that rainfall recharge uncertainty. However, a problem that is identified in this thesis is the fact that uncertainty stems from multiple causes. For example, soil moisture has a wide range of uncertainties, caused by: (1) soil heterogeneity; (2) technical sensor placement and calibration; (3) mathematical uncertainty of the inversion model; and (4) physics boundary conditions (that are shown to effect interferometric measurement). Furthermore, the use of a too simple vegetation model can cause extra uncertainty. Also, a too low resolution or low-quality terrain model caused uncertainty in rainfall recharge and soil moisture estimation.

The answer to question 3 is also mostly 'yes', but identification of data and model limitations before use of satellite data are important. Chapter 5 showed that use of multiple nation-wide data, amongst which are satellite data, helps to point out locations of alluvial aquifers on a regional to national scale, including its most likely water table. The method correlates well with groundwater tables and can thus be used to point out other areas where water tables are shallow. It is the only nation-wide groundwater model in New Zealand and because it covers the nation, it can: (1) identify unexplored areas where groundwater is likely to be close to surface; (2) point out where there is inconsistency between different regional groundwater models; and (3) aid in regional, inter-regional and national groundwater volume estimates. It furthermore helps to better estimate hydraulic conductivity at places with a well-known water level. This method however, shows to be limited to the quality of the terrain model when calculating water table depth from surface. The (partly satellite-derived) terrain model shows that large

errors in the terrain model propagate into the model outcome, which becomes significant when water tables are referenced to surface level. Although better terrain data (i.e. LIDAR) are available, these mostly constrain national use, as these models are local to regional. Furthermore, the model has shortcomings in areas where an aquifer is confined by impermeable layers at depth. Also, the model stops at the sea and it cannot therefore not (yet) calculate groundwater discharge in submarine springs. Like most other groundwater model, this nation-wide groundwater does not incorporate conduit groundwater flow, e.g. through faults, or tile drainage.

The concept of 'efficient combination' (explained in the introductory Chapter 1) is interwoven in my thesis. Chapter 2 explains that satellite data are more uncertain than ground-observed data, and therefore should always be used in conjunction with ground observations. A dedicated and efficient combination was therefore developed, which uses satellite data as 'part of the puzzle' and not as a separate entity. After all, if satellite data were used as a separate entity, it could be that they do not correlate well enough with ground observations of soil moisture or ET. One could conclude from that finding that satellite data are therefore not useful. In my opinion, that is a short-sighted conclusion. Of course, one cannot expect that a satellite signal, measuring from hundreds, or thousands, of kilometres from the Earth has the same data quality as ground-observed data. However, my research digs deeper, because it takes into account uncertainty of satellite measurements and also uncertainty of ground observations (that are usually treated as non-negotiable in terms of quality). Knowing the limitation of satellite data makes them a powerful additional tool to estimate terrestrial water cycle variables and even groundwater fluxes. This is especially shown in Chapter 2, where MOD16 data have higher uncertainty than ground observations, but can still be used to interpolate these ground observations to any national standard of ET (in this case Penman PET). From Chapter 3 one can surmise that ground observations can be constrained with soil moisture ranges and interpolated with soil moisture data trends (if satellite and ground-observed data compare well). Satellite data can also be used to better constrain bias in water cycle variables. An example is described in chapter 4, where an unknown bias of (ground-observed) rainfall, i.e. it can either underestimate or overestimate, introduces an unknown error in the error propagation model of rainfall recharge. This problem relates to all data, whether they are satellite or ground-observed. Although this problem is not solved in this thesis, it seems straightforward that the use of multiple data sources, e.g. satellite data, might aid in better quantification of that error. Further research is therefore recommended to better constrain bias in ground-observed or modelled water cycle variables. The use of satellite rainfall data, when used in an efficient way to fill gaps in unknown areas, might also aid a better rainfall estimate. Developments of such methods could be set up similar to the described ET estimation method. In my opinion, one should not rule out data just because they do not compare to what we expect or are used to. Satellite data should be used as one of the many available data resources, as similarly used in standard geophysical practice, where e.g. geophysical data is used as soft

information to interpolate between boreholes (see introductory chapter 1). I hope to have shown that the concept of efficient combination can be applied with large data sets, such as satellite data.

This research has led to multiple datasets of satellite-derived terrestrial water cycle variables. Using the findings of his thesis, further efficient combinations can be developed. For example, original MOD16 AET and PET can be linked to soil water deficit through empirical findings (Chapter 2). Using this nation-wide ET derived soil water deficit can be used in combination with satellite soil moisture data to better constrain the often large uncertainty of inverted microwave soil moisture, or in combination with soil moisture sensors. This was not tackled in my research, because of multiple reasons. First, data on Sentinel-1 is relatively new: currently, there is less than two years of historical data. Second, the ground-observed soil moisture currently used should be calibrated: preferably, multiple sensor stations should be used for one location to resolve better for soil heterogeneity. Satellite-derived data could also be used to constrain (too) high values of ground-observed soil moisture. Third, areas of dense vegetation, i.e. forests, should be identified, as satellite soil moisture does not penetrate the canopy in these areas. Using such an approach of efficient combination could lead to a better spatially resolved (nation-wide) soil water deficit input. In its turn, that could then be used in (national) rainfall recharge models. Future research should therefore focus on more of such efficient combination methods of satellite data with ground observations and models.

7 Conclusions

Satellite data of water cycle variables can play an important role in filling in data gaps in data-sparse regions and models. This thesis has applied water cycle variables of evapotranspiration, soil moisture and vegetation, mostly on a nation-wide scale, to better inform nation-wide models of groundwater and its recharge, including more knowledge on uncertainty. This was mainly done using the approach of an efficient combination between satellite data and existing ground data, databases and models. This concept of efficient combination, interwoven in this thesis, has been proven to be a successful approach when using satellite data to better estimate groundwater fluxes and other aquifer properties. This was already suggested in the introduction, proven in my research chapters, and further elaborated in an overarching synthesis. By digging deeper than standard practice and knowing uncertainties and limitations of satellite data, it has been shown that satellite data can be used as an additional dataset for groundwater assessment and characterisation in areas where other data are sparse. Satellite ET estimates are useful for interpolation of existing ground-observed ET data. Soil moisture can be derived from satellite data and might be used to constrain uncertainty in ground observations. Satellite data can help develop national datasets and models of rainfall recharge and groundwater flow. This research has resulted in several novel New Zealand nationwide models and datasets. Answers to the research questions have been mostly positive: (1) satellite-derived data of the terrestrial water cycle leads to better estimation of groundwater volume and flux changes and subsurface hydraulic properties in New Zealand; (2) uncertainty of these estimates can be quantified, although quantification of bias in measurements remains a problem; and (3) satellite-derived data of terrestrial water cycle parameters are useful to better indicate and characterise New Zealand's aquifers. Several important conclusions were drawn in the four main topics of this thesis, i.e., on evapotranspiration, soil moisture, rainfall recharge and groundwater flow models. These are outlined in the following topics.

Evapotranspiration

To obtain a national dataset of ET, MOD16 PET data were projected to Penman reference crop ET_0 (Penman PET). This has resulted in a nation-wide 1 km x 1 km monthly ET_0 estimation that validates well with ground-observed data. The method, using uncertainty of ground-observed ET_0, also estimates uncertainty of this national gridded product. Comparison of ground-observed ET_0 with original MOD16 PET data shows that original MOD16 PET data might fit real PET (and not reference crop ET) very well, as it follows expected seasonal trends and is the only estimate taking into account vegetation characteristics on a national scale. This research incorporates uncertainty of both ground-observed and satellite ET, where in most studies ground observations are treated as 'the gold standard'. Currently used ground-observed Penman ET_0 shows uncertainty in between 10% and 40% of ET_0, for high and low ET_0, respectively. It also shows that ET_0 is most sensitive to temperature, followed by solar radiation, cloudiness ratio and relative humidity. Using the uncertainty and the satellite data, a 'soft interpolator' between the ground observations has been built. The resulting ET_0 estimates also contain an uncertainty estimate. The proposed method enhances the capability of using global satellite data products on a catchment scale, hereby abiding local measurement standards. Comparison between the P-M derived MOD16 PET and ground-observed ET_0 suggests that it is very well possible that the original MOD16 can be applied directly in a PET and AET estimation. Original MOD16 AET resembles expected values, and also compares better than alternative modelled data at lysimeters in Canterbury. MOD16 PET, AET, and the newly derived ET_0 estimates, could serve as alternative to currently existing datasets in New Zealand. Penman PET has shown to be mistaken for real PET in some studies in New Zealand.

Soil moisture

Physics experiments and models were tested to develop more insight of the impact of use of Sentinel-1 SAR data in New Zealand. These experiments led to the following conclusions, summarised below.

First, minor differences in reflection properties of the material, such as a seasonal soil moisture change over time, can cause substantial differences in phase and amplitude of the backscatter. These differences are caused by the boundary conditions of electromagnetic reflection and transmission and lead to phase differences between different satellite overpasses. These phase difference translated to a distance of 5 - 8 mm for C-band microwave data, which can pose significant noise for interferometric (e.g. InSAR) data analyses of terrain motion.

Second, a synthetic model was built that calculates backscatter, based on a semi-empirical existing method to calculate backscatter from a soil (PRISM) and a method to calculate backscatter from vegetation (S^2RTR). This model was used in an analyses of the method to its input components (e.g., soil type, soil moisture,

incidence angle, soil density, vegetation optical depth). These numerical and visual analyses show that, for bare soil, microwave backscatter is most sensitive to surface roughness (when surface roughness is small), soil moisture, and incidence angle. Backscatter should be corrected for local terrain features when applied in synthetic models. Backscatter is also sensitive to vegetation, and as a result of that becomes relatively less sensitive to the other input components.

Third, the synthetic model was combined with a genetic algorithm-based model and with that was able to solve for surface soil moisture using satellite microwave backscatter data as an input. This iterative model, 'the inverse model', demands multiple pairs of backscatter (σ_0) and incidence angle θ as input data, i.e. it uses multiple neighbouring pixels of a satellite image. Using these multiple $\sigma_0 - \theta$ pairs solves for the non-uniqueness of the soil moisture solution and also solves for soil moisture in (light) vegetation scenarios. However, use of multiple pixels downscales the resolution of the solution (in my example from 10x10m to 1000x1000m). This model was tested with randomly 'pseudo-field' data, covering a range of incidence angles and backscatter values. The pseudo-field test shows that the genetic algorithm solves well for soil moisture in the range of 0 and 0.35 m^3 m^{-3} with an RMSE and standard deviation that are both lower than 0.05, if smart subsets are chosen (i.e. high incidence angle, high backscatter, and ks>2).

Sentinel-1 data was inverted using this algorithm and compared to monthly data from ground-observed soil moisture. Although some comparisons with ground stations seem to follow expected trends in soil moisture, in general the inverted results are not deemed reliable at this stage, and more research is needed to improve reliability. This research should focus on: the use of longer satellite time series; a more accurate terrain model; correlation between large model-data discrepancies and other land classifications (i.e. soil type, land-use, vegetation patterns, terrain slope); and anisotropy.

National rainfall recharge to groundwater

An approach was developed to estimate rainfall recharge across New Zealand using the available nation-wide datasets on rainfall, (satellite) evapotranspiration, (satellite) elevation, soil and geology. The result is a rainfall recharge model (NGRM), which estimates 1 km x 1 km monthly rainfall recharge from January 2000 to December 2013. All rainfall recharge estimates contain a model uncertainty estimate. National model output shows that national rainfall recharge compiles to approximately 3,538 m^3/s, or 421 mm/yr, with a model uncertainty (1σ) of 15%. Although the NGRM model is uncalibrated, its recharge estimates compare well to Canterbury lysimeter stations and the local models that have been applied there. They are lower than locally modelled recharge in the mid-Mataura, but still match those findings when taking tino account uncertainty, whereas they also appear to show a more realistic distribution of recharge values than the local polygon-based model. Furthermore, they match findings of mean annual recharge in the Waimakariri catchment in Canterbury, although also showing distinct spa-

tial difference in some areas. The nation-wide rainfall recharge model gives a valuable initial estimate when applied at the local or regional scale, and can thus also be used at areas as a valuable initial estimate in data-sparse areas. Some local application might require the model to be calibrated, but it is recommended to carefully consider model limitations and quality of input components (e.g. rainfall and ET) for local application, as these seem to cause the largest uncertainty. This research also provides improved insights into the uncertainty of rainfall recharge models, including the role of recharge model input components.

National (EWT) groundwater flow model and water table

The EWT method is useful for pointing out locations of possible alluvial aquifers on a regional to national scale, including its most likely water table. The improved EWT method shows that the high-resolution (i.e., 200 m x 200 m in my experiment) hydraulic head can be used on the regional scale,where it fills in the gaps or interpolates between sparse ground observations. In regional case studies EWT hydraulic head correlates well with ground observations and it can thus be used as an initial high-resolution estimate of hydraulic head for groundwater flow models in data-sparse areas. Improved EWT depths referenced to surface match ground observations better then the original EWT depths in the Canterbury Plains, and the improved EWT model is able to calculate improved estimates of hydraulic conductivity. The improved EWT method yields a higher resolution water table (200 m) than the original EWT (1000 m). It also calculates a correction for the rainfall recharge (i.e., where water tables are too shallow for the recharge to fit), and a qualitative indicator of where groundwater will discharge to surface and contribute to baseflow. Large remaining errors in the EWT depth, referenced to ground level, are most likely caused by wrong estimates of hydraulic conductivity K, errors in terrain models, but water abstraction and groundwater discharge to submarine springs or other catchments can also play a role. Iterative adjustments in K, embedded in the model, show that: K values in between the Canterbury major rivers are much higher than initially assumed; and iterative adjustment of these K values leads to better estimates of water tables in the Canterbury Plains and Waipa River catchment.

Recommendations

The above research chapters have led to valuable insights, as well as recommendations for further research, which are:

- temporal up-scaling of monthly satellite ET to daily ET estimates using existing gridded (VCS) data;
- replacement of Penman PET in current (VCS) data to a better estimate of FAO56 reference crop ET;

- a merge between MOD16 AET and other AET (e.g. from Woods et al. (2006)), as quality of satellite data decreases with topography and dense forest;
- use of MOD16 AET and PET to derive soil water deficit and estimation of irrigation volumes. Further combination of such a product with satellite microwave and ground-observed soil moisture;
- dedicated inversion schemes to derive vegetation properties from microwave backscatter data;
- focus on collaborative research in the fields of groundwater and surface water to improve estimates rainfall-runoff, snowmelt, river recharge, rainfall, and evapotranspiration;
- incorporation of heterogeneity in elevation, soil and geology in spatial scaling and fracture zones in the geology of mountainous areas on rainfall recharge;
- more advanced application of the national groundwater model to (1)further adjust K; (2) have flexible model time steps; (3) a better terrain model, once available; and (4) inclusion of reliable water abstraction data;
- more research on the role of satellite (soil moisture and ET) data to better constrain bias in other ground-observed or modelled (rainfall, ET and soil water deficit) estimates;
- similar algorithms for improvements of rainfall estimates through satellite data.

References

Ahnert, F., 1970. Functional relationships between denudation, relief, and uplift in large, mid-latitude drainage basins. American Journal of Science 268 (3), 243–263.

Ahrens, C. D., 2007. Meteorology today: an introduction to weather, climate, and the environment, 8th Edition. Thomson/Brooks/Cole, Belmont, CA.

Alkhaier, F., 2016. Land surface recharge calculations for the Waimakariri groundwater model. In review Report No. R16/10, Environment Canterbury Regional Council.

Allen, R. G., 1998. Crop evapotranspiration: guidelines for computing crop water requirements. No. 56 in FAO irrigation and drainage paper. Food and Agriculture Organization of the United Nations, Rome.

Allen, R. G., Bastiaanssen, W., Tasumi, M., Morse, A., 2001. Evapotranspiration on the watershed scale using the SEBAL model and Landsat images. ASAE Meeting Presentation, paper 01-2224.

Alley, W. M., 2002. Flow and storage in groundwater systems. Science 296 (5575), 1985–1990.

Alley, W. M., Leake, S. A., 2004. The journey from safe yield to sustainability. Groundwater 42 (1), 12–16.

Anderson, M. C., Norman, J. M., Mecikalski, J. R., Otkin, J. A., Kustas, W. P., 2007. A climatological study of evapotranspiration and moisture stress across the continental United States based on thermal remote sensing: 1. Model formulation. Journal of Geophysical Research 112 (D10117), 1 – 17.

Arnold, J., Allen, P., 1999. Automated methods for estimating baseflow and ground water recharge from streamflow records. Journal of the American Water Resources Association 35 (2), 411–424.

Attema, E. P. W., Ulaby, F. T., 1978. Vegetation modeled as a water cloud. Radio Science 13 (2), 357–364.

Auckland Regional Council, 1999. Guidelines for stormwater runoff modelling in the Auckland region. Technical Publication 108, prepared by Becca Carter Hollings and Ferner Ltd., Auckland Regional Council.

Australian National University, 2014. ANUSPLIN vrsn 4.4. Accessed October 31, 2014.
URL http://fennerschool.anu.edu.au/research/products/anusplin-vrsn-44

Baldocchi, D., Falge, E., Gu, L., Olson, R., Hollinger, D., Running, S., Anthoni, P., Bernhofer, C., Davis, K., Evans, R., Fuentes, J., Goldstein, A., Katul, G., Law, B., Lee, X., Malhi, Y., Meyers, T., Munger, W., Oechel, W., Paw, K. T., Pilegaard, K., Schmid, H. P., Valentini, R., Verma, S., Vesala, T., Wilson, K., Wofsy, S., 2001. FLUXNET: a new tool to study the temporal and spatial variability of ecosystemscale carbon dioxide, water vapor, and energy flux densities. Bulletin of the American Meteorological Society 82 (11), 2415–2434.

Bandaragoda, C., Tarboton, D. G., Woods, R., 2004. Application of TOPNET in the distributed model intercomparison project. Journal of Hydrology 298 (1-4), 178–201.

Barnhart, W. D., Lohman, R. B., 2013. Characterizing and estimating noise in InSAR and InSAR time series with MODIS: InSAR time series error analysis. Geochemistry, Geophysics, Geosystems 14 (10), 4121–4132.

Barrett, B., 2012. The use of C- and L-band repeat-pass Interferometric SAR coherence for soil moisture change detection in vegetated areas. The Open Remote Sensing Journal 5 (1), 37–53.

Bastiaanssen, W., Menenti, M., Feddes, R., Holtslag, A., 1998a. A remote sensing surface energy balance algorithm for land (SEBAL). Part 1: Formulation. Journal of Hydrology 212–213, 198–212.

Bastiaanssen, W., Noordman, E., Pelgrum, H., Davids, G., Thoreson, B., Allen, R., 2005. SEBAL model with remotely sensed data to improve water-resources

management under actual field conditions. Journal of Irrigation and Drainage Engineering 131 (1), 85–93.

Bastiaanssen, W., Pelgrum, H., Wang, J., Ma, Y., Moreno, J., Roerink, G., van der Wal, T., 1998b. A remote sensing surface energy balance algorithm for land (SEBAL).: part 2: Validation. Journal of Hydrology 212-213, 213–229.

Becker, M., 2006. Potential for satellite remote sensing of ground water. Groundwater 44 (2), 306–318.

Begg, J. G., Mouslopoulou, V., 2010. Analysis of late Holocene faulting within an active rift using lidar, Taupo Rift, New Zealand. Journal of Volcanology and Geothermal Research 190 (1-2), 152–167.

Beven, K. J., Kirkby, M. J., 1979. A physically based, variable contributing area model of basin hydrology / Un modéle à base physique de zone d'appel variable de l'hydrologie du bassin versant. Hydrological Sciences Bulletin 24 (1), 43–69.

Bojinski, S., Verstraete, M., Peterson, T. C., Richter, C., Simmons, A., Zemp, M., 2014. The concept of essential climate variables in support of climate research, applications, and policy. Bulletin of the American Meteorological Society 95 (9), 1431–1443.

Booker, D., Woods, R., 2014. Comparing and combining physically-based and empirically-based approaches for estimating the hydrology of ungauged catchments. Journal of Hydrology 508, 227–239.

Böttcher, C. J. F., 1978. Dielectrics in time-dependent fields, 2nd Edition. Elsevier Scientific Pub. Co, Amsterdam.

Breshears, D. D., Myers, O. B., Johnson, S. R., Meyer, C. W., Martens, S. N., 1997. Differential use of spatially heterogeneous soil moisture by two semiarid woody species: Pinus edulis and juniperus monosperma. The Journal of Ecology 85 (3), 289–299.

Brouwer, J., Helbig, K., 1998. Shallow high-resolution reflection seismics, 1st Edition. No. 19 in Handbook of geophysical exploration, seismic exploration. Elsevier, Amsterdam.

Brown, L., 2001. Canterbury. In: Rosen, M.R., White, P.A. eds. Groundwaters of New Zealand. New Zealand Hydrological Society, pp. 441–459.

Buis, A., 2011. NASA, Japan release improved topographic map of Earth. Ac-

cessed July 2013.
URL http://www.nasa.gov/topics/earth/features/aster20111017.html

Burberry, L., Moore, C., Dumbleton, B., 2013. Towards an improved understanding of the Knapdale aquifer: a modelling study of anomalous nitrate levels in the Knapdale groundwater zone. ESR Report Envirolink Grant 1206-ESRC254, ESR.

Burman, R. D., Pochop, L. O., 1994. Evaporation, evapotranspiration and climatic data. No. 22 in Developments in atmospheric science. Elsevier, Amsterdam.

Calmels, D., Galy, A., Hovius, N., Bickle, M., West, A. J., Chen, M.-C., Chapman, H., 2011. Contribution of deep groundwater to the weathering budget in a rapidly eroding mountain belt, Taiwan. Earth and Planetary Science Letters 303 (1-2), 48–58.

Carnec, C., Fabriol, H., 1999. Monitoring and modeling land subsidence at the Cerro Prieto geothermal field, Baja California, Mexico, using SAR interferometry. Geophysical Research Letters 26 (9), 1211–1214.

Chandrasekhar, S., 1960. Radiative transfer. Dover Publications, New York.

Cherkauer, D. S., Ansari, S. A., 2005. Estimating ground water recharge from topography, hydrogeology, and land cover. Ground Water 43 (1), 102–112.

Chunfeng Ma, Xin Li, Shuguo Wang, 2015. A Global Sensitivity Analysis of Soil Parameters Associated With Backscattering Using the Advanced Integral Equation Model. IEEE Transactions on Geoscience and Remote Sensing 53 (10), 5613–5623.

Clark, M., Örn Hreinsson, E., Martinez, G., Tait, A., Slater, A., Hendrickx, J., Owens, I., Gupta, H., Schmidt, J., Woods, R., 2009. Simulations of seasonal snow for the South Island, New Zealand. Journal of Hydrology (NZ) 48 (2), 41–58.

Clark, M. P., Rupp, D. E., Woods, R. A., Zheng, X., Ibbitt, R. P., Slater, A. G., Schmidt, J., Uddstrom, M. J., 2008. Hydrological data assimilation with the ensemble Kalman filter: Use of streamflow observations to update states in a distributed hydrological model. Advances in Water Resources 31 (10), 1309–1324.

Coleman, G., DeCoursey, D. G., 1976. Sensitivity and model variance analysis

applied to some evaporation and evapotranspiration models. Water Resources Research 12 (5), 873–879.

Cook, P., Stauffacher, M., Therrien, R., Halihan, T., Richardson, P., Williams, R., Bradford, A., 2001. Groundwater recharge and discharge in a saline, urban catchment. CSIRO technical report 39/01, CSIRO Land and Water.

Cronshey, R., 1986. Urban hydrology for small watersheds. Technical Report TR-55, 164p., US Dept. of Agriculture, Soil Conservation Service, Engineering Division.

Danielsen, J. E., Auken, E., Jørgensen, F., Søndergaard, V., Sørensen, K. I., 2003. The application of the transient electromagnetic method in hydrogeophysical surveys. Journal of Applied Geophysics 53 (4), 181–198.

Davis, J. L., Annan, A. P., 1989. Ground-penetrating radar for high-resolution mapping of soil and rock stratigraphy. Geophysical Prospecting 37 (5), 531–551.

De Jeu, R., Owe, M., 2003. Further validation of a new methodology for surface moisture and vegetation optical depth retrieval. International Journal of Remote Sensing 24 (22), 4559–4578.

De Jeu, R., Wagner, W., Holmes, T., Dolman, A., van de Giesen, N., Friesen, N., 2008. Global soil moisture patterns observed by space borne microwave radiometers and scatterometers. Surveys in Geophysics 28, 399–420.

De Roo, R., Du, Y., Ulaby, F., Dobson, M., Apr 2001. A semi-empirical backscattering model at L-band and C-band for a soybean canopy with soil moisture inversion. Geoscience and Remote Sensing, IEEE Transactions on 39 (4), 864–872.

Dean, T., 2013. Scalable neuroscience and the brain activity mapping project. Accessed September 2013.
URL `http://cs.brown.edu/people/tld/note/blog/13/07/26/`

Dee, D. P., Uppala, S. M., Simmons, A. J., Berrisford, P., Poli, P., Kobayashi, S., Andrae, U., Balmaseda, M. A., Balsamo, G., Bauer, P., Bechtold, P., Beljaars, A. C. M., van de Berg, L., Bidlot, J., Bormann, N., Delsol, C., Dragani, R., Fuentes, M., Geer, A. J., Haimberger, L., Healy, S. B., Hersbach, H., Hólm, E. V., Isaksen, L., Kållberg, P., Köhler, M., Matricardi, M., McNally, A. P., Monge-Sanz, B. M., Morcrette, J.-J., Park, B.-K., Peubey, C., de Rosnay, P.,

Tavolato, C., Thépaut, J.-N., Vitart, F., 2011. The ERA-Interim reanalysis: configuration and performance of the data assimilation system. Quarterly Journal of the Royal Meteorological Society 137 (656), 553–597.

DHI, 2016. MIKE 2016: MIKE SHE Integrated catchment modelling. Accessed April 2016.
URL `http://www.mikepoweredbydhi.com/products/mike-she`

Dingman, S. L., 2002. Physical hydrology, 2nd Edition. Prentice Hall, Upper Saddle River, NJ.

Dobson, M., Ulaby, F., Hallikainen, M., El-rayes, M., 1985. Microwave dielectric behavior of wet soil-part II: dielectric mixing models. IEEE Transactions on Geoscience and Remote Sensing GE-23 (1), 35–46.

Doherty, J., 2016. PEST, Model-independent parameter estimation. User Manual Part I, 6th Edition. Watermark Numerical Computing.

Döll, P., 2009. Vulnerability to the impact of climate change on renewable groundwater resources: a global-scale assessment. Environmental Research Letters 4 (3), 035006, 12p.

Döll, P., Fiedler, K., 2008. Global-scale modeling of groundwater recharge. Hydrology and Earth System Sciences 12 (3), 863–885.

Dorigo, W., 2013. Personal communication: ASCAT and topography. Senior Scientist Remote Sensing Research Group, Department of Geodesy and Geinformation, Vienna University of Technology, Austria.

Doubková, M., Van Dijk, A., Sabel, D., Wagner, W., Blöschl, G., 2012. Evaluation of the predicted error of the soil moisture retrieval from C-Band SAR by comparison against modelled soil moisture estimates over Australia. Remote Sensing of Environment 120, 188–196.

Doyle, J. M., Gleeson, T., Manning, A. H., Mayer, K. U., 2015. Using noble gas tracers to constrain a groundwater flow model with recharge elevations: A novel approach for mountainous terrain. Water Resources Research 51 (10), 8094–8113.

Du, Y., Ulaby, F., Dobson, M., 2000. Sensitivity to soil moisture by active and passive microwave sensors. IEEE Transactions on Geoscience and Remote Sensing 38 (1), 105–114.

Dubois, P., Van Zyl, J., Engman, T., 1995a. Measuring soil moisture with imaging radars. IEEE Transactions on Geoscience and Remote Sensing 33 (4), 915–926.

Dubois, P., VanZyl, J., Engman, T., 1995b. Corrections to "Measuring soil moisture with imaging radars". IEEE Transactions on Geoscience and Remote Sensing 33 (6), page 1340.

EartH2Observe, 2015. Earth2observe website. Accessed February 18, 2015. URL http://www.earth2observe.eu

Effersø, F., Auken, E., Ingvard Sørensen, K., 1999. Inversion of band-limited TEM responses. Geophysical Prospecting 47 (4), 551–564.

El-Rayes, M., Ulaby, F., 1987. Microwave Dielectric Spectrum of Vegetation-Part I: Experimental Observations. IEEE Transactions on Geoscience and Remote Sensing GE-25 (5), 541–549.

Ellison, W., Balana, A., Delbos, G., Lamkaouchi, K., Eymard, L., Guillou, C., Prigent, C., 1998. New permittivity measurements of seawater. Radio Science 33 (3), 639–648.

ESA, 2007. InSAR principles: guidelines for SAR interferometry processing and interpretation. Vol. 19. ESA Publications, ESTEC, Noordwijk, The Netherlands, Ch. Part C. InSAR processing: a mathematical approach, pp. 1–115.

ESA, 2015a. SAFE specification. Accessed November, 2015. URL https://sentinel.esa.int/web/sentinel/user-guides/sentinel-1-sar/data-formats/safe-specification

ESA, 2015b. Sentinel-1 SAR user guide introduction. Accessed May, 2015. URL https://sentinel.esa.int/web/sentinel/user-guides/sentinel-1-sar

ESA, 2015c. Sentinels scientific data hub. Accessed November, 2015. URL https://scihub.copernicus.eu/

Estévez, J., Gaviln, P., Berengena, J., 2009. Sensitivity analysis of a Penman-Monteith type equation to estimate reference evapotranspiration in southern Spain. Hydrological Processes 23, 3342–3353.

Fan, Y., Li, H., Miguez-Macho, G., 2013a. Global patterns of groundwater table depth. Science 339 (6122), 940–943.

Fan, Y., Li, H., Miguez-Macho, G., 2013b. Global patterns of groundwater table depth: Supplementary material. Science 339 (6122), 58p.

Fan, Y., Miguez-Macho, G., 2010a. Potential groundwater contribution to Amazon evapotranspiration. Hydrology and Earth System Sciences 14 (10), 2039–2056.

Fan, Y., Miguez-Macho, G., 2010b. A simple hydrologic framework for simulating wetlands in climate and earth system models. Climate Dynamics 37 (1-2), 253–278.

Fan, Y., Miguez-Macho, G., Weaver, C. P., Walko, R., Robock, A., 2007. Incorporating water table dynamics in climate modeling: 1. water table observations and equilibrium water table simulations. Journal of Geophysical Research 112 (D10125).

Faneca Sanchez, M., Gunnink, J. L., van Baaren, E. S., Oude Essink, G. H. P., Siemon, B., Auken, E., Elderhorst, W., de Louw, P. G. B., 2012. Modelling climate change effects on a Dutch coastal groundwater system using airborne electromagnetic measurements. Hydrology and Earth System Sciences 16 (12), 4499–4516.

Ferretti, A., Monti-Guarnieri, A., Prati, C., Rocca, F., Massonnet, D., 2007. InSAR Principles - guidelines for SAR interferometry. processing and interpretation. part C. InSAR processing: a mathematical approach. ESA Training Manual TM-19, 115 p., ESA.

Fitts, C. R., 2013. Groundwater science, 2nd Edition. Academic Press, Amsterdam.

Foth, H., 1990. Fundamentals of Soil Science, 8th Edition. John Wiley and Sons, New York, Ch. 3, pp. 22–40.

Freeze, R., Cherry, J., 1979. Groundwater. Prentice-Hall, Inc., Englewood Cliffs, NJ.

Fung, A., Eom, H., 1979. Multiple scattering and depolarization by a randomly rough Kirchhoff surface. Technical Report 369-4, University of Kansas, Remote Sensing Lab, Lawrence, Kansas.

Fung, A., Li, Z., Chen, K., 1992. Backscattering from a randomly rough dielectric surface. IEEE Transactions on Geoscience and Remote Sensing 30 (2), 356–369.

Funning, G. J., Parsons, B., Wright, T. J., Jackson, J. A., Fielding, E. J., 2005. Surface displacements and source parameters of the 2003 Bam (Iran) earthquake

from Envisat advanced synthetic aperture radar imagery. Journal of Geophysical Research: Solid Earth 110 (B09406).

Gadani, D., Rana, V., Bhatnagar, S., Prajapati, A., Vyas, A., 2012. Effect of salinity on the dielectric properties of water. Indian Journal of Pure & Applied Physics (IJPAP) 50 (6), 405–410.

GCOS, 2010. Implementation plan for the global observing system for climate in support of the UNFCCC (2010 update). Report Number GCOS-138, GCOS Secretariat.

Gedney, N., Cox, P. M., 2003. The Sensitivity of Global Climate Model Simulations to the Representation of Soil Moisture Heterogeneity. Journal of Hydrometeorology 4 (6), 1265–1275.

GEO, 2014a. The GEOSS Water Strategy: From Observations to Decisions. Japan Aerospace Exploration Agency, Genveva ; Tokyo, accessed December, 2014.
URL ftp://ftp.earthobservations.org/TEMP/Water/GEOSS_WSR_Full_Report.pdf

GEO, 2014b. Group on earth observation. Accessed December 10, 2014.
URL http://www.earthobservations.org

Geographx, 2012. Geographx new zealand DEM 2.1. Accessed November 2015.
URL http://geographx.co.nz/_wp/wp-content/uploads/2012/12/GX-Terrain-Metadata.pdf

Gerrits, M., 2010. The role of interception in the hydrological cycle. PhD thesis, Technical University Delft, Delft, accessed December 2015.
URL http://repository.tudelft.nl/assets/uuid:7dd2523b-2169-4e7e-992c-365d2294d02e/thesis_gerrits.pdf

Gesch, D. B., Verdin, K. L., Greenlee, S. K., 1999. New land surface digital elevation model covers the earth. Eos, Transactions American Geophysical Union 80 (6), 69p.

GEWEX, 2014. Global energy and water exchange project. Accessed December, 2014.
URL http://www.gewex.org

Gleeson, T., Smith, L., Moosdorf, N., Hartmann, J., Dürr, H. H., Manning, A. H.,

van Beek, L. P. H., Jellinek, A. M., 2011. Mapping permeability over the surface of the earth. Geophysical Research Letters 38 (2), l02401.

Gleeson, T., VanderSteen, J., Sophocleous, M. A., Taniguchi, M., Alley, W. M., Allen, D. M., Zhou, Y., 2010. Groundwater sustainability strategies. Nature Geoscience 3 (6), 378–379.

Gleeson, T., Wada, Y., Bierkens, M. F. P., van Beek, L. P. H., 2012. Water balance of global aquifers revealed by groundwater footprint. Nature 488 (7410), 197–200.

Glenn, E. P., Morino, K., Didan, K., Jordan, F., C. Carroll, K., Nagler, P. L., Hultine, K., Sheader, L., Waugh, J., 2008. Scaling sap flux measurements of grazed and ungrazed shrub communities with fine and coarse-resolution remote sensing. Ecohydrology 1 (4), 316–329.

GLOWASIS, 2015. GLOWASIS website. Accessed February, 2015.
URL http://glowasis.eu

GNS Science, 2012. QMAP. Accessed March 2014.
URL http://www.gns.cri.nz/Home/Our-Science/Earth-Science/Regional-Geology/Geological-Maps/1-250-000-Geological-Map-of-New-Zealand-QMAP

Goldman, M., Neubauer, F. M., 1994. Groundwater exploration using integrated geophysical techniques. Surveys in Geophysics 15 (3), 331–361.

Gong, L., Xu, C.-y., Chen, D., Halldin, S., Chen, Y. D., 2006. Sensitivity of the Penman-Monteith reference evapotranspiration to key climatic variables in the Changjiang (Yangtze River) basin. Journal of Hydrology 329 (3-4), 620–629.

Grobe, H., 2000. Albedo-e_hg.png (PNG image, 1588x2220 pixels). Accessed July 2014.
URL http://upload.wikimedia.org/wikipedia/commons/e/e0/Albedo-e_hg.png

Gunnink, J., Maljers, D., van Gessel, S., Menkovic, A., Hummelman, H., 2013. Digital Geological Model (DGM): a 3D raster model of the subsurface of the Netherlands. Netherlands Journal of Geosciences 92 (1), 33–46.

Günther, T., Rcker, C., Spitzer, K., 2006. Three-dimensional modelling and inversion of dc resistivity data incorporating topography - II. Inversion. Geophysical Journal International 166 (2), 506–517.

Hallikainen, M. T., Ulaby, F. T., Dobson, M. C., El-Rayes, M. A., Wu, L.-K., 1985. Microwave dielectric behavior of wet soil-part 1: empirical models and experimental observations. IEEE Transactions on Geoscience and Remote Sensing 1, 25–34.

Hanson, C., Abraham, P., 2009. Depth and spatial variation in groundwater chemistry, Central Canterbury Plains. Environment Canterbury, Environment Canterbury, Investigations and Monitoring Group, Christchurch (NZ).

Hanssen, R. F., 1998. Atmospheric heterogeneities in ERS tandem SAR interferometry. Technical Report DUP 98.1, Delft University of Technology.

Hanssen, R. F., 2001. Radar interferometry: data interpretation and error analysis. No. 2 in Remote sensing and digital image processing. Kluwer Academic, Dordrecht, The Netherlands.

Harding, D., Gesch, D., Carabajal, C., Luthcke, S., 1999. Application of the shuttle laser altimeter in an accuracy assessment of GTOPO30, a global 1-kilometer digital elevation model. In: Proceedings of the International Society for Photogrammetry and Remote Sensing. Vol. Volume XXXII-3/W14. La Jolla, USA, pp. 81 – 85.

Heath, R., 1995. Basic ground-water hydrology. United States Geological Survey Water Supply Paper 2220, USGS.

Hendriks, M. R., 2010. Introduction to physical hydrology. Oxford University Press, Oxford, UK.

Hohenbrink, T. L., Lischeid, G., Schindler, U., Hufnagel, J., 2016. Disentangling the effects of land management and soil heterogeneity on soil moisture dynamics. Vadose Zone Journal 15 (1), 12p.

Hong, T., White, P., 2014. Rainfall recharge estimation based on a nonlinear Bayesian technique with a dynamic state-space formulation in the Canterbury Plains. GNS Science Report 2014/37, 44p, GNS Science.

Hooijer, A., Page, S., Jauhiainen, J., Lee, W. A., Lu, X. X., Idris, A., Anshari, G., 2012. Subsidence and carbon loss in drained tropical peatlands. Biogeosciences 9 (3), 1053–1071.

Howard, K., Lloyd, J., 1979. The sensitivity of parameters in the Penman evaporation equations and direct recharge balance. Journal of Hydrology 41 (3-4), 329–344.

Irmak, A. (Ed.), 2012. Evapotranspiration - Remote Sensing and Modeling, Hardcover Edition. InTech, DOI: 10.5772/725.

Jarvis, P., 1976. The interpretation of the variations in leaf water potential and stomatal conductance found in canopies in the field. Philosophical Transactions of the Royal Society of London, series B, Biological Sciences 273 (927), 593–610.

Jin, Y.-Q., Wang, Y., 2001. A genetic algorithm to simultaneously retrieve land surface roughness and soil wetness. International Journal of Remote Sensing 22 (16), 3093–3099.

Jorgensen, D. G., Petricola, M., 1995. Research borehole-geophysical logging in determining geohydrologic properties. Ground Water 33 (4), 589–596.

Kerr, Y. H., Waldteufel, P., Richaume, P., Wigneron, J. P., Ferrazzoli, P., Mahmoodi, A., Al Bitar, A., Cabot, F., Gruhier, C., Juglea, S. E., Leroux, D., Mialon, A., Delwart, S., 2012. The SMOS Soil Moisture Retrieval Algorithm. IEEE Transactions on Geoscience and Remote Sensing 50 (5), 1384–1403.

Klein, L., Swift, C., 1977. An improved model for the dielectric constant of sea water at microwave frequencies. IEEE Journal of Oceanic Engineering 2 (1), 104–111.

Kluiving, S. J., Aleid Bosch, J., Ebbing, J. H., Mesdag, C. S., Westerhoff, R. S., 2003. Onshore and offshore seismic and lithostratigraphic analysis of a deeply incised Quaternary buried valley system in the Northern Netherlands. Journal of Applied Geophysics 53 (4), 249–271.

Korvin, G., Boyd, D. M., O'Dowd, R., 1990. Fractal characterization of the South Australian gravity station network. Geophysical Journal International 100 (3), 53.

Landcare Research, 2014. LRIS portal. Accessed March 2016.
URL `https://lris.scinfo.org.nz/p/about-lris-portal/`

Landcare Research, 2015. SMAP Online - the digital soil map for New Zealand. Accessed June 2015.
URL `http://smap.landcareresearch.co.nz`

Lane, J., Saxton, J., 1952. Dielectric dispersion in pure polar liquids at very high radio frequencies. III. The effect of electrolytes in solution. Proceedings of the Royal Society, Series A, Mathematical and Physical Sciences 214 (1119), 513–545.

Larned, S. T., Scarsbrook, M. R., Snelder, T. H., Norton, N. J., Biggs, B. J. F., 2004. Water quality in lowelevation streams and rivers of New Zealand: Recent state and trends in contrasting landcover classes. New Zealand Journal of Marine and Freshwater Research 38 (2), 347–366.

Lauknes, T., Piyush Shanker, A., Dehls, J., Zebker, H., Henderson, I., Larsen, Y., 2010. Detailed rockslide mapping in northern Norway with small baseline and persistent scatterer interferometric SAR time series methods. Remote Sensing of Environment 114 (9), 2097–2109.

Leathwick, J. R., Stephens, R. T. T., 1998. Climate surfaces for New Zealand. Landcare Research Contract Report LC9798 126, 1–19.

Li, Z., Cribb, M., Chang, F.-L., 2005. Natural variability and sampling errors in solar radiation measurements for model validation over the atmospheric radiation measurement southern Great Plains Region. Journal of Geophysical Research 110 (D15).

Lin, X., Hubbard, K. G., 2004. Uncertainties of derived dewpoint temperature and relative humidity. Journal of Applied Meteorology 43 (5), 821–825.

Lin, Y.-F., Wang, J., Valocchi, A., 2008. Making groundwater recharge and discharge estimate maps in one day. an arcgis 9.2 application for water resources research. Accessed January 2017.
URL `http://www.esri.com/news/arcuser/0408/groundwater.html`

Loke, M., Barker, R., 1996. Practical techniques for 3D resistivity surveys and data inversion1. Geophysical Prospecting 44 (3), 499–523.

Long, D., Chen, X., Scanlon, B. R., Wada, Y., Hong, Y., Singh, V. P., Chen, Y., Wang, C., Han, Z., Yang, W., 2016. Have GRACE satellites overestimated groundwater depletion in the Northwest India Aquifer? Scientific Reports 6, 24398.

Lorrain, P., Corson, D. R., Lorrain, F., 1988. Electromagnetic fields and waves: including electric circuits, 3rd Edition. Freeman, New York.

Lough, H., Williams, H., 2009. Vertical flow in Canterbury groundwater systems and its significance for groundwater management. Environment Canterbury, Investigations and Monitoring Group, Christchurch, New Zealand.

Lundgren, P., Casu, F., Manzo, M., Pepe, A., Berardino, P., Sansosti, E., La-

nari, R., 2004. Gravity and magma induced spreading of Mount Etna volcano revealed by satellite radar interferometry. Geophysical Research Letters 31 (4).

MacCary, L. M., 1983. Geophysical Logging in Carbonate Aquifers. Ground Water 21 (3), 334–342.

Mandel, S., 1974. The groundwater resources of the Canterbury Plains, 59p. Lincoln papers in water resources 12, New Zealand Agricultural Engineering Insititute.

Margat, J., van der Gun, J., 2013. Groundwater around the world: a geographic synopsis. CRC Press, Taylor & Francis Group, Boca Raton.

Marinoni, O., 2003. Improving geological models using a combined ordinaryindicator kriging approach. Engineering Geology 69 (1-2), 37–45.

Marshall, S. J., Clarke, G. K., 1999. Modeling North American freshwater runoff through the last glacial cycle. Quaternary Research 52 (3), 300–315.

Mathworks, 2014. Multivariate normal distribution - MATLAB & Simulink - MathWorks Australia. Accessed December 2014.
URL http://www.mathworks.com.au/help/stats/multivariate-normal-distribution.html

Mathworks, 2015a. Genetic algorithm. Accessed November 2015.
URL http://mathworks.com/discovery/genetic-algorithm.html

Mathworks, 2015b. Smoothing splubes - MATLAB & Simulink - MathWorks Australia. Accessed June 2015.
URL http://www.mathworks.com.au/help/curvefit/smoothing-splines.html

Maxwell, J. C., 1865. A dynamical theory of the electromagnetic field. Philosophical Transactions of the Royal Society of London 155, 459–512.

McMahon, T. A., Peel, M. C., Lowe, L., Srikanthan, R., McVicar, T. R., 2013. Estimating actual, potential, reference crop and pan evaporation using standard meteorological data: a pragmatic synthesis. Hydrology and Earth System Sciences 17 (4), 1331–1363.

Meekes, J., Scheffers, B., Ridder, J., 1990. Optimisation of high-resolution seismic reflection parameters for hydrogeological investigations in The Netherlands. First Break 8, 263–270.

Meijerink, A., 2007. Remote Sensing Applications to Groundwater. No. 16 in IHP-VI, Series on Groundwater. United Nations Educational, Scientific and Cultural Organization, France.

Miguez-Macho, G., Fan, Y., Weaver, C. P., Walko, R., Robock, A., 2007. Incorporating water table dynamics in climate modeling: 2. formulation, validation, and soil moisture simulation. Journal of Geophysical Research 112 (D13).

Miguez-Macho, G., Li, H., Fan, Y., 2008. Simulated water table and soil moisture climatology over North America. Bulletin of the American Meteorological Society 89 (5), 663–672.

Milsom, J., 2003. Field geophysics, 3rd Edition. The geological field guide series. John Wiley and Sons, Chichester, West Sussex, England.

Ministry for the Environment, 2013. Proposed amendments to the National Policy Statement for Freshwater Management 2011: A discussion document. Report ME1130, Ministry for the Environment, Wellington (NZ).

Miralles, D., De Jeu, R., Gash, J., Holmes, T., Dolman, A., 2011a. Magnitude and variability of land evaporation and its components at the global scale. Hydrology and Earth System Sciences 15, 967–981.

Miralles, D. G., Holmes, T. R. H., De Jeu, R. A. M., Gash, J. H., Meesters, A. G. C. A., Dolman, A. J., 2011b. Global land-surface evaporation estimated from satellite-based observations. Hydrology and Earth System Sciences 15 (2), 453–469.

Monteith, J., 1965. Evaporation and environment. Symposium of the society of experimental biology 19, 205–224.

Moreau, M., Bekele, M., 2015. Groundwater Component of the Water Physical Stock Account (WPSA). GNS Science Consultancy Report 2014/290, GNS Science.

Moreau-Fournier, M., Cameron, S., 2011. Update of national groundwater volume stock account. GNS Science Letter Report 2011/99LR, GNS Science.

Mu, Q., Heinsch, F., Zhao, M., Running, S., 2007. Development of a global evapotranspiration algorithm based on MODIS and global meteorology data. Remote Sensing of Environment 111, 519–536.

Mu, Q., Zhao, M., Running, S., 2011. Running, improvements to a MODIS

global terrestrial evapotranspiration algorithm. Remote Sensing of Environment 115 (8), 1781–1800.

Murray, F., 1967. On the computation of saturation vapor pressure. Journal of Applied Meteorology 6, 203–204.

Newsome, P., Wilde, R., Willoughby, E., 2008. Land resource information system spatial data layers - data dictionary, 75p. Technical report, Landcare Research New Zealand Ltd, Palmerston North, New Zealand.

NIWA, 2002a. January 2002 New Zealand storm (2002-01-01). Historical Weather events report 2002-01-01, NIWA, accessed January 2016.
URL hwe.niwa.co.nz/event/January_2002_New_Zealand_Storm

NIWA, 2002b. January 2002 South Island and Waikato Flooding (2002-01-11). Historical Weather events report 2002-01-11, NIWA, accessed January 2016.
URL hwe.niwa.co.nz/event/January_2002_South_Island_and_Waikato_flooding

NIWA, 2014. CliFlo: the national climate database. Accessed January 2015.
URL http://cliflo.niwa.co.nz/

NIWA, 2015. Cliflo soil moisture help. Accessed November 2015.
URL http://cliflo-niwa.niwa.co.nz/pls/niwp/wh.do_help?id=ls_soilm

NTSG, 2013. MODIS global evapotranspiration project (MOD16). Accessed January 2016.
URL http://www.ntsg.umt.edu/project/mod16

Oh, Y., 2004. Quantitative retrieval of soil moisture content and surface roughness from multipolarized radar observations of bare soil surfaces. IEEE Transactions on Geoscience and Remote Sensing 42 (3), 596–601.

Oh, Y., 2006. Robust inversion technique for retrieving soil moisture from multipolarised backscatter of bare surface. Electronics Letters 42 (7), 414.

Oh, Y., Sarabandi, K., Ulaby, F., 1992. An empirical model and an inversion technique for radar scattering from bare soil surfaces. IEEE Transactions on Geoscience and Remote Sensing 30 (2), 370–381.

Oh, Y., Sarabandi, K., Ulaby, F., 2002. Semi-empirical model of the ensemble-averaged differential mueller matrix for microwave backscattering from bare soil

surfaces. IEEE Transactions on Geoscience and Remote Sensing 40 (6), 1348–1355.

Oke, T. R., 1992. Boundary layer climates, 2nd Edition. Routledge, London.

Ortega-Guerrero, A., Rudolph, D. L., Cherry, J. A., 1999. Analysis of long-term land subsidence near Mexico City: Field investigations and predictive modeling. Water Resources Research 35 (11), 3327–3341.

Pain, H., 2005. The Physics of Vibrations and Waves, 6th Edition. John Wiley & Sons, Ltd, West Sussex, England.

Palmer, K., 2013. Personal communication. Groundwater data scientist, Environment Canterbury.

Park, T., 2015. Personal communication. PhD student at Boston University, Department of Earth and Environment, Boston University, Cliveg Research Group.

Penman, H., 1948. Natural evaporation from open water, bare soil and grass. Proceedings of the Royal Society, Series A, 193, 120–145.

Penman, H., 1963. Vegetation and hydrology. Vol. 53 of Tech. Comm. Commonwealth Bureau of Soils, Harpenden, England.

Phreatos, 2007. Mid-Mataura groundwater model. Environment Southland Report U04/97, 91p., Phreatos.

Priestley, C., Taylor, R., 1972. On the assessment of surface heat flux and evaporation using large-scale parameters. Monthly Weather Review 100 (2), 81–92.

Rajanayaka, C., Donaggio, J., McEwan, H., 2010. Update of water allocation data and estimate of actual water use of consented takes 2009-2010. Aqualinc Research Report H10002/3, New Zealand Ministry for the Environment.

Rawlinson, Z., 2014. Waipa River Catchment: requirements for conceptual groundwater model development. GNS Science consultancy report 2014/147, 87p., GNS Science.

Rawlinson, Z., Westerhoff, R., White, P., Schaller, K., Moore, C., 2015. Estimation of rainfall recharge to groundwater in the Waipa River catchment from three independent models. GNS Science Consultancy Report 2015/212, 88p., GNS Science.

Reeves, J. A., Knight, R., Zebker, H. A., Schreder, W. A., Shanker Agram, P., Lauknes, T. R., 2011. High quality InSAR data linked to seasonal change in

hydraulic head for an agricultural area in the San Luis Valley, Colorado. Water Resources Research 47 (12), 1–14.

Reynolds, C. A., Jackson, T. J., Rawls, W. J., 2000. Estimating soil water-holding capacities by linking the food and agriculture organization soil map of the world with global pedon databases and continuous pedotransfer functions. Water Resources Research 36 (12), 3653–3662.

Rodell, M., Chen, J., Kato, H., Famiglietti, J. S., Nigro, J., Wilson, C. R., 2007. Estimating groundwater storage changes in the Mississippi River basin (USA) using GRACE. Hydrogeology Journal 15 (1), 159–166.

Rodell, M., Famiglietti, J., Chen, J., Seneviratne, S., Viterbo, P., Holl, S., Wilson, C., 2004. Basin scale estimates of evapotranspiration using GRACE and other observations. Geophysical Research Letters 31 (20).

Rose, C., Smith, M., 1996. The multivariate normal distribution. The Mathematica Journal 6 (1), 32–37.

Rushton, K., Eilers, V., Carter, R., 2006. Improved soil moisture balance methodology for recharge estimation. Journal of Hydrology 318 (1-4), 379–399.

Sahoo, A., Pan, M., Troy, T., Vinukollu, R., Sheffield, J., Wood, E., 2011. Reconciling the global terrestrial water budget using satellite remote sensing. Remote Sensing of Environment 115, 1850–1865.

Samanta, A., Costa, M. H., Nunes, E. L., Vieira, S. A., Xu, L., Myneni, R. B., 2011. Comment on "Drought-Induced Reduction in Global Terrestrial Net Primary Production from 2000 Through 2009". Science 333 (6046), 1093–1093.

Sambridge, M., 1999. Geophysical inversion with a neighbourhood algorithm-II. Appraising the ensemble. Geophysical Journal International 138 (3), 727–746.

Saxton, K. E., 1975. Sensitivity analyses of the combination evapotranspiration equation. Agricultural Meteorology 15 (3), 343–353.

Scanlon, B. R., Healy, R. W., Cook, P. G., 2002. Choosing appropriate techniques for quantifying groundwater recharge. Hydrogeology Journal 10 (1), 18–39.

Scott, D., 2004. Groundwater allocation limits: land-based recharge estimates. Tech. Rep. Environment Canterbury U04/97, 39p., Environment Canterbury.

Seibert, J., McDonnell, J. J., 2002. On the dialog between experimentalist and

modeler in catchment hydrology: Use of soft data for multicriteria model calibration. Water Resources Research 38 (11), 23–1–23–14.

Siemon, B., Christiansen, A., Auken, E., 2009. A review of helicopter-borne electromagnetic methods for groundwater exploration. Near Surface Geophysics 7 (1303).

Sims, A., Cox, S., Fitzsimmons, S., Holland, P., 2015. Seasonal infiltration and groundwater movement in schist bedrock, Southern Alps, New Zealand. Journal of Hydrology (NZ) 54 (1), 33–52.

Smith, B., Sandwell, D., 2003. Accuracy and resolution of shuttle radar topography mission data. Geophysical Research Letters 30 (9), 4p.

Smith, K. A., Mullins, C. E. (Eds.), 2001. Soil and environmental analysis: physical methods, 2nd Edition. Books in soils, plants, and the environment. M. Dekker, New York.

Srinivasan, M., 2015. Personal communication. Hydrologist at NIWA.

Statistics New Zealand, 2011. Water Physical Stock Account 1995-2010. Statistics New Zealand.

Stewart, J., 1988. Modelling surface conductance of pine forest. Agricultural and Forest Meteorology 43 (1), 19–35.

Stogryn, A., 1971. Equations for calculating the dielectric constant of saline water. IEEE Transaction of Microwave Theory and Techniques 19 (8), 733–736.

Su, Z., 2002. The surface energy balance system (SEBS) for estimation of turbulent heat fluxes. Hydrology and Earth System Sciences 6, 85–100.

Summerfield, M. A., Hulton, N. J., 1994. Natural controls of fluvial denudation rates in major world drainage basins. Journal of Geophysical Research 99 (B7), 13871–13883.

Tait, A., 2014. Personal communication. Principal Scientist at the National Climate Centre, NIWA.

Tait, A., Henderson, R., Turner, R., Zheng, X., 2006. Thin plate smoothing spline interpolation of daily rainfall for New Zealand using a climatological rainfall surface. International Journal of Climatology 26 (14), 2097–2115.

Tait, A., Woods, R., 2007. Spatial interpolation of daily potential evapotranspira-

tion for New Zealand using a spline model. Journal of Hydrometeorology 8 (3), 430–438.

Tait, A., Zheng, X., 2007. Analysis of the spatial interpolation error associated with maps of median annual climate variables. NIWA report, 21p. Accessed July 2015.
URL https://www.niwa.co.nz/sites/niwa.co.nz/files/import/attachments/Climate_Maps_Error_Analysis.pdf

Taylor, J. R., 1997. An introduction to error analysis: the study of uncertainties in physical measurements, 2nd Edition. University Science Books, Sausalito, California, USA.

Tellinghuisen, J., 2001. Statistical error propagation. The Journal of Physical Chemistry A 105 (15), 3917–3921.

Tetens, O., 1930. Uber einige meteorologische begriffe. Zeitschrift für Geophysik 6, 297–309.

The Engineering Toolbox, 2012. Salinity of water. http://www.engineeringtoolbox.com/water-salinity-d_1251.html.

Thornthwaite, C., 1948. An approach toward a rational classification of climate. Geographical Review 38 (1), 55–94.

Thornthwaite, C., Mather, J., 1957. Instructions and tables for computing potential evapotranspiration and the water balance, Centerton, N.J., Laboratory of Climatology. Publications in Climatology 10 (3), 185–311.

Toebes, C., 1972. The water balance of New Zealand. Journal of Hydrology (NZ) 11 (2), 127–139.

Tomás, R., Li, Z., Lopez-Sanchez, J. M., Liu, P., Singleton, A., 2016. Using wavelet tools to analyse seasonal variations from InSAR time-series data: a case study of the Huangtupo landslide. Landslides 13 (3), 437–450.

Tschritter, C., Cameron, S., White, P., 2014. Incorporation of hydraulic properties in three-dimensional geological models. GNS Science Report 2013/53, 26p., GNS Science.

UCAR, 2014. Unidata | NetCDF. Accessed July 2014.
URL http://www.unidata.ucar.edu/software/netcdf/

Ulaby, F., Bengal, T., Dobson, M., East, J., Garvin, J., Evans, D., 1990. Mi-

crowave dielectric properties of dry rocks. IEEE Transactions on Geoscience and Remote Sensing 28 (3), 325–336.

Ulaby, F., Long, D., 2014. Microwave Radar and Radiometric Remote Sensing, 1st Edition. University of Michigan Press, Ch. 4, pp. 122–162.

Ulaby, F., Tavakoli, A., Thomas, B., 1987. Microwave Propagation Constant for a Vegetation Canopy With Vertical Stalks. IEEE Transactions on Geoscience and Remote Sensing GE-25 (6), 714–725.

Ulaby, F. T., 1981. Microwave response of vegetation. Advances in Space Research 1 (10), 55–70.

Ulaby, F. T., Long, D. G., Blackwell, W. J., Elachi, C., Fung, A. K., Ruf, C., Sarabandi, K., Zebker, H. A., Van Zyl, J., 2014. Microwave radar and radiometric remote sensing. University of Michigan Press, Ann Arbor.

Ulaby, F. T., Moore, R., Fung, A., 1982. Microwave remote sensing - Active and Passive. Vol. II of Advanced Level Textbooks and Reference Works. Addison-Wesley, Reading, Massachusetts.

Ulaby, F. T., Moore, R., Fung, A., 1986. Microwave remote sensing - Active and Passive, Volume III: From Theory to Applications. Artech House, Massachusetts.

Urish, D. W., Frohlich, R. K., 1990. Surface electrical resistivity in coastal groundwater exploration. Geoexploration 26 (4), 267–289.

U.S. Naval Observatory, 2012. Duration of daylight/darkness table for one year. Accessed July 2014.
URL http://aa.usno.navy.mil/data/docs/Dur_OneYear.php

USDA, 1987. United States Department of Agriculture, soil mechanics level I, module 3, USDA textural soil classification, study guide. Soil conservation service USDA, USDA, accessed February 2015.
URL ftp://ftp.wcc.nrcs.usda.gov/wntsc/H&H/training/soilsOther/soil-USDA-textural-class.pdf

USDA, 2015. Personal communication. Steven Speidel, Computer Specialist, COOP Coordinator, Soils Hotline USDA - Natural Resources Conservation Service, National Soil Survey CenterIT, Department of USDA - United States Department of Agriculture.

USGS, Global Land Cover Facility, U., 2006. Shuttle Radar Topography Mission

(SRTM), unfilled finished version B. Accessed March 2014.
URL http://www.landcover.org

Van der Tol, C., Parodi, G., 2012. Guidelines for remote sensing of evapotranspiration. In: Evapotranspiration - Remote Sensing and Modeling. InTech, pp. 227–250.

Van Overmeeren, R., 1998. Radar facies of unconsolidated sediments in The Netherlands: A radar stratigraphy interpretation method for hydrogeology. Journal of Applied Geophysics 40 (1-3), 1–18.

Van Zyl, J., Chapman, B., Dubois, P., Shi, J., 1993. The effect of topography on SAR calibration. IEEE Transactions on Geoscience and Remote Sensing 31 (5), 1036–1043.

Verhoef, A., Egea, G., 2014. Modeling plant transpiration under limited soil water: Comparison of different plant and soil hydraulic parameterizations and preliminary implications for their use in land surface models. Agricultural and Forest Meteorology 191, 22–32.

Wada, Y., van Beek, L. P. H., Bierkens, M. F. P., 2012. Nonsustainable groundwater sustaining irrigation: A global assessment. Water Resources Research 48 (6), W00L06.

Wada, Y., van Beek, L. P. H., van Kempen, C. M., Reckman, J. W. T. M., Vasak, S., Bierkens, M. F. P., 2010. Global depletion of groundwater resources. Geophysical Research Letters 37 (20), 1–5.

Wagner, W., Borgeaud, M., Rott, H., 1999. A study of vegetation cover effects on ERS scatterometer data. IEEE Transactions on Geoscience and Remote Sensing 37 (2), 938–948.

Wagner, W., Naeimi, V., Scipal, K., Jeu, R., Martnez-Fernández, J., 2007. Soil moisture from operational meteorological satellites. Hydrogeology Journal 15 (1), 121–131.

Wang, Y., Day, J. L., Davis, F. W., 1998. Sensitivity of Modeled C- and L-Band Radar Backscatter to Ground Surface Parameters in Loblolly Pine Forest. Remote Sensing of Environment 66 (3), 331–342.

Weerts, A. H., El Serafy, G. Y. H., 2006. Particle filtering and ensemble Kalman filtering for state updating with hydrological conceptual rainfall-runoff models. Water Resources Research 42 (9), W09403.

Westenbroek, S., Kelson, V., Dripps, W., Hunt, R., Bradbury, K., 2010. SWB - A Modified Thornthwaite-Mather Soil-Water-Balance Code for Estimating Groundwater Recharge. Tech. Rep. U.S. Geological Survey Techniques and Methods 6-A31, 60 p., USGS.

Westerhoff, R., 2015. Using uncertainty of Penman and Penman-Monteith methods in combined satellite and ground-based evapotranspiration estimates. Remote Sensing of Environment 169, 102–112.

Westerhoff, R., Karaoulis, M., de Kleine, M., Rawlinson, Z., 2014. Evaluation of the use of helicopter electromagnetic (HEM) measurements for aquifer characterisation in the Otago region, New Zealand. Deltares Science Report 1204708-000-BGS-0004, Deltares.

Westerhoff, R., Kleuskens, M., Winsemius, H., Huizinga, H., Brakenridge, G., Bishop, C., 2013. Automated global water mapping based on wide-swath orbital synthetic-aperture radar. Hydrology and Earth System Sciences 17, 651–663.

Westerhoff, R., White, P., 2013. Application of equilibrium water table estimates using satellite measurements to the Canterbury Region, New Zealand. GNS Science Report 2013/43.

White, P., 2001. Groundwater resources in New Zealand. In: Rosen, M.R., White, P.A. eds., Groundwaters of New Zealand. New Zealand Hydrological Society, pp. 45–75.

White, P., 2006. Some future directions in hydrology. Invited editorial. Journal of Hydrology NZ 45 (2), 63–68.

White, P., 2007. Snow storms in canterbury and recharge to groundwater. GNS Science Consultancy Report 2007/87, 46p., GNS Science.

White, P., 2008. Central Plains water. Evidence appearing for Ngai Tahu in support of their submission to the Central Plains water hearing committee.

White, P., Hong, Y.-S., Murray, D., Scott, D., Thorpe, H., 2003. Evaluation of regional models of rainfall recharge to groundwater by comparison with lysimeter measurements, Canterbury, New Zealand. Journal of Hydrology (NZ) 42 (1), 39–64.

White, P., Kovacova, E., Zemansky, G., Jebbour, N., Moreau-Fournier, M., 2012. Groundwater-surface water interaction in the Waimakariri River, New Zealand,

and groundwater outflow from the river bed. Journal of Hydrology (NZ) 51 (1), 1–24.

White, P., Moreau-Fournier, M., Thorpe, H., Lovett, A., 2014a. Summary of rainfall recharge measurements with lysimeters and ground-level rainfall observations 1952-1978 and 1997-2011, Canterbury. GNS Science Report 2013/10. 31p+CD., GNS Science.

White, P., Reeves, R., Zhan, X., 1996. Geological and fracture flow modelling of the Pukekohe aquifer system. Institute of Geological and Nuclear Sciences Science report 96/8, 64p., Institute of Geological and Nuclear Sciences.

White, P., Tschritter, C., 2014. Water budgets in the Piako catchment, Hauraki Plains. Report CR2014-139LR for Waikato Regional Council, 10p., GNS Science.

White, P., Tschritter, C., Davidson, P., 2016. Groundwater-surface water interaction in a coastal aquifer system, Wairau Plain, Marlborough, New Zealand. Journal of Hydrology (NZ) 55 (1), 25–43.

White, P., Tschritter, C., Rawlinson, Z., Moreau, M., Dewes, K., S., E., 2015. Groundwater resource characterisation in the Waikato River catchment for the Healthy Rivers Project. GNS Science consultancy report 2015/95, 75p + appendices (99p), Draft in Review, GNS Science.

White, P., Tschritter, C., Westerhoff, R., Lovett, A., 2014b. Rainfall recharge models of the Heretaunga Plains. GNS Science Report 2013/50, 48 p., GNS Science.

White, P., Zemansky, G., Hong, T., Kilgour, G., Wall, M., 2007. Lake Rotorua groundwater and Lake Rotorua nutrients phase 3 science programme technical report. GNS Client report 2007/220 to Environment Bay of Plenty, 402p., GNS Science.

White, P. A., 2013. Personal communication: lysimeters in the Canterbury Plains. Senior scientist at GNS Science.

Willis, B. J., White, C. D., 2000. Quantitative Outcrop Data for Flow Simulation. Journal of Sedimentary Research 70 (4), 788–802.

Wilson, K., Goldstein, A., Falge, E., Aubinet, M., Baldocchi, D., Berbigier, P., Bernhofer, C., Ceulemans, R., Dolman, H., Field, C., Grelle, A., Ibrom, A., Law, B., Kowalski, A., Meyers, T., Moncrieff, J., Monson, R., Oechel, W., Ten-

hunen, J., Valentini, R., Verma, S., 2002. Energy balance closure at FLUXNET sites. Agricultural and Forest Meteorology 113 (1-4), 223–243.

Woods, R., Hendrikx, J., Henderson, R., Tait, A., 2006. Estimating mean flow of New Zealand rivers. Journal of Hydrology (NZ) 45 (2), 95–110.

World Meteorological Organization, 2008. Guide to meteorological instruments and methods of observation. World Meteorological Organization, Geneva, Switzerland.

Wu, J., Shi, X., Xue, Y., Zhang, Y., Wei, Z., Yu, J., 2007. The development and control of the land subsidence in the Yangtze delta, China. Environmental Geology 55 (8), 1725–1735.

Yang, J., McMillan, H., Zammit, C., Horrel, G., 2015. Modelling Surface water groundwater interaction in New Zealand: Model development and application. In: EGU Geophysical Research Abstract. Vol. 17. Vienna, pp. EGU2015–7450.

Yeh, H.-F., Lin, H.-I., Lee, S.-T., Chang, M.-H., Hsu, K.-C., Lee, C.-H., 2014. GIS and SBF for estimating groundwater recharge of a mountainous basin in the Wu River watershed, Taiwan. Journal of Earth System Sciences 123 (3), 503–516.

Yi-Cheng Lin, Sarabandi, K., May 1999. Retrieval of forest parameters using a fractal-based coherent scattering model and a genetic algorithm. IEEE Transactions on Geoscience and Remote Sensing 37 (3), 1415–1424.

Zemansky, G., Westerhoff, R., 2013. Evaluation of a set of satellite remote sensing methods for application to characterization of New Zealand aquifers. GNS Science Report 2013/28, 128p., GNS Science.

Zhang, L., Hickel, K., Dawes, W. R., Chiew, F. H. S., Western, A. W., Briggs, P. R., 2004. A rational function approach for estimating mean annual evapotranspiration. Water Resources Research 40 (2), W02502.

Zhou, M., Ishidaira, H., Hapuarachchi, H., Magome, J., Kiem, A., Takeuchi, K., 2006. Estimating potential evapotranspiration using ShuttleworthWallace model and NOAA-AVHRR NDVI data to feed a distributed hydrological model over the Mekong River basin. Journal of Hydrology 327 (1-2), 151–173.

A

Inversion solutions of soil moisture at ground stations

This Appendix is a continuation of Chapter 3. Genetic Algorithm solutions for soil moisture at 62 NIWA ground stations. Each plot contains the solution for: all recorded backscatter (top); separate timeseries binned to timeseries of similar global incidence angles θ (middle); and the median of solutions of the θ timeseries (bottom), where the spread between the timeseries is denoted with δ_θ. Leaf Area Index (LAI) is plotted in green and was shown as 0.1 LAI so that it matched the same y-axis. Dotted lines are the standard deviations of the GA solutions (see section 3.4.3).

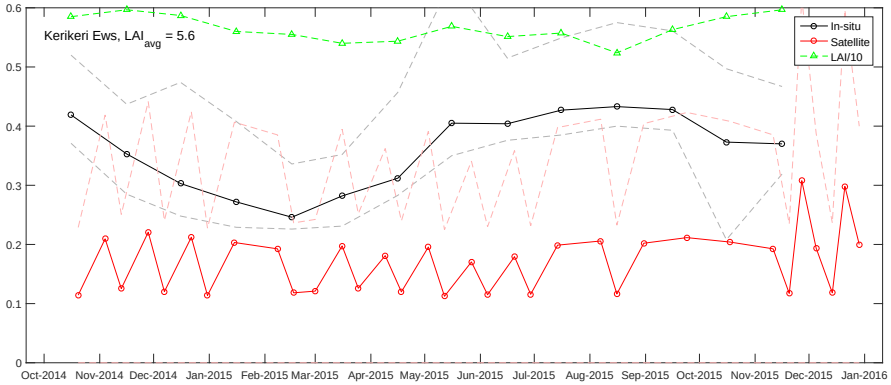

(a) All

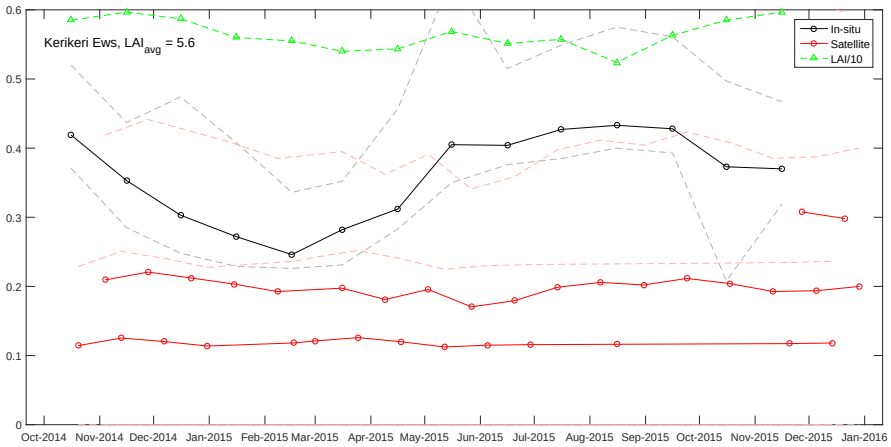

(b) Separate timeseries binned to global incidence θ

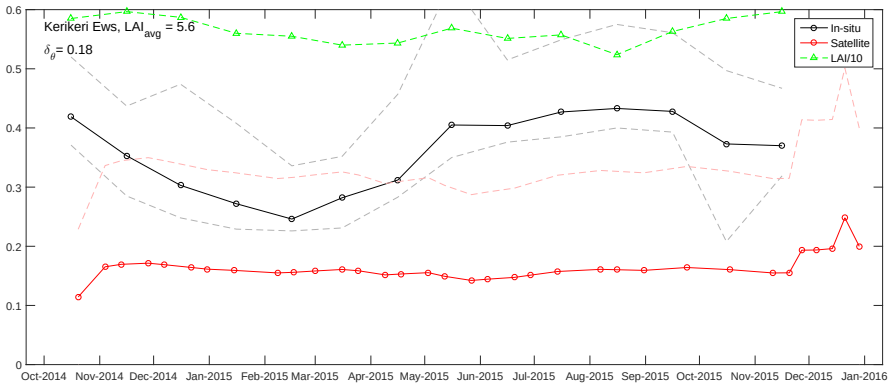

(c) Mean values, based on the θ time series

Figure A1: Inverted soil moisture at NIWA soil moisture ground station 'Kerikeri Ews'.

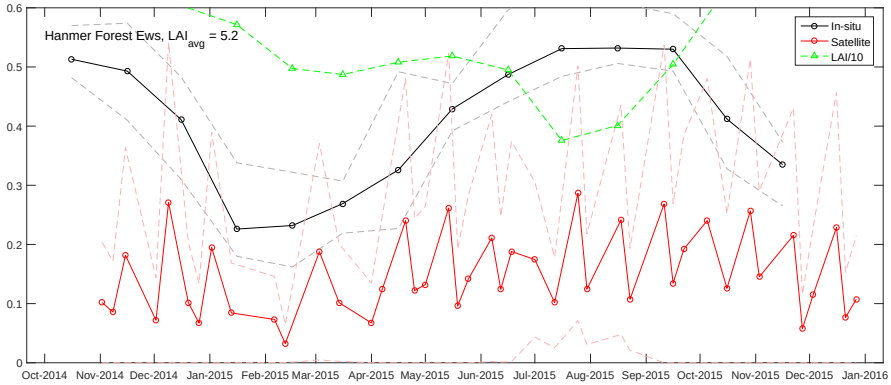

(a) All

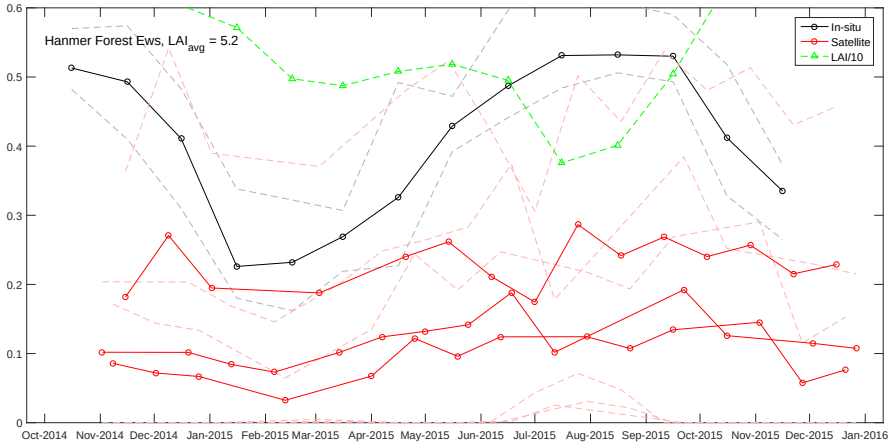

(b) Separate timeseries binned to global incidence θ

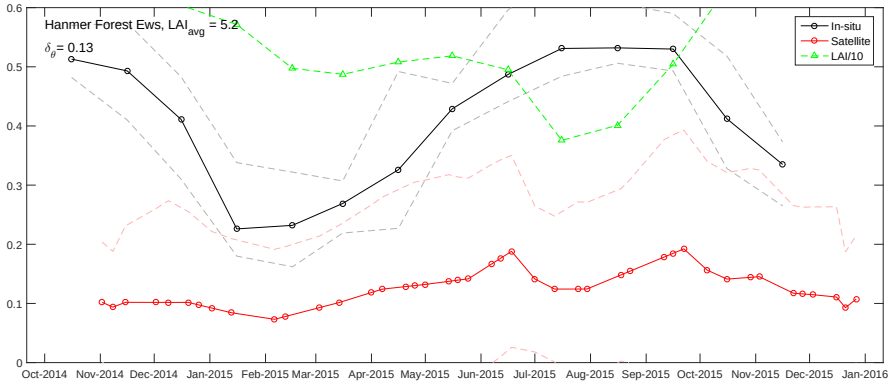

(c) Mean values, based on the θ time series

Figure A2: Inverted soil moisture at NIWA soil moisture ground station 'Hanmer Forest Ews'.

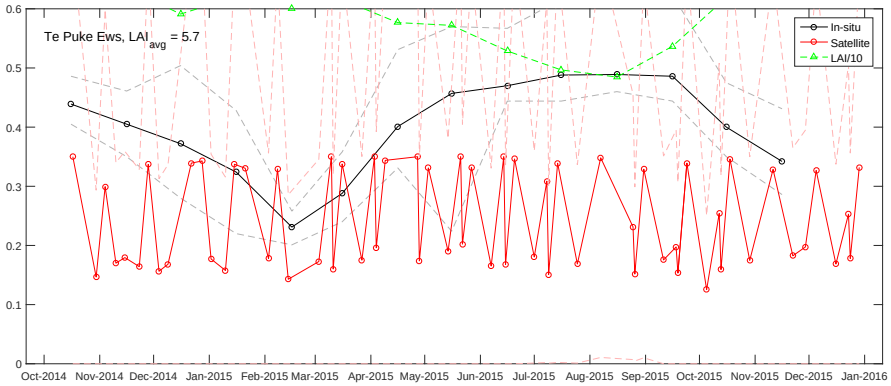

(a) All

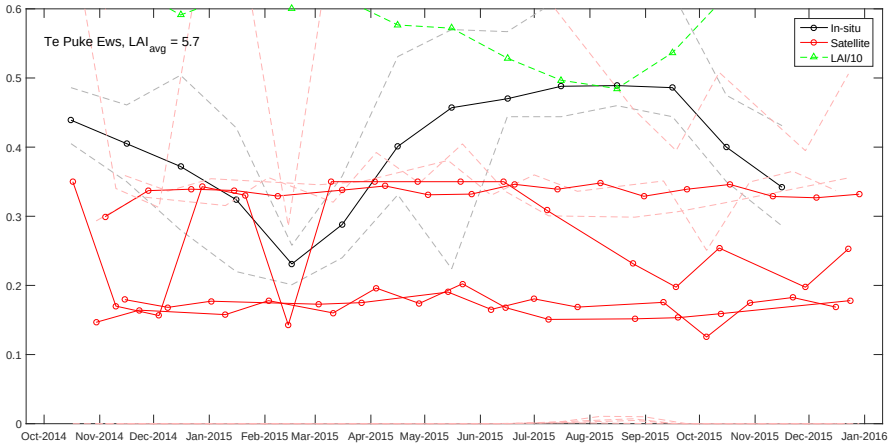

(b) Separate timeseries binned to global incidence θ

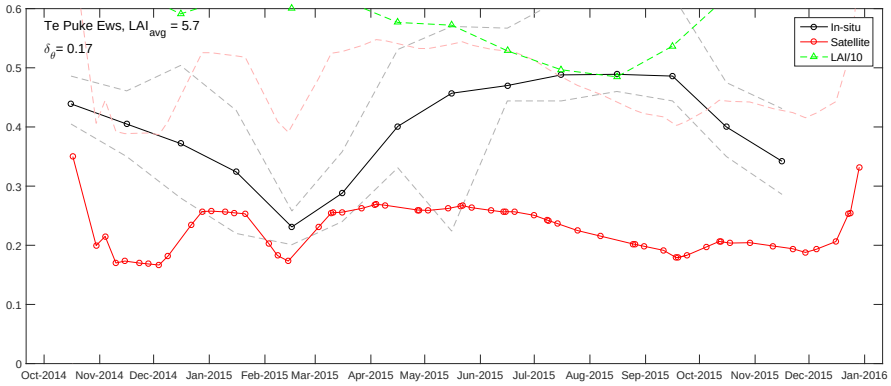

(c) Mean values, based on the θ time series

Figure A3: Inverted soil moisture at NIWA soil moisture ground station 'Te Puke Ews'.

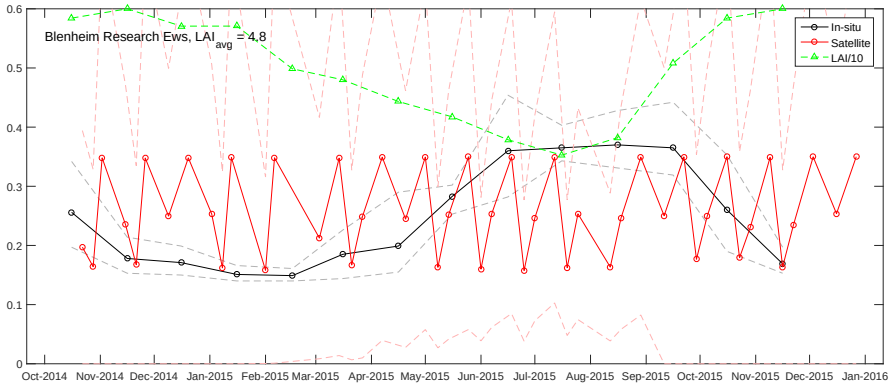

(a) All

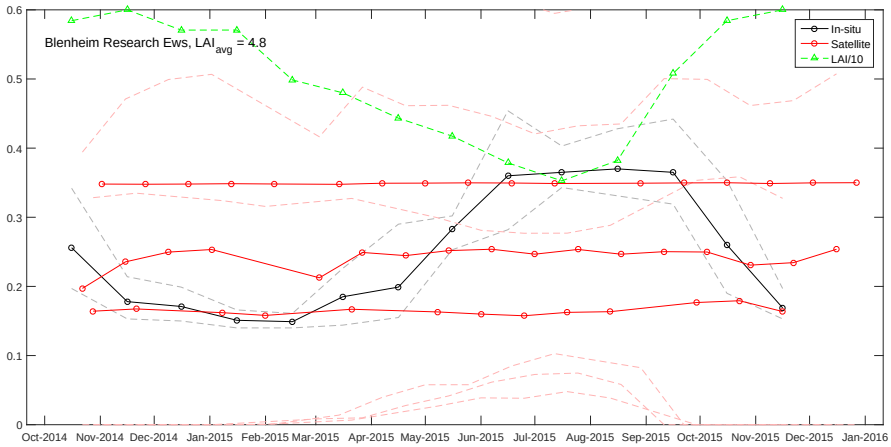

(b) Separate timeseries binned to global incidence θ

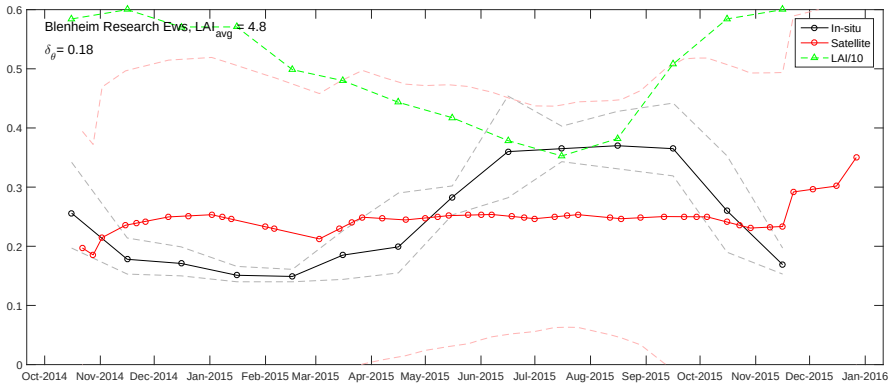

(c) Mean values, based on the θ time series

Figure A4: Inverted soil moisture at NIWA soil moisture ground station 'Blenheim Research Ews'.

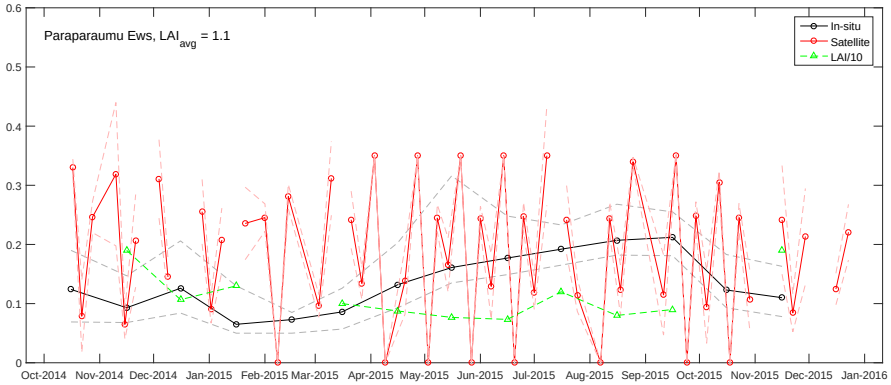

(a) All

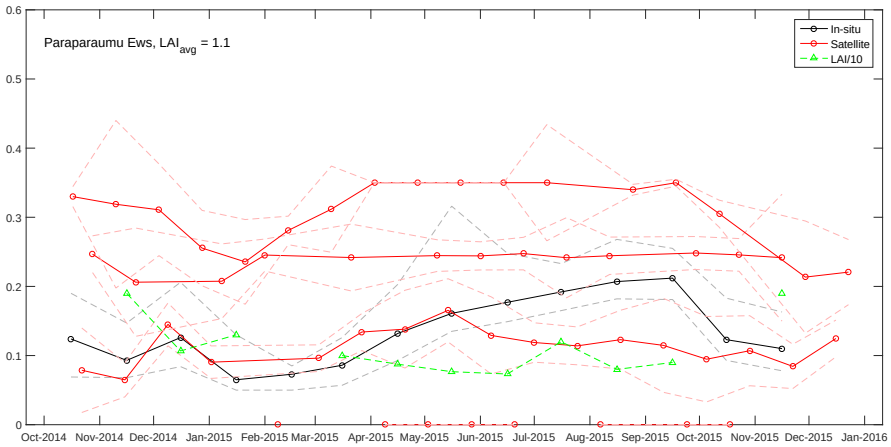

(b) Separate timeseries binned to global incidence θ

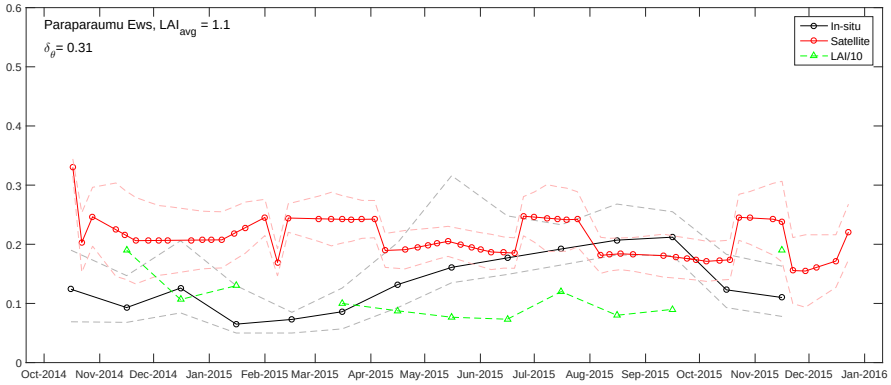

(c) Mean values, based on the θ time series

Figure A5: Inverted soil moisture at NIWA soil moisture ground station 'Paraparaumu Ews'.

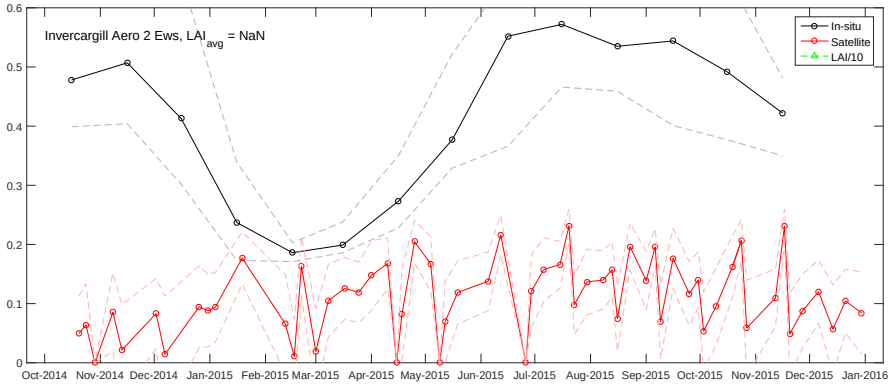

(a) All

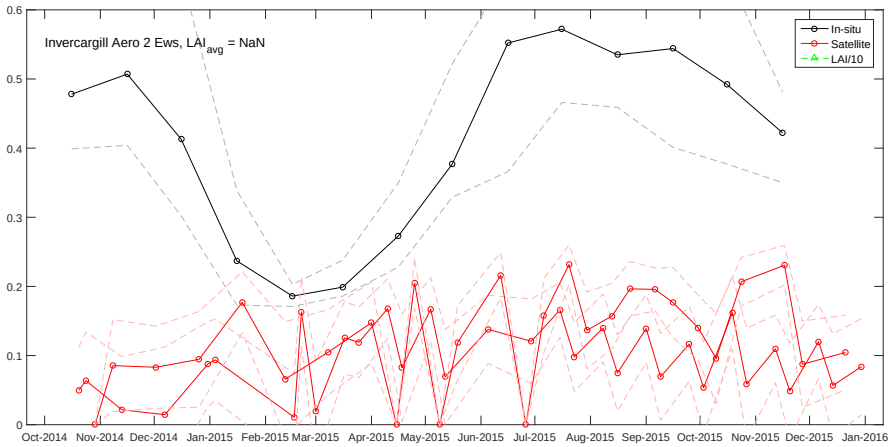

(b) Separate timeseries binned to global incidence θ

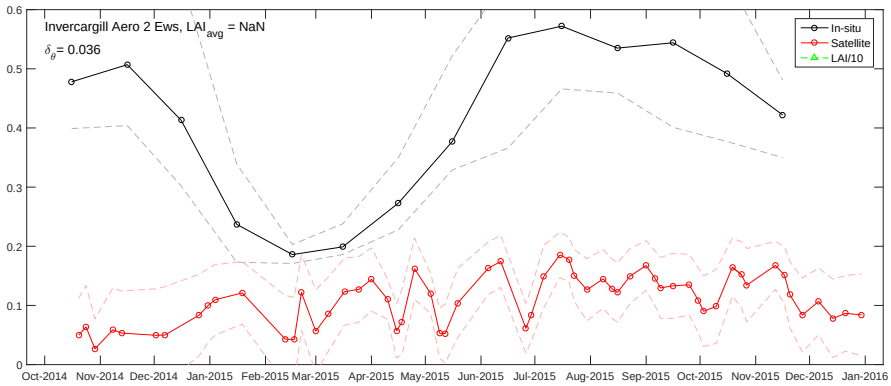

(c) Mean values, based on the θ time series

Figure A6: Inverted soil moisture at NIWA soil moisture ground station 'Invercargill Aero 2 Ews'.

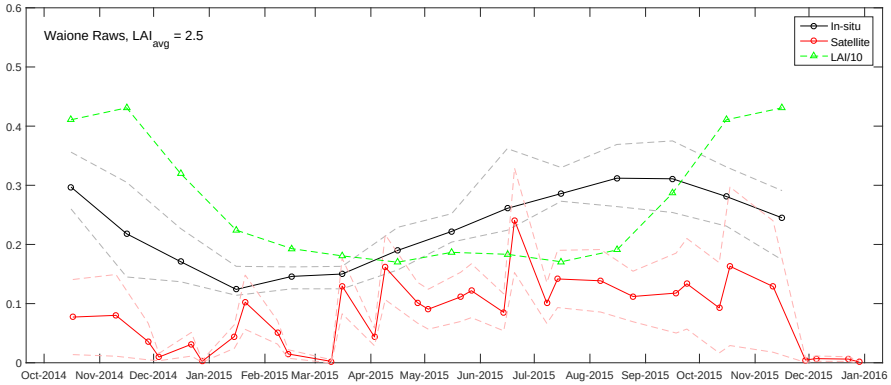

(a) All

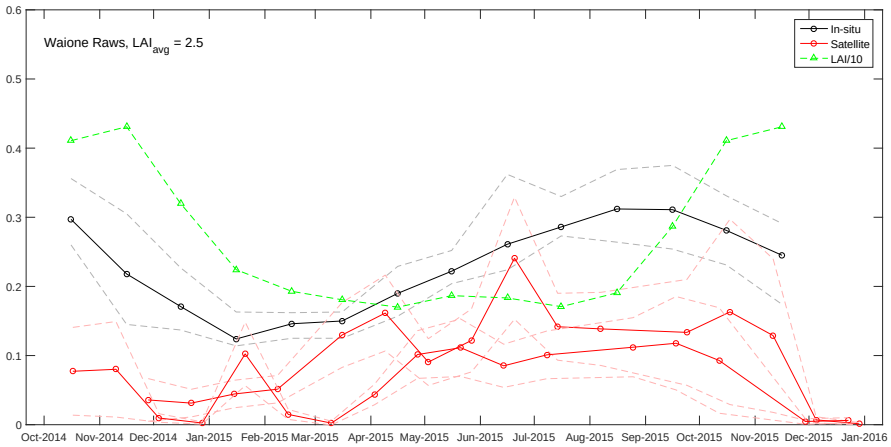

(b) Separate timeseries binned to global incidence θ

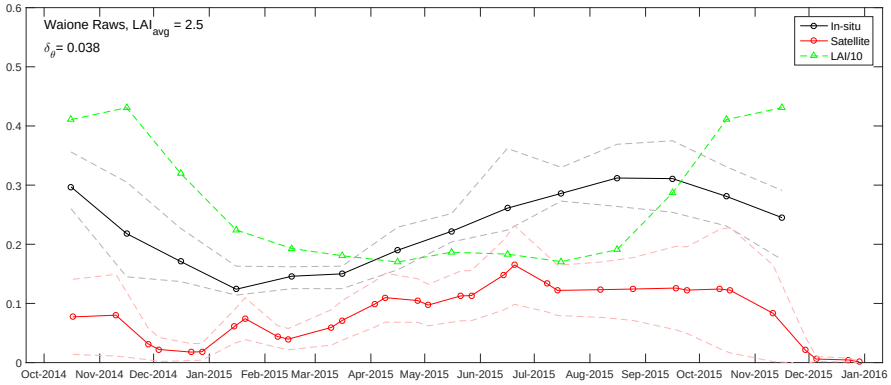

(c) Mean values, based on the θ time series

Figure A7: Inverted soil moisture at NIWA soil moisture ground station 'Waione Raws'.

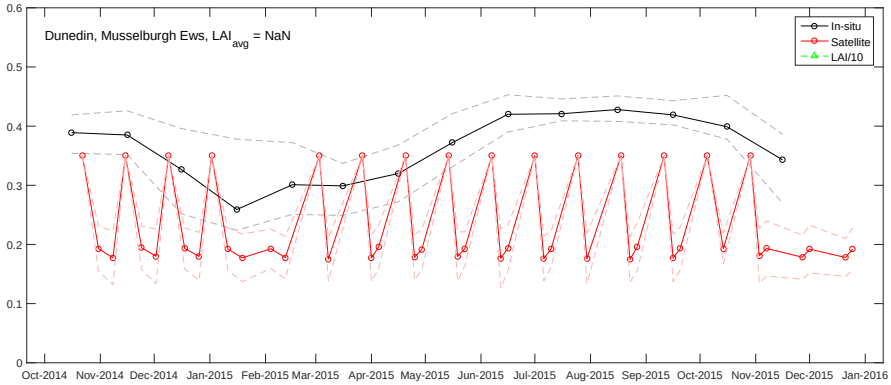

(a) All

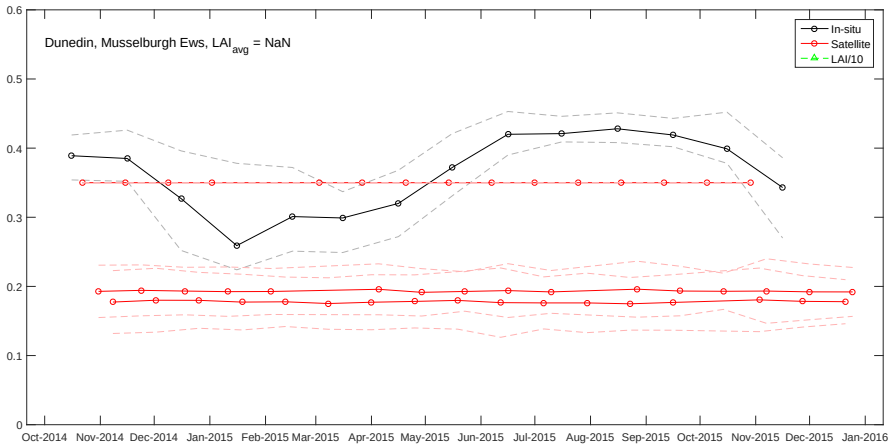

(b) Separate timeseries binned to global incidence θ

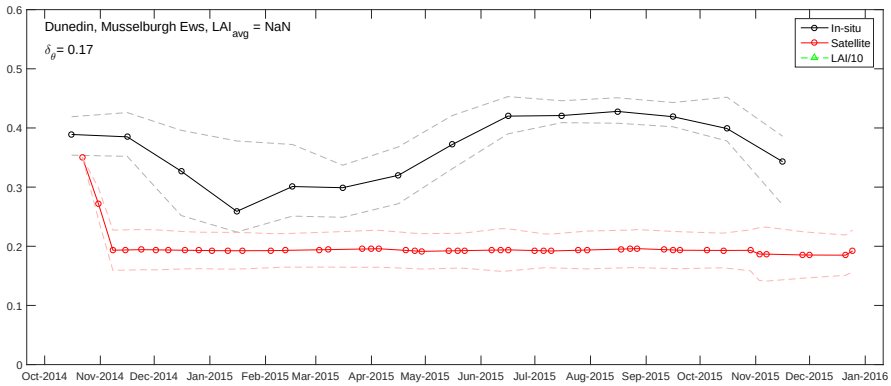

(c) Mean values, based on the θ time series

Figure A8: Inverted soil moisture at NIWA soil moisture ground station 'Dunedin, Musselburg Ews'.

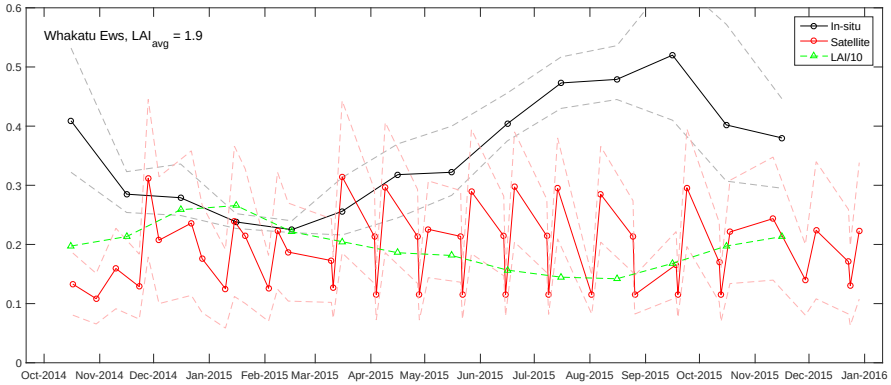

(a) All

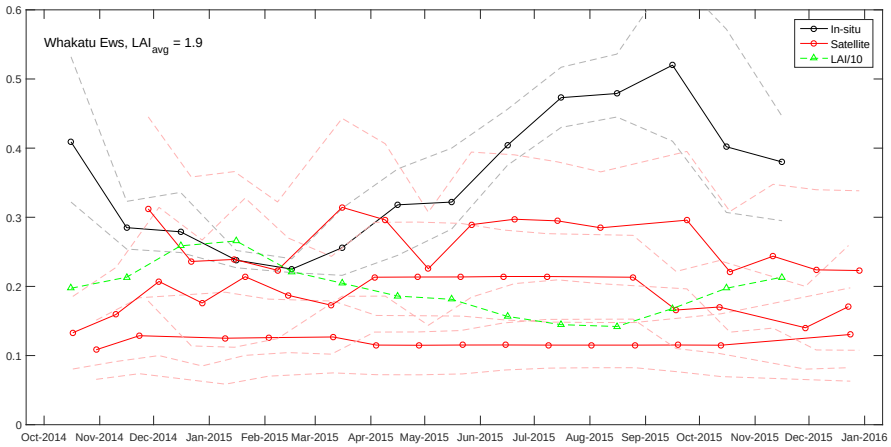

(b) Separate timeseries binned to global incidence θ

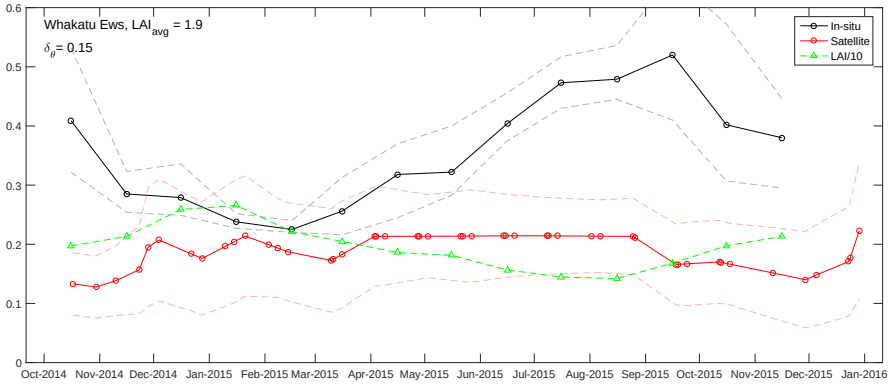

(c) Mean values, based on the θ time series

Figure A9: Inverted soil moisture at NIWA soil moisture ground station 'Whakatu Ews'.

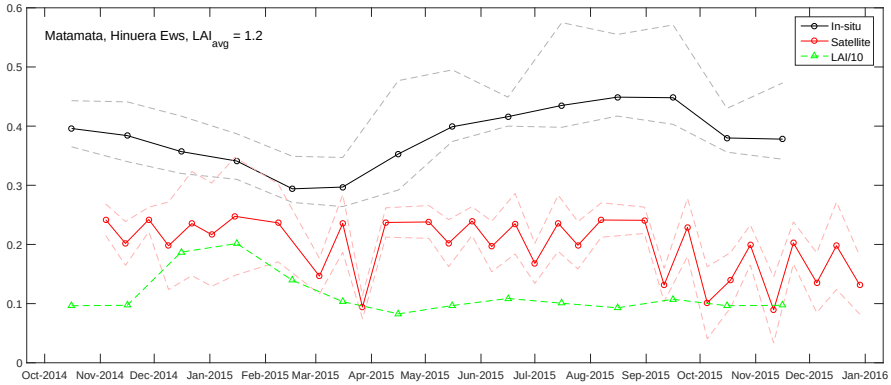

(a) All

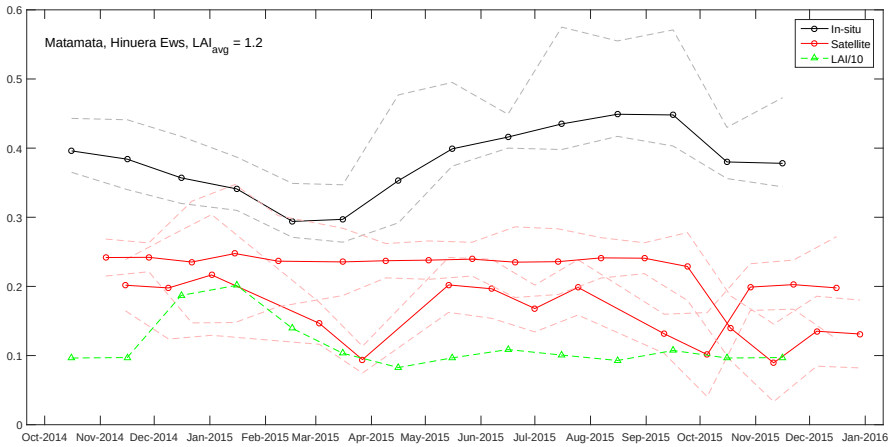

(b) Separate timeseries binned to global incidence θ

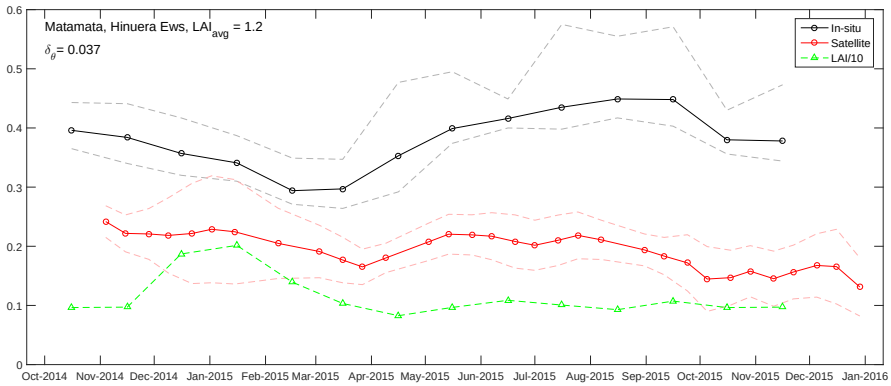

(c) Mean values, based on the θ time series

Figure A10: Inverted soil moisture at NIWA soil moisture ground station 'Matamata, Hinuera Ews'.

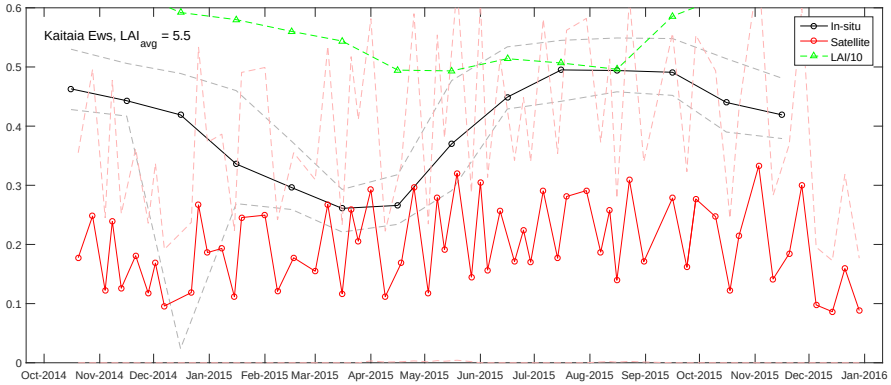

(a) All

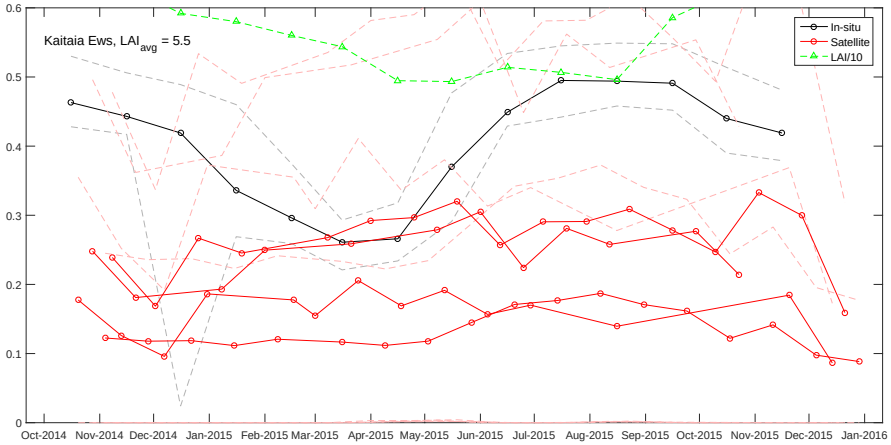

(b) Separate timeseries binned to global incidence θ

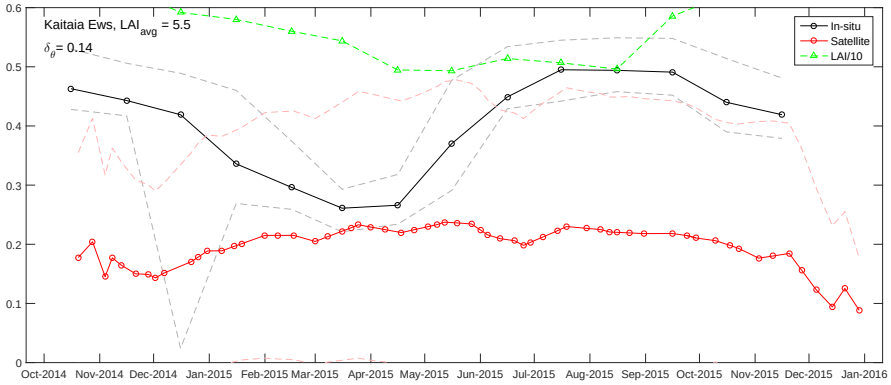

(c) Mean values, based on the θ time series

Figure A11: Inverted soil moisture at NIWA soil moisture ground station 'Kaitaia Ews'.

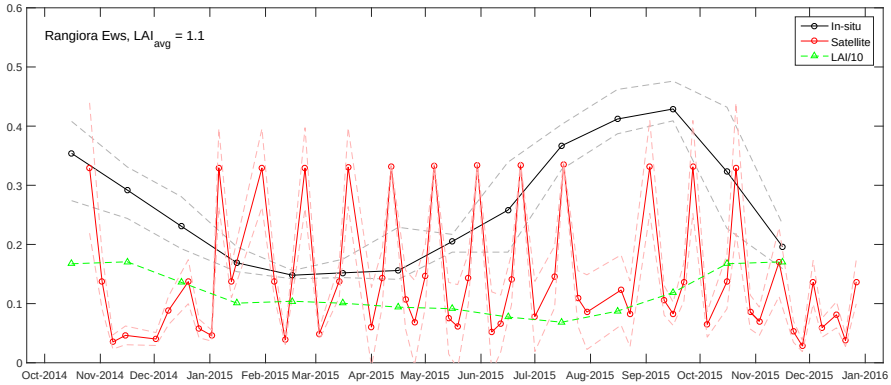

(a) All

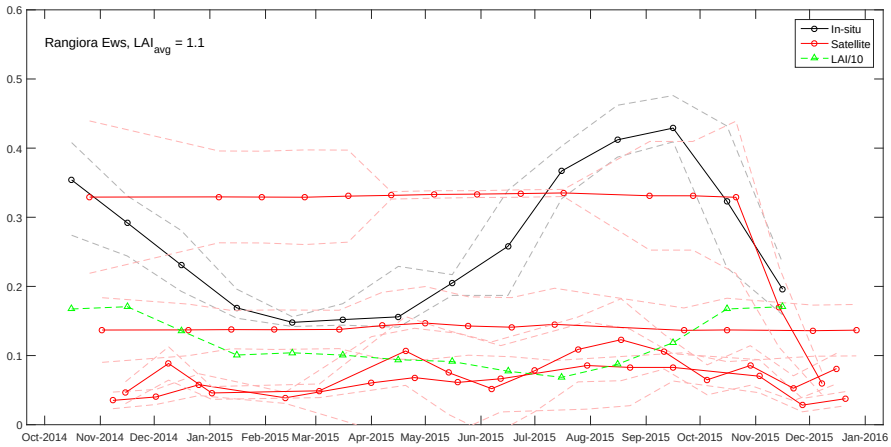

(b) Separate timeseries binned to global incidence θ

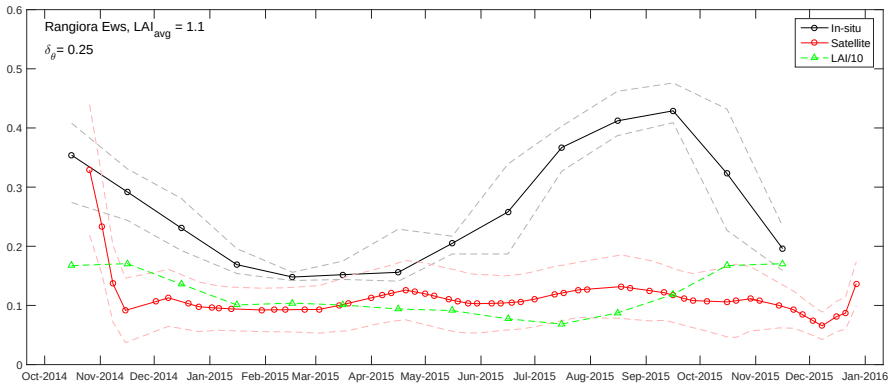

(c) Mean values, based on the θ time series

Figure A12: Inverted soil moisture at NIWA soil moisture ground station 'Rangiora Ews'.

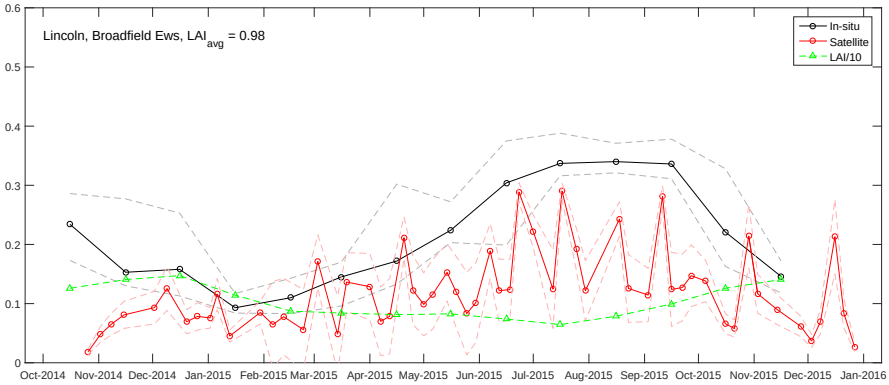

(a) All

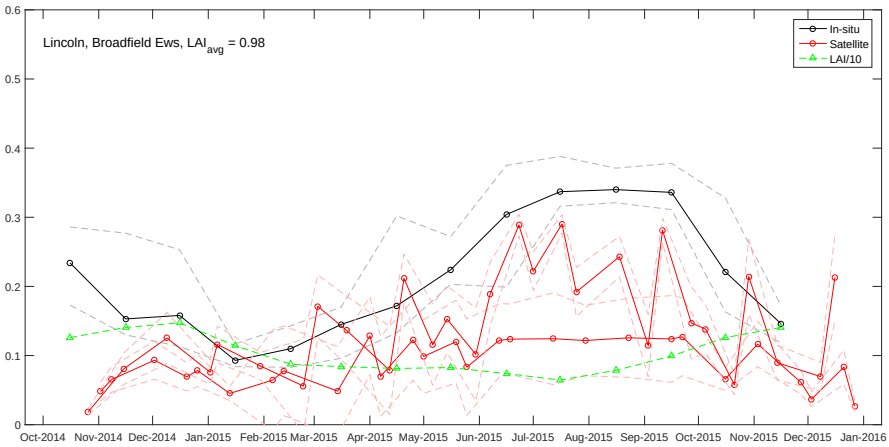

(b) Separate timeseries binned to global incidence θ

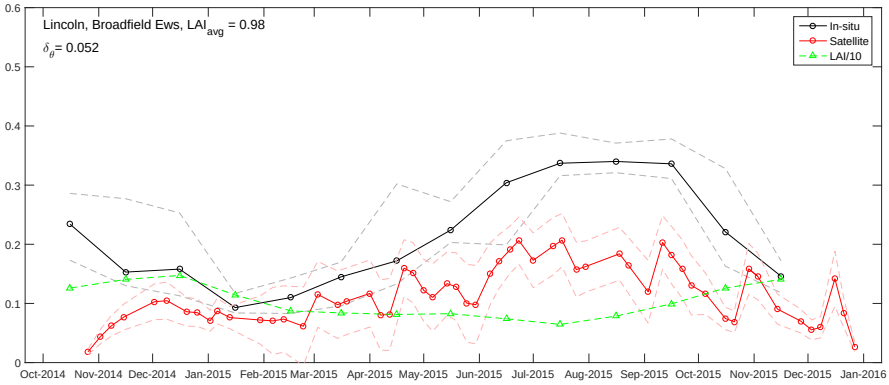

(c) Mean values, based on the θ time series

Figure A13: Inverted soil moisture at NIWA soil moisture ground station 'Lincoln, Broadfield Ews'.

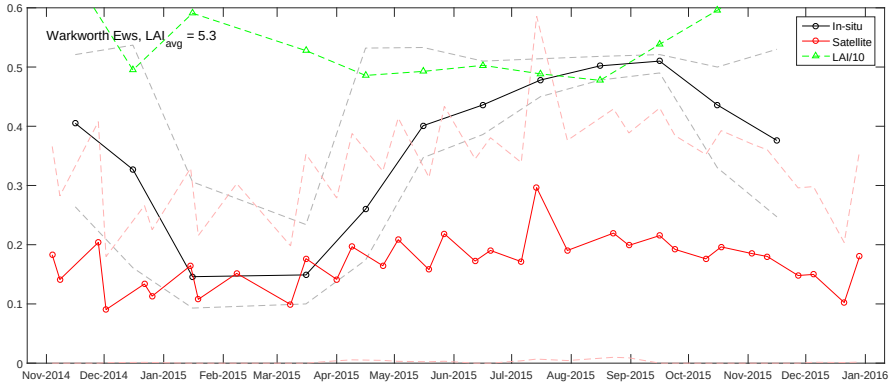

(a) All

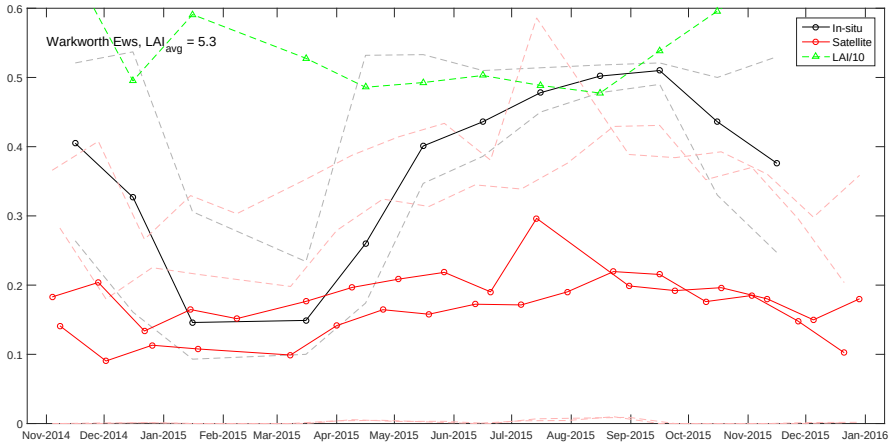

(b) Separate timeseries binned to global incidence θ

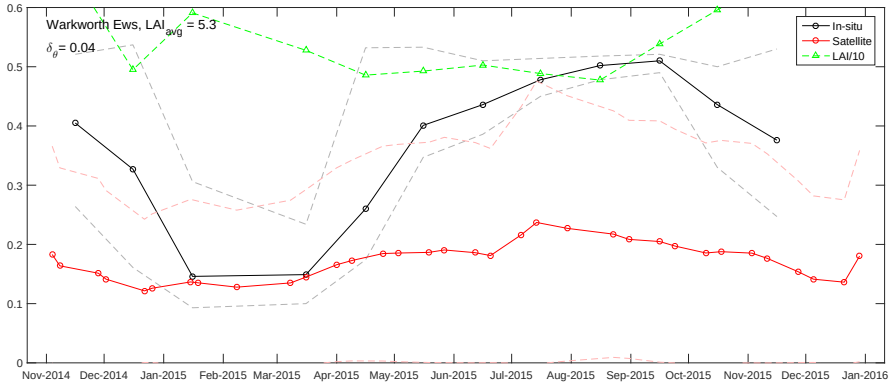

(c) Mean values, based on the θ time series

Figure A14: Inverted soil moisture at NIWA soil moisture ground station 'Warkworth Ews'.

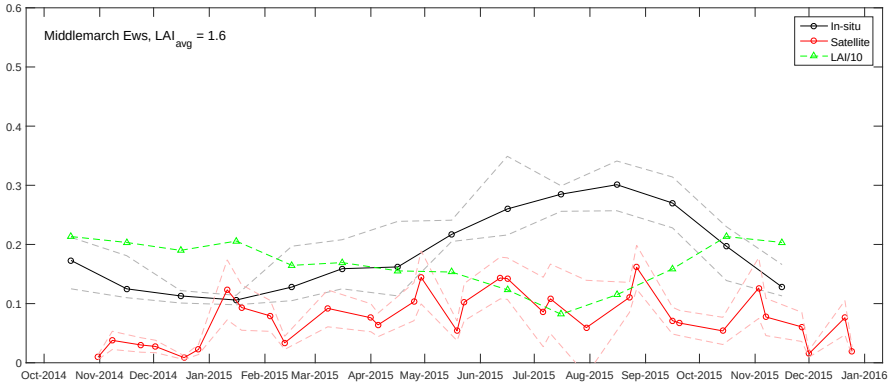

(a) All

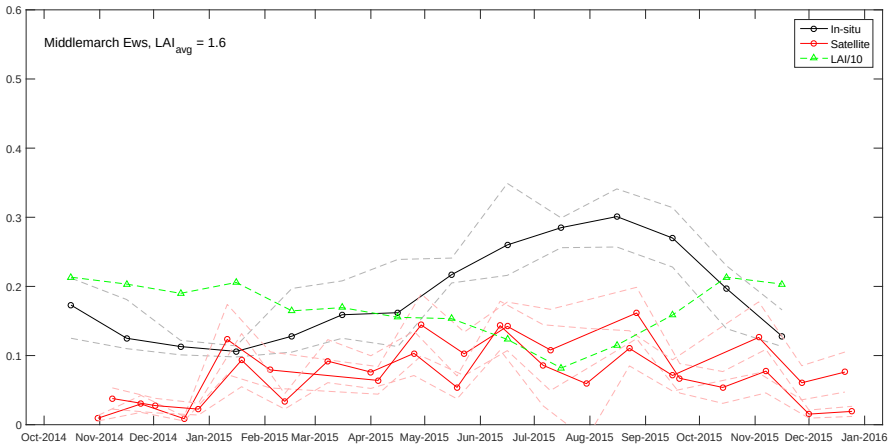

(b) Separate timeseries binned to global incidence θ

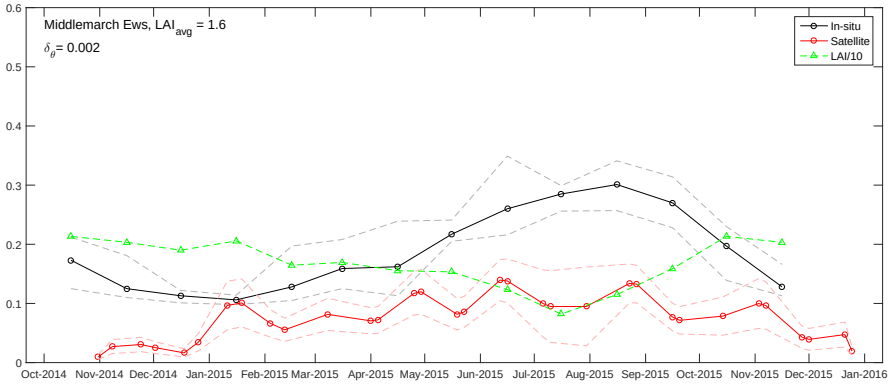

(c) Mean values, based on the θ time series

Figure A15: Inverted soil moisture at NIWA soil moisture ground station 'Middlemarch Ews'.

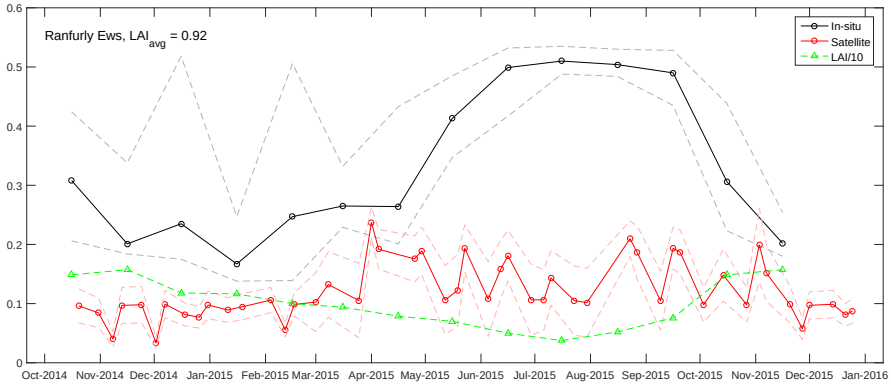

(a) All

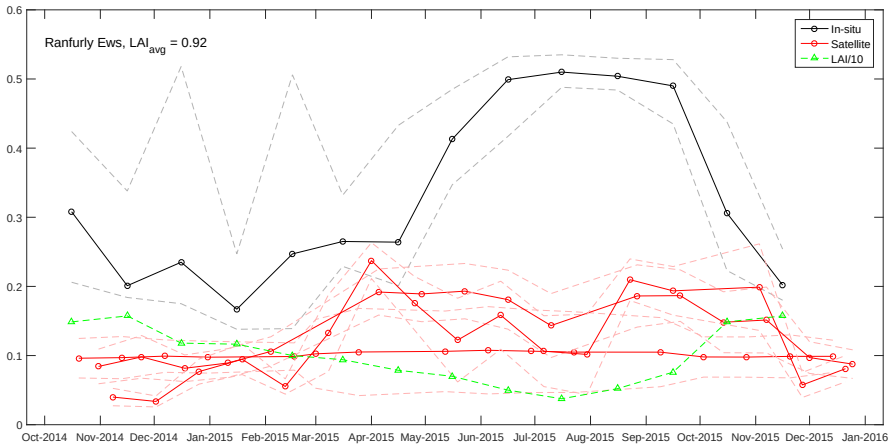

(b) Separate timeseries binned to global incidence θ

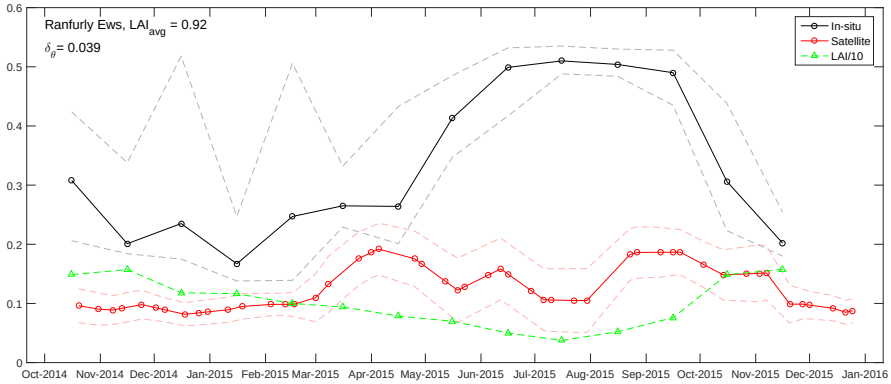

(c) Mean values, based on the θ time series

Figure A16: Inverted soil moisture at NIWA soil moisture ground station 'Ranfurly Ews'.

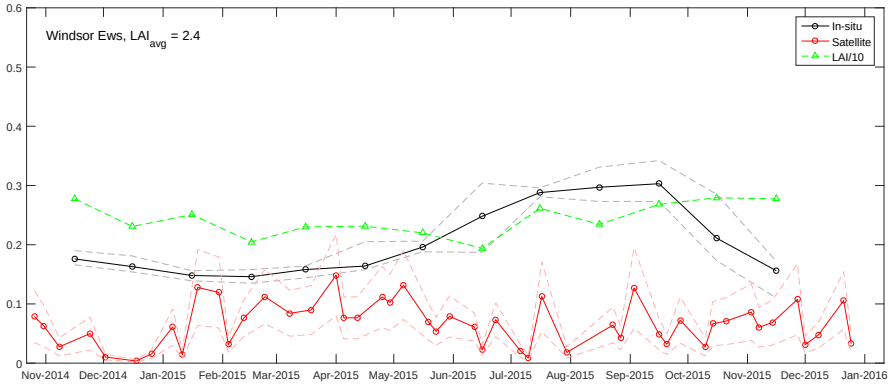

(a) All

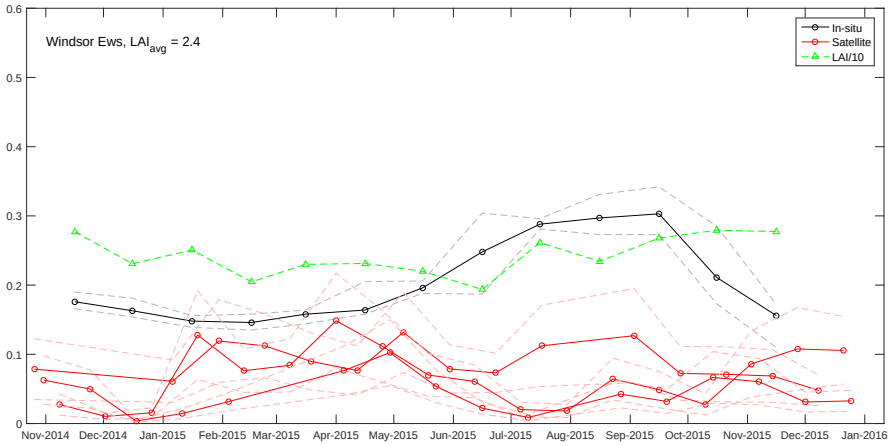

(b) Separate timeseries binned to global incidence θ

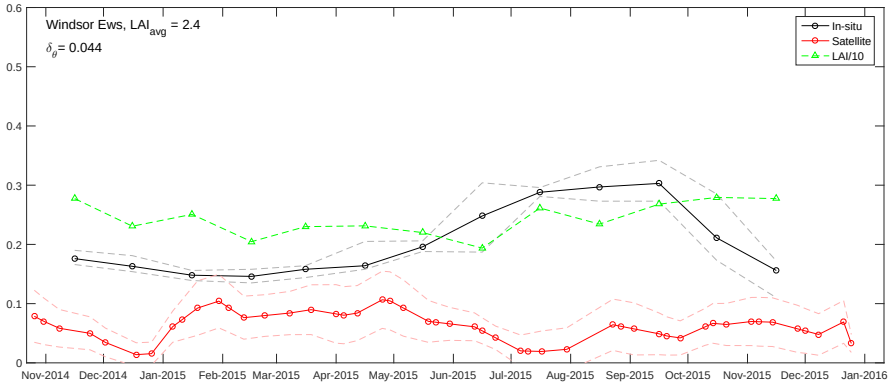

(c) Mean values, based on the θ time series

Figure A17: Inverted soil moisture at NIWA soil moisture ground station 'Windsor Ews'.

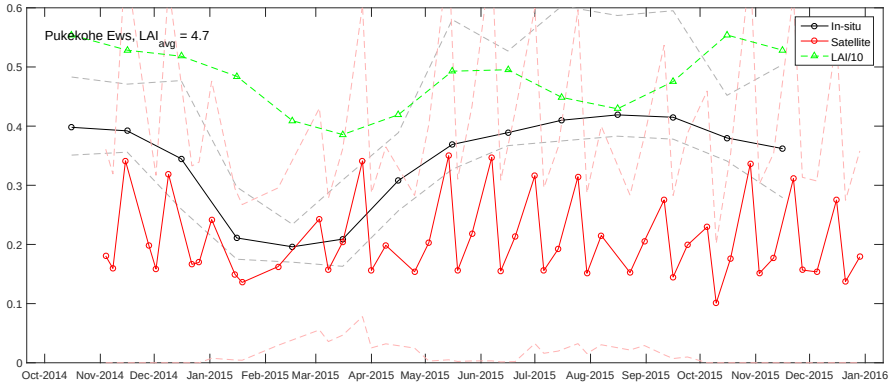

(a) All

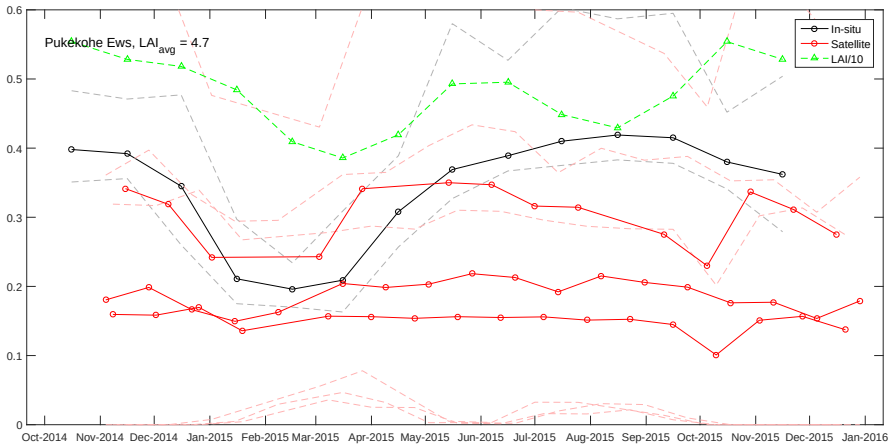

(b) Separate timeseries binned to global incidence θ

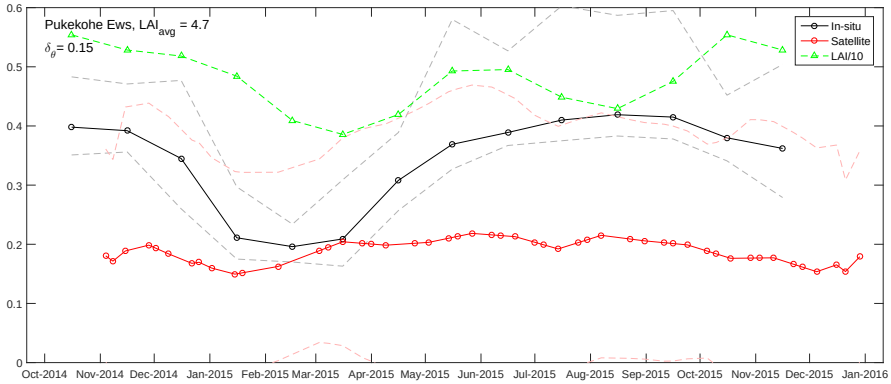

(c) Mean values, based on the θ time series

Figure A18: Inverted soil moisture at NIWA soil moisture ground station 'Pukekohe Ews'.

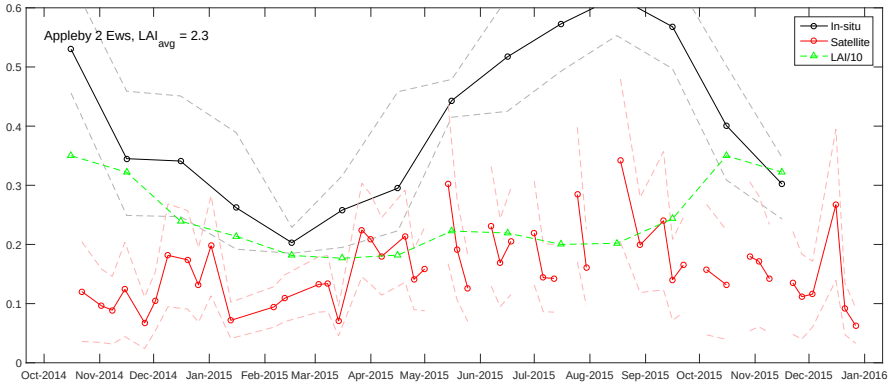

(a) All

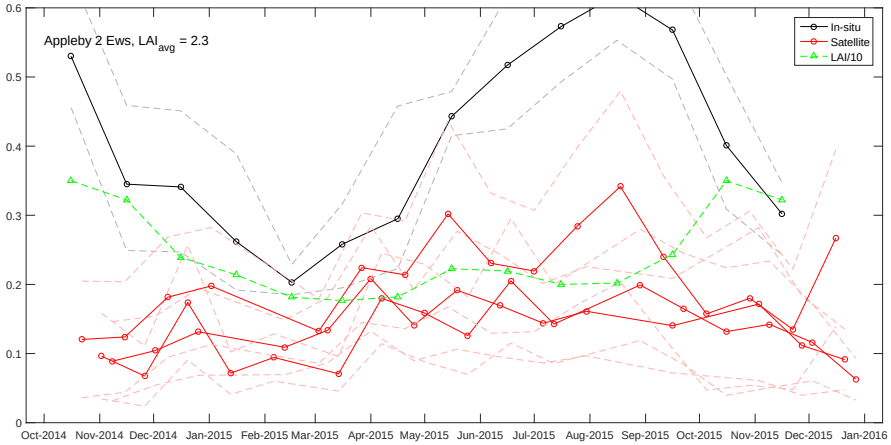

(b) Separate timeseries binned to global incidence θ

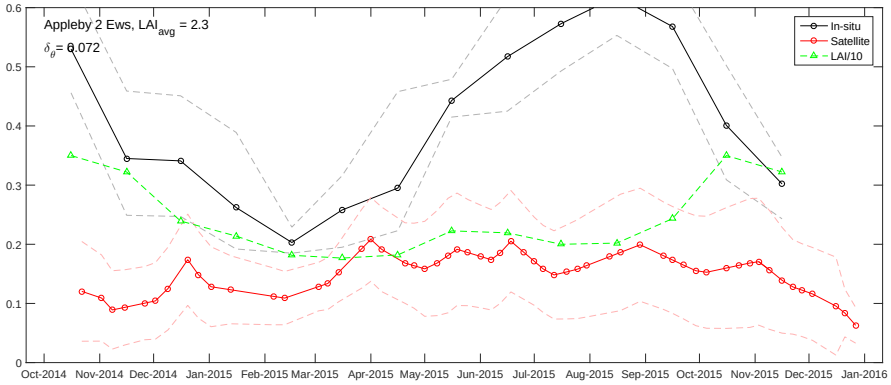

(c) Mean values, based on the θ time series

Figure A19: Inverted soil moisture at NIWA soil moisture ground station 'Appleby 2 Ews'.

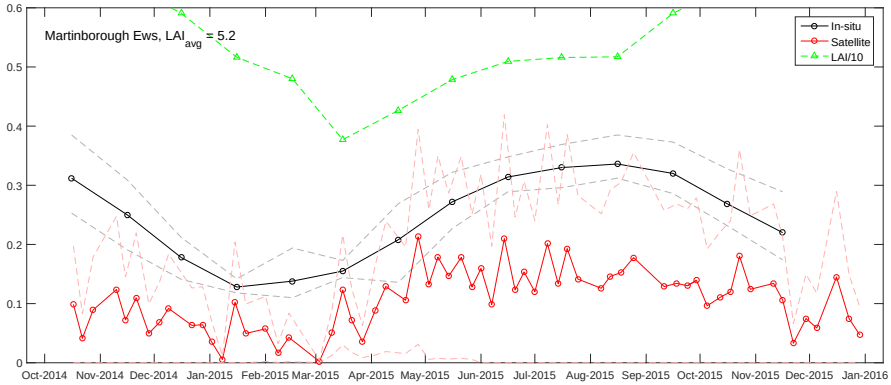

(a) All

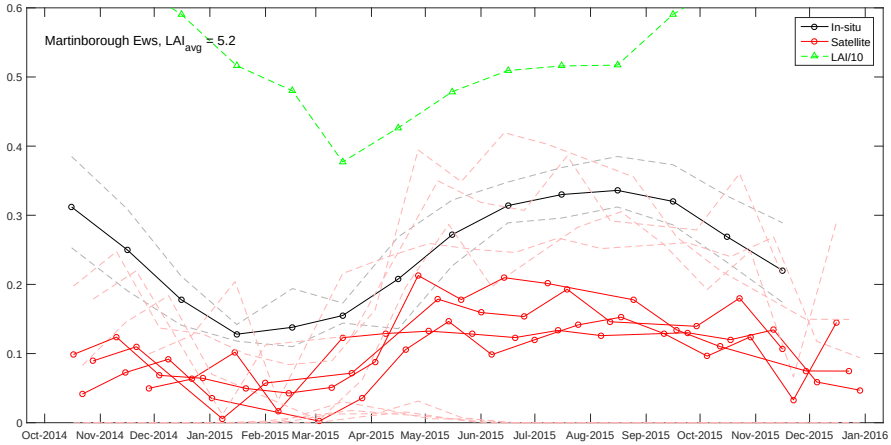

(b) Separate timeseries binned to global incidence θ

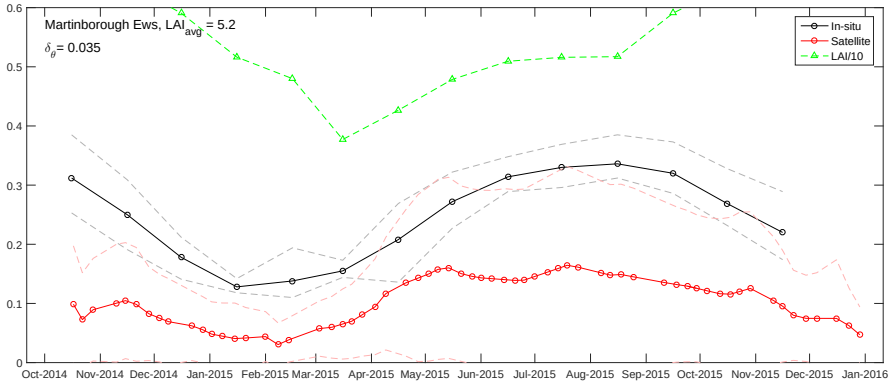

(c) Mean values, based on the θ time series

Figure A20: Inverted soil moisture at NIWA soil moisture ground station 'Martinborough Ews'.

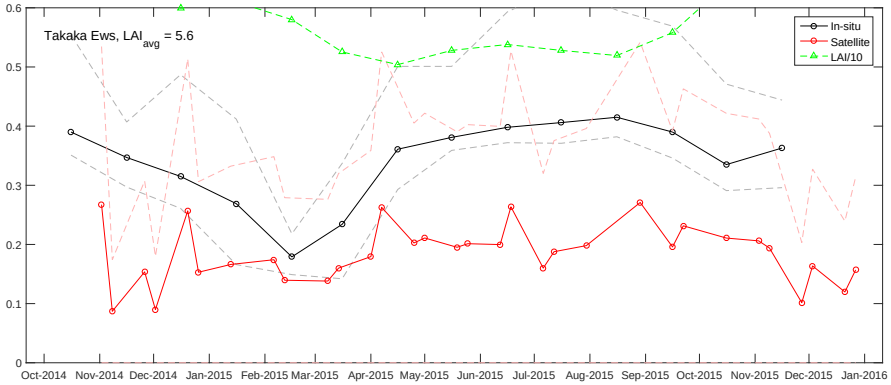

(a) All

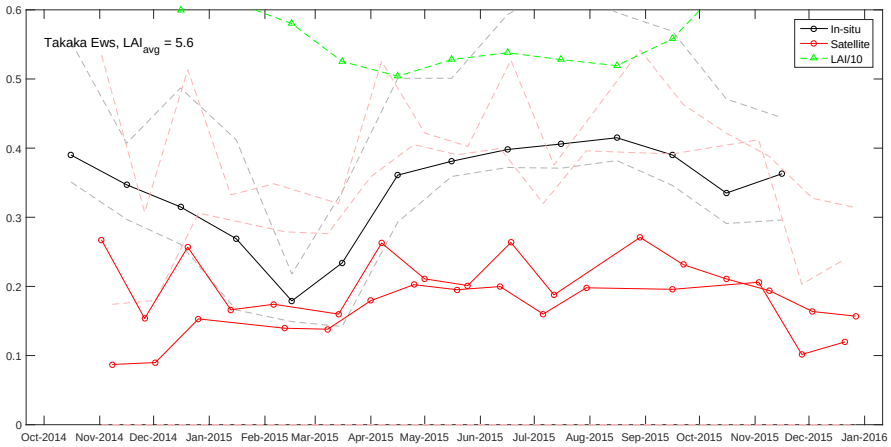

(b) Separate timeseries binned to global incidence θ

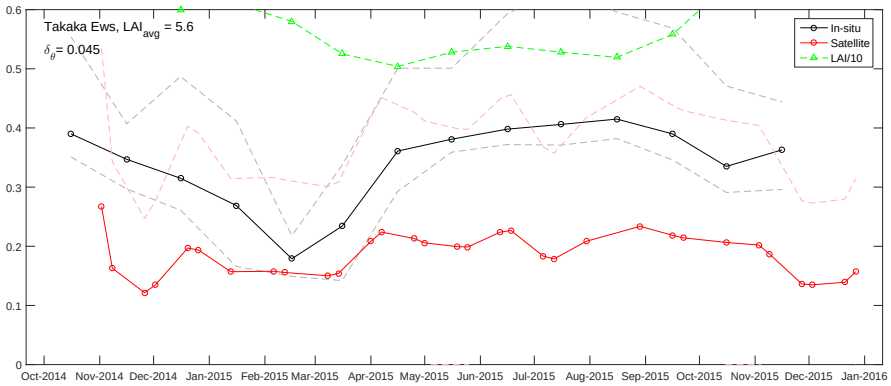

(c) Mean values, based on the θ time series

Figure A21: Inverted soil moisture at NIWA soil moisture ground station 'Takaka Ews'.

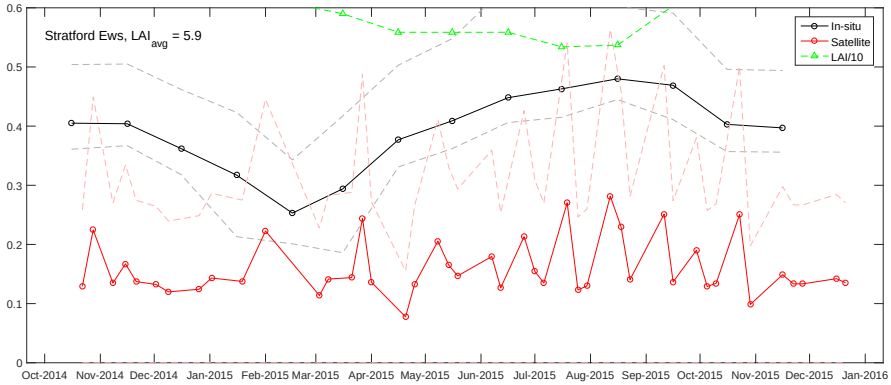

(a) All

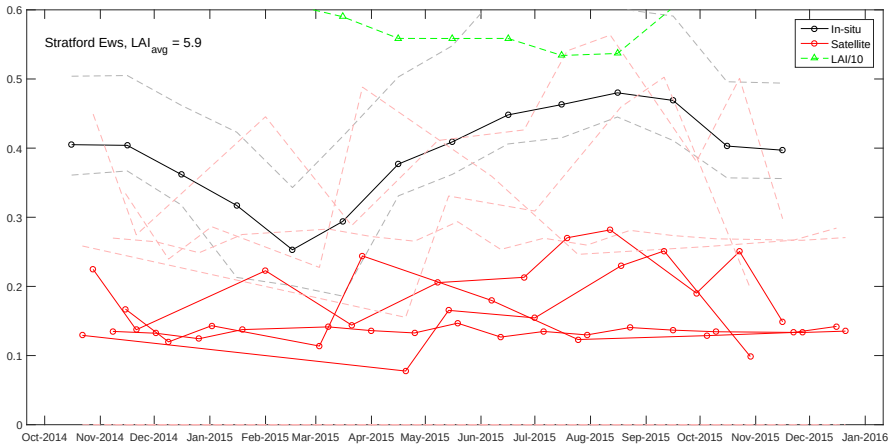

(b) Separate timeseries binned to global incidence θ

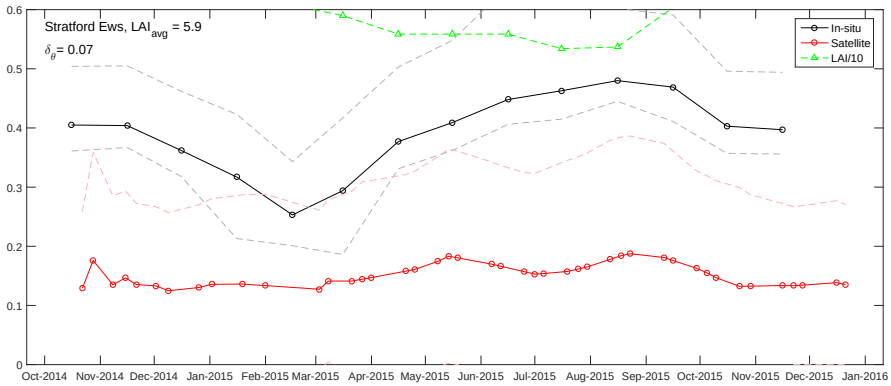

(c) Mean values, based on the θ time series

Figure A22: Inverted soil moisture at NIWA soil moisture ground station 'Stratford Ews'.

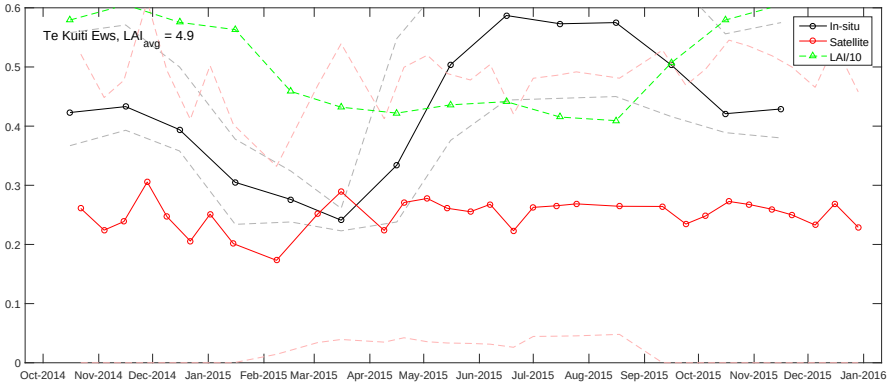

(a) All

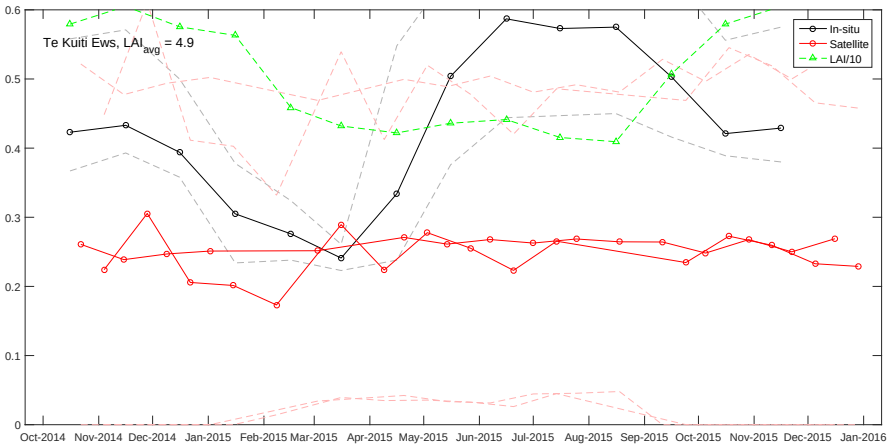

(b) Separate timeseries binned to global incidence θ

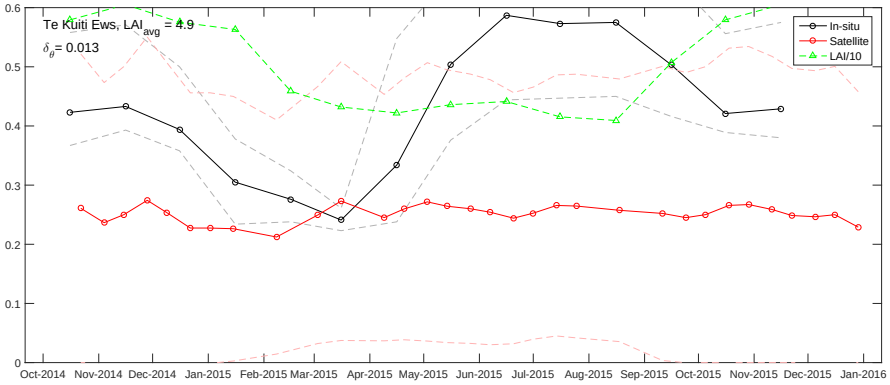

(c) Mean values, based on the θ time series

Figure A23: Inverted soil moisture at NIWA soil moisture ground station 'Te Kuiti Ews'.

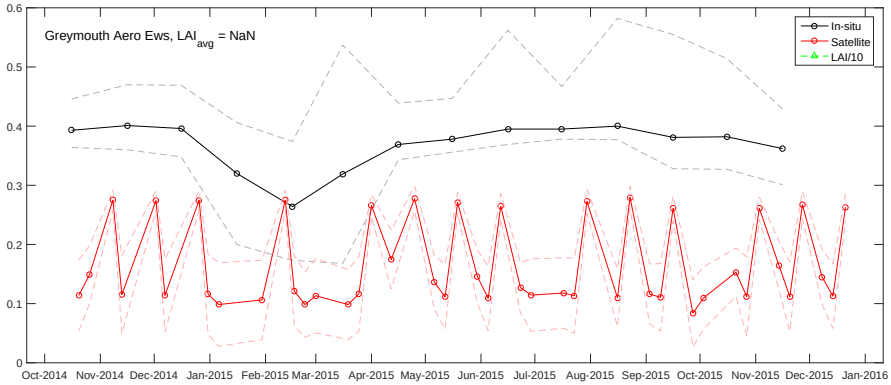

(a) All

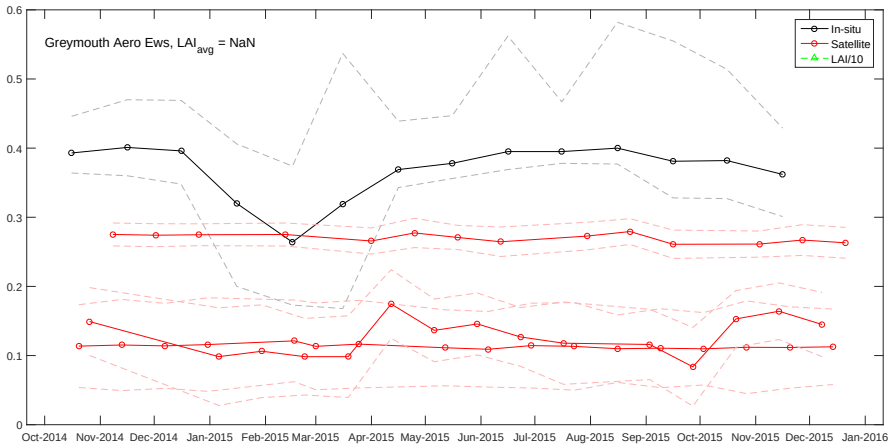

(b) Separate timeseries binned to global incidence θ

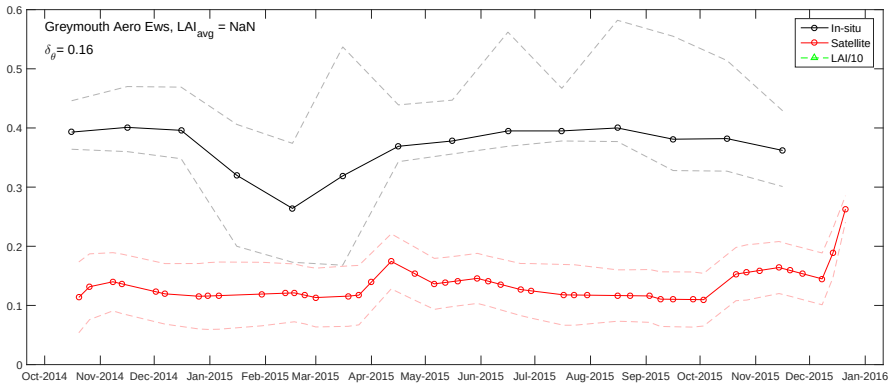

(c) Mean values, based on the θ time series

Figure A24: Inverted soil moisture at NIWA soil moisture ground station 'Greymouth Aero Ews'.

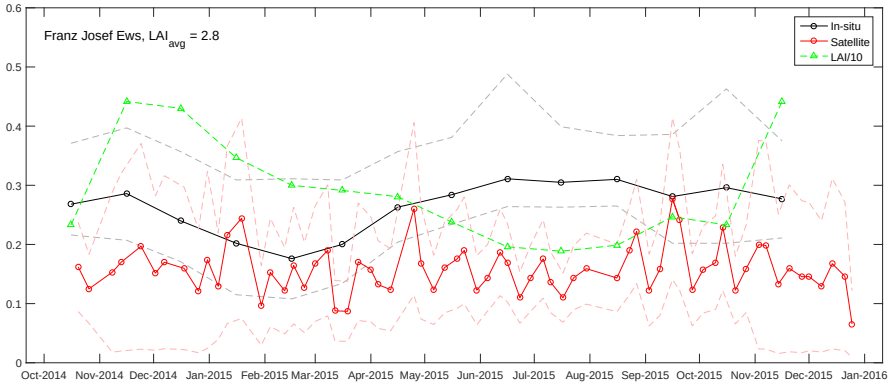

(a) All

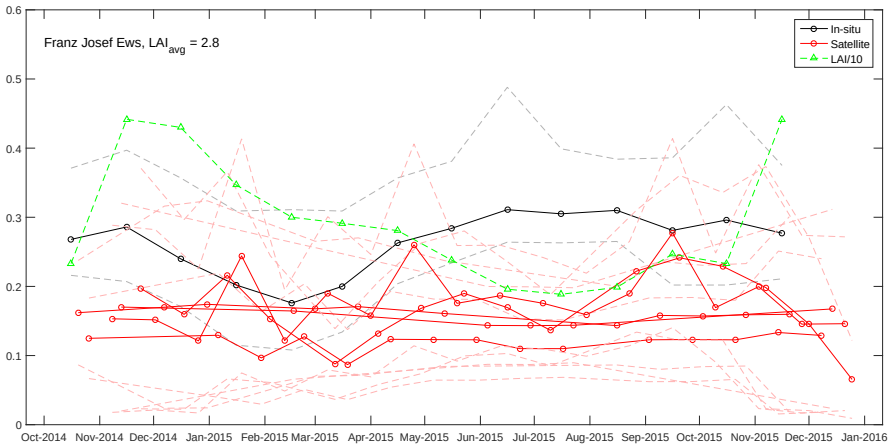

(b) Separate timeseries binned to global incidence θ

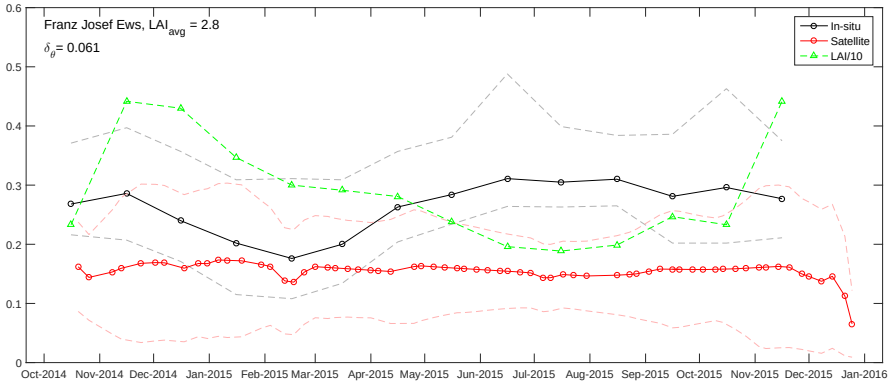

(c) Mean values, based on the θ time series

Figure A25: Inverted soil moisture at NIWA soil moisture ground station 'Franz Josef Ews'.

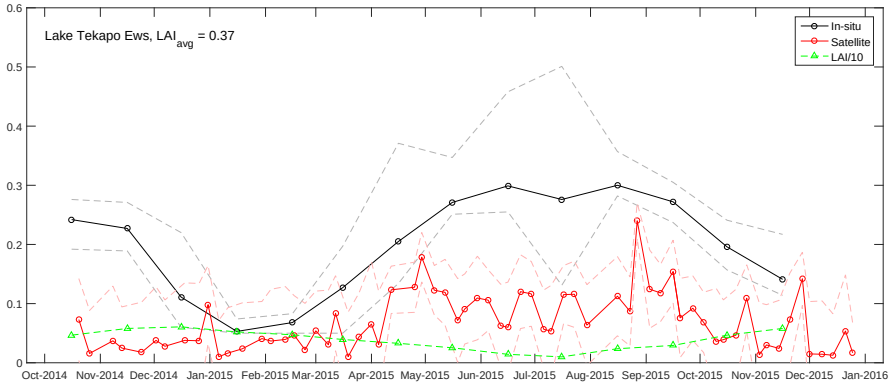

(a) All

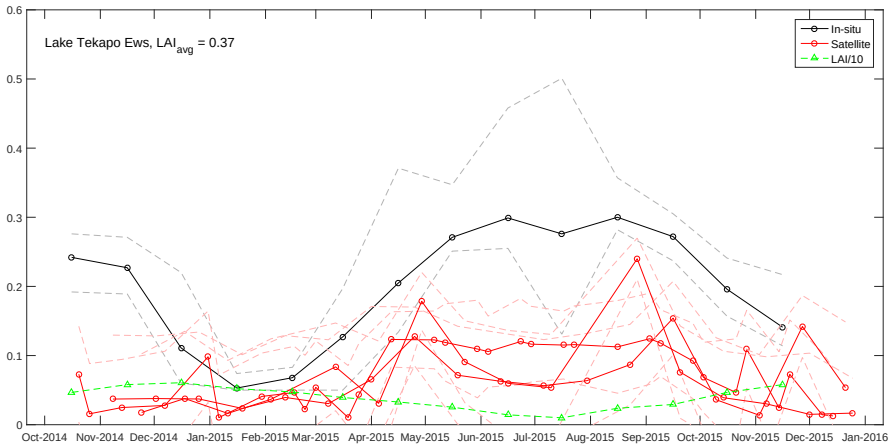

(b) Separate timeseries binned to global incidence θ

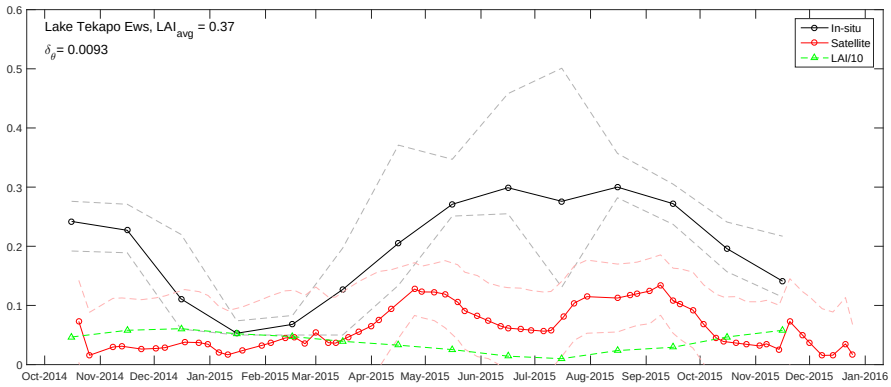

(c) Mean values, based on the θ time series

Figure A26: Inverted soil moisture at NIWA soil moisture ground station 'Lake Tekapo Ews'.

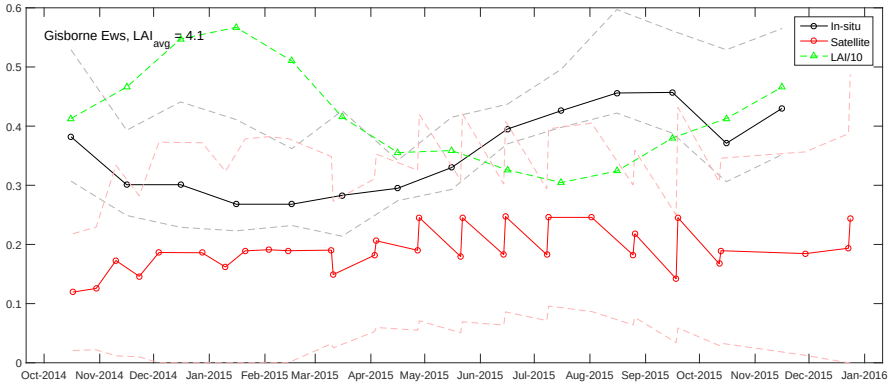

(a) All

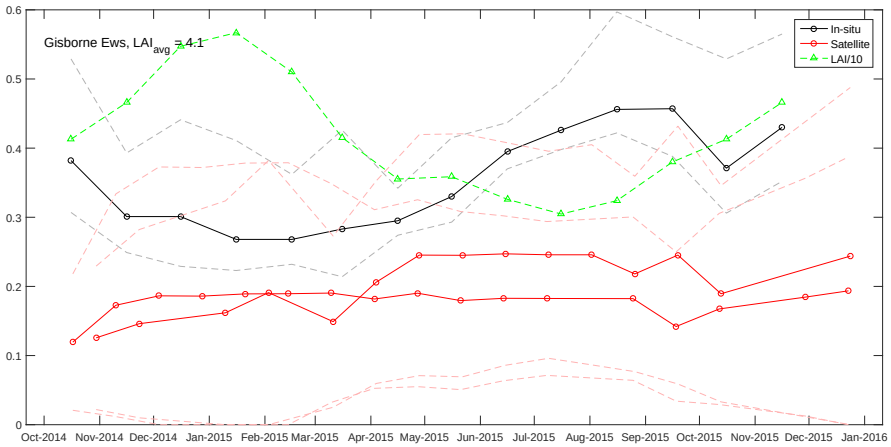

(b) Separate timeseries binned to global incidence θ

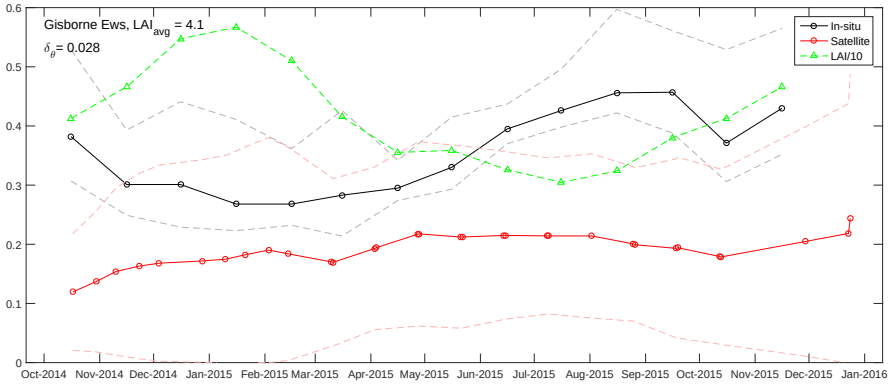

(c) Mean values, based on the θ time series

Figure A27: Inverted soil moisture at NIWA soil moisture ground station 'Gisborne Ews'.

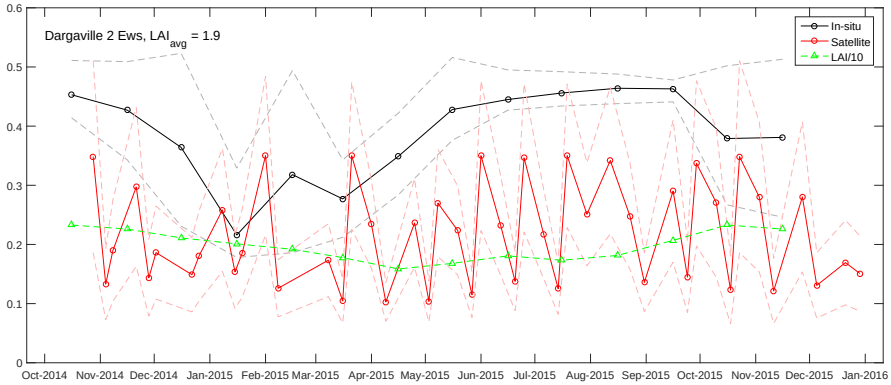

(a) All

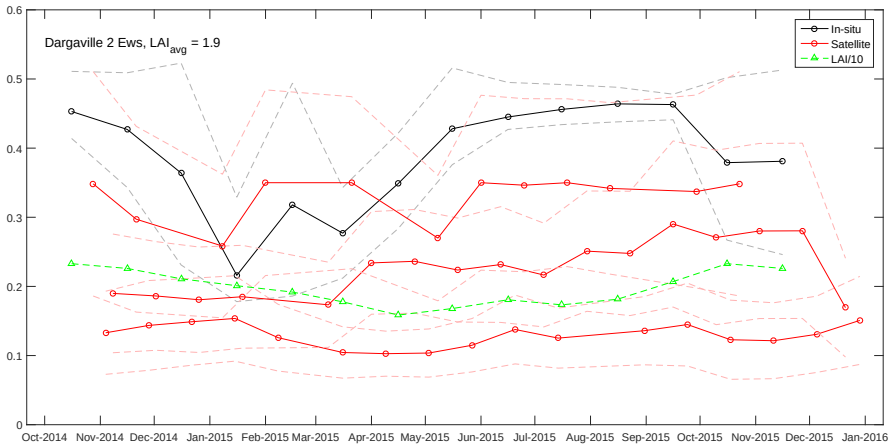

(b) Separate timeseries binned to global incidence θ

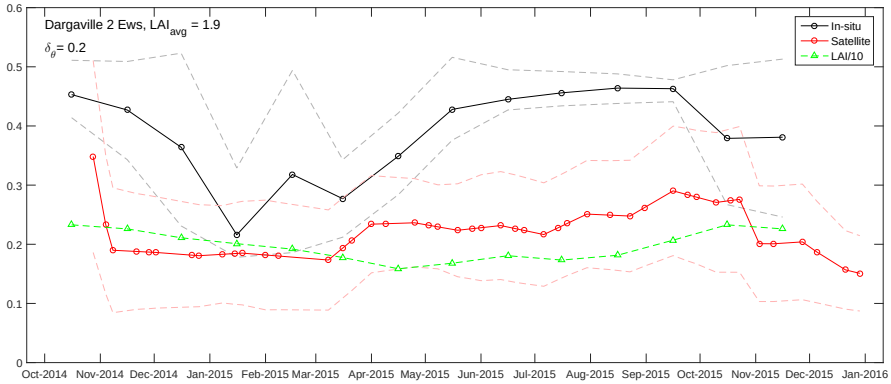

(c) Mean values, based on the θ time series

Figure A28: Inverted soil moisture at NIWA soil moisture ground station 'Dargaville 2 Ews'.

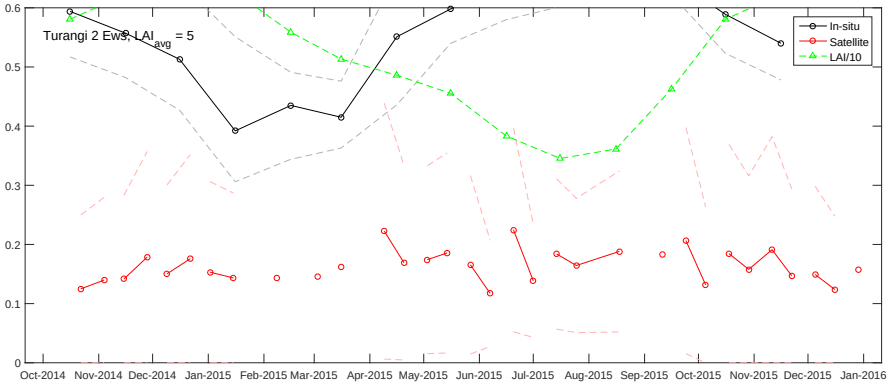

(a) All

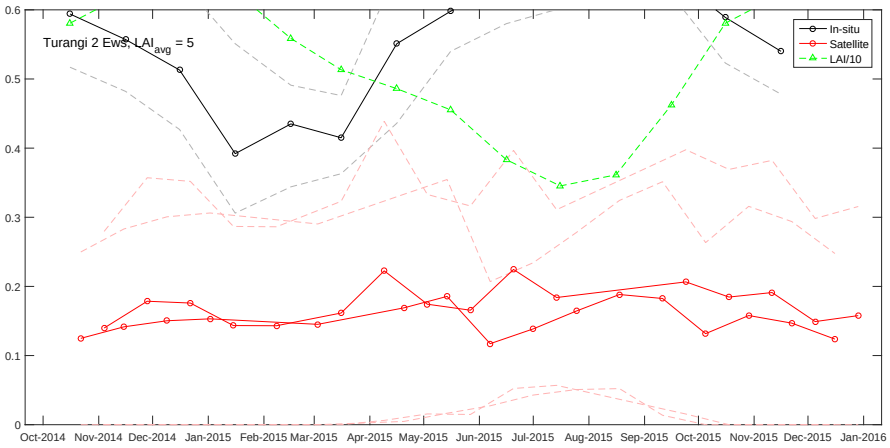

(b) Separate timeseries binned to global incidence θ

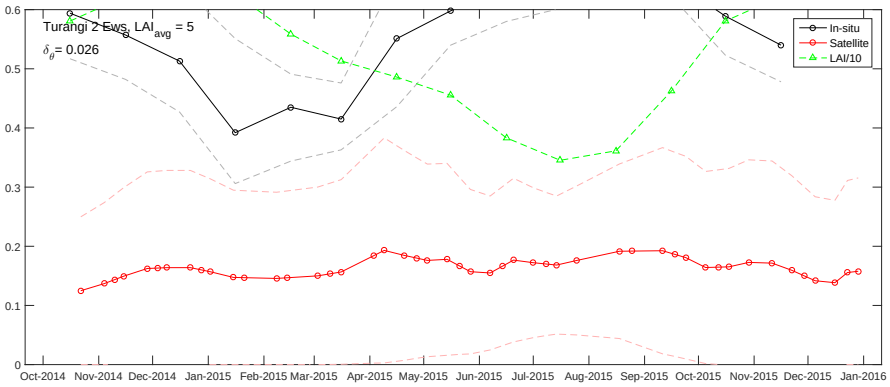

(c) Mean values, based on the θ time series

Figure A29: Inverted soil moisture at NIWA soil moisture ground station 'Turangi 2 Ews'.

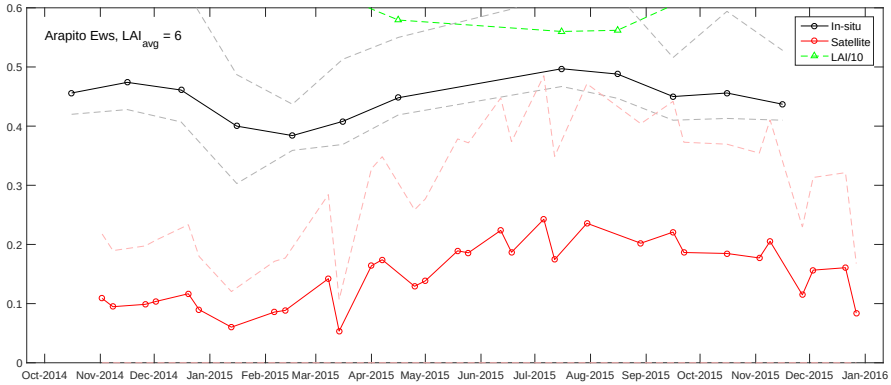

(a) All

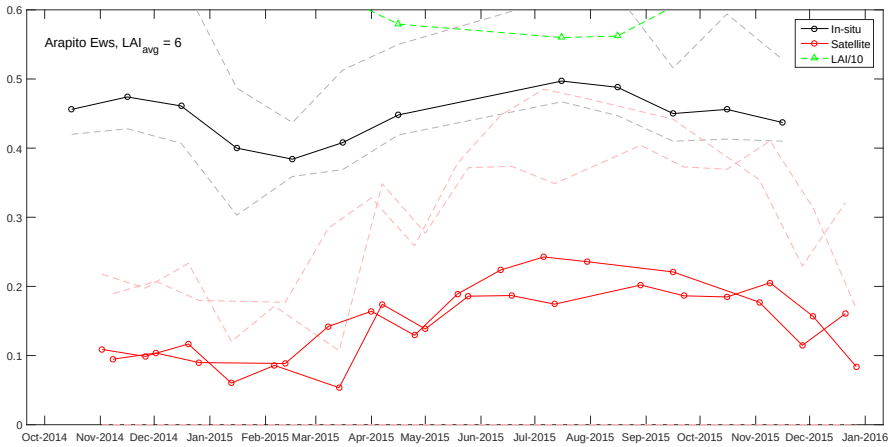

(b) Separate timeseries binned to global incidence θ

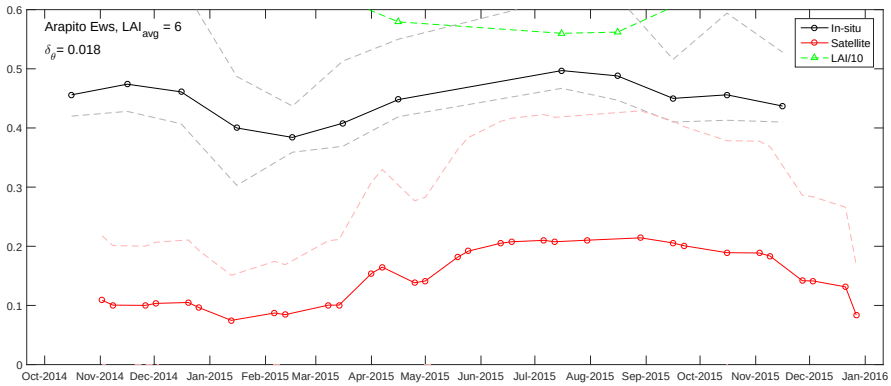

(c) Mean values, based on the θ time series

Figure A30: Inverted soil moisture at NIWA soil moisture ground station 'Arapito Ews'.

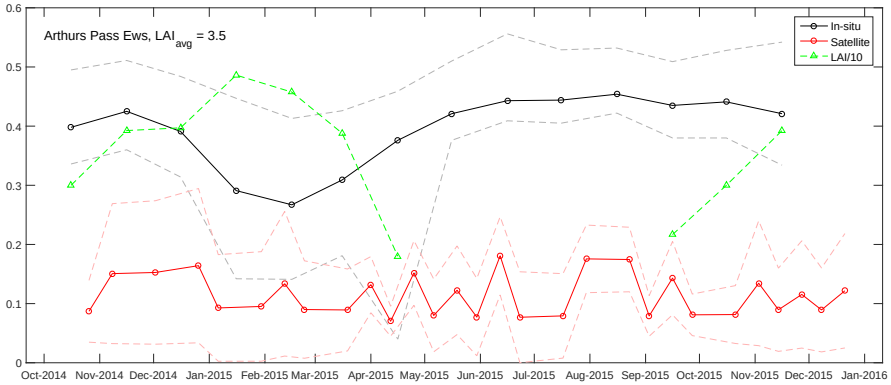

(a) All

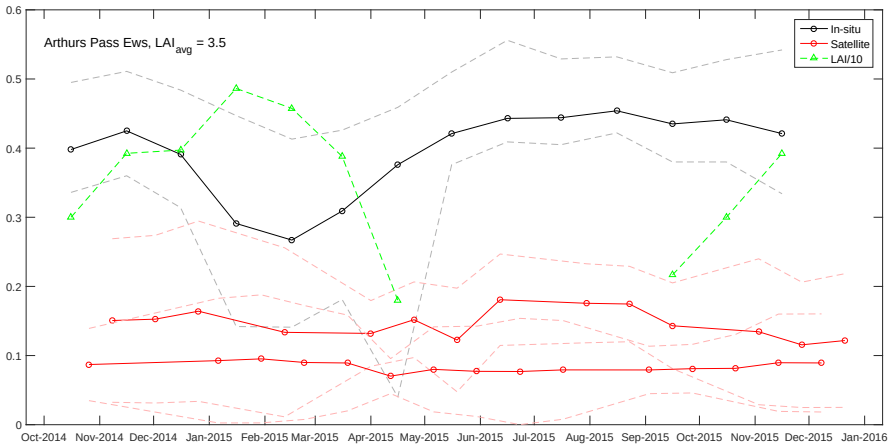

(b) Separate timeseries binned to global incidence θ

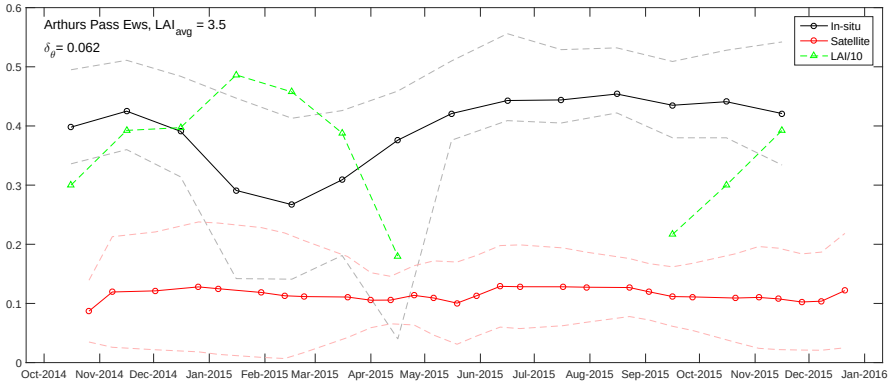

(c) Mean values, based on the θ time series

Figure A31: Inverted soil moisture at NIWA soil moisture ground station 'Arthurs Pass Ews'.

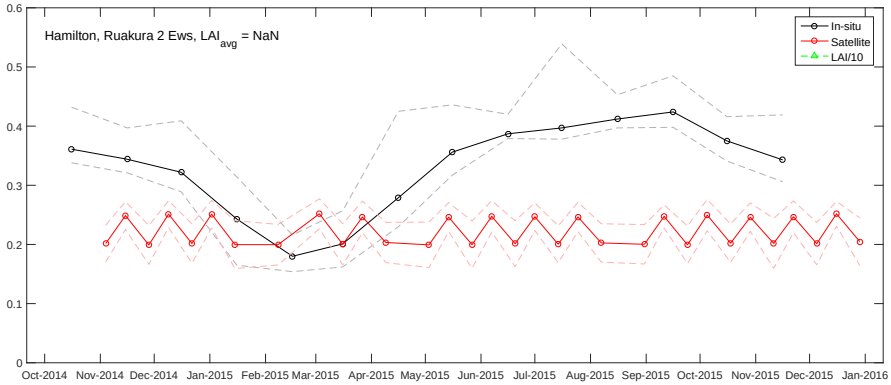

(a) All

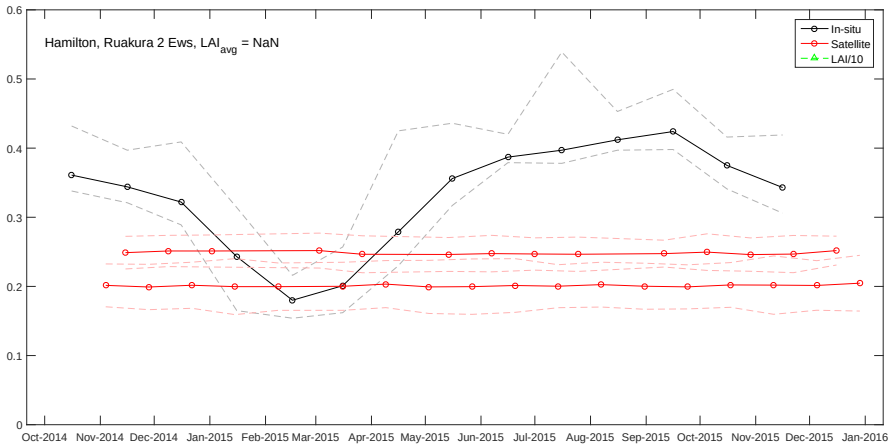

(b) Separate timeseries binned to global incidence θ

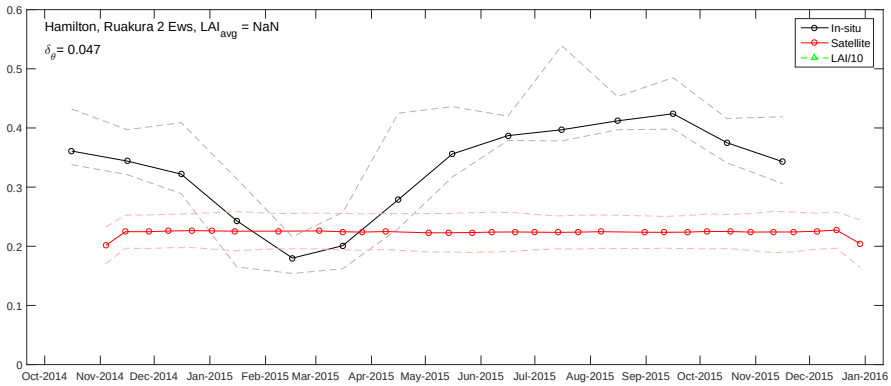

(c) Mean values, based on the θ time series

Figure A32: Inverted soil moisture at NIWA soil moisture ground station 'Hamilton, Ruakura 2 Ews'.

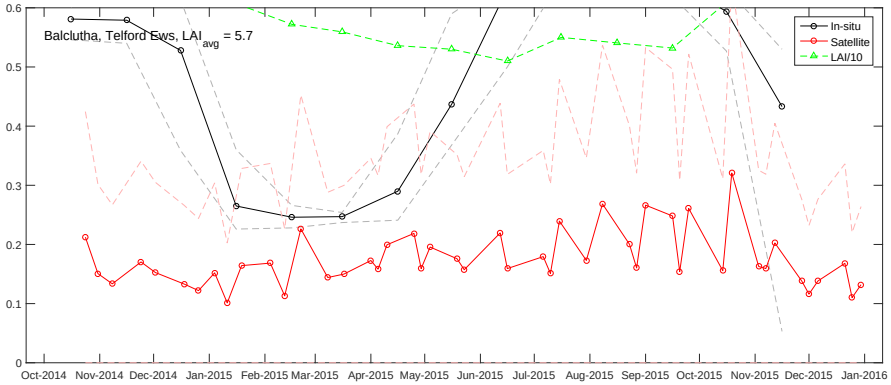

(a) All

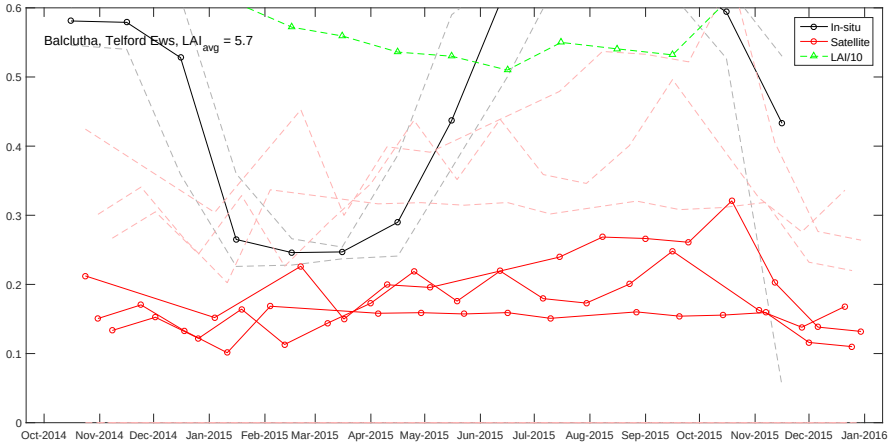

(b) Separate timeseries binned to global incidence θ

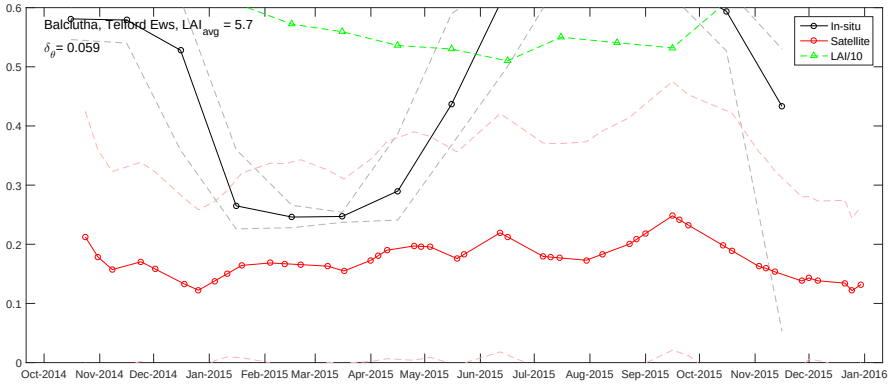

(c) Mean values, based on the θ time series

Figure A33: Inverted soil moisture at NIWA soil moisture ground station 'Balclutha, Telford Ews'.

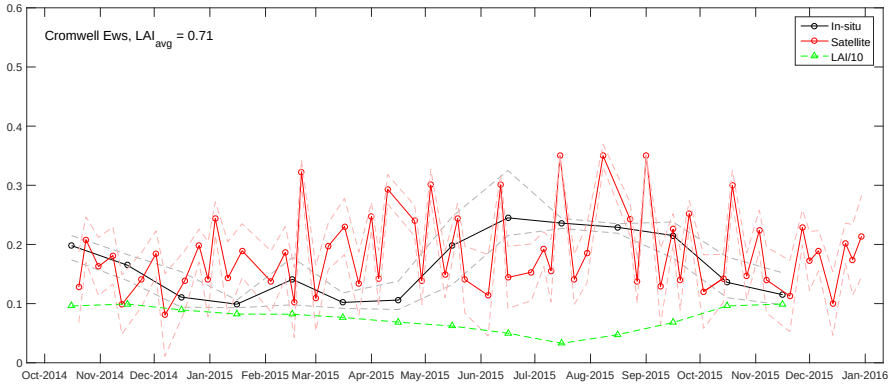

(a) All

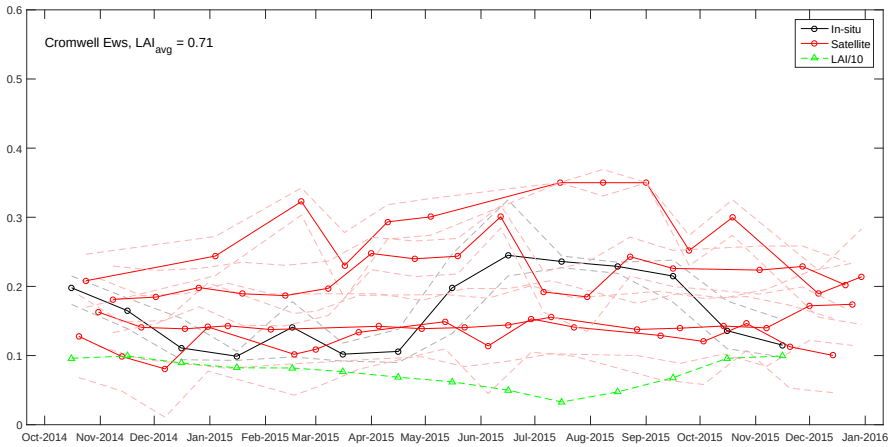

(b) Separate timeseries binned to global incidence θ

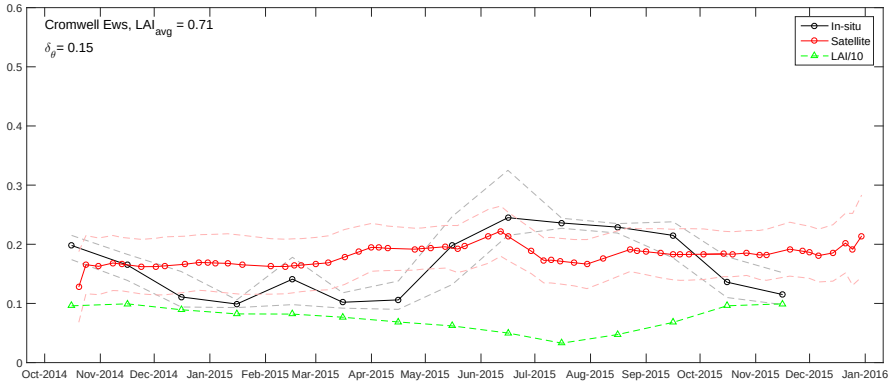

(c) Mean values, based on the θ time series

Figure A34: Inverted soil moisture at NIWA soil moisture ground station 'Cromwell Ews'.

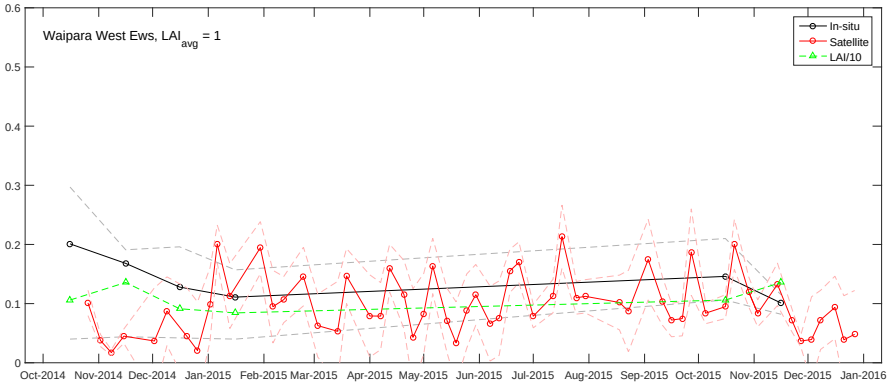

(a) All

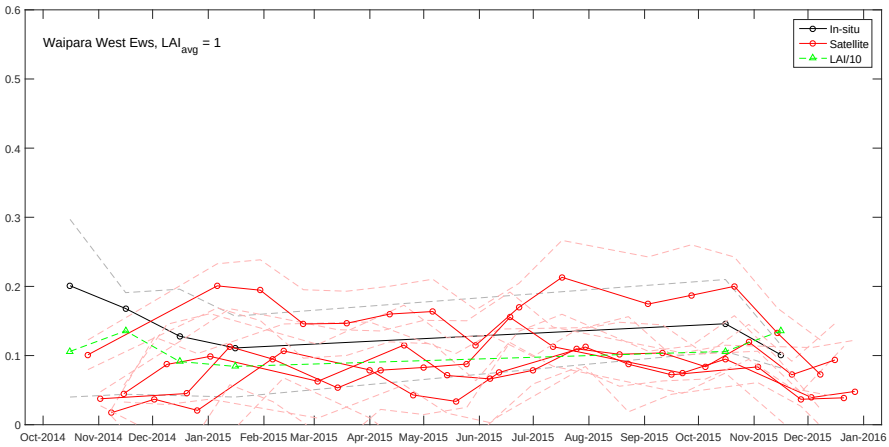

(b) Separate timeseries binned to global incidence θ

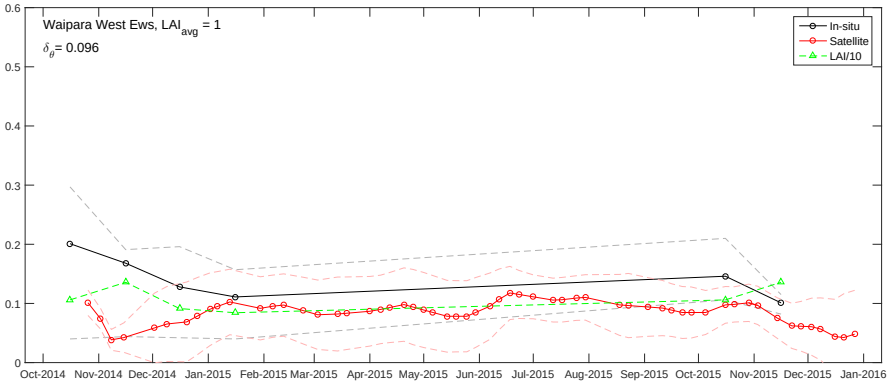

(c) Mean values, based on the θ time series

Figure A35: Inverted soil moisture at NIWA soil moisture ground station 'Waipara West Ews'.

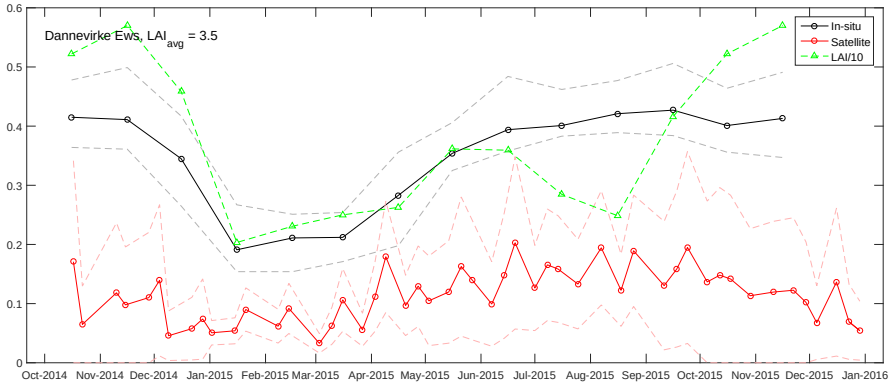

(a) All

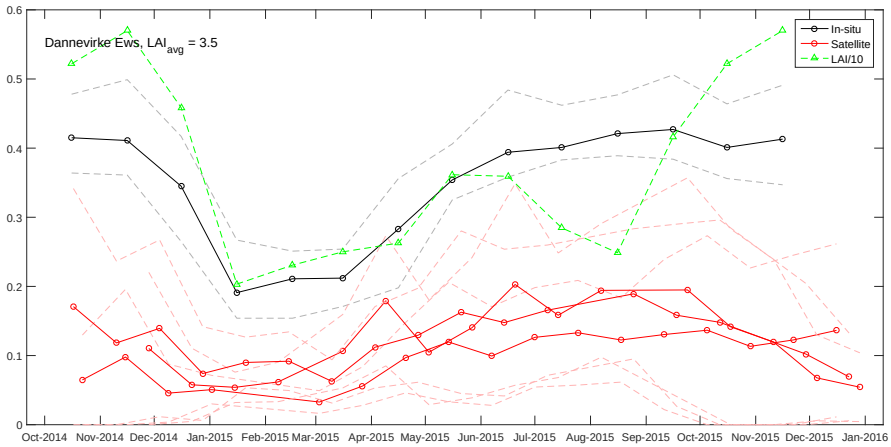

(b) Separate timeseries binned to global incidence θ

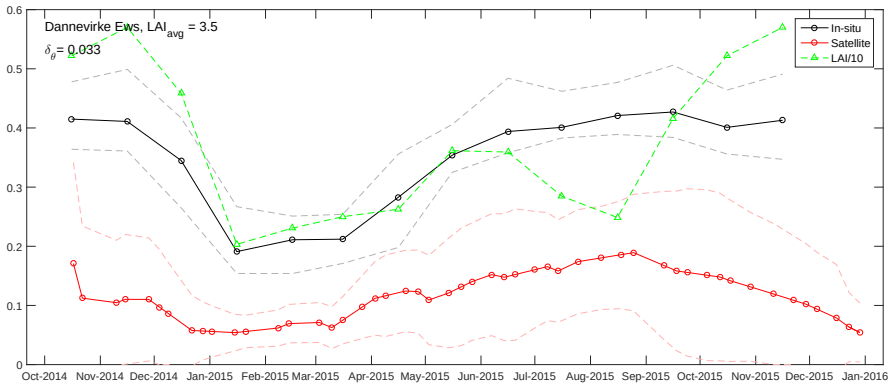

(c) Mean values, based on the θ time series

Figure A36: Inverted soil moisture at NIWA soil moisture ground station 'Dannevirke Ews'.

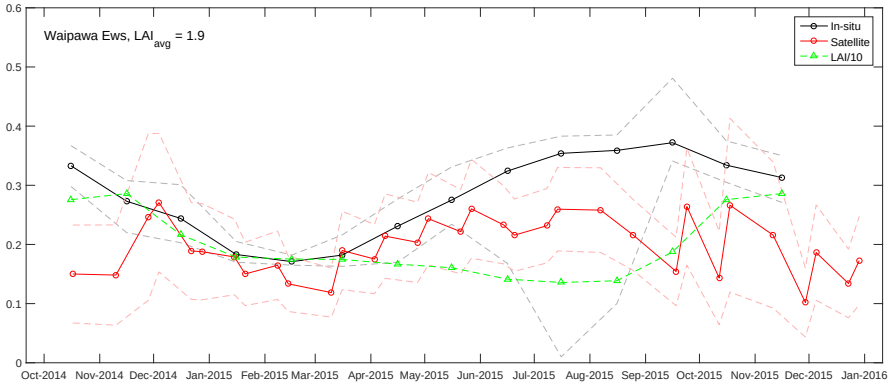

(a) All

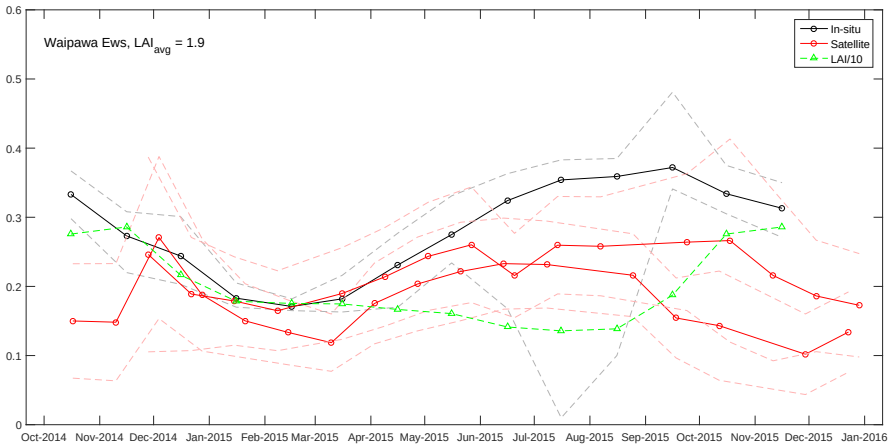

(b) Separate timeseries binned to global incidence θ

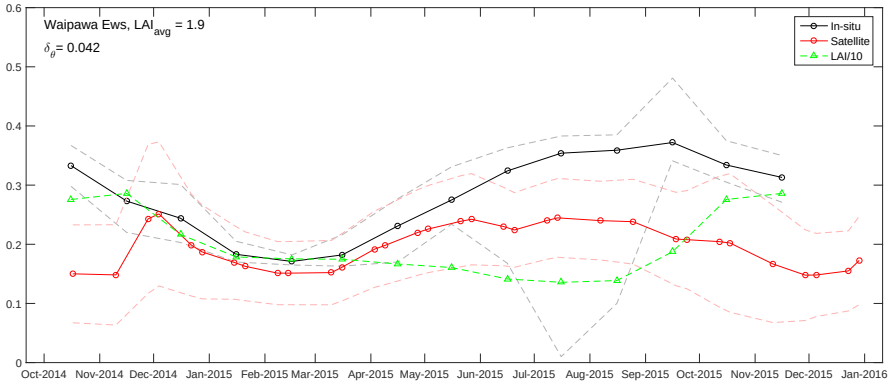

(c) Mean values, based on the θ time series

Figure A37: Inverted soil moisture at NIWA soil moisture ground station 'Waipawa Ews'.

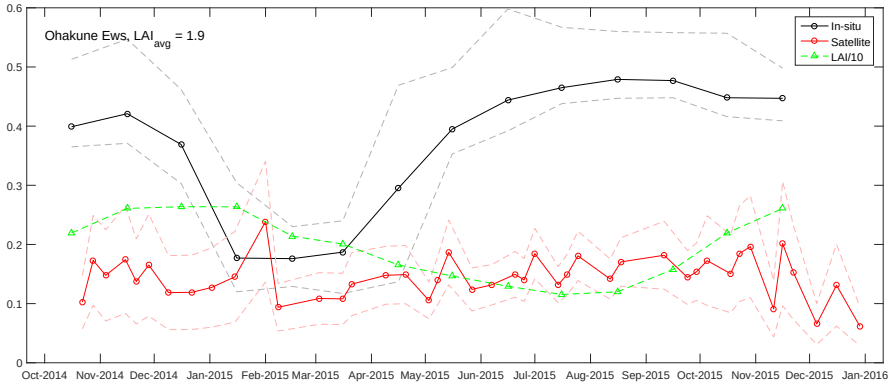

(a) All

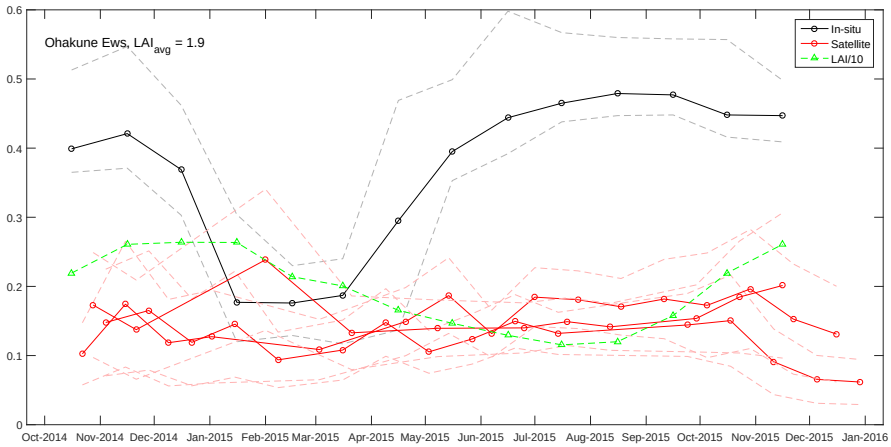

(b) Separate timeseries binned to global incidence θ

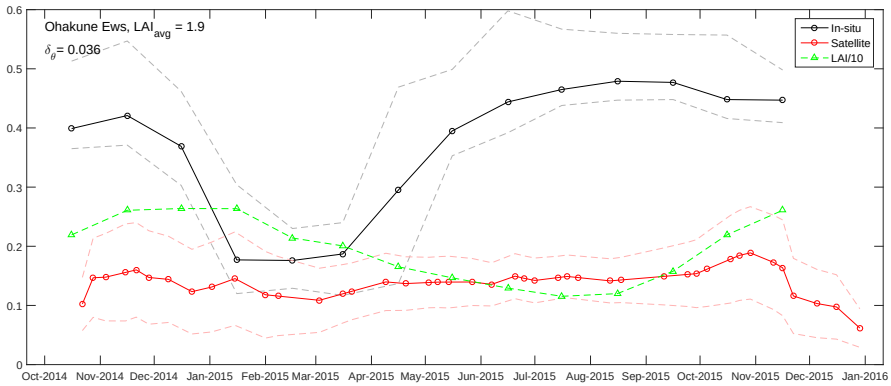

(c) Mean values, based on the θ time series

Figure A38: Inverted soil moisture at NIWA soil moisture ground station 'Ohakune Ews'.

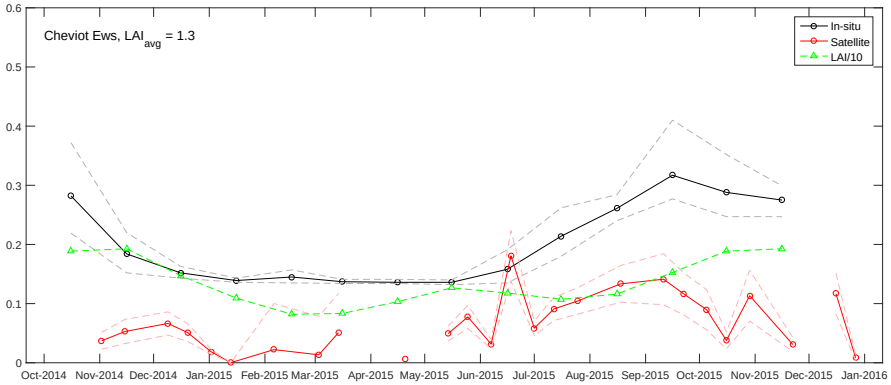

(a) All

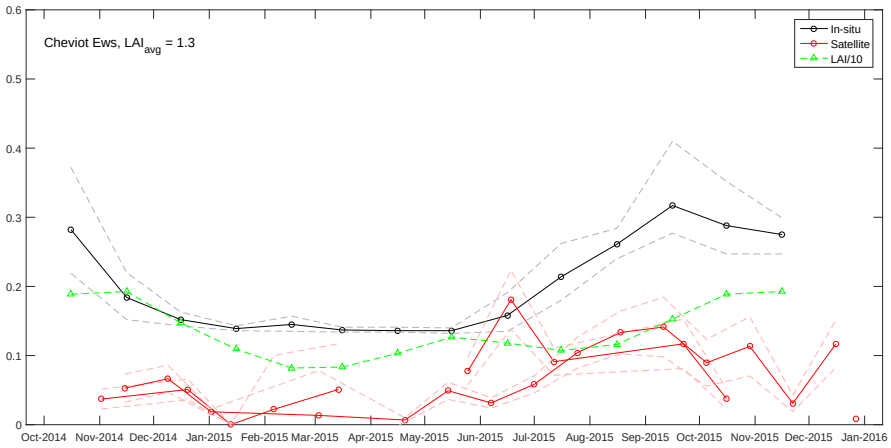

(b) Separate timeseries binned to global incidence θ

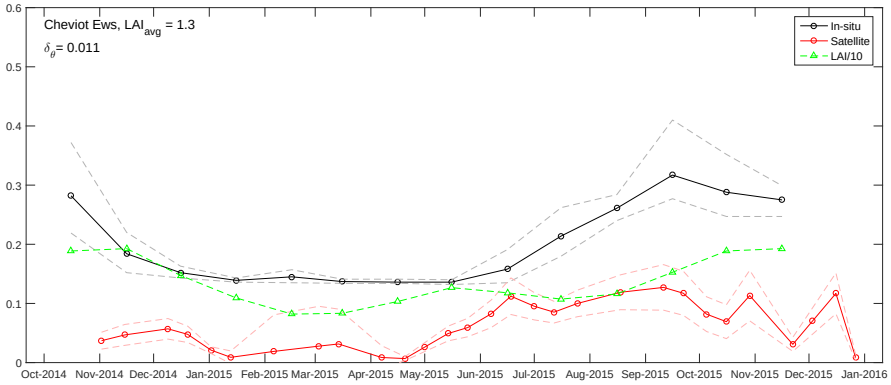

(c) Mean values, based on the θ time series

Figure A39: Inverted soil moisture at NIWA soil moisture ground station 'Cheviot Ews'.

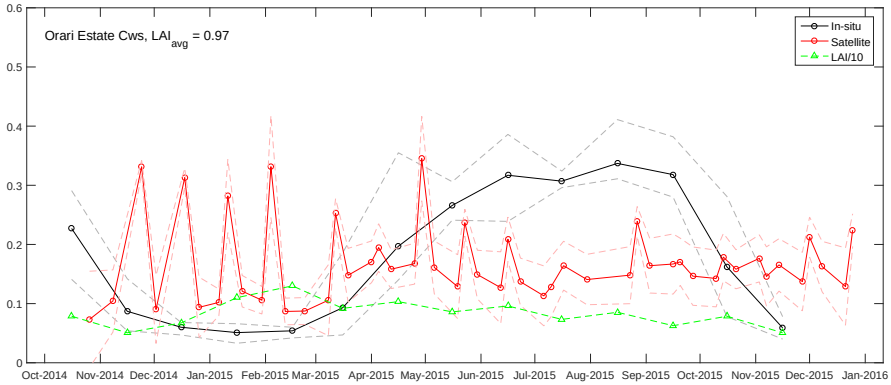

(a) All

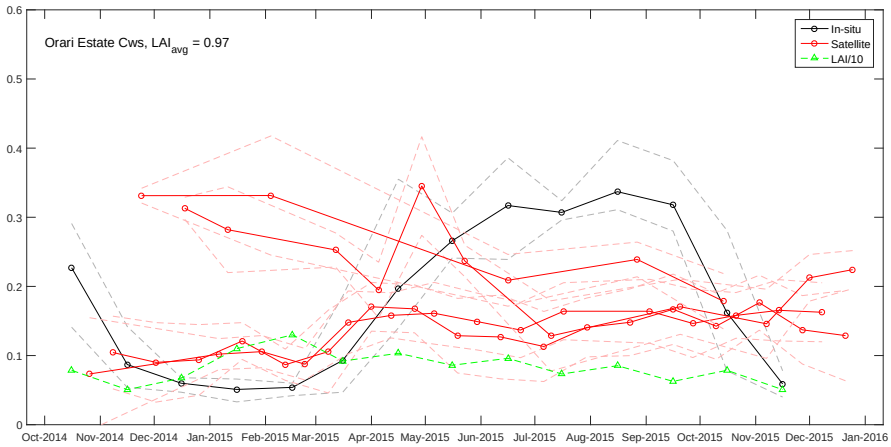

(b) Separate timeseries binned to global incidence θ

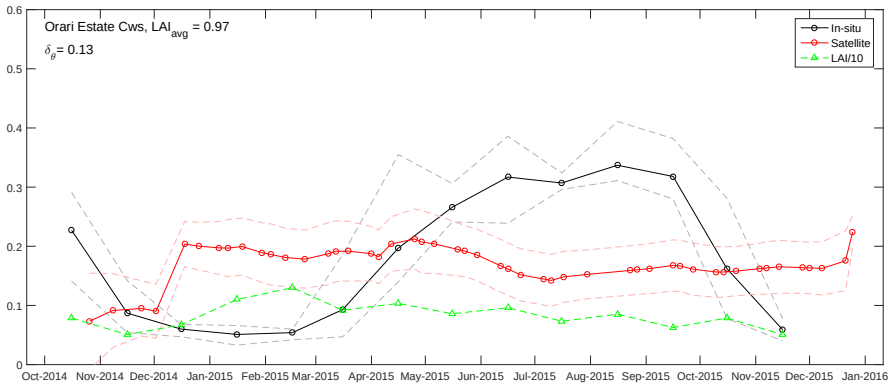

(c) Mean values, based on the θ time series

Figure A40: Inverted soil moisture at NIWA soil moisture ground station 'Orari Estate Cws'.

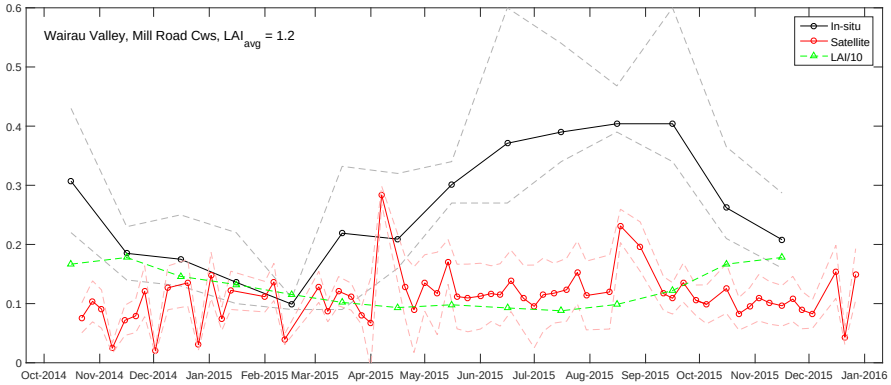

(a) All

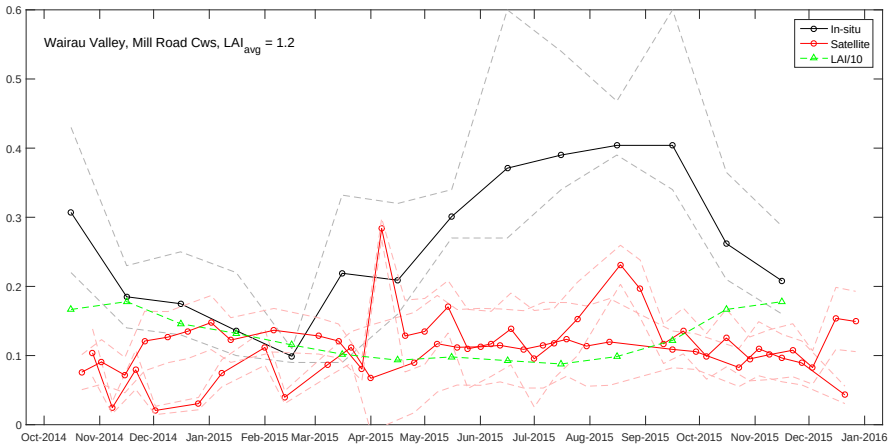

(b) Separate timeseries binned to global incidence θ

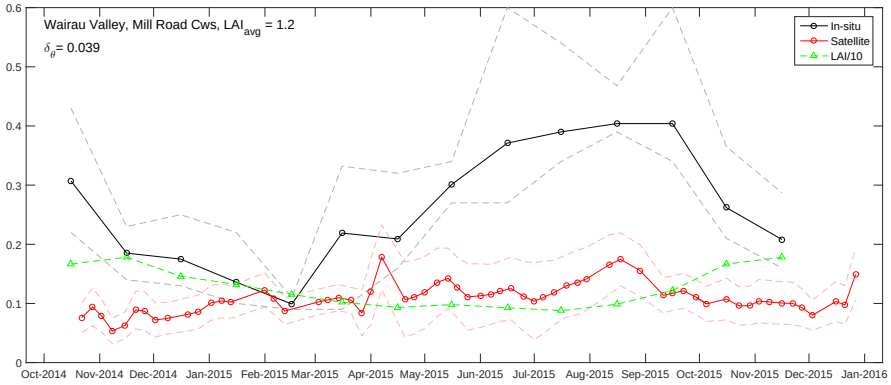

(c) Mean values, based on the θ time series

Figure A41: Inverted soil moisture at NIWA soil moisture ground station 'Wairau Valley, Mill Road Cws'.

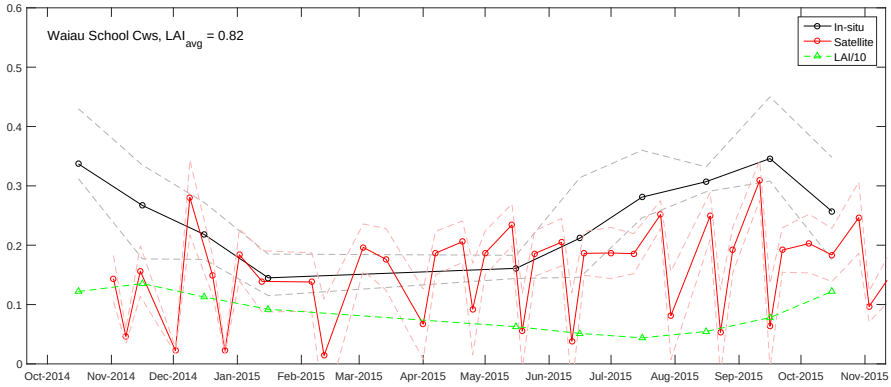

(a) All

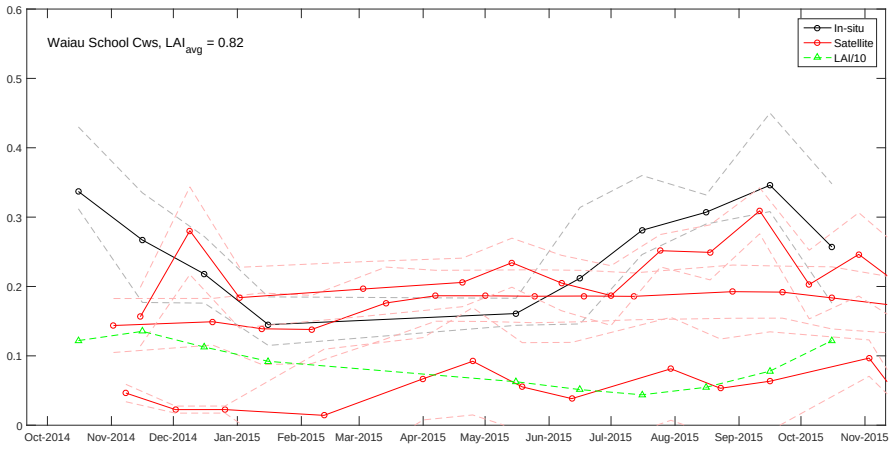

(b) Separate timeseries binned to global incidence θ

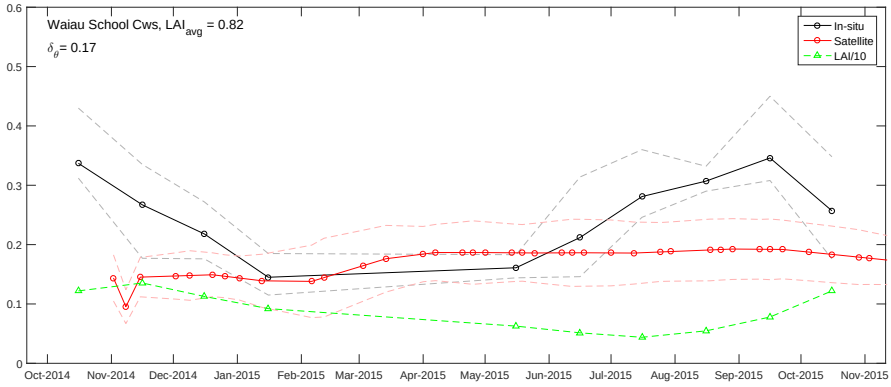

(c) Mean values, based on the θ time series

Figure A42: Inverted soil moisture at NIWA soil moisture ground station 'Waiau School Cws'.

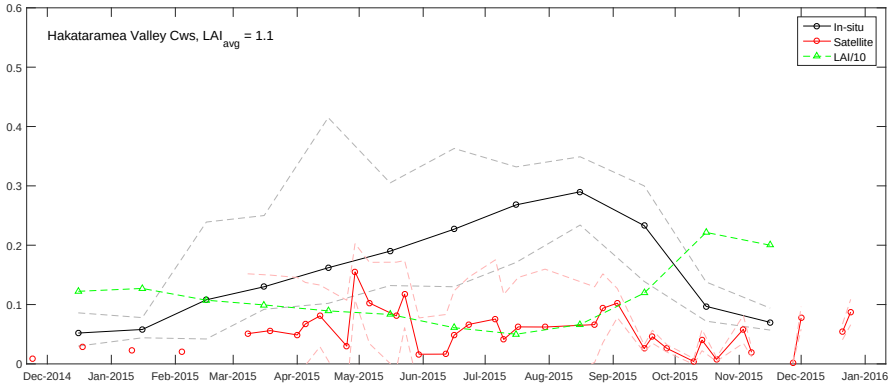

(a) All

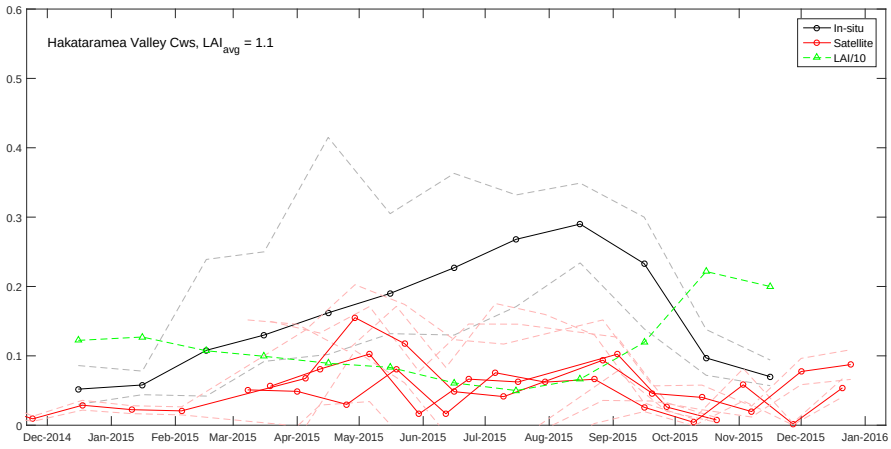

(b) Separate timeseries binned to global incidence θ

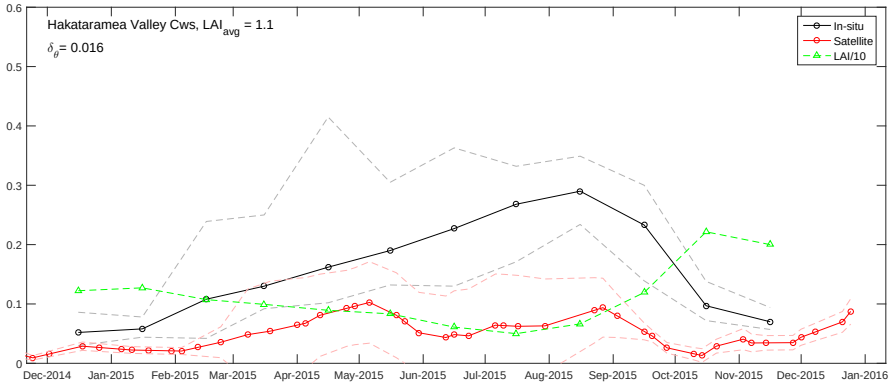

(c) Mean values, based on the θ time series

Figure A43: Inverted soil moisture at NIWA soil moisture ground station 'Hakataramea Valley Cws'.

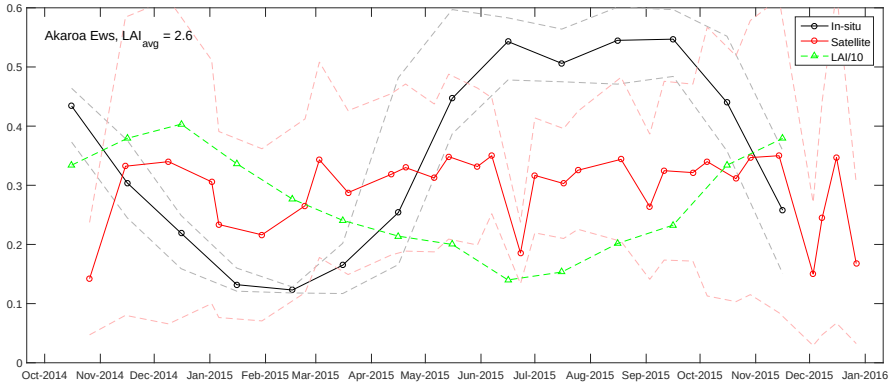

(a) All

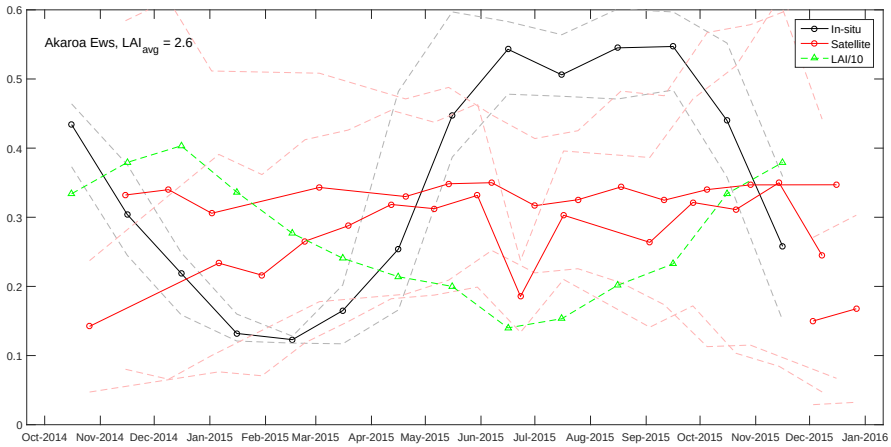

(b) Separate timeseries binned to global incidence θ

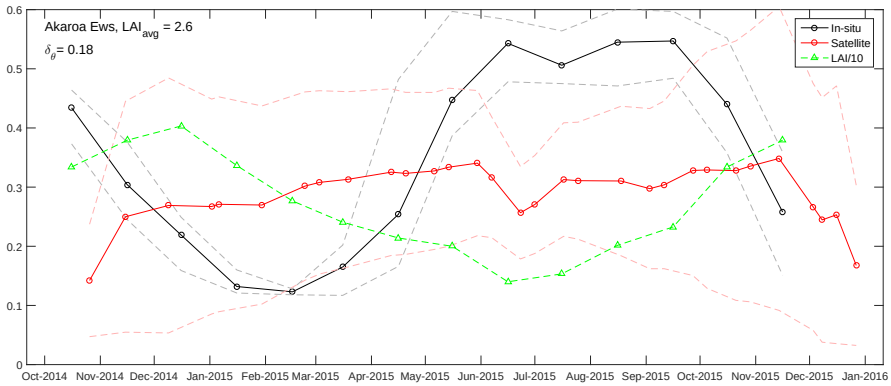

(c) Mean values, based on the θ time series

Figure A44: Inverted soil moisture at NIWA soil moisture ground station 'Akaroa Cws'.

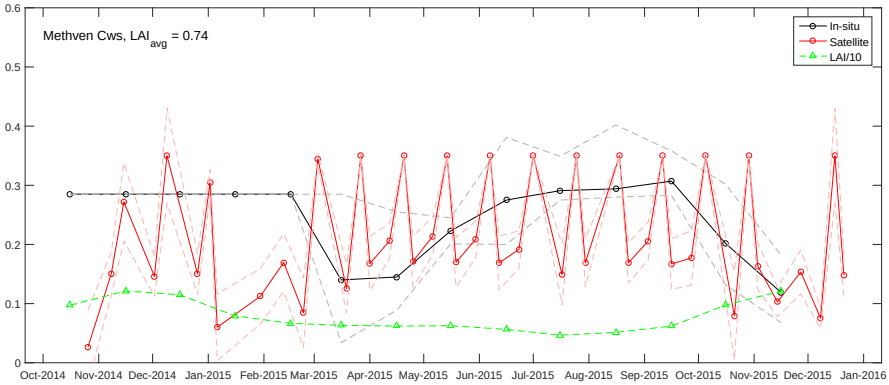

(a) All

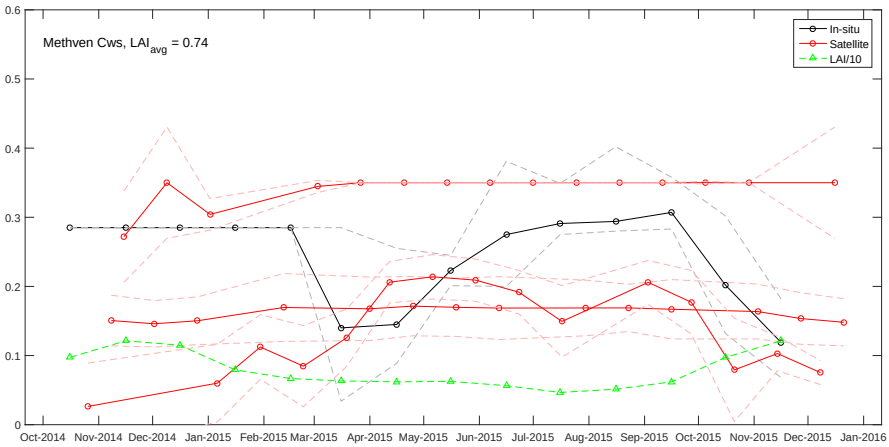

(b) Separate timeseries binned to global incidence θ

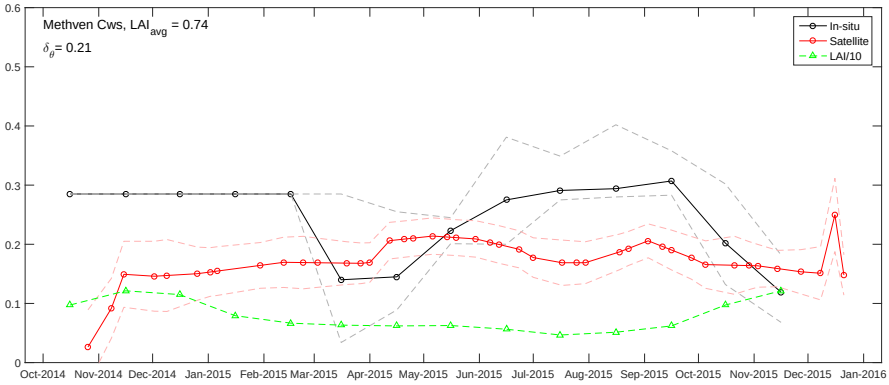

(c) Mean values, based on the θ time series

Figure A45: Inverted soil moisture at NIWA soil moisture ground station 'Methven Cws'.

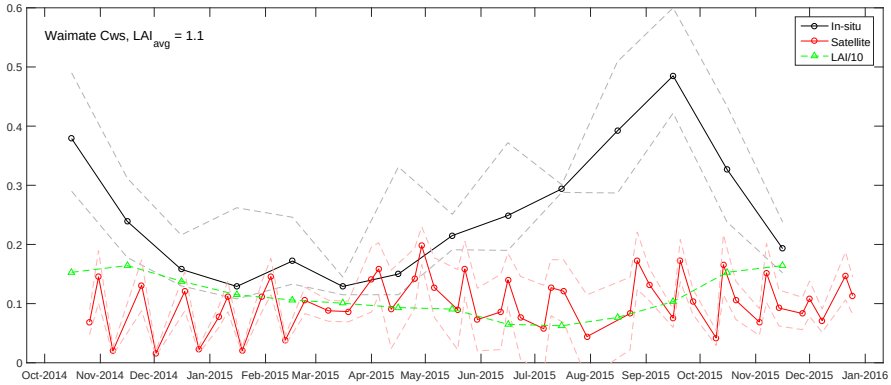

(a) All

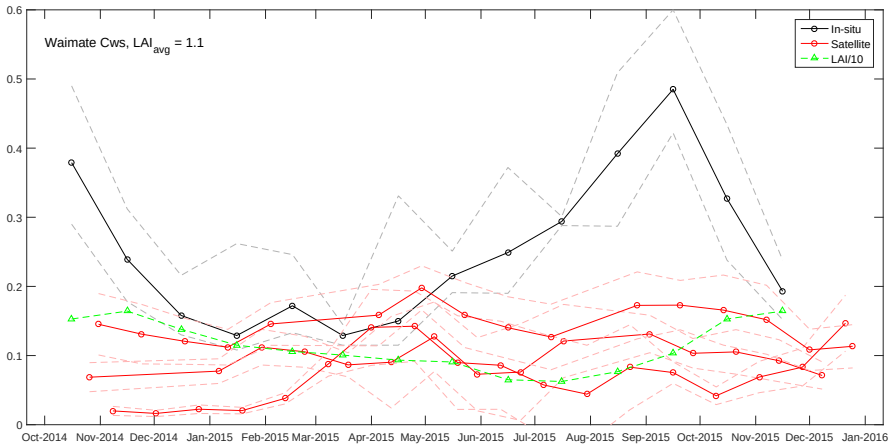

(b) Separate timeseries binned to global incidence θ

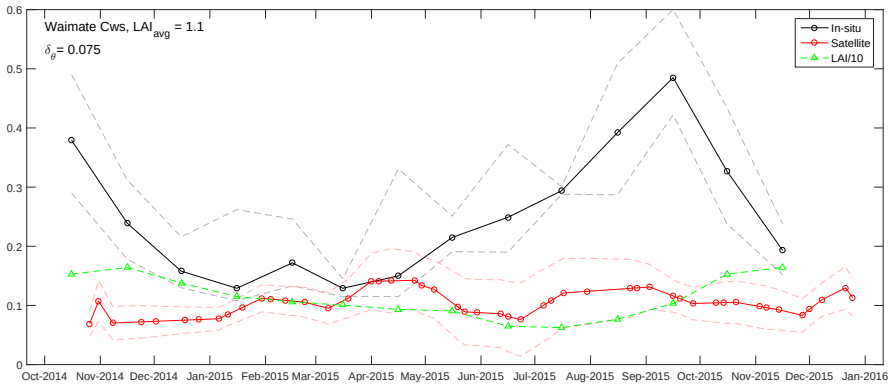

(c) Mean values, based on the θ time series

Figure A46: Inverted soil moisture at NIWA soil moisture ground station 'Waimate Cws'.

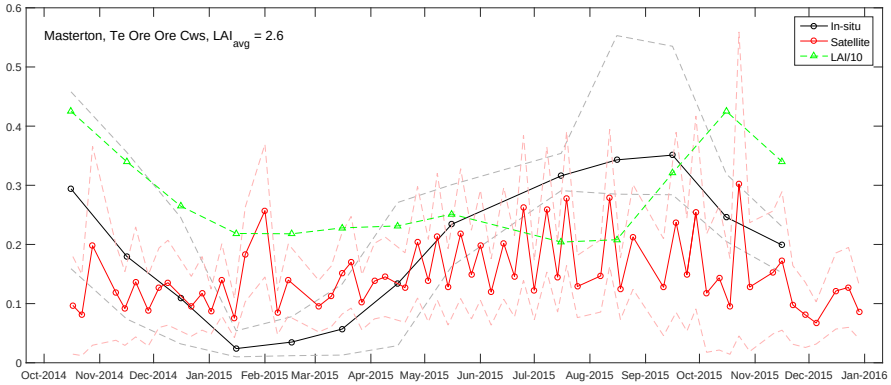

(a) All

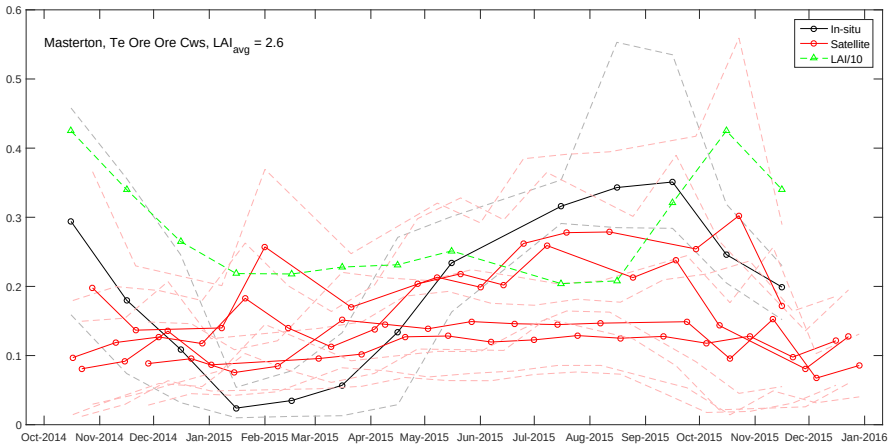

(b) Separate timeseries binned to global incidence θ

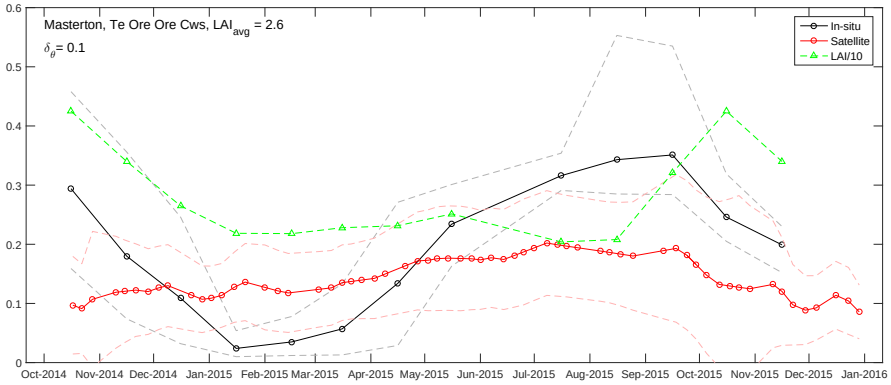

(c) Mean values, based on the θ time series

Figure A47: Inverted soil moisture at NIWA soil moisture ground station 'Masterton, Te Ore Ore Cws'.

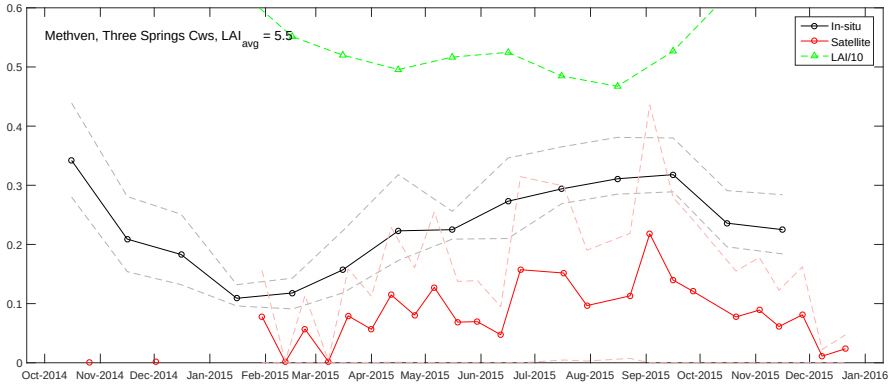

(a) All

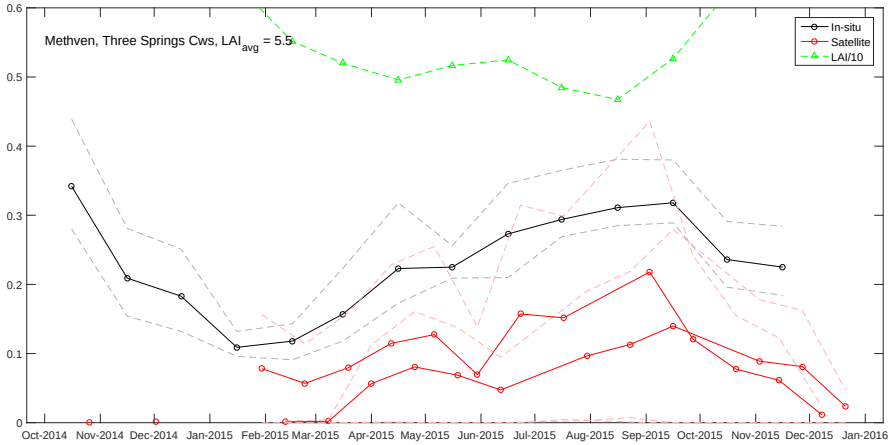

(b) Separate timeseries binned to global incidence θ

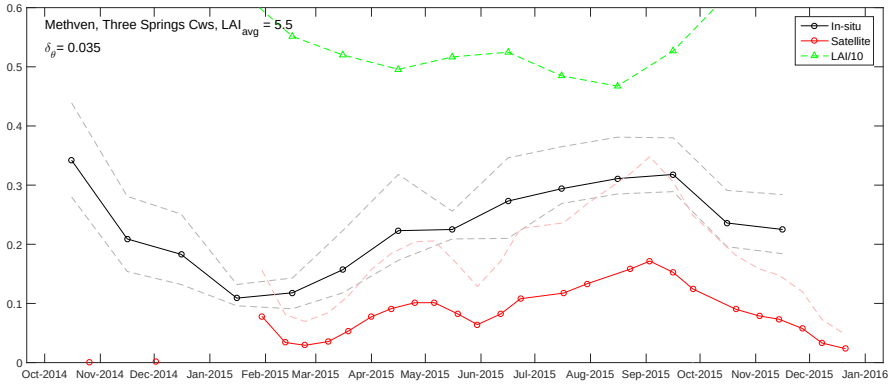

(c) Mean values, based on the θ time series

Figure A48: Inverted soil moisture at NIWA soil moisture ground station 'Methven, Three Springs Cws'.

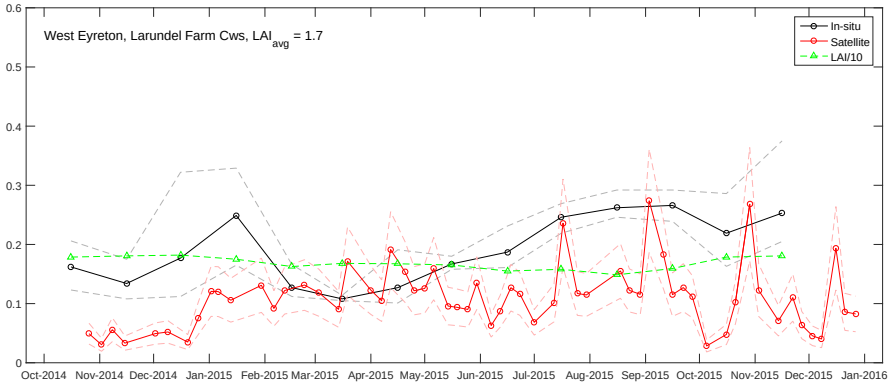

(a) All

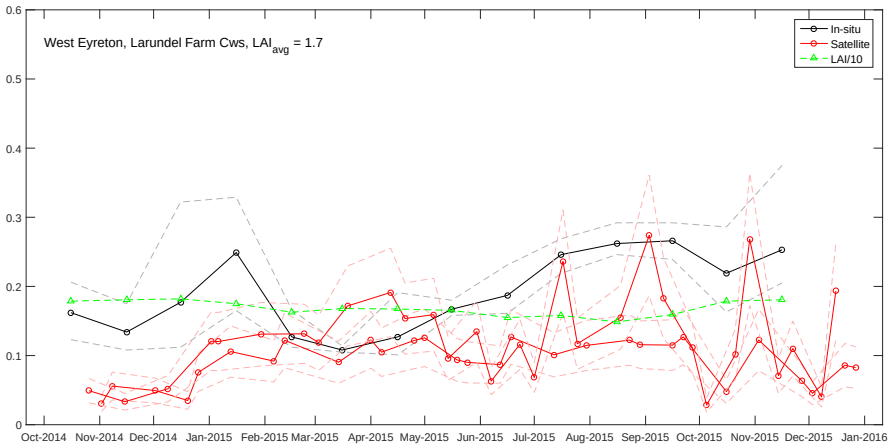

(b) Separate timeseries binned to global incidence θ

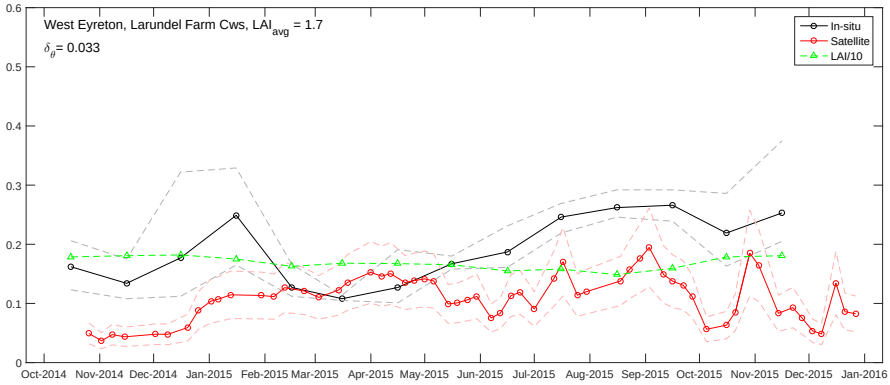

(c) Mean values, based on the θ time series

Figure A49: Inverted soil moisture at NIWA soil moisture ground station 'West Eyreton, Larundel Farm Cws'.

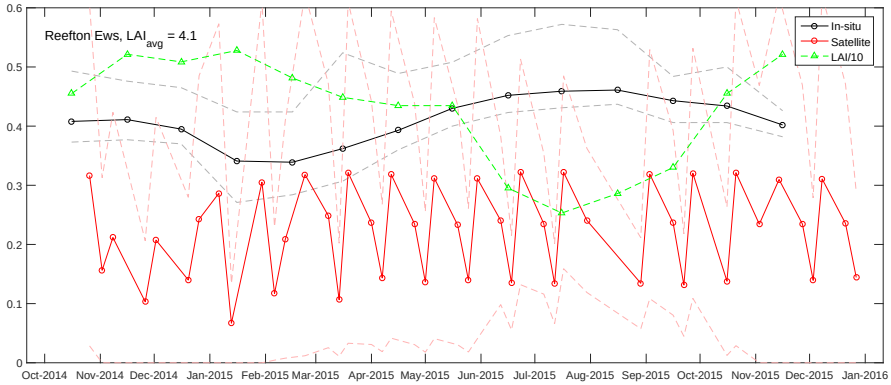

(a) All

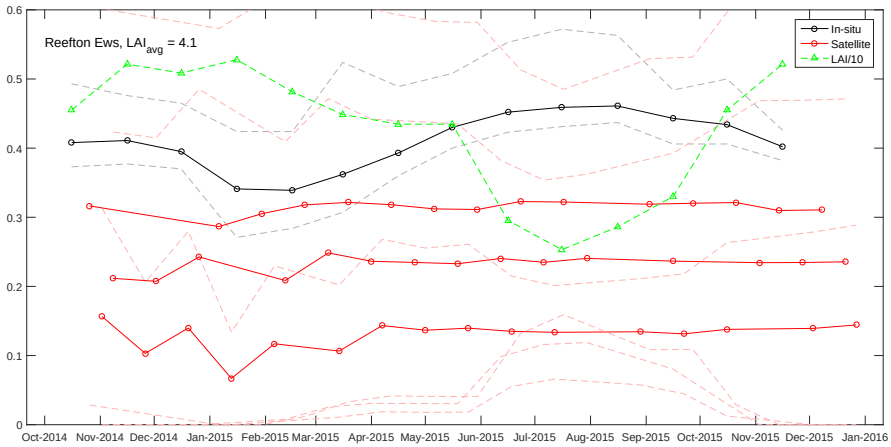

(b) Separate timeseries binned to global incidence θ

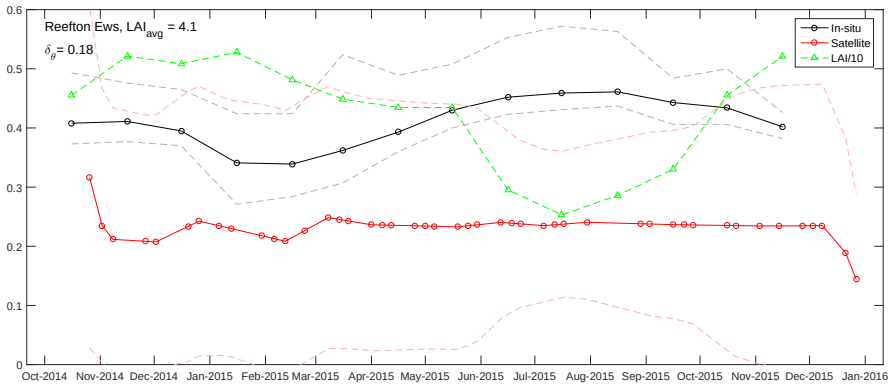

(c) Mean values, based on the θ time series

Figure A50: Inverted soil moisture at NIWA soil moisture ground station 'Reefton Ews'.

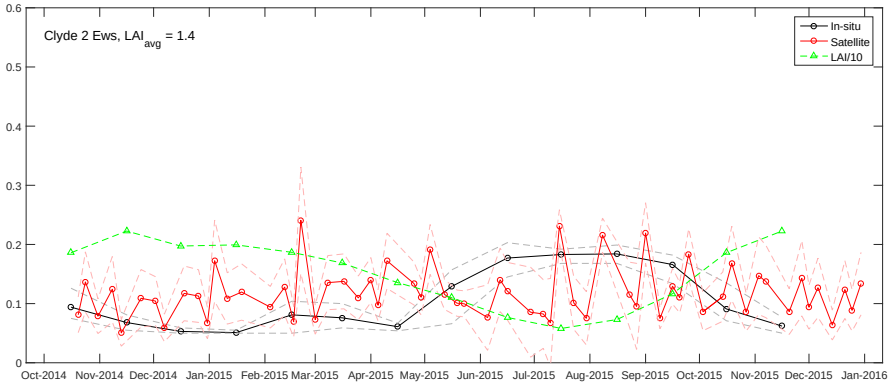

(a) All

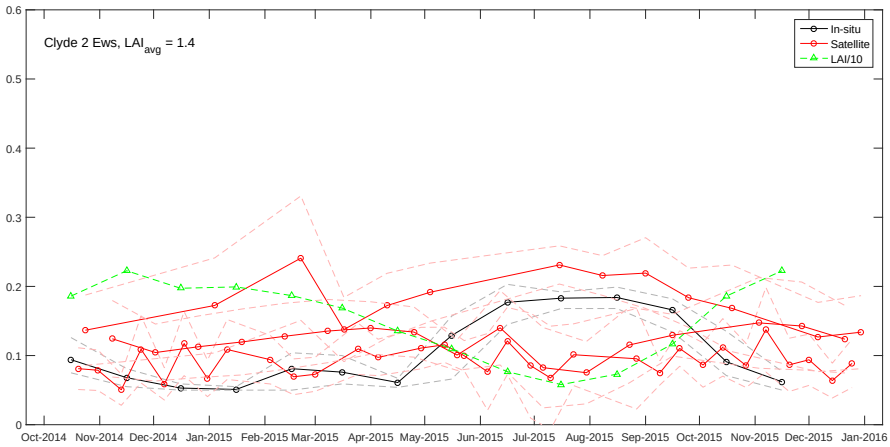

(b) Separate timeseries binned to global incidence θ

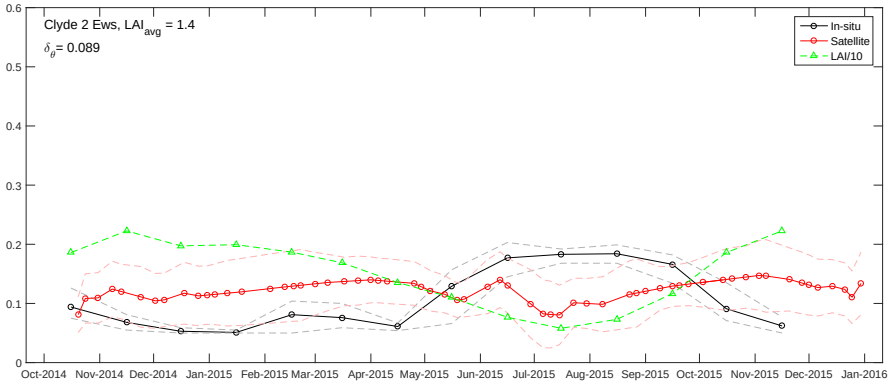

(c) Mean values, based on the θ time series

Figure A51: Inverted soil moisture at NIWA soil moisture ground station 'Clyde 2 Ews'.

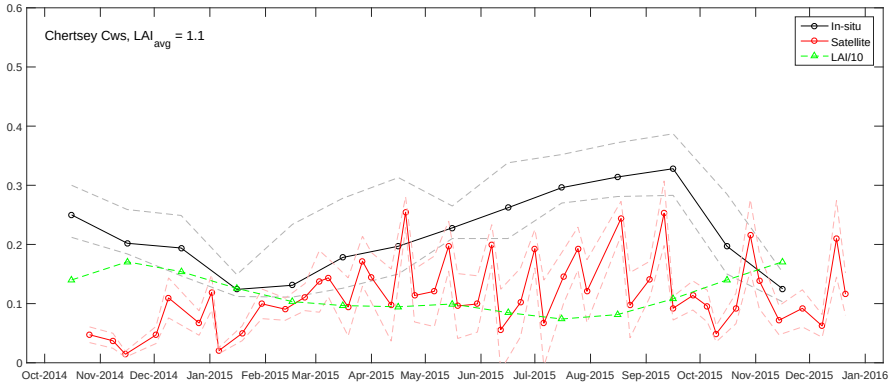

(a) All

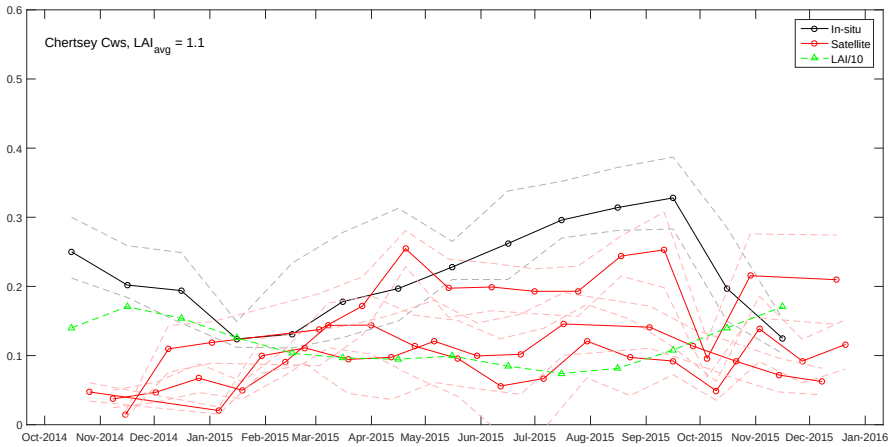

(b) Separate timeseries binned to global incidence θ

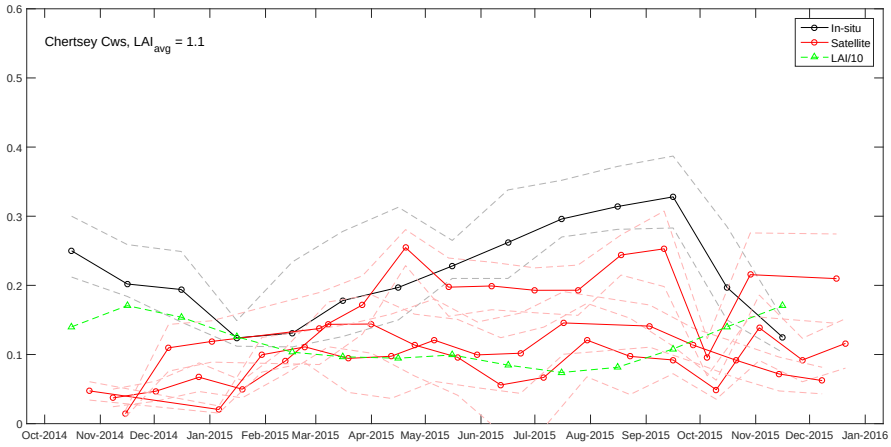

(c) Mean values, based on the θ time series

Figure A52: Inverted soil moisture at NIWA soil moisture ground station 'Chertsey Cws'.

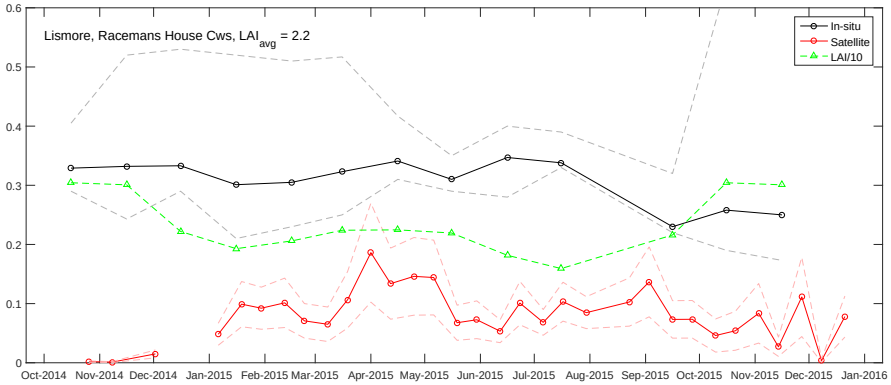

(a) All

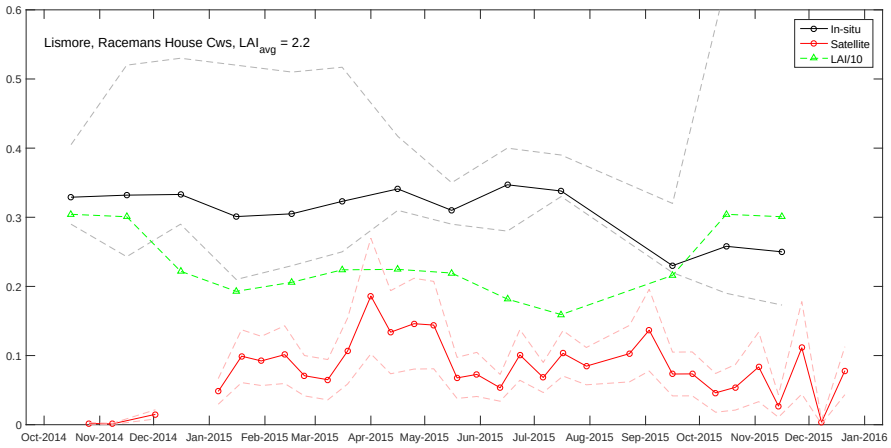

(b) Separate timeseries binned to global incidence θ

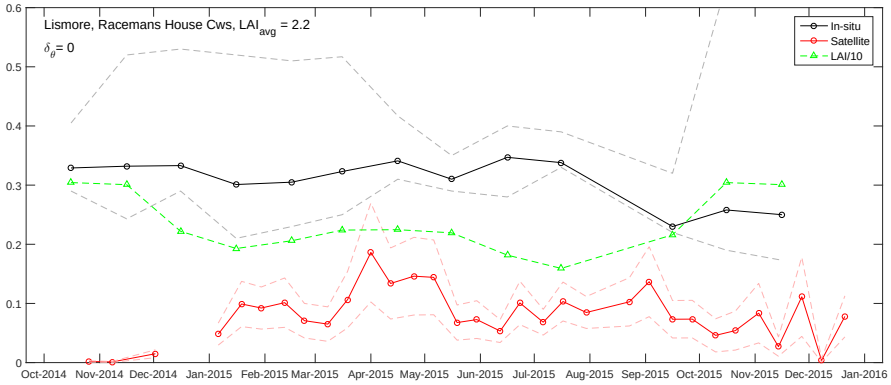

(c) Mean values, based on the θ time series

Figure A53: Inverted soil moisture at NIWA soil moisture ground station 'Lismore, Racemans House Cws'.

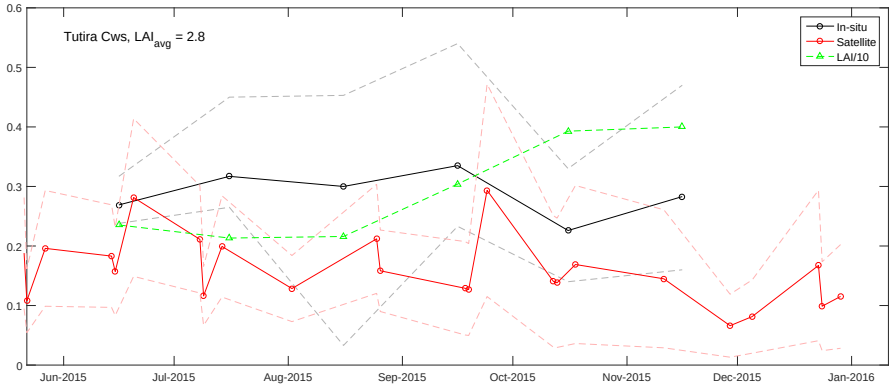

(a) All

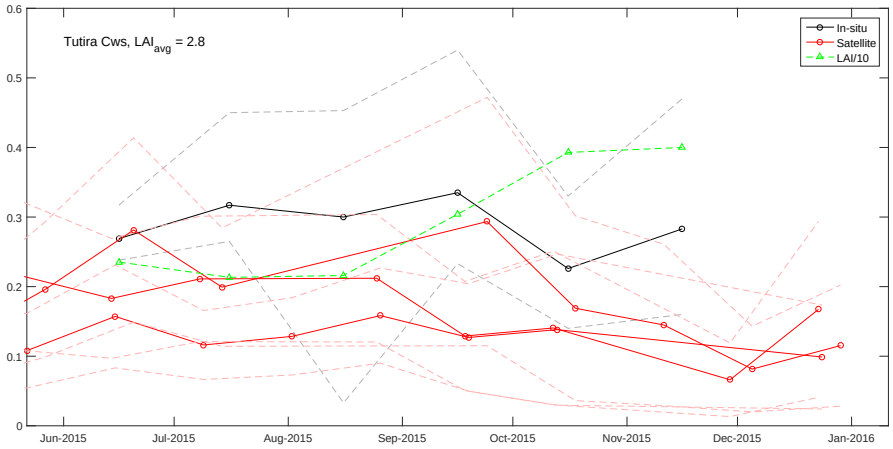

(b) Separate timeseries binned to global incidence θ

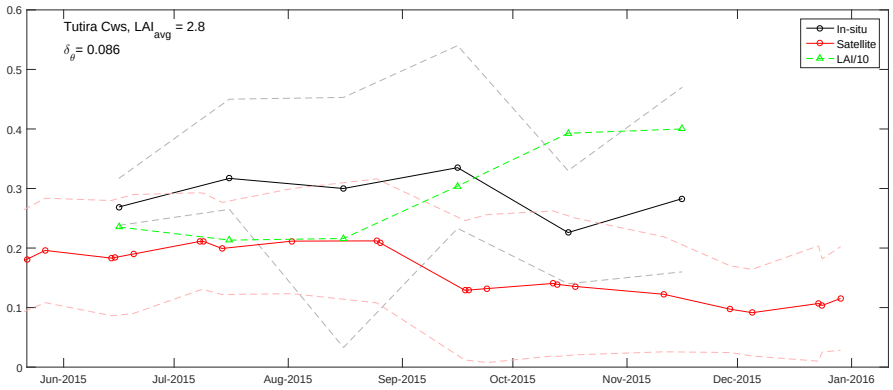

(c) Mean values, based on the θ time series

Figure A54: Inverted soil moisture at NIWA soil moisture ground station 'Tutira Cws'.

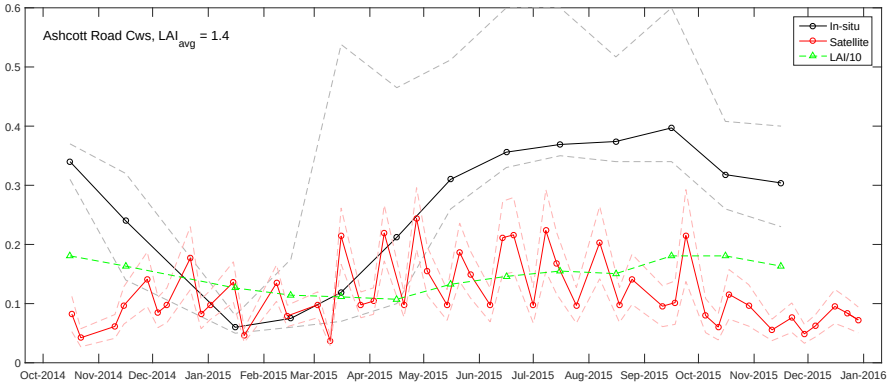

(a) All

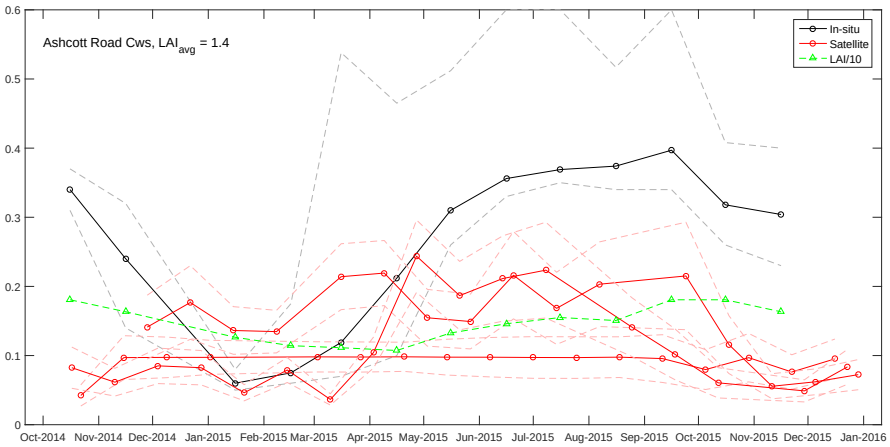

(b) Separate timeseries binned to global incidence θ

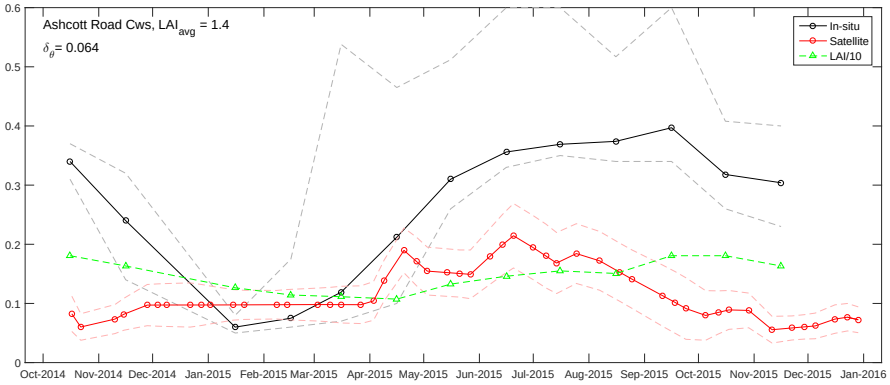

(c) Mean values, based on the θ time series

Figure A55: Inverted soil moisture at NIWA soil moisture ground station 'Ashcott Road Cws'.

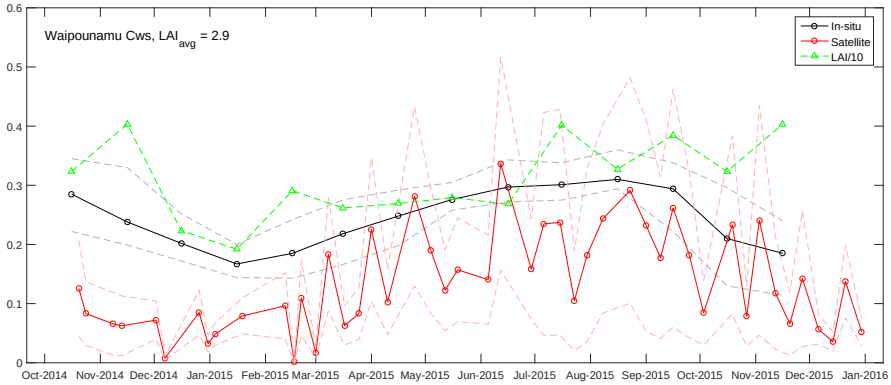

(a) All

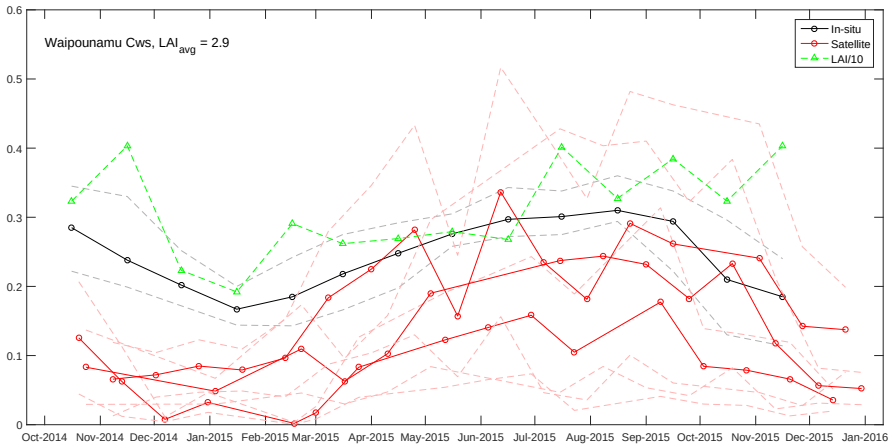

(b) Separate timeseries binned to global incidence θ

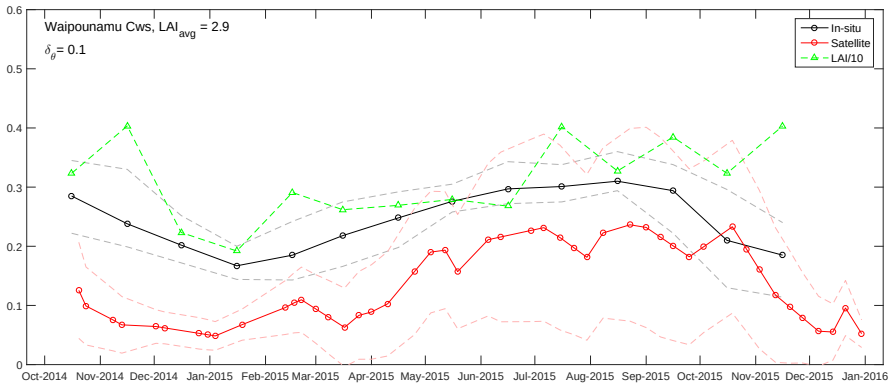

(c) Mean values, based on the θ time series

Figure A56: Inverted soil moisture at NIWA soil moisture ground station 'Waipounamu Cws'.

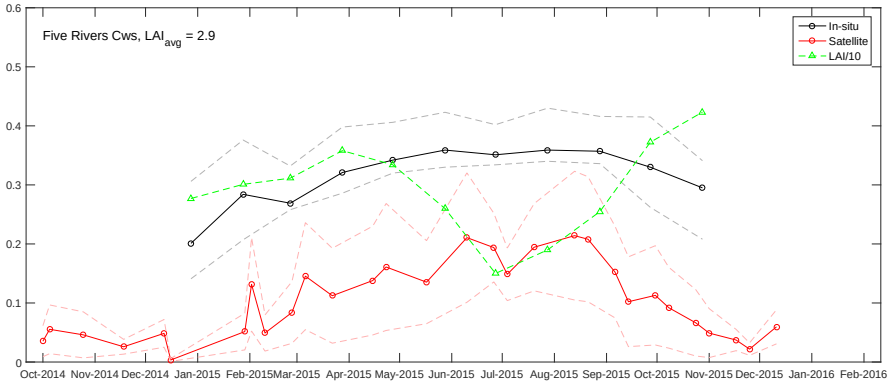

(a) All

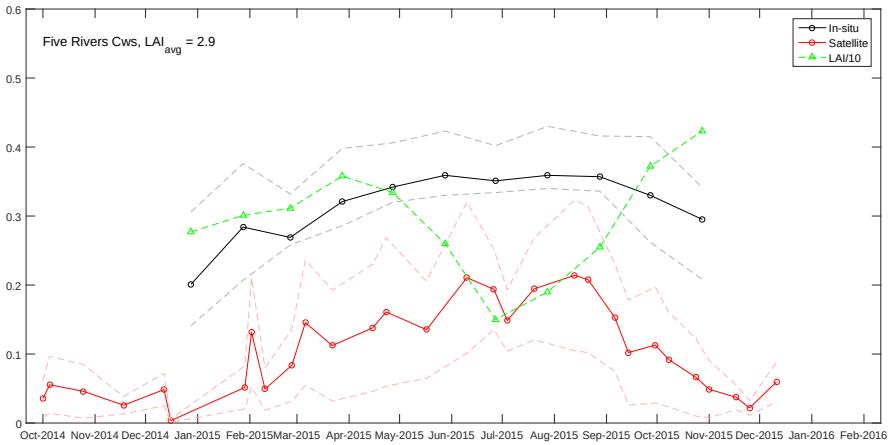

(b) Separate timeseries binned to global incidence θ

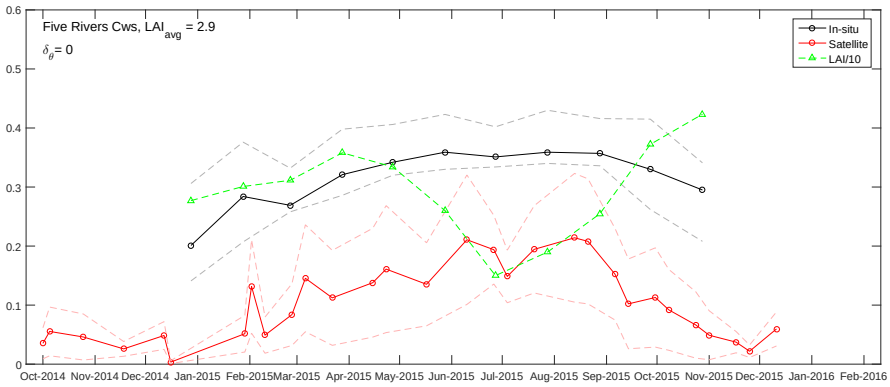

(c) Mean values, based on the θ time series

Figure A57: Inverted soil moisture at NIWA soil moisture ground station 'Five Rivers Cws'.

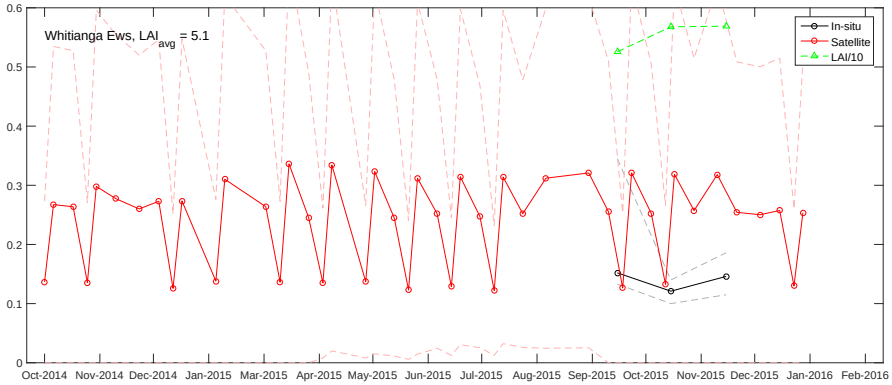

(a) All

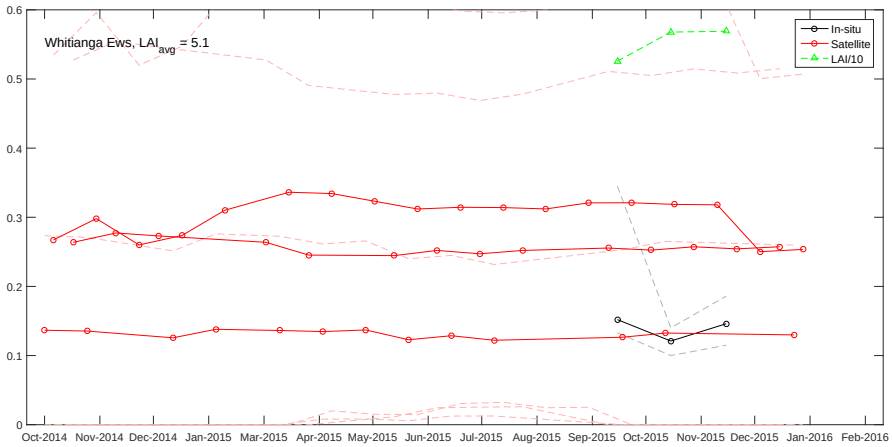

(b) Separate timeseries binned to global incidence θ

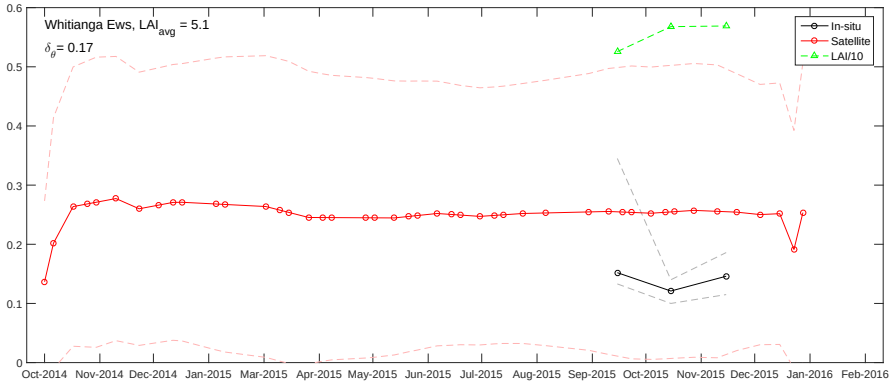

(c) Mean values, based on the θ time series

Figure A58: Inverted soil moisture at NIWA soil moisture ground station 'Whitianga Ews'.

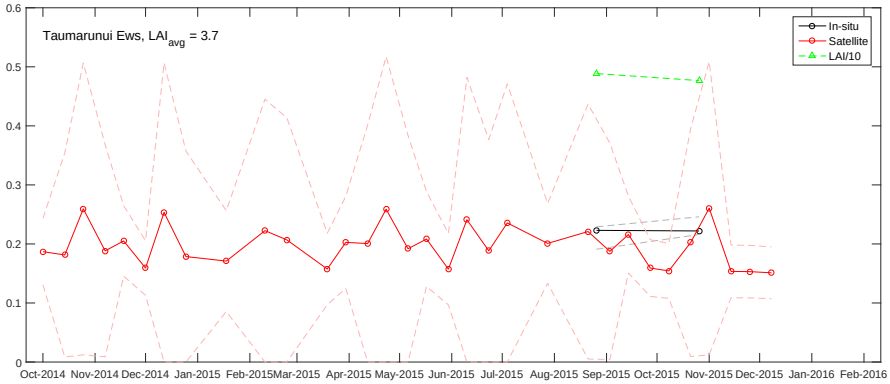

(a) All

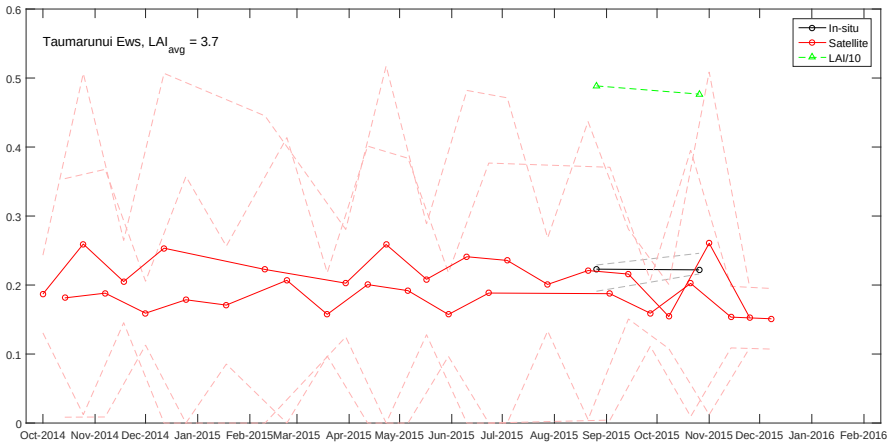

(b) Separate timeseries binned to global incidence θ

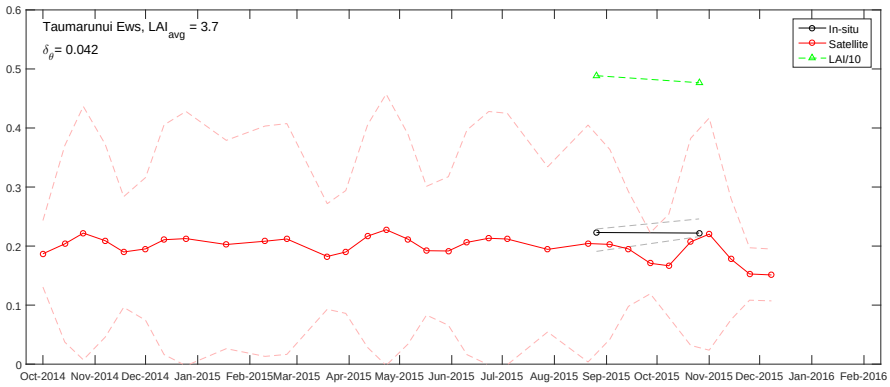

(c) Mean values, based on the θ time series

Figure A59: Inverted soil moisture at NIWA soil moisture ground station 'Taumaranui Ews'.

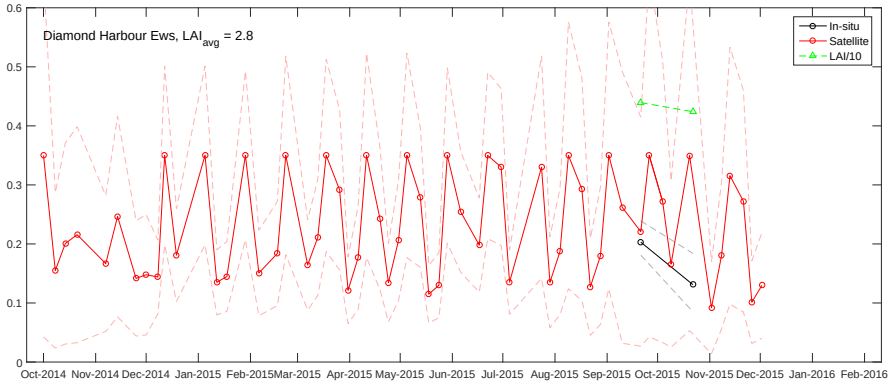

(a) All

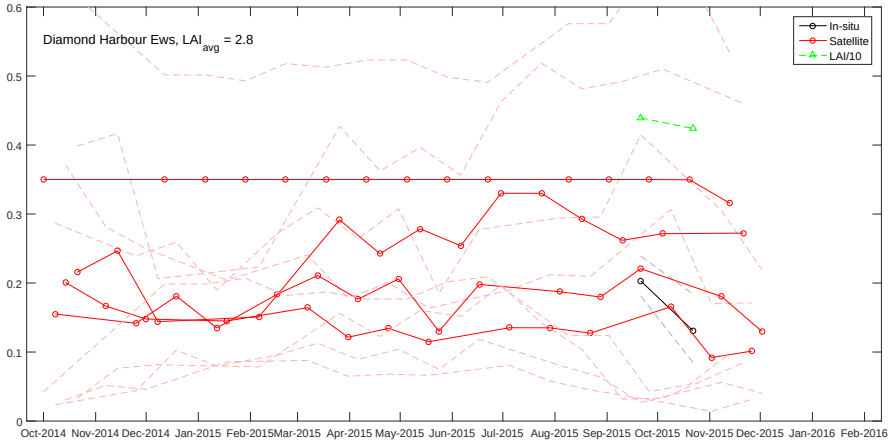

(b) Separate timeseries binned to global incidence θ

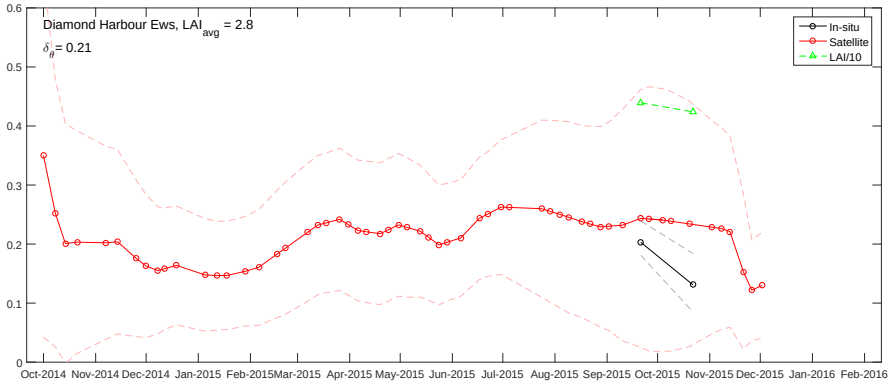

(c) Mean values, based on the θ time series

Figure A60: Inverted soil moisture at NIWA soil moisture ground station 'Diamond Harbour Ews'.

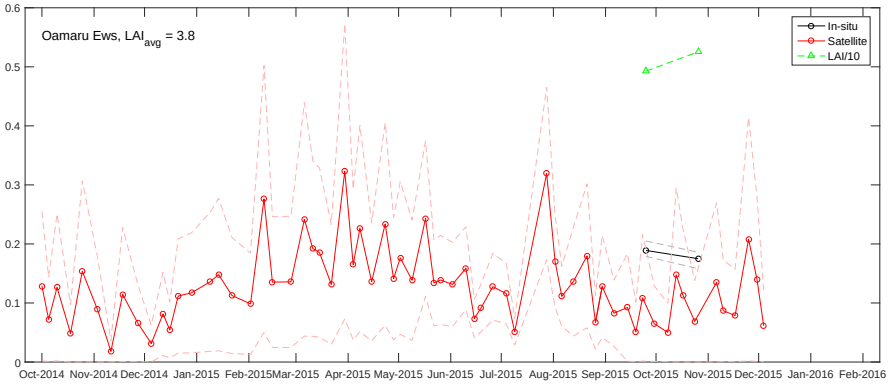

(a) All

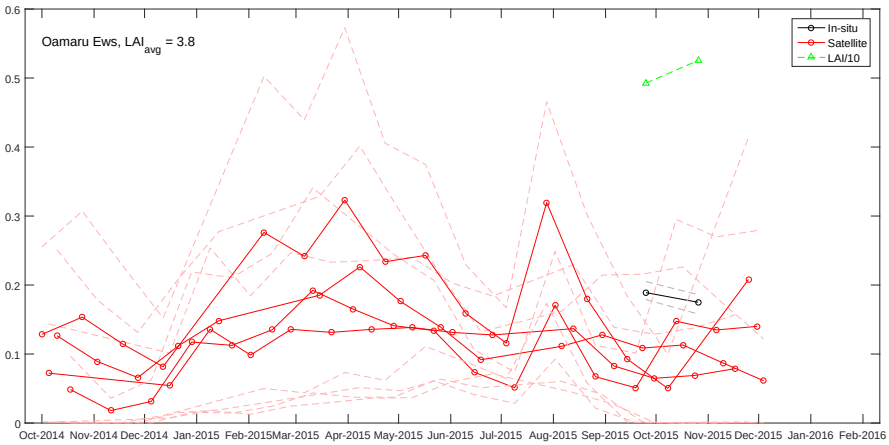

(b) Separate timeseries binned to global incidence θ

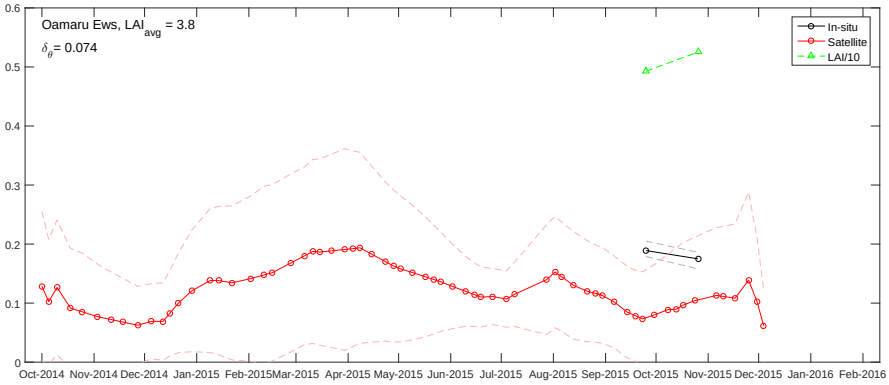

(c) Mean values, based on the θ time series

Figure A61: Inverted soil moisture at NIWA soil moisture ground station 'Oamaru Ews'.

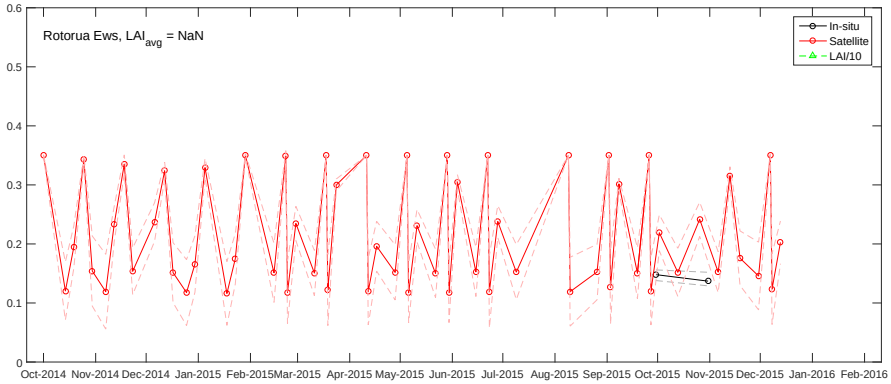

(a) All

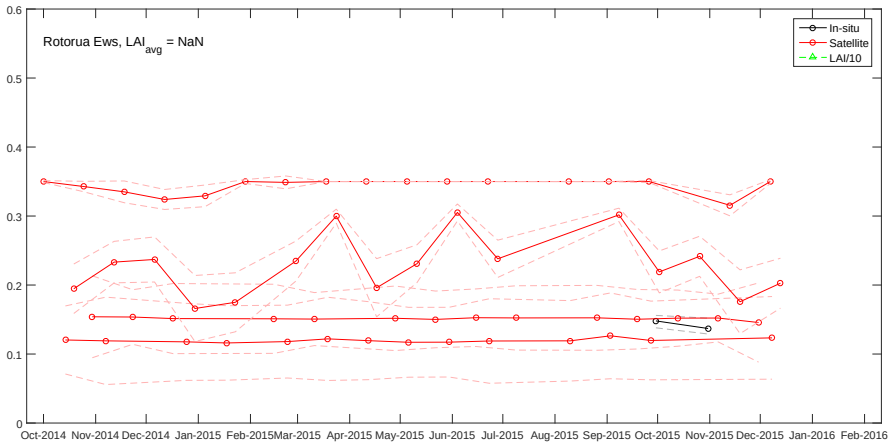

(b) Separate timeseries binned to global incidence θ

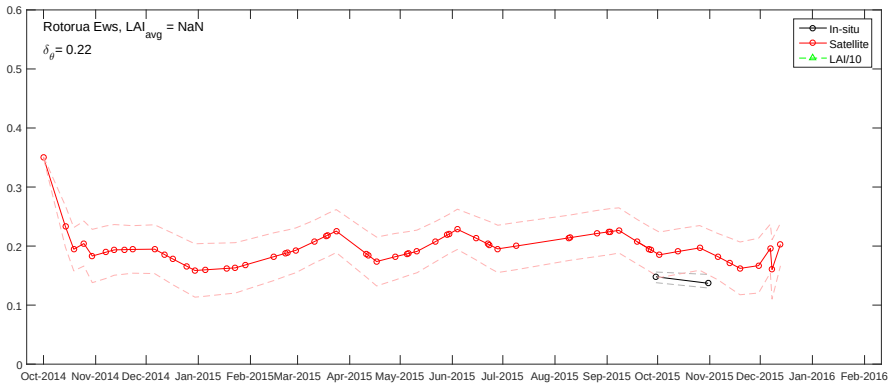

(c) Mean values, based on the θ time series

Figure A62: Inverted soil moisture at NIWA soil moisture ground station 'Rotorua Ews'.

B

Basic theory of uncertainty propagation

Methods of propagation of errors and uncertainty are used throughout this thesis. The term 'uncertainty' is mostly used in this thesis, which here means the combined effect of measurement errors or the effect of averaging multiple values over time or area. Some basics of error propagation that are used are explained here.

The variance of a function f, ${\sigma_f}^2$, is ultimately given by (Tellinghuisen, 2001):

$$ {\sigma_f}^2 = \boldsymbol{g}^T \boldsymbol{V} \boldsymbol{g}, \tag{B1} $$

which has $n = 1 : N$ input components; $\boldsymbol{g}$ is a vector of input component $\partial f / \partial n_i$; $\boldsymbol{V}$ is the $N \times N$ variance-covariance matrix; and $\boldsymbol{g}^T$ is the transpose of $\boldsymbol{g}$. This function is used mostly in this research.

Several other notations for Eq. B1 are often used in research. For example, for a function f with only two components x and y, for any function $f_i = f(x_i, y_i), (i = 1, ..., N)$, where both x and y have an uncertainty or standard deviation σ, the *variance* ${\sigma_f}^2$ is defined as (Taylor, 1997):

$$ {\sigma_f}^2 = \left(\frac{\partial f}{\partial x}\right)^2 {\sigma_x}^2 + \left(\frac{\partial f}{\partial y}\right)^2 {\sigma_y}^2 + 2\frac{\partial f}{\partial x}\frac{\partial f}{\partial y}\sigma_{xy}, \tag{B2} $$

where σ_{xy} is the *covariance*:

$$ \sigma_{xy} = \frac{1}{N}\sum_{i=1}^{N} \left(x_i - \bar{x}\right)\left(y_i - \bar{y}\right). \tag{B3} $$

When errors are normally distributed, σ_{xy} is zero and the standard deviation simplifies to:

$$ {\sigma_q}^2 = \left(\frac{\partial q}{\partial x}\right)^2 {\sigma_x}^2 + \left(\frac{\partial q}{\partial y}\right)^2 {\sigma_y}^2. \tag{B4} $$

Asuming no covariance, Eq. B4 can thus be expanded for any set V_j counting N_V variables:

$$\sigma_{q(V_j)}{}^2 = \sum_{j=1}^{N_V} \left(\frac{\partial q}{\partial V_j} \right)^2 \sigma_{V_j}{}^2. \tag{B5}$$

I assume that uncertainty or errors are random (at least, within the normal distribution) and not systematic (bias) unless it is specifically mentioned.

When taking the mean or median of a dataset over a temporally and spatially distributed estimate, one can also quantify the variability of that distribution. Usually that is done with a standard deviation of the spatial distribution. To avoid confusion of terminology, in this research we will define this as 'the standard deviation of the spatial distribution', or 'the standard deviation of the temporal distribution'. If these estimates contain uncertainty, the summed uncertainty for these datasets are averaged over time or space (denoted as dimension i) as the square root of the mean of the squared uncertainties over i:

$$\sigma = \sqrt{\frac{1}{N_i} \sum_{i=1}^{N_i} \sigma_i{}^2} \tag{B6}$$

C

Permeability in hydrolithologies

Gleeson et al. (2011) compile hydrolithologies in North America and at a global scale. These are shown in Table C1.

Table C1: Hydrolithologies according to Gleeson et al. (2011).

Hydrolithology class name	log κ (m^2)	log σ (m^2)
coarse-grained unconsolidated	-10.9	1.2
fine-grained unconsolidated	-14.0	1.8
coarse-grained siliclastic sedimentary	-12.5	0.9
fine-grained siliclastic sedimentary	-12.5	0.9
carbonate	-11.8	1.5
crystalline	-14.1	1.5
volcanic	-12.5	1.8

Hydrolithologies from Table C1 were compared to values found in aquifers in the Waikato Region in Tschritter et al. (2014). These are summarised in Table C2 and shown in Figure C1. As these are values for formations, which can hold several lithologies, an interpretation of the range of hydrolithology class names from table C1 was made.

Table C2: Median hydraulic conductivities from Tschritter et al. (2014) interpreted in hydrolithologies from Gleeson et al. (2011). C.g. = coarse-grained, f.g.=fine-grained.

Formation/group name	K (m/day)	log κ (m^2)	Interpretation of hydrolithology
Basement	0.1	-12.8	in between c.g. and f.g. siliclastic sedimentary
Lake sediment	1.1	-11.8	in between c.g. and f.g. unconsolidated
Tauranga Group	2.8	-11.4	in between c.g. and f.g. unconsolidated
Oranui Formation	1.6	-11.6	in between c.g. and f.g. unconsolidated
Kapenga caldera deposits	2.2	-11.5	in between c.g. unconsolidated and volcanic
Western domes	4.2	-11.2	in between c.g. unconsolidated and volcanic
Earthquake Flat breccia	3.3	-11.3	in between c.g. unconsolidated and volcanic
Mamaku Plateau	0.01	-13.8	in between f.g. siliclastic sedimentary and crystalline
Ohakuri Caldera deposits	0.09	-12.9	in between f.g. unconsolidated and volcanic
Pre-Whakamaru volcanics	0.02	-13.5	in between f.g. unconsolidated and volcanic
Mangakino volcanics	0.3	-12.4	volcanic
Maroa ignimbrite	0.7	-12.0	volcanic
Whakamaru ignimbrite	0.5	-12.1	volcanic
Kaingaroa ignimbrite	0.4	-12.2	volcanic
Western volcanics	0.1	-12.8	volcanic

For the conversion of permeability κ [m^2] to hydraulic conductivity K [m s^{-1}] we used this relation (Freeze and Cherry, 1979, , their equation 2.28):

$$\kappa = K\frac{\mu}{\rho g} \tag{C1}$$

where

- μ is the dynamic viscosity of fresh water at 13°C (= 1.2155×10^{-3} kg m^{-1} s^{-1})
- ρ is the density of fresh water (= 1000 kg m^{-3})
- g is the gravitational acceleration (= 9.80 m^2 s^{-1})

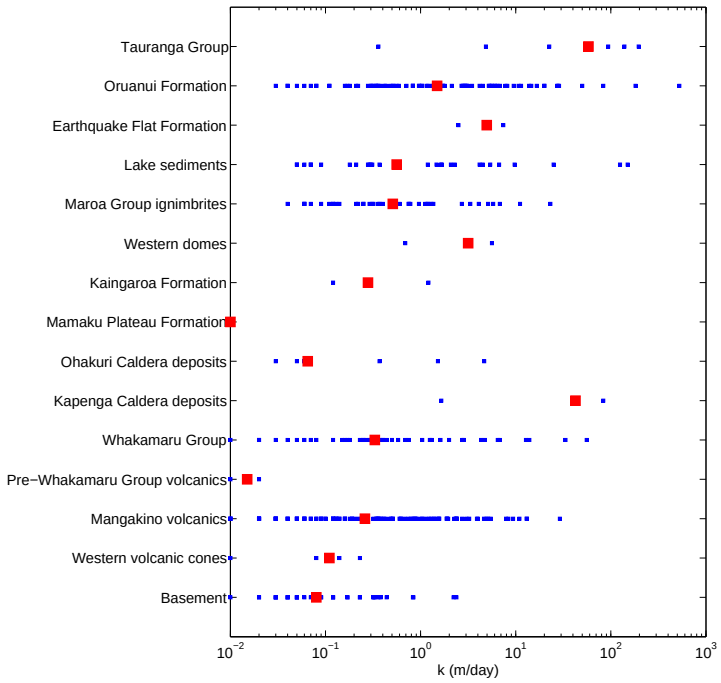

Figure C1: Compilation of K- values for 16 geological formations (Tschritter et al., 2014).

All main rock units in QMAP ArcGIS were translated to hydrolithologies from C1, where three extra changes/additions were made:

- ignimbrite was set to a log κ value of -11.7 ($\approxeq$ K=1.75 m/day), after the median value found by Tschritter et al. (2014).
- gravel was set to a log κ value of -10.2 (K=44 m/day), as the most coarse grained unconsolidated material.
- all crystalline rocks were set to a log κ value of -15.0, to accommodate for low hydraulic conductivity in high-rainfall mountaineous ranges.

This resulted in a description of hydrolo-lithological classes as listed in Table C3. The result of classification of all QMAP main rock units is a table of 122 main rock types with an associated hydro-lithological class, including an according κ and K value and standard deviation. It is shown in Table C4.

Table C3: Description of hydro-lithological classes used in this research.

Class	Description
1	fine-grained sedimentary
2	crystalline and metasediments (e.g. greywacke, semischist)
3	fine-grained unconsolidated
4	carbonate
5	volcanic
6	(poorly sorted) in between fine-grained and coarse-grained sedimentary
7	(poorly sorted) in between fine-grained and coarse-grained unconsolidated
8	coarse-grained sedimentary
9	highly permeable volcanic (ignimbrite)
10	coarse-grained unconsolidated

Hydraulic permeabilities are shown in Figure C2, where the standard deviation is shown in Figure C3.

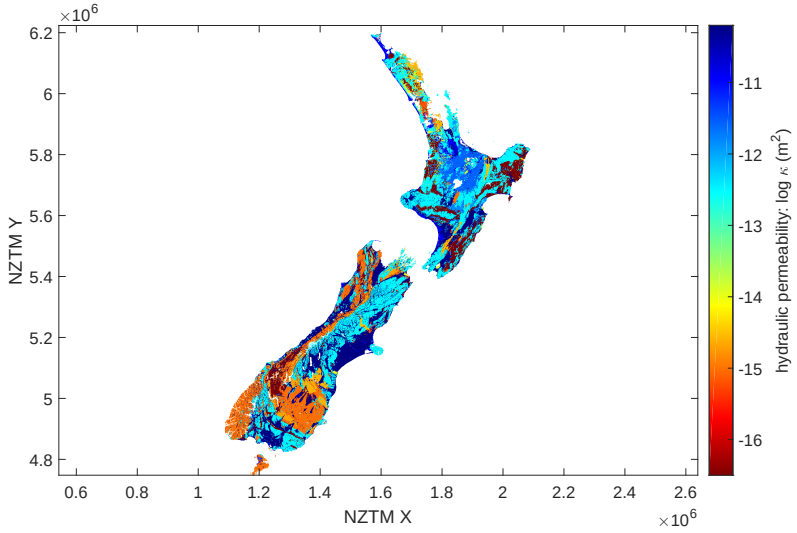

Figure C2: Hydraulic permeabilities [log m^2] of surface geology for New Zealand.

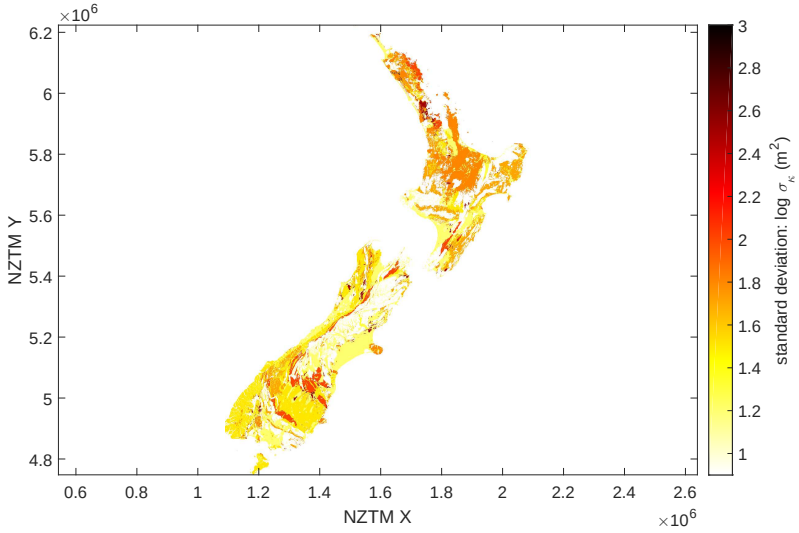

Figure C3: standard deviation [log m^2] of hydraulic permeability of surface geology for New Zealand.

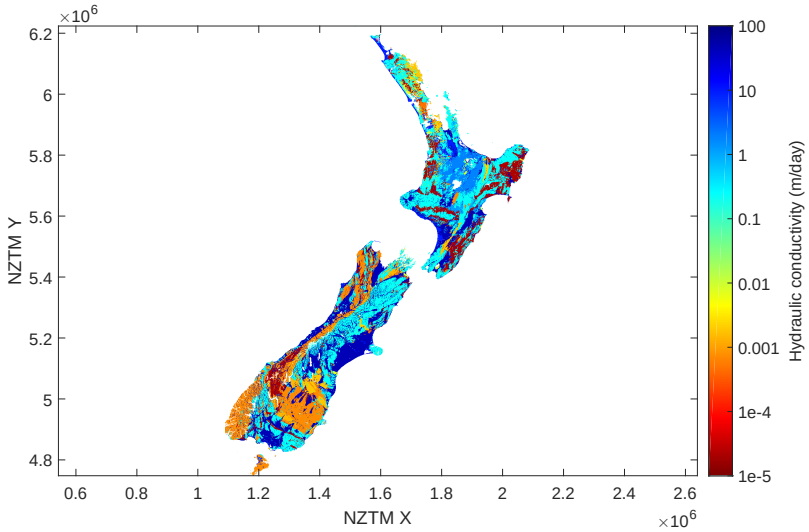

Figure C4: Hydraulic conductivities [m/day] of surface geology for New Zealand.

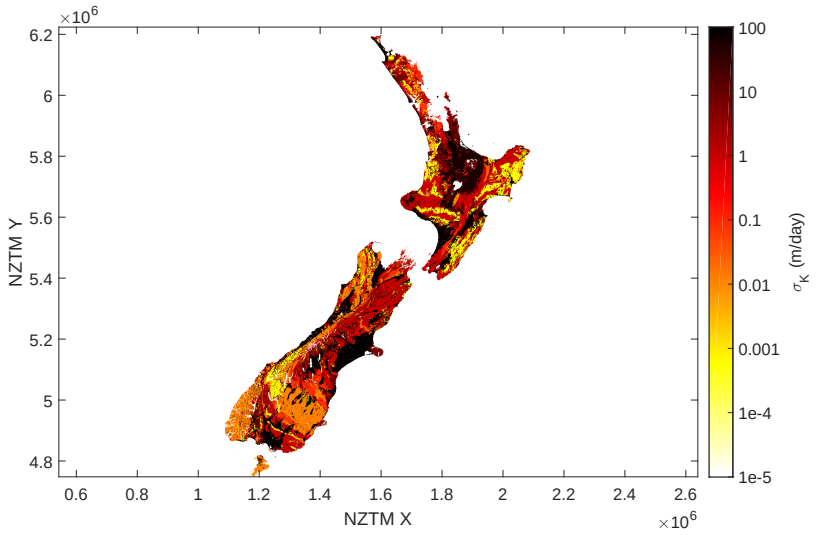

Figure C5: standard deviation [m/day] of hydraulic conductivity of surface geology for New Zealand.

Table C4: Mean hydraulic permeability (κ) for QMAP main rock types; uncertainty σ_κ; and mean values for k converted to hydraulic conductivity (K, m/day)

Main rock type	**log k (m^2)**	**log σ_k (m^2)**	**K (m day^{-1})**	**Class**
basalt	-12.5	1.8	0.220	5
sandstone	-12.5	0.9	0.220	8
peridotite	-12.5	1.8	0.220	5
gabbro	-12.5	1.8	0.220	5
granitoid	-15	1.5	0.001	2
sand	-10.9	1.2	8.770	10
conglomerate	-15.2	2.5	0.000	6
mudstone	-16.5	1.7	0.000	1
volcanic breccia	-12.5	1.8	0.220	6
andesite	-12.5	1.8	0.220	5
greywacke	-14.6	2	0.002	2
mud	-14	1.8	0.007	3
breccia	-14.5	1.3	0.002	6
melange	-14.5	1.3	0.002	6
limestone	-11.8	1.5	1.104	4
chert	-15	1.5	0.001	2
micrite	-15	1.5	0.001	2
rhyolite	-12.5	1.8	0.220	5
scoria	-12.5	1.8	0.220	5
landslides	-12.5	3	0.220	7
peat	-12.5	1.5	0.220	7
biosparite	-11.8	1.5	1.104	4

Continued on next page

Table C4 – *Continued from next page*

Main rock type	**log k (m^2)**	**log σ_k (m^2)**	**K (m day^{-1})**	**Class**
basaltic andesite	-12.5	1.8	0.220	5
dacite	-12.5	1.8	0.220	5
siltstone	-16.5	1.7	0.000	1
coal	-11.8	1.5	1.104	4
olivine basalt	-12.5	1.8	0.220	5
ignimbrite	-11.7	1.8	1.75	9
volcanic sandstone	-12.5	1.8	0.220	5
rhyodacite	-12.5	1.8	0.220	5
turbidite	-15.2	2.5	0.000	7
debris	-12.5	0.9	0.220	7
vitric tuff	-12.5	1.8	0.220	5
fill	-14	1.8	0.007	3
granodiorite	-15	1.5	0.001	2
gravel	-9.9	1.2	90	10
quartz diorite	-15	1.5	0.001	2
tuff	-12.5	1.8	0.220	8
sinter	-15.2	2.5	0.000	6
volcanic conglomerate	-12.5	1.8	0.220	5
pyroclastics	-12.5	1.8	0.220	5
clay	-14	1.8	0.007	3
pumice	-12.5	1.8	0.220	5
tephra	-12.5	1.8	0.220	5
boulders	-10.9	1.2	8.770	10
broken formation	-14.5	1.3	0.002	6
none	-14.5	1.3	0.002	6
silt	-14	1.8	0.007	3
travertine	-11.8	1.5	1.104	4
harzburgite	-15	1.5	0.001	2
greensand	-12.5	0.9	0.220	8
claystone	-16.5	1.7	0.000	1
andesite lava	-12.5	1.8	0.220	5
schist	-15	1.5	0.001	2
pyroclastic breccia	-12.5	1.8	0.220	5
coquina	-11.8	1.5	1.104	4
algal limestone	-11.8	1.5	1.104	4
granite	-15	1.5	0.001	2
argillite	-16.5	1.7	0.000	1
greenschist	-15	1.5	0.001	2
serpentinite	-15	1.5	0.001	2
quartzite	-15	1.5	0.001	2
amphibolite	-15	1.5	0.001	2
diorite	-15	1.5	0.001	2

Continued on next page

Table C4 – *Continued from next page*

Main rock type	**log k** ($\mathbf{m^2}$)	**log σ_k** ($\mathbf{m^2}$)	**K** ($\mathbf{m\ day^{-1}}$)	**Class**
semischist	-14.7	2	0.001	2
clinopyroxenite	-15	1.5	0.001	2
monzogranite	-15	1.5	0.001	2
phyllonite	-15	1.5	0.001	2
gabbronorite	-15	1.5	0.001	2
gneiss	-15	1.5	0.001	2
migmatite	-15	1.5	0.001	2
paragneiss	-15	1.5	0.001	2
metaconglomerate	-14.7	2	0.001	2
pyroxenite	-15	1.5	0.001	2
tonalite	-15	1.5	0.001	2
shale	-16.5	1.7	0.000	1
orthogneiss	-15	1.5	0.001	1
calcareous mudstone	-16.5	1.7	0.000	1
mylonite	-15	1.5	0.001	2
syenite	-15	1.5	0.001	2
till	-12.5	1.5	0.220	7
hornfels	-15	1.5	0.001	2
metavolcanics	-15	1.5	0.001	2
olivine nephelinite	-15	1.5	0.001	2
cataclasite	-15	1.5	0.001	2
monzodiorite	-15	1.5	0.001	2
dolerite	-15	1.5	0.001	2
loess	-12.5	1.5	0.220	7
hawaiite	-12.5	1.8	0.220	5
pelite	-16.5	1.7	0.000	1
metasandstone	-15	1.5	0.001	2
trachyte	-15	1.5	0.001	2
psammite	-15	1.5	0.001	2
metapelite	-15	1.5	0.001	2
spilite	-15	1.5	0.001	2
lamprophyre	-15	1.5	0.001	2
trondhjemite	-15	1.5	0.001	2
dioritic orthogneiss	-15	1.5	0.001	2
dunite	-15	1.5	0.001	2
granulite	-15	1.5	0.001	2
ultramafics	-15	1.5	0.001	2
quartz monzodiorite	-15	1.5	0.001	2
metachert	-15	1.5	0.001	2
diatomite	-16.5	1.7	0.000	1
marble	-15	1.5	0.001	2
syenogranite	-15	1.5	0.001	2

Continued on next page

Table C4 – *Continued from next page*

Main rock type	**log k (m^2)**	**log σ_k (m^2)**	**K (m day^{-1})**	**Class**
quartz monzonite	-15	1.5	0.001	2
hornblendite	-15	1.5	0.001	2
anorthosite	-15	1.5	0.001	2
calc-silicate	-15	1.5	0.001	2
keratophyre	-15	1.5	0.001	2
phonolite	-15	1.5	0.001	2
lignite	-11.8	1.5	1.104	4
metamudstone	-15	1.5	0.001	2
shell beds	-11.8	1.5	1.104	4
norite	-15	1.5	0.001	2
porphyry	-15	1.5	0.001	2
gabbroic orthogneiss	-15	1.5	0.001	2
microdiorite	-15	1.5	0.001	2
lapilli tuff	-12.5	1.8	0.220	5
epidiorite	-15	1.5	0.001	2